



HAL
open science

Use of CFD for the extrapolation of attrition and hydrodynamic phenomena in circulating fluidized beds

Benjamin Amblard

► **To cite this version:**

Benjamin Amblard. Use of CFD for the extrapolation of attrition and hydrodynamic phenomena in circulating fluidized beds. Chemical engineering. Université de Lyon, 2020. English. NNT : 2020LYSE1080 . tel-03306229

HAL Id: tel-03306229

<https://theses.hal.science/tel-03306229v1>

Submitted on 29 Jul 2021

HAL is a multi-disciplinary open access archive for the deposit and dissemination of scientific research documents, whether they are published or not. The documents may come from teaching and research institutions in France or abroad, or from public or private research centers.

L'archive ouverte pluridisciplinaire **HAL**, est destinée au dépôt et à la diffusion de documents scientifiques de niveau recherche, publiés ou non, émanant des établissements d'enseignement et de recherche français ou étrangers, des laboratoires publics ou privés.



N°d'ordre NNT : 2020LYSE1080

THESE de DOCTORAT DE L'UNIVERSITE DE LYON

opérée au sein de
l'Université Claude Bernard Lyon 1

Ecole Doctorale N° 206
(Ecole Doctorale de Chimie de Lyon)

Spécialité de doctorat : Procédés
Discipline : Génie Chimique

Soutenue publiquement le 21/07/2020, par :
Benjamin Amblard

Use of CFD for the extrapolation of attrition and hydrodynamic phenomena in circulating fluidized beds

Devant le jury composé de :

Fede, Pascal	Maître de conférences	IMFT Toulouse	Rapporteur
Ocone Raffaella	Professeure	Université Heriot Watt,	Rapporteur
Cocco Ray	Directeur R&D	Particulate Solids Research Inc	Examineur
Lance Michel	Professeur des universités	Université Lyon 1	Président du jury Examineur
Rode Sabine	Professeure des universités	Université de Lorraine	Examineur
Yazdanpanah Mahdi	Ingénieur	Total	Invité
Gauthier Thierry	Ingénieur de recherche	IFP Energies nouvelles	Directeur de thèse

Thèse en VAE préparée au sein de:

Département Génie Chimique et Technologies
Direction Conception Modélisation Procédés
IFP Energies Nouvelles
Etablissement de Lyon
Rond-point de l'échangeur de Solaize - BP 3
69360 Solaize – France

Le doute est la clé de toute connaissance
Proverbe persan

Doubt is the key to knowledge
Persian proverb

A mes grand-mères, Alice et Claire

ACKNOWLEDGMENTS

First, I would like to thank Thierry Gauthier, my thesis director, who helped me, oriented me and supported me from the beginning to the end of this PhD project. It was a real pleasure to have all these intense scientific discussions and you definitely improved the work presented in this manuscript. It was also an honor to work with such an internationally well-known name in the field of fluidization. Merci beaucoup Thierry !

Second, I would like to thank all the members of my PhD evaluation committee who took part of their valuable time to read this manuscript and evaluate my work. Thank you, merci, grazie, با سپاس از شما

Then I want to thank the people who helped me to get all the experimental data presented in this work, Florian Montjovet, Charly Rogeon, Robert Beaumont, Stéphane Poncet, Maurizio Troiano from the University of Napoli, Denis Roux, Carole Bobin and Arnaud Si Djilani.

Then, I thank all the people who helped me and gave me useful advices during this PhD project, Jean-Marc Schweitzer, Sina Tebianian, Pascal Alix, Lionel Gamet (the openFOAM master), Martine Glo and Claire Herri-Mongardien. I would like to thank especially Stéphane Bertholin with who I shared the adventure on attrition from the beginning.

I also want to acknowledge my fluidization masters, Ted Knowlton, Reddy Karri and Ray Cocco. I have known you and worked with you for more than 12 years now, your extended knowledge and your humility is a source of inspiration to me.

I also thank IFP Energies nouvelles management, Philippe Maurel, Pierre Porot, Fabrice Giroudière and Denis Guillaume for giving me the opportunity of doing this PhD project.

I then want to thank the Particulate Solids Research Inc (PSRI) for letting me use and present their experimental data acquired on a large size fluidized bed.

Finally, grazie a Manuela the mother of my young kids who was really patient while I was writing my thesis manuscript. An advice for the future PhD students reading this words, write your thesis before having children ☺

Thank you, merci, grazie, با سپاس از شما, 谢谢

EXTENDED ABSTRACT

Extrapolation from lab to industrial scale is challenging when dealing with gas-particles flows encountered in Circulating Fluidized Bed (CFB) processes and technologies. Extrapolation relates in a first step, to the understanding of physical phenomena at accessible scales through dedicated and focused experiments. In a second step, modeling is often used to transpose observation from lab scale to an industrial perspective. In my Ph.D. project, we present how Computational Fluid Dynamic (CFD) tools can be used for both steps with first the characterization of local phenomena which allows a better understanding of lab scale experiments in a context of attrition phenomena extrapolation. Second, we present how CFD tools can be used for the scale extrapolation of hydrodynamic phenomena through a relevant simulation strategy.

Concerning the first topic, it is essential in the early stage of the process development, to quantify attrition phenomena expected at industrial scale when selecting the solid particles to be used. Indeed, attrition can first be the cause of particles circulation problems, and second it can induce important particle inventory losses which may then impact the process economics. We faced this situation during the development of the Chemical Looping Combustion (CLC) process where little information is available concerning long term operation of the oxygen carrier particles used in this process. In our work, we propose a new procedure using a jet cup apparatus to compare the mechanical resistance to attrition of particles used in the CLC process under development with particles used in the Fluid Catalytic Cracking (FCC) process (hundreds of units in operation for more than seventy years). The latter is then used as a reference since attrition data are available both at lab and industrial scales for FCC catalyst. In this study, we use CFD tools for the understanding of local physical phenomena in our testing apparatus to then orientate the experimental strategy to assess and compare the mechanical resistance to attrition of the different powders of interest in a context of early stage extrapolation. Experimental results confirmed the findings from the CFD simulations with the attrition rate being dependent on the initial particles volume implemented in the jet cup. The experimental methodology was then applied on three solids (equilibrium FCC catalyst, fresh and equilibrium oxygen carriers). The results obtained showed that the fresh and equilibrium oxygen carriers performed respectively better and worse than the reference FCC catalyst. The effect of the CLC process conditions on the mechanical resistance of the particles considered was therefore clearly emphasized by the test. This experimental procedure can therefore be used in the future to evaluate the mechanical resistance of other oxygen carriers and evaluate also the effect of the CLC process conditions on the particles mechanical structure. Finally, the main perspective is then to correlate lab scale experimentation with the main sources of attrition in circulating fluidized bed for finally implementing a population balance modeling to assess attrition at industrial scale as a function of precise design criteria. A PhD in partnership with the university of Leeds and Total was launched in 2015 to develop such a multi-scale approach with the use of CFD tools.

Concerning the second topic with the use of CFD tools to extrapolate hydrodynamic phenomena in circulating fluidized beds, we propose a simulation strategy in order to assess the CFD models extrapolation capability and their potential limits in term of fluidization regimes representativeness. For this purpose, different experimental set ups were used with first a 20 cm turbulent fluidized bed to characterize different gas injection configurations, second a 90 cm turbulent fluidized bed where several gas superficial velocities were investigated and finally a 30 cm riser to characterize transport regime conditions. In the three experiments, FCC catalysts with similar physical properties were used in order to focus

mainly on gas distribution, scale-up and fluidization regime effects. Local and global experimental flow characterizations were acquired. All the information collected was then used to evaluate CFD prediction of gas distribution, multi scale and operating conditions effects. Two CFD approaches were evaluated with first the Multiphase Particle In Cell (MP-PIC) approach with the software Barracuda VR[®] and second the Euler/Euler with the Kinetic Theory of Granular Flows (KTGF approach) using the open source software openFOAM. In the first simulation strategy steps we demonstrated that for both approaches, default parameters with the Gidaspow drag law failed predicting the 20 cm fluidized bed density and local solid volume fraction profiles. We therefore develop dedicated drag laws and boundary conditions to get satisfactory hydrodynamic predictions of the different 20 cm fluidized bed operating conditions. In the next simulation strategy step, the CFD model parameters developed from the 20 cm fluidized bed simulations were applied for the 90 cm fluidized bed simulation. This step was crucial since it was a differentiator between both approaches with the parameters developed for Barracuda VR[®] failing to predict the bed hydrodynamic while the parameters developed for openFOAM predicted well the change of bed density and the particles entrainment trends for the different superficial gas velocities simulated. This step is therefore essential since it justifies the evaluation of CFD models at different scales and it also shows that CFD can be used for extrapolation. In the last simulation strategy step, the openFOAM modeling parameters developed were then applied for the simulation of the riser transport regime. The simulation failed capturing the riser pressure drop and local solid flux profiles. A dedicated drag law was then developed to capture reasonably well these riser experimental data. This last step shows that the drag models developed are fluidization regime dependent and it is therefore important to investigate the limits of the models developed. For the perspectives of this work, the same simulation strategy could be developed against a wider set of experimental data in term of fluidized bed characterizations (bubbling structures, mixing and local velocities characterization) as well as in term of fluidization regimes (minimum fluidization to transport regime). Other extrapolation parameters to industrial conditions such as pressure and temperature could be investigated following a similar strategy developed in this work with the final objective being to simulate an industrial size Circulating Fluidized Bed.

KEYWORDS –

Extrapolation, Circulating Fluidized Beds, Computational Fluid Dynamic, attrition, hydrodynamic.

RESUME ETENDU

L'extrapolation de l'échelle laboratoire à l'échelle industrielle est un réel challenge pour les écoulements gaz-particules rencontrés dans les procédés et technologies en lit fluidisé circulant. L'extrapolation consiste dans une première étape à la compréhension des phénomènes physiques à des échelles accessibles basée sur des expérimentations dédiées. Dans une deuxième étape, la modélisation est souvent utilisée pour transposer les observations effectuées à échelle laboratoire à une perspective industrielle. Dans mon projet de thèse, nous présentons comment les outils de simulation numériques des écoulements (CFD) peuvent être utilisés dans ces deux étapes. En effet, dans une première étude nous avons employé la CFD pour la caractérisation et la compréhension d'une expérimentation afin d'orienter notre procédure expérimentale dans un contexte d'extrapolation des phénomènes d'attrition. Dans une deuxième étude, nous présentons comment les outils CFD peuvent être utilisés pour l'extrapolation des phénomènes hydrodynamiques à travers une stratégie de simulation pertinente.

Concernant la première étude, il est essentiel dans les premières étapes d'un développement de procédé en lit fluidisé circulant, de quantifier l'attrition à l'échelle industrielle des particules sélectionnées. En effet, les phénomènes d'attrition peuvent être à l'origine de problème de circulation dans l'unité mais peuvent aussi générer des pertes d'inventaire qui vont impacter directement les coûts de fonctionnement du procédé. Nous avons rencontré ce type de problématique lors du développement du procédé de combustion en boucle chimique (CLC) pour lequel peu d'informations sont disponibles concernant les opérations sur le long terme des particules porteuses d'oxygène utilisées dans le procédé. Dans notre travail, nous proposons une nouvelle méthode utilisant un dispositif expérimental caractéristique de l'attrition appelé « Jet Cup » pour comparer la résistance mécanique des particules utilisées dans le procédé CLC avec les particules utilisés dans le procédé de craquage catalytique FCC pour lequel des centaines d'unités industrielles sont en opération depuis plus de 70 ans. Les particules de FCC sont donc utilisées comme référence puisque des données d'attrition sont disponibles aussi bien à l'échelle de laboratoire qu'à échelle industrielle. Dans cette étude, nous avons utilisé les outils CFD pour la caractérisation et la compréhension de l'écoulement dans notre dispositif expérimental afin d'orienter notre stratégie de test pour la comparaison de l'attrition générée sur les différents types de particules d'intérêts. Les résultats expérimentaux ont ensuite confirmés les conclusions de l'étude CFD avec une attrition générée dans le test proportionnelle au volume initial de particules inséré. La méthodologie expérimentale développée a ensuite été appliquée sur trois types de particules (un catalyseur d'équilibre FCC, un porteur d'oxygène frais et un porteur d'oxygène d'équilibre). Les résultats montrent que les porteurs d'oxygène frais et d'équilibre ont respectivement une meilleure et moins bonne performance comparés au catalyseur FCC de référence. Les effets des conditions opératoires du procédé CLC sur la résistance mécanique des particules ont donc été clairement mis en avant par notre procédure expérimentale. Celle-ci peut donc être utilisée dans le futur pour évaluer d'autres porteurs d'oxygènes ainsi que les effets des conditions opératoires du procédé sur les particules. La principale perspective de ce travail est la corrélation des phénomènes d'attrition sur pilote dédié aux phénomènes d'attrition générés par les principales sources dans les procédés en lit fluidisé circulant (cyclone, jet) afin d'implémenter un modèle de population pour la prédiction quantitative de l'attrition dans les unités industrielles. Une thèse a été lancée en 2015 en partenariat avec Total et l'université de Leeds pour développer une telle approche multi-échelle.

Dans la deuxième étude sur l'utilisation des outils CFD pour l'extrapolation des phénomènes hydrodynamiques en lit fluidisé circulant, nous avons proposé une stratégie de simulation afin

d'évaluer les capacités d'extrapolation des modèles CFD et aussi d'évaluer leurs potentielles limites en terme de représentativité des différents régimes de fluidisation. Pour cela, différentes expérimentations ont été utilisées avec premièrement un lit fluidisé turbulent de 20 cm de diamètre pour la caractérisation de différentes configuration d'injection gaz, deuxièmement un lit fluidisé turbulent de 90 cm de diamètre avec lequel différentes vitesses superficielles de gaz ont été étudiées et troisièmement un riser de 30 cm de diamètre pour la caractérisation du régime de transport des particules. Dans toutes les expérimentations, des catalyseurs FCC avec des propriétés physiques similaires ont été utilisés afin de se concentrer uniquement sur les effets de distribution gaz, d'échelle et de régime de fluidisation. Des données de caractérisation locale et globale des écoulements ont été recueillies. Toutes ces données sont ensuite utilisées pour évaluer la capacité des modèles CFD à prédire les différents effets mentionnés auparavant (distribution gaz, échelle et régime de fluidisation). Deux approches CFD ont été évaluées avec tout d'abord l'approche « Multiphase Particle in Cell » (MP-PIC) et le logiciel Barracuda VR[®] et deuxièmement une approche Euler/Euler avec la théorie cinétique des écoulements granulaires (KTGF) en utilisant le logiciel open-source openFOAM. Dans la première étape de notre stratégie, nous avons démontré que les paramètres par défaut des deux approches, en utilisant la corrélation de Gidaspow pour la force de traînée, échouent à prédire l'hydrodynamique du lit fluidisé turbulent de 20 cm. Nous avons donc développé pour chaque approche un modèle de force de traînée et des conditions limites spécifiques pour obtenir des prédictions satisfaisantes de l'hydrodynamique du lit fluidisé de 20 cm pour les différentes configurations d'injection gaz étudiées. Dans l'étape suivante, les modèles CFD développés à partir des simulations du lit fluidisé turbulent de 20 cm ont été appliqués pour la simulation du lit fluidisé turbulent de 90 cm. Cette étape est fondamentale puisqu'elle a permis de mettre en évidence la différence entre les deux modèles CFD utilisés ; les prédictions de Barracuda VR[®] ont échoué à prédire l'hydrodynamique du lit alors que les simulations openFOAM arrivent à prédire quantitativement l'évolution de la masse volumique du lit en fonction de la vitesse superficielle de gaz dans le lit et que la tendance de l'entraînement des particules est qualitativement prédite. Cette étape est donc essentielle puisqu'elle justifie l'évaluation des modèles CFD à différentes échelles et qu'elle démontre aussi la possibilité ou non de prédire les effets d'extrapolation avec ces outils. Dans la dernière étape de notre étude, le modèle CFD développé avec le logiciel openFOAM a été appliqué pour la simulation du régime de transport des expérimentations riser. Les résultats obtenus sont insatisfaisants avec une sous-estimation importante de la perte de charge dans le riser et des profils locaux de flux solide différents de ceux mesurés. Un nouveau modèle corrélatif de force de traînée a ensuite été développé avec une prédiction satisfaisante des paramètres expérimentaux étudiés. Cette dernière étape démontre donc que les modèles de traînées développés dans cette étude sont dépendants du régime de fluidisation simulé et qu'il est donc important d'étudier et d'évaluer les limites de ces modèles. Pour les perspectives de cette étude, une stratégie de simulation similaire pourrait être développée basée sur une base de données élargies en terme de caractérisation expérimentale de l'hydrodynamique des lits fluidisées (structure gaz, mélange particules/gaz, caractérisation des vitesses locales) mais aussi en terme de régime de fluidisation (minimum de fluidisation jusqu'au transport de particules). D'autres paramètres d'extrapolation aux conditions industrielles telles que les effets de pressions et de température pourraient être étudiés en utilisant une stratégie de simulation similaire avec pour objectif final de simuler un réacteur industriel en lit fluidisé circulant.

MOT CLES –

Extrapolation, lit fluidisé circulant, Simulation numérique des écoulements, attrition, hydrodynamique.

CONTENTS

INTRODUCTION	1
---------------------------	----------

I. LITERATURE REVIEW	3
-----------------------------------	----------

1 CIRCULATING FLUIDIZED BED PROCESSES.....	3
1.1 CHEMICAL LOOPING COMBUSTION (CLC) PROCESS	4
1.2 FLUID CATALYTIC CRACKING (FCC) PROCESS	6
2 FLUIDIZATION PHENOMENA	8
2.1 CHARACTERIZATION OF PARTICLES	8
2.1.1 PARTICLE SIZE DISTRIBUTION	8
2.1.2 DENSITIES	10
2.1.3 MISCELLANEOUS	10
2.1.4 INTER-PARTICLE FORCES AND CLUSTERING	11
2.1.5 GELDART CLASSIFICATION	12
2.2 REGIME OF FLUIDIZATION	13
2.2.1 FIXED BED AND MINIMUM OF FLUIDIZATION REGIME	14
2.2.2 BUBBLING AND TURBULENT REGIMES	15
2.2.3 TRANSPORT REGIME IN A VERTICAL UPSTREAM FLOW.....	18
2.3 ENTRAINMENT OF PARTICLES IN FLUIDIZED BED.....	21
2.4 EFFECT OF PRESSURE AND TEMPERATURE	23
3 EXPERIMENTATION AND MEASUREMENT TECHNIQUES	24
3.1 GLOBAL HYDRODYNAMIC CHARACTERIZATION	24
3.2 LOCAL CHARACTERIZATION	25
4 COMPUTATIONAL FLUID DYNAMIC FOR GAS PARTICLES FLOW	27
4.1 EULER/EULER WITH KTGF APPROACH	29
4.2 MULTIPHASE PARTICLE IN CELL (MP-PIC) APPROACH	32
4.3 DISCUSSION ON EULER/EULER KTGF AND MP-PIC APPROACHES.....	34
4.4 DRAG CLOSURE LAWS.....	35
5 EXTRAPOLATION OF CIRCULATING FLUIDIZED BED PROCESSES THROUGH MODELLING	37
5.1 EXTRAPOLATION USING THE TWO-PHASE FLOW THEORY	37
5.2 EXTRAPOLATION USING CFD TOOLS.....	39
6 PARTICLES ATTRITION IN CIRCULATING FLUIDIZED BED AND ATTRITION TESTING.....	40
6.1 ATTRITION PHENOMENA AND THEIR CHARACTERIZATION	40
6.2 JET CUP ATTRITION INDEX.....	42
6.3 CFD STUDIES CARRIED OUT ON THE JET CUP	43
7 CONCLUSIONS	44

II. ATTRITION PHENOMENA EXTRAPOLATION AT THE EARLY STAGE OF A PROCESS DEVELOPMENT.....	45
---	-----------

1 INTRODUCTION	45
2 MATERIAL AND METHODS	46
2.1 PARTICLES PROPERTIES	46
2.2 JET CUP ATTRITION TESTING.....	47
2.3 CHOICE OF THE JET VELOCITY FOR ATTRITION TESTING	49
2.4 CFD SIMULATION	51
2.5 CONCLUSIONS.....	55

3 CFD INVESTIGATION	56
3.1 INTRODUCTION	56
3.2 CHARACTERIZATION OF THE PARTICLES CIRCULATION RATE WITHIN THE JET	56
3.3 CONCLUSIONS.....	58
4 MECHANICAL RESISTANCE TO ATTRITION CHARACTERIZATION	59
5 DISCUSSION	64
6 CONCLUSIONS AND PERSPECTIVES	65

III. USE OF CFD FOR EXTRAPOLATION MATERIAL AND METHODS 66

1 INTRODUCTION	66
2 POWDER CHARACTERISTICS USED IN EXPERIMENTS	68
3 FLUIDIZED BED OF 20 CM	70
3.1 EQUIPMENT AND OPERATING CONDITIONS.....	70
3.2 EXPERIMENTAL TECHNIQUES	71
3.3 OPTICAL PROBE SIGNAL POST-PROCESSING.....	74
3.3.1 OPTICAL SIGNAL CHARACTERIZATION	74
3.3.2 EXPERIMENTAL PROCEDURE AND SOLID VOLUME FRACTION RECONSTRUCTION.....	77
4 FLUIDIZED BED OF 90 CM	84
4.1 EQUIPMENT	84
4.2 EXPERIMENTAL TECHNIQUES	85
5 RISER OF 30 CM	87
5.1 EQUIPMENT	87
5.2 EXPERIMENTAL TECHNIQUES	90
5.2.1 SOLID FLUX MEASUREMENTS	90
5.2.1 RISER PRESSURE DROP MEASUREMENTS	92
5.2.1 LOCAL FLUX MEASUREMENT	93
6 CFD APPROACHES	96
6.1 EULER/EULER WITH KTGF APPROACH: OPENFOAM v17.12 CFD SOFTWARE	96
6.1.1 GAS PHASE TURBULENCE MODEL.....	96
6.1.2 SOLID PHASE FRICTIONAL MODEL.....	97
6.1.3 WALL BOUNDARY CONDITIONS	98
6.1.4 SIMULATION PARAMETERS AND MODELS SUMMARY	99
6.1.5 MP-PIC APPROACH: BARRACUDA VR®	100
7 CONCLUSIONS	101

IV. USE OF CFD FOR EXTRAPOLATION EXPERIMENTAL RESULTS..... 103

1 INTRODUCTION	103
2 FLUIDIZED BED OF 20 CM	103
2.1 EXPERIMENT N°1: HOMOGENEOUS FLUIDIZATION	104
2.2 EXPERIMENT N°2: GAS INJECTION WITH JET	106
2.3 CONCLUSIONS.....	107
3 FLUIDIZED BED OF 90 CM	108
3.1 EXPERIMENTAL RESULTS	108
3.2 CONCLUSIONS.....	110
4 RISER OF 30 CM	111
4.1 EXPERIMENTAL RESULTS	111
4.2 CONCLUSIONS.....	114
5 CONCLUSIONS ON THE EXPERIMENTAL RESULTS	114

V. USE OF CFD FOR EXTRAPOLATION SIMULATION RESULTS	115
1 INTRODUCTION	115
2 FIRST SIMULATION STRATEGY STEP: INVESTIGATION ON THE CFD MODELS PARAMETERS	115
2.1 MP-PIC APPROACH, BARRACUDA VR®	116
2.2 EULER/EULER WITH KTGF APPROACH: OPENFOAM	125
2.3 EFFECT OF MESH SIZE, CLOUD NUMBERS AND MESH TYPE	135
2.3.1 EFFECT OF MESH CELL SIZE	136
2.3.1 EFFECT OF CLOUDS NUMBER.....	138
2.3.1 EFFECT OF MESH CELL TYPE FOR OPENFOAM SIMULATIONS	139
2.4 DISCUSSIONS	141
3 SECOND SIMULATION STRATEGY STEP: CFD CODES PREDICTION WHEN CHANGING OPERATING CONDITIONS	146
3.1 BASE CASE.....	147
3.2 INFLUENCE OF THE MESH SIZE AND MESH TYPE	150
3.2.1 MESH SIZE.....	151
3.2.2 EFFECT OF MESH CELL TYPE FOR OPENFOAM SIMULATIONS	152
3.3 DISCUSSIONS	154
4 THIRD SIMULATION STRATEGY STEP: CFD CODES PREDICTIONS AT LARGER SCALE	155
4.1 GEOMETRY, MESH AND BOUNDARY CONDITIONS	155
4.2 BASE CASE.....	160
4.3 OTHER OPERATING CONDITIONS.....	165
4.4 DISCUSSION.....	168
5 FOURTH SIMULATION STRATEGY STEP: CFD CODE PREDICTION AT LARGER SCALE AND DIFFERENT OPERATING CONDITIONS (CHANGE OF FLUIDIZATION REGIME)	172
5.1 GEOMETRY, MESHING AND BOUNDARY CONDITIONS.	173
5.2 BASE CASE.....	175
5.3 INVESTIGATION ON THE DRAG MODEL FOR THE RISER SIMULATION	178
5.4 DISCUSSIONS	184
6 USE OF CFD FOR EXTRAPOLATION: CONCLUSIONS AND PERSPECTIVES	185
GENERAL CONCLUSIONS AND PERSPECTIVES	187
VI. REFERENCES	189
APPENDIX.....	198
CURRICULUM VITAE.....	237

Nomenclature

LATIN LETTERS		
SYMBOL	DESCRIPTION	UNITS
A_H	Hamakar constant for the calculation of the Van Der Walls force	
$A_{ORIFICE}$	Valve orifice surface	m^2
Ar	Archimede number	
$B_{attrition\ rate}$	Initial attrition generated characteristic constant	
C	Smagorinsky Barracuda VR® coefficient	
$C_{attrition\ rate}$	Attrition rate characteristic constant	
Cd	Valve orifice coefficient	
$d_b(z)$	Bubble diameter at height z in the bed	m
$d_{b_MAXIMUM}$	Maximum bubble diameter	m
d_p	Particle diameter	m
$d_{p,i}$	Particle diameter of the class i	m
$d_{p,50}$	Particle distribution mean diameter	m
$d_{p,sv}$	Particle distribution Sauter diameter	m
$\frac{dP}{dz}$	Pressure gradient over a height dz	$Pa.m^{-1}$
e_s	coefficient of restitution for particles collisions	
E_r	total particle entrainment rate	$kg.m^{-2}.s^{-1}$
E_i^∞	Entrainment rate of particles having a diameter $d_{p,i}$	$kg.m^{-2}.s^{-1}$
$f_{particles\ in\ jet}$	Averaged particles contacting frequency with the jet	s^{-1}
$f(x,u_p,m,t)$	Probability function in the MP-PIC approach	
F	Mass fraction of particles lower than 45 microns in the Abrahamsen correlation for the minimum bubbling gas velocity	
Fr	Froude number	
Fr_t	Froude number with particle terminal velocity	
F_s	Solid flowrate through valve	kg/s
F_{vp_jet}	Global volume flux of particles circulating in the jet	$m^3.s^{-1}$
F_{VW}	Van der Walls force	N
g	Gravitational acceleration	$m.s^{-2}$
$g_{0,s}$	radial distribution function	
G_s	Particles mass flux	$kg.m^{-2}.s^{-1}$
H	Bed height	m
H_{mf}	Bed height at minimum of fluidization	m
i	Particle class number	
k	kinetic turbulent energy	$m^2.s^{-2}$
K_d	Drag coefficient	
$K_{d_default}$	Default Drag coefficient	
$K_{d_MULTIPLIER}$	Drag coefficient with multiplier	

n	number of classes of particle diameters in the fluidized bed	
N	Number of holes per square meter of distributor in the Darton correlation	m ⁻²
P	Pressure	Pa
PC_1	Particle contacting frequency with the air jet	s ⁻¹
PC_tracer	Particle tracer contacting frequency with the jet	s ⁻¹
Ps	Solid pressure	Pa
$P_{s,KTGF}$	Solid pressure from Kinetic Theory of Granular Flow	Pa
$P_{s,frictional}$	Frictional solid pressure	Pa
$(Re)_c$	Particulate Reynold number at turbulent fluidization	
Re_p	Particulate Reynold number	
$Re_{p,mf}$	Particulate Reynold number at minimum of fluidization	
$S_{particles}$	Surface of particles	m ²
TDH	Transport Disengaging Height	m
$U_{annular\ to\ homogeneous}$	Gas superficial velocity at the transition between annular to homogeneous regime in transport conditions	m.s ⁻¹
U_c, U_k	Superficial gas velocities characteristic of the turbulent regime	m.s ⁻¹
$U_{chocking}$	Gas superficial velocity at chocking conditions	m.s ⁻¹
U_{mb}	Gas superficial velocity at minimum bubbling conditions	m.s ⁻¹
U_{mf}	Gas superficial velocity at minimum fluidization conditions	m.s ⁻¹
U_{sg}, V_{sg}	Gas superficial velocity	m.s ⁻¹
u_m	Velocity of phase m (m=g for the gas phase, m=s for the solid phase)	m.s ⁻¹
u_p	Particle cloud velocity in the MP-PIC approach	m.s ⁻¹
u'	Velocity fluctuations	m.s ⁻¹
Vsample	Jet cup particle sample volume	m ³
V_t	particle terminal velocity	m.s ⁻¹
$Vol_{particles}$	Volume of particles	m ³
x_{cloud}^n	Clouds position at t in the MP-PIC approach	m
x_{cloud}^{n+1}	Clouds position at t+Δt in the MP-PIC approach	m
x_i	weight fraction of particles in fluidized bed having a diameter dp,i	%wt
z	Height coordinate	m

GREEK LETTERS		
SYMBOL	DESCRIPTION	UNITS
Φ	specularity coefficient for particle wall collisions	
θ_s	Granular temperature	J/kg
λ_s	Bulk viscosity	kg/m.s
τ_m	Stress tensor of phase m (m=g for the gas phase, m=s for the solid phase)	Pa
α_m	Volume fraction of phase m (m=g for the gas phase, m=s for the solid phase)	
$\alpha_{s,max}$	Maximum solid volume fraction	
$\alpha_{s,min}$	Minimum solid volume fraction for the particle frictional model	
ρ_m	Density of phase m (m=g for the gas phase, m=s for the solid phase)	kg/m ³
Φ_s	Particle sphericity	
μ_g	Gas viscosity	kg/m.s
μ_s	Solid viscosity	kg/m.s
$\mu_{s,col}$	Solid viscosity due to particles collisions	kg/m.s
$\mu_{s,kin}$	Solid kinetic viscosity	kg/m.s
μ_t	Turbulent viscosity	kg/m.s
δ	Distance between particles for the calculation of the Van der Walls force	m
β	Constant in the MP-PIC particles stress model	
ε	kinetic turbulent dissipation rate	m ² s ⁻³
ε_g	gas volume fraction	
ε_s	solid volume fraction	
$\varepsilon_{s,bubble}$	Solid volume fraction in bubble phase of the fluidized bed	
$\varepsilon_{s,dense}$	Solid volume fraction in dense phase of the fluidized bed	
ε_{mf}	Gas volume fraction at minimum of fluidization	
$\varepsilon_{s,mf}$	Solid volume fraction at minimum of fluidization	
ε_{pores}	Volume fraction of pores inside the particles	
ρ_{BED}	Fluidized bed density	kg/m ³
ρ_{Bulk}	Bulk density	kg/m ³
ρ_P	Particle density	kg/m ³
$\rho_{skeletal}$	Skeletal density	kg/m ³
$\rho_{Stand-pipe}$	Stand-pipe density	kg/m ³
ΔP	Pressure drop	Pa
Δt	Delta time	s

ABBREVIATIONS		
SYMBOL	DESCRIPTION	UNITS
CFD	Computational Fluid Dynamic	
CFB	Circulating Fluidized bed	
CLC	Chemical Looping Combustion	
FCC	Fluid Catalytic Cracking	
PSD	Particle Size distribution	
TPGI	Total Particles Generated Index	wt%

INTRODUCTION

Research and development dedicated to multiphase flow still faces challenging extrapolation/scale-up issues, especially in the field of energy where processes reach very large capacities and sizes to minimize production cost. Extrapolation relates to first the understanding of physical phenomena at accessible scales through dedicated and focused experiments. In a second step, modeling is often used to transpose observation from lab scale to an industrial perspective. Minimizing the risk of extrapolation is mandatory when developing processes both from an economical and technology feasibility point of view [1].

Extrapolating is particularly difficult when dealing with gas-solid flows encountered in Circulating Fluidized Bed (CFB) processes and technologies. In this field, physical phenomena and corresponding reactor technologies are complex with regard to hydrodynamics, reaction kinetics, mass and heat transfers [2]. In my Ph.D. dissertation, two topics of interest regarding extrapolation of circulating fluidized beds are investigated with first the extrapolation of attrition phenomena and second the extrapolation of hydrodynamic phenomena.

Concerning the first topic, it is essential in the early stage of the process development, to quantify attrition phenomena expected at industrial scale when selecting the solid particles to be used. Indeed, attrition can first be the cause of particles circulation problems, and second it can induce important particle inventory losses which may then impact the process economics. We faced this situation during the development of the Chemical Looping Combustion (CLC) process [3] where little information is available concerning long term operation of the oxygen carrier particles used in this process. In our work, we propose a new procedure using a jet cup apparatus [4] to compare the mechanical resistance to attrition of particles used in the CLC process under development with particles used in the Fluid Catalytic Cracking (FCC) process (hundreds of units in operation for more than seventy years). The latter is then used as a reference since attrition data are available both at lab and industrial scales for FCC catalyst. In this study, we use Computational Fluid Dynamic (CFD) tools for the understanding of local physical phenomena in our testing apparatus to then develop a relevant experimental strategy to assess and compare the mechanical resistance to attrition of the different powders of interest in a context of early stage extrapolation.

The second part of this PhD project explores extrapolation of hydrodynamic phenomena encountered in fluidized bed systems using CFD. Indeed, CFD tools are increasingly used for the understanding, the development, and the extrapolation of processes and technologies [5]. However, concerning CFD for circulating fluidized beds, modeling the fundamental gas-particles and particles-particles interactions phenomena still remain challenging [6,7]. We therefore, face a situation where CFD tools are essential for extrapolation purposes [8,9], but their prediction capacities need to be evaluated for each configuration simulated in order to check the validity and put into perspectives the simulation results. When using CFD for extrapolation, it is therefore important to investigate if CFD tools predictions can capture scaling up effects. Indeed, most of the CFD developments found in the literature focus on the simulation of a specific equipment with a rather narrow range of operating conditions [10–13]. Then authors investigate the modeling of different phenomena such as the gas/particles, particles/particles and wall/particles interactions with effects of mesh refinement on their simulation results. There is however, no precise characterization against experimental data concerning the use of a CFD model, developed from experiments at a given scale, for the simulation at larger scales where larger mesh cell sizes have to be used because of computational power limitation. In my PhD research, I investigate this issue. For this purpose, we developed a specific simulation strategy focusing on Geldart Group A particles hydrodynamic. We used two CFD tools with first Barracuda VR[®], which uses the MP-PIC approach [14]

and second the OpenFOAM solver “twoPhaseEulerFOAM” which uses a Euler/Euler approach [15]. We then followed our simulation strategy which consists in a first step to modify the code modeling parameters (gas/particles drag model and boundary conditions) to best match the experimental data from a specific experiment at specific operating conditions. It is important to point out that this first step corresponds to most of the study found in the literature. In the following steps, keeping the same CFD model parameters, simulations are then evaluated against experimental data of equipment at larger scales. We discovered that a code showing good prediction results at a given scale does not necessarily have the same prediction quality when used for larger scale simulations. It is therefore necessary to implement such a multi-scale evaluation step when using CFD for extrapolation purposes.

The manuscript is organized as follow:

- In the first chapter, the general context of this work is presented in a literature review with a presentation of the industrial processes which motivated these R&D efforts followed by a focus on circulating fluidized bed characterization and on CFD tools for gas/particles flow simulations. Extrapolation modeling tools are then presented and discussed. Finally, a focus on attrition phenomena is given.
- In a second chapter, the study carried out on the evaluation of the attrition phenomena using a jet cup apparatus is presented.
- Chapters 3 to 5 present the study on the hydrodynamic phenomena extrapolation using CFD tools. Chapter 3 present the simulation strategy developed in this work and the material and methods used to carry out this strategy. Chapter 4 presents the experimental results used to evaluate the CFD predictions and Chapter 5 actually shows the simulations results based on the simulation strategy. The conclusions and perspectives of this study are also presented in Chapter 5.

A general conclusion with perspectives is finally presented.

I. LITERATURE REVIEW

The literature review presented in this chapter sets the global context of this PhD project and focuses on the main topics investigated with the extrapolation of particles attrition and hydrodynamic phenomena.

The general context is first presented with a focus on the Circulating Fluidized Bed (CFB) processes which motivated our R&D efforts. Then, a literature review on hydrodynamic phenomena extrapolation is carried out, many of the items addressed being common with the topic on attrition phenomena extrapolation. A focus on the different fluidization hydrodynamic regimes and their characteristics is first carried out followed by a focus on the experimentation and measurement techniques for the characterization of CFB hydrodynamic. Computational Fluid Dynamic (CFD) approaches for gas/particles flow are then addressed in a dedicated chapter. Finally, the modeling of CFB for extrapolation purposed is investigated.

Eventually, the topic of the attrition phenomena extrapolation is addressed in the last chapter of this literature review.

Despite the large number of industrial CFB processes in operation for a very long time, and the extended amount of literature in the field of fluidization, it will be shown that there are still important efforts to conduct to improve the understanding and modeling of CFB systems for scale-up purposes.

1 Circulating fluidized bed processes

Circulating Fluidized Beds (CFB) technologies are used in many industrial processes among various fields such as refining for the conversion of heavy feedstock [16], petro-chemistry with the ethylene and propylene polymerization [17], coal and waste combustion/ gasification [18], biomass pyrolysis for bio-oil or bio-chemicals production [19].

In CFB technologies, the principle of fluidization is used. It consists in mixing particles with gas, the mixture of the two behaving as a pseudo fluid (more details are given in Chapter II-2). This technique presents many advantages from a process point of view:

- First, it allows operating reactors with a high continuous catalyst circulation. It is therefore a great advantage when continuous regeneration of catalyst is necessary in a process.
- Second, the particle mixing allows having an efficient heat transfer and therefore a good reactor temperature control which is crucial in case of highly exothermic reactions. Moreover particles can also be used as heat carrier between different sections of the process.
- Finally, fluidization allows using fine particles with reasonable reactor pressure drops. The use of fine particles helps preventing diffusional limitations in the catalyst.

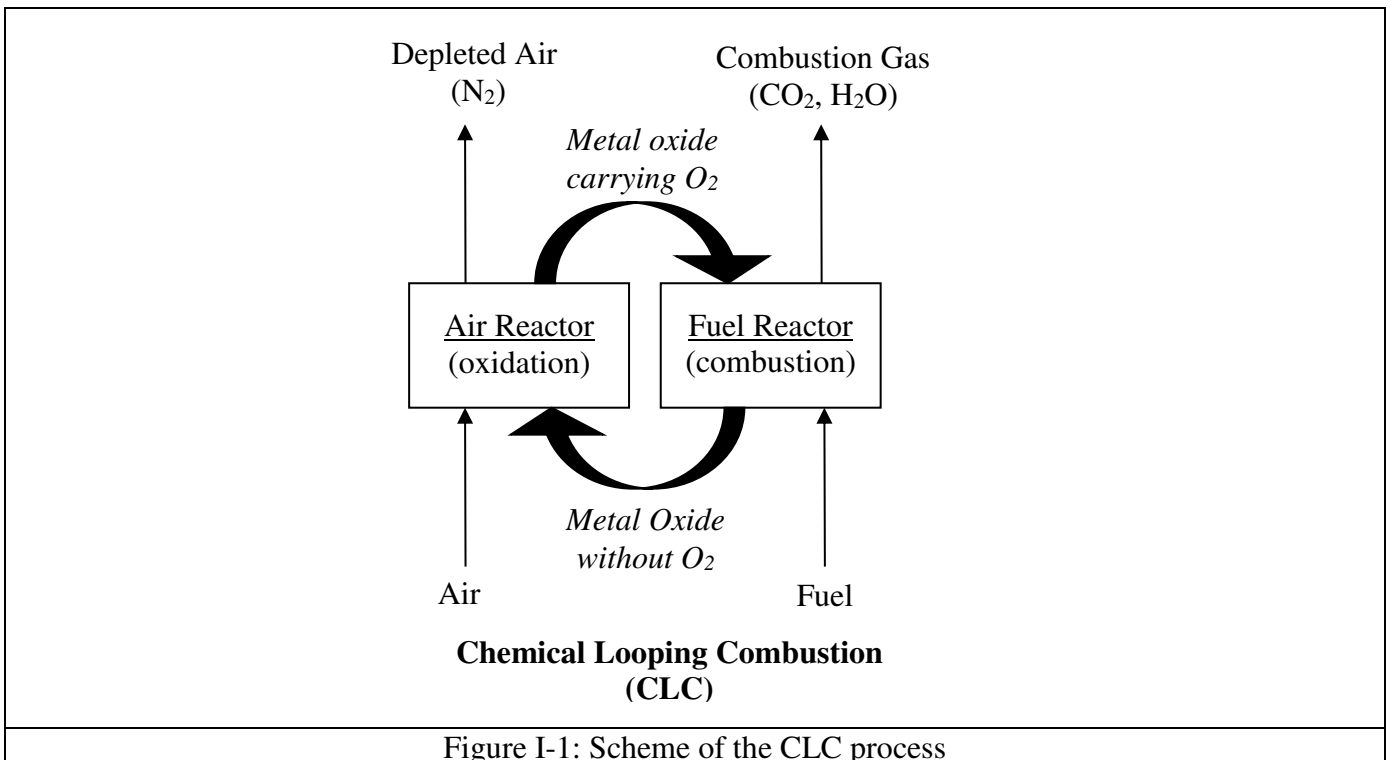
In this chapter, a focus is made on the two processes which motivated our R&D efforts presented in this PhD project:

- First, the Chemical Looping Combustion (CLC) process. It is a promising concept under intensive development for carbon dioxide (CO₂) capture. The investigation presented in Chapter II is related to attrition prediction at industrial scale for this process.
- Second the Fluid Catalytic Cracking (FCC) process. It is a well-known and established process in refining. The study presented in the second part of this PhD project deals with the use of Computational Fluid Dynamic (CFD) tools for circulating fluidized beds with FCC type of catalyst.

1.1 Chemical Looping Combustion (CLC) process

The Chemical Looping Combustion (CLC) process is currently under development [3] in a context where carbon dioxide (CO₂) emission reduction has become the main target to mitigate global warming. Indeed, in a context where CO₂ emissions from fuel combustion has increased from 23.2 Gtons/year in 2000 to 33.4 Gtons/year in 2018 [20], the International Energy Agency (IEA) [21] predicted the need for capturing over 7 Gtons/year of CO₂ by 2050 in order to limit the earth global temperature increase below 2°C.

Different technologies can be considered to reduce CO₂ emissions from fuel combustion in industrial applications with post-combustion, oxy-fuel combustion and pre-combustion systems. The CLC process is an oxy-combustion like technology with low energy penalty costs compared to other technologies [22]. It is therefore a promising concept even if technical challenges as well as economic issues still need to be solved in order to reach the industrial demonstration [3,22,23]. Several type of reactors have been considered for CLC going from fixed beds to fluidized beds systems [24]. For large scale applications such as power generation from coal combustion, fluidized bed technology is promising since it is already demonstrated at industrial scale with coal CFB boilers having large power generation [25]. Circulating fluidized bed technology has been therefore chosen by IFP Energies nouvelles and Total for their CLC development [3,22]. Figure I-2 presents the global concept of the process.



The process is divided into two main sections, the Air reactor and the Fuel reactor. Metal oxide particles circulate in a loop between the two sections where they get oxidized in the air reactor and become oxygen carriers. They are then separated from the depleted air, composed mainly of nitrogen, and sent to the Fuel Reactor where they bring the oxygen necessary for the combustion and then get sent back to the Air Reactor. Since only oxygen is used for combustion, the gas generated from the combustion is composed of CO₂ and water and it is therefore not diluted in nitrogen (N₂). The water can thus be easily separated by condensation and the CO₂ compressed for storage.

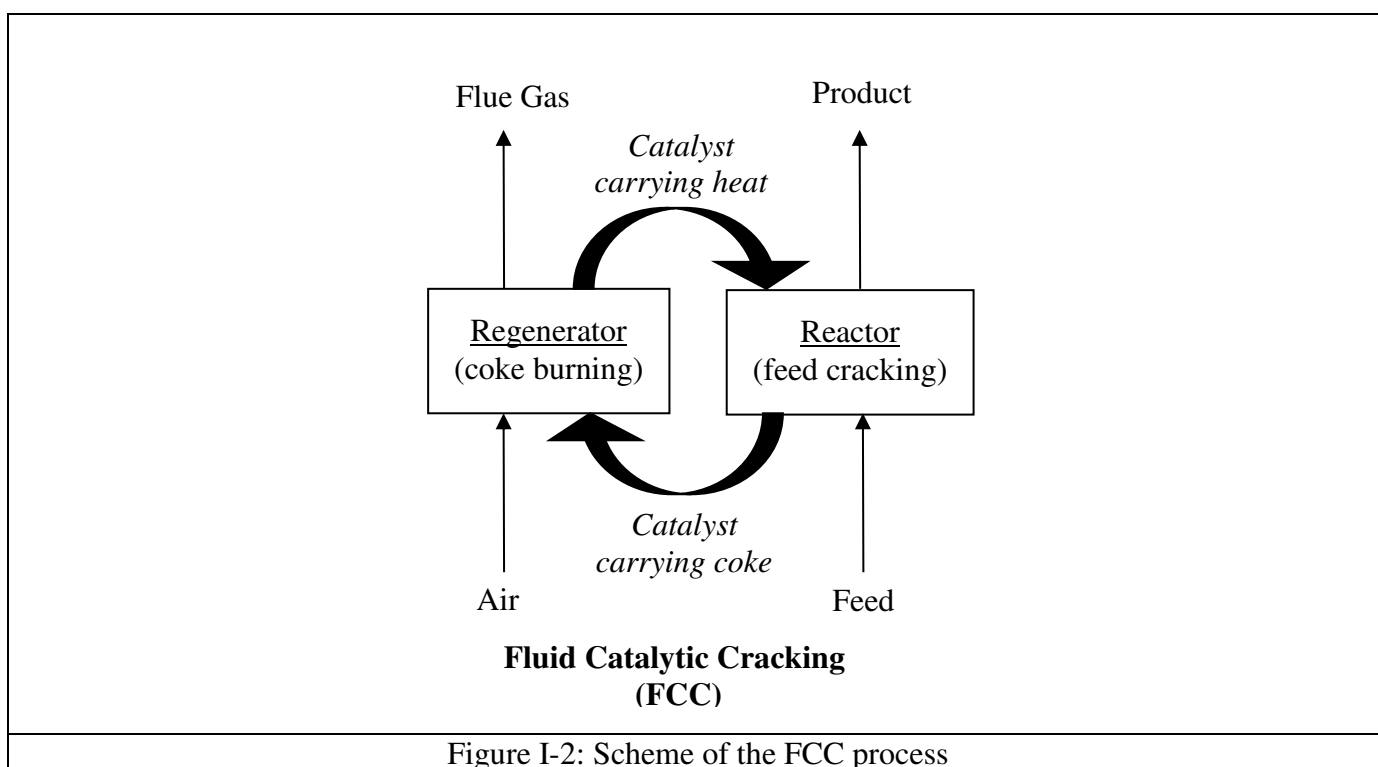
Different technical challenges can be pointed out for the development of this process [3]:

- The first one is the limitation of the pressure drop in the Air Reactor since it is directly connected to the cost of the air compression and therefore the economics of the process. This issue has been investigated at IFP Energies nouvelles [26] in order to develop a model predicting the pressure drop in an air reactor.
- The second one is the control of the particles circulation at high temperature where mechanical devices such as slide valves cannot be used. A possible alternative studied at IFP Energies nouvelles is the use of a non-mechanical L-Valve where gas injections control the particles circulation [27].
- The third crucial point is the choice of the oxygen carrier particles. Many different oxygen carriers have been tested for the CLC process [28], the criteria of selection being the high conversion rates and reactivity, low rate of agglomeration, the resistance to the attrition phenomena and the cost of production.

It is in the context of the oxygen carrier selection regarding its resistance to attrition that my work presented in Chapter III has been conducted.

1.2 Fluid Catalytic Cracking (FCC) process

Fluid Catalytic Cracking (FCC) is one of the most important conversion processes used in refineries all over the world. It is used for the conversion of heavy oil feedstock with high boiling temperature to produce gasoline, diesel and light olefins. In this process, a zeolite-based catalyst is used to crack the long hydrocarbon molecules of the feed; detailed information on the catalyst structure and the catalytic cracking reactions can be found in [29]. The FCC process has continuously evolved over the last 80 years going from a fixed bed technology to the current circulating fluidized bed technology [16,30]. It is now a key process in refineries and is used in more than half of them. Figure I-2 presents the scheme of a circulating fluidized bed FCC process. The feed is injected into the riser section of the reactor where it gets vaporized and cracked in contact with the zeolite-based catalyst. The cracking reactions deposit coke on the catalyst as a reaction by-product, which causes its deactivation. The deactivated catalyst is then sent to a regenerator where the coke on catalyst is burnt in contact with air and where part of the combustion heat is absorbed by the catalyst. Finally, the catalyst carries the heat generated by the combustion back to the reactor, where it is then consumed for the vaporization of the feed and the endothermic cracking reactions.



The evolution toward heavier FCC feedstock as well as the complex hydrodynamic of gas / particles flows led to the development of dedicated technologies [31,32]. One example is the development of the R2R™ Resid FCC, concept developed to process feedstock with a high Conradson Carbon Residue [33]. This technology is developed and licensed by the FCC Alliance which comprises of Axens, TechnipFMC, Total and IFP Energies nouvelles (IFPEN), the schematic diagram is presented in Figure I-3.

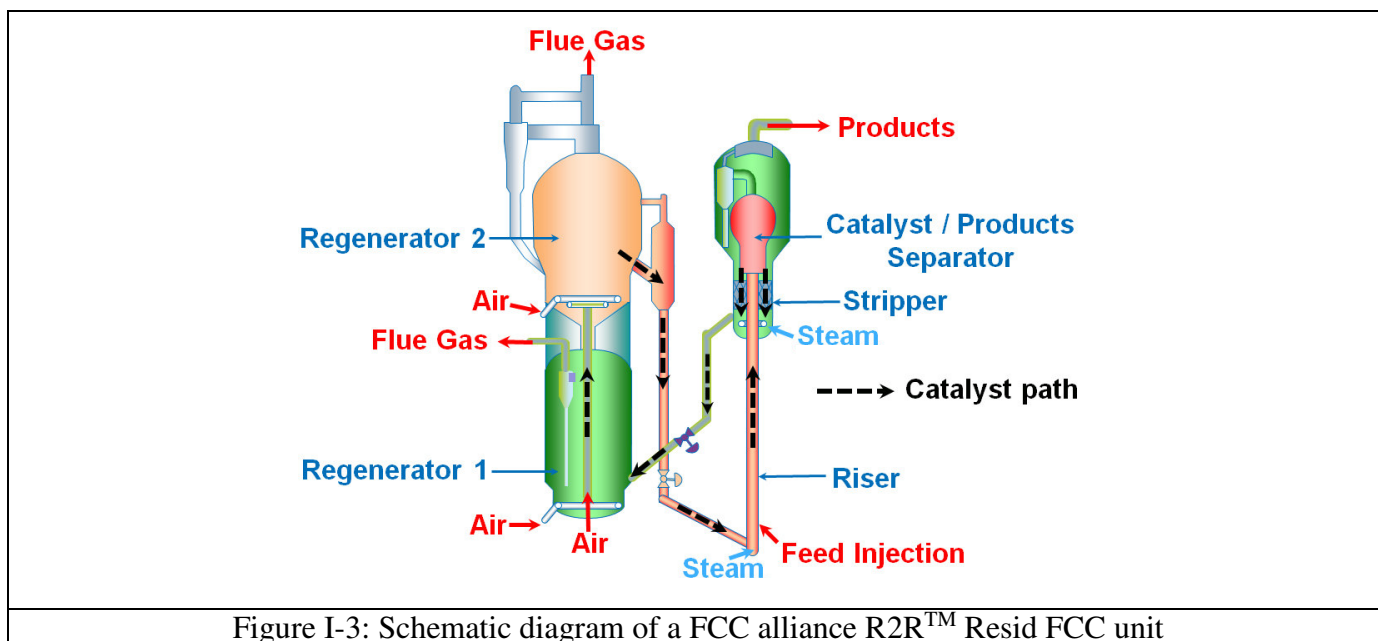


Figure I-3: Schematic diagram of a FCC alliance R2R™ Resid FCC unit

As shown in Figure I-3, hot regenerated catalyst flows from the second stage regenerator to the riser bottom where it is contacted with finely atomized feedstock. At the riser top, a termination device called RS² rapidly disengages vapor products from the catalyst to reduce further thermal and catalytic cracking. The spent catalyst then flows down a stripper section where it is contacted counter-currently with steam. Steam plays the role of fluidization and stripping media, strips the hydrocarbons from the catalyst before it leaves the stripper. The hydrocarbon stripped spent catalyst is then sent to the regeneration section to burn the coke deposit. The particular two stages regenerator configuration allows treating heavier feedstock compared to previous FCC units. The first regenerator operates in partial combustion mode with oxygen in default, it allows burning 50% to 70% of the coke on catalyst while limiting the heat generation. The rest of the coke is then burnt in a second stage regenerator in full combustion mode with oxygen in excess. Limiting the heat generation in the regeneration section for heavy feedstock is the key in order to maintain a reasonable catalyst circulation and a reasonable temperature in the reaction section.

One can appreciate the complexity of the FCC process where the comprehension and characterization of the catalyst flow is essential in many different areas of the process: in the riser for an efficient feed vaporization, in the riser termination device for an efficient gas/particles separation, in the stripper for an efficient steam/catalyst contacting, in the transfer lines (stand-pipes) for a good pressure recovery and in the regenerator for an efficient air/catalyst contacting leading to an efficient combustion. The main difficulties to better understand all this phenomena and to develop technologies are first the flow characterization at laboratory scale where it can be challenging to investigate gas/particles flows with local measurements (as discussed in Chapter I.3) and second the extrapolation of the laboratory results to the industrial scale and operating conditions. It is in this context of extrapolation for technology development that the work presented in Chapter IV has been conducted.

2 Fluidization phenomena

Fluidization consists in mixing gas and particles in order to give to the mixture the properties of a fluid. Indeed, when gas transfers to the particles enough momentum to compensate their weight and their internal friction forces, particles starts moving and the mixture behaves as a pseudo-fluid.

Fluidization has been studied intensively already since 1930 with the development of the FCC process [30] and other processes then. The objective of this chapter is to present an overview of fluidization phenomena and their characterization. The reader will appreciate the difficulty of understanding and characterizing fluidization going from evaluating particles physical properties to then investigate fluidization regimes and phenomena such as the influence of fine particles content, pressure and temperature as well as particles clustering. Fluidization remains difficult to characterize with fundamental physical phenomena, the consequences being that empirical correlations are most of the time used to predict characteristics of interest. This chapter gives a non-exhaustive list of correlations to better illustrate this characterizing approach.

2.1 Characterization of particles

The first and crucial step when dealing with fluidization of particles is the characterization of their physical properties. It is important to realize that powders used in fluidization are composed of a high number of dispersed particles. As an example, 100 grams of FCC catalyst has a number of particles in the order of 10^8 . While it is relatively easy to characterize a single particle, it becomes complex and challenging to characterize a powder with a high number of particles having different properties such as the particle diameter and internal structure. Indeed, particles can have inner pores and interstices with complex structures that can vary and be influenced by the process operations.

This chapter presents the main properties needed in order to describe the particles behavior to fluidization [34].

2.1.1 Particle size distribution

Particle Size Distribution (PSD) is a key parameter to describe the particles behavior to fluidization. Moreover, Grace et al. [35] also showed that PSD can affect the performances of fluidized bed reactors. Different techniques exist to measure PSDs as described by Allen [36]:

- Mechanical sieving, which consist in separating the powder in different classes of diameter with different sieve sizes.
- Optical measurements with laser diffraction techniques where the particles flow in front of a laser cell, the particles size changing the diffraction pattern obtained.
- Coulter-counter measurements where particles flowing through an orifice of an electrode change the electrical intensity which allows getting a particle size distribution.

Mechanical sieving is a robust technique which presents the advantage that no mathematical reconstruction is needed. However, the measurement accuracy depends of the number of sieve classes used and it can be difficult to apply such a technique for fine powders with cohesive particles (diameter lower than 100 microns) where optical measurements are preferred [2,37]. The laser diffraction is a technique relatively easy to use especially for fine powders. However the diffraction phenomena need to be modeled and the final result therefore depends on the model used for the PSD reconstruction. The Coulter counter technique is a good compromise in term of accuracy and signal reconstruction influence

since the particle diameter directly influence the electrical signal measured. However, its application can be long with the use of multiple electrode pore diameter to get the full range of the PSD.

Once the PSD is measured different representative diameters can be defined:

- The mean diameter D_{p50} which is the diameter with 50% of the total particles being smaller in size and other 50% being larger.
- The Sauter diameter $d_{p,sv}$ defined by Equation 1

$d_{p,sv} = \frac{1}{\sum(\frac{x_i}{d_{p_i}})}$	Equation 1
--	------------

o where x_i is the mass fraction of particles having a particle size $d_{p,i}$.

The Sauter Diameter is more representative of the smaller particle diameter classes of the distribution. To illustrate this concept, Figure I-4 presents two PSDs with the same mean diameter D_{p50} of 80 microns.

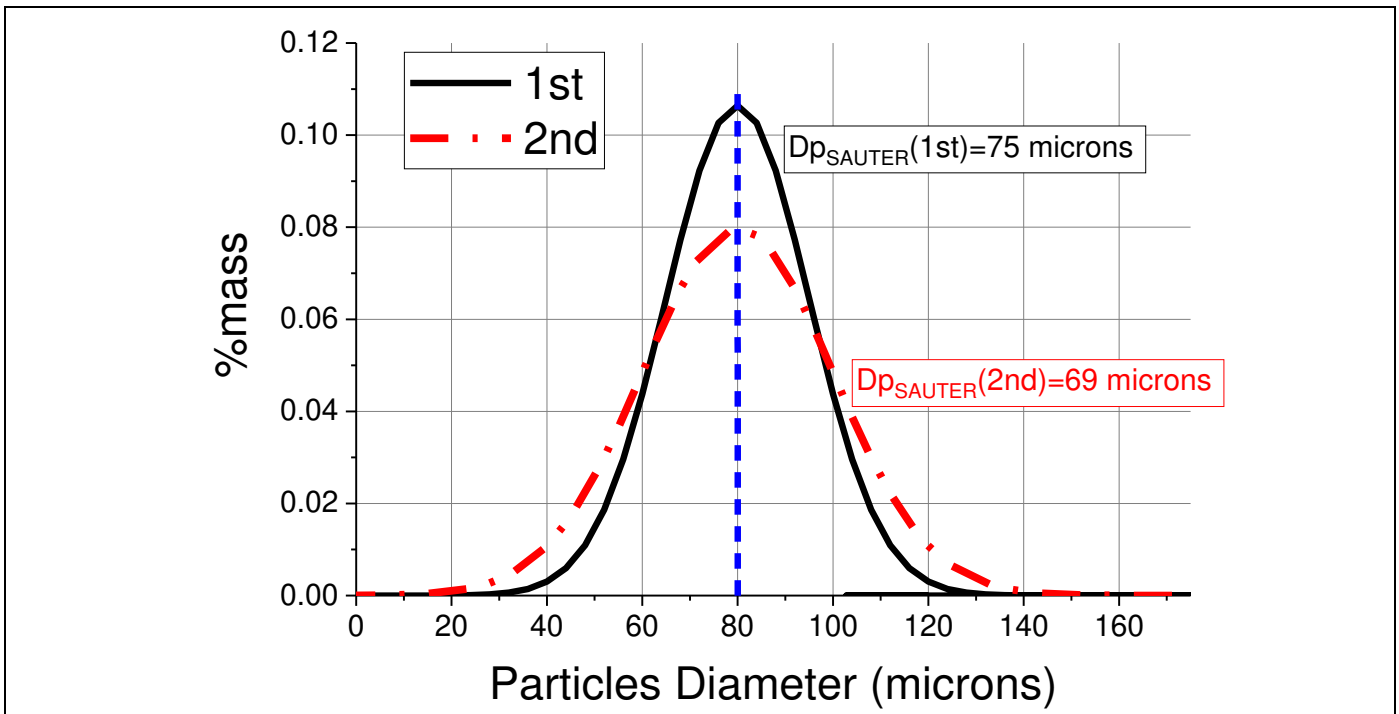


Figure I-4: Example of two Particle Size Distribution with the same mean diameter D_{p50} but with different Sauter Diameter D_{psv}

From Figure I-4, one can see the effect of fines particles for the second particle size distribution shown in red. Indeed the Sauter diameter is lower for this distribution due to the highest amount of fine particles compared to the first distribution shown in black.

Finally, another important parameter of the Particle Size Distribution is the content of fine particles. For FCC catalyst, fine particles are typically defined for particles below 40 microns [4].

To conclude, one can wonder if one representative diameter can fully characterized the powder behavior when fluidized. For example, in CFD simulations some approaches use a representative diameter which is often equal to the Sauter Diameter while other approaches consider different particle size classes. This topic is further discussed in Chapter I.4.

2.1.2 Densities

Density is a physical property as important as the particle size distribution. Different densities have to be considered as shown in Figure I-5:

- The bulk density corresponding to the mass of particles divided by the volume of the bed including the interstitial void between particles and the volume of particles with the pores.
- The particle density corresponding to the mass of particles divided by the volume of the particle including the particles pores volume.
- The skeletal density corresponding to the mass of particles divided by the volume of the particles without the pores volume.

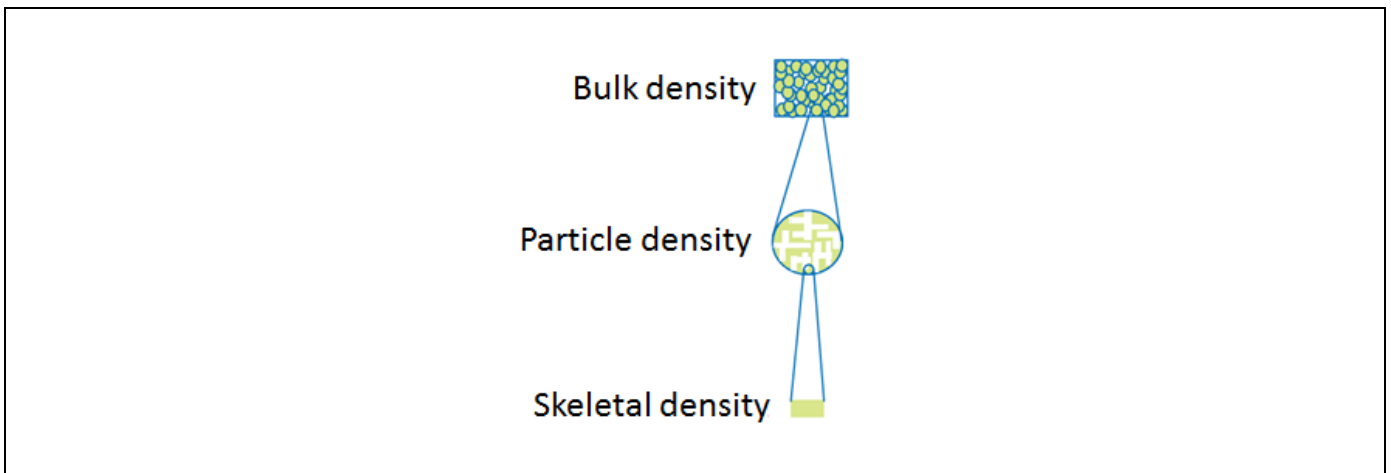


Figure I-5: Fluidization densities definition

Equation 2 presents the relation between the different densities.

$\rho_{Bulk} = (1 - \varepsilon_g)\rho_P = ((1 - \varepsilon_g)(1 - \varepsilon_{Pores})\rho_{Skeletal}$	Equation 2
--	------------

- With:
- ε_g Volume fraction of interstitial gas
 - ε_{Pores} Volume fraction of pores inside the particles
 - ρ_{Bulk} Bulk density
 - ρ_P Particle density
 - $\rho_{Skeletal}$ Particle skeletal density

For fluidization, bulk density and particle density are the main physical properties of interest for describing the gas/particles flows. Bulk density can be measured considering the particles weight and the volume they occupy in a vessel. However at rest the bulk density is very sensitive to the way the particles are packed with is influence by the tapped conditions. Particle and skeletal densities are more challenging to measure, techniques such as mercury porosimetry are often used [38].

2.1.3 Miscellaneous

Other physical properties are important to investigate:

- The particle sphericity which is defined by the ratio of the surface area of a sphere with the same volume as the given particle to the surface area of the particle as presented in Equation 3. In their

work, Rodrigues et al. [26] found that particles sphericity was a crucial parameter for the pressure drop in a vertical riser.

$Particle\ sphericity = \frac{\pi^{\frac{1}{3}}(6Vol_{particles})^{\frac{2}{3}}}{S_{particles}}$	Equation 3
--	------------

With:

- $Vol_{particles}$ Volume of the particles
- $S_{particles}$ Surface of the particles

- The particles frictional angle and repose angle respectively α and β in Figure I-6. These angles are important to characterize when designing internals to avoid local accumulation of particles in hoppers for example

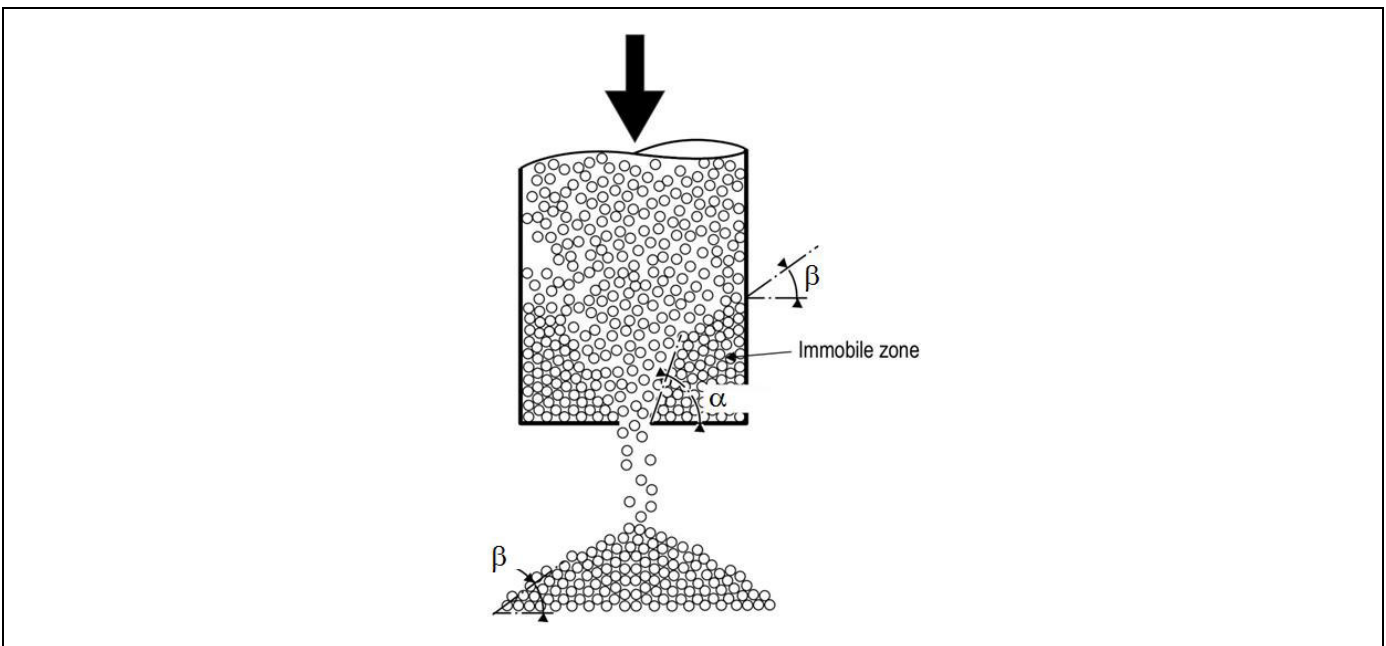


Figure I-6: Particles angle characteristics

2.1.4 Inter-particle forces and clustering

Different inter-particle forces are often mentioned when dealing with fluidized bed of fine particles with the electrostatic, the capillary and the Van der Walls forces. These forces can be at the origin of particles clusters formation which can then influence the hydrodynamic of the gas-particles flow. Indeed, clusters of particles will generate a different interaction with the gas phase compared to single particles.

Visser et al. [39] highlighted the contribution of the Van der Walls force on the clusters formation in fluidized beds. They stated that the Van der Walls force is dominant compared to the electrostatic and capillary forces. They also demonstrated that Van der Walls forces become dominant compared to the particle weight for small particle diameters which explain why clusters formation occur mostly for fine particles (Geldart Group A and Group C presented in the next chapter). For two smooth spheres, the Van der Walls force can be written with Equation 4[40]:

$F_{vw} = \frac{A_H d_p}{\delta}$	Equation 4
-----------------------------------	------------

Where A is the Hamakar constant which depends on the material and fluid properties and δ is the distance between particles. Van der Walls forces are considered non-negligible when distance between particles are in the order of 0.1 to 1 nanometer [39]. In fluidized bed, particles contact each other at a high frequency therefore the distance between particles is in the range where Van der Walls forces are noticeable. It is also important to mention that particle asperities and shapes have a great influence on the Van der Walls forces [41]. Then, Kaye and Boardman [42] stated that particle clustering becomes significant in many systems where particles volume concentration exceed 0.1% which is the case in circulating fluidized bed even for dilute regime flows.

Cahyadi et al. [43] and Cocco et al. [44] also highlighted that the formation of particles cluster can be connected to hydrodynamic phenomena with non-rigid clusters under the form of streamers while other rigid clusters are formed because of the inter-particle forces. It then becomes interesting to wonder if single particles or cluster of particles have to be considered for modeling the gas/particles interaction having in mind that cluster consideration will necessarily add complexity to the model. Indeed cluster formation is first difficult to characterize experimentally and it is then dependent on the particles properties, fluidization regimes and system used as demonstrated by Cahyadi et al. [43].

Many phenomena observed in fluidization are attributed to particle clustering as presented in the next chapters of this literature review.

2.1.5 Geldart classification

Geldart [45] defined in 1973 a classification of particles with respect to their behavior when fluidized with a gas. Four groups of particles were distinguished according to their physical properties as shown in Figure I-7 with first the difference between particles density and gas density ($\rho_{particles} - \rho_{Gas}$) and second the particle size distribution Sauter diameter (D_{pSV})

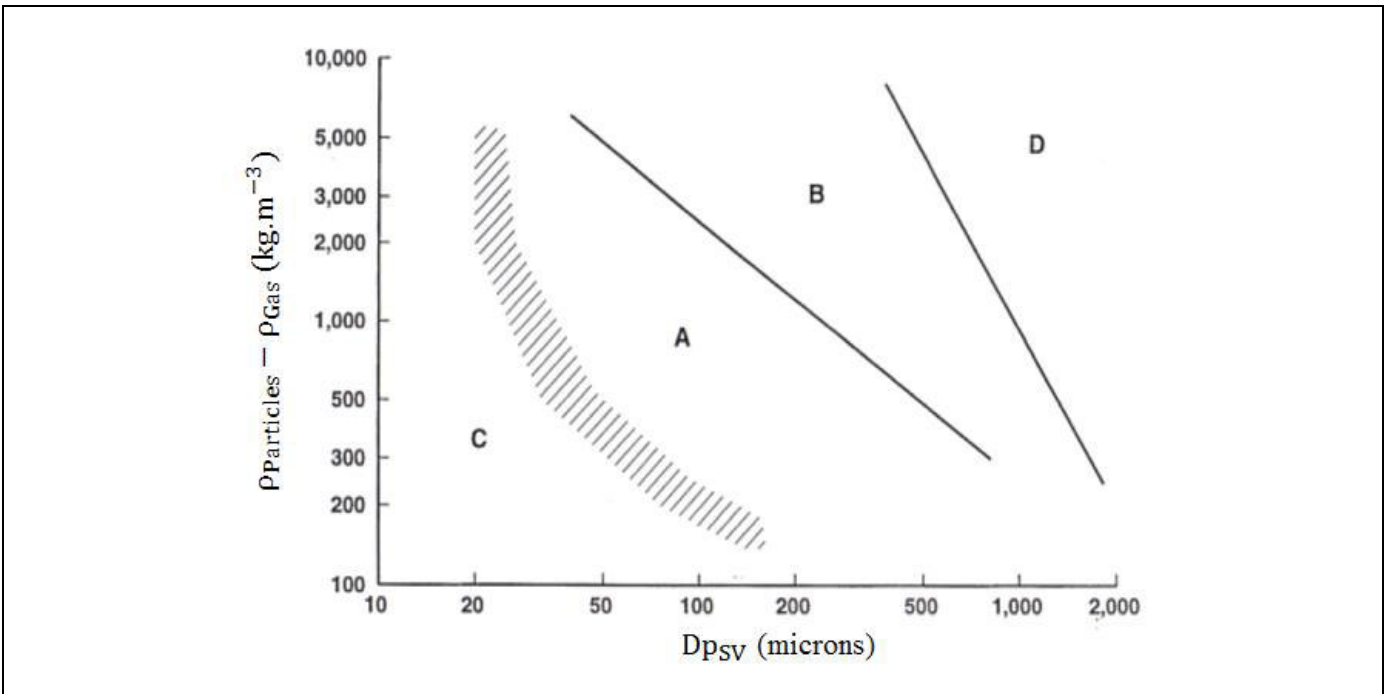


Figure I-7 : Geldart classification of powders with respect to their fluidization behavior

The characteristics of each group are:

- Group C: Fine particles difficult to fluidize. Inter-particle forces (electrostatics, van der Waals and capillary forces) have an important effect on the fluidization quality and gas tends to channel

through the bed [2]. FCC catalyst particles with a diameter below 20 microns are an example of Geldart Group C particles.

- Group A: Particles easy to fluidize and characterized by a homogenous fluidization regime where the bed expands without bubbles formation before reaching the bubbling regime. Bubbles generated in Geldart Group A particles present a maximum stable diameter even for large fluidized beds. Particle weight is rather small and inter-particles forces can affect particle flow [2]. FCC catalyst is an example of Geldart Group A particles.
- Group B: Particles having larger diameter and/or larger density than Geldart Group A particles. Bubbles are formed in the bed as soon as the minimum velocity of fluidization is reached. Inter-particles forces are less dominant, the bubbles size is not limited and can reached the vessel bed diameter. Large bubbles can be problematic in term of operation with slugging effects [2]. Sand is an example of Geldart Group B particles.
- Group D: large and heavy particles, stable spouted beds can be easily formed with this group of particles. In order to be fluidized beds of Geldart Group D, particles need very large quantities of gas.

2.2 Regime of fluidization

Fluidization of gas-solid systems depends on the particles properties as discussed in Chapter 2.1.5, as well as the fluidization gas velocity. Different regimes can be defined according to the flow structure observed when increasing the superficial gas velocity as described in Figure I-8.

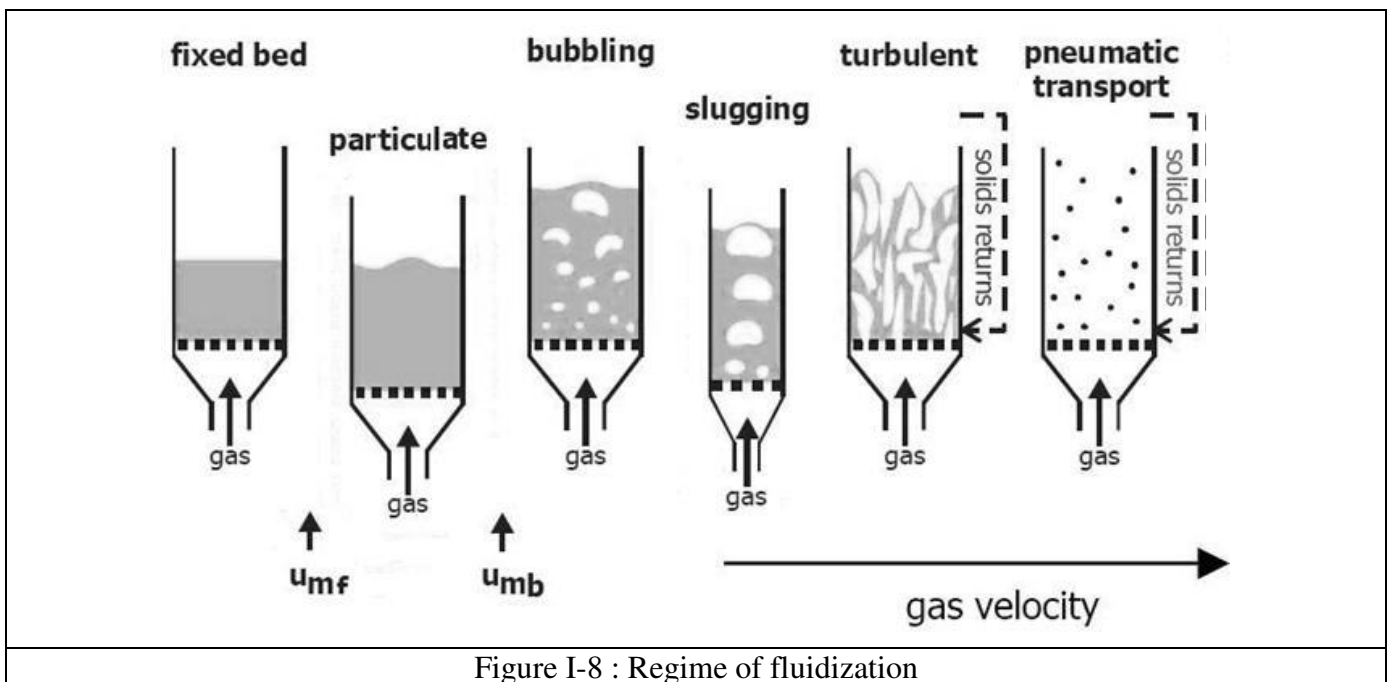


Figure I-8 : Regime of fluidization

The different fluidization regimes are presented below, when increasing the superficial gas velocity, from the fixed bed to the pneumatic transport regimes. The main flow characteristics are introduced for each regime.

2.2.1 Fixed bed and minimum of fluidization regime

In the fixed bed regime, particles do not move. The pressure drop through the bed can be calculated according to the Ergun's empirical equation presented below which takes into account the particle sphericity factor. For small particles, the second term can be neglected compared to the first one and the pressure drop thus increases linearly with the gas velocity.

$\frac{\Delta P}{H} = \frac{150(1 - \varepsilon_g)^2 \mu_g}{\phi_s^2 \varepsilon_g^3 d_p^2} U_{sg} + \frac{1.75(1 - \varepsilon_g) \rho_g}{\phi_s \varepsilon_g^3 d_p} U_{sg}^2$	Equation 5
--	------------

The minimum of fluidization is then defined as the transition from fixed bed to homogeneous fluidization regime, for Geldart Group A particles, and to bubbling regime for Group B particles. At the minimum of fluidization, the pressure drop through the bed can therefore be calculated according to Ergun's equation as shown in Equation 6 and according to the Equation 7 which describes the pressure drop through a fluidized bed where the mixture behaves as a liquid.

$\frac{\Delta P}{H_{mf}} = \frac{150(1 - \varepsilon_{mf})^2 \mu_g}{\phi_s^2 \varepsilon_{mf}^3 d_p^2} U_{mf} + \frac{1.75(1 - \varepsilon_{mf}) \rho_g}{\phi_s \varepsilon_{mf}^3 d_p} U_{mf}^2$	Equation 6
---	------------

$\frac{\Delta P}{H_{mf}} = g(\rho_p - \rho_g)(1 - \varepsilon_{mf})$	Equation 7
--	------------

Equalizing Equation 6 and Equation 7, the minimum fluidization equation is obtained as shown in Equation 8

$A_1 Re_{p,mf}^2 + A_2 Re_{p,mf} = Ar$ <p style="text-align: center;">with</p> $Re_{p,mf} = \frac{u_{mf} \phi d_p \rho_g}{\mu} ; Ar = \frac{(\phi d_p)^3 \rho_g (\rho_p - \rho_g)}{\mu^2} ; A_1 = \frac{1.75}{\varepsilon_{mf}^3 \phi} ; A_2 = \frac{150(1 - \varepsilon_{mf})}{\varepsilon_{mf}^3 \phi^2}$	Equation 8
---	------------

The analytical solution of Equation 8 being:

$Re_{p,mf} = \sqrt{\left(\frac{A_2}{2A_1}\right)^2 + \frac{Ar}{A_1}} - \frac{A_2}{2A_1}$	Equation 9
--	------------

The unknowns of the analytical solution presented in Equation 9 are ε_{mf} in the terms A_1 and A_2 and u_{mf} in $Re_{p,mf}$. Many authors have given empirical values for the coefficient A_1 and A_2 based on experimental investigation as shown in Table I-1.

Table I-1– Empirical values of A₁ and A₂ for minimum of fluidization conditions for Equation 9 [2]

	A ₁	A ₂
Wen and Yu (1966)	33.7	0.0408
Richardson (1971)	25.7	0.0365
Saxena and Vogel (1977)	25.3	0.0571
Babu et al. (1978)	25.25	0.0651
Grace (1982)	27.2	0.0408
Chitester et al. (1984)	28.7	0.0494

Values of A₁ and A₂ differ according to the authors and the experiments used to set the data base. This variation may be due to the discrepancy between experiments but also to the characteristic used for the powder description with only a representative diameter. Indeed, Bruni et al. [46] demonstrated that the fine content also influences the minimum fluidization velocity.

This first example illustrates the difficulty of characterizing experimentally basic parameters such as the minimum of fluidization velocity where many parameters must be characterized and taken into account.

2.2.2 Bubbling and turbulent regimes

In the bubbling regime, bubbles are formed and rise through the so-called emulsion phase with a regular frequency and burst at the top of the bed which has a stable and well defined level. The emulsion phase is often considered as particles fluidized at the minimum fluidization conditions ($\epsilon_g = \epsilon_{mf}$). The bubbling regime is characterized with the bubbling velocity U_{mb} with $\frac{U_{mb}}{U_{mf}} > 1$ for Geldart Group A particles and $\frac{U_{mf}}{U_{mb}} = 1$ for Geldart Group B particles. Abrahamsen and Geldart [47] proposed the correlation presented in Equation 10 for the ratio of $\frac{U_{mb}}{U_{mf}}$ for Geldart Group A particles where F is the solid mass fraction of particles lower than 45 microns:

$\frac{U_{mb}}{U_{mf}} = \frac{2300 \rho_g^{0.126} \mu_g^{0.523} \exp^{0.716F}}{(\phi d_{p,sv})^{0.8} g^{0.934} (\rho_p - \rho_g)^{0.934}}$	Equation 10
---	-------------

Many studies have been carried out in order to characterize the bubbles size and velocity in fluidized beds [2,48–52] with many correlations developed [34]. Darton et al. [50] proposed the correlation presented in Equation 11 for bubbles growth based on a theory that bubbles tend to rise in preferred paths and that the distance travelled by two neighboring bubbles coalescence is proportional to their lateral distance separation.

$d_b(z) = \frac{0.54 (U_{sg} - U_{mf})^{0.4} \left(z + 4 \sqrt{\frac{1}{N}} \right)^{0.8}}{g^{0.2}}$	Equation 11
---	-------------

- Where N is the number of holes per square meter of distributor.

The author found that the correlation worked quite well if the bubble size is not limited by the presence of fine particles and therefore more applicable for Geldart Group B particles. Indeed, Werther [53] and

Matsen [54] reported a stable bubble size for Geldart Group A particles. Geldart [55] proposed the following correlation to compute the maximum stable bubble size:

$d_{b_MAXIMUM} = 2 \frac{V_t^{*2}}{g}$	Equation 12
---	-------------

Where:

- $d_{b_MAXIMUM}$ is the maximum stable bubble size
- V_t^* is the terminal velocity of the a particle having the size of the PSD Sauter diameter times 2.7
- g is the gravitational acceleration equals to 9.81 ms^{-2} .

Hillgart and Werther [49] proposed a correlation for the local average bubble rise velocity for Geldart Group A and Group B particles presented in Equation 13 based on the assumption that all the gas which is not in the emulsion phase flows under the form of bubbles.

$u_b = \varphi(U_{sg} - u_{mf}) + 0.71\vartheta\sqrt{gd_b}$ <p style="text-align: center;">with</p> <p><i>Group A:</i> $\vartheta = 3.2 D^{0.33}$ for $0 < \frac{z}{D} < 1$ and $\vartheta = 3.2$ for $\frac{z}{D} > 1$</p> <p><i>Group B:</i> $\vartheta = 2.0 D^5$ for $0 < \frac{z}{D} < 1$ and $\vartheta = 2.5$ for $\frac{z}{D} > 1$</p>	Equation 13
--	-------------

In turbulent regime, bubbles are difficult to observe and the bed level is also hardly distinguishable. The transition from the bubbling regime to the turbulent regime is often characterized by the gas velocity U_c defined as the velocity when the maximum pressure fluctuations through the bed are reached as shown in Figure I-9. However, disagreement appears in the literature when defining turbulent fluidization, and transport regimes [56]. Indeed, another characteristic velocity U_k is defined where the pressure fluctuations of the bed reach a threshold as shown in Figure I-9. Yerushalmi et al. [57] considered that the turbulent regime starts from U_k while the most common approach proposed by Rhodes and Geldart considered that turbulent regime occurs from U_c to U_k .

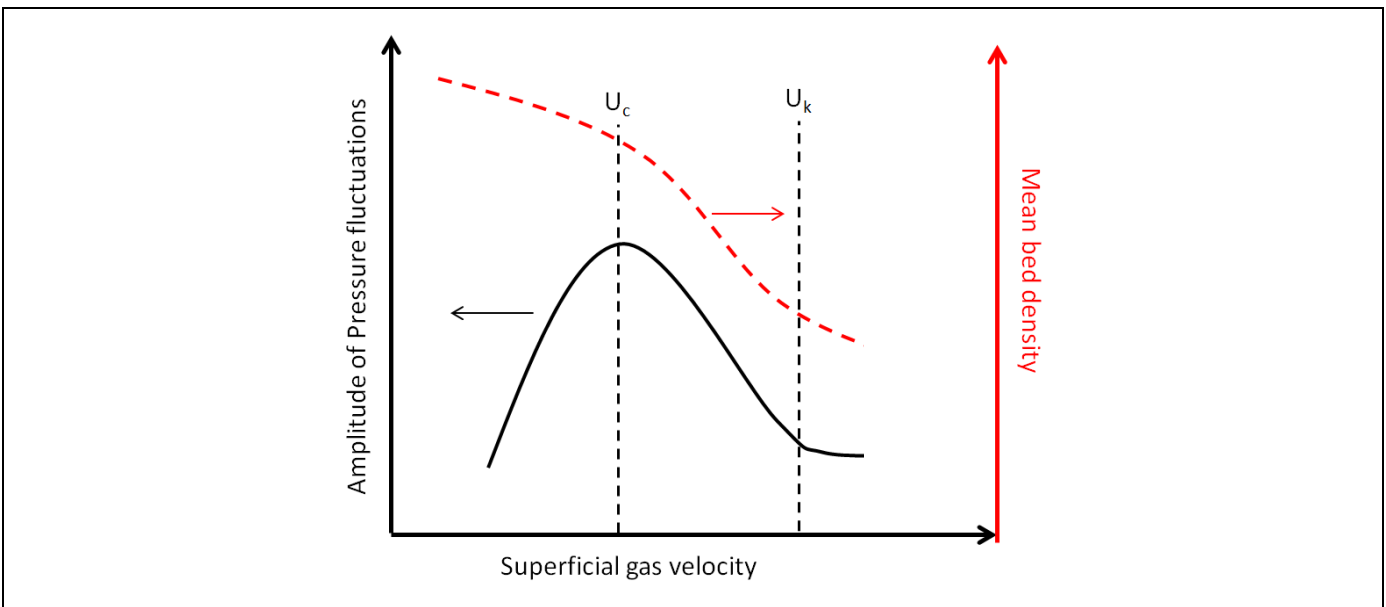


Figure I-9 : Transition between bubbling, turbulent, fast fluidization regimes according to Rhodes and Geldart [56]

Many correlations exist for the prediction of U_c and U_k [2]. Cai et al. [58] correlated the literature data based on absolute pressure fluctuation and bed expansion measurements up to 1989 with the turbulent Reynold number shown in Equation 14.

$(Re)_c = \frac{d_p \rho_f U_c}{\mu_g} = 0.57 Ar^{0.46}$	Equation 14
--	-------------

Later on Bi and Grace [59] proposed another correlation presented in Equation 15. They also demonstrated the influence of operating parameters, such as the bed level and solid cyclone return configuration, as well as the measurement techniques on the experimental determination of U_c and U_k [59].

$(Re)_c = \frac{d_p \rho_f U_c}{\mu_g} = 1.243 Ar^{0.447}$ <p style="text-align: center;">for $2 < Ar < 1 \times 10^8$</p>	Equation 15
---	-------------

Issangya et al. [60] also demonstrated for FCC catalyst that the fines content, defined by the amount of particles with a diameter lower than 40 microns, as well as bed level and internals influenced the pressure fluctuations and therefore the determination of the turbulent regime. The explanation highlighted by the authors was that high fines contents and internals had the tendency to mitigate the gas by-passing through the bed and the pressure drop fluctuations were consequently reduced.

From bubbling to turbulent fluidization regime, the pressure drop through the bed can be expressed with the bed average gas volume fraction as indicated in Equation 16:

$\frac{\Delta P}{H} = g(\rho_p - \rho_g)(1 - \varepsilon_g)$	Equation 16
--	-------------

Investigations were then carried out to predict the average gas volume fraction in a fluidized bed according to the superficial gas velocity. For this purpose, King [61] developed an empirical correlation for Geldart Group A particles for turbulent bed as shown in Equation 17.

$\varepsilon_g = \frac{U_{sg} + 1}{U_{sg} + 2}$	Equation 17
---	-------------

However, as highlighted by Bi et al. [62] in their state of the art on turbulent fluidization, parameters such as column diameter, fines content, internals in the bed clearly influence the hydrodynamic of turbulent beds. Issangya et al. [63] also showed the influence of the dilute phase pressure on the bed gas maldistribution. It is therefore difficult to develop predictive models including all these effects and correlations are consequently connected to the experiment used to set them up.

Finally, some authors investigated the formation of particles clusters in turbulent fluidized beds. Cocco et al. [44] studied the cluster formation in a dense and dilute part of a fluidized bed with polyethylene and FCC particles having both a mean diameter around 70 microns. They observed visually the flow with a high speed camera system (boroscope) inserted into the bed. For the polyethylene, they observed in the dilute phase particles cluster with a mean size of 240 microns. The observation in the dense phase was more difficult clusters being observed in the vicinity of gas bubbles. Concerning the FCC particles, smaller clusters were observed in the dilute phase with some pictures of clusters around 100 microns. The

authors proposed a mechanism for cluster formation where the granular temperature therefore the collision between the particles needs to decrease in a certain range in order to let the inter-particle forces act to form clusters.

2.2.3 Transport regime in a vertical upstream flow

Solid circulation in a CFB system is maintained through a circulation loop pressure balance. Figure I-10 gives an example of such a loop with solid circulating from a fluidized bed into a stand-pipe, a valve, then a riser with a vertical upstream flow and finally through a cyclone where particles recovered fall back into the fluidized bed.

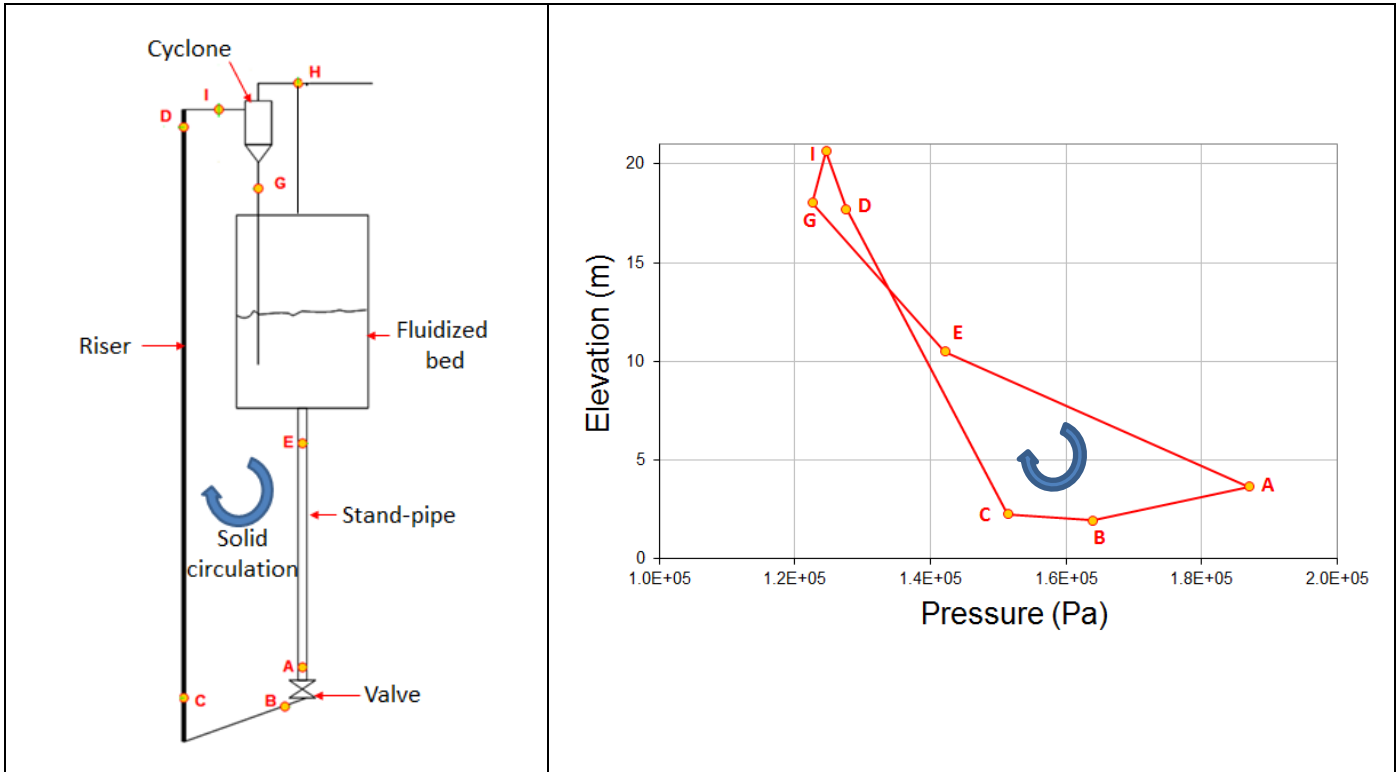


Figure I-10: Solid circulation loop pressure balance example

As shown in Figure I-10, there are parts in the circulating loop where pressure is recovered with an increase of pressure in the direction of the circulation and parts with a loss of pressure with a decrease of pressure in the direction of the circulation. The pressure balance in the loop can be written with Equation 18.

$\Delta P_{riser\ C \rightarrow D} = \Delta P_{bed\ G \rightarrow E} + \Delta P_{standpipe\ bed\ E \rightarrow A} - \Delta P_{VALVE\ A \rightarrow B} - \Delta P_{cyclone\ I \rightarrow G} - \Delta P_{termination\ D \rightarrow I}$	Equation 18
--	-------------

Where: - $\Delta P_{riser\ C \rightarrow D}$ is the pressure drop in the vertical upflow riser

- $\Delta P_{bed\ G \rightarrow E}$ is the pressure recovered in the bed and is equal to $\rho_{BED} \times g \times H_{BED}$ with ρ_{BED} and H_{BED} being the bed density and height

- $\Delta P_{standpipe\ bed\ E \rightarrow A}$ is the pressure recovered in the stand-pipe and is equal to $\rho_{SP} \times g \times H_{SP}$ with ρ_{SP} and H_{SP} being the stand-pipe density and height

- $\Delta P_{VALVE\ A \rightarrow B}$ is the pressure drop generated in the valve

- $\Delta P_{termination D \rightarrow I}$ is the pressure drop generated by the riser termination
- $\Delta P_{cyclone I \rightarrow G}$ is the pressure drop generated in the cyclone

From Equation 18 one can see that the maximum riser pressure drop is dependent on the circulating loop characteristics and the pressure recovery in the bed and stand-pipe. The pressure recovery of these elements being dependent on their height, a circulation loop with a high bed and stand-pipe length will have a high pressure recovery and can consequently reach high riser pressure drop and therefore high solid circulation rate. On the other hand, a circulating loop with a low pressure recovery will have a limited solid circulation rate.

Figure I-11 describes qualitatively the particle vertical upflow conveying in a riser with the pressure drop versus superficial gas velocity.

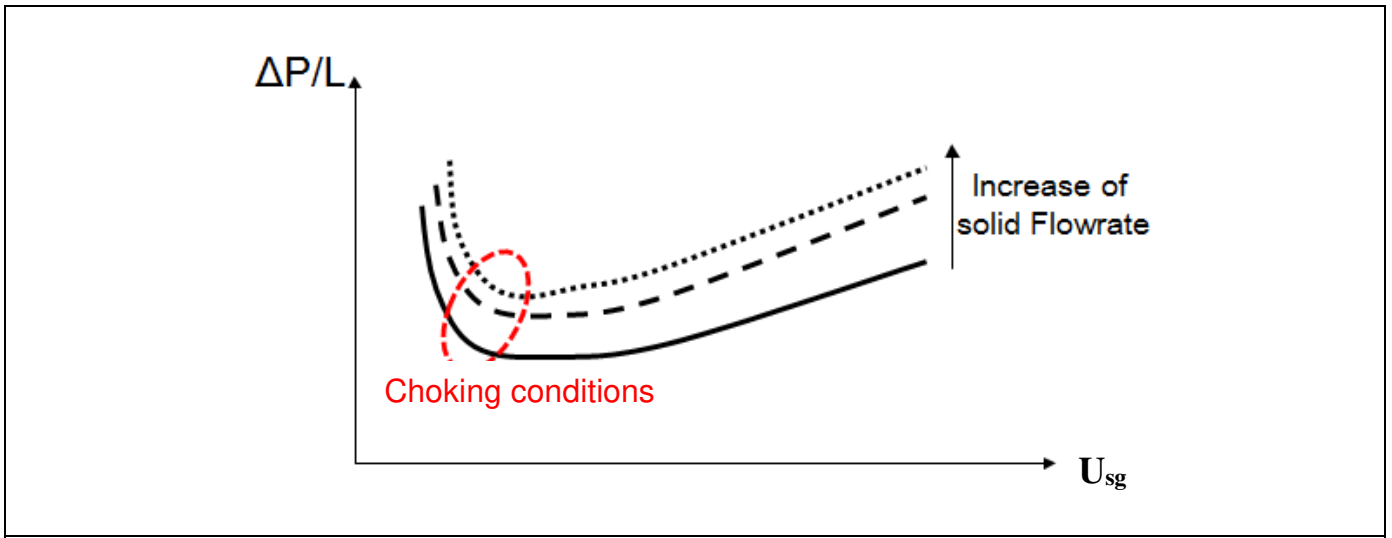


Figure I-11 : Qualitative characterization of vertical upflow pneumatic conveying

In transport regime, the pressure drop increases with the solid flowrate carried by the gas. At high velocity, the particles are transported in a dilute uniform type of flow. When decreasing the air velocity for the same solid flowrate transported (from right to left on Figure I-11), the solid volume fraction increases in the riser while the pressure drop related to the wall friction decreases, the overall pressure drop decreasing as shown in Figure I-11. At the choking velocity conditions, the suspension of gas and particles becomes unstable, the pressure drop through the riser increases dramatically, and particles are transported in a dense flow regime which can lead to slugging in some cases. Most of the studies carried out in the literature have been done for dilute transport with gas velocities above the choking velocity. Many correlations exist for the prediction of choking velocity [64]. Bi et al. [65] proposed the following correlation for Geldart Group A and Group B particles:

$\frac{U_{Chocking}}{\sqrt{gd_p}} = 21.6 Ar^{0.105} \left(\frac{Gs}{\rho_G U_{Chocking}} \right)^{0.542}$	Equation 19
--	-------------

It is interesting to point out that choking conditions are also connected to the pressure balance in the circulation loop where the pressure recovery available limits the riser pressure drop and therefore the solid circulation as explained above.

Bi et al. [65] then made a distinction between two types of transport regime with first the core-annular dilute transport regime occurring at lower gas velocities and second the homogeneous dilute transport

regime for higher gas velocities. The core-annulus regime [66,67] consists on the segregation of particles into a dilute core and a denser annulus with lower particles velocity as shown in Figure I-12 .

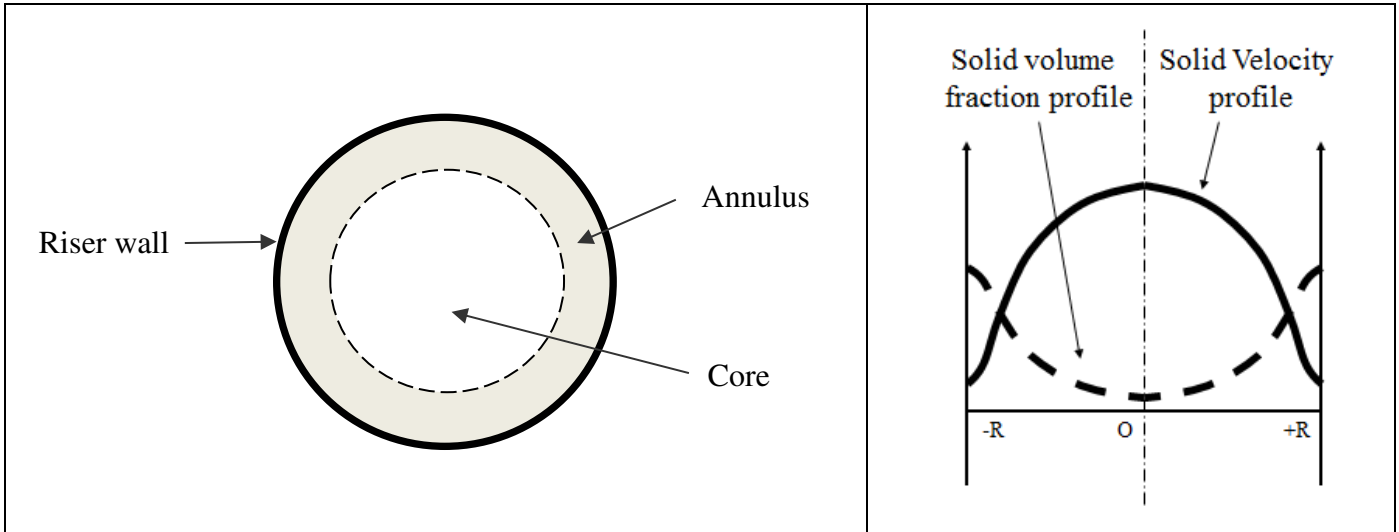


Figure I-12: Core-annulus structure in a riser

Bi et al. [65] proposed the following correlation as an attempt to estimate the transition between the core-annulus and homogeneous dilute transport regimes:

$U_{annular\ to\ homogeneous} = 10.1(gd_p)^{0.347} \left(\frac{Gs}{\rho_G}\right)^{0.31} \left(\frac{d_p}{D}\right)^{-0.139} Ar^{-0.021}$	Equation 20
---	-------------

Karri and Knowlton [68] then put in evidence with experiments on a 20 cm diameter riser with FCC catalyst that particles in the annulus region have a downward or upward velocity depending on the superficial gas velocity and particles mass flux.

Concerning the pressure drop prediction in risers, Nieuwland et al. [69] proposed a one dimensional model with Equation 21 which includes the sum of the following contributions :

- Pressure drops due to the acceleration of the gas and the particles.
- Pressure drops due to the friction of the gas and particles with the wall.
- Pressure drops due to the weight of the gas and particles.

$\frac{dP}{dz} = \left(\frac{dP}{dz}\right)_{Gas,Acc} + \left(\frac{dP}{dz}\right)_{Gas,Weight} + \left(\frac{dP}{dz}\right)_{Gas,Fric_wall} + \left(\frac{dP}{dz}\right)_{Par,Acc}$ $+ \left(\frac{dP}{dz}\right)_{Par,Weight} + \left(\frac{dP}{dz}\right)_{Par,Fric_wall}$	Equation 21
---	-------------

Using this approach, Rodrigues et al. [26] measured pressure profiles in a riser with Gerdart Group B particles. They assumed that particles were accelerated in the fully developed flow region where the pressure gradient versus height in the riser was constant. They then obtained the solid concentration in the accelerated zone modeling the pressure drops due to the gas and particles wall friction through the Fanning and Konno & Saito equations [69–71]. Finally, by discretizing the gas and particles momentum equation in the riser, they managed to get local velocities and concentrations for both gas and particles. They also obtained an expression of a one dimensional drag force between gas and particles depending on the operating conditions.

Patience et al. [72] in their study on scaling risers proposed the following correlation for the slip velocity factor in the fully developed flow region defined as the ratio of the particles velocity over the gas velocity.

$\text{Slip factor} = \frac{\epsilon V_s}{U_g} = \left(1 + \frac{5.6}{Fr} + 0.47 Fr_t^{0.41}\right)^{-1}$	Equation 22
---	-------------

- With :
- Fr: Froude number $Ug/(gD)^{0.5}$
 - Fr_t: Froude number with particle terminal velocity $V_t/(gD)^{0.5}$
 - V_t Particle terminal velocity

They then claimed that this ratio is around 0.5 for FCC industrial risers with diameters in the order of the meter.

Finally in their literature review, Cahyadi et al. [43] investigated the particles cluster formation phenomenon in risers. They mentioned its influence on the riser hydrodynamic with cluster of particles having a different interaction with the gas phase compared to single particles. They also demonstrated that the experimental characterization of particles clusters formation is difficult with a result dependency on the experimental set-up used. The question on the cluster consideration can then be raised when using equation 22 since the cluster will have a different terminal velocity compared to single particles.

2.3 Entrainment of particles in fluidized bed

In turbulent regime, particles can be entrained with the gas out of the fluidized bed vessel. The flux of particles entrained is referred as entrainment. The mechanism of entrainment is shown in Figure I-13.

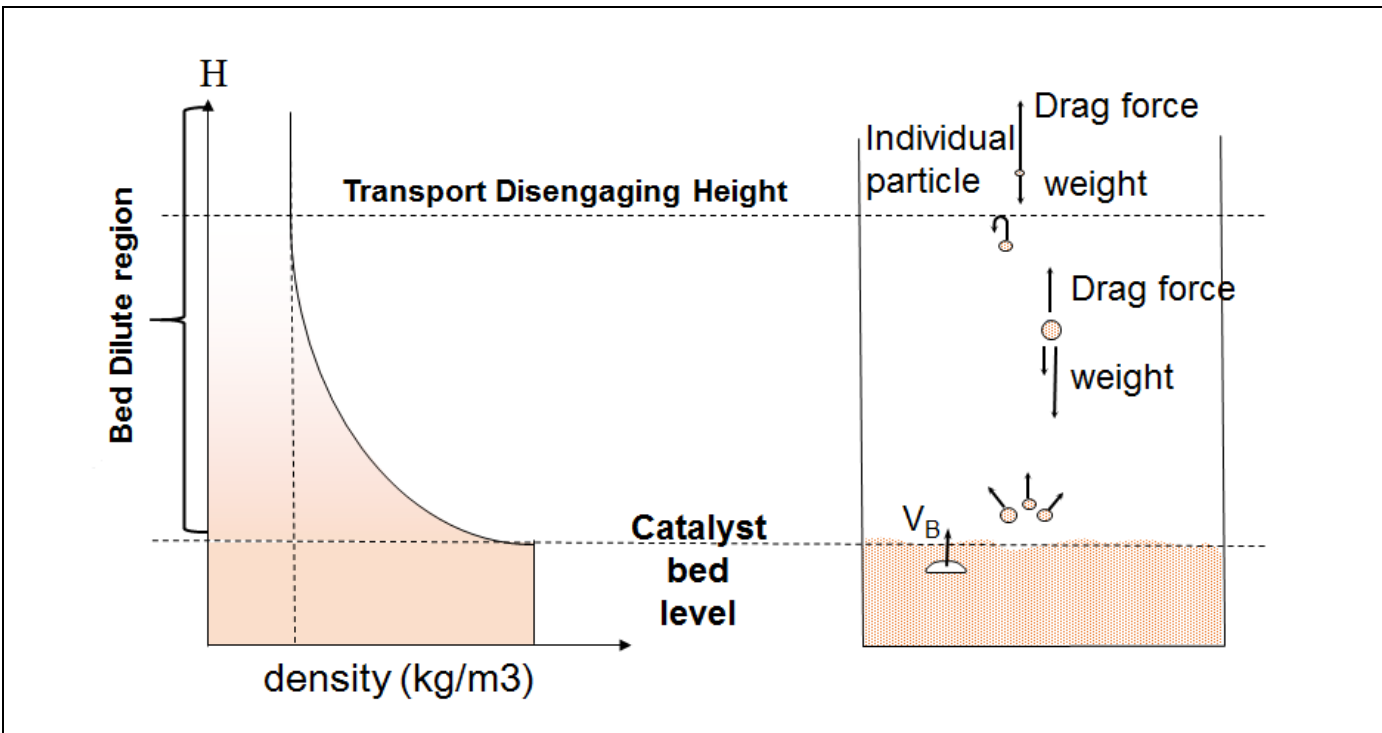


Figure I-13: Mechanism of entrainment in fluidized bed

Bubbles bursting at the bed level surface eject clouds of particles out of the bed into the dilute region. Different mechanisms have been observed for the particles ejection out of the bed with particles being ejected either by the roof or/and the wake of the bubbles as shown by Levy et al. [73]. Then in the dilute region, particles are subjected to two forces, their weight and the drag force due the interaction with the

gas. According to their size and potential cloud structure, particles can either fall back into the bed or being transported with the gas. The particles concentration in the dilute region of the bed decreased with the height until reaching a threshold where particles entrained do not fall back into the bed and are therefore entrained. This height is called the Transport Disengaging Height (TDH).

The effect on entrainment of different parameters has been investigated. The most influencing parameters are the particles properties and the superficial gas velocity. First, entrainment rate increases when decreasing the particle size and density which can be directly explained by a force balance on one particle. However, some authors found that entrainment rate can be decreased with the injection of fine particles for fluidization of Geldart Group A particles. This phenomenon is explained by the formation of particle clusters and it is discussed in Chapter II-2.4. The entrainment rate is then found increasing proportionally with the gas velocity to a power generally between 2 to 4 [2]. Colakyan et al. and Tasirin et al. [74,75] found no significant influence of the vessel diameter on the entrainment rate for bed diameters between 0.1 and 0.9 m with particles from Geldart Groups A and B. Choi et al. [76] found on their study on fluidized bed combustors that the bed level did not have a strong influence as long as the vessel height was above the TDH.

Different attempts were made to model entrainment [2,77,78]. One important parameter is the determination of the TDH. Correlations can be found in the literature [2], Chan and Knowlton [79] proposed from experiments with sand particles the correlation presented in Equation 23 taking into account only the superficial gas velocity:

$TDH = 0.85 U_{sg}^{1.2} (7.33 - 1.2 \log U_{sg})$	Equation 23
--	-------------

Sciazko et al. [80] proposed a correlation based on particle and fluidized bed height presented in

$TDH = \frac{1500 H Re_p}{Ar}$	Equation 24
--------------------------------	-------------

With :

- H fluidized bed height (m)
- Re_p particle Reynold number ($\rho_g U_g d_p / \mu_g$)
- Ar Archimede number $\rho_g (\rho_g - \rho_p) g d_p^3 / \mu_g^2$

Cahyadi et al. [81] demonstrated the high discrepancy obtained between 25 TDH correlations. The authors pointed the lack of fundamental understanding of the TDH phenomenon and the dependency of the empirical correlation on the experimental set up used to develop them.

The total entrainment rate above TDH is then modeled according to the entrainment rate per size of particles, and it is defined with Equation 25

$E_r = \sum_1^n x_i E_i^\infty$	Equation 25
---------------------------------	-------------

With:

- E_r : total entrainment rate (kg/m²/s)
- x_i : weight fraction of particles in fluidized bed having a diameter $d_{p,i}$
- E_i^∞ : entrainment rate of particles having a diameter $d_{p,i}$ rate (kg/m²/s)
- n: number of classes of particle diameters in the fluidized bed

Many correlations exist for the determination of E_i^∞ . Colakyan and Levenspiel [74] proposed the correlation presented in Equation 26 based on experiments on Geldart Group A and Group B particles.

$E_i^\infty = 0.011 \rho_p \left(1 - \frac{V_{t,i}}{U_{sg}} \right)^2$	Equation 26
---	-------------

Choi et al [82] proposed then a correlation based on a wider number of experiments including pressure and temperature effects, it is presented in Equation 27 :

$\frac{E_i^\infty d_p}{\mu_g} = Ar^{0.5} \exp \left(6.92 - 2.11 F_g^{0.303} - \frac{13.1}{F_d^{0.902}} \right)^2$	Equation 27
--	-------------

With :

- $F_g = g d_p (\rho_s - \rho_g)$ gravity force per projection area
- $F_d = K_d \frac{U^2}{2}$ drag force per projection area

Yang [2] and Chew [83] listed many correlations of entrainment rate. These authors compared some of the correlations with experimental data. A great discrepancy in the predicted entrainment was obtained according to the correlation used. An important scatter was also observed in the experimental data according to the authors. These comparisons clearly shows that entrainment modelling and experimental characterization remains a challenging topic where the influence of many parameters such as fines content, temperature, pressure, presence of internals are not clearly characterized and understood.

Finally, clustering effects on particle entrainment were also demonstrated. Geldart and Wong [84] observed the reduction of the particles entrainment rate when injecting fine particles in a Geldart Group A particles fluidized bed. The decrease was explained by the particles cluster formation due to the fines injection, particles cluster having a higher weight than single particles and being less prone to be entrained. Baeyens et al. [85] found similar results where the entrainment rate reached a threshold when decreasing the bed particle size at a diameter between 25 and 40 μm . Then as mentioned before, Cocco et al. [44] observed clusters of particles with a boroscope in the dilute phase of a turbulent bed.

2.4 Effect of pressure and temperature

Most of the experimental studies to characterize circulating fluidized bed are carried out at ambient conditions while industrial processes operate at elevated pressure and temperature. It is therefore necessary to investigate the effect of these two parameters to transpose lab scale results to industrial conditions.

The pressure and temperature affect the gas density and viscosity and therefore affect the interaction between the gas and solid phases. The characteristic such as the minimum, bubbling and turbulent velocities are therefore influenced, studies showing that the consequences are not identical for all particle Geldart fluidization groups. Indeed, the Wen-Yu minimum fluidization correlation shows that viscosity is the most influencing parameter for small particles while density is more influencing for large particles [86]. Therefore, as described by Rowe et al. [87] pressure affects the minimum fluidization velocity for particles higher than 100 microns so mostly Geldart Groups B and D particles. On the other hand, temperature decreases the minimum fluidization velocity for small particles and increases it for large particles. Pressure and temperature also affect the transition to the turbulent flow regime. Cai et al. [58] showed with experiments using particles from Geldart Groups A and B with temperature and pressure varying respectively from 50°C to 450°C and from 1 to 64 atmospheres that temperature increases and pressure decreases the transition to the turbulent regime. Concerning the bed expansion, it was shown that

pressure increases the dense phase voidage for Geldart Group A particles and had not influence for Geldart Group B particles [86]. Botterill et al. [88] found that temperature increases the bed voidage in the dense phase for all Geldart Groups except Group D.

Concerning the bubbles size, it was found that pressure decreases the bubble diameter for Geldart Group A particles while it does not have any influence for Geldart Group B particles [2]. A possible explanation is that more gas goes in the dense emulsion phase when increasing the pressure for Geldart Group A particles and therefore less gas is available for bubbles.

The particles entrainment rate is also greatly affected with an increase of pressure and temperature. Indeed, increasing the pressure and temperature leads to respectively a higher gas density and a higher gas viscosity which leads to an increase of the drag force between the gas and particles and therefore entrainment is increased. Chan and Knowlton [79] confirmed this mechanism with a significant increase of the entrainment rate with the pressure increase while Findley and Knowlton [86] confirmed the influence of the gas viscosity increase on entrainment.

Finally, Cui et al. [89] stated from their experiments on FCC catalyst at high temperature that particles tested increasingly shift from typical Geldart Group A towards Geldart Group B with increasing temperature due to a decrease of the inter-particle attractive forces and a simultaneous increase of inter-particle repulsive forces.

3 Experimentation and measurement techniques

Experimental characterization of hydrodynamic phenomena is essential in a purpose of modeling for process extrapolation. However multiphase flow in circulating fluidized beds are challenging to characterize with heterogeneous non-stationary moving structures such as gas bubbles and moving particles. The extent of work in the literature is extremely large with different regimes of fluidization investigated with a wide range of solids using multiple experimental techniques. Werther et al. [90], Van Ommen et al. [91], Yates et al. [92] published reviews on experimental techniques used for CFB characterization.

The purpose of this chapter is to discuss the different type of experimental techniques according to the scale of interest with first the characterization of macro scale hydrodynamic descriptors such as bed level, bed averaged gas volume fraction, and second the characterization of local parameters like gas and particles voidage and velocities. The challenges related to local measurements are also highlighted.

3.1 Global hydrodynamic characterization

A first challenge when investigating CFB systems is their characterization at a global scale, where macro-scale hydrodynamic descriptors are investigated.

The first and easy method to characterize the overall circulating fluidized beds hydrodynamic is flow observations. It is also important to point that such observations are most of the time carried out at ambient conditions where the implementation of transparent walls is possible. Flow visualization can help appreciating the bed hydrodynamic behavior through the different fluidization regimes transitions. Interesting phenomena can be observed such as bubble bursting at the bed surface in bubbling regimes [74], bed defluidization when interrupting the gas injection, the particles entrainment versus the gas velocity increase, etc. Flow visualization therefore helps understanding the fluidized bed hydrodynamic from a qualitative point of view and in some cases it can also confirm other measurements such as the bed level.

The most common experimental technique is then the use of pressure probes connected on the vessel wall in order to measure the pressure drop generated by the flow. This robust and easy to implement technique is used on industrial processes to follow global hydrodynamic parameters [90]. As described in Chapter II-2, the time averaged pressure drop allows getting the bed expansion and the average gas volume fraction in fluidized beds, it also allows distinguishing the acceleration and fully developed regions in transport regime risers. The time analysis of the pressure drop signal allows getting useful information as well. As mentioned before, the transition to the turbulent regime is measure with the peak of pressure fluctuations. Issangya et al. [63] also demonstrated the detection of bed gas by-passing phenomenon evaluating the bed pressure drop fluctuations. Pressure probes appears to be a robust and simple measurement technique however some issues need to be faced when carrying out such measurements in fluidized beds. Van Ommen et al. [91] reported the importance of pressure transducer dimensions in order to avoid resonance effects. They also highlighted the issue of pressure ports plugging due to particles infiltration and therefore the necessity of using a constant flush with a porous media to avoid particle blockage. Bi et al. [59] then demonstrated the influence of such porous media with flushing systems on the pressure fluctuations with a change of amplitude depending on the pressure drop generated by the porous media. This type of issue illustrates the challenge of fluidized bed experimental characterization where even measurements which appear to be easy to implement should be treated with great care.

Tracing is another technique for global hydrodynamic characterization. Tracer injection in a multiphase flow reactor and its time evolution measurement at various locations allows studying the hydrodynamic behavior of the phase traced. Once injected, the tracer evolution versus time is measured and it can then be modeled with theoretical flow models (plug-flow, CSTR, dispersed plug flow, ...) which can also be combined. Sane et al. [93] and Ege et al. [94] used this technique at laboratory scale in order to describe the gas phase hydrodynamic in a respectively bubbling and turbulent fluidized bed. Gauthier et al. [1] used radioactive tracing on an industrial FCC unit to characterize the gas hydrodynamic in a gas particles separator. The authors pointed out the challenges related to the implementation of such a technique at industrial scale with first the management of radioactive elements and second the careful implementation of the probes in order to describe the gas flow in the best way. Indeed, tracing is a standard method widely used in the chemical engineering field. However, its implementation in circulating fluidized bed is challenging where the presence of particles and the relative short flow characteristic time bring to the use of specific tracer injection and sampling methods.

Fluidized bed particles entrainment can also be characterized on a global hydrodynamic point of view. For this purpose, the entrained flux of particles recovered into the cyclone is measured by momentarily interrupting the particles return into the bed. Colakyan et al. [74] used a butterfly valve at the bottom of the cyclone return dipleg to momentarily orientate the flux of recovered particles toward a weighting scale. It is important which such technique to make sure that while interrupting the circulation of particles, the bed level is not decreased significantly since it would directly affect the bed TDH and therefore the entrainment flux itself. High entrainment fluxes are thus difficult to measure with this technique.

3.2 Local characterization

Global hydrodynamic descriptors such as bed level and density, entrainment, phase tracing descriptions are essential for hydrodynamic modeling. However local CFB characterization has shown flow heterogeneity with gradient of velocities and concentrations in fluidized beds and risers [1,26]. Therefore for rigorous hydrodynamic modeling such as Computational Fluid Dynamic simulations where non-stationary flows are simulated in three dimensions, local phase voidage and velocities are essential to fully estimate the model validity.

Local measurements are generally complex for multiphase CFB reactors. Indeed the flow opacity and the non-stationary moving structures make the estimation of local parameters difficult. To tackle this difficulty, advanced experimental techniques are used and can be split into two categories:

- The invasive techniques where probes are inserted inside the flow. Measurements are often carried out at different positions on a long period in order to have representative averaged values. It is important to evaluate the probes invasiveness effects with such techniques. Cocco et al. [95] discussed the effect of particles accumulation around an optical fiber probe in a riser transport regime flow while Tebianian [96] showed that the fiber optical probe presence did not affect the flow in a fluidized bed using X-Ray tomography.
- The non-invasive techniques where probes are located outside the flow with for example tomography methods (Electrical Capacitance Tomography, X-ray Tomography).

Table I-2 present a non-exhaustive list of experimental techniques used for CFB local hydrodynamic characterization. For more details, one can refer to the literature reviews on experimental techniques in CFB mentioned above.

Table I-2– Local measurements techniques for CFB local hydrodynamic characterization

<u>Technique</u>	<u>Probe</u>	<u>Measurements and principle</u>
Invasive	Fiber optical probes	Measurement of gas/particles voidage and velocity. Measurement of gas bubbles properties Based on the intensity signal measurement of a light source reflected on particles, the light intensity being proportional to the solid concentration [97]
	Capacitance probe	Measurement of gas/particles voidage and velocity. Measurement of gas bubbles properties Based on the capacitance measurement between two closely space electrodes, the signal intensity being proportional to the solid concentration
	Boroscope	Measurement of particles velocity Based on high frequency imaging and image particle tracking
	Extraction probes or isokinetic probes	Measurement of local solid fluxes Based on iso-kinetic sampling where the gas velocity at the tip of the extraction probe is equal to the measured gas flow velocity
Non-invasive	Electrical capacitance tomography	Measurement of gas/particles voidage. Measurement of gas bubbles properties Based on capacitance measurement between electrodes located around the vessel with dynamic electrodes excitation and their corresponding capacitance measurement with non-excited electrodes.
	X-ray, Gamma Ray tomography	Measurement of gas/particles voidage. Measurement of gas bubbles properties Based on the attenuation of a radioactive source signal located on the opposite side of the signal detectors.
	Radioactive Particle tracking	Measurement of particle velocity Based on the attenuation of moving radioactive particles measured by detectors located outside of the vessel

All these techniques come with complex signal post-processing which depends on the theory behind the experimental method but also on the calibration procedure [90–92]. Calibration is usually difficult for CFB experiments where it is easy to calibrate probes for maximum solid concentration with a fixed packed bed and for minimum solid concentration with an empty bed but where it is difficult to produce controlled conditions of solid concentrations between these two configurations. For example, different methods are used to calibrate optical fiber signals as reported by Dubrawski et al. [98] with some authors calibrating their probe on a fixed bed mixture of particles of interest with black particles to mimic void, others calibrating their probe in a stirred mixture of water and particles.

Then, for the same experimental technique, different methods are reported to obtain the hydrodynamic parameter of interest. With tomography techniques, different image reconstruction algorithms can be applied as reported by Van Ommen et al. [91]. With optical fiber probes, some authors used a direct conversion from the probes signal to the particle volume fraction based on their calibration as reported by Dubrawski et al. [98], on the other hand Schweitzer et al. [97] differentiated a bubble and an emulsion region on a signal histogram to get the mean particle volume fraction.

Tebianian et al. [96] carried out an interesting comparison between different experimental techniques for local particles voidage and velocity characterization in a fluidized bed of FCC and sand particles. They used the following measurement techniques: pressure probe, optical fiber, electrical capacitance tomography, X-Ray tomography and boroscope image analysis. They demonstrated that all techniques gave rather good qualitative results with for example the same trends obtain when investigating the bed voidage versus gas fluidization velocity. However the quantitative comparisons showed rather important discrepancies especially when measuring particle velocities. This study clearly highlights the challenge of measuring quantitatively local hydrodynamic parameters in CFBs, where results obtained should always be treated carefully and where trends might be the most important result to look at when comparing experimental data with models. Different authors reported the importance of connecting the measured local hydrodynamic parameters with macro-scale descriptors with for example the comparison of integrated radial profiles of gas volume fraction with the mean gas volume fraction obtained by pressure probes measurements [97,99]. Herbert et al. [100] also compared the global solid flux in a downer reactor with local particle concentration and velocity obtained with fiber optical probes. These types of comparison allow checking the pertinence of local measurements.

4 Computational Fluid Dynamic for gas particles flow

From the two previous chapters, the reader can apprehend the challenge of characterizing fluidization where local physical phenomena are difficult to apprehend and where correlative approaches are often used. In this context, Computational Fluid Dynamic (CFD) tools became popular for multiphase chemical engineering applications around 1990 with the work of Gidaspow et al. [101,102]. The authors indeed demonstrated the potential of using a multidimensional fluid mechanic approach to better characterize multiphase flows. CFD tools are nowadays used for the understanding and the characterization of CFB hydrodynamic from particles to industrial scales [103,104]. Indeed with the improvement of computational power, CFD tools allow characterizing flows in three dimensions on large scales taking into account complex geometrical features such as distributors and internals. However, CFD modeling of multiphase flow remains challenging with many developments on-going. The modeling of the key gas/particles and particle/particles interactions remains complex and is a source of great interest where models allowing predictions on a wide range of operating conditions have not yet been found. In this context, many gas/particles and particles/particles interactions model are available, authors often investigating these models predictions on a specified experiment with a rather narrow operating conditions range.

This chapter first presents the different approaches available for the modeling of gas/particles flow with a focus on the Euler/Euler and Multiphase Particle in Cell (MP-PIC) methods which are later on used in

this PhD project. A discussion is then carried out on the main differences between these two approaches followed by a focus on the different model available for gas/particles interactions.

F.Euzenat [104] summarized the different scales of gas /particles CFD investigations in an explicit sketch presented in Figure I-14.

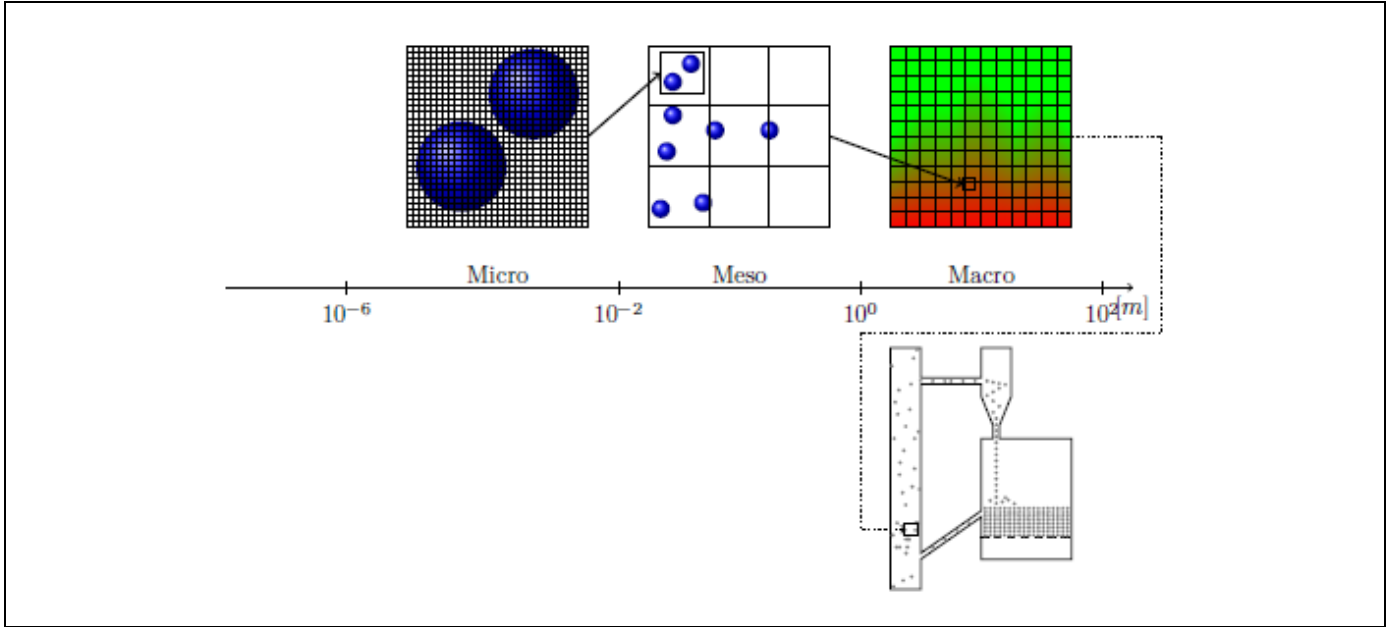


Figure I-14:Multi scales simulations of gas/particles flow from F.Euzenat[104]

Three different scales are identified:

- First, the micro scale where the CFD flow resolution is made at the particle size level through the so-called Direct Numerical Simulation (DNS). For this purpose, the mesh used to discretize the geometry volume is smaller than the particles size as shown in Figure I-14. The gas phase is considered continuous and resolved using an Eulerian approach. Particles are tracked individually using a Lagrangian approach, particle-particle and particle-wall collisions are detected and modeled with for example hard or soft sphere collisions models. No closure law is needed to compute the interaction force between the gas and particles since the fine mesh allows integrating this force over the particles surface. With the current computational power, this type of approach allows simulating in the order of 10^3 particles [104].
- Second, the meso-scale where the flow resolution is made at a larger scale than the particle size with a larger mesh as shown in Figure I-14. This approach is communally called CFD-DEM method where similarly to the DNS approach gas is treated as a continuum with an Eulerian approach and particles are tracked individually using a Lagrangian approach with collisions detected and modeled. The difference is that the force between gas and particles cannot be directly computed from integrating forces on particles surface since the mesh size is larger than particles. An interphase exchange closure law is therefore needed, this closure law being referred as the drag law. With the current computational power, this type of approach allows simulating in the order of 10^8 to 10^9 particles [104].
- Third, the macro scale where both gas and particles phase are considered as a continuum using an Eulerian approach. The modeling of the solid phase in an Eulerian frame is challenging especially for the solid phase “viscosity” representation via the solid stress tensor. For this purpose, the Kinetic Theory of Granular Flow (KTGF) [7] is often used, this theory is detailed below. This type of approach does not have a limit in term of particle number, the computational limitation coming from the number of cells in the mesh.

Each approach presents advantages and challenges. The DNS approach allows simulating directly the gas/particles and particles/particles interactions, however the meshing of geometry with moving particles and the modeling of particles/particles contact forces remain challenging. The CFD-DEM approach allows simulating larger geometry while simulating the contacts between particles. The modeling of the gas/particles interaction as well as the particles/particles forces however remains a source of development. Finally, the Euler/Euler approach allows simulating large and complex geometry but as mentioned before the closure models are still a source of intensive development.

Table I-3 presents a particle number estimation for fluidized bed going from lab scale to industrial scales. Particles are assumed to be monosized and spherical at a volume concentration of 0.52. Two sizes are investigated with first sphere of 75 microns corresponding to Geldart Group A particles and sphere of 250 microns corresponding to Geldart Group B particles.

Table I-3– Particles number assuming sphere of monosized particles at a volume concentration of 0.52

Bed Diameter (m)	0.2	1	5	10
Bed Length over Diameter Ratio	2.5	3	1.5	0.7
Bed length (m)	0.5	3	7.5	7
Bed volume (m ³)	0.02	2.4	147.3	549.8
Number of particles with Particle size of 75 microns	3.07E+10	4.60E+12	2.88E+14	1.07E+15
Number of particles with Particle size of 250 microns	1.01E+09	1.51E+11	9.42E+12	3.52E+13

It is obvious when looking at Table I-3 that the DNS and CFD-DEM methods are not suitable for CFD simulations of fluidized beds from lab to industrial scales with Geldart Groups A and B solids where the number of particles exceeds the capacity of these approaches. It is however important to point out that these micro and meso scale approaches are intensively used in the literature to better characterize the gas/particles and particles/particles interactions in order to provide closure models for macro scale approaches [104,105].

A focus is now given on macro scale Eulerian methods which are used in this PhD project, with first the Euler/Euler approach using the Kinetic Theory of Granular Flow (KTGF) and second the Multiphase Particle In Cell approach.

4.1 Euler/Euler with KTGF approach

The most common approach when simulating fluidized bed in an Eulerian frame is the use of the Kinetic Theory of Granular Flow (KTGF) in order to model the particle phase stress tensor. The equations from the work of Gidaspow [7] are presented below. In all equations, variables are averaged over a region that is large compared with the particle spacing but much smaller than the flow domain.

First, conservation equation of both gas and solid phases is presented in Equation 28, where “m” stands for both gas and solid phases.

$\frac{\partial(\alpha_m \rho_m)}{\partial t} + \nabla \cdot (\alpha_m \rho_m \overline{u_m}) = 0$	Equation 28
--	-------------

The Equation 29 and Equation 30 present respectively the gas momentum balance equation and its stress force tensor τ_g .

$\frac{\partial(\alpha_g \rho_g \overline{u_g})}{\partial t} + \nabla \cdot (\alpha_g \rho_g \overline{u_g} \overline{u_g}) = -\alpha_g \nabla P + \alpha_g \rho_g \vec{g} + \nabla(\tau_g) + K_d(\overline{u_g} - \overline{u_s})$	Equation 29
---	-------------

$\tau_g = \mu_g (\nabla \overline{u_g} + \nabla^T \overline{u_g}) - \frac{2}{3} \mu_g \nabla \overline{u_g} I$	Equation 30
--	-------------

A turbulence contribution can also be added in the gas stress force tensor with a turbulent viscosity according to the Boussinesq approach.

The determination of the gas/particles exchange term K_d is crucial for CFB simulations and it has been widely investigated in the literature. This aspect is discussed in Chapter I.4.4.

The Equation 31 and Equation 32 present respectively the solid momentum balance equation and its stress force tensor τ_s .

$\frac{\partial(\alpha_s \rho_s \overline{u_s})}{\partial t} + \nabla \cdot (\alpha_s \rho_s \overline{u_s} \overline{u_s}) = -\alpha_s \nabla P + \nabla P_s + \alpha_s \rho_s \vec{g} + \nabla(\tau_s) + K_d(\overline{u_s} - \overline{u_g})$	Equation 31
--	-------------

$\tau_s = \mu_s (\nabla \overline{u_s} + \nabla^T \overline{u_s}) + \left(\lambda_s - \frac{2}{3} \mu_s \right) \nabla \overline{u_s} I$	Equation 32
---	-------------

Different terms appear compared to the gas phase equations in order to model the solid phase internal forces with the solid pressure P_s , the solid shear viscosity μ_s and the solid bulk viscosity λ_s , representing the resistance of the solid to compression. The expressions of these terms presented below are the one used in this PhD project. One can refer to [106] for other models formulation available.

The Lun solid pressure expression is presented with Equation 33:

$P_s = \rho_s \alpha_s \theta_s + 2\rho_s (1 + e_s) \alpha_s^2 g_{0,s} \theta_s$	Equation 33
--	-------------

Where e_s is the coefficient of restitution for particles collisions, θ_s is the granular temperature defined in Equation 34 from the solid phase velocity fluctuations and $g_{0,s}$ is the radial distribution which describes the probability of particle collisions which becomes infinite at the highest solid concentration. Different expressions exist for the radial distribution, Equation 35 presents the Sinclair Jackson formulation used in this thesis.

$\theta_s = \frac{1}{3} \langle \overline{u_s} \rangle^2$	Equation 34
---	-------------

$g_{0,s} = \frac{1}{1 - \left(\frac{\alpha_s}{\alpha_{s,max}} \right)^{1/3}}$	Equation 35
--	-------------

The shear viscosity is expressed in Equation 36 with the contributions of the collisions and kinetics viscosities expressed respectively in Equation 37 and Equation 38 with the Gidaspow formulation.

$\mu_s = \mu_{s,col} + \mu_{s,kin}$	Equation 36
-------------------------------------	-------------

$\mu_{s,col} = \frac{4}{5} \alpha_s^2 \rho_s d_p g_{0,s} (1 + e_s) \sqrt{\frac{\theta_s}{\pi}}$	Equation 37
---	-------------

$\mu_{s,kin} = \frac{10 \sqrt{\pi \theta_s}}{96 g_{0,s} (1 + e_s)} \rho_s d_p \left[1 + \frac{4}{5} \alpha_s g_{0,s} \right]^2$	Equation 38
--	-------------

The bulk viscosity is expressed in Equation 39 with the Shaeffer formulation

$\lambda_s = \frac{4}{3} \alpha_s^2 \rho_s d_p g_{0,s} (1 + e_s) \sqrt{\frac{\theta_s}{\pi}}$	Equation 39
---	-------------

The granular temperature is described with a transport equation presented in Equation 40. It is derived by writing the Boltzmann integral-differential conservation equation for the probability distribution of random particle motion [7].

$\frac{3}{2} \left[\frac{\partial(\alpha_s \rho_s \theta_s)}{\partial t} + \nabla \cdot (\alpha_s \rho_s \vec{u}_s \theta_s) \right] = (-P_s + \tau_s) : \nabla \vec{u}_s + \nabla(K_s \nabla \theta_s) - \gamma_s - J_{vis}$	Equation 40
--	-------------

With:

- $(-P_s + \tau_s) : \nabla \vec{u}_s$ Production term
- $+\nabla(K_s \nabla \theta_s)$ Granular energy diffusion flux
- $-\gamma_s$ Dissipation due to inelastic collisions
- $-J_{vis}$ Dissipation due to fluid viscosity

The diffusion coefficient K_s is expressed with Equation 41 with the Gidaspow formulation

$K_s = \frac{150 \sqrt{\pi \theta_s} \rho_s d_p}{384 g_{0,s} (1 + e_s)} \left[1 + \frac{6}{5} \alpha_s g_{0,s} (1 + e_s) \right]^2 + 2 \alpha_s^2 \rho_s d_p g_{0,s} (1 + e_s) \sqrt{\frac{\theta_s}{\pi}}$	Equation 41
--	-------------

The dissipation due to inelastic collisions γ_s is expressed with Equation 42 with the Shaeffer formulation

$\gamma_s = \frac{12(1 - e_s^2) g_{0,s}}{d_p \sqrt{\pi}} \rho_s \alpha_s^2 (\theta_s)^{3/2}$	Equation 42
--	-------------

The dissipation due to fluid viscosity J_{vis} is expressed with Equation 43 with the Shaeffer formulation

$J_{vis} = 3K_s \theta_s$	Equation 43
---------------------------	-------------

The Euler/Euler with KTGF approach allows considering the particles phase as a continuum thanks to a complex modeling of the particle-particle interactions. It is important to point out that this model takes into account a single particle diameter which is usually taken as the mean or Sauter diameter for particles

with a distribution of sizes. If several particles diameter should be considered with such model, several particle phases must be defined for each particle diameter multiplying the number of equations by the number of phases. This type of approach can become time and computational resource consuming. Moreover interactions between the solid phases should also be defined and modeled.

4.2 Multiphase Particle In Cell (MP-PIC) approach

The MP-PIC approach has been described by Andrew, O'Rourke and Snider [14,107]. The main advantage of this method is that it allows taking into account particle size distributional for a low computation cost. For this purpose, authors use a so-called "hybrid Eulerian/Lagrangian" approach for the particles phase as detailed below.

The gas phase is considered in an Eulerian frame as the Euler/Euler with KTGF approach. The gas mass and momentum balance equations are therefore the same as shown with Equation 44 to Equation 46.

$\frac{\partial(\alpha_g \rho_g)}{\partial t} + \nabla \cdot (\alpha_g \rho_g \vec{u}_g) = 0$	Equation 44
---	-------------

$\frac{\partial(\alpha_g \rho_g \vec{u}_g)}{\partial t} + \nabla \cdot (\alpha_g \rho_g \vec{u}_g \vec{u}_g) = -\alpha_g \nabla P + \alpha_g \rho_g \vec{g} + \nabla(\tau_g) + F$	Equation 45
---	-------------

$\tau_g = \mu_g (\nabla \vec{u}_g + \nabla^T \vec{u}_g) - \frac{2}{3} \mu_g \nabla \vec{u}_g I$	Equation 46
---	-------------

The solid phase mass and momentum equations are derived from the Liouville equation presented in Equation 47 which describes the transport of a particle probability distribution function $f(x,v,m,t)$ in an Eulerian frame. $f(x,u_p,m,t)$ represents the probability of having particles at a position "x" with a velocity " u_p ", with a mass "m" at a time "t".

$\frac{\partial f}{\partial t} + \nabla_x \cdot (f \vec{u}_p) + \nabla_{u_p} \cdot (f A) = 0$ <p style="text-align: center;">with</p> $A = K_d (\vec{u}_g - \vec{u}_p) - \frac{1}{\rho_p} \nabla P + g - \frac{1}{\alpha_s \rho_s} \nabla \tau$	Equation 47
---	-------------

The mass and momentum balance equations for the particle phase can be obtained by taking the moments of Equation 47 as explained by O'Rourke , they are presented respectively in Equation 48 and Equation 49.

$\frac{\partial(\alpha_s \rho_s)}{\partial t} + \nabla \cdot (\alpha_s \rho_s \vec{u}_s) = 0$	Equation 48
---	-------------

$\begin{aligned} \frac{\partial(\alpha_s \rho_s \vec{u}_s)}{\partial t} + \nabla \cdot (\alpha_s \rho_s \vec{u}_s \vec{u}_s) + \nabla \tau + \alpha_s \nabla P \\ = \alpha_s \rho_s g + \iint f m K_d (\vec{u}_g - \vec{u}_p) dm du_p \\ - \nabla \left[\iint f m (\vec{u}_p - \vec{u}_s) (\vec{u}_p - \vec{u}_s) dm dv \right] \end{aligned}$	Equation 49
---	-------------

With the solid volume fraction and the mean solid velocity defined by respectively Equation 50 and Equation 51.

$\alpha_s = \iint f \frac{m}{\rho_s} dm du_p \text{ with}$ $\alpha_g + \alpha_p = 1$	Equation 50
--	-------------

$\vec{u}_s = \frac{1}{\alpha_s \rho_s} \iint f m \vec{u}_p dm du_p$	Equation 51
---	-------------

The second term on the right hand of Equation 49 corresponds to the interphase drag momentum exchange while the third term accounts for the kinematic stress from the particle velocity fluctuations with respect to the mean solid velocity. All this terms are expressed with the integration of the particles probability distribution function $f(x, u_p, m, t)$.

The particle normal stress model τ is expressed with Equation 52 [108].

$\tau = P_s \frac{\alpha_s^\beta}{\max[(\alpha_{s,max} - \alpha_s), \epsilon_{barracuda}(1 - \alpha_s)]}$	Equation 52
---	-------------

With:

P_s	Constant of pressure (Pa)
β	Model constant recommended to be between 2 and 5
$\alpha_{s,max}$	Maximum close packing solid volume fraction
$\epsilon_{barracuda}$	Small number in the order of 10^{-7} to remove singularity

The MP-PIC method consists then in using a hybrid Eulerian/Lagrangian approach to solve the gas and particles mass and momentum balances. For this purpose, the particles distribution function $f(x, u_p, m, t)$ is discretized into clouds of particles, each cloud having a certain number of real particles N_p with the same diameter, mass and velocity. The number of real particles per cloud therefore becomes a simulation parameter. Then at a given simulation time t , clouds properties (N_p , velocity, mass, diameter) are interpolated to the Eulerian mesh using interpolation functions [14,107]. The integrals of the distribution function in Equation 49 to Equation 51 become then summations over interpolated clouds properties. From this point, gas and solid phases mass and momentum equations are solved to get flow properties at $t+\Delta t$ on the Eulerian mesh. Once the solution found, clouds position is updated at $t+\Delta t$ using Equation 53 and Equation 54 where Eulerian mesh flow properties such as the gas velocity, the pressure and particle stress are interpolated to the clouds positions.

$x_{cloud}^{n+1} = x_{cloud}^n + \Delta t u_{cloud}^{n+1}$	Equation 53
--	-------------

$u_{cloud}^{n+1} = \frac{u_{cloud}^n + \Delta t \left[K_d u_{g,cloud}^{n+1} - \frac{1}{\rho_p} \nabla P_{cloud}^{n+1} + g - \frac{1}{\theta_p \rho_p} \nabla \tau_{cloud}^{n+1} \right]}{1 + \Delta t K_d}$	Equation 54
--	-------------

With:

$u_{g,cloud}^{n+1}$	gas velocity at $t+\Delta t$ interpolated to the cloud position
P_{cloud}^{n+1}	pressure at $t+\Delta t$ interpolated to the cloud position
τ_{cloud}^{n+1}	solid stress at $t+\Delta t$ interpolated to the cloud position

As explained by Snider [14], Equation 54 is first used in the Eulerian resolution of the momentum balances to express the cloud particle velocity at $t+ \Delta t$ with to Eulerian flow properties. Snider also pointed out that for this resolution, the solid volume fraction α_s at $t+ \Delta t$ is not implicitly coupled with the parcels positions at $t+ \Delta t$, meaning that at $t+ \Delta t$ there is a difference between the Eulerian solid volume fraction and the solid volume fraction calculated from the updated clouds positions.

4.3 Discussion on Euler/Euler KTGF and MP-PIC approaches

This chapter discusses the comparison of the Euler/Euler KTGF and the MP-PIC approaches from the equations presented in Chapter II-4.2 and Chapter II-4.3.

First concerning the inter-particle forces, one can notice the more advanced modeling in term of physical phenomena considered with the Euler/Euler KTGF. Indeed, this approach takes into account different parameters such as solid pressure, solid bulk and shear viscosities all depending of the granular temperature which is transported with a dedicated equation taking into account physical phenomena such as granular energy diffusion, inelastic particles collisions and fluid viscosity dissipations. On the other hand, the MP-PIC approach presents a rather simplistic modeling of particle interactions with an orthogonal stress tensor correlative model and with the kinematic stress from the particle velocity fluctuations contribution taken into account. As described with the last term of Equation 49, this kinematic stress is calculated with the following term, where u_p is the particle velocity and u_s is the mean volume particle velocity defined in Equation 51:

$\text{MP - PIC Kinematic stress} = \nabla \left[\iint f m (\vec{u}_p - \vec{u}_s) (\vec{u}_p - \vec{u}_s) d m d v \right]$	Equation 55
--	-------------

As explained in Chapter II-4.3, clouds are used to discretize the distribution function and their properties are interpolated on the Eulerian mesh, the integral term presented in Equation 55 becoming a summation on interpolated clouds properties. It is then interesting to analyze the difference between the mean clouds velocity and the clouds velocity presented in Equation 54. Indeed, from this equation, one can see that the cloud velocity is calculated from the drag, pressure and particle stress contributions. For clouds being close to each other in space, the pressure and particle stress contributions can be considered similar since they are interpolated from the Eulerian mesh to the clouds positions. Therefore, the only term which can create a difference for the velocity calculation of two clouds being close to each other is the drag term K_d in Equation 54. Thus, the kinematic stress with the difference between mean particles velocity and particle velocity of Equation 55 is mainly influence by drag which is itself influence by particle size for a given drag correlation.

The second point of discussion is the difference in term of particle size taken into account in the two approaches. Indeed, with the Euler/Euler KTGF method, only one representative diameter is considered. As explained before, several classes of diameter can be considered by having different solid phases, the number of equations solved being multiplied by the number of phases. This method is time consuming in term of computational power moreover interactions between the different solid phases must also be described. Concerning the MP-PIC approach, the full particle size distribution can be taken into account for a low computational cost.

It appears that each approach have its own advantage. The Euler/Euler KTGF method describes with a more complex model the particle interactions but only a representative particle diameter is considered while the MP-PIC method takes into account the full particle size distribution through the population of clouds but with a rather simplistic modeling of particles interactions. One can then wonder if the combination of the two approaches could be possible with the more complex particles interaction model from the Euler/Euler KTGF approach incorporated in the MP-PIC approach.

To conclude, both approaches are used on the same simulation cases in this dissertation. It should be added that these two approaches are the most commonly used in the literature for gas/particles flow simulations, investigations and development being mainly carried out on the gas/particles and particles/particles interactions models.

4.4 Drag closure laws

Both Euler/Euler KTGF and MP-PIC approaches use a drag closure law through the term K_d for the gas/particles exchange in the momentum Equation 31 and Equation 49. The modeling of K_d has been widely investigated and proven crucial for CFBs hydrodynamic predictions [7,8,10,12,26,109–112].

Different common drag closure laws are often mentioned in the literature, a non-exhaustive list being presented in Table I-4.

Table I-4– Common drag closure laws

Ergun model [113]	$K_d = \frac{150\alpha_s^2\mu_g}{\alpha_g^2 d_p^2} + \frac{1.75\alpha_s\rho_g}{\alpha_g^2 d_p} u_g - u_s $
Wen-Yu model [114]	$K_d = \frac{3}{4} Cd \frac{\alpha_s\alpha_g\rho_g u_g - u_s }{d_p} \alpha_g^{-2.65}$ <p style="text-align: center;">with</p> $Cd = \frac{24}{Re_p} (1 + 0.15Re_p^{0.687}) \text{ for } Re_p < 1000 ; Cd = 0.44 \text{ for } Re_p \geq 1000$ $Re_p = \frac{\rho_g d_p u_g - u_s }{\mu_g}$
Gidaspow model [7]	$K_d = \text{Ergun model for } \alpha_s > 0.2 \text{ and } K_d = \text{WenYu model for } \alpha_s < 0.2 \text{ (no physical continuity at the transition between the Ergun and Wen-Yu model)}$
Syamlal&O'Brien model [115]	$K_d = \frac{3 Cd \alpha_s \alpha_g \rho_g u_g - u_s }{4 d_p v_{rs}^2}$ <p style="text-align: center;">with</p> $v_{rs} = 0.5(A - 0.06Re_p + \sqrt{(0.06Re_p)^2 + 0.12Re_p(2B - 1) + A^2}) +$ <p style="text-align: center;">with $A = \alpha_g^{4.14}; B = 0.8\alpha_g^{1.28} \text{ for } \alpha_g \leq 0.85 \text{ and } B = \alpha_g^{2.65} \text{ for } \alpha_g \geq 0.85$</p>

Simulations with Geldart Group A particles are often reported to fail using these common drag laws [6]. Indeed, authors showed for Geldart Group A fluidized bed simulations that common drag laws overestimate the momentum exchange between gas and solid phases with over prediction of the bed expansion in bubbling regimes [109] and no dense phase predicted for turbulent bed simulations as shown by Li et al. [10]. A first simple corrective approach proposed by Cocco et al. [116] in order to reduce the gas/particles drag force was to multiply the drag coefficient K_d by a factor between 0 and 1, the factor being set according to experimental data. Then two schools of thoughts can be found in the literature to explain the particle drag overestimation phenomena. First authors claim that the formation of clusters due to the inter-particle forces in the fluidized bed changes the effective diameter of the solid phase and the drag closure law should be calculated with this larger effective diameter. Li et al. [10] simulated a turbulent bed of FCC particles having a mean diameter of 60 microns. They used an effective particle diameter of 300 microns in their drag closure law at high solid volume fraction where clustering is

supposed to occur and an effective diameter equals to the particles mean diameter of 60 microns at low solid volume fraction. With this approach they managed to predict the bed density of their turbulent bed. Motlagh et al. [12] used a more complex physical clustering model based on a force balance between inter-particle forces to compute an effective diameter for the drag closure law. With this method they managed to predict with accuracy bed expansions for different superficial gas velocity in a FCC fluidized bed. The other school of thought claims that the overestimation of the particles drag comes from the non-resolved structure when using a coarse mesh and a large time step. The non-resolved structure refers to the formation of particles streamers or clusters that are due only to hydrodynamic phenomena and not inter-particle forces. Authors developed strategy when they resolve the gas/particles flow with a fine mesh where they can actually solve the structures such as hydrodynamic streamers and cluster. They then develop filter approaches to modify the drag closure law for coarser mesh simulations. Ozel et al. [8] proposed a drag filter formulation with a drift velocity formulation based on the well-resolve simulation of a periodic FCC riser using 17 million cells. Parmentier et al. [117] used the same approach with a well-resolved two dimensional dense fluidized bed. Another method for considering the effect of non-resolved structure on the drag is the Energy Minimization Multi Scale (EMMS) approach proposed by Li [118,119]. This approach consists in considering for the drag calculation, a particle dense cluster phase and a particle dilute phase. Then gas/particles interactions are considered separately in the dense and dilute phases. An additional drag interaction terms is then considered between the particles dense and dilute phases. The consideration of the additional phases brings additional parameters and equations to be solved. The closing of this equation sets is made through the minimization of the mass-specific energy consumption for suspending and transporting particles. Indeed, as stated by Ghadirian et al. [120], the fundamental concept in the EMMS approach is the fact that in a fluidized bed, the gas and solid phase interact with each other so that the net energy transfer between phases is minimized. In their work, Wang et al. [119] showed good agreement with experimental data for their riser simulations using the EMMS drag model.

To conclude, gas/particles drag closure law development remains a challenge with many developments on-going and where models allowing predictions on a wide range of systems and operating conditions have not yet been found.

5 Extrapolation of circulating fluidized bed processes through modelling

Extrapolating the circulating fluidized bed lab scale characterization to the industrial scale is a major challenge and topic of interest for processes performance prediction and trouble-shooting. This chapter presents different modelling methodology for such extrapolation with first the phases flow theory and seconds the use of CFD tools.

5.1 Extrapolation using the two-phase flow theory

The two-phase flow theory consists in representing the different phases or structures of a fluidized bed or riser with theoretical flow models (plug-flow, CSTR, dispersed plug flow, ...). Figure I-15 presents an example of a fluidized bed representation with the distinction of an emulsion, a bubble and a dilute phase used by Davidson et al. [121].

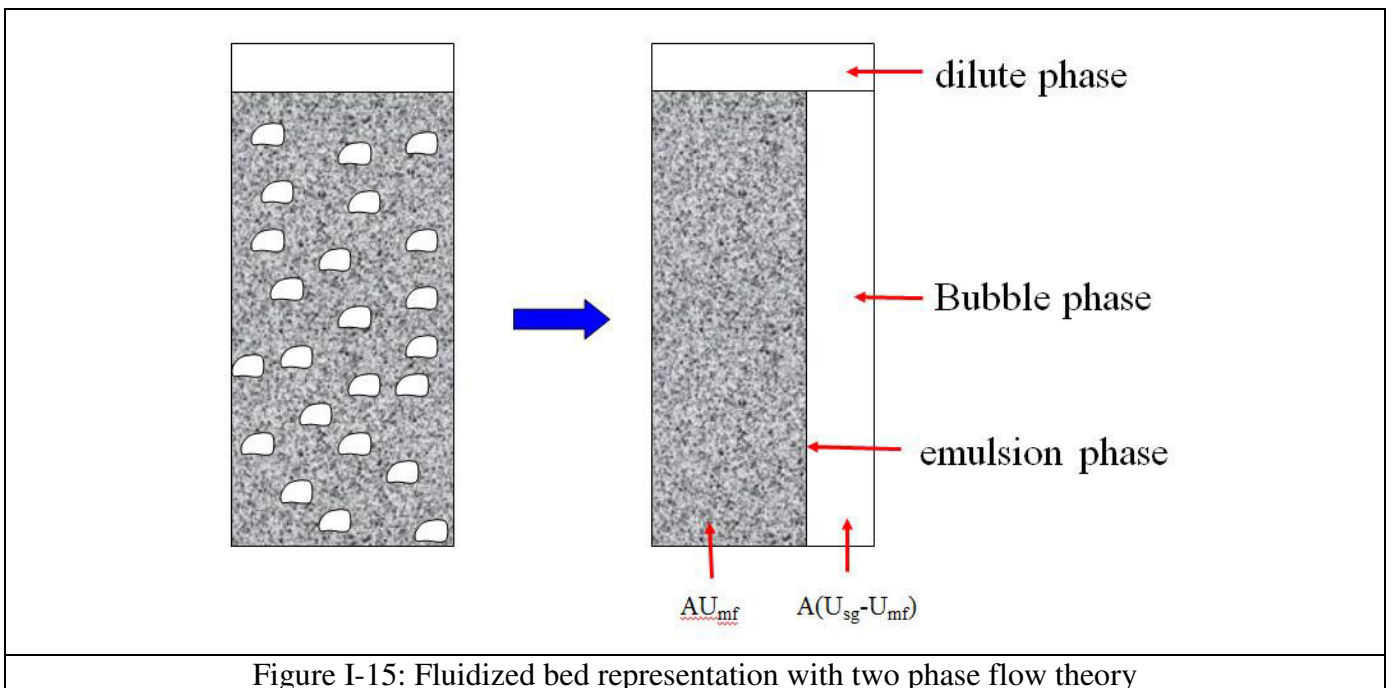


Figure I-15: Fluidized bed representation with two phase flow theory

In this model, authors considered the emulsion phase as a plug dispersed flow at minimum fluidization conditions with a gas volume fraction and a gas velocity of respectively ϵ_{mf} and U_{mf} . The bubble phase is considered as a plug dispersed flow while the dilute phase is considered as a plug flow. Parameters such as bubble diameter and velocity as well as particles entrainment are calculated with correlations developed from experiments as presented in Chapter I.2.2. The main assumption with this model is that all the gas which is not in the emulsion phase at ϵ_{mf} flows under the form of bubbles. More complex models have then been developed with kinetic reactions, heat and mass transfers between the different phases [122]. Lee et al. [123] used a phase theory model similar to Davidson et al. model [121] coupling kinetic and heat balance to simulate an industrial FCC regenerator. They also included a jet grid model to take into account the air distributor effect. The model predicted more qualitative than quantitative results in term of temperature and coke combustion rate. A similar approach was used by Filho et al. [124] to simulate the regenerator of an industrial FCC unit operated by Petrobras. In their hydrodynamic model, they assumed a jet zone above the air injection where no reaction occurs. Good agreement was found between the experimental and predicted regenerator temperatures. Soundararajan et al. [125] used a phase flow theory approach to model Methanol to Olefin (MTO) reactions in a riser. As presented in Figure I-18, they distinguished a gas/particles acceleration zone at the riser bottom followed by an established zone

divided into a core and annulus region. Authors also implemented a riser termination effect on hydrodynamic based on experimental measurements.

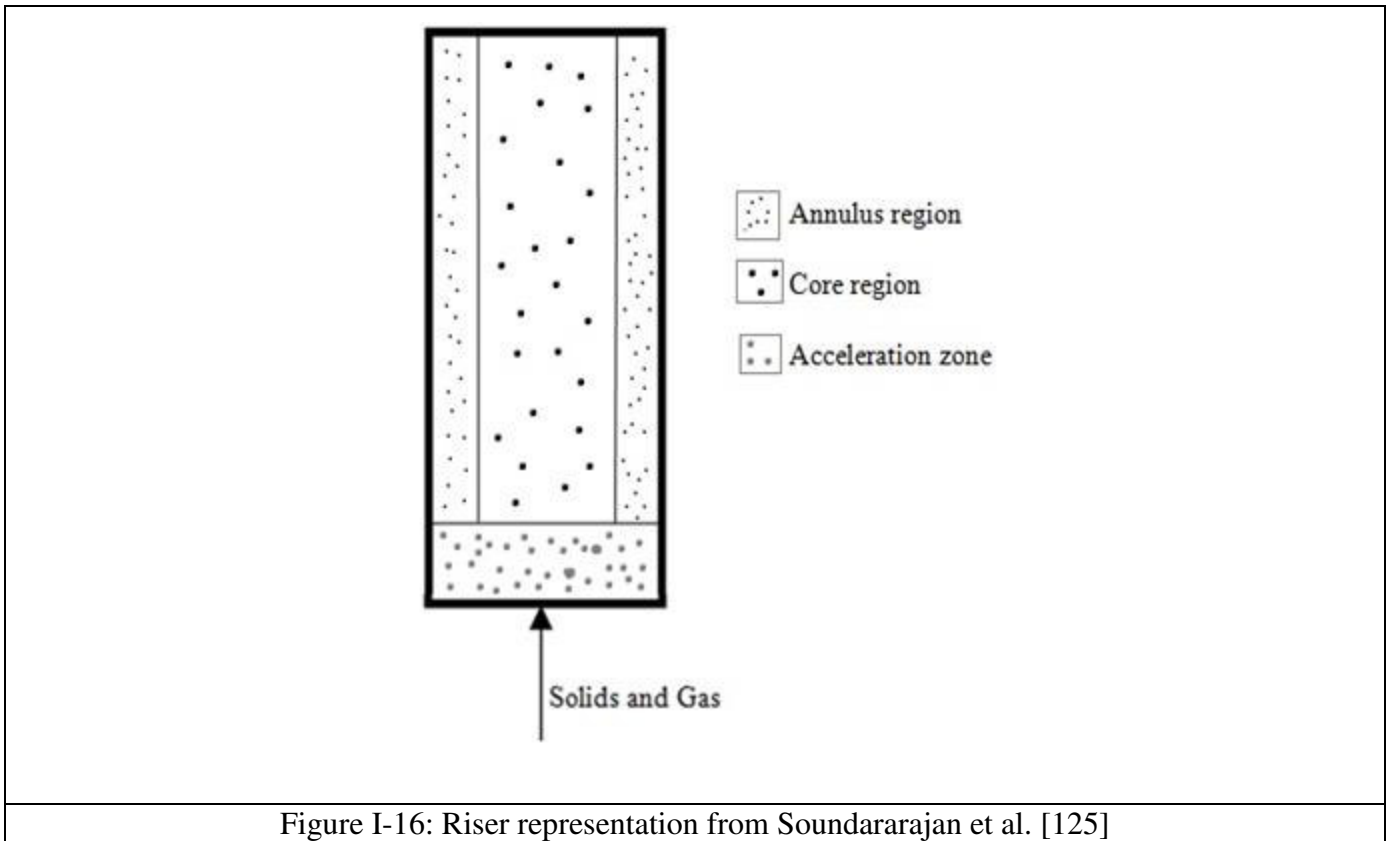


Figure I-16: Riser representation from Soundararajan et al. [125]

The extrapolation capacity of two phase flow theory models depends on the extrapolation capacity of the hydrodynamic, kinetic heat and mass transfers parameters input in the model. Indeed these parameters characterization rely on the experimentation and measurement techniques set up to determine them, the way they have been modeled/correlated and how these modeling/correlations extrapolate to industrial conditions. For example, in fluidized bed modeling shown in Figure I-15, bed expansion will be dependent on the bubble properties (diameter, velocity), these properties being first difficult to characterize experimentally especially in turbulent regime and second it is difficult to assess their extrapolability at industrial conditions. Mass transfer characterization is also crucial when modeling reactive systems. The development of precise mass transfer model is therefore necessary but challenging. This issue is however not investigated in this dissertation.

Finally, two phase flow models allow investigating the extrapolation of global parameters such as bed expansions, entrainment, and reactor yields for reactive systems. However, local information and three-dimensional effects with complex geometries (internals, gas injectors design, solid injections) are difficult to characterize with such a modeling strategy. In this context, CFD tools became another modeling alternative as presented in the next chapter.

5.2 Extrapolation using CFD tools

Compared to phases flow theory, CFD relies on the more fundamental but complex physical modeling of gas/particles and particles/particles interactions as presented in Chapter II-4. Within the last twenty years and the continuous improvement of computational power, CFD tools became a topic of great interest for modeling fluidized beds. The main advantage is that geometrical and three-dimensional effects are directly taken into account with local phases properties determined in the entire simulated geometry. Therefore, CFD tools allow investigating potential design changes as carried out by Lopes et al. [126] who studied the effect of different riser termination for an FCC industrial unit with an Euler/Euler with KTGF approach. CFD tools also allow studying phenomena at industrial scale which are difficult or almost impossible to characterize experimentally on site. Amblard et al. [9] simulated using the MP-PIC approach an industrial FCC regenerator coupling hydrodynamic with a coke combustion kinetic model. Authors highlighted the potential useful insights obtained which are not accessible on the industrial unit in term of gas distribution, temperature profiles and coke combustion rate. However, Amblard et al. also highlighted the difficulty to estimate directly the validity of CFD modeling versus industrial data where only macroscopic daily averaged data are available and where it is difficult to decouple the effects of the different phenomena occurring (hydrodynamic, kinetic, heat transfer).

CFD modeling at industrial scale is therefore challenging for two main reasons, the computational resources available with the limitation of the mesh size that can be used and the estimation of results validity. Indeed, precise investigation of CFD modeling predictions is carried out at laboratory scale where local measurements can be carried out (bed expansion, entrainment rate, local volume fraction and velocities). It should be pointed out that such validations are already not trivial since experimental local characterization can be challenging and should be considered with care as presented in Chapter II-3.2. With lab scale simulations, authors usually investigate the gas/particles and particle/particles interactions models and the results independency with respect to the mesh cell size [10,12,127]. However, due to computational power limitations, it is usually impossible to keep the same cell size between lab scale and industrial scale simulations. Table I-5 presents an estimation of mesh sizes with different hexahedral cell size for vessel diameters from 0.2 meter to 10 meters.

Table I-5– Mesh size estimation for different geometries with hexahedral cells

Vessel Diameter (m)	0.2	1	5	10
Vessel length (m)	1	5	15	25
Vessel volume (m ³)	0.03	3.9	294.5	1963.5
number of cells with hexahedral cells of 0.5 cm	2.51E+05	3.14E+07	2.36E+09	1.57E+10
number of cells with hexahedral cells of 1 cm	3.14E+04	3.93E+06	2.95E+08	1.96E+09
number of cells with hexahedral cells of 5 cm	2.51E+02	3.14E+04	2.36E+06	1.57E+07

Assuming that transient CFD simulations can be obtained in a reasonable time frame with meshes lower than 10 million cells, it is clear from Table I-5 that large industrial scale simulations cannot be run with a mesh size lower than 5 cm. Shah et al. [128] simulated an industrial fluidized bed furnace with cell sizes of 10 cm. They then adjusted the model drag closure law based on the industrial pressure drop measurements. However, one can wonder about the hydrodynamic representativity of such model where the drag closure law had been adjusted based on a global averaged measurement characteristic for one operating condition. Ozel et al. [8] developed a filtered approach to modify their drag and particle/particles models according to the cell size used. Authors evaluated their filtered approach from a

numerical point of view and highlighted that comparisons between filtered simulations and experimental data should also be carried out. Amblard et al. [9] with their simulation of the coke combustion in an industrial FCC regenerator compared the combustion gas composition of the plant with the simulation data. Even if a good agreement was obtained, authors highlighted that such a comparison is not enough to fully validate all the model parameters (kinetic rates, heat transfer, ...). Indeed, at industrial scale, the data available to estimate the simulation predictions are global and averaged (bed level, temperature, gas composition) and even if a certain agreement is reached with the simulation, it is difficult to estimate if local properties such as gas and solid velocities are also well predicted by the simulation.

It therefore appears that the extrapolation capacity of CFD gas/particles simulations is a topic where further investigation is needed. The work presented in this dissertation is an attempt to bring a methodology to study this issue.

6 Particles Attrition in circulating fluidized bed and attrition testing

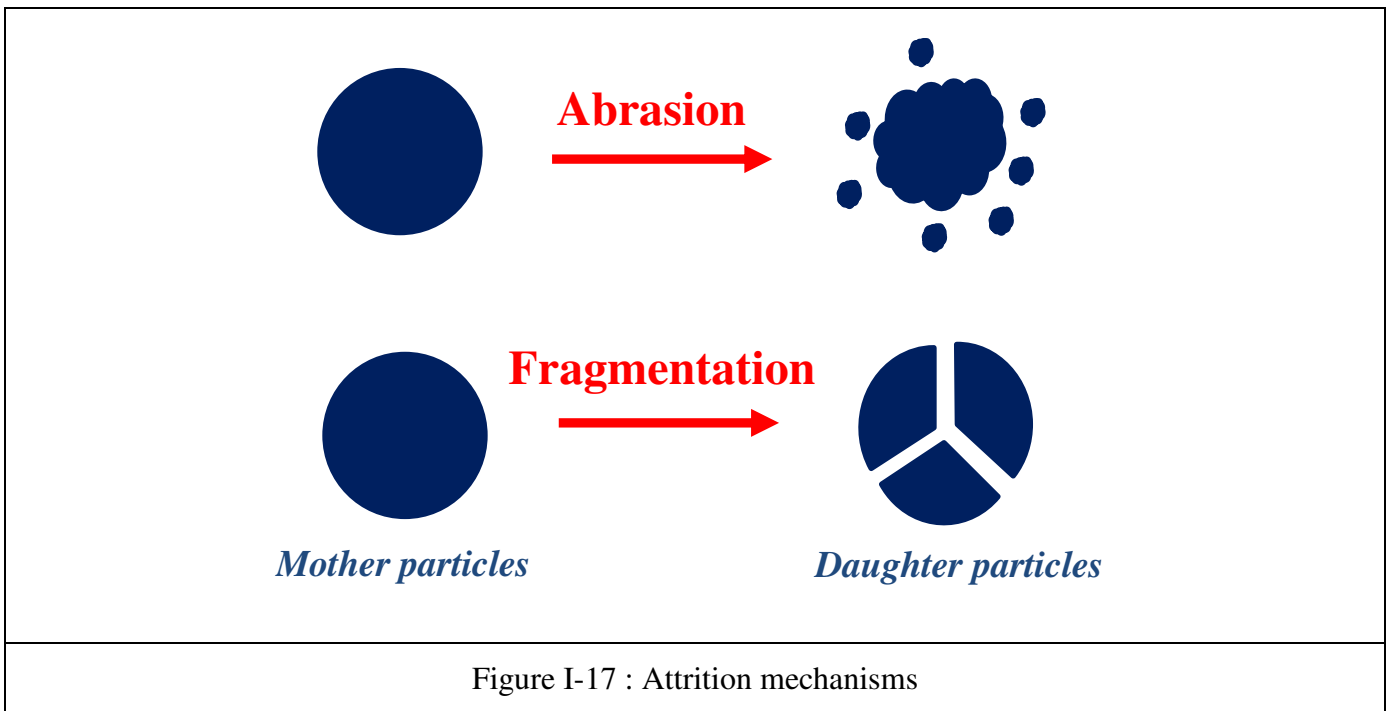
From the previous chapters, we have seen that circulated fluidized bed put particles under a high mechanical stress with continuous particles/particles and particles/wall interactions. The consequence of this stress is the degradation of the particles structure also commonly named attrition. Attrition linked to fluidization is a topic of interest intensively studied in the industry. Indeed, generation of fines due to attrition causes many problems such as inventory loss, which has a strong economic impact on the process, as well as change in the flow hydrodynamic with difficulties to operate the units. Therefore, two main issues related to attrition can be pointed out when developing new circulating particles and/or a new CFB process:

- First, it is important to reach a good compromise between particles resistance to attrition and particles reactivity. Indeed, better particle reactivity requires a higher porosity in order to increase the internal particle surface area but a higher porosity also weakens the particles mechanical structure.
- Second, it is important to estimate at industrial scale the particles losses for the process economics and operations.

The study presented in Chapter III investigates attrition phenomena and their extrapolation for the development of the CLC process. This chapter therefore presents a literature review on this topic.

6.1 Attrition phenomena and their characterization

Abrasion and fragmentation are the two mechanisms that govern attrition. As shown in Figure I-17, abrasion corresponds to daughter particles removed from the surface of a mother particle which generates fines while fragmentation corresponds to daughter particles generated from the splitting of a mother particle which generates intermediate size particles.



In fluidization, the physics behind these mechanisms is not quite understood and difficult to model, therefore attrition studies remain correlative. J. Werther and J. Reppenhagen [129] summarize the work and techniques used to study particles attrition. Different approaches and many apparatus exist to characterize attrition. The two main issues investigated being to characterize the resistance to attrition for a given solid and then predict attrition in a CFB system as a function of operating conditions for the same given solid.

A first approach consists in characterizing attrition due to the principal sources of breakage such as cyclones, gas injections and gas bubbles in fluidized beds. The attrition sources modeling remains correlative with attrition rates expressed in function of attrition source dimensions (injection orifice diameter, bed height, ...), gas properties (velocity, density) and empirical terms depending on the materials as carried out by Ghadiri et al. [132] for the prediction of jet attrition. The modeling of attrition sources can then be used in a population balance model in order to predict attrition at an industrial case. J. Werther and E. Hartge [130] used this method to predict the attrition generated in a reactor/regenerator system. Based on this approach, more recently, Kramp et al. [131] made an attempt to simulate attrition in a CLC process. This method is probably the most precise in order to evaluate attrition at industrial scale, however it requires a tedious experimental work and a large quantity of material of interest in order to characterize the different sources of attrition. Moreover, experiments to estimate attrition phenomena are often made at ambient conditions which differ from the industrial conditions.

A second approach consists in using attrition test in order to evaluate the attrition potential of a material. Such tests allow ranking different materials with respect to their mechanical resistance to attrition and can give useful information during catalyst and process development. Many attrition tests exist. A first category such as the shear and crushing tests evaluate the mechanical resistance of particles applying a well-defined mechanical stress. Discussions exist concerning on how the results of such tests can be correlated to attrition in a circulating fluidized bed. Knight and Bridgwater [133] showed that when comparing the mechanical resistance of different solids with the shear and crushing tests, the rank is different depending on which test is used. Magnus Rydén et al. [134] found no strong correlation between the crushing test and the attrition data from their continuous chemical looping experiments in reactors at Chalmers University of Technology. A second category of attrition test consists in applying a “less-controlled” mechanical stress by putting particles under a mechanical stress similar to conditions in circulating fluidized beds. For example, the standard method ASTM D-5757 [135] consists in putting 50 grams of a solid sample in a mini-fluidized bed with three vertical air injections at high velocity during 5

hours, the attrition being characterized by the amount of fine elutriated. This method has been design for FCC catalyst only. Cocco et al. [4] developed a jet cup test where air is injected tangentially at high velocity in a conical shape container where the particles sample is placed. The high gas velocity injection reproduces the mechanical stress of gas injectors while the tangential inlet induces a swirling flow that reproduces a mechanical stress similar to cyclones. In their study, Cocco et al. [4] compared for several types of FCC catalyst, the attrition generated in a 30 cm fluidized bed with the attrition generated in the Jet Cup. They found that their jet cup results correlated well with attrition rate measured on the 30 cm fluidized bed. Moreover, Magnus Rydén et al. [134] found that their jet cup results correlated well with attrition rates measured on their continuous chemical looping experiments at Chalmers University of Technology with Group B oxygen carriers. Therefore, the jet cup seems to be a relevant tool to characterize the attrition generated in fluidized beds.

The effects of thermal and chemical stresses on particles attrition were also investigated. Knight et al. [136] studied the effect of temperature on attrition by carrying out tests on an oxygen sorbent at ambient temperature and at 500 degrees Celsius. They used an air jet attrition test apparatus based on the standard ASTM D5727. Knight et al. clearly report that when temperature is increased, if the gas mass flowrate is kept constant, the attrition generated in the test increases since the jet velocity increases because of the gas density change. Therefore, the authors reduced the gas mass flowrate in order to keep the jet velocity constant compared with the ambient conditions testing. It resulted that the attrition generated became similar to the one observed at ambient temperature. Concerning the chemical stress, Magnus Rydén et al. [134] investigated the impact of the chemical reaction in a Chemical looping Combustion process by comparing Jet Cup attrition results on fresh particles and on particles that have been through several chemical cycles.

6.2 Jet cup attrition index

Different indexes are used to characterize the attrition generated during a jet cup test. The first method consists in comparing the particles size distribution of the tested sample before and after the test. Figure I-18 shows the particle size distributions of a FCC catalyst sample before and after a jet cup test. Cocco et al. [4] use two indexes AI(20) and AI(44) which corresponds to the weight of particles generated by attrition below respectively 20 μm and 44 μm.

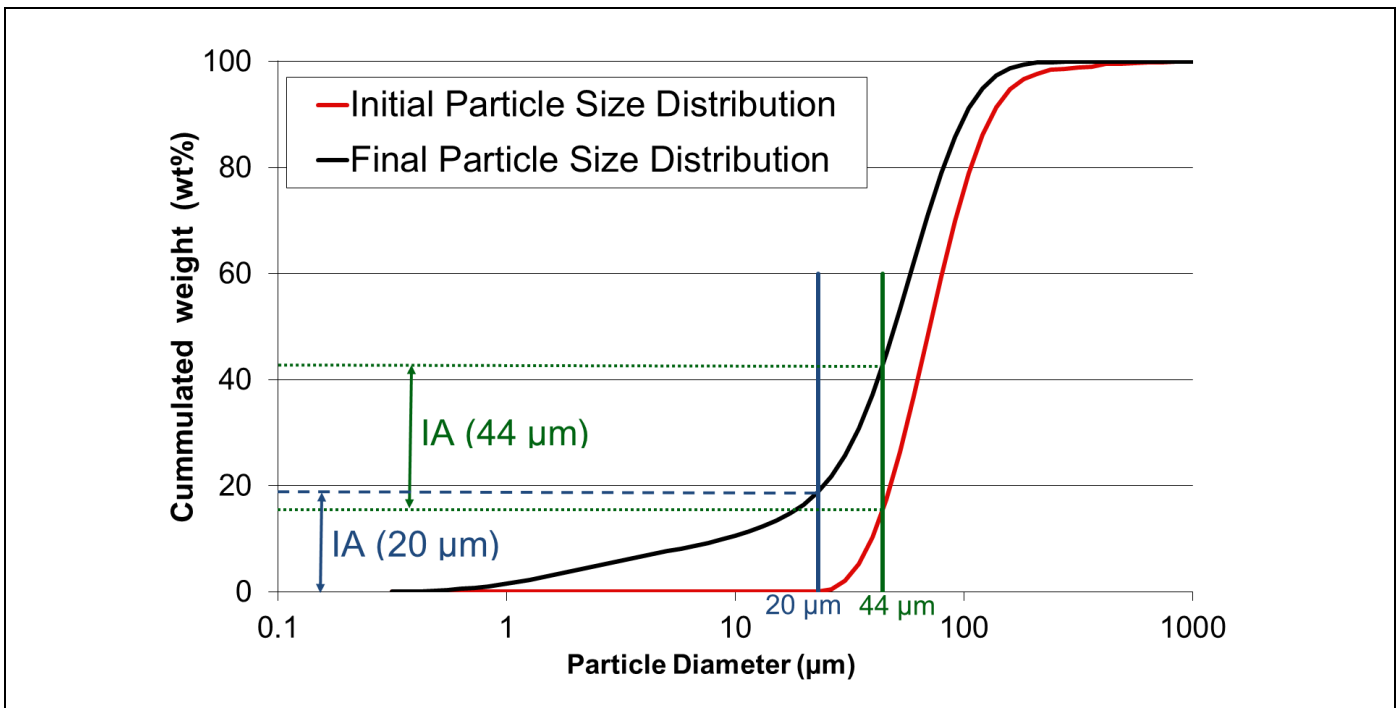


Figure I-18: Definition of the attrition indexes used by Cocco et al.

These two indexes have limitations when comparing solids with large particles. Indeed, when considering group B powders that are used for the CLC process, generation of fine particles below 20 or 44 microns is not enough to describe particles breakage since the particle size generated by attrition might be higher.

Magnus Rydén et al. [134] characterize the attrition in the jet cup test by measuring the weight of fines that are elutriated and recovered in a filter. The advantage of this method is that it is independent from the measure of particle size distributions which can be challenging. However, one problem is that the amount of particles elutriated at a constant gas velocity depends also on the particles properties such as the density. Therefore when comparing two solids with different densities, the amount of fines elutriated to the filter might be lower for the heaviest solids but it does not mean that the attrition rate is lower.

6.3 CFD studies carried out on the Jet Cup

In order to better understand the hydrodynamic and the breakage mechanisms within the jet cup, several Computational Fluid Dynamic (CFD) studies have been carried out.

Cocco et al. carried out CFD simulations in order to study the influence of the jet cup shape on the gas-solid flow hydrodynamic. For this purpose they used the commercial code Barracuda VR[®] from CPFD-Software. Barracuda VR[®] uses the multiphase particle-in-cell (MP-PIC) method presented in Chapter I.4.2. The particle–fluid drag force was expressed using the Gidaspow drag function [7] which combines the Wen-Yu and Ergun models. Cocco et al. simulated jet cup tests in three dimensions with 100 grams of FCC catalyst that represents about 10^8 real particles. The simulations took into account a particle size distribution with a mean diameter of about 80 microns. It is important to notice that attrition is not simulated and therefore the particle size distribution stays constant during the simulations. CFD simulations revealed that with the cylindrical shape jet cup, a large part of the particles remains stagnant. This result was confirmed experimentally with a cold flow study. The problem is that stagnant particles do not go under stress and are not subject to attrition which makes the results from the jet cup test difficult to interpret. Afterwards they studied a jet cup configuration with a conical shape. Both experimental CFD studies confirm that almost all particles were in motion with this configuration, the experimental attrition rates found were higher than with the previous cylindrical shape configuration.

Wei Xu et al. [137] used another approach to simulate the jet cup gas-solid hydrodynamic. They carried out CFD simulations using the open source code MFI_X–DEM where the gas phase is treated as a continuum in a Eulerian framework while the solid phase is treated in a Lagrangian framework using a Discrete Element Method (DEM). Real particles are directly represented and the main advantage of this approach is that particles inter-collisions are directly detected and modeled using the soft-sphere approach [138]. Moreover, Wei Xu et al. [137] also implemented a model for particle size reduction due to chipping and abrasive wear from particle–particle and particle–wall interactions. The particle interactions are therefore described in a more precise way and at a lower physical scale compared to the MP-PIC method presented before. However, with the DEM approach the number of particles is limited by the expensive computational cost of the method. Wei Xu et al. [137] simulated a jet cup in two dimensions with about 10^3 particles taken into account. Both polydispersed and monodispersed particle size distributions were simulated with particle size going from 200 to 600 microns. Moreover, the particle size is limited at 100 microns in order to avoid numerically the generation by attrition of particles smaller than this diameter. They studied the influence of different parameters on the attrition rate: the air jet velocity, the initial diameter of a mono-dispersed distribution going from 200 to 600 microns, the particles density and the jet cup shape. First, they found that attrition increases with the air jet velocity. Then there was no direct correlation between the attrition and the initial diameter of the mono-dispersed distribution. The attrition decreases with the particle density the explanation being that although higher density can increase the particle inertia, it will reduce the particle mobility that appears to be more dominant in the attrition process. Finally, they found that changing the shape of the jet cup can create regions where particles are stagnant and therefore the attrition rates is decreased, this is confirmed by the experimental work done by Cocco et al. [4].

7 Conclusions

This literature review sets the context of the different investigations carried out in this dissertation.

First concerning attrition, the reader could appreciate the importance of estimating attrition phenomena when developing a new circulating fluidized bed process and the difficulty to estimate the particles resistance to attrition with tests using a well-defined mechanical stress. Different studies then demonstrated that jet cup tests are representative of the mechanical stress applied to particles in a fluidized bed and that it can be used to evaluate the resistance to attrition of different types of particles. However, based on the literature, it is not a well-defined methodology to compare attrition resistance of particles having different sizes and densities. The investigation presented in Chapter III therefore introduces a methodology using a jet cup test to evaluate and compare the resistance to attrition of Geldart Group B particles used in the CLC process with Geldart Group A particles used in the FCC process. The purpose of such a comparison is to use FCC particles, where industrial attrition data are available, as a reference to assess the resistance to attrition of the potential oxygen carriers where data at industrial scale are not available.

The reader could then appreciate the difficulty of characterizing CFB hydrodynamic with complex flow structures where many physical parameters such as superficial gas velocity, solid circulation rate, fines content, pressure, temperature, geometry and internals have a strong influence, while their characterization and modeling remaining mostly correlative due to a lack in fundamentals for describing gas-particle interactions. The challenges connected to experimentation were also presented, highlighting the difficulty to get precise local hydrodynamic descriptors. These different issues make the CFB hydrodynamic extrapolation challenging whatever the approach:

- If using phase flow theory, the challenge for scale-up is to develop correlative models used to describe the hydrodynamic phenomena at macroscopic scale. Three dimensional effects with complex geometry are then difficult to take into account with this approach.
- If using CFD, three dimensional effects and complex geometries can be described but the challenge relies on the more fundamental but complex modeling of gas/particles and particles/particles interactions.

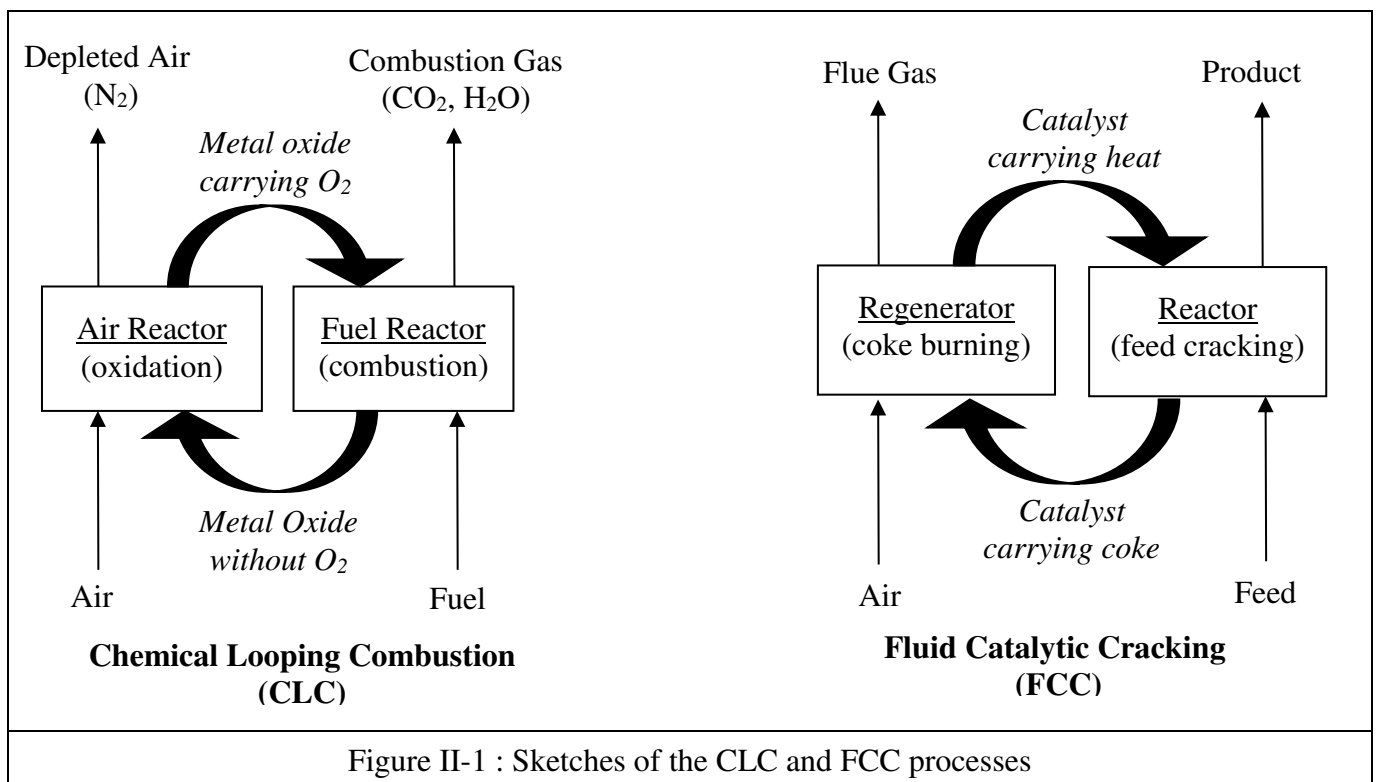
With the improvement of computational power, CFD tools allows characterizing multiphase flows in three dimensions on large scales taking into account complex geometrical features such as distributors and internals. Two CFD approaches for large scale simulations were introduced in the literature review with the Euler/Euler KTGF and the MP-PIC approaches. For both approaches, modeling of the gas/particles drag closure law is proven to be critical but it remains challenging and complex. Indeed, many models exist in the literature which are often investigated and tuned for simulations of a specified experiment with a rather narrow range of operating conditions. The use of the same mesh cell size between lab and industrial scales is impossible due to computational power limitations. Therefore, different methodology were then introduced for CFD simulations at industrial scale with authors investigating their drag closure law based on industrial data, other others proposing filtered drag closures law in order to take into account the large mesh cell size effect. Validation of CFD models extrapolation capability by analyzing simulation results on a wide range of conditions is a topic of interest but it is not yet clearly addressed. The work presented in in this dissertation is therefore an attempt to bring a methodology to study this issue. We conducted or used experiments at different scales that were then simulated using both Euler/Euler with KTGF and MP-PIC approaches.

II. ATTRITION PHENOMENA EXTRAPOLATION AT THE EARLY STAGE OF A PROCESS DEVELOPMENT

1 Introduction

The present study is part of the process study conducted together by IFP Energies nouvelles and Total to develop a Chemical Looping Combustion process [3]. As presented in the literature review, the CLC process is an oxy-combustion like technology for CO₂ capturing where oxygen-carrying particles are used to supply oxygen for combustion. The process uses group metal oxide particles as an oxygen carrier to transfer oxygen in a circulating fluidized bed from an air reactor to a fuel reactor where combustion takes place. The choice of the oxygen carrier particles is a key parameter for the process development. Apart from reactivity, oxygen transfer capacity, fluidization properties and cost, it is also important to study attrition. Indeed, during their life-time, particles go through a high mechanical stress due to their circulation between the different reactors. Particles with low mechanical resistance will produce fines which can cause operating issues such as solid circulation upset as well as loss of material which may impact significantly the operating costs of the unit considering that the solid inventory at industrial scale is several hundred tons.

Particles belonging to Group B powders may be more suitable to control circulation in the CLC process [139] and also to separate more easily oxygen carriers from unburnt particles [140]. However, there is presently very little information available concerning long term operation with Group B oxygen carriers and industrial data are not available for the CLC process. It is therefore difficult to predict attrition at industrial scale based on existing tools and methodologies for the different oxygen carriers available in limited quantities at the early stage of the process development. Therefore, we propose to compare the resistance to attrition of the different potential oxygen carriers with the one of catalyst used for the Fluid Catalytic Cracking process (FCC), where industrial attrition data already exist. Indeed, the CLC process is similar in its configuration to the FCC process with particles circulating in a loop between different reactors as shown in Figure II-1.



As presented in the literature review, in the FCC process particles circulate in a loop between the reactor sections, where the feed is cracked by catalytic reaction, and the regenerator section where the coke formed during the reaction is burnt in order to regenerate the catalyst. Therefore, in both CLC and FCC processes, particles go through a mechanical stress proportional to the solid circulation due to different attrition sources like cyclones, gas injections, fluidized beds and so on. Thus, comparing the different potential oxygen carriers with FCC catalyst gives a good indication to rank their mechanical resistance and evaluate their potential use at an industrial scale considering only mechanical attrition.

This investigation presents a method to compare the mechanical resistance to attrition of a Group A FCC catalyst with Group B oxygen carriers using a jet cup apparatus originally developed to characterize FCC catalysts. The goal is to compare the mechanical resistance to attrition of the different solids on the same mechanical stress basis in the jet cup. For this purpose, CFD was used to characterize the particles circulation within the jet cup for solids with different properties (FCC catalyst, oxygen carriers) which would be very difficult to measure experimentally. This work therefore shows how CFD can help understanding physical phenomena difficult to characterize experimentally and how CFD can orientate the testing method development.

In the following, materials and methods are first introduced with the presentation of the powders characteristics used in the investigation, followed by a description of the experimental jet cup apparatus and procedure and CFD tools and methods. Then, we present the CFD investigation conducted to characterize the jet cup hydrodynamic. Finally, we show experimental results using CFD findings to adjust the testing method.

2 Material and methods

This study was conducted in order to compare attrition resistance of an equilibrium FCC and two oxygen carriers using a jet cup apparatus. This chapter presents first the physical properties of the different powders used. A presentation of the jet cup apparatus and procedures is then carried out, and the CFD tools and method used to characterize the jet cup hydrodynamic are finally introduced since CFD was used to characterize the hydrodynamic within the jet cup of the different solids.

2.1 Particles properties

Three solids are used for this investigation:

- First a Geldart Group A equilibrium FCC catalyst which comes from the Total refinery in Feyzin, France.
- Second a fresh Group B oxygen carrier which is a crushed natural manganese ore.
- Third, a Group B equilibrium oxygen carrier. It is actually the fresh oxygen carrier presented above collected after being used in IFP Energies nouvelles hot pilot [3] under real CLC process conditions with several oxydo-reduction cycles.

The particle size distribution (PSD) and physical properties of the different solids can be found in respectively Figure II-2 and Table II-1. PSDs are measured by laser diffraction with a master sizer 3000 and particle densities are measured by mercury porosimetry.

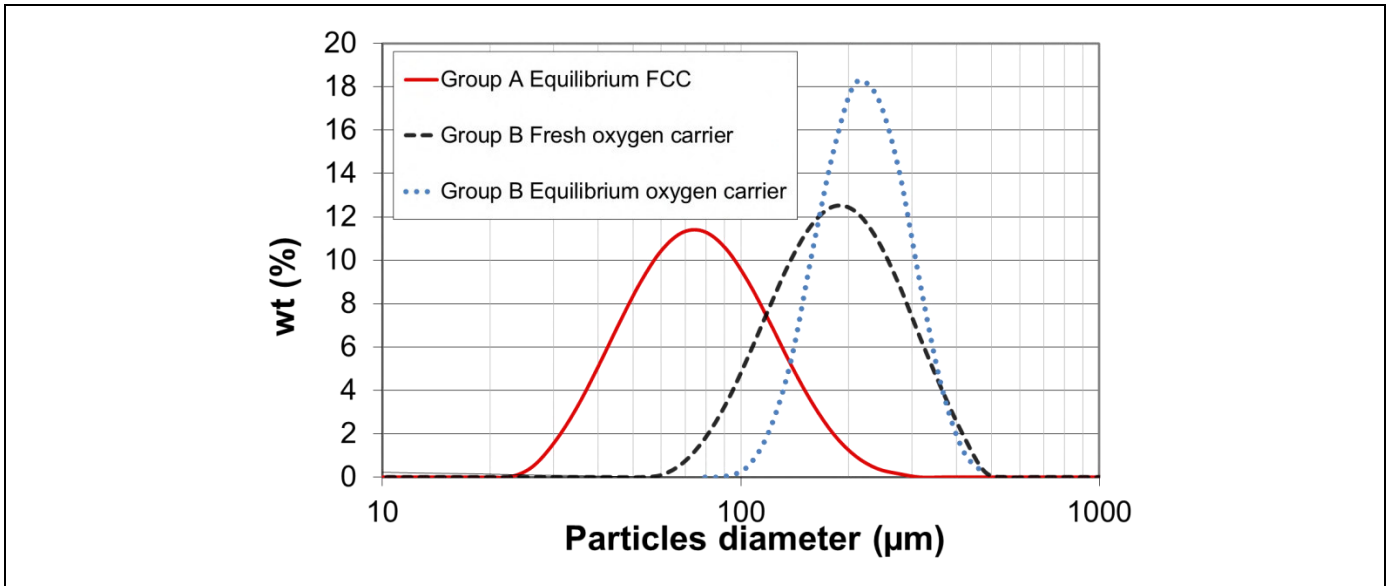


Figure II-2 : Particle size distribution of the material investigated

Table II-1– Particles physical properties

	Equilibrium FCC	Fresh oxygen carrier particles	Equilibrium oxygen carrier particles
Particle Density (kg/m ³)	1 450	3 600	3300
Particles mean diameter dp ₅₀ (µm)	70	180	210
Particles Sauter Diameter (µm)	51	170	205

One can see that the fresh and equilibrium CLC oxygen carriers have similar mean physical properties. The equilibrium CLC presents a narrower particle size distribution with less fine particles as shown in Figure II-2.

Oxygen carrier particles and FCC particles have very different properties. One can therefore wonder how to handle these different powders in a jet cup test that has been developed for FCC catalysts and how we can evaluate and compare properly their attrition resistance. These questions are investigated in the next sections.

Finally, it is important to point out that the amount of equilibrium oxygen carrier particles available is low compared to the two other solids. Therefore, most of the tests to characterize and develop the jet cup attrition method were carried out with the equilibrium FCC and the fresh oxygen carrier particles. The equilibrium oxygen carrier particles were used only for the final comparison tests. This is a classical issue for process development. In early stages, particle quantities available are limited and it is important to be able to reach conclusions based on tests with limited solid amounts.

2.2 Jet cup attrition testing

The jet cup used for the attrition testing is presented in Figure II-3. It consists in a conical cup where air is injected tangentially in the bottom at high velocity through a 5 mm diameter orifice as presented by Cocco et al. [4]. The jet cup is connected to a disengagement vessel where the superficial air velocity is

low which allows particles above a certain size to go back into the jet cup, precise dimensions can be found in Appendix 1. Elutriated fines are collected with a filter placed into the disengagement vessel.

The air flowrate is controlled with a flowmeter Brooks 2580S. The accumulation of particles on the filter makes the pressure in the vessel increasing which affects the air jet velocity. For this reasons a maximum pressure variation of 100 mbars is tolerated during the test. In order to limit electrostatic effects that make particles stick to the walls, air is humidified before entering the jet cup.

After testing, all materials collected inside the jet cup and on the filter are weighed. A material balance is conducted to ensure that at least 95% of the material is accounted for. Attrition generated is characterized with the difference between the particle size distribution before and after the test. The particle size distribution at the end of the test is reconstructed with the particles collected on the filter and inside the cup. Particle size distributions are measured by laser diffraction technique using a Malvern Mastersizer 3000.

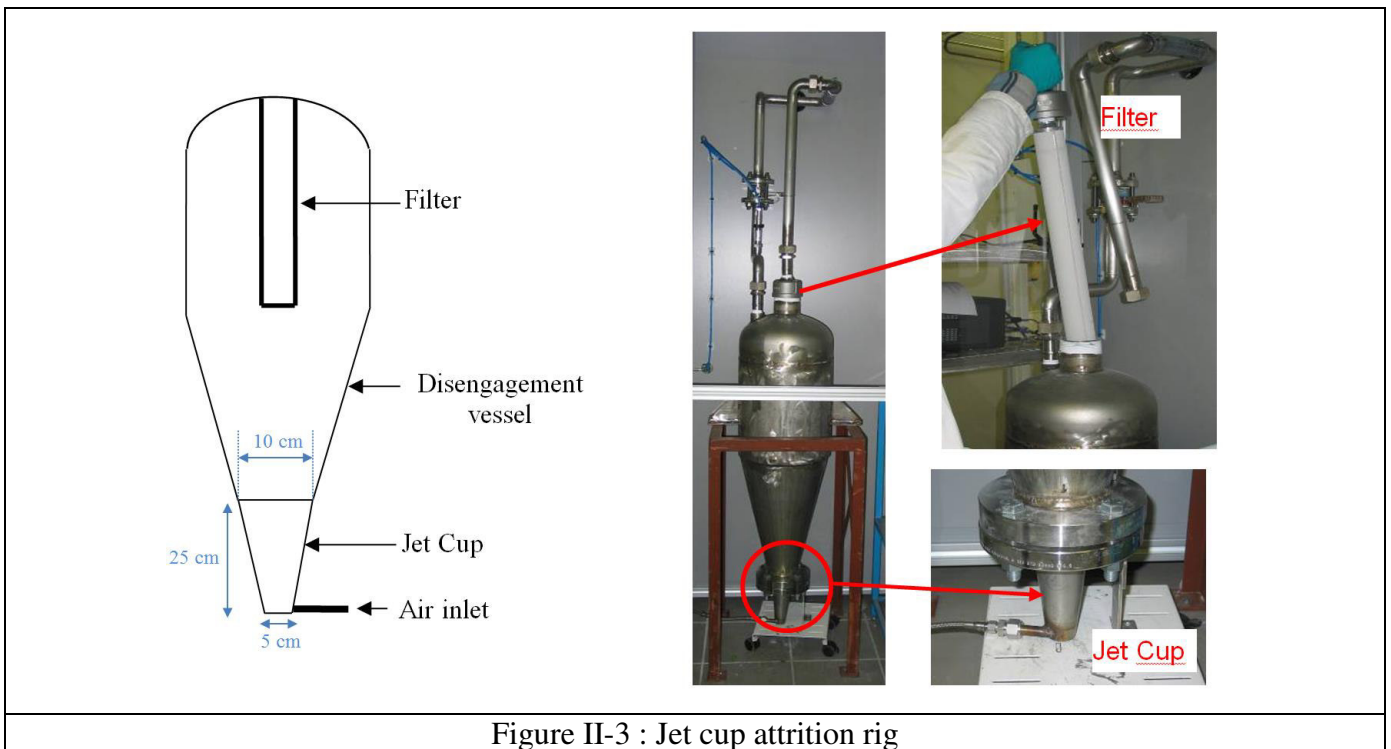


Figure II-3 : Jet cup attrition rig

Figure II-4 and Figure II-5 show the particle size distributions (PSD) of jet cup tests carried out respectively with the Group A FCC catalyst and the Group B fresh oxygen carrier. The red and black curves correspond respectively to the initial and the final particle size distributions. The blue curve corresponds to the difference between the initial and the final particle size distribution. The positive area delimited by the differential blue curve corresponds to the amount of particles generated by attrition while the negative area corresponds to the amount of particles, which went through attrition phenomena. When the blue curve cut the x-axis it indicates the maximum diameter of the particles generated by attrition which is shown by the red arrow on the Figures. With FCC catalyst, the maximum diameter is in the range of 50 microns. Usually when people conduct investigations on FCC catalyst, they characterize the fine particles generation below 20 or 44 microns [4], which is consistent with the maximum diameter found in our case . However, when considering large particles such as the oxygen carrier studied, attrition indexes based on the generation of fine particles below 20 or 44 microns are not sufficient to describe particle breakage mechanisms as shown in Figure II-5 where the maximum diameter of the particles generated by attrition is 110 microns. Therefore, in order to compare both solids on the same basis, we propose to introduce a new attrition index that does not depend upon a given particle size [141]. This index is based on the total percentage of particles generated by attrition which corresponds to the positive

area delimited by the differential blue curve shown with the green lines on Figure II-4 and Figure II-5. This index is referred as TPGI (Total Particles Generated Index) in the rest of the investigation.

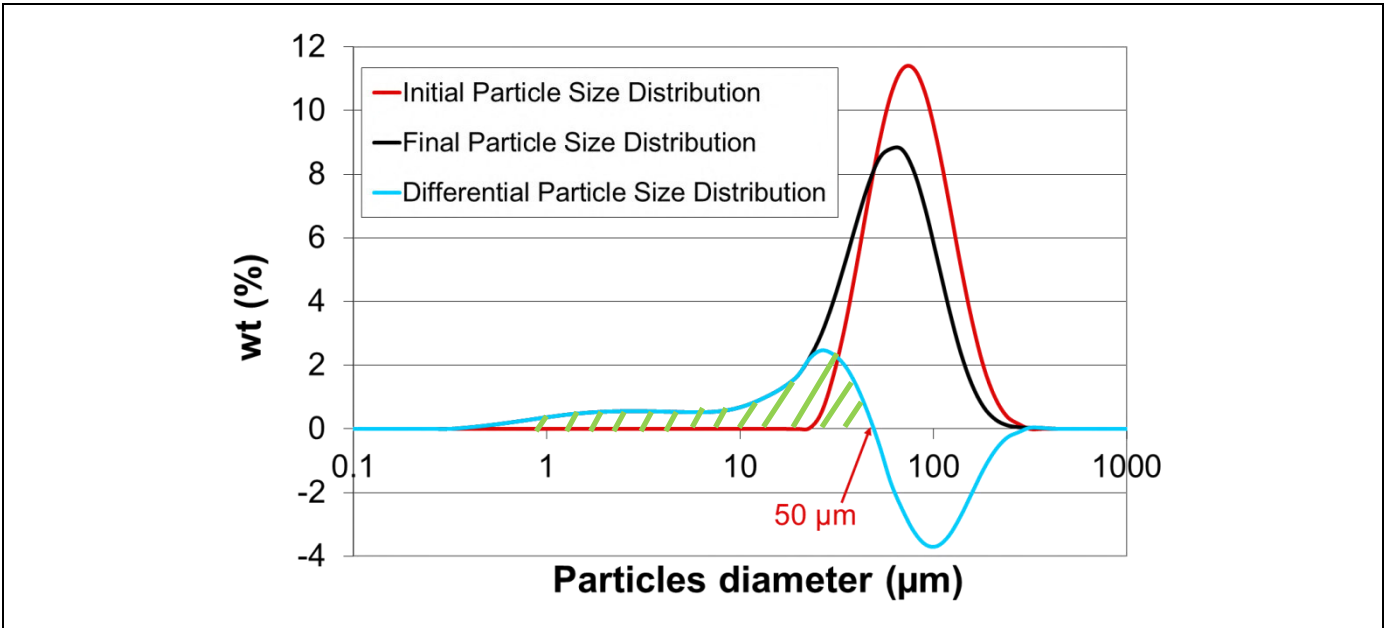


Figure II-4 : equilibrium FCC ; Particle Size Distributions for a jet cup test ; sample mass of 100 grams air jet velocity: 90 m/s; test duration: 6 hours

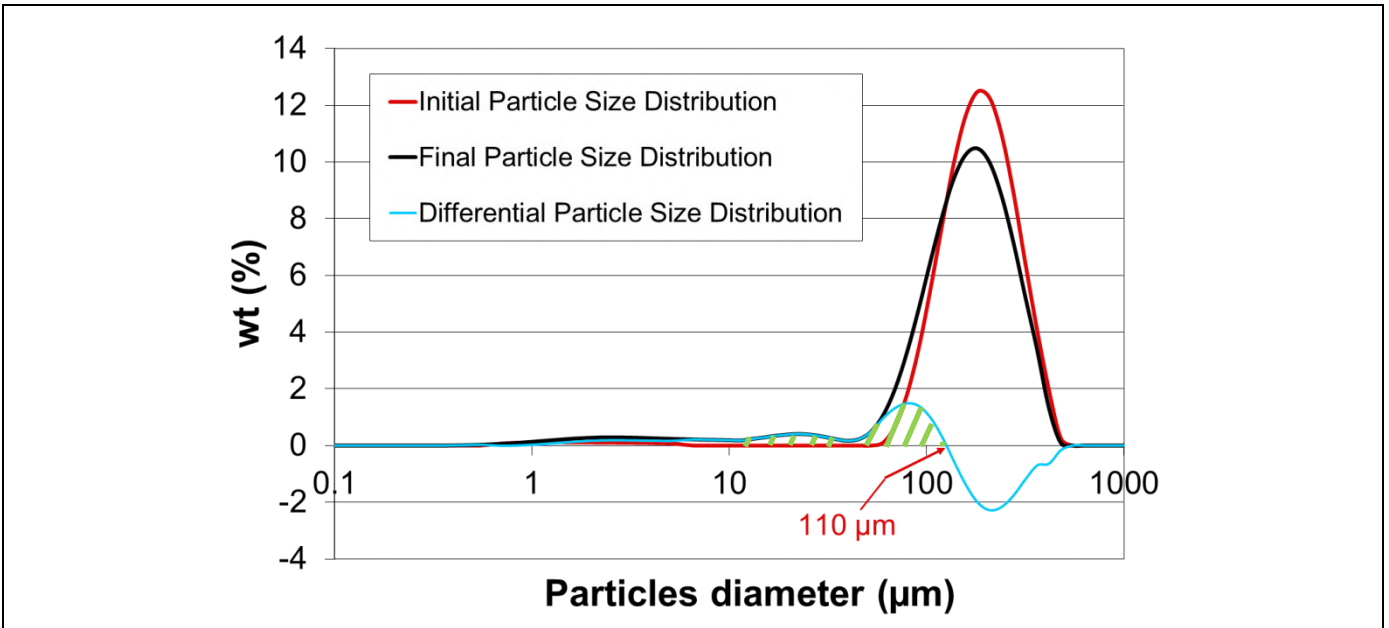


Figure II-5 : fresh oxygen carrier ; Particle Size Distributions for a jet cup test ; sample mass of 250 grams air jet velocity: 90 m/s; test duration: 6 hours

2.3 Choice of the jet velocity for attrition testing

When using the jet cup, the main parameter to determine is the velocity of the air jet implemented at the jet cup inlet. It is important to choose a jet velocity that first generates attrition in a reasonable test duration frame without applying a mechanical stress which would generate attrition phenomena to be avoided in circulating fluidized bed processes such as particle fragmentation [129,130].

Several tests were then carried out with air jet velocities of 30, 60, 90, 120, 150 and 180 m/s with the equilibrium FCC and with the fresh oxygen carrier. Figure II-6 presents the Total Particle Generated Index (TPGI) against the air jet velocity for tests of one hour carried out with 100 grams of both solids.

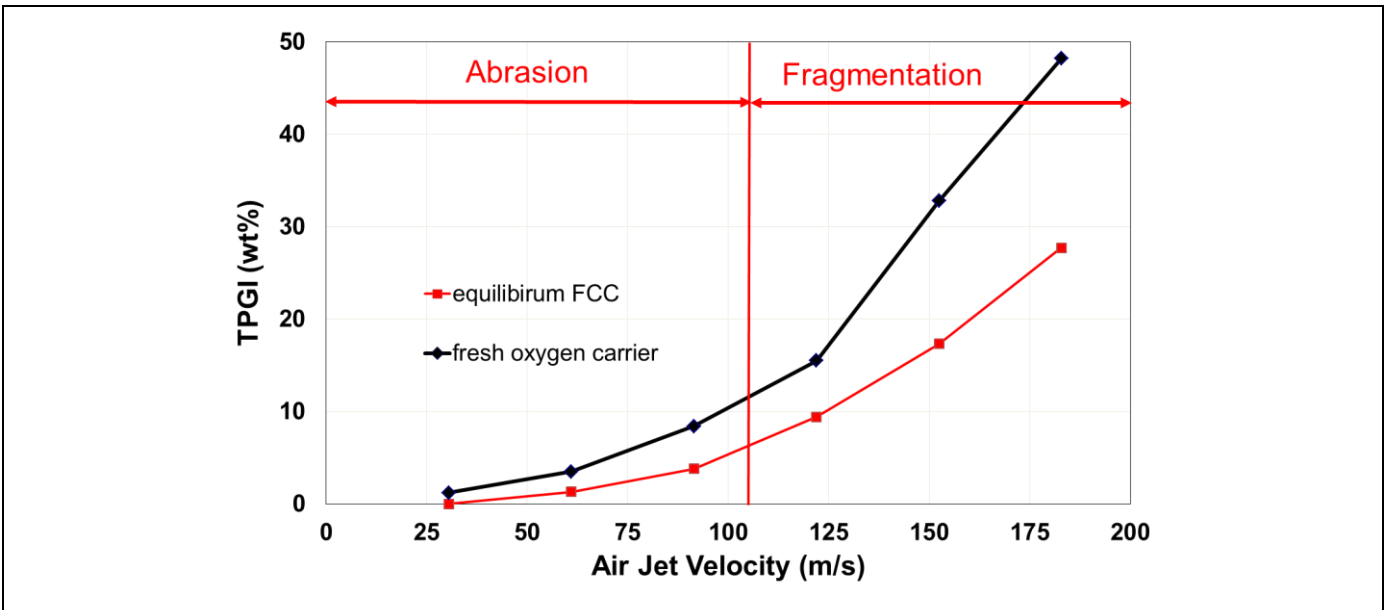


Figure II-6 : TPGI index against air jet velocity for a sample mass of 100 grams test duration of 1 hour

Two ranges of velocities can be pointed out. In the first range of velocities from 30 m/s to 90 m/s, the TPGI increases moderately with respect to the air jet velocity for both solids. This corresponds to the zone where abrasion phenomena are dominant. Figure II-7 shows the initial and final particle size distribution for the fresh oxygen carrier test with an air injection of 90 m/s. The difference between the two curves is a typical example of abrasion where only fines are generated. In the second range of velocities from 120 m/s to 180 m/s, the TPGI increases dramatically with respect to the air jet velocity, it corresponds to the zone where fragmentation phenomena are dominant. Figure II-8 shows the initial and final Particle Size Distribution for the fresh oxygen carrier test with an air injection of 180 m/s. The difference between the two curves is a typical example of fragmentation where the breakage of the big particles leads to intermediate size particles. Similar results are obtained with the equilibrium FCC as shown in Appendix 1.

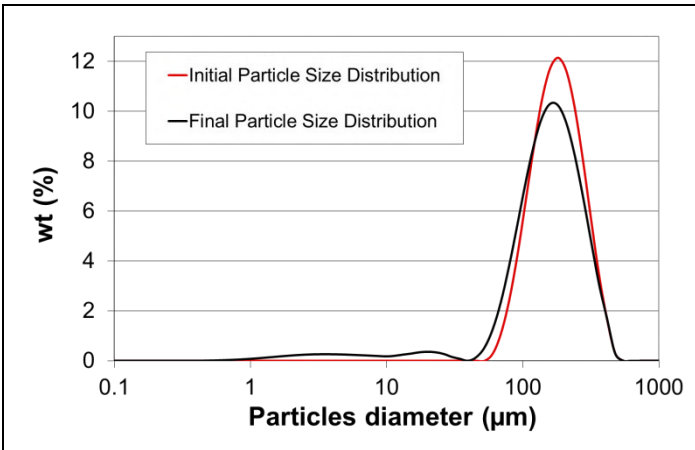


Figure II-7 : Initial and Final Particle Size Distribution for a test with 100 grams of fresh oxygen carrier particles during one hour ; Air Injection velocity = 90 m/s

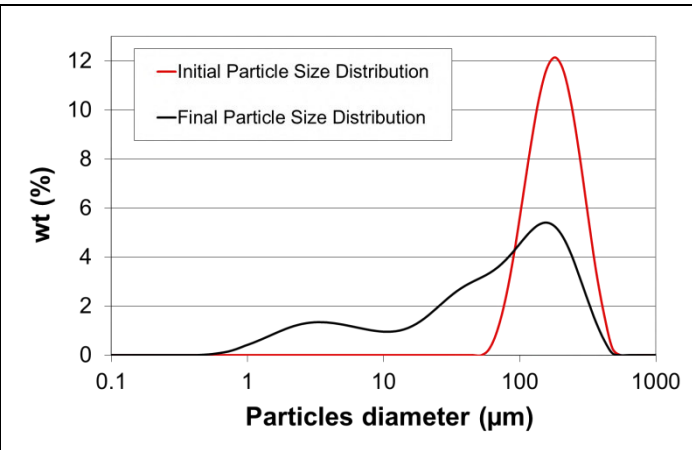


Figure II-8 : Initial and Final Particle Size Distribution for a test with 100 grams of fresh oxygen carrier particles during one hour ; Air Injection velocity = 180 m/s

From these results, it was decided to take an air injection velocity for the comparison method of 90 m/s which is at the limit between the zone where abrasion phenomena are dominant and the zone where fragmentation is dominant. Cocco et al. [4] and Rydén et al. [134] used jet velocities in the same range for their tests with respectively FCC and CLC particles.

2.4 CFD simulation

CFD simulations were carried out in order to investigate the impact of particles properties on the jet cup hydrodynamics and especially on the internal particles contact frequency with the jet. Indeed, as explained in Chapter II.3, it is assumed that the attrition within the jet cup is generated through the particles contacting frequency with the jet. It is therefore important to estimate the circulation rate of particles within the jet in order to characterize and compare their resistance to attrition. This chapter presents the CFD approach and parameters used.

The Barracuda VR[®] v17.2 software was used for the jet cup CFD simulations. Barracuda VR[®] uses the Multiphase Particle In Cell (MP-PIC) approach presented in Chapter I.4.2. Moreover, a contribution of the gas phase turbulence is modeled and taken into account in the calculation of the gas stress tensor, Equation 46 therefore becomes:

$\tau_g = \mu(\nabla \vec{u}_g + \nabla^T \vec{u}_g) - \frac{2}{3}\mu\nabla \vec{u}_g I$	Equation 56
--	-------------

$\mu = \mu_g + \mu_t$	Equation 57
-----------------------	-------------

Where μ_t is the turbulence viscosity from a Smagorinsky turbulence model [142,143] presented in Equation 67. Large eddies are calculated and the unresolved sub-grid turbulence is modeled by an eddy-viscosity

$\mu_t = C\rho_f\Delta^2 \sqrt{\left(\frac{\partial u_i}{\partial x_j} + \frac{\partial u_j}{\partial x_i}\right)^2}$	Equation 58
---	-------------

where Δ is the sub-grid length scale which is the cube root of the sum of the product of distances across a calculation cell in the three orthogonal directions. The Smagorinsky Barracuda VR[®] default coefficient C used in all simulations is constant and is equal to 0.01.

Concerning the meshing, Barracuda VR[®] has its own meshing software which generates a structured hexahedral mesh. For this reason, the 5 mm cylindrical jet inlet at the bottom of the jet cup was modified with a hexahedral shape of the same surface to facilitate the geometry meshing. The mesh used has 500 000 cells with an average cell size of 2.5 mm. A picture of the hexahedral structure mesh can be found in Appendix 1. The default Barracuda VR[®] parameters set a maximum Courant number of 1.5, the resulting time step used was in the order of $4 \cdot 10^{-5}$ seconds for a total simulation time of 20 seconds.

The domain simulated is presented in Figure II-9. Only part of the disengagement vessel is taken into account. A pressure value of 2 kPag is imposed at the top surface of the geometry with a pressure boundary condition, particles cannot escape. The air injection is set with a mass flow boundary condition. The air density and viscosity are automatically calculated by the software according to the air temperature which is fixed at 25°celcius. The solids density and particle size distribution are taken from the experimental values presented in Figure II-2 and Table II-1.

The objective of the simulation is to determine particle circulation pattern in the jet cup. Attrition is not simulated and the particle size distribution remains constant during the simulations. We therefore assume that attrition phenomena do not affect the particles circulation rate within the jet cup.

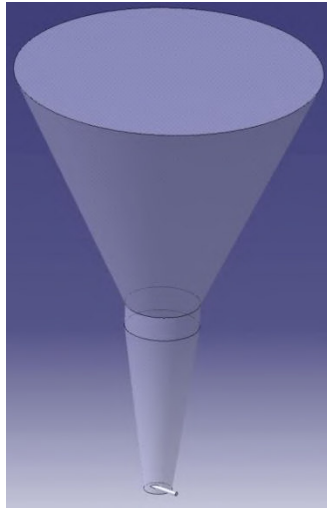


Figure II-9 : Domain simulated for the CFD study

The particle gas drag interaction model used is the default Barracuda VR[®] Gidaspow model presented in Equation 59.

$K_d = D1 = \text{Ergun model for } \alpha_s > 0.85\alpha_{s,max}$ $K_d = D2 = \text{WenYu model for } \alpha_s < 0.75\alpha_{s,max}$ $K_d = (D2 - D1) \frac{\alpha_s - 0.75\alpha_{s,max}}{0.85\alpha_{s,max} - 0.75\alpha_{s,max}} + D1 \text{ for } 0.75\alpha_{s,max} < \alpha_s < 0.85\alpha_{s,max}$	Equation 59
--	-------------

It is important to point out that with this model the transition between the Ergun and WenYu model occurs at a higher solid volume fraction of around 0.5 compared to the classical Gidaspow model where the transition occurs at a solid volume fraction of 0.2 as shown in Table I-4.

A no slip wall boundary condition is used for the gas phase. No clear description of the solid wall boundary condition was found in the literature. The software provider then gave the following information [144] “the particles at the wall see the velocity of the cell at the walls. Due to this, the boundary will occasionally appear as a partial slip condition. The momentum retention factors are then used during the advection of the particles to determine how any particles that intersect a wall will be reflected back into the domain and this is not closely coupled to the fluid and pressure solvers”. Therefore, the normal and tangential retention factors are used to compute the clouds properties which are in contact with the wall when computing their new positions as explained in Chapter I.4.2. It appears that the new positioning of the particles contacting the wall is not coupled with the fluid solver.

Finally, Table II-2 presents the parameters for the three simulations carried out. The same drag, turbulence, solid stress models as well as boundary conditions were used by Cocco et al. [4] for their jet cup simulations using Barracuda VR[®].

Table II-2– Simulations parameters

	Simulation n°1	Simulation n°2	Simulation n°3
Mesh size	500 000 hexahedral cells		
Cell size	2.5 mm		
Particles type	FCC catalyst	Fresh oxygen carrier	Fresh oxygen carrier
Particle Size Distribution	From Figure II-2		
Particle density (kg/m ³)	1 450	3 600	3 600
Pressure at top boundary condition (kPa g)	2 kPag		
Bottom air flowrate through jet (kg/hr)	7.8 (to get a jet velocity of 90 m/s)		
Air temperature (°C)	20		
particles mass (g)	100	100	250
Total number of particles	8 10 ⁸	1.34 10 ⁷	3.34 10 ⁷
Averaged Number of Particles per Cloud	5.2 10 ⁴	2.2 10 ³	2.2 10 ³
Number of clouds	1.53 10 ⁴	6.2 10 ³	1.53 10 ⁴
Simulation time step (s)	in the order of 4.10 ⁻⁵ (CFL<1.5)		
Simulation time (s)	25		
Drag Law model	Barracuda VR [®] Wen-Yu/Ergun		
Gas Wall boundary condition	No slip		
Solid stress model	model of Equation 52, $P_s = 1$; $\beta = 3$; $\epsilon_{barracuda} = 10^{-8}$, $\alpha_{s,max} = 0.62$		
Solid Wall boundary condition	Particle to wall normal retention coefficient: 0.3 Particle to wall tangential retention coefficient: 0.99		

CFD simulations were carried out to evaluate the particles circulation frequency within the air jet at the bottom of the cup. Basically, the objective here is to simply evaluate how many times in average the particles will go through the air jet during a given test duration. To get this circulation rate, a virtual plane is set just above the air injection as shown in Figure II-10.



Figure II-10 : Virtual plane above the air injection to evaluate the solid circulation

Barracuda VR[®] allows tracking the cumulated mass flow rate of particles going up and down through a virtual plane. Then, we defined the total particles contacting frequency within the air jet PC₁ with Equation 60:

$PC_{1}(s^{-1}) = \left(\frac{\text{Cumulated mass flowrate going down through the virtual plane}}{\text{Solid Sample mass}} \right) \times \frac{1}{\text{Simulation time}}$	Equation 60
--	-------------

PC₁ represents a percentage of inventory passing into the air jet per second. For example, when simulating a jet cup test with a 100 grams inventory, if after ten seconds there is 200 grams of cumulated particles that went down through the virtual plane, PC₁ is equal to 0.2 s⁻¹ which means that in one second 20% of the inventory passed into the air jet. With this definition of PC₁, we assume that the flow is homogeneous, that all particles go exactly the same number of time in the air jet. However, there is the possibility that some particles remain stagnant while others go several times within the air jet. In order to evaluate the homogeneity of the solid flow, two groups of particles within the solid inventory are taken randomly as tracers and two contacting frequency PC_{tracer1} and PC_{tracer2} are calculated from Equation 61 and Equation 62:

$PC_{tracer1}(s^{-1}) = \left(\frac{\text{Cumulated tracer1 mass flowrate going down through the virtual plane}}{\text{Tracer1 mass}} \right) \times \frac{1}{\text{Simulation time}}$	Equation 61
---	-------------

$PC_{tracer2}(s^{-1}) = \left(\frac{\text{Cumulated tracer2 mass flowrate going down through the virtual plane}}{\text{Tracer2 mass}} \right) \times \frac{1}{\text{Simulation time}}$	Equation 62
---	-------------

Figure II-11 presents pictures taken during the simulation of 100 grams of FCC catalyst. The first picture shows the solid volume fraction of the entire sample, while the two other pictures show the position of particles of respectively tracer n°1 and tracer n°2.

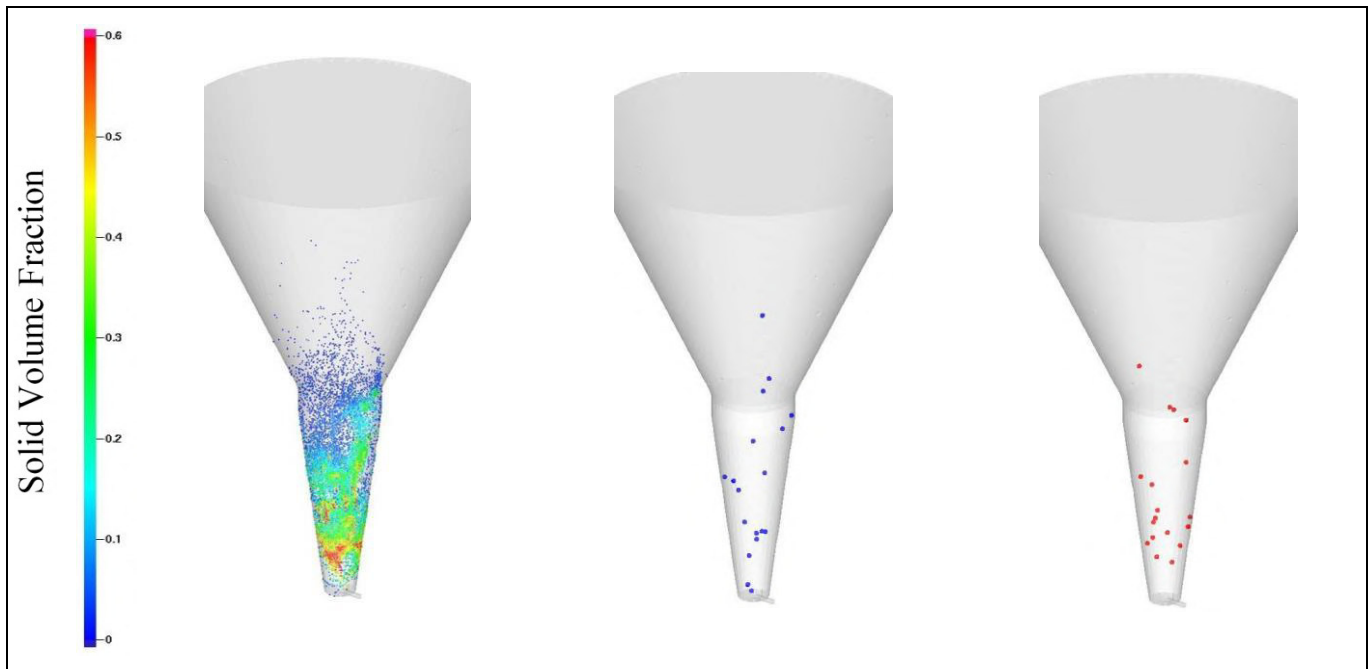


Figure II-11: equilibrium FCC catalyst ; sample mass of 100 grams ; Pictures taken at a certain simulation time ; Air injection velocity of 90 m/s; from left to right: Volume fraction of the entire sample ; Particles of Tracer n°1; Particles of Tracer n°2

The comparison of the particles contacting frequencies obtained with the two random groups of particles (PC_{tracer1} and PC_{tracer2}) and the particles contacting frequencies obtained with the entire inventory (PC₁) gives a characteristic parameter to estimate the homogeneity of the solid circulation rate into the

jet. Indeed, in the case the three values are close it means that all the particles are circulating in the same way and that there is no stagnant region.

It is important to highlight that the method applied, which consists in isolating and tracking a group of particles, can be easily implemented with the MP-PIC approach where clouds are tracked through a hybrid Eulerian/Lagrangian method. It is more challenging to implement such a method with a classic Euler/Euler KTGF approach and this is the main reason why we chose to use Barracuda VR[®] in the first place.

2.5 Conclusions

The main goal of this investigation is the development of a method to assess and compare the mechanical resistance of FCC particles and CLC oxygen carriers using the conical jet cup. We therefore presented in this chapter the properties of the different powder used in this investigation with first an equilibrium FCC catalyst taken as a reference from a mechanical resistance to attrition point of view. Two CLC solids were then introduced which are actually the same oxygen carrier one being fresh the other one being considered as an equilibrium oxygen carrier since it was used in the IFP Energies Nouvelles hot pilot under CLC process conditions.

The jet cup apparatus used was then introduced with first the presentation of the equipment where attrition is generated through hydrodynamic phenomena with a high jet velocity. Second a new attrition index named TGPI was defined, it allows the mechanical resistance comparison of particles with different properties. This TPGI index, based on the particle size distribution before and after the test, characterizes the total amount of particles generated by attrition. The jet velocity used in the experiments was then chosen at 90 m/s based on tests carried out on both FCC catalyst and fresh oxygen carrier.

Finally, a method was developed using CFD in order to characterize the jet cup hydrodynamics and the particles contacting frequency with the jet. It is important to highlight that CFD is used in this investigation to characterize the particles contacting frequency with the jet since it would have been very difficult to characterize this phenomenon experimentally.

The next chapters present the results obtained with first the CFD investigation followed by the experimental results and method developed.

3 CFD investigation

3.1 Introduction

The next step of this investigation is to implement tests conditions which results in a similar mechanical stress exposure for the different solids tested. For this purpose, an analogy was made between the attrition generated in CFB processes and the attrition generated in the jet cup.

In CFB processes, attrition is generated by attrition sources such as cyclones and gas distributor [129]. However, the main parameter controlling attrition is the particles circulation between the different elements/reactors of the CFB process related to the particles inventory. Indeed, the particle circulation, for a given particle inventory, will directly determine the particles contacting frequency with attrition sources. The same analysis can be made in the jet cup: the main attrition source is the high velocity jet and the main parameter impacting the overall attrition rate is the particles contacting frequency with the jet for a given inventory. Therefore, to compare attrition of the different solids on the same basis with the jet cup, the particle contacting frequency with the jet should be equal for both solids. However, the jet cup particles internal circulation is not easily accessible experimentally and it may also depends upon particle properties. The objective is, thus, to evaluate particles circulation and therefore particle contacting frequency within the jet using CFD.

3.2 Characterization of the particles circulation rate within the jet

The particles circulation is determined for both equilibrium FCC and fresh oxygen carrier particles using the CFD method presented in Chapter II.2.4. Simulations with the equilibrium oxygen carrier were not carried out since its mean physical properties are close to the fresh oxygen carrier properties.

One potential parameter identified, which can impact the particle contacting frequency with the jet, is the inventory of particles initially implemented in the jet cup. One can indeed wonder with particles having such a large difference of density if they should be compared with the same initial mass or the same initial volume. To answer this question, three simulations were carried out as presented in Table II-2. First the reference case with 100 grams of equilibrium FCC was simulated. It is important to highlight that the jet cup standard method developed by Cocco et al. [4] uses 100 grams of material. Then two other cases were simulated with the fresh oxygen carrier, one with the same mass than the reference case ($M=100\text{g}$), the other one with the same initial particles volume than the reference case ($M=250\text{g}$). All simulations were run for 20 second of simulation times, the simulation was considered at steady state when the average particles contacting frequency with the jet does not vary anymore with the simulation time. Steady state was therefore reached after about 10 seconds of simulation and results were then averaged from 10 to 20 seconds.

As expected, the flow pattern obtained for the simulations with the fresh oxygen carrier is quite different than with the equilibrium FCC as shown in Figure II-12. With the equilibrium FCC, all particles are suspended and go once in a while into the air jet, where they are carried upward again with a high velocity. With the fresh oxygen carrier, there is an accumulation on the side of the air injection. Particles going into the air jet are then carried upward with a high velocity and fall at the top of the particles accumulation zone where they flow slowly downward toward the air injection. A qualitative validation of the flow pattern was carried out at PSRI using a transparent jet cup. The same trend was visually observed.

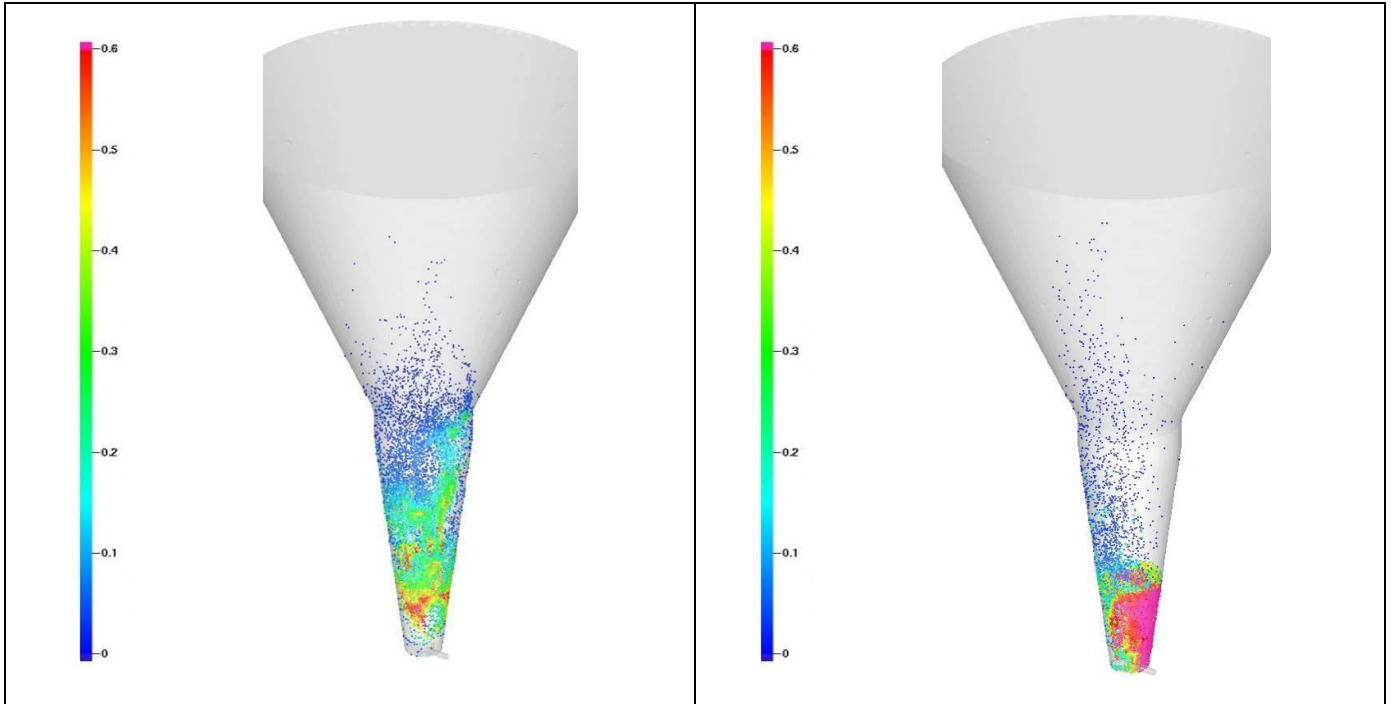


Figure II-12: Solid volume fraction ;simulation with the same volume of solids ; Air injection velocity of 90 m/s On the left: equilibrium FCC; On the right: fresh oxygen carrier

Then, Barracuda VR[®] allows tracking the cumulated impact of particles on the geometry wall. For this purpose an impact number is defined and it is proportional to the particles velocity and mass, a correction factor is then applied according to the impact angle, Barracuda VR[®] default parameters were used. Barracuda VR[®] then calculates the cumulated impact number over the entire simulation time.

Figure II-13 presents the cumulated impact number for the simulations with respectively the equilibrium FCC catalyst and the fresh oxygen carrier.

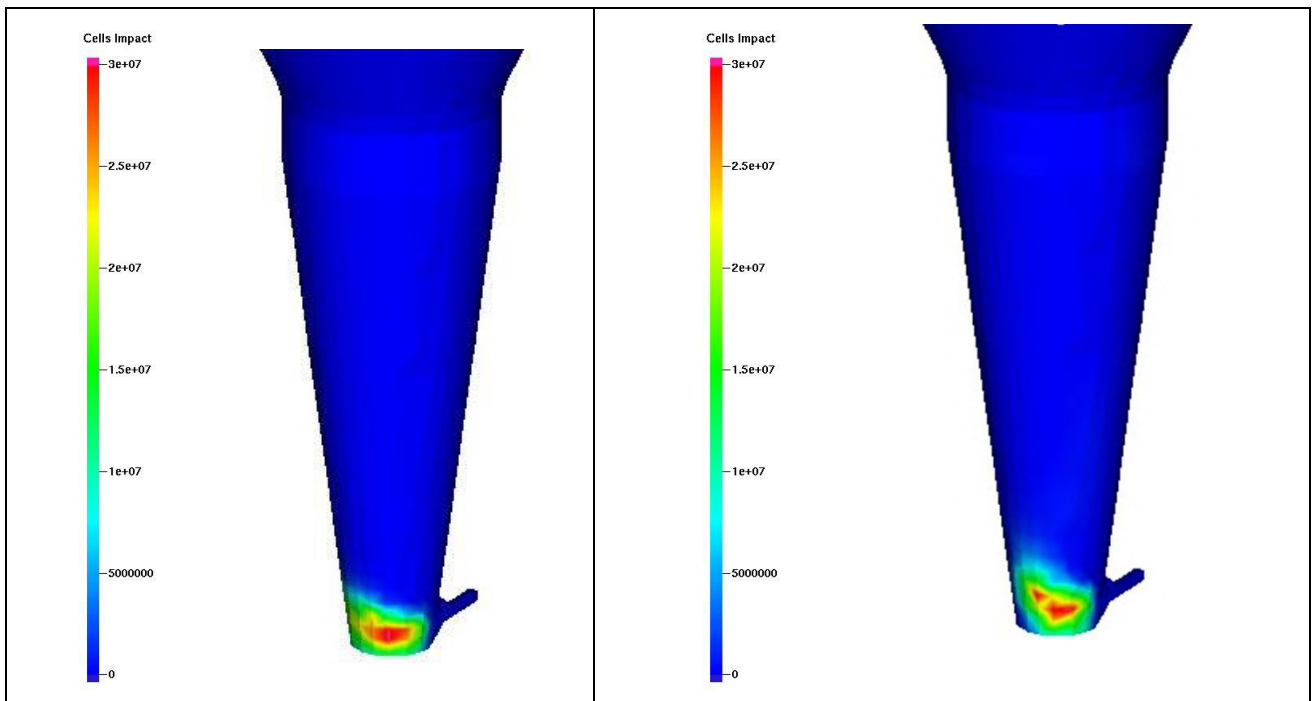


Figure II-13: Barracuda VR[®] impact number at the end of the simulation ;
Air injection velocity of 90 m/s
On the left: Group A equilibrium FCC; On the right: Group B fresh oxygen carrier

For both solids, the higher cumulated impact number and therefore the higher mechanical stress applied on particles due to the wall is located exactly on the opposite side of the air injection. One can then assume that the most important stress applied on particles is carried out in this region of the jet cup and therefore even if the global hydrodynamic is different for both solids tested, the mechanical stress applied remains similar for the same particles circulation frequency into the jet.

The results obtained for the three particle contacting frequency with the jet PC_1, PC_tracer1 and PC_tracer2 are presented in Table II-3.

Table II-3 : Jet particles contacting frequency PC_1, PC_tracer1 and PC_tracer2

	Solid	Solid Density (kg/m ³)	Solid Mean Diameter D ₅₀ (µm)	Solid Sample mass (g)	Initial Volume (cm ³)	PC_1 (s ⁻¹)	PC_tracer1 (s ⁻¹)	PC_tracer2 (s ⁻¹)
n°1	Group A equilibrium catalyst	1 450	70	100	115	0.26	0.25	0.28
n°2	Group B Fresh Oxygen carrier	3 600	180	100	46	0.68	0.65	0.69
n°3	Group B Fresh Oxygen carrier	3 600	180	250	115	0.24	0.25	0.27

First, for the three simulations the particles contacting frequency with the jet measured with the tracers (PC_tracer1 and PC_tracer2) are similar to the one measured with the entire inventory (PC_1) which shows that the solid flow tends to be homogeneous in all cases.

When comparing results for the two simulations conducted with the fresh oxygen carrier, one can see that PC_1 changes dramatically with the solid initial inventory. Indeed, the PC_1 frequency is inversely proportional to the inventory. Then comparison between simulation n°1 and n°3 further suggests that the particle contacting frequency with the jet is set by the initial sample volume since similar PC_1 values were obtained for both cases. Thus, in order to have the same particles contacting with the jet and therefore compare solids on the same mechanical stress exposure, the comparison between the FCC equilibrium catalyst and the fresh oxygen carrier should be done with the same initial volume of particles in the jet cup.

3.3 Conclusions

The CFD investigation allowed the determination of test conditions to compare solids with the same mechanical stress exposure using a similar contacting frequency with the jet. Based on results obtained, the same particles initial volume should be used in order to evaluate and compare attrition resistance of the powders of interest.

As mentioned before, this study is a clear example on how CFD can be used to help characterizing physical phenomena that are difficult to access experimentally. It allowed for a better comprehension of the jet cup test and a better exploitation of the attrition results obtained in the context of the CLC process extrapolation.

It is then important to remind that experimental flow characterization based on visual observation confirmed qualitatively simulations for both solids. In a future work, one could develop a more precise experimental procedure to measure the actual solid contacting frequency with the jet using tracers for example. At present, based on our CFD results, an experimental strategy is proposed as presented in the next chapter with the jet cup experimental results.

4 Mechanical resistance to attrition characterization

From the previous discussions, the jet cup testing was adapted in order to compare the different solids of interest:

- First, the Total Particle Generated Index (TPGI), based on global PSD evolution, is used to characterize attrition in the jet cup for all solids.
- Second an air injection velocity of 90 m/s was chosen based on preliminary testing of each solid.
- Third, the comparison of attrition results is carried out with the same particle initial volume as suggested by the CFD study.

Tests were then conducted as a function of time and initial inventory in the jet cup in order to quantify attrition experimentally for each solid.

Figure II-14 presents the Total Particle Generated Index (TPGI) against several test durations for both equilibrium FCC catalyst and fresh oxygen carrier in comparative conditions (same initial volume of 115 cm³ equivalent of 100 grams of the equilibrium FCC catalyst, jet velocity of 90m/s). The equilibrium oxygen carrier was not tested in these conditions (sample amounts limited).

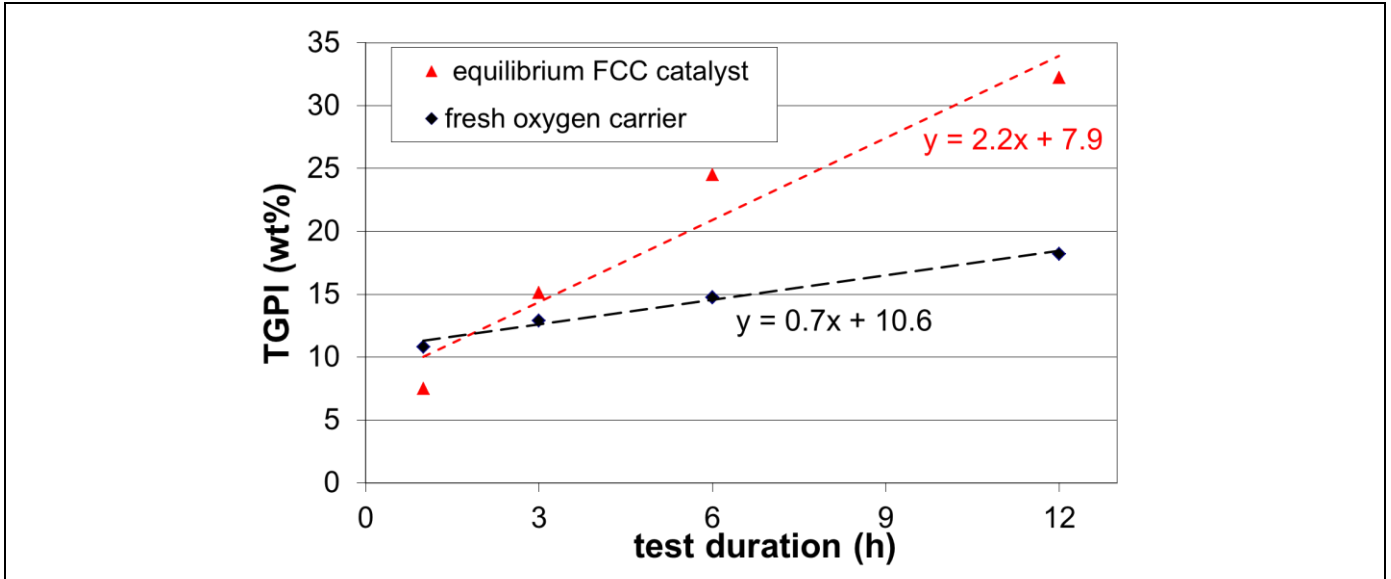


Figure II-14 : Comparison of the Group A FCC catalyst with the Group B oxygen carrier TPGI versus test duration ; comparison at iso initial particles volume ; air velocity injection at 90 m/s

For both solids, one can see that the TPGI increases proportionally to the testing time. The particles mechanical resistance is then characterized by the TPGI linear increasing rate equation against time which can be expressed in the general form shown in equation 63:

$TPGI (\%) = C_{attrition\ rate} \times Test\ duration + B_{initial\ attrition}$	equation 63
--	-------------

Where $C_{attrition\ rate}$ is the TPGI increase rate constant versus test duration and $B_{initial\ attrition}$ characterizes the initial attrition generation. Indeed, we considered the attrition increase linear over the range of test duration tested but one should not forget that at a test duration of 0 hour the attrition rate is necessarily 0. Therefore, the term $B_{initial\ attrition}$ characterizes the attrition generation in the first period of the test. It is then interesting to wonder if $B_{initial\ attrition}$ is dependent only on intrinsic particle mechanical properties or if is dependent on the test operating conditions with for example the sample initial inventory. This question is investigated further with the next experimental results.

The parameters $C_{attrition\ rate}$ and $B_{initial\ attrition}$ can then be used as a comparison basis for the characterization of the solid mechanical resistance to attrition demonstrating that the fresh oxygen carrier shows better performances. Different questions were then raised: can we apply the same procedure for a lower initial sample volume since powder inventories can be limited? What is the effect of using a smaller sample volume on the characterizing coefficients $C_{attrition\ rate}$ and $B_{initial\ attrition}$? Will we get the same ranking of powders concerning their resistance to attrition? In order to investigate these different issues, another series of tests were carried as explained below.

Tests were first carried out for all solids with a percentage of 100, 80, 65, 50, 35, 30 and 25 of the initial volume equivalent to 100 grams of FCC. Figure II-15 presents the TPGI versus the inverse of the initial sample volume.

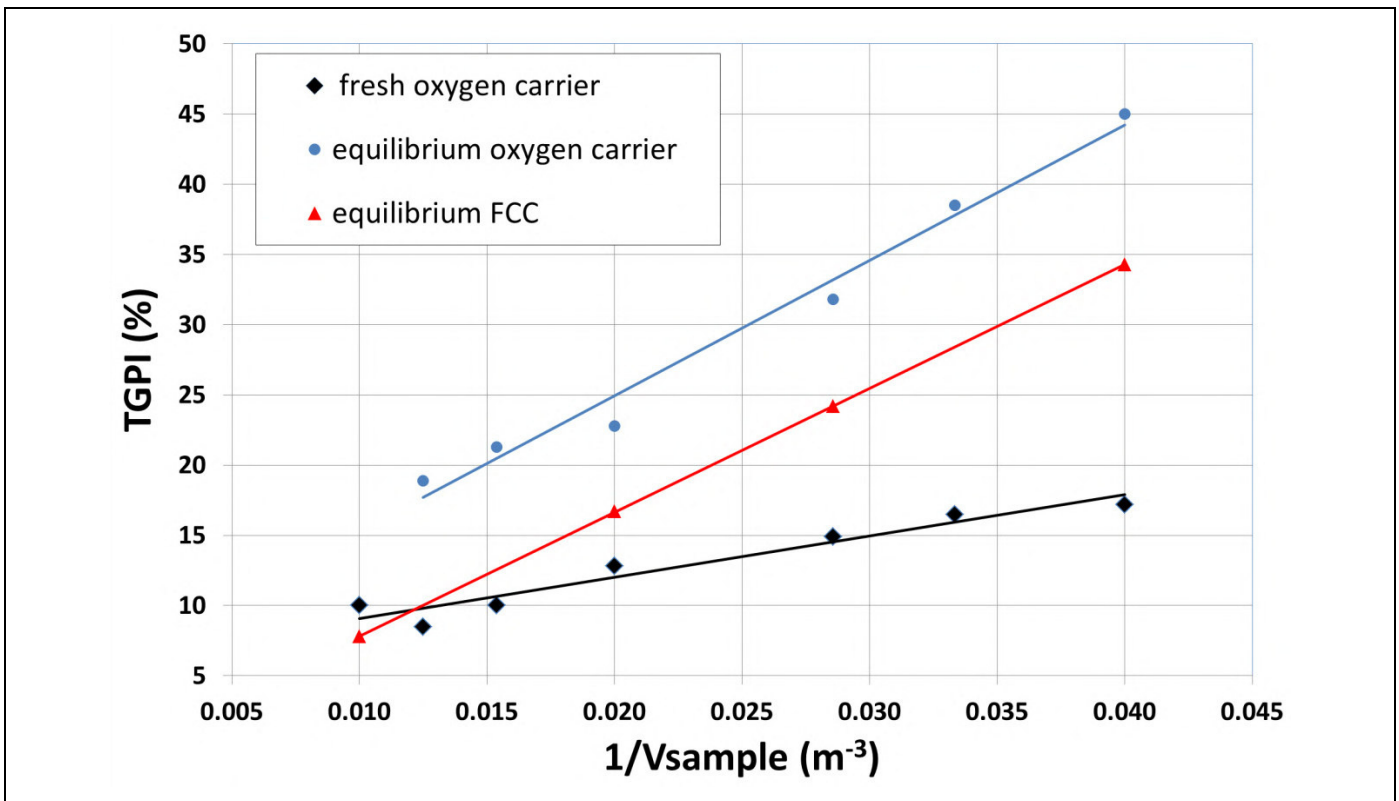


Figure II-15 : TPGI against the inverse of the initial sample volume ;
Air injection velocity of 90 m/s ; Test duration of 2 hours

One can see that the TPGI index increases almost linearly against the inverse of the initial sample volume for all solids tested. This trend therefore confirms the hypothesis that attrition in the jet cup is proportional to the particles contacting frequency with the jet for all cases. Indeed, one can express the averaged particle contacting frequency with the jet using Equation 64:

$$f_{particles\ in\ jet} = \frac{F_{vp_jet}}{Total\ Volume\ of\ particles}$$

Equation 64

Where:

- $f_{particles\ in\ jet}$ Averaged particles contacting frequency with the jet (s^{-1})
- F_{vp_jet} Global volume flux of particles circulating in the jet (volume of particles per second)

The results presented in Figure II-15 clearly demonstrate that the global volume flux of particles circulating in the jet F_{vp_jet} is constant between all experiments. Using a smaller amount of particles will then generate a higher contact frequency and a higher attrition rate since the volume of particles circulating in the jet F_{vp_jet} is constant and since the global particle volume in the jet cup is smaller. Moreover it also confirms that all solids can be compared with a lower initial sample volume since the attrition remains proportional to the circulation rate in these conditions.

Finally, one could conclude that the test procedure with the variation of the initial sample volume can be suitable to compare the different solids. Indeed, from the comparison of the three solids curves increase rate in Figure II-15, one can see that the fresh oxygen carrier presents the best resistance to attrition performances, followed by the equilibrium FCC and finally the equilibrium oxygen carrier with the poorest performances. However, this test procedure is not considered suitable since it requires solid inventories that might not always be available. Second, it is difficult to interpret the curves tendency when the inverse to the volume “ $1/V$ ” tends to 0 meaning an infinite inventory. Indeed, an infinite inventory is of course not possible and large inventories will anyway affect the flow hydrodynamic with a jet cup full of particles. The procedure with the variation of the test duration is therefore preferred since the two coefficients $C_{attrition\ rate}$ and $B_{initial\ attrition}$ can be used to characterize the solids resistance to attrition.

The following method was then applied on the three solids using an equivalent volume of 35 grams of FCC for all solids (volume around $40\ cm^3$).

- Two test durations were investigated with respectively two and three hours. These shorter test durations were chosen in order to repeat the test more rapidly and also because attrition rates obtained are higher when using smaller amount of particles. The test duration can therefore be reduced.
- For all solids, the same solid sample is used for the two tests durations. Therefore, after two hours, an amount of particles lower than 2 grams is taken to measure the TPGI and the test is ran for another hour to get the TPGI at three hours.
- The test with the two durations is repeated 6 times for the equilibrium FCC and the Group B fresh oxygen carrier. Tests were repeated only 2 times for the equilibrium oxygen carrier because of the low amount of particles available.

Using this procedure we assume that the small amount of particles taken from the test to measure the TPGI at two hours does not influence the result for the TPGI at three hours. The amount of particles withdrawn represents about 5%wt of the total inventory.

Figure II-16 presents all TPGI values obtained for the three solids. The line connecting two points indicates the experiments carried out on the same solid sample.

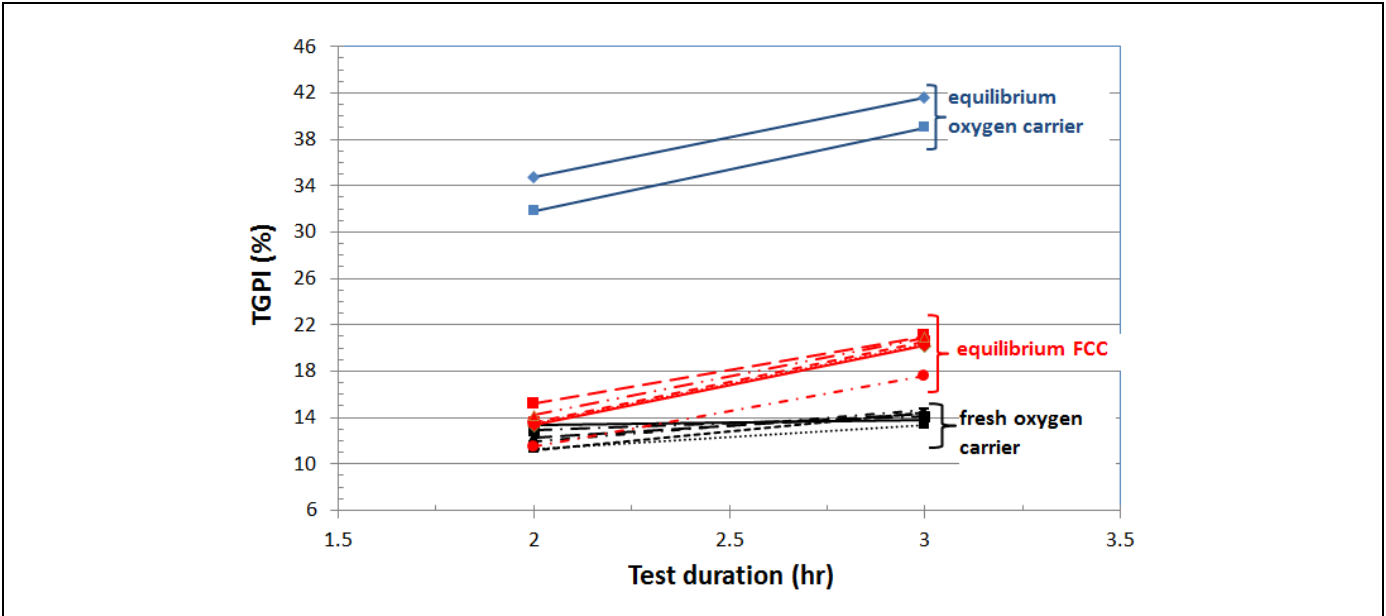


Figure II-16 : Comparison of the three solids of interest TGPI versus test duration ; comparison at iso initial particles volume ; air velocity injection at 90 m/s

Table II-4 shows the average values and standard deviation of the coefficient $C_{attrition\ rate}$ and $B_{initial\ attrition}$ for the three solids. All coefficients $C_{attrition\ rate}$ and $B_{initial\ attrition}$ corresponding to individual on each solid can be found in Appendix 1.

Table II-4 : Average values and standard deviation of the coefficient $C_{attrition\ rate}$ and $B_{initial\ attrition}$ for the three solids with a volume equivalent to 35 grams of FCC (40 cm³)

Solids	Coefficient $C_{attrition\ rate}$ Average value / standard deviation	Coefficient $B_{initial\ attrition}$ Average value / standard deviation
equilibrium FCC	6.5 / 0.5	13.5 / 1.2
fresh oxygen carrier	2 / 1	12.15 / 0.8
equilibrium oxygen carrier	7.1 / 0.2	33.2 / 2

Different remarks can be pointed out:

- First, concerning the evaluation of the resistance to attrition of the three solids, one can see a clear ranking with the equilibrium oxygen carrier showing poor performances while the fresh oxygen carrier has the best resistance to attrition. Equilibrium oxygen carrier is clearly more fragile than fresh oxygen carrier. This is consistent with observation made by Nelson et al. [145] and can be explained by the fact that oxygen transfer cycles and temperature effects tend to weaken the particle mechanical structure.
- Second, it is interesting to notice that both coefficients $C_{attrition\ rate}$ and $B_{initial\ attrition}$ have to be considered to compare the solids. Indeed, looking only at coefficient $C_{attrition\ rate}$, one could assume that the Group A equilibrium FCC and Group B equilibrium oxygen carrier demonstrate similar attrition performances. However, the initial attrition characterized by the coefficient $B_{initial\ attrition}$ is much higher for the second solid.
- Third, concerning the repeatability, one can see that tests with the Group B fresh oxygen carrier show an important variation in term of slopes with a high standard deviation for coefficient $C_{attrition\ rate}$. This important variation can be explained by the fact that it is more challenging

with the fresh solid to have a good repeatability in term of homogeneous solid samples compared to equilibrium solids.

For FCC catalyst and fresh oxygen carrier particles, experimental results have been obtained as function of time for various inventories (shown respectively in Figure II-14 and Figure II-16). We can then compare the two coefficients values for the experiments with an initial volume equivalent to respectively 100 grams and 35 grams of FCC as shown in Table II-5.

Table II-5 : Comparison of $C_{attrition\ rate}$ and $B_{initial\ attrition}$ as a function of the sample inventory with an equivalent volume of 100 grams and 35 grams of FCC

Solids	equilibrium FCC coefficient $C_{attrition\ rate}$	fresh oxygen carrier coefficient $C_{attrition\ rate}$
Tests with an initial volume equivalent of 100 g of FCC	$C_{attrition\ rate}(100) = 2.2$	$C_{attrition\ rate}(100) = 0.7$
Tests with an initial volume equivalent of 35 g of FCC	$C_{attrition\ rate}(35) = 6.5$	$C_{attrition\ rate}(35) = 2$
Ratio $C_{attrition\ rate}(35)$ over $C_{attrition\ rate}(100)$	2.95	2.85
Ratio Volume (V_{100}/V_{35})	2.86	

Solids	equilibrium FCC coefficient $B_{initial\ attrition}$	fresh oxygen carrier coefficient $B_{initial\ attrition}$
Tests with an initial volume equivalent of 100 g of FCC	$B_{initial\ attrition}(100) = 7.9$	$B_{initial\ attrition}(100) = 10.6$
Tests with an initial volume equivalent of 35 g of FCC	$B_{initial\ attrition}(35) = 13.5$	$B_{initial\ attrition}(35) = 12.15$
Ratio $B_{initial\ attrition}(35)$ over $B_{initial\ attrition}(100)$	1.71	1.15
Ratio Volume (V_{100}/V_{35})	2.86	

One can see from Table II-5 that the attrition increase rate coefficient $C_{attrition\ rate}$ increases for both solids when decreasing the initial sample volume. The most interesting result is that the ratio $C_{attrition\ rate}(35)$ over $C_{attrition\ rate}(100)$ is in the same range for both solids and it is also in the same range than the ratio of the highest volume divided by the smallest volume (V_{100}/V_{35}). This result demonstrates that for both solids the attrition rate is linearly proportional to the sample volume and therefore when decreasing the initial sample volume the attrition rate is affected in the same way for both solids. Moreover, it comforts the CFD simulation results. Indeed, CFD indicated that having the same initial sample volume is the parameter to respect to compare solids on the same mechanical stress basis. The results of Table II-5 confirm this result since for both solids the attrition rate is changed in the same proportion between the two initial volume tests.

Concerning the coefficient $B_{initial\ attrition}$, one can see that it is less affected by the change of the sample inventory especially for the fresh oxygen carrier. Therefore, the coefficient $B_{initial\ attrition}$ could be dependent on the intrinsic particle mechanical property. Indeed, its variation was important between the two oxygen carriers tested (see Figure II-16) and one can then conclude that the mechanical properties of the equilibrium solid has been affected by the CLC process conditions which is in accordance with the results of Nelson et al. [145]. Further work is however needed to connect $B_{initial\ attrition}$ attrition to the intrinsic particle properties.

5 Discussion

Several points can be discussed concerning the comparison method developed based on the results presented.

- To characterize the attrition resistance of our solids of interest, we first defined the attrition index TPGI and we then chose the jet velocity based on experiments carried out on different solids. The CFD investigation suggested that solids should be compared with the same initial sample volume in order to be exposed to a similar mechanical stress. Experimental results comforted this result with the attrition rate evolving in the same proportion for both solids when changing the initial sample volume. One can then wonder about the need to develop a precise experimental measurement of the particle contacting frequency with the jet. The experimental results clearly suggest that the trends highlighted by CFD simulations are valid.
- Based on our results, we demonstrated that the fresh oxygen carrier shows better resistance to attrition than equilibrium FCC catalyst while the equilibrium oxygen carrier shows the poorest performances. Therefore, oxygen carrier properties were modified and deteriorate during the CLC process operations. Attrition resistance was strongly affected and we therefore need to find alternative oxygen carriers showing better performances after reaction or to apply different CLC process operating conditions to minimize oxygen carrier changes. The strategy developed in this work will then allow for a fast screening of the future oxygen carriers resistance to attrition after testing in process condition, using a comparison with the reference equilibrium FCC catalyst.
- It is also important to point out that if we had used standard jet cup testing conditions with a sample mass of 100 grams for all solids, we would have concluded that the fresh oxygen carrier is less resistant to attrition. But in fact, in this case, with a smaller initial volume, the particles contacting frequency with the jet is increased as well as the attrition generated. It is therefore crucial to understand the jet cup mechanisms and phenomena to orientate the test strategy if one wants to reach the correct conclusions.
- It was demonstrated that the coefficient $C_{attrition\ rate}$ is clearly dependent of the attrition resistance related to jet contacting. Further work is then needed to connect coefficient $B_{initial\ attrition}$ to intrinsic particle mechanical resistance and also jet cup testing conditions. In the future, the effect of the jet velocity on the coefficients $C_{attrition\ rate}$ and $B_{initial\ attrition}$ could also be investigated in order to characterize the attrition kinetics rates on a large range of gas velocities. These results could then be used to connect the jet cup attrition rates to the fluidized bed main sources of attrition (cyclones, jets).
- Then, the methodology developed allows screening different solids with respect to their resistance to attrition. However, these data are difficult to extrapolate if one wants to estimate precisely the attrition due to mechanical stress in an industrial circulating fluidized bed process. In general, a better characterization of the attrition rates and hydrodynamic in the jet cup is needed in order to connect the jet cup attrition with the circulating fluidized bed sources of attrition such as cyclone and distributor jets. If such connection is carried out, one could then implement a multi scale approach with the characterization of the process sources of attrition using the jet cup and then the use of a population balance model to estimate the attrition at industrial scale as carried out by Werther et al. [129,130].
- Finally, the study clearly shows that particles properties are affected when exposed to process conditions (and most likely to reduction/oxidation cycles) as shown by the difference exhibited between fresh and equilibrium oxygen carriers. It is therefore critical to relate particle attrition resistance to their process conditions exposure.

6 Conclusions and perspectives

We have shown that that it is important to assess the attrition phenomena at the early stage of a process development but that there is little information available on attrition at industrial scale for the Group B oxygen carriers used in the CLC process. A methodology was then proposed in order to compare the resistance of attrition of the oxygen carriers with FCC catalyst for which attrition at industrial scale is well characterized.

A methodology using a jet cup test developed by Cocco et al. [116] was then developed in order to compare different solids with regard to attrition. The jet cup allows assessing the resistance to attrition using a small amount of particles which is an advantage at the early stage of the CLC process development where different oxygen carriers can potentially be used and where the quantities of solids available are limited.

In order to compare solids with different Particle Size Distributions, we first defined a new attrition index that does not depend upon a given particle size. This index is based on the total percentage of particles generated by attrition and it is called TPGI (Total Particles Generated Index). This index also gives the possibility to estimate the maximum diameter of particles generated by attrition. We then chose a jet velocity of 90 m/s based on the attrition phenomena generated in the jet cup, particle abrasion being the phenomena targeted. As suggested by CFD, solids were compared with the same initial sample volume. The particles mechanical resistance was then characterized by the TPGI increase rate versus test duration equation, this increase being considered linear.

The methodology was applied on three solids (equilibrium FCC catalyst and fresh and equilibrium oxygen carriers). It provided satisfying results with the fresh and equilibrium oxygen carriers performing respectively better and worse than the reference FCC catalyst. The effect of the CLC process conditions on the mechanical resistance of the particles considered was therefore clearly emphasized by the test.

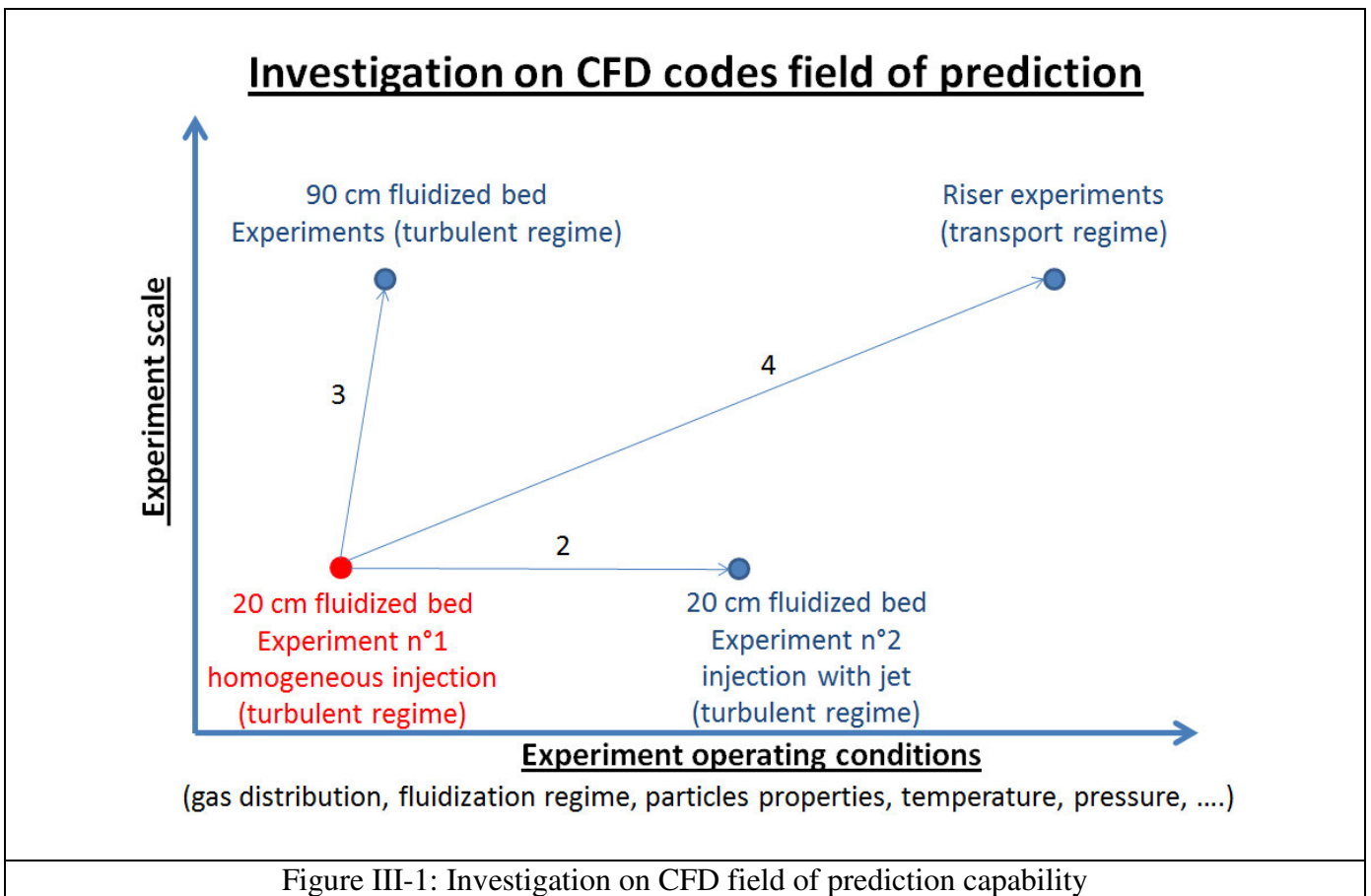
The use of CFD allowed a better characterization and understanding of the jet cup test. We indeed demonstrated that solids should be compared with the same initial sample volume in order to apply a similar mechanical stress, which was not obvious at all when starting the present work. This CFD result was then confirmed experimentally when we showed that the attrition increase rate was linearly proportional to the initial sample volume for both solids and changing the initial sample volume affected both solids attrition increase rate in the same proportion. A global validation of CFD simulations was therefore achieved, meaning that the relevant hydrodynamic aspects were captured. It is then important to highlight that the prediction of local parameters such as particle and gas velocities in the jet cup cannot be considered validated and further work is needed for this purpose. **This study therefore shows that CFD can be used to characterize physical phenomena that are difficult to access experimentally and how it can improve and orientate the data analysis in the context of attrition phenomena extrapolation.**

Finally, the methodology developed allows for a first screening of solids with respect to their mechanical resistance to attrition in a jet cup. Useful information can be obtained from such a test especially at the early stage of a process development. Further work is however needed if one wants to extrapolate attrition results from a lab scale experiment such as the jet cup to an industrial scale. For this purpose, a better characterization of the particles kinetic rates versus hydrodynamic conditions is necessary. Then the next step consists in correlating lab scale experimentation with the main sources of attrition in circulating fluidized bed for finally implementing a population balance modeling to assess attrition at industrial scale as a function of precise design criteria. A PhD in partnership with the university of Leeds and Total was launched in 2015 to develop such a multi-scale approach [146,147].

III. USE OF CFD FOR EXTRAPOLATION MATERIAL AND METHODS

1 Introduction

Minimizing the risk of extrapolation is mandatory when developing processes and technologies. Extrapolation relates to first the understanding of physical phenomena at accessible scales through dedicated and focused experiments. In a second step, modeling is utilized to transpose observation from lab scale to an industrial perspective. CFD modeling tools are increasingly used for the development and extrapolation of processes and technologies. However, as discussed in the literature review concerning CFD for Circulating Fluidized Beds (CFB), modeling of the crucial gas-particles and particles-particles interactions remain challenging. Thus, most of the CFD studies in the literature usually focus on a given configuration at a given scale where mesh refinement dependency and closure models such as drag laws are investigated against experimental data when available. However, there is a lack of published studies to evaluate the reliability of simulation results when using a CFD model validated at a given scale and operating conditions to another scale or to different operating conditions. This is however essential since one of the CFD ultimate goals is to facilitate scale-up which remains a very complex task for multiphase flow systems such as fluidized bed. The work presented in the second part of this PhD is therefore an attempt to study this issue. Our strategy is presented in Figure III-1.



In this figure, the CFD field of prediction is defined against two axis with first the experiment scale and second the experiment operating conditions which gather a certain number of parameters such as particles properties, fluidization regimes, gas distribution, temperature, pressure, etc. To be rigorous, each of these

parameter should be represented on a separate axis, but for a better understanding and simplicity, we put them on the same axis in Figure III-1. During a scale-up study, it is important to focus on the most important parameters to be carefully studied. The choice of these relevant parameters is critical and relies mostly on knowledge and experience. One can therefore consider for instance that it is more important to focus on changes related to operating conditions than on changes on particles properties if the solid to be used industrially is the solid used during cold flow testing.

It is important to highlight that we focused only on fluidized bed with Geldart Group A particles since this work has been carried out in the context of FCC process developments. The simulation strategy that we proposed then consists in the following steps:

- First, as carried out in many CFD investigations, an experiment is taken as a reference to study and optimize simulation predictions as a function of the CFD code parameters such as drag law and boundary conditions. This experiment is indicated in red on Figure III-1, it consists of a turbulent 20 cm fluidized bed of FCC particles with a homogeneous gas injection as detailed later.
- In a second step, the parameters found in the first step are used to investigate the codes capability to predict a different operating condition at the same scale. In our case, we chose the same 20 cm fluidized bed experiment with FCC particles but with a different gas injection configuration.
- Third, the CFD code predictions capability are investigated at another scale with experiments carried out on a 90 cm fluidized bed using solids and operating conditions similar to the reference case.
- Finally, the CFD code predictions capability for another scale with different operating conditions in a different fluidization regime is investigated using riser experiments with FCC particles.

Different points can be discussed regarding the choices taken for this strategy:

- First, we chose to focus on the FCC process. The reason is that technology development and extrapolation using CFD for this process is a topic of great interest [1,148,149]. Moreover, this type of development is also interesting for other Circulating Fluidized Bed processes using Geldart Group A particles [17,19].
- Second, we focused in the second step of the simulation strategy on the effect of gas injection distribution in turbulent beds. We chose to investigate this aspect since it is an important factor for turbulent bed reactor performances [9]. It is therefore important to study if CFD can predict gas distribution effects.
- For the third step, we focused on the effect of size extrapolation. We therefore chose a larger 90 cm fluidized bed with operating conditions similar to the 20 cm fluidized bed experiments in order to evaluate size effect keeping the same fluidization regime.
- Finally, we also chose to investigate CFD predictions by changing operating conditions but also fluidization regime to investigate the potential limits of the CFD model. Indeed, it is also important to be able to model different fluidization regimes in the same simulation if one wants to investigate for example the injection of a dilute transported mixture of gas and particles in a turbulent fluidized bed as it is the case for the second stage regenerator of the R2RTM Resid FCC [33].

This work is divided in three chapters:

- In this chapter, we present the material and methods used to develop our simulation strategy. Three different experimental set-up are used with first a 20 cm fluidized bed, second a 90 cm fluidized bed and finally a 30 cm riser. The characteristics of the FCC powders used in the three different experiments are first presented. Then, each experimental set-up with their corresponding measurement techniques is introduced. Finally, the CFD approaches and codes as well as the common simulation parameters are presented.
- Then in the next Chapter VI, experimental results obtained are presented and discussed.
- Finally, in Chapter VII we present the CFD developments and results based on the experimental results presented in Chapter V.

2 Powder characteristics used in experiments

Three different FCC catalyst powders were respectively used in the three experimental set ups. A fresh catalyst powder was used for the 20 cm fluidized bed experiments, equilibrium FCC catalyst powders coming from industrial units were used for the 90 cm fluidized bed and 30 cm riser experiments.

It is first important to point out that we targeted experimental systems at different scales and operating conditions having similar powder properties. Indeed, if particles with different properties are used between experiments, it then becomes an effect to be investigated and characterized. We do not target to study this effect and we therefore chose experiments with powders having similar properties. Figure III-2 and Table III-1 present respectively the particle size distribution and the characteristics of the powders used in the three different experimental systems. The particle size distribution was measured by laser diffraction while the particle density was measured by mercury porosimetry technique.

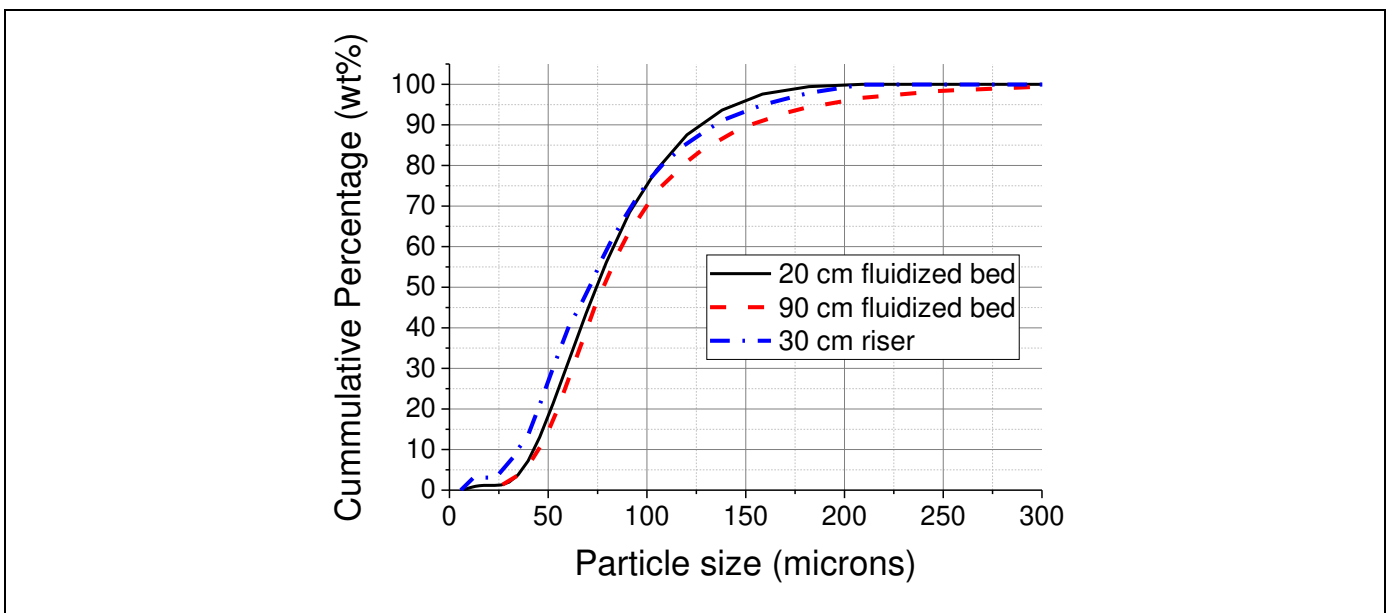


Figure III-2. Particle size distribution of the powders used in the three experiments

Table III-1: Characteristics of the powders used in the three experiments

	20 cm fluidized bed	90 cm fluidized bed	30 cm riser
Particle density (kg/m ³)	1 260	1490	1450
dp ₅₀ (microns)	75	78	73
d _{p,sv} (microns)	71	74	55
Percentage of fines below 40 microns (wt%)	7.2	6.4	13.8

First, one can notice differences between the powders characteristics which shows that FCC catalyst properties are not standard and can vary according to the catalyst formulation and fabrication as well as the catalyst life cycles in the industrial unit with phenomena of attrition and change of internal structure [150]. It is therefore challenging to obtain results from different experimental systems using the exact same powder properties.

Then from Table III-1, one can observe a 13% variation between the highest and the lowest particle density values. The mean diameters are in the same range for the three powders while the Sauter diameters are in the same range for the 20 cm and 90 cm fluidized beds powders, it is however lower for the 30 cm riser powder because of the higher fines content.

In the experiments CFD simulations, particles density is an input of the solid phase description. Then, in the MP-PIC CFD approach used in this study, the particle size distributions presented in Figure III-2 are used as an input. For the second CFD Euler/Euler approach investigated in this study, the Sauter mean diameter is initially used as an input to describe the full particle size distribution. This parameter was then modified with larger diameters to model particles clustering phenomena as described in Chapter V.2.2.

Finally, the solid volume fraction at the minimum of fluidization was determined for the catalyst used in the 20 cm fluidized bed. This value is used for the optical probe signal post-processing as presented in Chapter III.3.3.2. The minimum of fluidization was determined on a 4 cm fluidized bed using 90 grams of catalyst. The minimum of fluidization velocity was evaluated with the bed pressure drop evolution versus gas flowrate method [2] and the solid volume fraction was then obtained measuring the bed height. Table III-2 presents the characteristics at minimum of fluidization obtained.

Table III-2: Characteristics at the minimum of fluidization for the catalyst used in the 20 cm fluidized bed

Minimum fluidization velocity (mm/s)	Solid volume fraction at minimum of fluidization
2.8	0.58

3 Fluidized bed of 20 cm

The 20 cm fluidized bed experimental results are used in the simulation strategy Steps 1 and 2 in order to evaluate the CFD code predictions at lab scale for different operating conditions. We chose a fluidized bed of this size for several reasons. First, it is a simple configuration where instrumentation can be easily implemented. It also allows having a column diameter larger than gas bubbles in a turbulent Geldart Group A fluidized bed.

3.1 Equipment and operating conditions

Figure III-3 presents the configuration of the 20 cm fluidized bed used to study turbulent fluidization with two different gas distribution systems as presented in the simulation strategy.

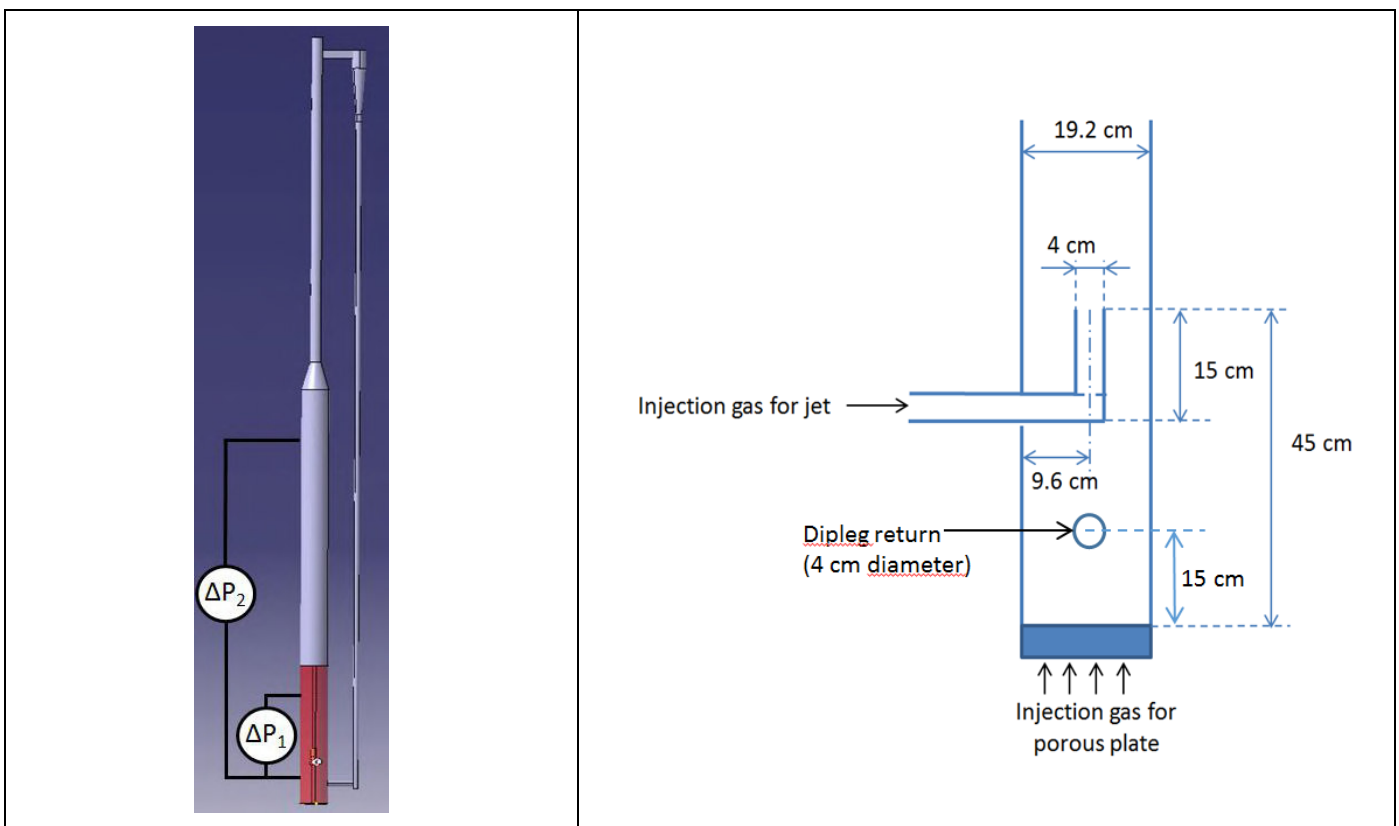


Figure III-3. 20 cm fluidized bed configuration.
 Left: entire cold flow model; right: detail of the column bottom.

The cold flow mockup, located at IFP Energies nouvelles in Solaize, consists in a fluidized bed vessel with an inner diameter of 19.2 cm and a height of 3 meters. A 7.5 cm restriction is then implemented at the top of the bed before the cyclone. The entire equipment is made of PVC material except for the cyclone which is made of metal. All equipment parts are grounded and electrostatic effects such as electrical arcs in the column were not observed during experiments. The particles recovered by the cyclone are then sent back to the bed with a 4 cm dipleg. As shown in Figure III-3, the dipleg returns into the bed 15 cm above the column bottom where gas is injected through a porous plate. The porous plate characteristics and pressure drop curve can be found in Appendix 2. Another gas injection is implemented inside the bed through a 4 cm tube with an elbow connected to a side tube, precise dimensions being indicated in Figure III-3.

The air used for fluidization comes from the research center utility network. It is dry compressed air supplied in the lab at ambient condition with an average temperature of 20°C.

Two operating conditions are investigated as shown in Table III-3.

Table III-3: Operating conditions for the 20 cm fluidized bed experiments

	Injection through Porous plate (Nm ³ /hr)	Injection through jet tube (Nm ³ /hr)	Bed superficial velocity (m/s)
Experiment n°1	66	0	0.64
Experiment n°2	16.5	49.5 (V _{jet} =12 m/s)	0.64

The pressure in the dilute phase is measured before the restriction at the top of the bed and was equal to 6kPg for all experiments.

In both experiments, the same superficial turbulent regime velocity is used. In experiment n°1 all the gas is injected in the porous media. In experiment n°2, 75% of the gas is injected through the jet, the jet velocity being around 12 m/s, the other 25% of the gas being injected through the bottom porous plate. The choice of the jet velocity is based on the superficial gas velocity criteria used in the R2R™ Resid FCC [33] units for the injection of the dilute gas/catalyst mixture through a transport line into the second stage regenerator (one can refer to Figure I-3 for a schematic diagram of a FCC alliance R2R™ Resid FCC unit). Indeed, one objective is to investigate if CFD is able to predict the effect of such a gas distribution. For this purpose, our experimental set up allows generating two well controlled gas repartitions with the experimental characterization of their effects on the bed hydrodynamic. The experimental results will then be used to investigate if the CFD codes can predict these effects in a context of extrapolation where gas distribution is a key factor for turbulent bed reactors performances.

3.2 Experimental techniques

Two Keller differential pressure probes are used to measure the bed density and bed level, their implementation is shown in Figure III-4. The acquisition signal frequency is 5 Hz. All the probes branches have a diameter of 4 mm and are flushed with an air flowrate in the range of 15 to 20 liters per hour. The flushing air flowrate is controlled separately in each branch in order to have a pressure drop measurement of zero when the bed is empty.

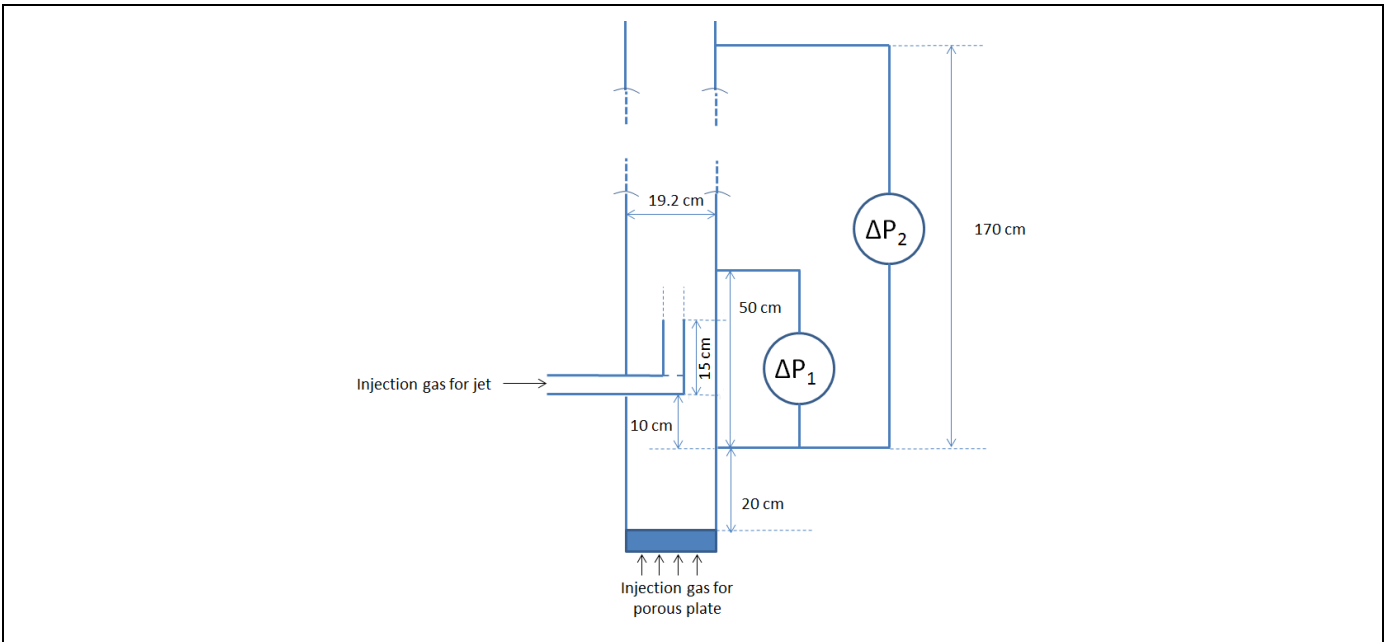


Figure III-4: Pressure probes implementation on the 20 cm fluidized bed

The bed density and level are then obtained with Equation 65 and Equation 66.

$\rho_{BED} \left(\frac{kg}{m^3} \right) = \frac{\Delta P_1}{g \times H1} = \frac{\Delta P_1}{g \times 0.5}$	Equation 65
$H_{BED} = \frac{\Delta P_2}{g \times \rho_{BED}}$	Equation 66

Optical probes are then used to measure solid volume fraction profiles in the column. Figure III-5 presents the optical probes used in this investigation which have been supplied by the University of British Columbia in Vancouver. Similar probe has already been used by Tebianian [96] to measure local solid volume fractions as well as local particles velocity in a 13.3 cm fluidized bed. Liu [99] also used similar probes to characterize solid volume fraction and particles velocity in a dense riser.

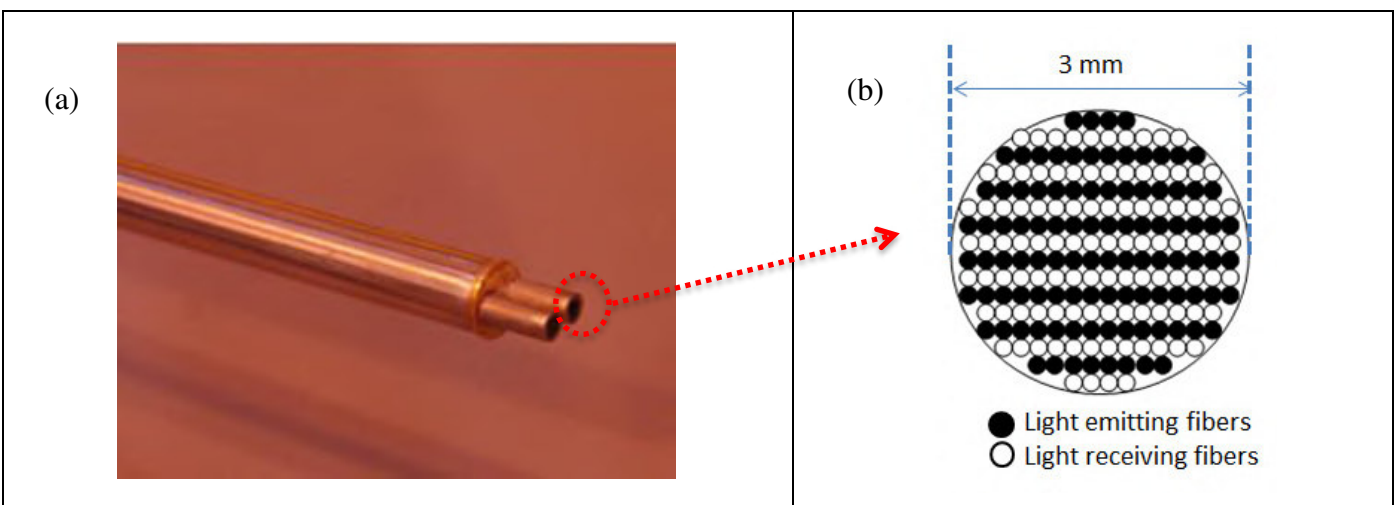


Figure III-5: Fiber optic probes used
(a) Dual probe ; (b) Emitting and receiving fibers arrangement

The probe consists in two 3 mm diameter channels next to other, each channel being composed of light emitting and light receiving fibers in a parallel arrangement. The signal of each channel is post-processed separately as presented in the next chapter. The light receiving fibers signal is converted into an electric signal with a photodiode. The electric signal can then be modified with an amplifying circuit using gain and off-set options and finally the electric signal is numerically converted using an acquisition card. A user interface software allows choosing the acquisition frequency and duration.

The probe is inserted in the bed through dedicated taps to conduct in situ measurements. In total, six profiles are acquired as shown in Figure III-6. First, three different height are investigated with respectively position 1 (low), position 2 (intermediate) and position 3 (high). These 3 heights are located respectively 5cm, 10cm and 15 cm above the jet outlet. For each height, two profiles are then acquired in the “West/East” and “North/South” directions as shown in Figure III-6.

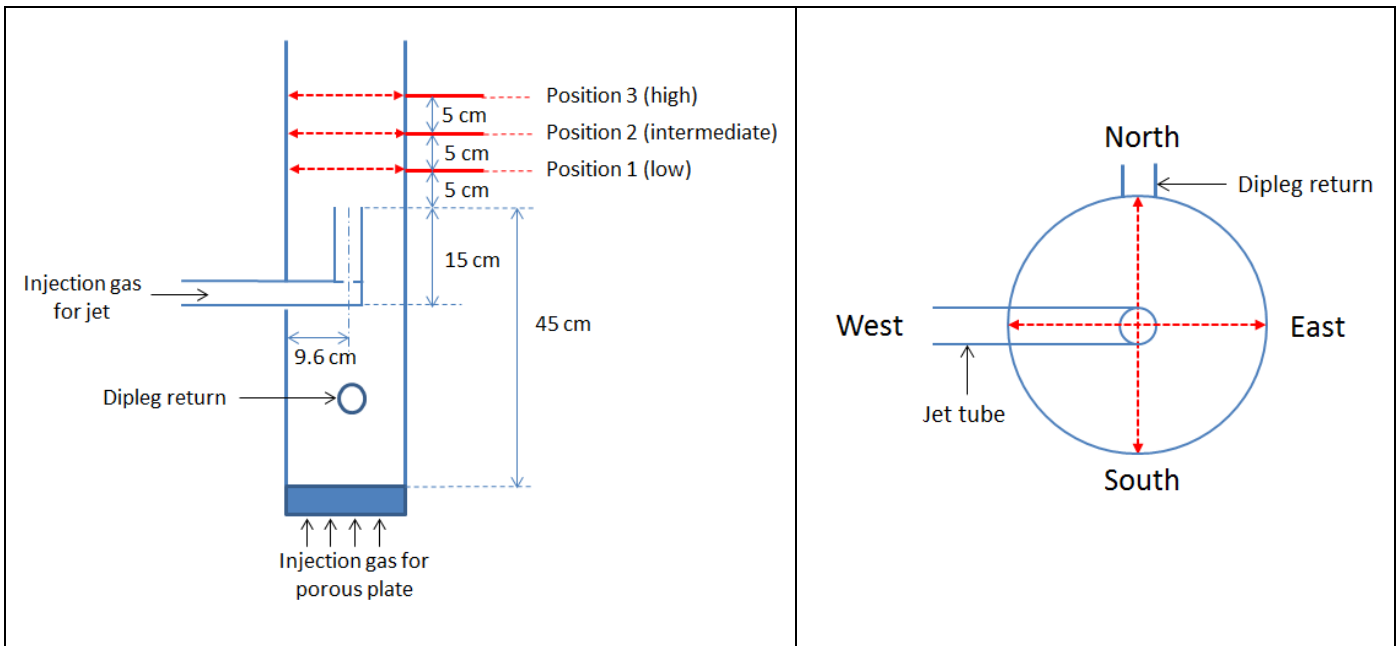


Figure III-6: Optical probes profiles positions

It is interesting to notice that the jet side tube is located in the same direction than the West/East profile while the dipleg return is located in the North/south direction. Eleven points are acquitted for each profile as shown in Table III-4. The six profiles represent therefore a total of 66 acquisition points.

Table III-4. Optical probe profile points locations

Measurement distance from the column center (mm)	-90 ; -72 ; -54 ; -36 ; -18 ; 0 ; +18 ; +36 ; +54 ; +72 ; +90
Measurement distance from the jet (mm)	50 – 100 – 150

3.3 Optical probe signal post-processing

As mentioned in the literature review, different methods are used to calibrate and post-process the optical probe signals in order to get local solid volume fractions [97,98]. This chapter presents the methodology used in this study, with first a simple characterization of the probes signal response and second the experimental procedure developed to convert the probes signal into a local solid volume fraction.

3.3.1 Optical signal characterization

Before using the probe in complex situations as encountered in the fluidized bed, we spent some time to evaluate / understand the way the probes work using basic and well defined configurations.

A graduation of black and white printed on a sheet of paper shown in Figure III-7 was first used to characterize and understand better the probe signal response. The system acquisition system shown in Appendix 2 allows setting the light intensity of the emitting fibers and the offset and gain of the received signal. For this characterization, the signal offset and gain were set to the value “0”. Then the probe was faced to the pure white part of the graduation sheet presented in Figure III-7 and the light intensity of the emitting fibers was set in order to have a signal of 4V. The probe was then moved through the different black and white graduations.

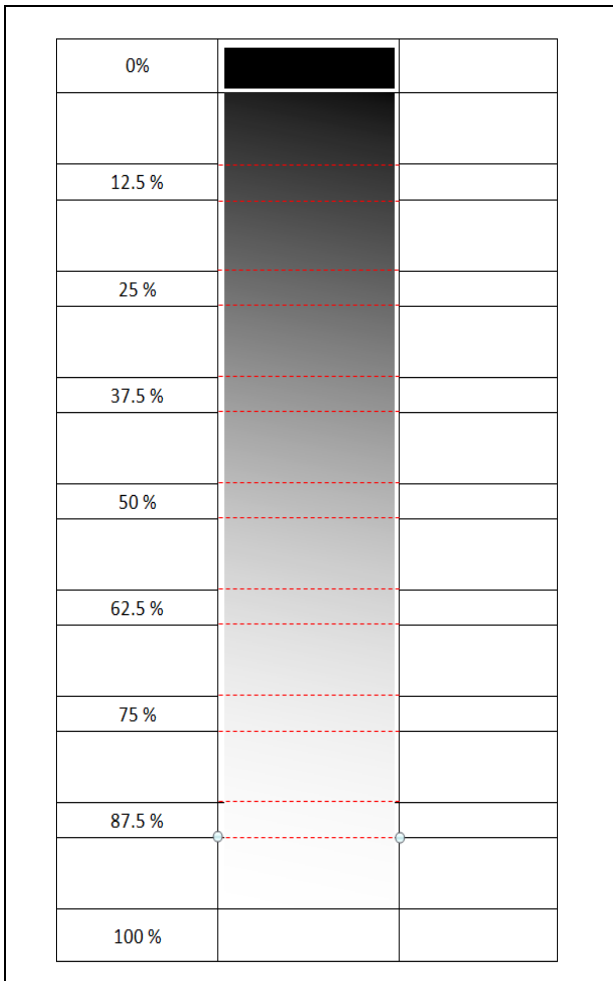


Figure III-7: Black and white graduation used for the probe signal characterization

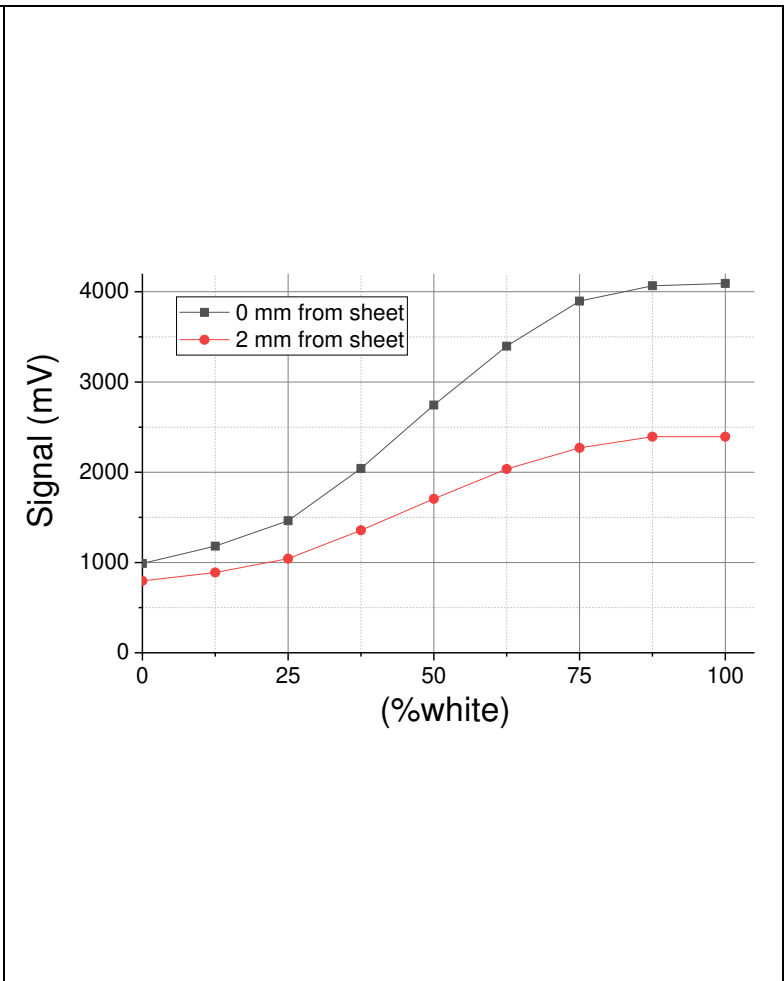


Figure III-8: Probe Signal at different elevation

Figure III-8 presents the signal results obtained with two elevations of the probe with respect to the graduation sheet. The black curve corresponds to the case where the probe was faced to the sheet (elevation of 0 mm), the red curve corresponds to the case where the probe is located 2 mm above the sheet. First, one can see that the signals obtained are not linear over the entire graduation scale. Then an interesting point is there are two possibilities for the signal value of 2400 mV: the first one with the black curve and a graduation of about 45% and the second one with the red curve and a graduation of 100%. Therefore, in a real test condition with particles, the same voltage could lead to two possibilities as shown in Figure III-9.

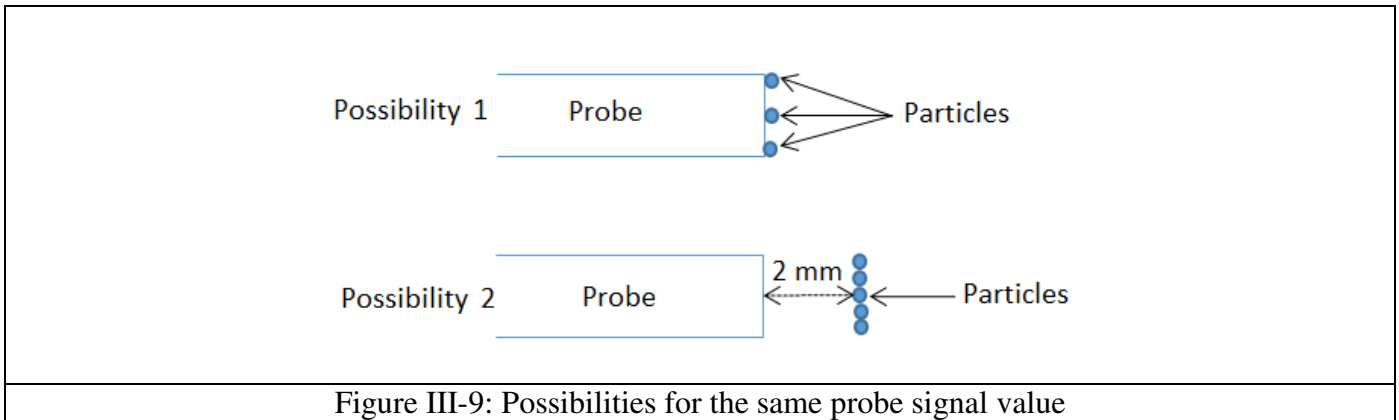


Figure III-9: Possibilities for the same probe signal value

In possibility n°1, there are particles located at “0 mm” of the probe with a certain concentration. In possibility n°2, particles at the maximum volume fraction are located at a distance of 4 mm from the probe. Based on this observation one can conclude that in a real test condition with particles, the same voltage can lead to infinity of possibilities related to particle concentration and distance from the probe.

This first simple characterization shows that the probe signal is affected by particles which are located within a certain distance with respect to the probe, this distance defining a volume of measurement which is important to characterize. It is also worth noticing that the calibration method with a mixture of black and white particles to get the signal value versus white particles concentration [98] cannot work for the probe used in this study since it does not take into account the fact that particles can be located at different distances from the probe with void between them.

In order to evaluate the optical probe measurement volume, its signal value was plotted against the distance with respect to a white surface, the results is shown in Figure III-10.

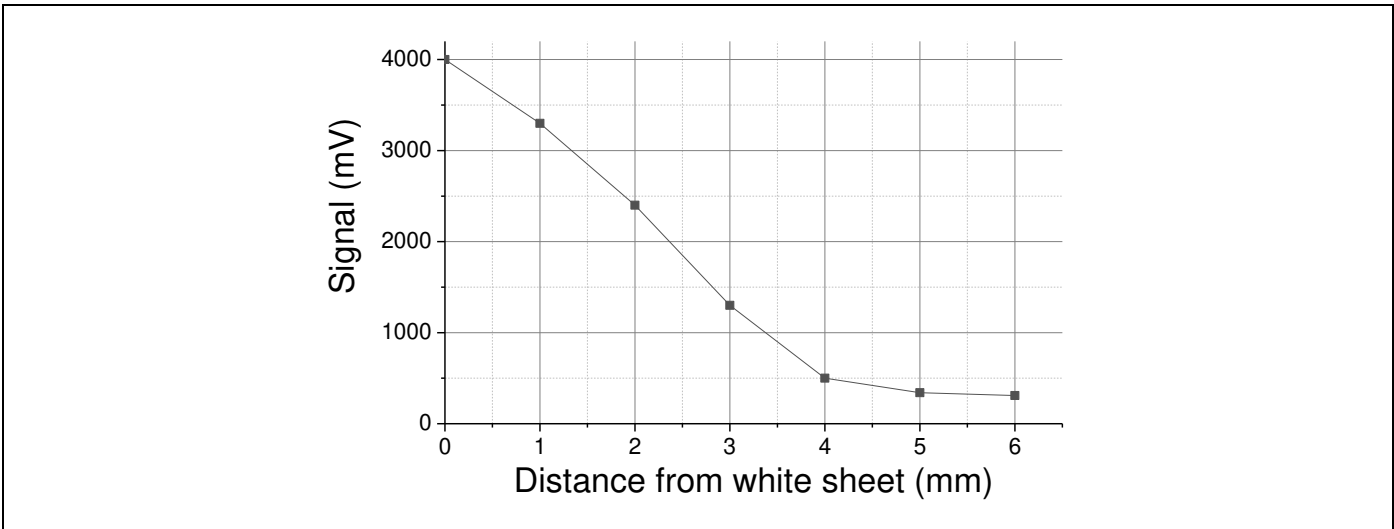


Figure III-10: Signal versus probe height with respect to a white surface

One can see that the volume of measurement has a length of about 4 mm. All particles flowing in this volume will therefore influence the probe signal value. Figure III-11 present a theoretical examples of 80 microns spherical particles positions with respect to the probe for different solid volume fractions.

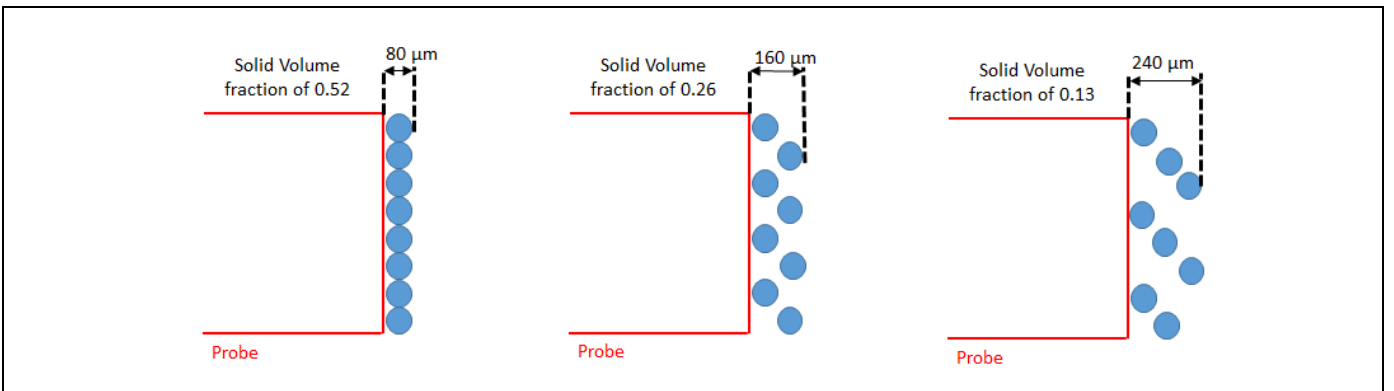


Figure III-11: Theoretical examples of particles positions with respect to the probe for different solid volume fraction, particles are considered as 80 microns spheres

It is interesting to notice that for all these solid volume fraction configurations, the light emitted by the probe will be reflected within a distance of maximum 240 microns where the signal presented in Figure III-10 is varying from 4000 mV to 3750 mV. This theoretical example demonstrates that even relative low solid volume fraction can generate a high signal voltage due to the signal generated by the light reflection on particles within the measuring volume.

This first signal characterization study showed that the fiber probes used in this study performed measurement which are affected by particles flowing within a 4 mm distance in front of the probe, the consequences being that first one signal voltage can correspond to different solid volume fraction possibilities and that low solid volume fraction can still generate a high signal voltage. For these reasons, in real life with complex systems, the post-processing approach used in this study relates on a statistical evaluation of the signal as presented in the next chapter.

3.3.2 Experimental procedure and solid volume fraction reconstruction

The procedure carried out for the calibration of the probe is the following:

- The probe is first inserted in the bed which is not fluidized.
- Light intensity is set to get a signal at a value around 4000 mV. It is important mentioning that reaching exactly 4000 mV is difficult due to the acquisition set sensitivity; a spread of +/- 200 mV was usually obtained. This value is then taken as the upper voltage reference.
- The probe is then withdrawn from the bed and inserted in a dark environment to get the lower voltage reference value corresponding to 100% voidage.
- The probe is then re-inserted in the bed for the experiment.
- Signal from both channels are post-processed separately and they always show similar values, the averaged of both signal post-processing is therefore considered.
- At the end of the experiment, another measurement is made in the bed non-fluidized to observe if there is a shift compared to the same measurement before the test. A maximum shift of 100 mV was considered to validate the experiment, which has always been respected.

It is also interesting to mention that the probe light intensity was increased from 5.1 to 6 on a scale of 10 over one month of experiments showing that the probe gets damaged over time and it is therefore important to track this phenomena as carried out in this study.

The data acquisition was conducted with a frequency of 1 kHz. Table III-5 presents the number of acquisition points where the probe is inserted in the bubble according to its diameter and velocity, the velocity being calculated with Equation 13 (see Chapter I.2.2.2).

Table III-5. Acquisition points where the probe is inserted in bubbles according to their properties

bubble diameter (m)	bubble velocity calculated from Equation 13 (m/s)	period of probe inserted in the bubble (s)	Number of acquisition point in the bubble
0.003	0.9	0.003	3
0.005	1.1	0.005	5
0.01	1.3	0.008	8
0.02	1.6	0.013	13
0.03	1.8	0.017	17
0.04	2.0	0.020	20
0.05	2.1	0.023	23

One can see that the acquisition frequency chosen allows detecting the presence of a large range of bubbles with the probes being inserted in the bubbles for always more than two acquisition points. It is also worth mentioning that this acquisition frequency is well suited for solid volume fraction measurements, but a higher frequency is necessary if one wants to measure bubbles/ particles velocities. Indeed, Schweitzer et al. [97] and Herbert et al. [100] used an acquisition frequency of respectively 5kHz and 50 kHz to measure respectively bubbles and particles velocities.

Figure III-12 presents an optical probe signal example when inserted in the fluidized bed with a superficial velocity of 0.7 m/s. One can see different peaks with low signal values corresponding to the case where the probe is within a dilute phase or bubble where the light emitted is not reflected by particles which then generates a low signal value. One can also see peaks with intermediate value corresponding to a phase with higher concentrations of particles.

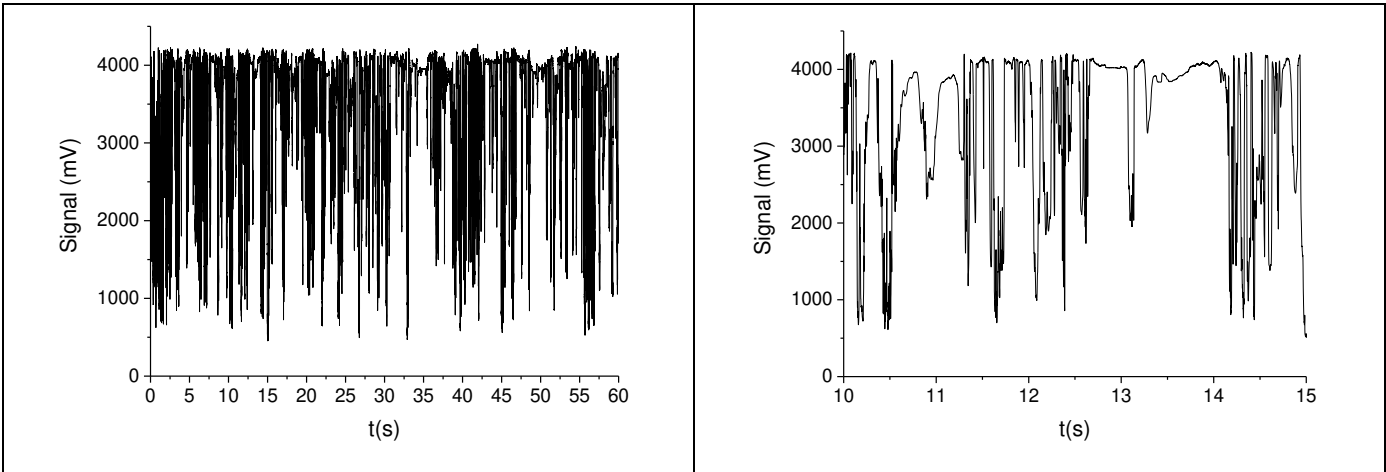


Figure III-12: Example of optical probe signal in the 20 cm fluidized bed

In order to extract the local voidage fraction of the fluidized bed from the signals, the same method introduced by Schweitzer et al. [97] was applied on the optical probe signal with a differentiation of a dense and a bubble phase from a signal values histogram. The key with this method is the definition of the voltage threshold which defines the limit between the two phases. For this purpose, a histogram is used as shown in Figure III-13 where the signal measured values are numbered in different voltage classes of 20 mV each. The blue bars indicates the number of measured values per class, the red curve their accumulation over the entire range of classes. Figure III-14 shows all cumulative curves of the different points of a profile measured for experiment n°1 with a homogeneous injection.

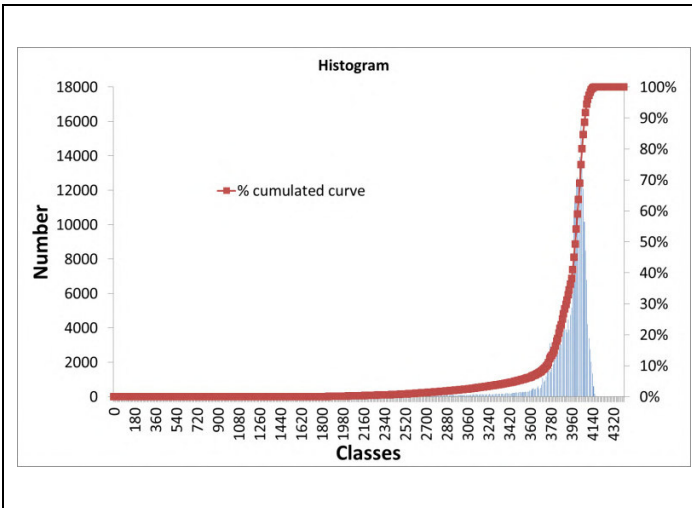


Figure III-13: Example of an histogram obtained for one acquisition with cumulative curve

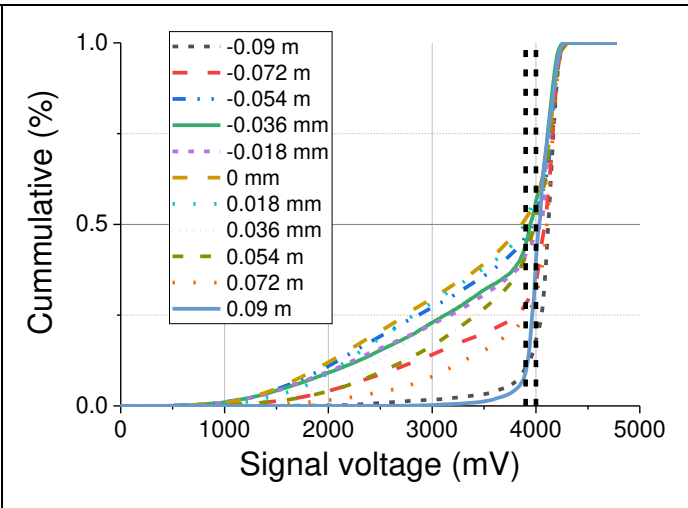


Figure III-14: Signals cumulative curves profile carried out for experiment n°1 with homogeneous injection

One can notice from Figure III-14 that the cumulative curves present a sharp increase at classes around 3900 mV shown with the black dotted lines. High voltage classes on the right correspond to bubbles

while lower voltage classes on the left correspond to emulsion phase. It is also important to notice that before this sharp increase, the shape of the cumulative curves differs depending on the profile probe position with higher cumulative values when the probe is located at the center. We therefore considered that the point where the cumulative curves show a sharp increase is representative of the transition between bubble and emulsion phase. Indeed, depending of the position in the column, the cumulative curves shows different values at this transition point which is representative of the bubble concentration at that position.

In order to have a precise determination of this transition, the derivative of the cumulative curve was plotted as shown in Figure III-15.

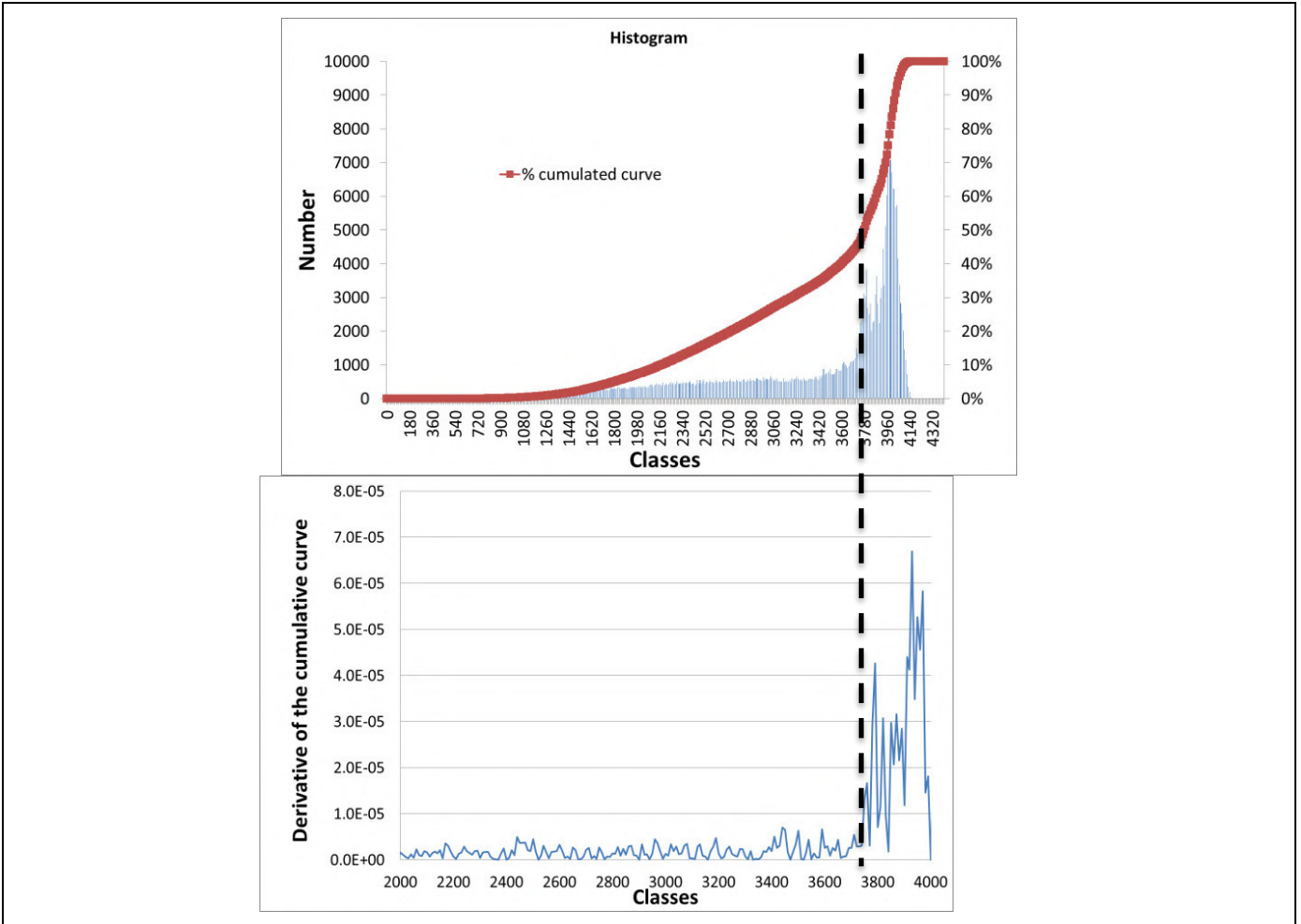


Figure III-15: Example of signal histogram cumulative curve and its derivative

The transition point is considered when the derivative curve shows a high variation with a sudden increase as shown in Figure III-15. The solid volume fraction is then calculated from the optical probe signal histogram with Equation 67

$\epsilon_s = \frac{\text{Number of signal values below transition}}{\text{Total Number of signal values}} \epsilon_{s,bubble} + \frac{\text{Number of signal values above transition}}{\text{Total Number of signal values}} * \epsilon_{s,dense}$	Equation 67
---	-------------

Figure III-14 and Figure III-16 present the signal cumulative curves of a profile measured for experiment n°1 and its corresponding solid volume fraction profile with $\epsilon_{s,bubble}=0$ and $\epsilon_{s,dense} = \epsilon_{s,mf} = 0.58$.

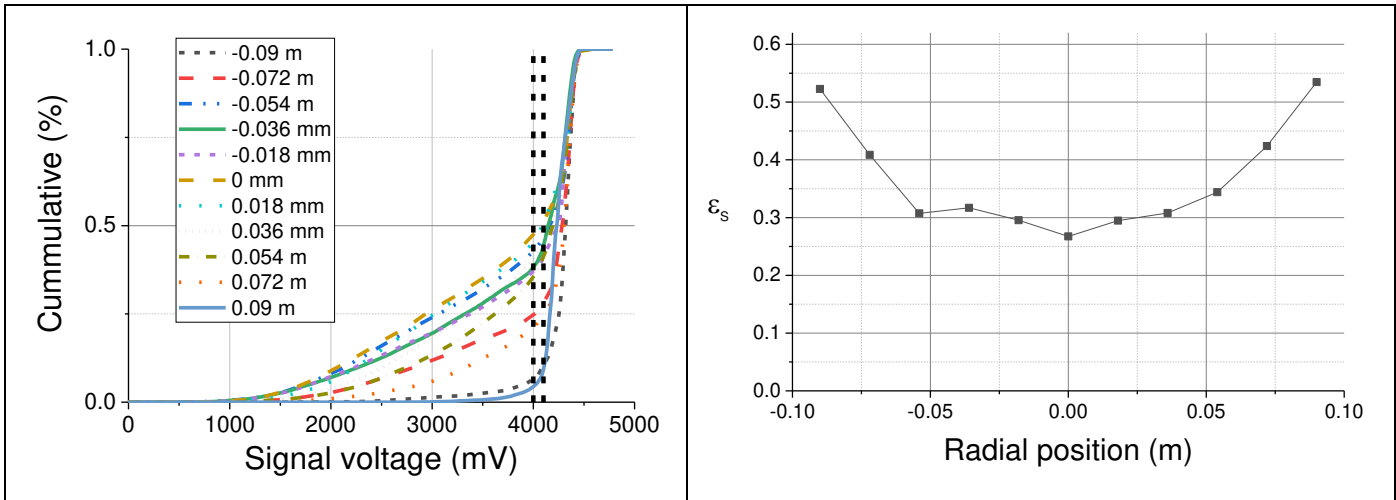


Figure III-14: Signals cumulative curves profile carried out for experiment n°1 with homogeneous injection

Figure III-16: Solid volume fraction profile from cumulative curves of Figure III-14 post-processing with $\epsilon_{s,bubble}=0$ and $\epsilon_{s,dense} = \epsilon_{s,mf} = 0.58$

It is important to point out that this method to determine the transition between emulsion and bubble phases from the histogram was developed in this study and it differs from the method used by Schweitzer et al. [97]. Indeed, in their work they considered that the emulsion phase from the histogram was symmetric with respect to the maximum peak value. They then determine the transition voltage from the voltage at the peak and the maximum voltage. One can refer to Appendix 2 for more details. Figure III-18 presents the effect of the transition determination between the emulsion and bubbles phases with the method used in this study and the one from Schweitzer et al. [97].

Different sampling durations (30 s, 60 s, 120 s) were investigated in order to minimize the sampling time without compromising reproducibility of average concentration profiles. Figure III-17 presents the effect of the sampling duration on a solid volume fraction profile obtained with $\epsilon_{s,bubble}=0$ and $\epsilon_{s,dense} = \epsilon_{s,mf} = 0.58$.

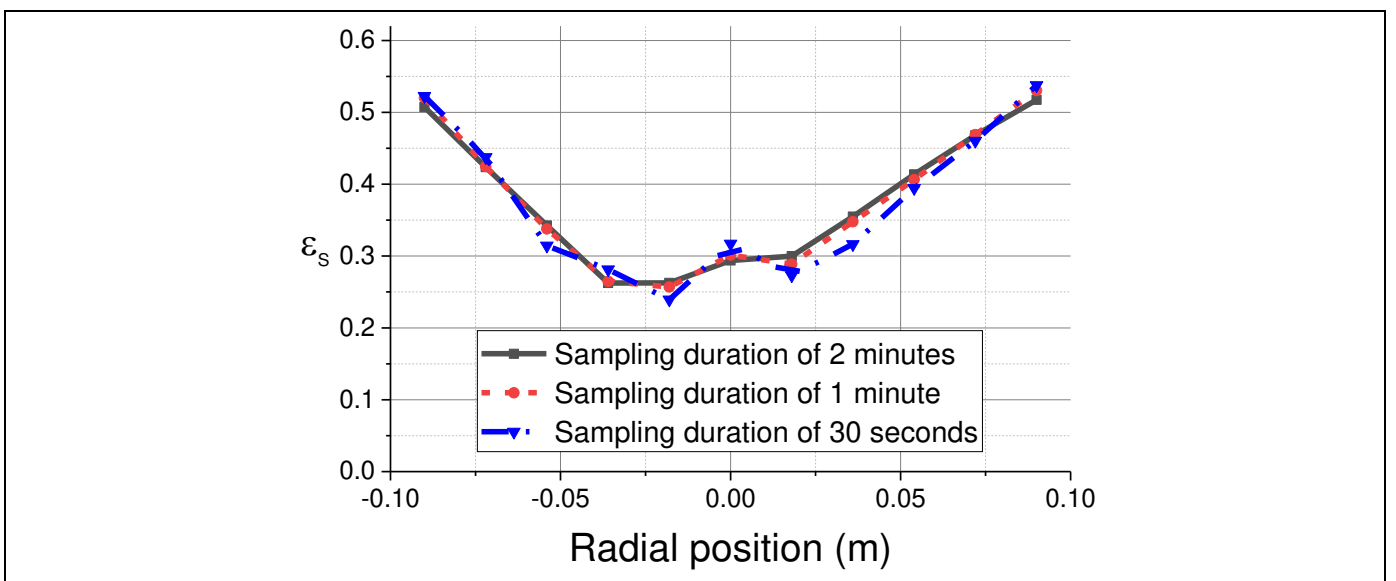


Figure III-17: Solid volume fraction profile post-processing with $\epsilon_{s,bubble}=0$ and $\epsilon_{s,dense} = \epsilon_{s,mf} = 0.58$ Effect of the sampling duration

One can see that the profiles for the sampling time of one and two minutes are similar with an average relative error over all solid volume fraction values lower than 2%. On the other hand, the 30 seconds sampling duration profile presents a relative error compared to the profile with a 2 minutes sampling duration profile of 6.5%. The sampling duration of 1 minute was therefore chosen since it minimizes the test duration without affecting the solid volume fraction values obtained.

Different points can be discussed concerning the signal post-processing method presented here above:

- First, it is important to point out that the method presented to determine the transition between emulsion and bubble phases from the histogram was developed in this study and it differs from the method used by Schweitzer et al. [97]. Indeed, in their work they considered that the emulsion phase from the histogram was symmetric with respect to the maximum peak value. They then determine the transition voltage from the voltage at the peak and the maximum voltage. One can refer to Appendix 2 for more details. Figure III-18 presents the effect of the transition determination between the emulsion and bubbles phases with the method used in this study and the one from Schweitzer et al. [97].

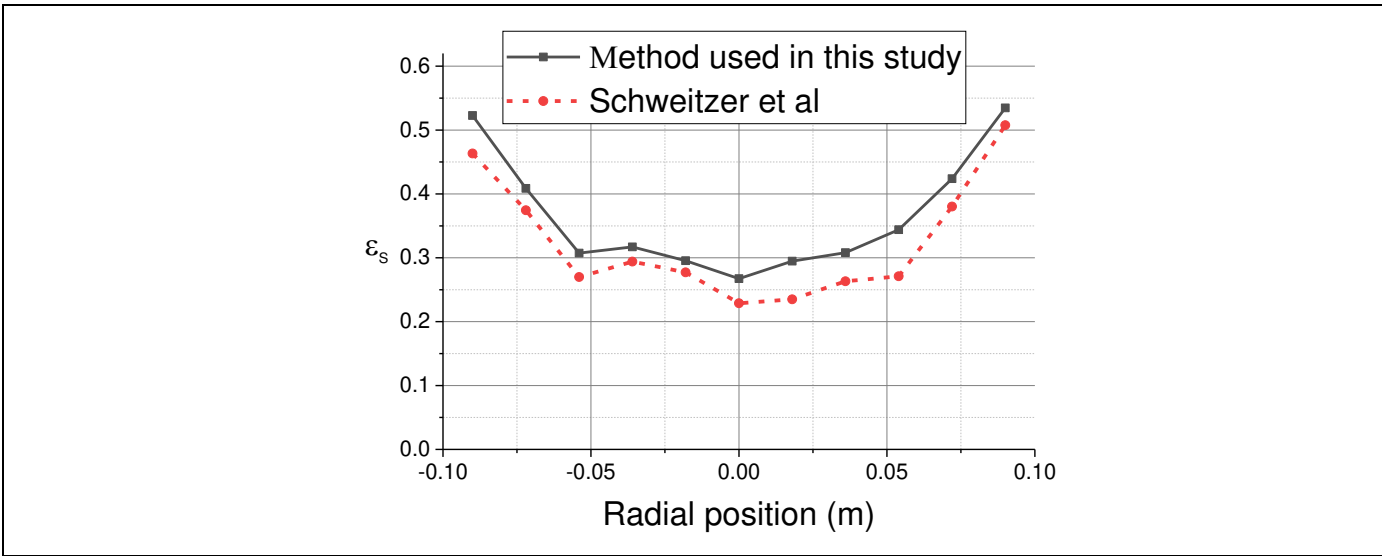


Figure III-18: Effect of the transition determination, Solid volume fraction profile from cumulative curves post-processing with $\epsilon_{s,bubble}=0$ and $\epsilon_{s,dense} = \epsilon_{s,mf} = 0.58$

One can see that the profile shapes remain the same for both method but the one from Schweitzer et al. [97] gives lower solid volume fraction values since the transition between the emulsion and gas phases always occur at higher voltages with this method. This comparison shows that the post-processing of the optical probe signal depends on different hypothesis and the results therefore need to be validated against other experimental data as discussed below.

- When calibrating the probe signal on the catalyst fixed bed, it is difficult to set a precise maximum value of 4000 mV due to the lack of sensitivity of the acquisition system settings, therefore the maximum value can reach values up to 4300 mV. However, the determination of the transition between the bubble and dense phase is independent of the initial probe calibration since the transition value is determined based on the derivative of the cumulative curve for each measurement and not based on a fixed threshold value for all measurements.

- The transition between bubble and dense phase occurs at high voltages implying that low solid concentration generates also high signal values. This phenomenon was explained in the previous chapter with Figure III-11.
- The influence of the transition voltage value on the solid volume fraction profile was also investigated for our post processing method. For this purpose, the solid volume fraction profile presented in Figure III-16 was plotted considering different voltage transitions as shown in Figure III-19. As a reminder, each class represents voltage values number within a range of 20 mV.

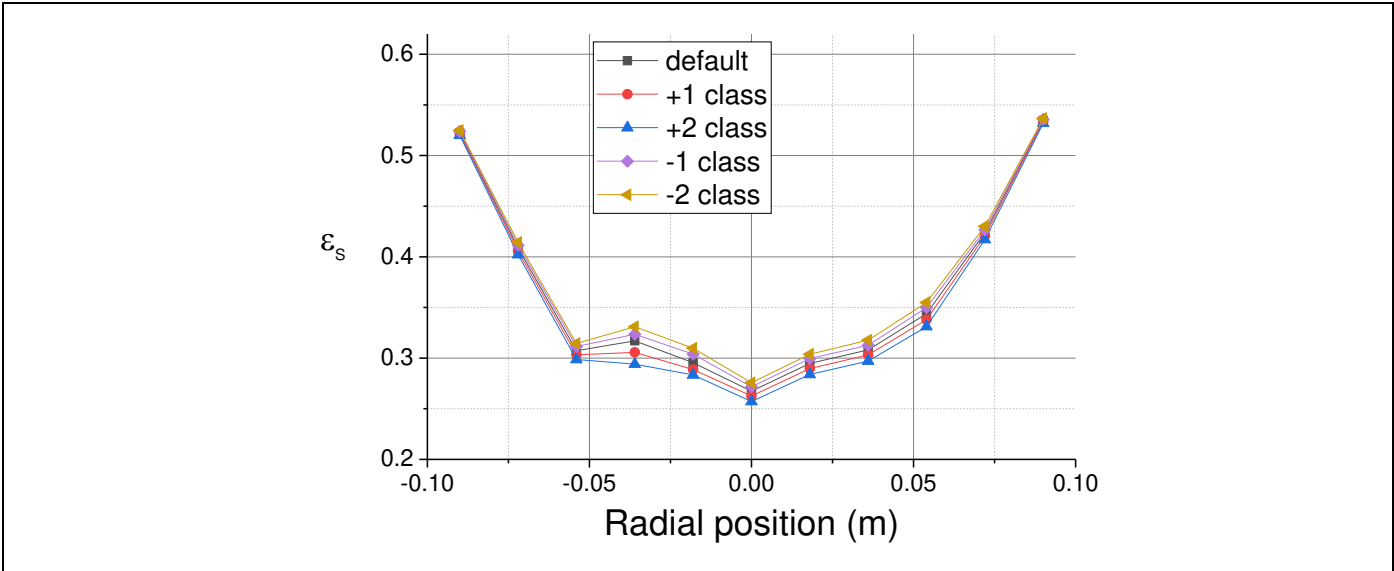


Figure III-19: Effect of transition voltage value

The default curve is the same as the one shown in Figure III-16. The transition values were then set with one and two classes above and below the default transition value. Table III-6 presents the averaged solid volume fraction obtained from the profile integration over the column surface for the different transition voltages. One can see from Figure III-19 and Table III-6 that the transition voltage has almost no influence on the solid volume fraction profile shape and averaged value.

Table III-6. Averaged solid volume fraction from profile integration, influence of the transition voltage

Class	Default	- 1 class	- 2 class	+1 class	+2 class
Averaged solid volume fraction	0.43	0.42	0.42	0.43	0.42
%error	-	1.0%	2.0%	0.9%	1.7%

- The solid volume fraction obtained is obviously connected to the values of $\epsilon_{s,bubble}$ and $\epsilon_{s,dense}$ in Equation 67. In the previous examples, $\epsilon_{s,bubble}$ and $\epsilon_{s,dense}$ were considered as indicated in the two phases theory equal to respectively 0 and the solid volume fraction at the minimum of fluidization 0.58. However, when observing the histogram cumulative curves on Figure III-14, the bubble and dense phases cover a certain range of voltages implying that $\epsilon_{s,bubble}$ and $\epsilon_{s,dense}$ correspond to an average value of different solid concentrations. Figure III-20 and Figure III-21 presents the effect of the $\epsilon_{s,dense}$ and $\epsilon_{s,bubble}$ values on the solid volume fraction profile presented before. Table III-7 presents the averaged solid volume fraction obtained from the profiles integration.

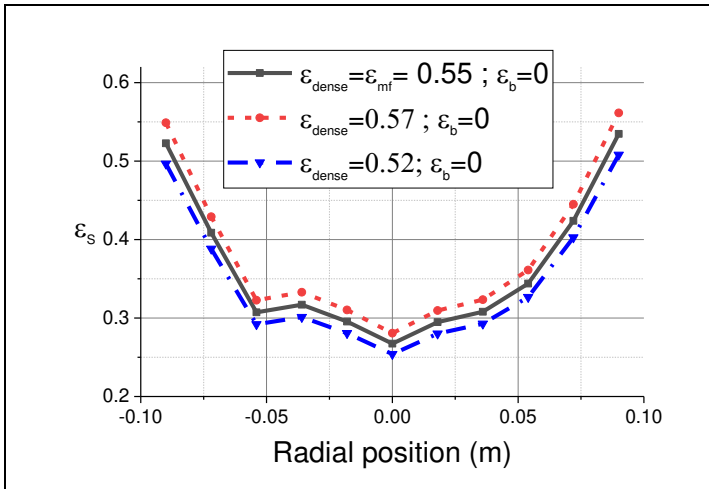


Figure III-20: Effect of $\epsilon_{s,dense}$ values on the solid volume fraction profile

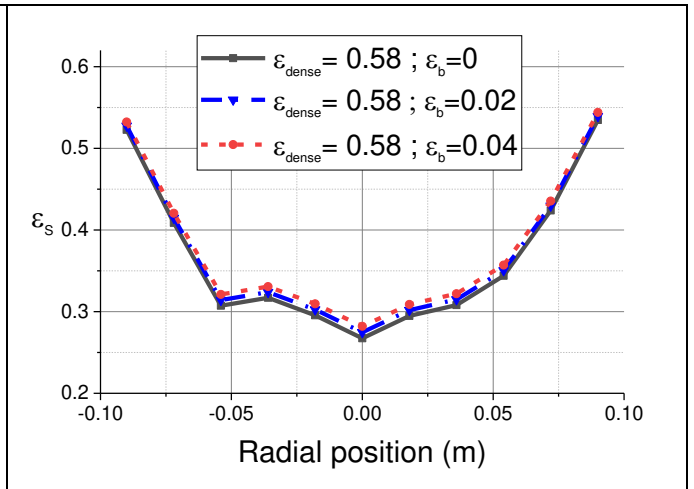


Figure III-21: Effect of $\epsilon_{s,bubble}$ values on the solid volume fraction profile

Table III-7. Effect of $\epsilon_{s,dense}$ and $\epsilon_{s,bubble}$ on averaged solid volume fraction

ϵ_{dense}	0.58	0.55	0.52	0.58	0.58
ϵ_{bulle}	0	0	0	0.02	0.04
Averaged solid volume fraction	0.43	0.41	0.39	0.43	0.44
%error	-	5%	10%	1.5%	2.9%

All profiles present a similar shape. Depending on $\epsilon_{s,dense}$ and $\epsilon_{s,bubble}$ value considered, the average averaged solid volume fraction is affected, the most influencing parameter being $\epsilon_{s,dense}$ which results from independent measurement. $\epsilon_{s,bubble}$ is evaluated to 0 considering the two phase theory but it remains an hypothesis.

One can see from the discussion above that the evaluation of local bed voidage using optical probes relies on several hypothesis / assumptions. In order to gain confidence into the measurement method as well as the signal processing and to check that the probe does not have a strong intrusiveness impact, it is essential to validate the optical probes results with experimental data obtained from other independent measurement techniques. For this purpose, we compared the averaged solid volume fraction resulting from optical fibers profile integration with macroscopic measurement of bed density resulting from the pressure drop measurements probe. This comparison is presented in Chapter IV.2.

4 Fluidized bed of 90 cm

This chapter presents the 90 cm fluidized bed equipment and related instrumentation. It is located at Particulate Solid Research Incorporation (PSRI) in Chicago. Experiments were conducted for PSRI consortium and the results were used in this dissertation with their agreement.

The 90 cm fluidized bed experimental results are used in the simulation strategy Step 3 to evaluate the prediction of CFD at a larger scale compared to the 20 cm fluidized bed experiments and simulations.

4.1 Equipment

Figure III-22 presents a general sketch of the PSRI 90 cm fluidized bed with the air injector used at the bottom.

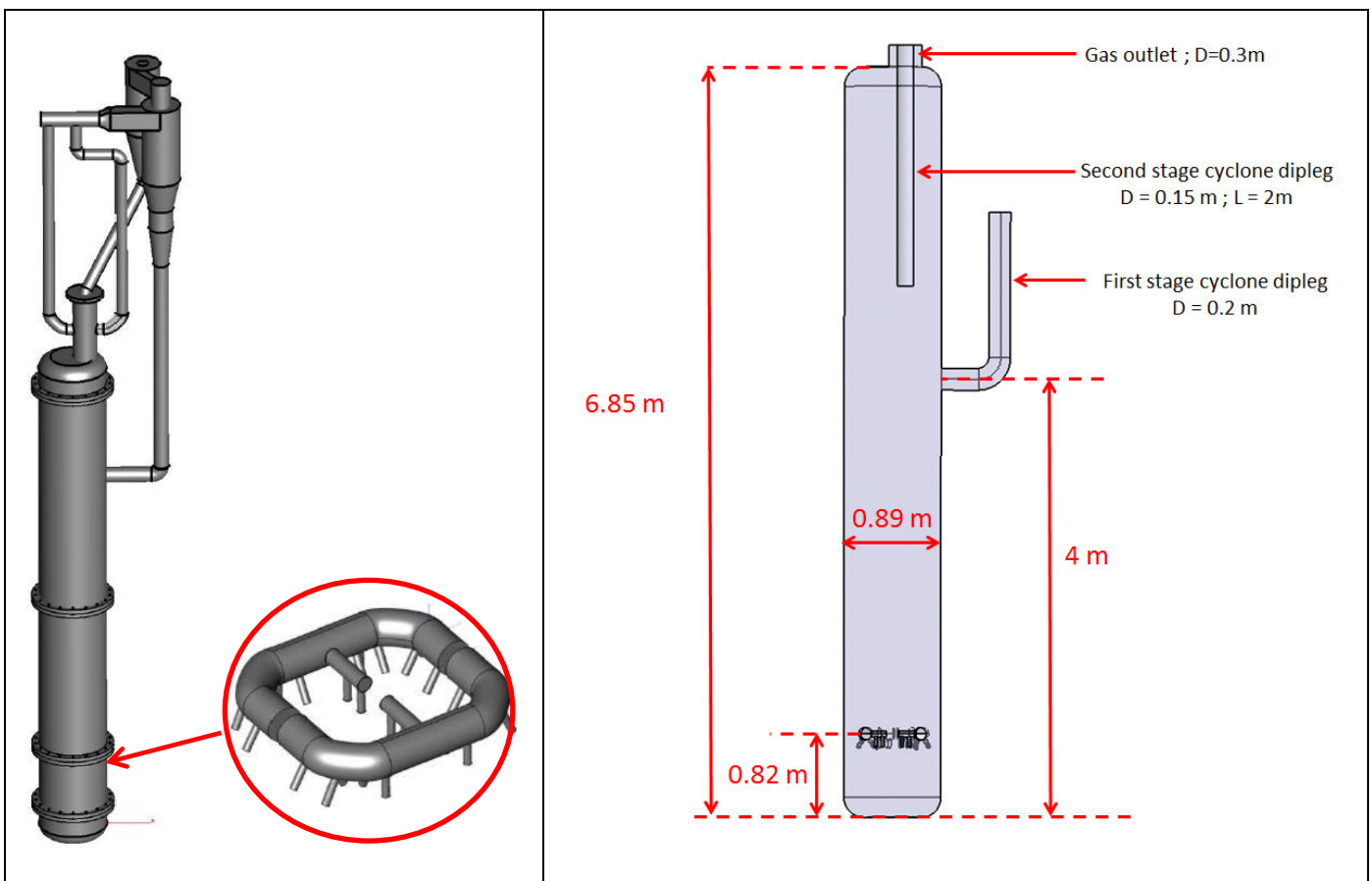


Figure III-22: PSRI 90 cm fluidized bed

The experimental set up consists of a cylindrical carbon steel vessel with an inner diameter of 0.89 m and a total height of 6.85m. The vessel and cyclones are made of metal. A distributor is located at 0.82m from the vessel bottom and consists of 36 nozzles with a diameter of 2.5cm connected to a main rectangular ring. Details of the distributor design can be found in Appendix 3. The gas outlet at the top of the bed is connected to a series of two cyclones. The particles recovered by the first cyclone are recycled back to the bed through a 0.2m dipleg using an automatic L-valve system that prevents gas leakage through the dipleg [151,152]. The particles recovered by the second cyclone are sent back to the bed through a 0.2m second stage dipleg. A flapper valve is located at the tip of the second stage cyclone dipleg to prevent gas from the fluidized bed to flow up through the dipleg.

Compressed dry air at ambient conditions is used for fluidization with a temperature assumed to be 20°C. The pressure in the dilute phase of the bed is maintained at a pressure of 35kPag. Table III-8 presents the operating conditions of the three tests carried out with a superficial gas velocity of respectively 0.3 m/s, 0.6 m/s and 0.85 m/s. The superficial velocities are calculated at the top the bed with the dilute pressure of 35 kPag.

Table III-8. Acquisition points where the probe is inserted in bubbles according to their properties

	Bed superficial velocity (m/s)
Test 1	0.3
Test 2	0.6
Test 3	0.85

Finally, it is important to point out that the 90 cm fluidized bed experiment has a gas distribution system different compared to the 20 cm fluidized bed where gas is injected at the bottom through a porous media. This difference is discussed here: the two experiment set ups were chosen to investigate the CFD predictions when extrapolating a CFD model from a given scale to a larger one. In this case, the main extrapolation parameter considered is the change of scale for the same fluidization regime. Then, for an ideal comparison meaning only the change of scale effect is investigated, it would be necessary to have two experiments at different scales with the same gas distribution system, one could also add the use of the same powder and experimental techniques. It is not the case for our comparison since porous plate distributors are rarely used at large scales because of potential mechanical issues and homogeneous gas distribution problems [2]. Nevertheless, we still consider that the choice of these two experiments is pertinent since they have in common particles with similar properties fluidized at similar superficial gas velocities and since the effect of the gas distribution system is taken into account directly in the simulations through the choice of pertinent boundary conditions as shown in Chapter IV.

4.2 Experimental techniques

Two different experimental techniques were used to characterize the fluidized bed hydrodynamic with first density profile measurements using differential pressure probes and second particle entrainment measurements

Figure III-23 presents the ports location for the differential pressure probes measurements that are used to get the density profile with respect to the vessel height.

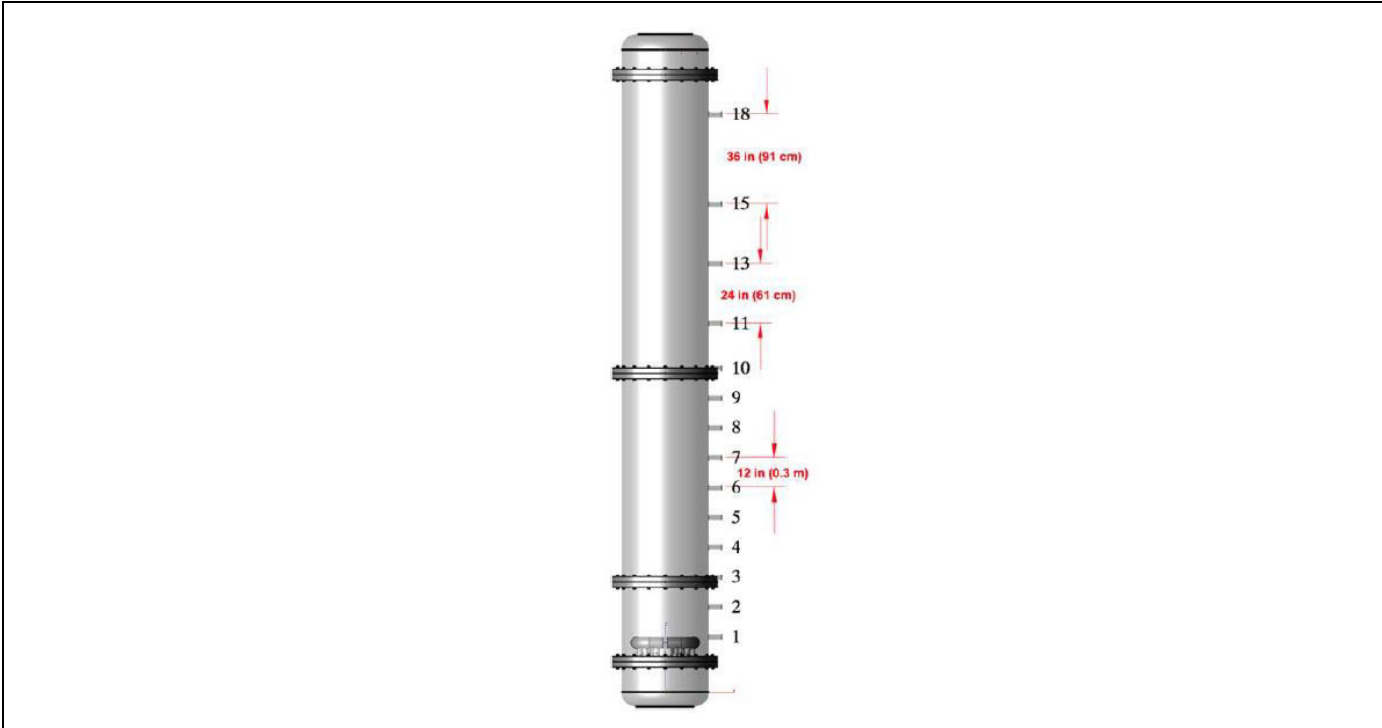


Figure III-23. Ports location for differential pressure probes

The pressure transmitters (Honey well Model STD904) are connected with 6 mm diameter polyethylene tubes to the array of pressure ports that had high porosity snubbers (McMaster Carr, Model 3820K27) to prevent the tubes from getting plugged with solids. The pressure ports are located 0.3 m apart starting from the sparger and continued to the 3rd steel section. Above this section, the pressure ports were placed at 0.6 m increments to the top of the column in the freeboard. The responses were time averaged, normalized to the spacing of the ports multiplied by gravity to give an axial and localized bed density.

The overall particle entrainment rate of the fluidized bed was measured by closing a pneumatically operated butterfly valve located at the bottom of the first stage cyclone dipleg. The accumulation of particles in the dipleg versus time was then measured with a differential pressure probe. The measurement period never exceeded 30 seconds in order to limit the variation of particles inventory in the fluidized bed. The main assumptions for this measurement are:

- During the measurement, the entrainment is not affected by the variation of the fluidized bed level due to the interruption of the particles return from the first stage cyclone dipleg.
- The particles losses that are not recovered in the first stage cyclone are neglected which is acceptable since the first cyclone efficiency is estimated above 99%.

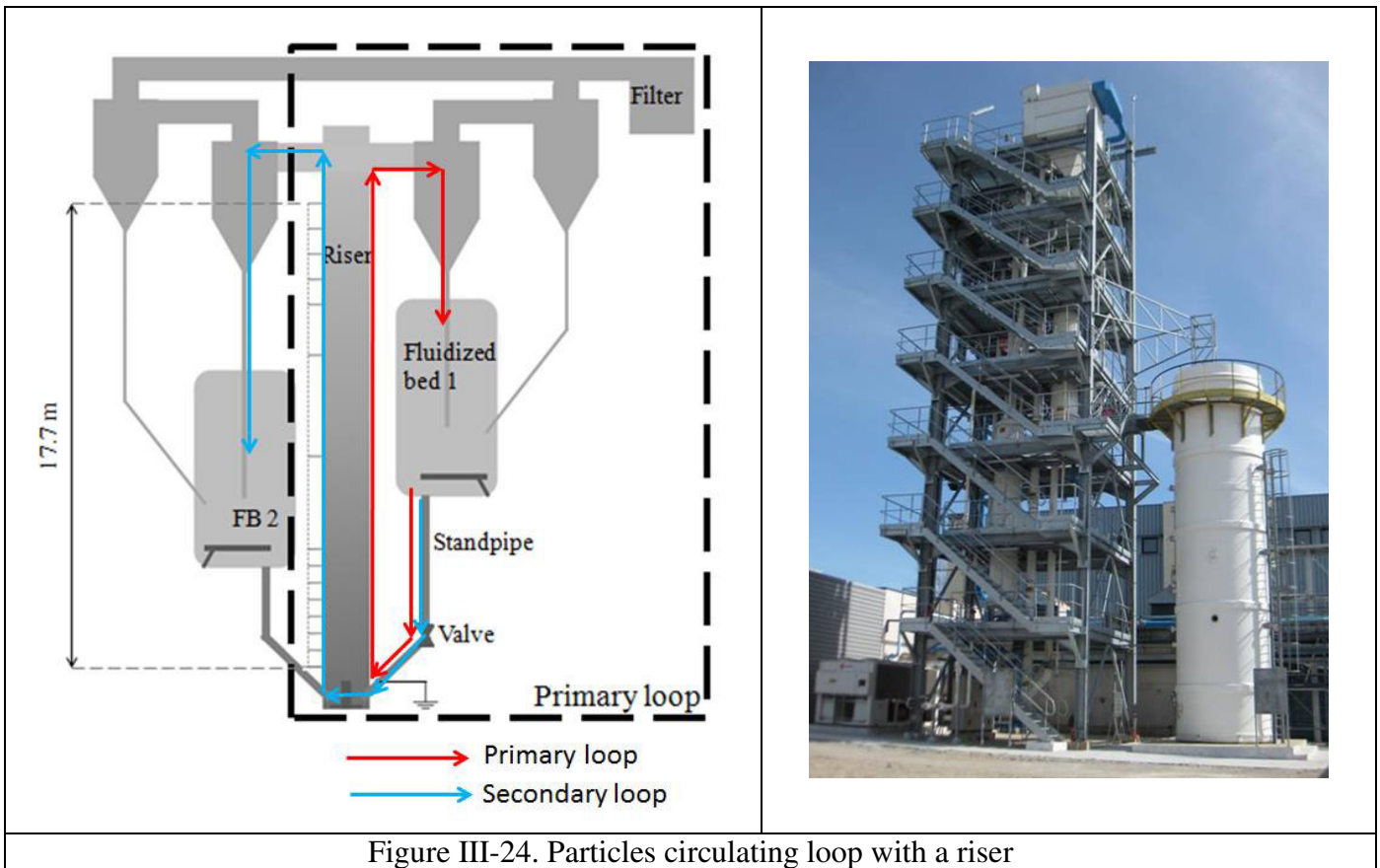
5 Riser of 30 cm

The experiments for the vertical transport regime in a riser were carried out on a large circulating fluidized bed loop at IFP Energies nouvelles Solaize.

These experiment results are used in the simulation strategy step n°4 in order to evaluate the CFD predictions at large scale with operating conditions different compared to the previous steps.

5.1 Equipment

Figure III-24 presents a sketch and a picture of the CFB set up.



The cold flow mock-up is composed of two solid loops. The primary loop shown in Figure III-24 is used for stationary hydrodynamic experiments where the solid circulate in a loop from the fluidized bed n°1 into a stand-pipe then through a valve, then to a riser and it is finally separated from the riser gas into two cyclones in series and sent back to the fluidized bed n°1. The second loop, operated in batch mode, is used for solid flowrate calibration. It consists in emptying the fluidized bed n°1 into the fluidized bed n°2 through the riser and the cyclones located on the left side. Solid flowrate is estimated by measuring the decrease of the fluidized bed n°1 level and is correlated to the valve pressure drop as explained below.

The main characteristics of the mock up are:

- Fluidized bed n°1 and n°2: Internal diameter of 1 meter, height of 6 meters
- Standpipe: Internal diameter of 26 cm, total height of 9 meters.
- Riser: Internal diameter of 30 cm, total length of 18 meters.
- Catalyst inventory: around 2.5 tons

Figure III-25 presents the riser bottom gas injection configuration. As for the other experimental set-ups already described it is specific and different from the previous distributors. Indeed, in CFB risers, gas flow is much larger than in fluidized beds and solid circulation has also to be accounted for. Inlet configuration is important as discussed by Cocco et al. [95] and Grace et al. [2]. Indeed, in order to achieve well distributed flows, it is better to feed the solid into a fluidized bed below the main gas injection. Gas can then be fed all around the riser through multiple points or axially with an internal injection system. Wang et al. [153] also demonstrated that feeding the particles above the gas injection can lead to asymmetric particles profile in the riser.

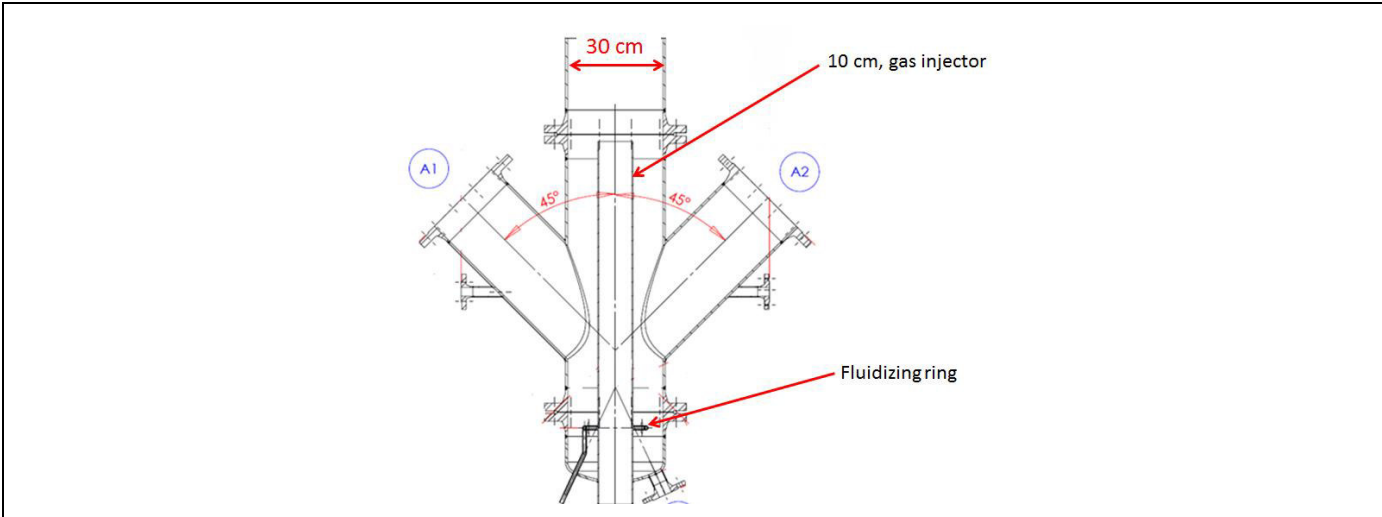


Figure III-25: Riser bottom gas injection configuration

In our system shown on Figure III-25, the catalyst from the fluidized bed n°1 comes from a standpipe connected to the riser bottom through a 45° inclined pipe shown with the “A2” symbol on Figure III-25. This inclined pipe is located 30 cm below the 10 cm tube main riser gas inlet as shown in Figure III-25. A ring located at the riser bottom allows maintaining the solid coming from the standpipe fluidized at a superficial velocity around 10 cm/s.

The solid circulation in the loop is maintained through an appropriate pressure balance. An example of pressure balance corresponding to a solid circulation of 220 kg/m²/s and a superficial velocity in the riser of 8.15 m/s is presented in Figure III-26.

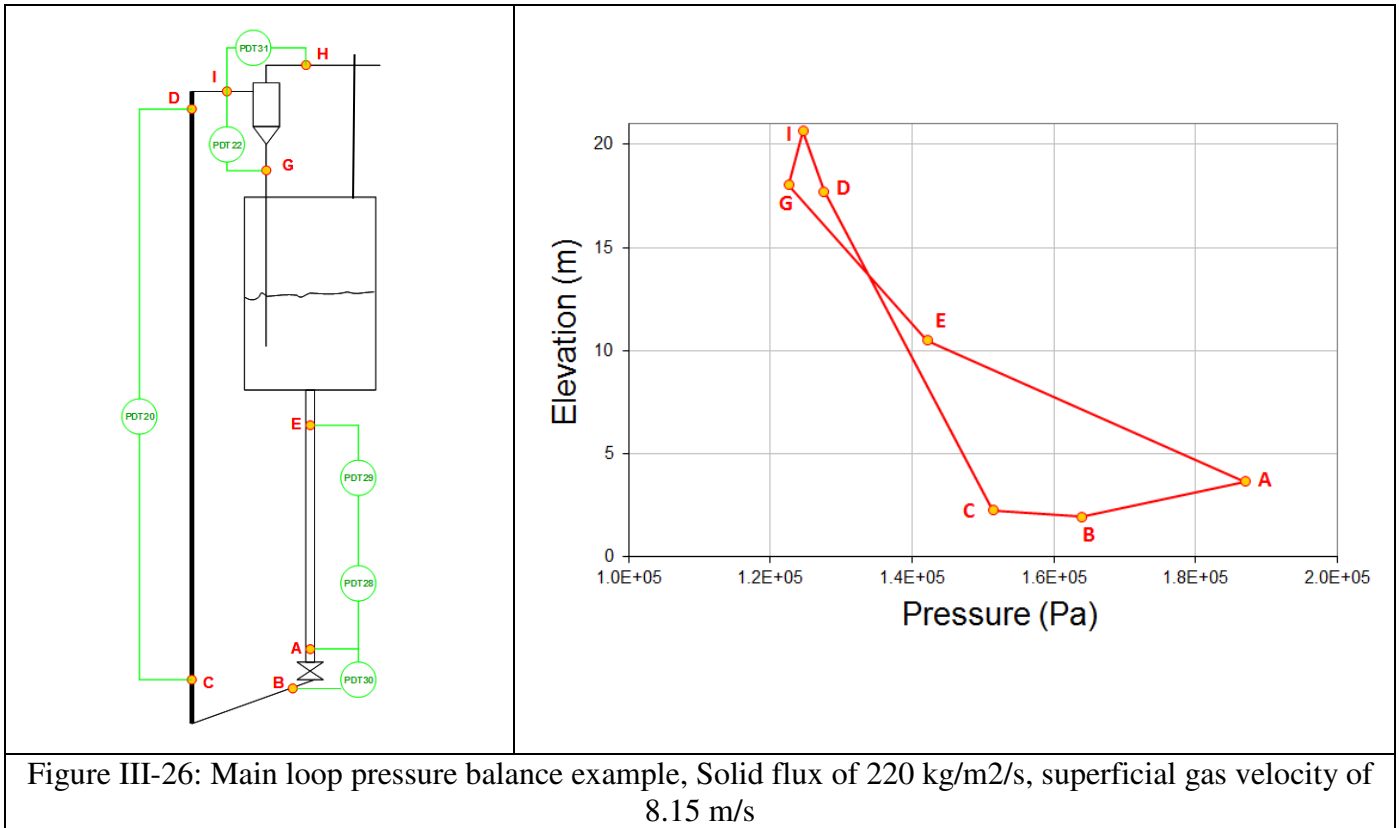


Figure III-26: Main loop pressure balance example, Solid flux of 220 kg/m²/s, superficial gas velocity of 8.15 m/s

As explained in the literature review, the pressure balance in the loop can be written with Equation 68.

$\Delta P_{VALVE\ A \rightarrow B} = \Delta P_{recovery\ bed\ G \rightarrow E} + \Delta P_{standpipe\ bed\ E \rightarrow A} - \Delta P_{riser\ C \rightarrow D} - \Delta P_{cyclone\ I \rightarrow G}$	Equation 68
--	-------------

Table III-9 presents the tests matrix for the riser experiments that were conducted in the present work. Superficial gas velocity is calculated using the absolute pressure measured at the top of the riser which is constant for all tests and equal to 110 kPa abs (+/- 1 kPa).

Table III-9: Tests matrix for riser experiments

	Superficial velocity at riser top (m/s)	Solid Flux in riser (kg/m ² /s)
Test 1	6.9	80
Test 2	8.15	160
Test 3	8.15	220

The procedure used to determine the solid flowrate circulating in the loop is presented in the next section.

5.2 Experimental techniques

5.2.1 Solid flux measurements

There is no direct method to measure the solid flowrate while circulating in the loop. Therefore, the solid flux in the loop was calibrated against the orifice valve pressure drop using the secondary loop where the fluidized bed n°1 is emptied in to the fluidized bed n°2 (see Figure III-24). Three valve orifices were used with respectively 3.5cm, 5cm and 7cm.

Figure III-27 presents the different pressure drop recordings while running the cold flow mock-up in batch mode through the secondary loop using the 3.5 cm orifice. The curve in red is the pressure drop across the orifice valve, the curve in blue represents the level in the fluidized bed n°1 and the two other curves represent the ΔP in the standpipe.

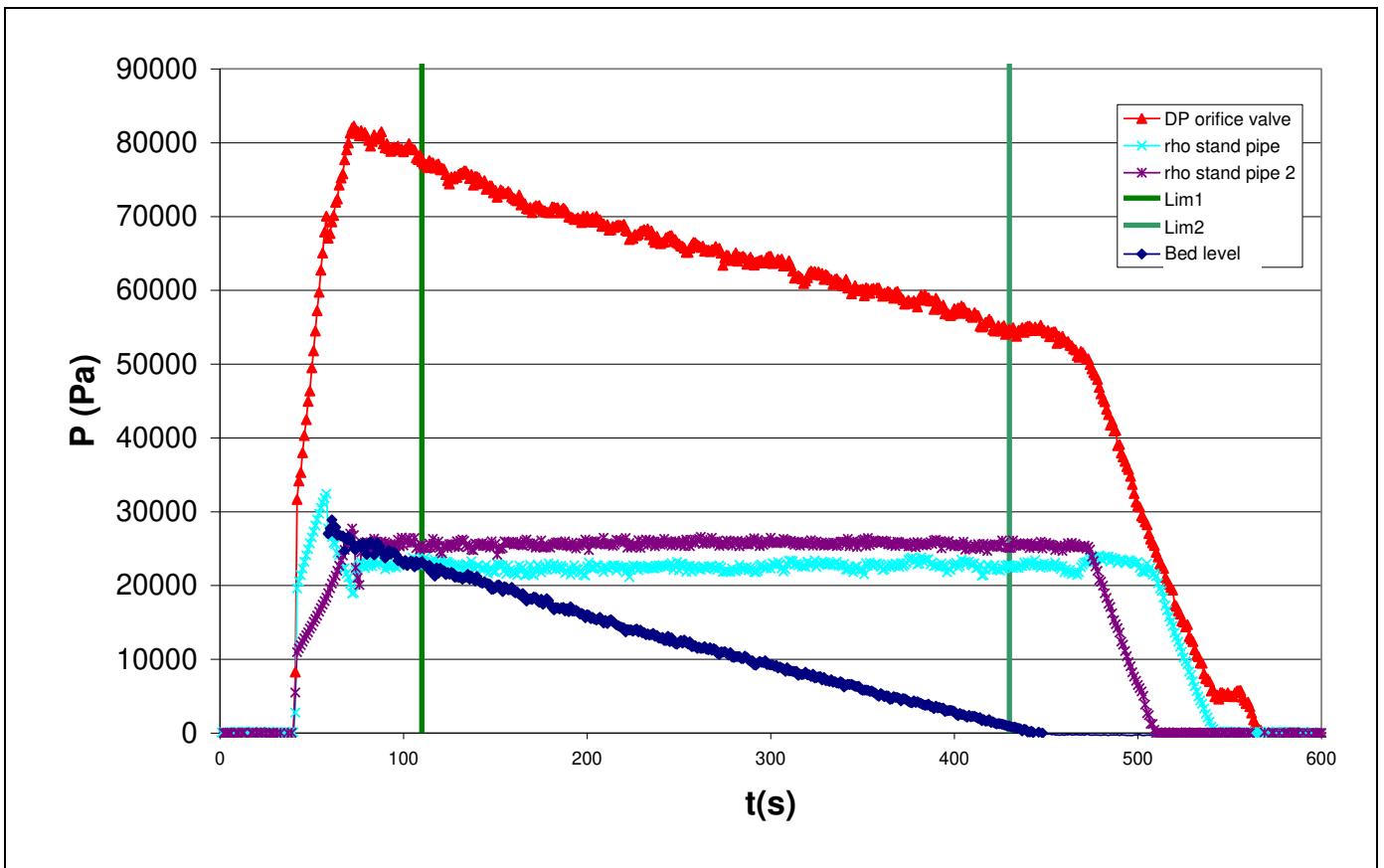


Figure III-27: Pressure drops measurement in transfer mode with an valve orifice of 3.5 cm

The solid mass flow rate going through the orifice valve is classically expressed with Equation 69:

$$F_s = C_d \times A_{ORIFICE} \times \sqrt{2 \times \rho_{STAND-PIPE} \times \Delta P_{ORIFICE}}$$

Equation 69

Where:

- $A_{ORIFICE}$ is the surface area of the orifice (m²)
- F_s is the solid flowrate (kg.s⁻¹)
- C_d is the orifice coefficient
- $\rho_{stand\ pipe}$ is the density in the stand-pipe (kg.m⁻³)
- $\Delta P_{orifice}$ is the pressure across the orifice (Pa)

The solid mass flowrate is also given by the level decrease in fluidized bed n°1 with Equation 70.

$F_S = \frac{\Delta P_{BED}(t) - \Delta P_{BED}(t+1)}{g} \times S_{bed}$	Equation 70
--	-------------

Where: ΔP_{BED} is the pressure corresponding to the level of catalyst in T01 (Pa)
 S_{bed} is the surface area of the fluidized bed n°1 (m²)

The coefficient Cd is then calculated combining Equation 69 and Equation 70, its value is averaged over the period of time indicated by the green bars on Figure III-27.

Table III-10 presents the values obtained for the orifice coefficients. For each orifice, four tests were carried out.

Table III-10: Valve Cd coefficient determination

Orifice	3.5 cm			
Test N°	1	2	3	4
Value	0.6411	0.6246	0.6635	0.6379
Cd Averaged value	0.6418			
Difference with averaged value	0.1%	2.7%	3.4%	0.6%
Orifice	5 cm			
Test N°	1	2	3	4
Value	0.6837	0.6757	0.6718	0.6574
Cd Averaged value	0.6721			
Difference with averaged value	1.7%	0.5%	0.1%	2.2%
Orifice	7 cm			
Test N°	1	2	3	4
Value	0.7138	0.7101	0.6926	0.6812
Cd Averaged value	0.6994			
Difference with averaged value	2.1%	1.5%	1.0%	2.6%

The coefficients presented above were then used to calculate the solid flux in the riser during experiments.

5.2.1 Riser pressure drop measurements

Pressure drops measurements were carried out during experiments along the riser height as shown in Figure III-28. Different pressure drop sensors are installed on the riser. PDT16 and PDT41 allows measuring the riser pressure drop profile by switching through the different ports shown in Figure III-28 with a higher space definition at the riser bottom to better characterize the pressure drop due to particle and gas accelerations.

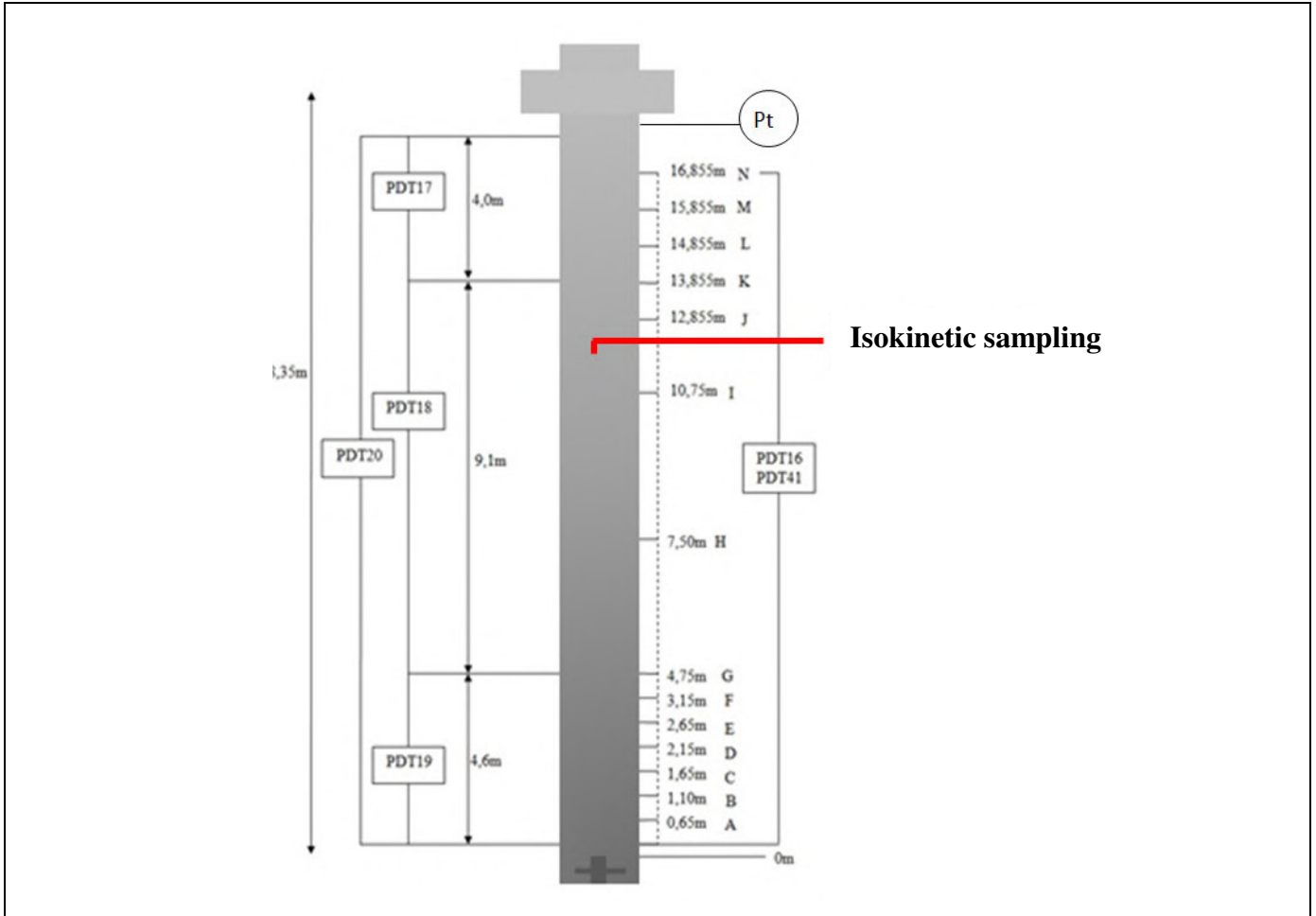


Figure III-28: Riser pressure drop and pseudo isokinetic sampling measurements

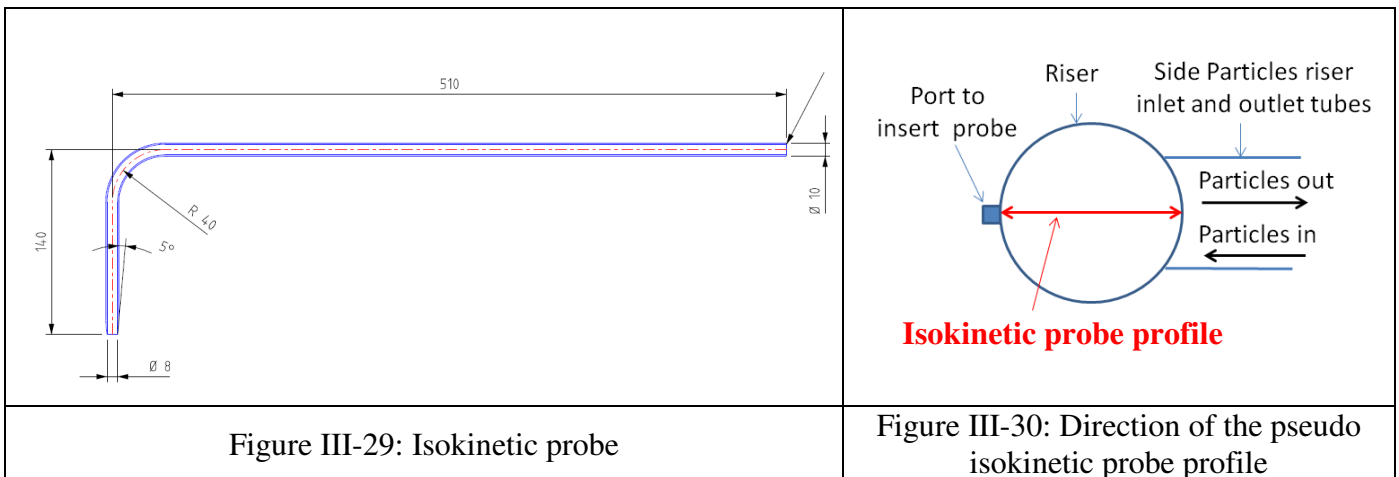
Data acquisition of pressure drop signals was conducted at 1Hz by Keller pressure sensors for a minimum period of three minutes. To avoid pressure taps plugging, continuous air aeration was set and controlled through a rotameters system. The taps aeration was set to generate zero pressure drop when there was no circulation inside the riser. The average aeration flowrate was 25 NL/h. Finally, an absolute pressure sensor is located at the riser top before the riser blind-tee.

It is important to mention that the pressure profiles were measured with the same pressure sensor PDT41. A system of valves allowed changing the position of the riser pressure taps the sensor was connected to. It took in average one hour and a half to measure a full profile, during this period it was checked that the total riser pressure drop measured by the PDT 20 remained constant. An example of a pressure profile measurement versus time can be found in Appendix 4. The consistency of the pressure values from PDT41 and PDT20 was checked by comparisons with other pressure drop measurements from the sensor PDT19, PDT 18 and PDT 17.

5.2.1 Local flux measurement

The pseudo isokinetic sampling technique was used to measure local flux profiles in our experimental set up. As presented in detail below, the technique consists in inserting a tube connected to a vacuum pot in order to withdraw locally particles from the flow to measure a local flux. This technique has been already used and discussed in the literature. Herbert [154] validated this technique in a downer flow by comparing the local solid flux profile obtained with an pseudo isokinetic probe with the combination of local particles concentration and velocity profiles obtained from an optical probe. They also found a good agreement between the particles circulation in the system and the total particles flux calculated from the pseudo isokinetic probe profile integration. Issangya et al. [155] used pseudo isokinetic probes to measure particles fluxes in a riser of FCC particles with solid fluxes from 70 to 700 kg/m²/s and superficial gas velocity going from 9 to 17 m/s. They use a probe with a diameter of 13 mm bent smoothly at 90 degrees. The authors demonstrated with their measurements the influence of the solid riser side inlet on the asymmetry of the solid profiles.

In our work, we use isokinetic sampling technic to measure a riser local flux profile in one direction at a height of 12 meters above the main gas injection as shown in Figure III-28. This height was chosen in order to be in the fully developed section of the flow without being influenced by the riser termination effect presents a sketch of the pseudo- isokinetic probe used to during the tests. Figure III-29 presents the dimensions of the pseudo isokinetic probe used. Dimensions and shape are similar to the probe used by Issangya et al. [155]. Then, as shown in Figure III-30 the profile measured is in the same direction that the side particles riser inlet and outlet tubes. Only one profile was measured using one port to insert the probe located on the opposite side of the particle inlet tube. Previous investigations carried out at IFP Energies nouvelles using a 31 cm riser with FCC particles and similar operating conditions demonstrated the repeatability of the pseudo isokinetic profiles using two ports to insert the probe opposite to each other with an angle of 180°. These results demonstrate the limited intrusiveness of the pseudo isokinetic probe, one can refer to Appendix 4 for more details.



As shown in Figure III-31, the probe is connected to a particle collection pot that is operated under vacuum. The vacuum pressure is set in order that the velocity at the probe tip is equal to the superficial gas flow velocity in the riser. The weight of the collection pot is measured over time in order to get the local mass flux. For each profile point time was measured in order to get 1 kg of particles. For the riser chord investigated, two profile measurements are carried out with the probe facing respectively downward and upward.

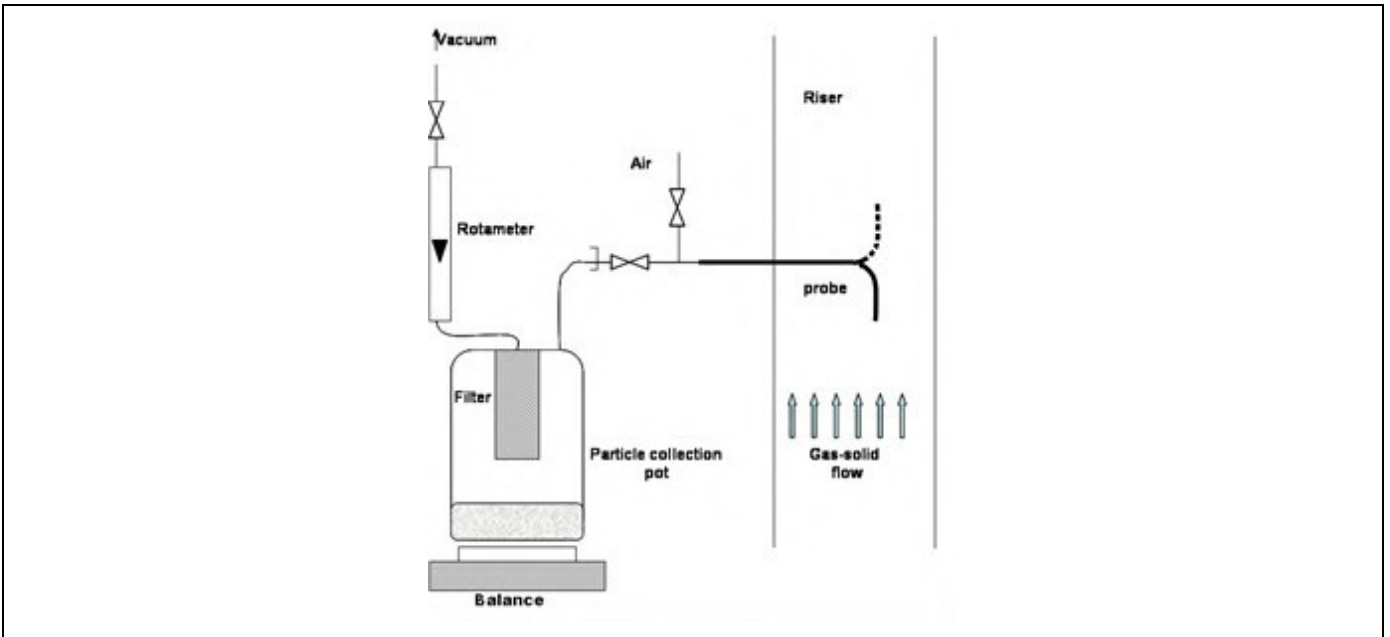


Figure III-31: Isokinetic probe measurement set

The pseudo isokinetic probe is moved along the diameter in different points as shown on Figure III-32, Table III-11 presents the different sampling points locations.

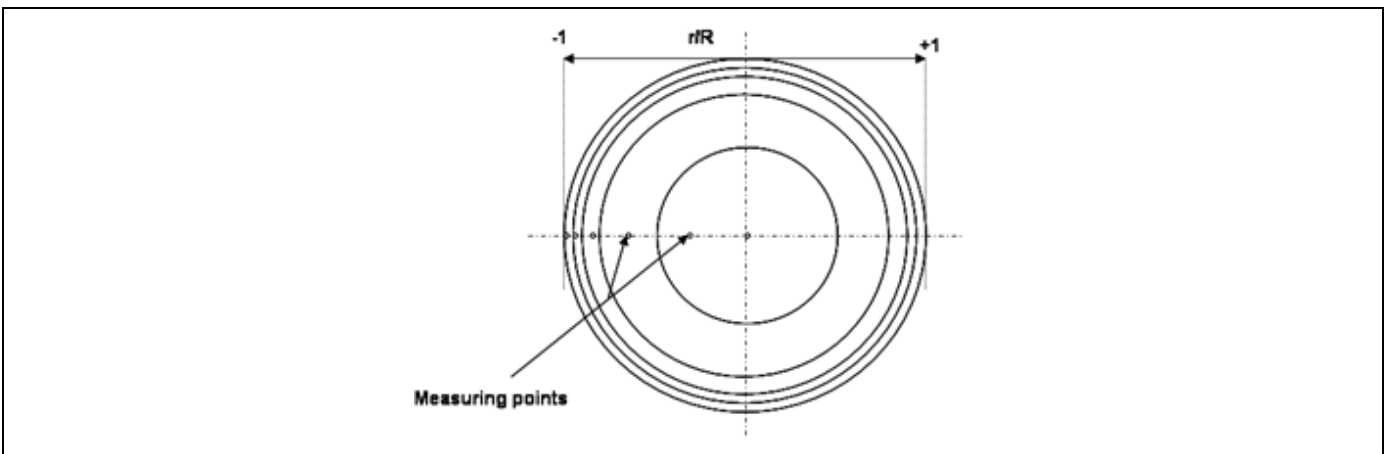


Figure III-32: Profile measurements with the isokinetic probe

Table III-11. Isokinetic probe profile points locations

Measurement distance from the column center (cm)	-14.7 ; -12.9 ; -10.9 ; -8.4 ; -3.5 ; 0 ; +3.5 ; +8.4 ; +10.9 ; +12.9 ; +14.7
Measurement Height in Figure III-28 (m)	10

Local solid flux measurement to characterize a flux distribution is a classical approach but it remains a complex measurement. Indeed it relies on different measurements over a certain test duration. In our case, 22 measurement points have to be made to get a full profile for a period depending on the flux measured as shown in Table III-12 with the averaged sampling duration per probe profile point.

Table III-12. Averaged sampling duration per probe profile points to extract 1 kg of particles

Riser flux	Flux of 80 kg/m ² /s	Flux of 160 kg/m ² /s	Flux of 220 kg/m ² /s
Averaged sampling time per profile point to get 1 kg of solid (s)	240	125	75

The cold flow has therefore to be run in steady state conditions for the entire profiles measurements. Due to all these different experimental challenges, it is necessary to check the consistency of data by comparing the mass flux estimated through the local flux measurements with global solid mass flux estimated through orifice pressure drop calibration. For this purpose, the global mass flux is calculated integrating the local flux profile with Equation 71.

$G_{s_{TOTAL}} = \frac{\sum_1^t \frac{M_i}{t \times A_{PROBE}} \times \frac{A_i}{2}}{A_{TOTAL}}$	Equation 71
--	-------------

- Where:
- $G_{s_{TOTAL}}$ is the total mass flux (kg.m².s⁻¹)
 - t is the number of measuring point
 - A_{PROBE} is the surface area of the tip of the isokinetic probe (m²)
 - M_i is the mass of the collection pot (kg)
 - t is the time over the collection pot mass is measured (s)
 - A_i is the surface area of the ring i (m²)
 - A_{TOTAL} is the surface area of the total section (m²)

The comparison between the global flux from the orifice valve calibration and the integration of the local flux profile is presented in Chapter IV.4.

6 CFD approaches

The simulation strategy is developed using two CFD approaches, the MP-PIC and Euler/Euler KTGF approach. The main reason is to study if two different approaches can first predict experimental results in step n°1 and n°2 for the 20 cm fluidized bed and then study the predictions of the two approaches when extrapolating at a larger scale with the 90 cm fluidized bed in step n°3.

As discussed in the literature review, the Euler/Euler KTGF approach describes better the particle interactions but only a representative particle diameter is considered for the solid phase while the MP-PIC method takes into account the full particle size distribution through a population of computational clouds but with a rather simplistic modeling of particles interactions. These two approaches were used in this investigation with the software OpenFOAM v17.12 for the Euler/Euler KTGF approach and Barracuda VR® for the MP-PIC approach

For a better understanding, the simulations set up description with the geometry, mesh, boundary conditions and drag law is described together with the simulation results in Chapter IV in order to have all information in the same chapter. This section therefore focusses on general information to describe the conditions in which simulations were conducted and to give more details on the two approaches models.

All simulations are transient, the time step being taken to get a Courant number defined by Equation 72 always lower than one (1.0) in the entire simulation domain.

$Courant\ number = \frac{u_g \Delta t}{\Delta x}$	Equation 72
---	-------------

With:

- u_g gas velocity (m/s)
- Δt simulation time step (s)
- Δx cell size (m)

6.1 Euler/Euler with KTGF approach: OpenFOAM v17.12 CFD software

Open Source Field Operation And Manipulation (OpenFOAM) is an open-source C++ CFD software with different solvers, each solver corresponding to a particular application. The solver twoPhaseEulerFOAM version 17.12 developed for the fluidized bed simulation with the Euler/Euler KTGF approach was used in this project. One can refer to Rollins [15] and Engen [127] for more details on the code development and structure.

The mass and momentum conservation equations solved for both phases are presented in Chapter I.4.1. However, OpenFOAM takes into account an additional turbulence model for the gas phase and a friction model for the solid phase as presented below.

6.1.1 Gas phase turbulence model

The standard Launder and Spalding [156] “k-ε” model is considered for the gas phase turbulence, the gas stress tensor presented in Equation 30 then becomes:

$\tau_g = (\mu_g + \mu_t) \left(\nabla \vec{u}_g + \nabla^T \vec{u}_g - \frac{2}{3} \nabla \vec{u}_g I \right)$	Equation 73
--	-------------

With μ_t corresponding to the turbulent viscosity defined by Equation 74:

$\mu_t = \rho_g C_\mu \frac{k^2}{\epsilon}$	Equation 74
---	-------------

Where k is the kinetic turbulent energy defined by the sum of the gas velocity fluctuations components squared as presented in Equation 75.

$k = \frac{1}{2} (u_x'^2 + u_y'^2 + u_z'^2)$	Equation 75
--	-------------

ϵ is the kinetic turbulent dissipation rate and C_μ is a constant.

k and ϵ are transported with respectively Equation 76 and Equation 77.

$\frac{\partial(\alpha_g \rho_g k)}{\partial t} + \nabla \cdot (\alpha_g \rho_g \vec{u}_g k) = \nabla \left[\left(\mu_g + \frac{\mu_t}{\sigma_k} \right) \nabla k \right] + 2\alpha_g \mu_t S_{ij} S_{ij} - \alpha_g \rho_g \epsilon$	Equation 76
---	-------------

With: $-S_{ij}$ mean strain rate tensor equals to $\frac{\partial U_i}{\partial x_j} + \frac{\partial U_j}{\partial x_i}$

$\frac{\partial(\alpha_g \rho_g \epsilon)}{\partial t} + \nabla \cdot (\alpha_g \rho_g \vec{u}_g \epsilon) = \nabla \left[\left(\mu_g + \frac{\mu_t}{\sigma_\epsilon} \right) \nabla \epsilon \right] + \alpha_g C_{\epsilon 1} \frac{\epsilon}{k} 2\mu_t S_{ij} S_{ij} - \alpha_g C_{\epsilon 2} \rho_g \frac{\epsilon^2}{k}$	Equation 77
--	-------------

C_μ , σ_k , σ_ϵ , $C_{\epsilon 1}$ and $C_{\epsilon 2}$ are constant taken from the study of Launder and Spalding [156] on experimental characterization of monophasic turbulent flows and are equal respectively to 0.09, 1, 1.3, 1.44 and 1.92. The use of a turbulent model developed for monophasic flow in a multiphase simulation is discussed in Chapter V.

6.1.2 Solid phase frictional model

When solid volume concentration is high the particle collision are no longer instantaneous, as it is assumed in kinetic theory. The resulting frictional stress due to sustained contact between the particles is therefore taken into account by adding a frictional stress component to the solid pressure equation and the viscous stress equation with the model of Johnson and Jackson [157].

$P_s = P_{s,KTGF} + P_{s,frictional}$	Equation 78
---------------------------------------	-------------

With: $-P_{s,KTGF}$: the solid pressure from the Kinetic Theory of Granular flow with the Lun model presented in Equation 33.

The Johnson and Jackson solid pressure from particle friction model is presented in Equation 79, it is implemented only when the solid volume concentration is greater than a specified minimum solid volume

fraction value. This minimum value chosen for this study is the openFOAM default value of 0.55. This parameter was not investigated in this work.

$P_{s,frictional} = Fr \frac{(\alpha_s - \alpha_{s,min})^n}{(\alpha_{s,max} - \alpha_s)^p} \text{ if } \alpha_s > \alpha_{s,min}$ $P_{s,frictional} = 0 \text{ if } \alpha_s < \alpha_{s,min}$	Equation 79
--	-------------

With :

- $\alpha_{s,min}$ equals to 0.55 in this study
- $\alpha_{s,max}$ equals to 0.62 in this study
- Fr constant equals to 0.05
- n constant equals to 2
- p constant equals to 5

The solid viscosity is then calculated from Equation 80:

$\mu_s = \mu_{s,KTGF} + \mu_{s,frictional}$	Equation 80
---	-------------

With: - $\mu_{s,KTGF}$: solid viscosity from the Kinetic Theory of Granular flow with the Gidaspow model presented in Equation 33 to Equation 38.

The Johnson and Jackson solid viscosity from particle friction model is presented in Equation 79, it is implemented only when the solid volume concentration is greater than a specified minimum solid volume fraction value.

$\mu_{s,frictional} = P_{s,frictional} \sin(\varphi)$	Equation 81
---	-------------

With: φ : internal flow angle taken at 28.5° in this study

6.1.3 Wall boundary conditions

Wall boundary conditions for gas/particles flow is a topic of great interest already discussed in the literature. Fede et al. [13] and Li et al. [158] investigated and showed the influence of the particle wall boundary conditions on their fluidized bed simulations but no general agreement can be found in the literature concerning this particles wall boundary conditions modeling. It therefore remains a challenging topic.

In our study, we chose the Johnson and Jackson [157] partial slip wall boundary condition for the particle phase which is one of the most common model for fluidized bed simulation [159]. The Equation 82 and Equation 83 present respectively the wall velocity and granular temperature conditions.

$\vec{n} \mu_s \nabla \vec{V}_{p,w} = \frac{\pi \Phi \rho_s \alpha_s \vec{V}_{p,w} g_{0,s} \sqrt{3\theta_s}}{6 \alpha_{s,max}}$	Equation 82
---	-------------

$\vec{n} K_s \nabla \theta_s = \frac{\pi}{6} \sqrt{3} \frac{\alpha_s}{\alpha_{s,max}} \rho_s g_{0,s} \sqrt{\theta_s} V_{p,w}^2 - \frac{\pi}{4} \sqrt{3} \frac{\alpha_s}{\alpha_{s,max}} (1 - e_w^2) \rho_s g_{0,s} \theta_s^{3/2}$	Equation 83
--	-------------

- With:
- \vec{n} unit normal vector to the wall
 - $V_{p,w}$ particle slip velocity parallel to the wall (m/s)
 - $\alpha_{s,max}$ equals to 0.62 in this study
 - Φ specularity coefficient for particle wall collisions taken at 0.01 in this study
 - $g_{0,s}$ radial distribution from Equation 35 with the Sinclair Jackson model
 - θ_s granular temperature
 - K_s granular temperature conductivity coefficient K_s from Equation 41 with the Gidaspow model
 - e_w coefficient of restitution for particle wall collisions equals to 0.85 in this study

The specularity and restitution coefficients Φ and e_w were set with the default openFOAM values of respectively 0.01 and 0.85. These values were also used in the work of Engen [127] with the simulations of Geldart Group A and Group B particles using openFOAM. It is also important to point out that Motlagh et al. [12] showed that the variation of the specularity coefficient from 0.001 to 0.1 did not affect significantly the results of his Geldart Group A turbulent bed simulations. Then Fede et al. [13] showed that the restitution coefficient e_w variation from 0.86 to 1 did not affect their Geldart Group B fluidized bed simulation results.

Concerning the gas phase, a no slip condition is applied at the wall as it is usually applied in gas/particles simulations [159]. The code default wall boundary conditions were used for the turbulence k and ϵ parameters.

6.1.4 Simulation parameters and models summary

Table III-13 presents the parameters and models summary of the simulations carried out with openFOAM.

Table III-13: Simulation parameters and models summary for OpenFOAM simulations

Gas turbulence model	
Standard k-ε Launder and Spalding [156] ; $C_\mu = 0.09$, $\sigma_k = 1$, $\sigma_\epsilon = 1.3$, $C_{\epsilon 1} = 1.44$ and $C_{\epsilon 2} = 1.92$	
Kinetic theory of Granular Flow	
$\alpha_{s,max}$	0.62
Coefficient of restitution for particles collisions e_s	0.9
Granular Pressure $P_{s,KTGF}$ model	Lun (Equation 33)
Viscosity $\mu_{s,KTGF}$ model	Gidaspow (Equation 33 to Equation 38)
granular temperature conductivity coefficient K_s model	Gidaspow (Equation 41)
Radial distribution $g_{0,s}$	Sinclair Jackson model (Equation 35)
Frictional stress	
$P_{s,frictional}$ and $\mu_{s,frictional}$ model	Johnson and Jackson [157]
$\alpha_{s,min}$	0.55
Angle φ	28.5
r	2
Fr	0.05

s	5
---	---

Wall boundary conditions	
model	Johnson and Jackson [157]
$\alpha_{s,max}$	0.62
specularity coefficient Φ	0.01
coefficient of restitution for particle wall collisions e_w	0.85

Particle density
Input from the experimental measurements (Table III-1)

Particle mass
1 815 kg

Parameters investigated and/or discussed in Chapter III
Mesh size and mesh type
Gas/ particles drag Law
particle representative diameter
Geometry simulated and boundary conditions imposed
Simulation time step and duration

The solver and numerical schemes selected are detailed in Appendix 5 and Appendix 6 which include respectively the fvSolution and fvSchemes files of the openFOAM simulations.

6.1.5 MP-PIC approach: Barracuda VR[®]

Barracuda VR[®] and the MP-PIC approach have already been introduced in Chapter I.4.2 and Chapter II.2.4. Table III-14 presents the parameters and models used for Barracuda VR[®] simulations.

Table III-14: Simulation parameters and models summary for Barracuda VR[®] simulations

Gas turbulence model
Smagorinsky (1963) turbulence model, Smagorinsky coefficient C=0.01

Solid stress model
model of Equation 52, $P_s = 1$; $\beta = 3$; $\epsilon_{barracuda} = 10^{-8}$, $\alpha_{s,max} = 0.62$

Wall boundary conditions
Particle to wall normal retention coefficient: 0.3 Particle to wall tangential retention coefficient: 0.99

Particle size distribution
Input from the experimental particle size distribution measurements (Figure II-2)

<u>Particle density</u>
Input from the experimental measurements (Table II-1)
<u>Particle mass</u>
1 815 kg
<u>Parameters investigated and/or discussed in Chapter IV</u>
Mesh size
Gas/ particles drag Law
Number of particles per cloud
Geometry simulated and boundary conditions imposed
Simulation time step and duration

The constants used in the turbulence, solid stress and wall boundary conditions models are the default values of the software Barracuda VR[®]. Many authors [9,11,160] used the same values for their circulating fluidized bed simulations with Geldart Group A particles. No investigation on the effect of changing these models constants were found in the literature.

7 Conclusions

In this chapter, we first proposed a strategy to evaluate the use of CFD models in a context of extrapolation with an investigation of two CFD approaches predictions at different scales and different fluidization regimes. For this purpose, we then presented the three experimental set-ups used to investigate scale and operating conditions effects. The 20 cm fluidized bed experiments allowed measuring local solid volume fraction and bed density for two gas distributions. It is indeed important to evaluate if CFD can predict gas distribution effects in a context of extrapolation where it directly affects industrial fluidized bed reactors performances [9]. The 90 cm fluidized bed experiments then allowed measuring bed density profiles and entrainment rates for different superficial gas velocities. These experiments are used to evaluate the extrapolation capacity of the CFD predictions from the 20 cm fluidized bed scale toward the 90 cm fluidized bed scale with similar fluidization regimes and operating conditions. The riser experiments allows measuring for different solid circulation rates macro and local data with respectively the riser pressure drop profile and a riser local flux profile. This data are used to evaluate the extrapolation capacity of CFD predictions from the 20 cm fluidized bed scale using turbulent regime operating conditions toward the riser scale with a different fluidization regime (transport regime) and different operating conditions (increasing gas velocity and increasing solid flowrate).

It is important to highlight that all experiments are run at ambient conditions with FCC catalyst particles having similar properties. We therefore do not investigate temperature, pressure and particle properties effects in this work. As mentioned before, only the scale and operating conditions effects are investigated.

Finally, we introduced the two CFD approaches used in this dissertation. The first MP-PIC approach allows taking into account the full particle size distribution with a rather simplistic particle interactions model. The second Euler/Euler KTGF approach has a more complex modeling of particle interactions and uses a single representative particle diameter. The objective is first investigating if two different approaches can predict experimental results at a given scale with the 20 cm fluidized bed experiments and then investigate the two approaches predictions at another scale with the 90 cm fluidized bed experiments.

Experimental results obtained with the three experimental set up are presented in Chapter IV. The experiments simulations results and the investigation of the CFD approaches extrapolation capabilities are presented in Chapter V.

IV. USE OF CFD FOR EXTRAPOLATION EXPERIMENTAL RESULTS

1 Introduction

This chapter presents and discusses all experimental results which are then used as comparison basis in the CFD simulation strategy. The results of the 20 cm fluidized bed results are first presented, followed by the experimental results obtained in the 90 cm fluidized bed. The experimental results obtained with the riser experiments are finally presented.

2 Fluidized bed of 20 cm

The 20 cm fluidized bed is used to study axial and radial distribution of solid volume fraction in the bed as a function of gas distribution.

Table IV-1 presents the bed density and equivalent averaged solid volume fraction obtained from the pressure probe measurements for both experiments with homogeneous and jet gas injections. The values are averaged over five experiments of 15 minutes each. Values in parenthesis show the standard deviation over all experiments.

Table IV-1: Bed density and equivalent averaged solid volume fraction from pressure probe measurements ($V_{sg} = 0.64$ m/s)

	Experiment n°1: homogeneous gas injection	Experiment n°2: gas injection with jet
Bed density (kg/m ³)	504 (+/- 5)	631 (+/- 4)
Averaged Solid volume fraction	0.4 (+/- 0.005)	0.50 (+/- 0.003)

The averaged solid volume fraction found in Experiment n°1 is in agreement with the results found by Taxil [161] using a 20 cm fluidized bed of FCC particles. The bed density and averaged solid volume fraction are higher in experiment n°2 with the jet. This phenomenon is expected since the jet injection promotes gas by-passing which results in a higher bed density and averaged solid volume fraction. Similar results were found by Issangya et al. [162].

Particles entrainment was not measured experimentally but it was evaluated from a PSRI model that cannot be disclosed (due to confidentiality), it actually uses an approach similar to the one presented in the literature review [2,74]. The model takes into account the column diameter, the particle size distribution, the particle density and the superficial gas velocity. The model assumes a homogeneous gas distribution, it is therefore applied to experiment n°1 only. The entrainment rate from the model was estimated at 0.07 kg/s. It is important to highlight that this value is used here only as a qualitative comparator to assess if the CFD modeling predicts entrainment rate in the same range.

The two next sections present the results from the optical probe measurement to characterize the solid volume fraction in the bed for both experiments.

2.1 Experiment n°1: homogeneous fluidization

As discussed in Chapter III.3.3, the solid volume fraction reconstruction from the optical probe signal depends on the bubble and dense phase solid volume fraction, for the following results they were chosen at respectively $\epsilon_{s,bubble}=0$ and $\epsilon_{s,dense}=\epsilon_{s,mf}=0.58$. This choice is then discussed when comparing the averaged solid volume fraction from pressure probe and from optical probe measurements.

Figure IV-1 and Figure IV-2 present the solid volume fraction profiles obtained from optical probes for respectively the north-south and west-east directions. The results presented are averaged over five experiment repetitions and the error bars show the standard deviation over all experiments.

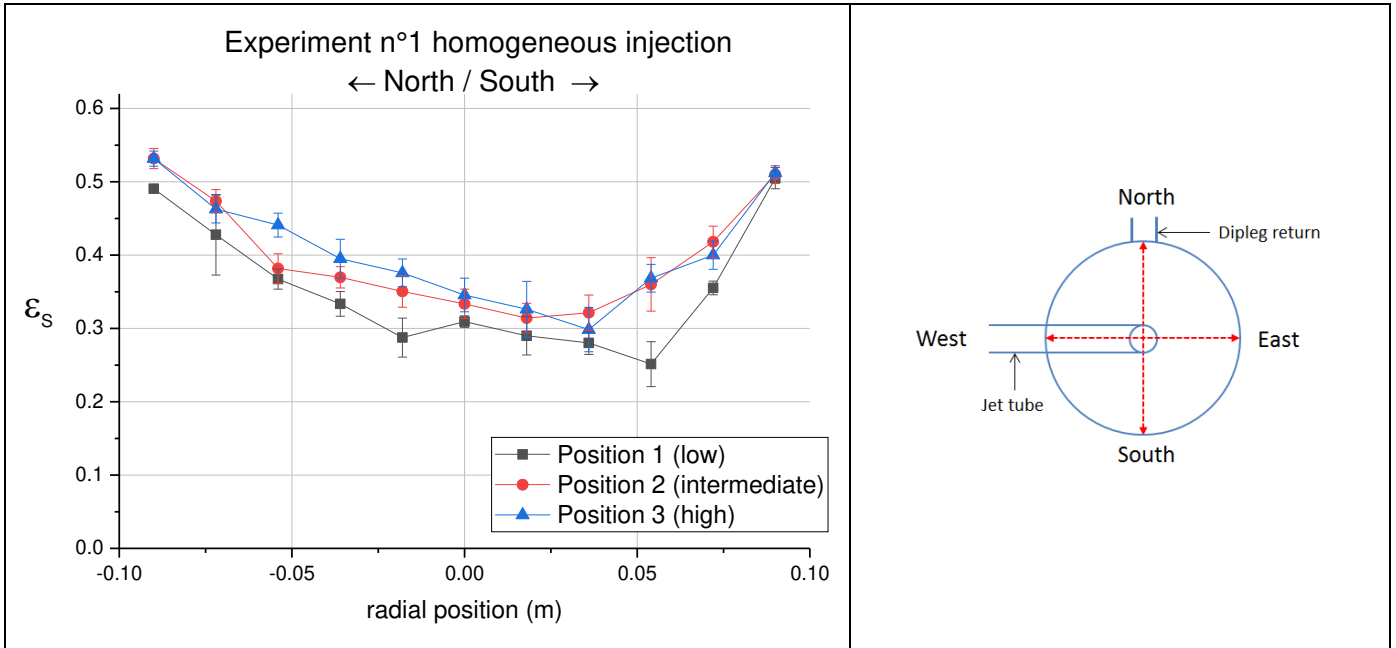


Figure IV-1: Homogeneous fluidization, solid volume fraction profiles North-South direction, $V_{sg} = 0.64 \text{ m/s}$

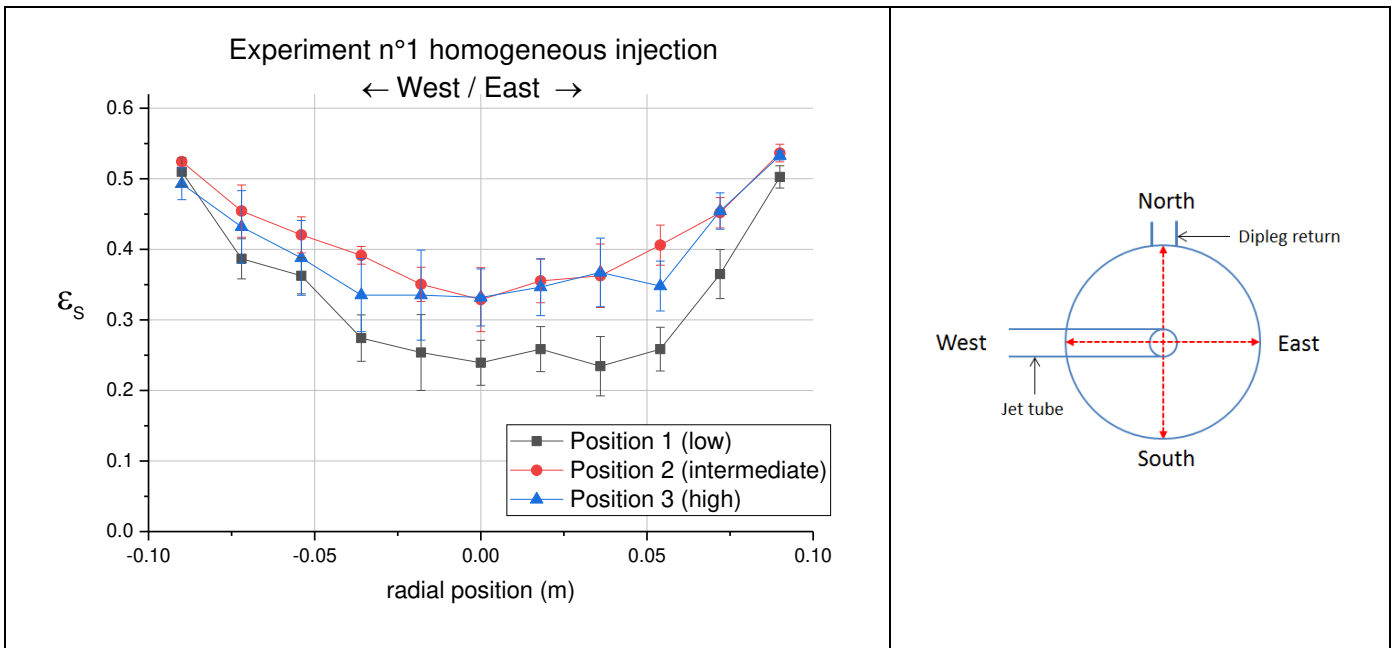


Figure IV-2: Homogeneous fluidization, solid volume fraction profiles West-East direction $V_{sg} = 0.64 \text{ m/s}$

Different points can be highlighted:

- The solid volume fraction profiles obtained are elliptical and almost symmetrical with respect to the bed axis which shows that gas bubbles have a tendency to flow in the column center. These results are in accordance with the findings of Schweitzer et al. [97] and their experiments on a 20 cm fluidized bed with FCC catalyst.
- The “north-south” profiles tend to shift toward the south direction. One explanation for this shift could be the non-symmetrical nature of the column configuration with the return of the cyclone dipleg located on the bottom north side. The particles recovered by the cyclone and re-entering in the bed could therefore influence the solid volume profiles and gas repartition in the column. To verify this hypothesis, it would be interesting in a future investigation to switch the dipleg return on the south side of the column and check if the solid volume fraction profiles shift in the other direction.
- The profiles at the lowest position 1 give lower solid volume fraction values, then profiles at position 2 and 3 are similar. One can wonder if this difference can be connected to a tube effect. Experiments without tube could therefore be carried out in the future to answer this question.

Considering the symmetrical aspect of the profiles, the averaged solid volume fraction was calculated integrating the profiles with respect to the column radius with Equation 84:

$\epsilon_{S,AVERAGED} = \frac{\sum_1^n \epsilon_{S,Ri} \times \frac{Ai}{2}}{A_{TOTAL}}$	Equation 84
--	-------------

Where:

- $\epsilon_{s,averaged}$ averaged solid volume fraction
- $\epsilon_{s,Ri}$ solid volume fraction at the location of radius Ri with respect to column center
- n is the number of measuring point
- Ai is the surface area of the ring with a center of radius Ri (m²)
- A_{TOTAL} is the surface area of the total section (m²)

The averaged solid volume fraction obtained from the profile integration was then calculated for the six profiles (two profiles for the three elevations) and the six values were then averaged. Table IV-2 present the comparison between this averaged value and the one obtained from the pressure probe measurement.

Table IV-2 : Comparison of averaged solid volume fraction from optical probe and pressure measurement

	Averaged value from optical probe profiles integration	Averaged pressure probe (bed density)	Relative error (%)
Averaged Solid volume fraction	0.42	0.40	4.6%

One can notice that both values are close to each other with a relative error of 4.6% between the two experimental techniques. This result is satisfying since the local bed hydrodynamic characterization is in a reasonable accordance with the macro scale measurement from the pressure probe. It therefore comforts the choice of $\epsilon_{s,bubble}=0$ and $\epsilon_{s,dense}=\epsilon_{s,mf}=0.58$ for the optical probe signal post-processing.

2.2 Experiment n°2: Gas injection with jet

Figure IV-3 and Figure IV-4 present the solid volume fraction profiles obtained from optical probes for respectively the north-south and west-east directions. The results presented are averaged over five experiment repetitions and the error bars show the standard deviation over all experiments.

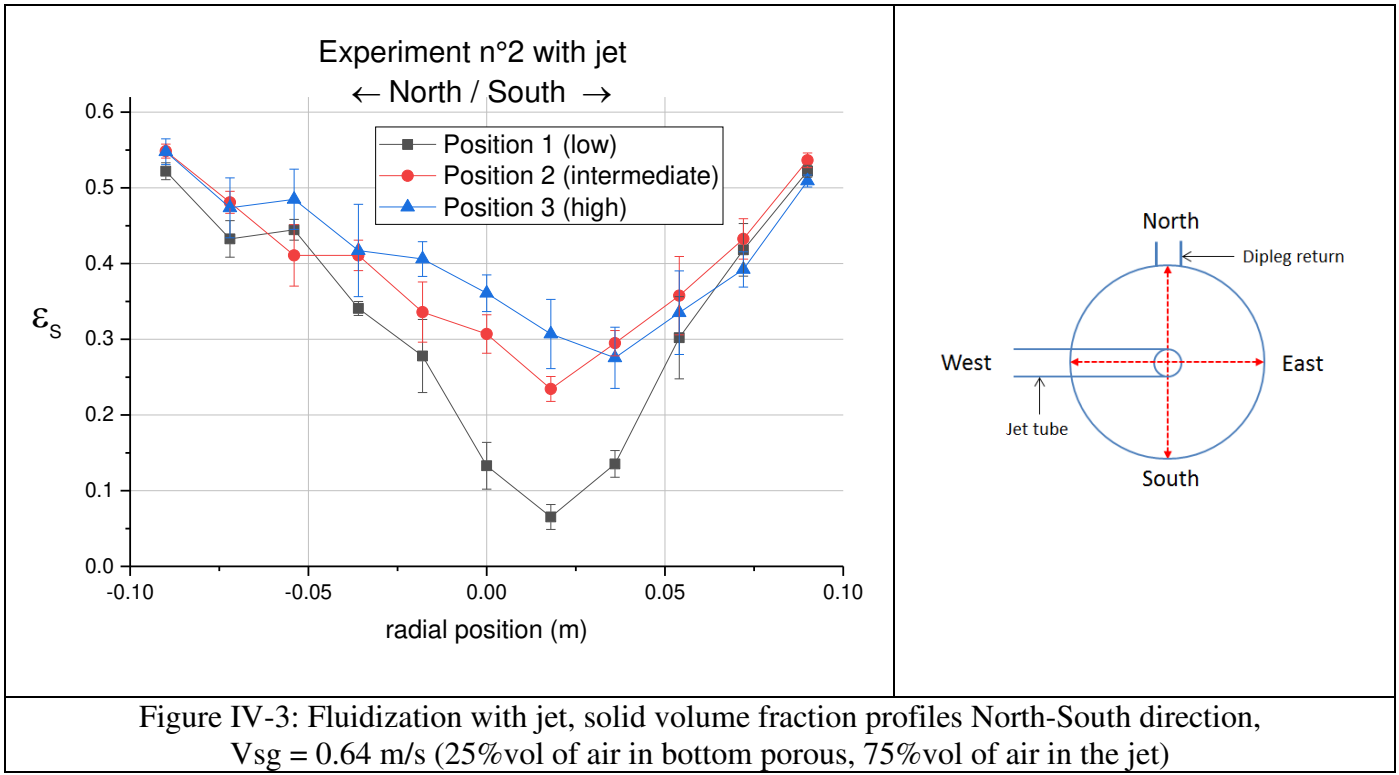


Figure IV-3: Fluidization with jet, solid volume fraction profiles North-South direction, $V_{sg} = 0.64 \text{ m/s}$ (25%vol of air in bottom porous, 75%vol of air in the jet)

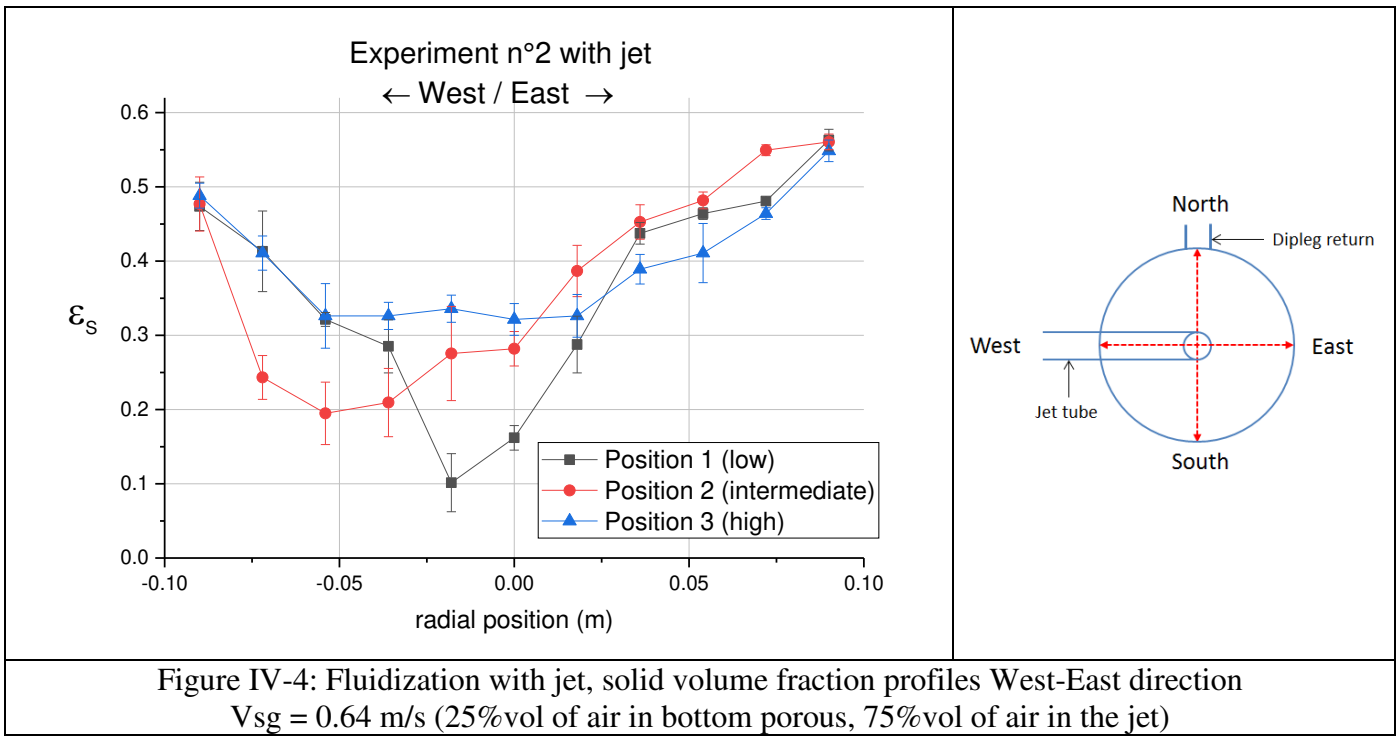


Figure IV-4: Fluidization with jet, solid volume fraction profiles West-East direction $V_{sg} = 0.64 \text{ m/s}$ (25%vol of air in bottom porous, 75%vol of air in the jet)

Different points can be highlighted:

- First, one can clearly notice the effect of the jet by comparing the results obtained to the profiles of experiment n°1 especially for the lowest position 1 with low solid volume fraction close to the column center where the jet injection is located.
- Second, the flow is now clearly asymmetric:
 - o The gas stream from the jet is shifted toward the south side on the north-south direction. Similarly to the results obtained in experiment n°1, this shift can be explained by the presence of the dipleg return on the north side. Again this hypothesis could be verified by moving the dipleg return on the south side and observe if the profiles shifts on the other direction.
 - o In the other direction, the jet gas stream shifts toward the west side with the position 2 profile highly shifted. This result can be explained by the non-symmetrical aspect of the column configuration in this direction with the presence of the tube for the jet injection. To verify this hypothesis, the tube position could be modified in order to observe if it affects the profile shifting.
 - o The important shift observed for the position 2 profile in the west-east direction is surprising. Indeed when looking at Figure IV-1, Figure IV-2 and Figure IV-3 the profiles of position 2 and 3 are always similar in shape. In Figure IV-4, the position 2 and position 3 profiles are different with the important shift observed at position 2 being cancelled at position 3 the difference of height being 5 cm between the two profiles.
- As a consequence, since profiles shapes are not symmetrical with respect to the bed axis, the procedure of integrating these profiles to obtain an average solid volume fraction as carried out for experiment n°1 is not possible. Indeed, additional profiles in other directions are needed to reconstruct precisely the solid volume fraction over the bed section at a given height, this could be done in a future study.
- The effect of the jet is dissipated at the highest position 3 where profiles have a shape similar to experiment n°1 profiles is obtained. Therefore, jet dissipation is quite fast and occurs within 10 to 15 cm from the jet inlet cm with a ratio of the dissipation length over jet diameter between 2.5 and 3.75.

2.3 Conclusions

The experiments carried out allowed characterizing local flow structure in a turbulent fluidized bed with the measurement of solid volume fraction profiles at different height. Two gas injection distributions were investigated. The results obtained with the homogeneous injection showed that gas tend to flow in the center of the column which is in accordance with results from the literature [161]. When the gas distribution was modified with the implementation of a gas injection through the jet, the local flow structure was affected with by-passing phenomena and asymmetric solid volume fraction profiles. The averaged bed solid volume fraction was also affected with a lower value compared to the homogeneous injection case result.

In a context of extrapolation and scaling up of fluidized beds, gas distribution is therefore an important parameter to consider. We now have experimental data characterizing two well controlled gas distributions. It is then important to evaluate if CFD can predict the differences obtained between the two configurations in order to potentially use CFD as an extrapolation tool to characterize gas distributions at a larger scale.

3 Fluidized bed of 90 cm

This section presents the results for the 90 cm fluidized bed experiments carryout at PSRI. The main objective with these experimental results is first the evaluation of the size effect between the 20 cm and the 90 cm fluidized beds using similar operating conditions (superficial gas velocity of 0.64 m/s and 0.60 m/s for respectively the 20 cm and 90 cm fluidized beds). We can then evaluate if CFD can predict the change of scale effects which is of course a necessary condition if one wants to use this tool for extrapolation purposes. Moreover, the 90 cm fluidized bed experiments with a superficial gas velocity of respectively 0.3 and 0.85 m/s allow evaluating CFD predictions capabilities for different operating conditions at large scale.

3.1 Experimental results

Figure IV-5 presents the bed density profiles for the different superficial gas velocities tested.

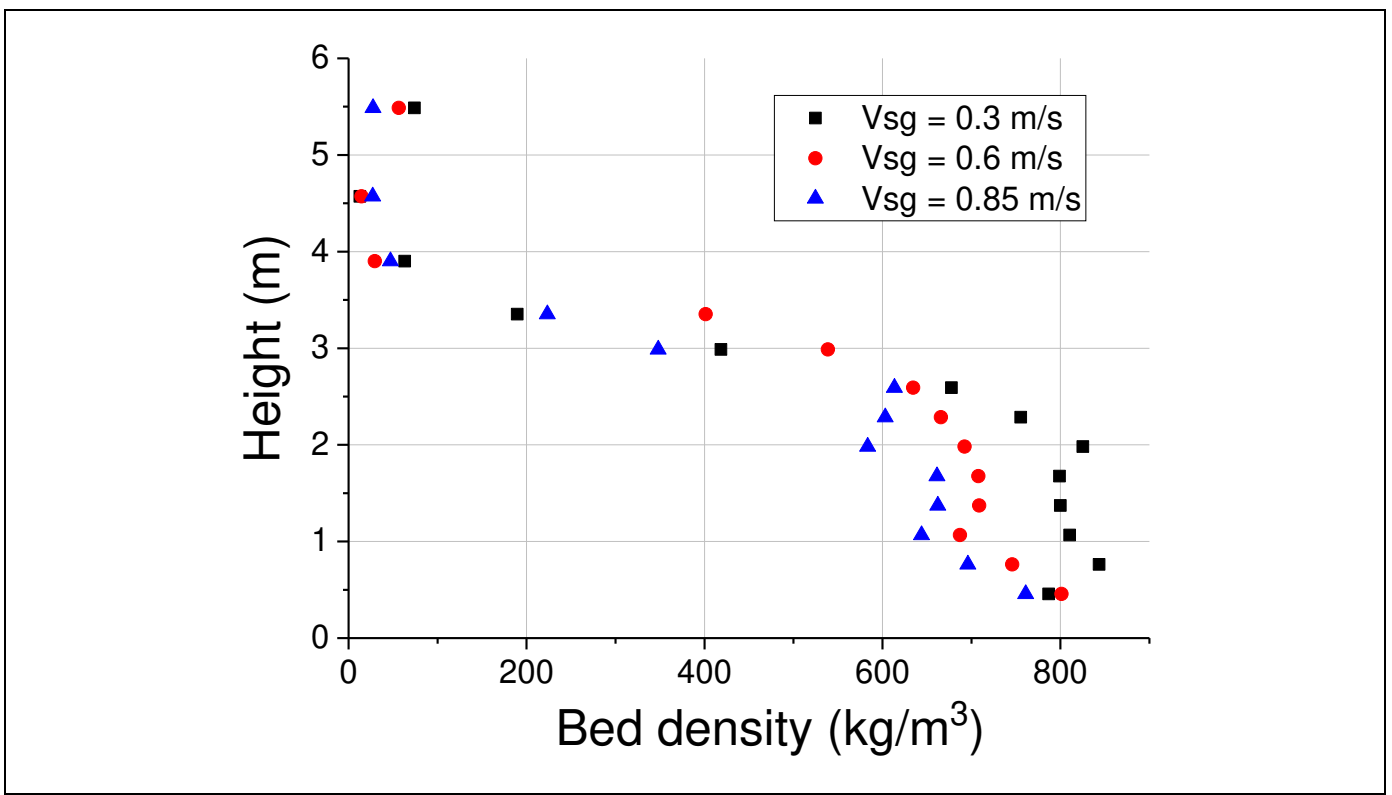


Figure IV-5: Bed density profiles for the different superficial gas velocities

One can see clearly observe for all profiles three different zones with first the dense bed with high bed density values, then the transition between the dense and dilute phases and finally the dilute phase with low bed density value. Concerning the dense bed, the density values decrease with the increase of superficial gas velocity which is in accordance with the literature [61]. Concerning the dilute phase, one can wonder why the bed density values and therefore the pressure drop measured are more important at the top of the column for lower superficial gas velocities. One could expect the opposite trend since pressure drop is supposed to be more important at higher gas velocities especially since the particles entrainment is also higher as shown below. This issue was not investigated further since our main interest concerns predictions of the bed hydrodynamic characteristics and not boundary effects such as this variation of pressure at the top of the bed.

Figure IV-6 then presents the bed overall density for the 20 cm and 90 cm fluidized bed experiments versus the superficial gas velocities. The King correlation, which expresses the bed solid volume fraction as a function of the superficial gas velocity (see Equation 17 in Chapter I.2.2.2), is also plotted.

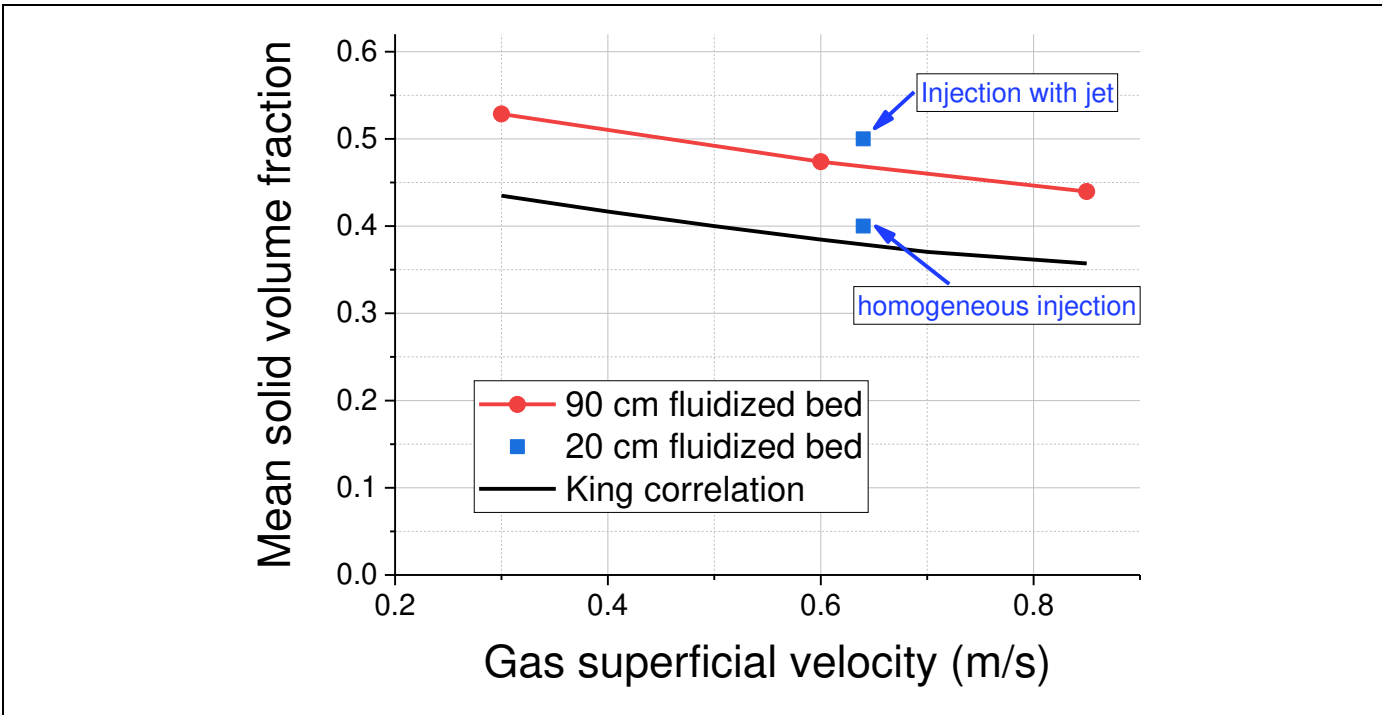


Figure IV-6: Overall bed density for the different superficial gas velocities

Different remarks can be made:

- First, the 90 cm fluidized bed solid volume fraction decreases with the superficial gas velocity which is in accordance with the results presented in Figure IV-5.
- The decrease of solid volume fraction observed from the 90 cm fluidized bed experiments follows the same trend than the King correlation, however, experimental values obtained are higher compared to the correlation.
- The solid volume fraction obtained in the 20 cm fluidized bed experiment with a homogeneous injection is also lower compared to the 90 cm fluidized bed experiment and closer to the King correlation result. The higher value obtained in the case of an injection with jet for the 20 cm fluidized bed was already explained by the fact the gas bypassing phenomena.

The higher solid volume fraction obtained with the 90 cm fluidized bed show that the gas goes through the bed with a higher velocity compared to the 20 cm fluidized bed experiment for similar operating conditions. This phenomenon can be explained through scale effects. Indeed, as highlighted by Bi et al. [62] in their state of the art on turbulent fluidization, parameters such as the column diameter can clearly influence the hydrodynamic of turbulent beds. It can also be explained by gas distribution effects as demonstrated with the experiments on the 20 cm fluidized bed where gas distribution affects the averaged bed volume fraction. As mentioned in the literature review it is difficult to develop predictive models including all these effects. It therefore explains the differences observed between experimental results and the King correlation. It is now interesting to evaluate if CFD is able to predict these different effects which is the main objective of our simulation strategy.

Finally, Figure IV-7 presents the particle entrainment measured versus superficial gas velocities for the 90 cm fluidized bed experiments as well as values predicted from the PSRI model for the 90 cm and 20 cm fluidized bed experiments.

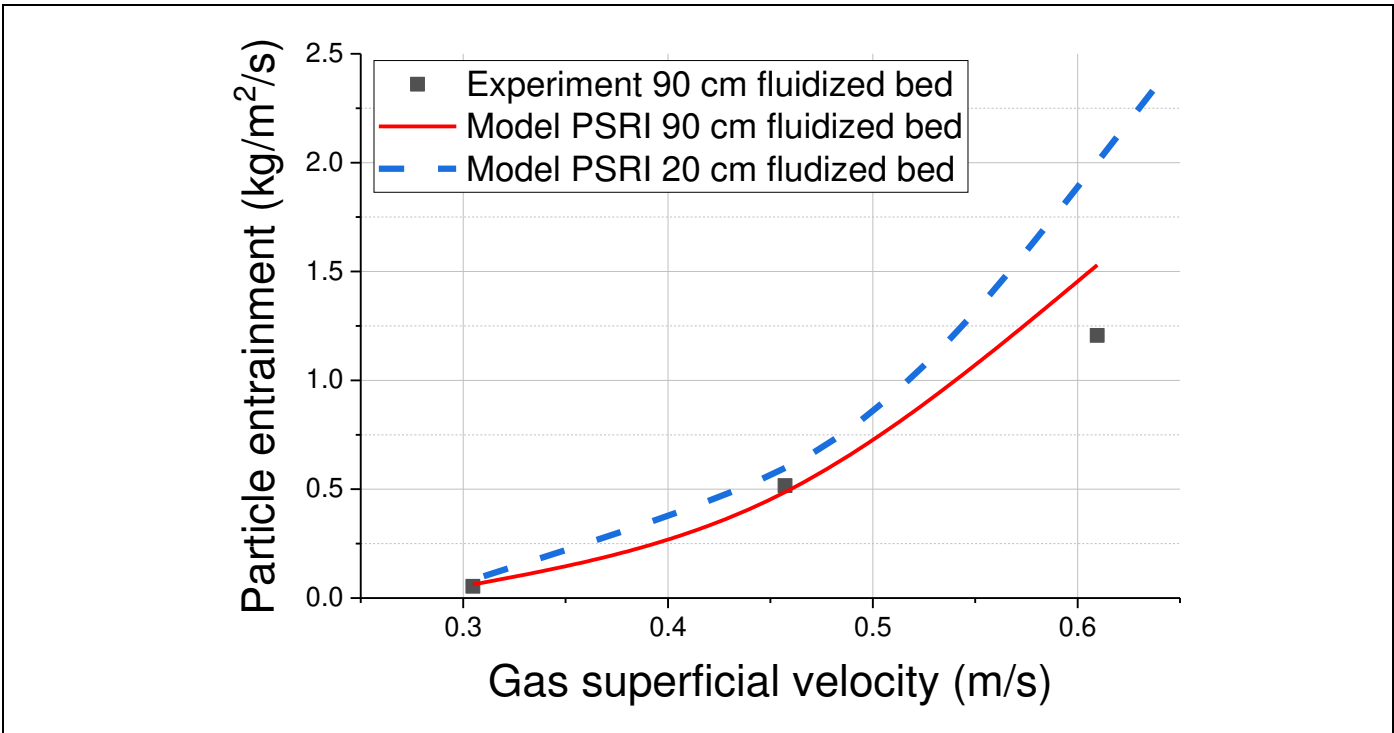


Figure IV-7: Particle entrainment versus superficial gas velocities

First, the velocities at which entrainment was measured are lower compared to the results for the bed density. This comes from the fact that entrainment rate for a superficial velocity of 0.85 m/s was too high to be measured with the experimental technique used. Therefore, entrainment values are reported only up to 0.6 m/s.

Then, one can see that entrainment increases with the superficial velocity as expected and as reported in the literature [2]. It is also interesting to notice that the PSRI model predicts reasonably well the evolution of the entrainment rate with a slight overestimation for the highest velocity. However, experimental error bars are not indicated and one can imagine that the entrainment rate for the gas superficial velocity of 0.6 m/s can be challenging considered that measurement at 0.85 m/s was not possible. It would be interesting in future work to indicate the error bars obtained from experiments repetitions. The model predictions are still considered satisfactory which then comforts its use to evaluate the entrainment of the 20 cm fluidized bed experiment n°1 with a homogeneous injection. It should also be pointed out that no column diameter effect is taken into account in the PSRI model for entrainment rates above TDH. The difference of the predicted entrainment between the 20 cm and 90 cm fluidized beds comes from the difference of particles properties with a lower density for the 20 cm fluidized bed experiments.

3.2 Conclusions

The data acquired with the 90 cm fluidized bed experiments are interesting and pertinent for our simulation strategy. We now have experimental data at two different scales where usual correlations fail to predict the experimental differences obtained between the two scales. It therefore becomes relevant

from an extrapolation point of view to investigate if CFD can predict these differences which is exactly the purpose of our simulation strategy.

Moreover the entrainment data acquired are also interesting from a CFD point of view with an increase of the particle circulation rate depending only on superficial gas velocity and representing a transition to the transport regime. It is therefore interesting to investigate if CFD is able to predict the entrainment rate trend with a perspective of simulating other regimes.

4 Riser of 30 cm

This chapter presents the results of the riser experiments. It is first important to highlight that the regime investigated in these experiments is different from the turbulent fluidized bed experiments presented before. Indeed, as presented in the literature review, the transport regime hydrodynamic depends on both superficial gas velocity and particles circulation compared to the turbulent regime where superficial gas velocity is the main characterizing parameter.

The riser experiments are used in the simulation strategy to evaluate if the CFD model developed from turbulent fluidized bed experiments can also predict such transport regime. It is indeed important to evaluate the CFD prediction over a large range of fluidization regime in order first to potentially target physical phenomena that should be taken into account or modeled differently depending on the fluidization regime. It is also important to assess if the CFD model predict different regimes in the same simulation with for example the injection of the gas/particle mixture into a turbulent bed through a riser as it is the case in the R2R™ Resid FCC [33] (see Figure I-3)

4.1 Experimental results

Figure IV-8 presents the riser pressure drop profiles for the three operating conditions tested. As mentioned before, the superficial velocity are calculated at the riser top before the blind tee where the absolute pressure is measured and was equal to 110 000 Pa abs for all experiments. Tests were not repeated therefore no error bars are indicated.

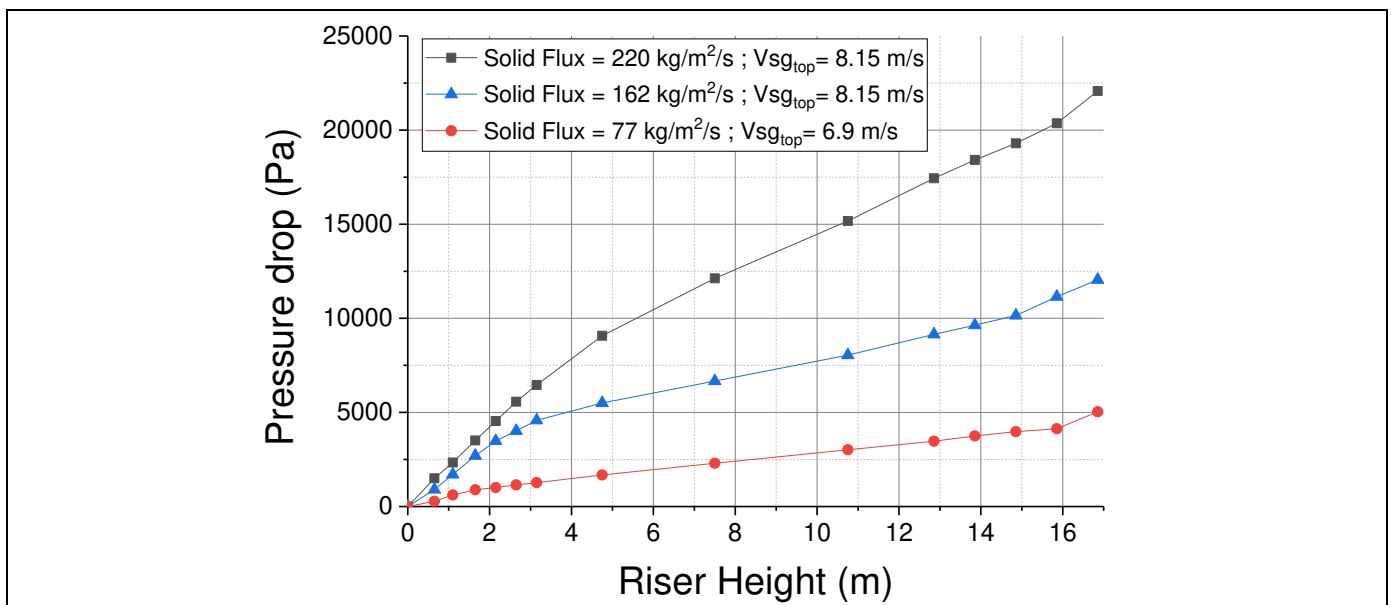


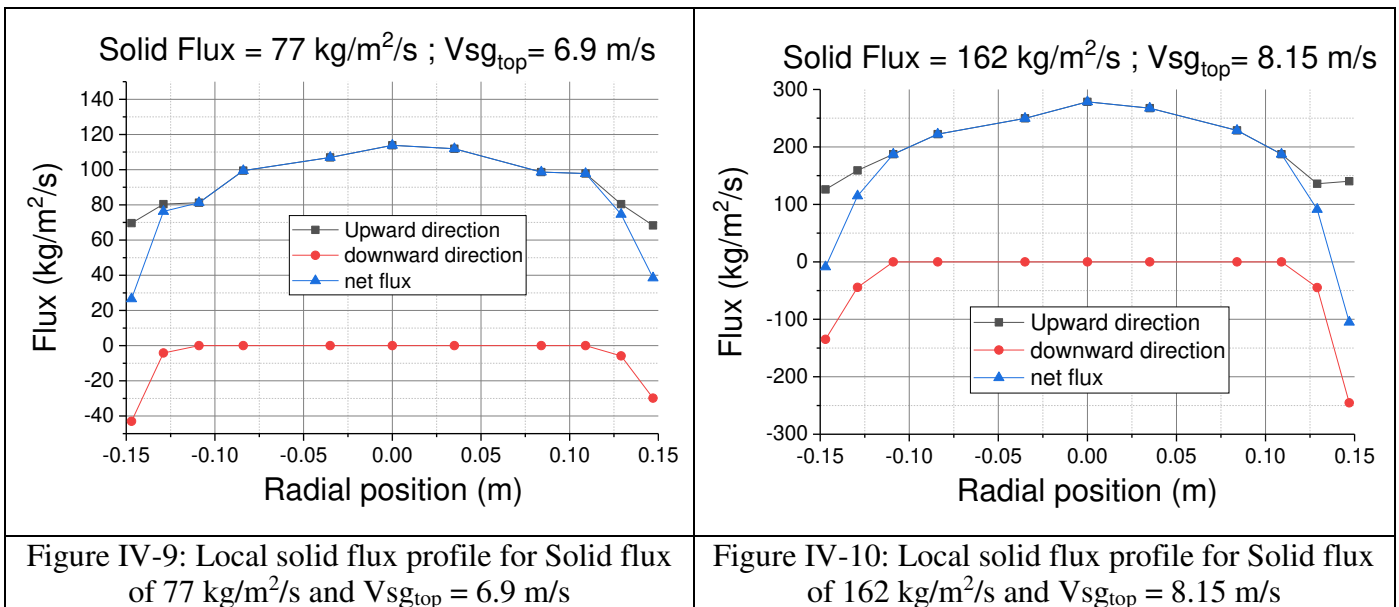
Figure IV-8: Riser pressure drop profile for the three operating conditions tested

Different remarks can be pointed out:

- First, the riser pressure drop increases with the solid flux which was expected.
- As mentioned in the literature review, each profile can be split into three zones:
 - o The particles acceleration zone with an important pressure drop increase. The pressure drop for particles acceleration increases with the solid flux. It takes also a longer riser height for particles acceleration, from 0 to around 2 meters for the solid flux of 77 kg/m²/s, from 0 to around 3 meters for the solid flux of 162 kg/m²/s and from 0 to around 5 meters for the solid flux of 220 kg/m²/s.
 - o The second zone corresponds to a linear pressure drop increase with height where the particles seem to be fully accelerated due to the linear pressure gradient obtained.
 - o Finally, the last zone at the top of the riser with the effect of the riser termination with an increase of the pressure drop. This zone is located at a height of 15 to 16 meters.

The global hydrodynamic in the riser is also different from the turbulent fluidized bed hydrodynamic. The flow is indeed more dilute with low solid volume fraction in the range of 0.1 at the riser bottom to 0.01 in the riser developed region while the fluidized bed exhibited solid volume fraction in the range of 0.4 to 0.5.

Figure IV-9, Figure IV-10 and Figure IV-11 present the local flux profiles measured for a solid flux of respectively 77 kg/m²/s, 162 kg/m²/s and 220 kg/m²/s. Tests were not repeated therefore no error bars are indicated. The black and red curves correspond to measurements of the upward and downward fluxes. The blue curve corresponds to the net flux which is the difference between the black and red curves.



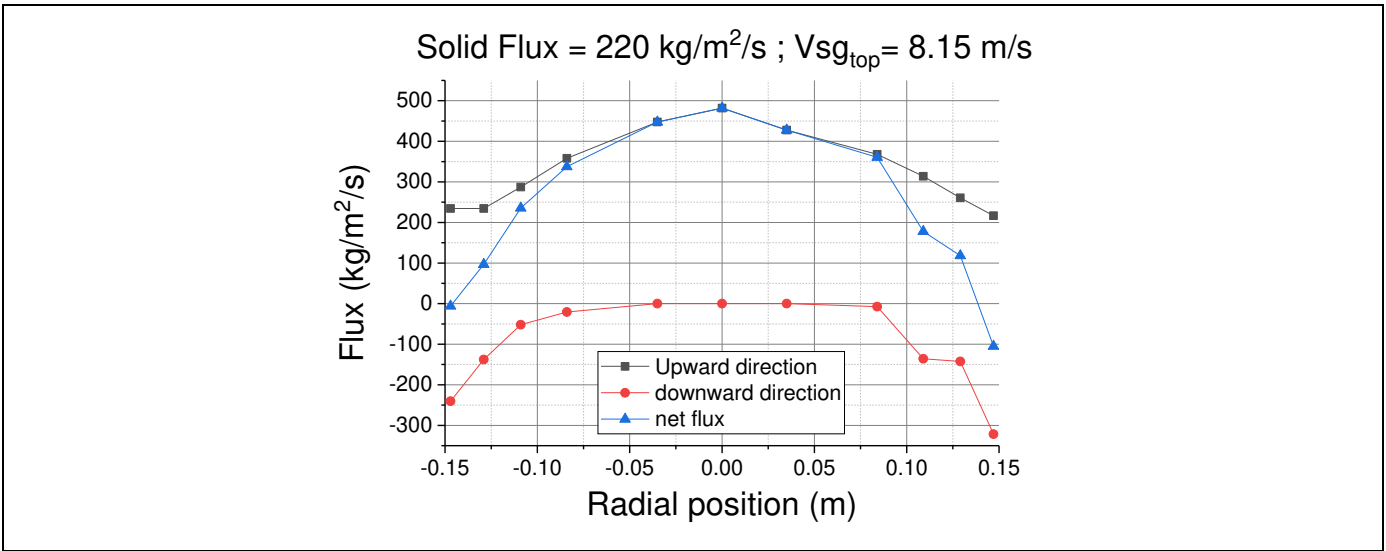


Figure IV-11: Local solid flux profile for Solid flux of 220 kg/m²/s and Vsg_{top} = 8.15 m/s

Different remarks can be pointed out regarding the core annulus type of flow obtained:

- First all net flux profiles obtained are symmetrical. Therefore even if only one profile in one direction was measured, one can make the hypothesis of a symmetrical profile with respect to the riser axis and then calculate the total flux by integrating the profiles over the riser surface. The measurement of other profiles in other directions could be carried out in a future work to check this hypothesis.
- There is a clear core annulus structure, already reported in the literature [66,67], with upward flow only in the center, and both upward and downward flow close to the wall.
- When the solid mass flux increases, the annulus size seems to increase as well as the absolute downward fluxes.

Table IV-3 presents the comparison of the total solid mass fluxes circulating in the riser based on valve calibration and based on local fluxes profiles integration.

Table IV-3 : Comparison of total solid fluxes from valve calibration and local fluxes profiles integration

Solid flux from valve calibration (kg/m ² /s)	77	162	220
Solid From local flux profile integration (kg/m ² /s)	74	154	208
Relative error (%)	3.9	4.9	5.5

One can notice that for all three cases, the total fluxes from valve calibration and profiles integration are close with a relative error lower than 6%. This result is satisfying since the local riser hydrodynamic characterization is in accordance with the macro scale measurement from the valve calibration.

Finally, it is important to mention that similar experimental results with the effect of solid circulation on the riser pressure drop and local fluxes were obtained by Issangya et al. [155].

4.2 Conclusions

The experiments presented in this section allowed characterizing the riser hydrodynamic for different solid circulation rate at a similar superficial gas velocity with both local and global measurements. One could notice the important differences compared to the fluidized bed experiments with a more dilute flow where all particles are entrained and are circulating. Then, the pressure profiles obtained allowed the differentiation of axial physical phenomena with the particles acceleration region at the riser bottom and the fully developed region in the upper part. On the other side the local flux profiles measurements allowed the characterization of radial structures with the core annulus flow. In future work, one could investigate the effect of the superficial gas velocity in order to complete the characterization map of the transport regime. However the data collected can already be used to assess the CFD predictions for such regime which is the aim of the simulation strategy step n°4.

5 Conclusions on the experimental results

This chapter presented all experimental results collected in order to develop our simulation strategy. Both local and global characterizations were investigated allowing the experimental demonstration of gas distribution effects, scale effects between the 20 cm and 90 cm fluidized beds with different bed volume fraction for a similar fluidization velocity, allowing also the experimental demonstration of fluidization regime effects with the important hydrodynamic differences obtained between the turbulent bed and riser experiments. One could appreciate the complexity of the experimental procedure and how results rely on calibrations and signal post-processing hypothesis. It is therefore important to check the consistency of experimental results. In this study, satisfactory results were obtained by comparing the integrated profiles of local voidages in the turbulent bed with the average voidage deduced from global pressure drop measurements. In the riser, the integrated local solid mass flux profiles were consistent with the global solid circulation in the CFB loop. It is finally important to mention that experiments results found are globally in accordance with the literature.

The experimental results collected represent a complete set of data for the investigation of CFD prediction for scale and operating conditions extrapolation. Results of these experiments simulations carried out with the two CFD approaches are presented in the next chapter to evaluate the reliability of their predictions in a context of extrapolation.

V. USE OF CFD FOR EXTRAPOLATION SIMULATION RESULTS

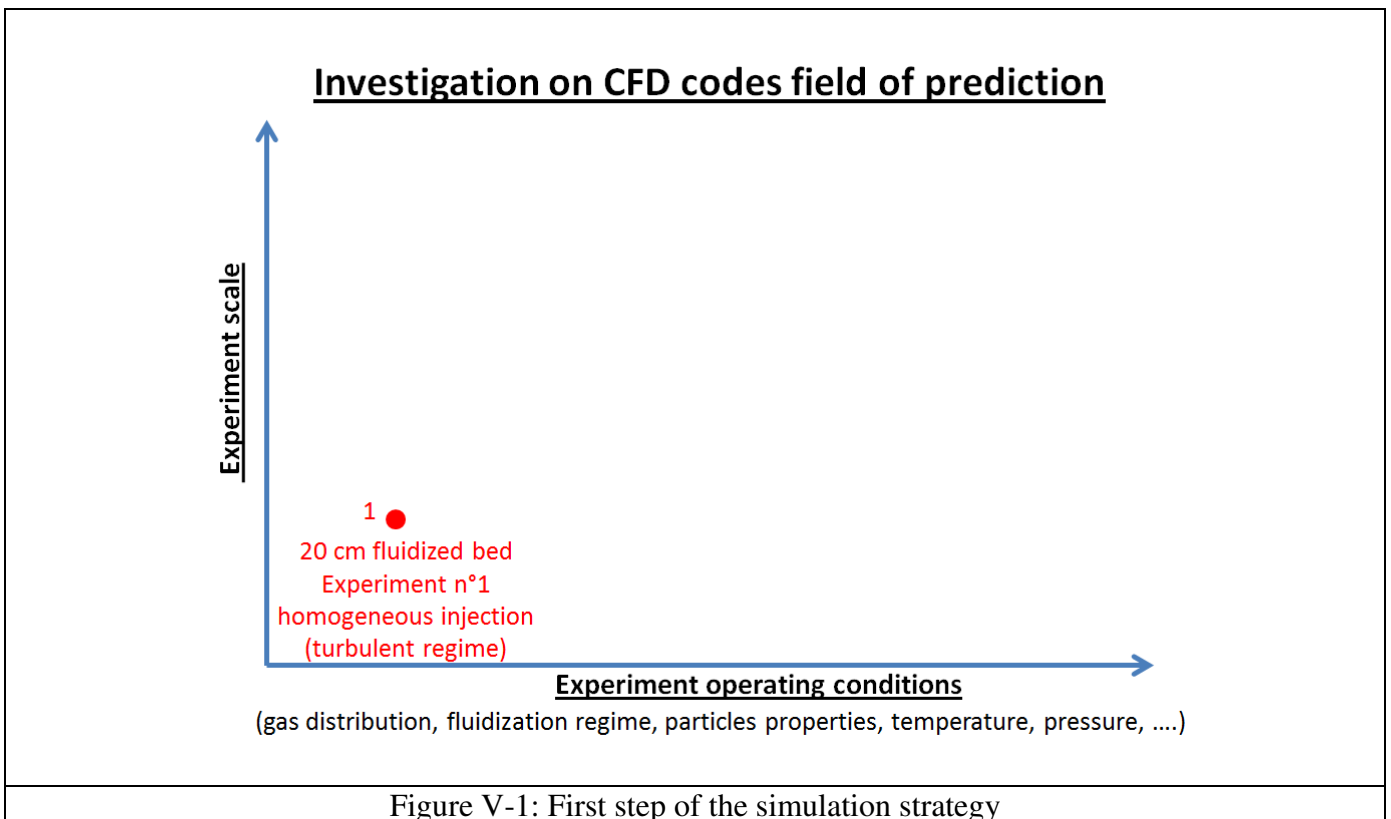
1 Introduction

We have conducted experiments in fluidized beds and circulating fluidized beds at different size and in different operating conditions to collect global and local experimental data. These data will now be used to challenge CFD capabilities according to the strategy presented before. Each step of the simulation strategy is presented in a dedicated chapter.

It is important to remind that all simulations carried out in this investigation are transient and three dimensional; the results presented are averaged once the simulation is considered at steady state. The definition of the steady state is presented for each type of simulation. As a reminder all CFD code parameters that are not investigated (turbulence models, particles interactions models, wall boundary conditions) and that are common to all simulations have already been presented and can be found in Table III-13 and Table III-14 for respectively OpenFOAM and Barracuda VR[®].

2 First simulation strategy step: investigation on the CFD models parameters

As indicated in Figure V-1, the first step of the simulation strategy consists in investigating CFD models parameters using the 20 cm fluidized bed experiment n°1 with a homogeneous injection. For this purpose, we studied the influence of the drag models and simulations boundary conditions in order to best match the experimental results available.

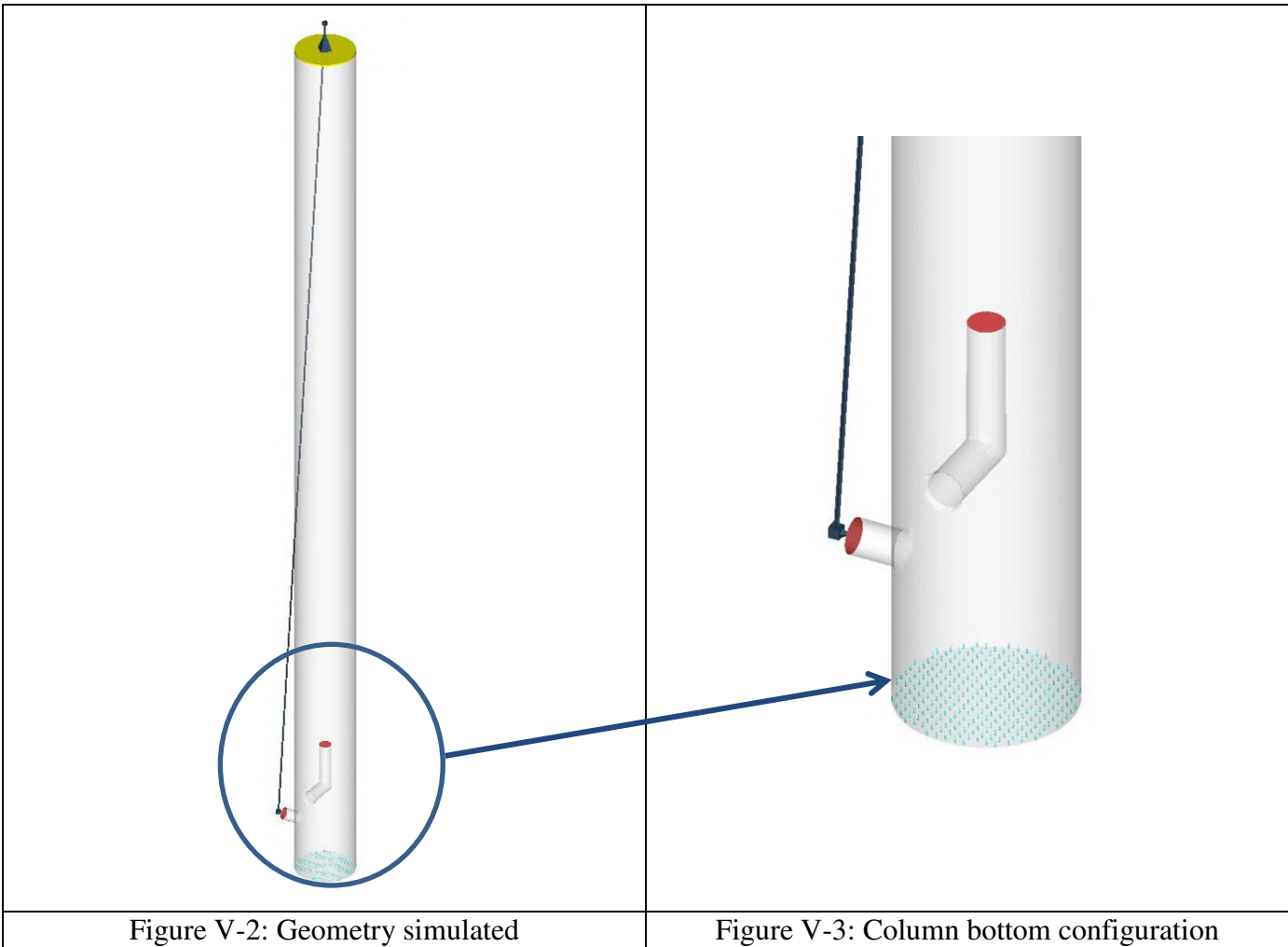


For all simulations carried out, the steady state was considered once the particle entrainment rate at the top of the bed and the bed pressure profile reached steady state values. For the 20 cm fluidized bed simulations, steady state happens at around 6 seconds of simulation time, results presented are then averaged from 6 to 20 seconds of simulation time. The MP-PIC approach was investigated first followed by the Euler/Euler with KTGF approach. Results showing the steady state determination and the influence on the average period can be found in Appendix 9.

For the investigation on each approach, the simulation strategy was first, to choose a mesh cell size of 6 mm to investigate different parameters (drag model and boundary conditions) in order to best match the experimental results and then to investigate the cell size effect by reducing and enlarging the mesh cell size in order to study the results mesh dependency. Indeed, it is important to remind that for large scale simulations, a large cell size will have to be used (see Chapter I.5.2), it is therefore necessary to investigate the effect of using large cells.

2.1 MP-PIC approach, Barracuda VR®

Figure V-2 and Figure V-3 presents respectively the column geometry simulated and the bottom column configuration.



The column height considered is three meters which correspond to the height before the restriction shown in Figure III-3. The piping above this height, the cyclone and cyclone dipleg are not taken into account in the simulation.

The boundary conditions imposed are:

- Bottom porous plate gas injection: injections points where gas mass flowrate and velocity are imposed for each injection point. As shown in Figure V-3 the injection points repartition is uniform with a spacing of 5 mm between each injection in order to insure that there is at least one injection per mesh cell. The injection point gas velocity is imposed at a value given by Equation 85:

$V_{injection} = \frac{U_{superficial\ gas\ bottom}}{\alpha_{bed}} = 1.5\ m/s$	Equation 85
--	-------------

Where $V_{superficial\ gas\ bottom}$ is the superficial gas velocity calculated from experimental data considering the gas bottom mass flowrate and the gas density with the pressure at the column bottom. α_{bed} is the bed averaged solid volume fraction equals to 0.4.

- Top outlet: A pressure value is imposed at 6kPag corresponding to the experiment measurement.
- Dipleg return:
 - o Solid Phase: Barracuda VR[®] allows connecting the top outlet boundary condition to the dipleg return as shown in Figure V-2. In this way, the particle clouds escaping at the top outlet at a certain time step are re-injected through the dipleg return at the next time step resulting in a constant particles mass in the simulation.
 - o Gas phase: the gas phase mass flowrate is imposed dynamically according to the particle phase mass flowrate with the following expression:

$Q_g = Q_{particle\ phase} \left(\frac{1}{\rho_{dipleg}} - \frac{1}{\rho_{particle}} \right) \rho_g$	Equation 86
---	-------------

Where:

- Q_g is the imposed gas mass flowrate (kg/s)
- $Q_{particle\ phase}$ is the mass flowrate of particles re-injected through the dipleg (kg/s)
- ρ_{dipleg} is the cyclone dipleg density taken at 600 kg/m³
- $\rho_{particle}$ is the particle density equals to 1 260 kg/m³
- ρ_g gas density at dipleg return conditions (kg/m³)

- jet injection inlet: wall boundary conditions since no gas is injected through the jet for experiment n°1.

One can wonder about the choice regarding the bottom gas injection condition with injections points instead of a uniform mass flowrate condition. The reason of this choice is to have the possibility of imposing a non-uniform gas profile at the bottom which was proven necessary as explained below.

The drag law model used was the default Barracuda VR[®] Wen-Yu/Ergun model presented in Equation 59 (see Chapter II.2.4). Different remarks can be pointed out when comparing the Barracuda VR[®] model compared to the classic Wen-Yu/Ergun or Gidaspow model presented in Table I-4.

- First, the Barracuda VR[®] drag law presents a smooth transition between the Ergun and Wen-Yu models for solid volume fraction between 0.75 $\alpha_{s,max}$ and 0.85 $\alpha_{s,max}$

- Second, the transition between the Ergun and Wen-Yu models occurs at higher solid volume fraction values for the Barracuda VR[®] drag law. Indeed, for the classic drag model the transition occurs at a solid volume fraction of 0.2 while with the Barracuda VR[®] model the transition starts at a solid volume fraction of 0.53 and finishes at a solid volume fraction of 0.47.

Three different simulations were carried out in order to determine the Barracuda VR[®] code parameters to best match the experimental results, all simulations parameters are presented in Table V-1. The development of these three simulations is presented below.

Table V-1 : 20 cm fluidized bed experiment n°1 homogeneous gas injection, simulations parameters

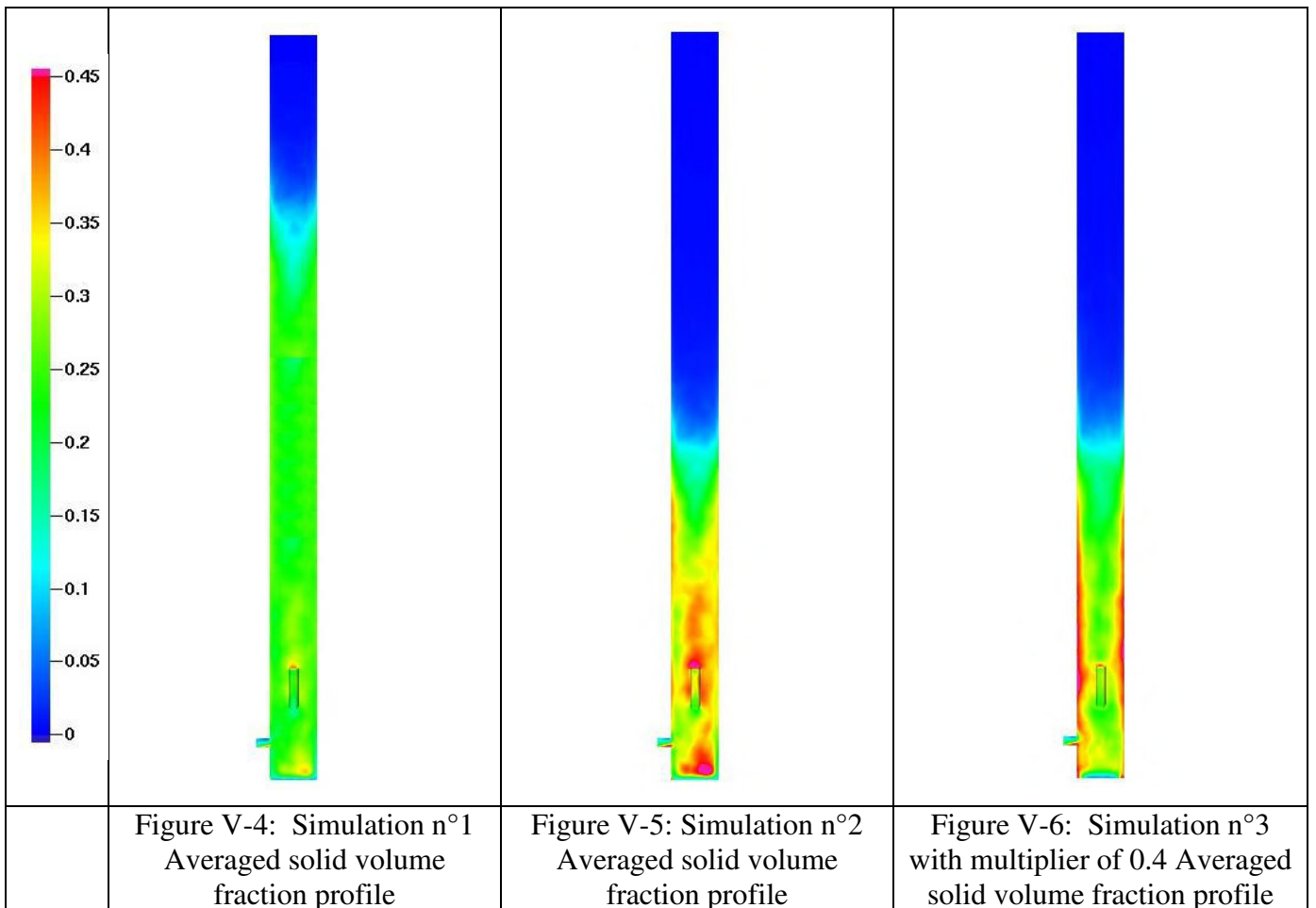
	Simulation n°1	Simulation n°2	Simulation n°3
Mesh size	470 000 hexahedral cells		
Cell size	6 mm		
Particle Size Distribution	From Figure III-2		
Particle density (kg/m ³)	1 260		
Pressure at top boundary condition (kPa g)	6 kPag		
Bottom gas flowrate injected through injection points (kg/s)	0.0238		
Air temperature (°C)	20		
Bed mass (kg)	17		
Averaged Number of Particles per Cloud	41 10 ³		
Number of clouds	8.64 10 ⁶		
Simulation time step (s)	in the order of 1.10 ⁻⁴		
Simulation time (s)	20		
Gas repartition through the injection points	Uniform	Uniform	Reduced close to the wall (see Figure V-10)
Drag Law model	Barracuda VR [®] Wen-Yu/Ergun	Barracuda VR [®] Wen-Yu/Ergun with multiplier of 0.4	Barracuda VR [®] Wen-Yu/Ergun with multiplier of 0.4 and 0.6

The mesh is composed of 470 000 hexahedral cells with a size of 6 mm, one can refer to Appendix 7 for a mesh visualization.

The comparison of the bed density and particle entrainment between experiment/PSRI model and the simulations are shown in Table V-2 for all simulations. Then, Figure V-4, Figure V-5, and Figure V-6 present the bed averaged volume fraction profile for respectively simulation n°1, simulation n°2 and simulation n°3 with the multiplier of 0.4.

Table V-2 : Bed density and Particle entrainments from experiment and Barracuda VR® simulations

Bed density (kg/m ³)				
Experimental	Simulation n°1 with default parameters	Simulation n°2 with drag law multiplier of 0.4	Simulation n°3 with drag coefficient multiplier + bottom boundary condition modified	
			Multiplier of 0.4	Multiplier of 0.6
504	295	517	513	461
Relative error	42%	2.6 %	1.8%	8.5%
Particle entrainment (kg/s)				
PSRI model	Simulation n°1 with default parameters	Simulation n°2 with drag law multiplier	Simulation n°3 with drag coefficient multiplier + bottom boundary condition modified	
			Multiplier of 0.4	Multiplier of 0.6
0.07	0.6	0.06	0.05	0.04



One can see from the table and figures above that simulation n°3 with the multiplier of 0.4 predicts better the experimental/PSRI model results. The investigation which led to these results is presented in detailed below with also the comparison of experimental and simulation local solid volume fraction profiles. The first simulation uses Barracuda VR® default parameters with a homogeneous bottom gas injection with the same amount of gas injected through all injection points. Figure V-7 presents the comparison between experimental and simulation solid volume fraction profile in the North-South direction. The profile in the other West-Est direction can be found in Appendix 7. The predicted bed density and entrainment rate are presented in Table V-2. Finally, Figure V-4 presents the simulation average solid volume fraction in a plane crossing the column center.

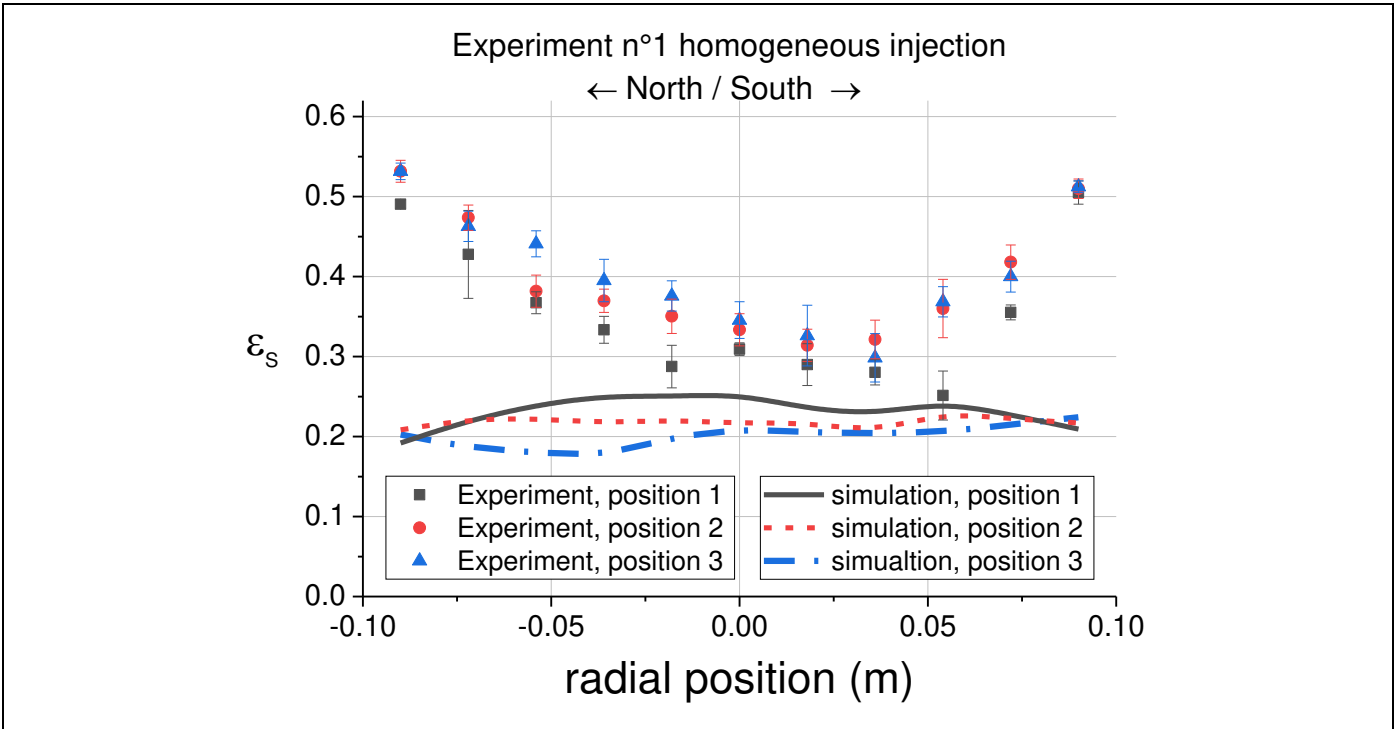


Figure V-7: Simulation n°1 Barracuda VR®, default parameters, Comparisons of solid volume fraction profiles in the North South direction, experiment n°1 homogeneous injection

One can clearly conclude that simulation n°1 underestimates the solid volume fraction in the bed, with the overall bed density underestimated by 42% compared to the experiment and with flat solid volume fraction profiles with values around 0.2. Moreover, as presented in Table V-2, the predicted entrainment rate is almost 10 times higher than the PSRI model value. The results of simulation n°1 show similar result compare to the literature where standard drag model overestimates the gas/particles interactions for Group A particles.

In the second simulation, we used a similar approach than Cocco et al. [116] which consists in multiplying the drag law model by a constant multiplier factor between 0 and 1 to reduce the drag overestimation found in simulation n°1. By experience with similar simulations, the multiplier was set at 0.4. The drag correlation is then calculated with Equation 87:

$K_{d_multiplier} = Multiplier * K_{d_DEFAULT}$	Equation 87
---	-------------

- Where:
- $K_{d_multiplier}$ drag coefficient calculated with multiplier
 - $K_{d_DEFAULT}$ Default Wen-Yu/Ergun Barracuda VR® drag law
 - Multiplier equals to 0.4 in simulation n°2

Figure V-8 presents the comparison between experimental and simulation n°2 solid volume fraction profile in the North-South direction. The profile in the other West-Est direction can be found in Appendix 7. The predicted bed density and entrainment rate are presented in Table V-2. Finally, Figure V-5 presents the simulation average solid volume fraction in a plane crossing the column center.

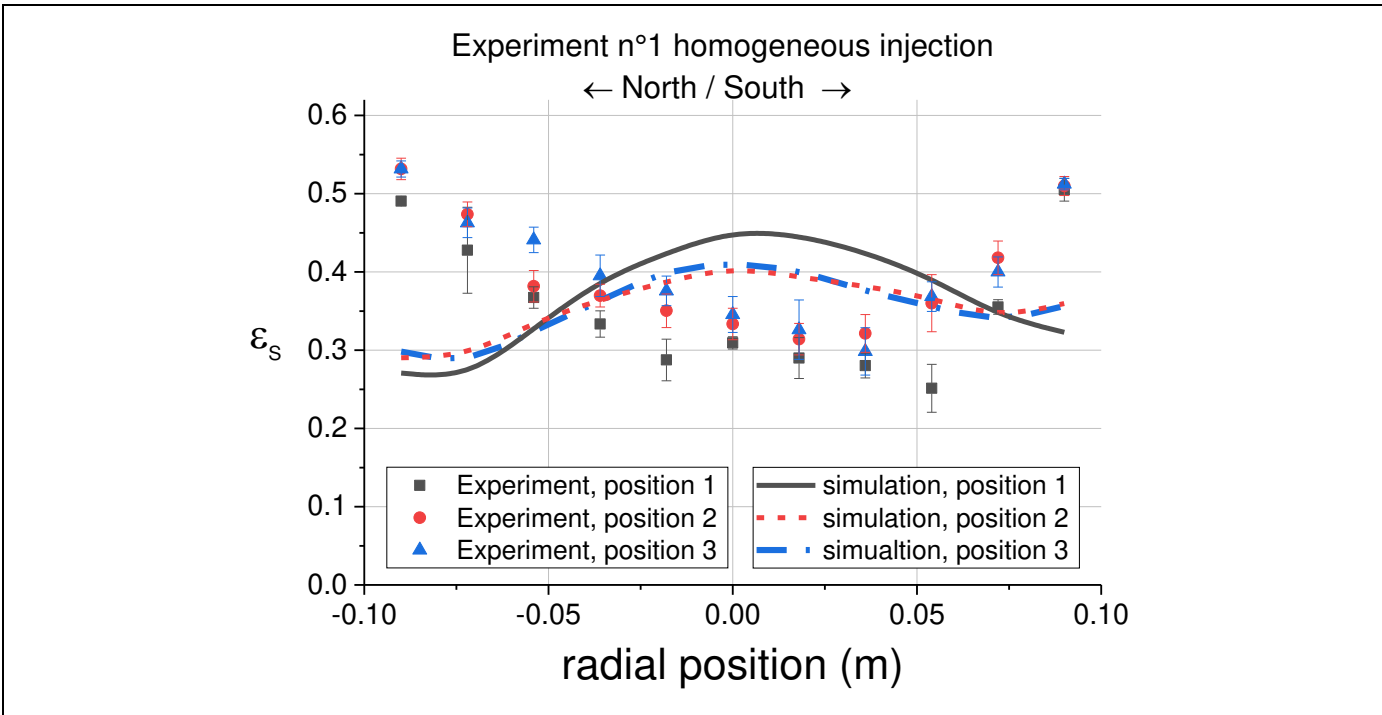


Figure V-8: Simulation n°2 drag modified with multiplier, Comparisons of solid volume fraction profiles in the North South direction, experiment n°1 homogeneous injection

From Table V-2 one can see that the predicted bed density and entrainment are in really good accordance with data from respectively experiments and PSRI model. However, the solid volume fraction profiles are not well predicted with a reverse tendency with lower solid volume fraction close to the wall and higher ones in the center. This profile shape can be explained with the bottom boundary condition effect presented in Figure V-9 which shows the averaged solid volume fraction profile at the column bottom.

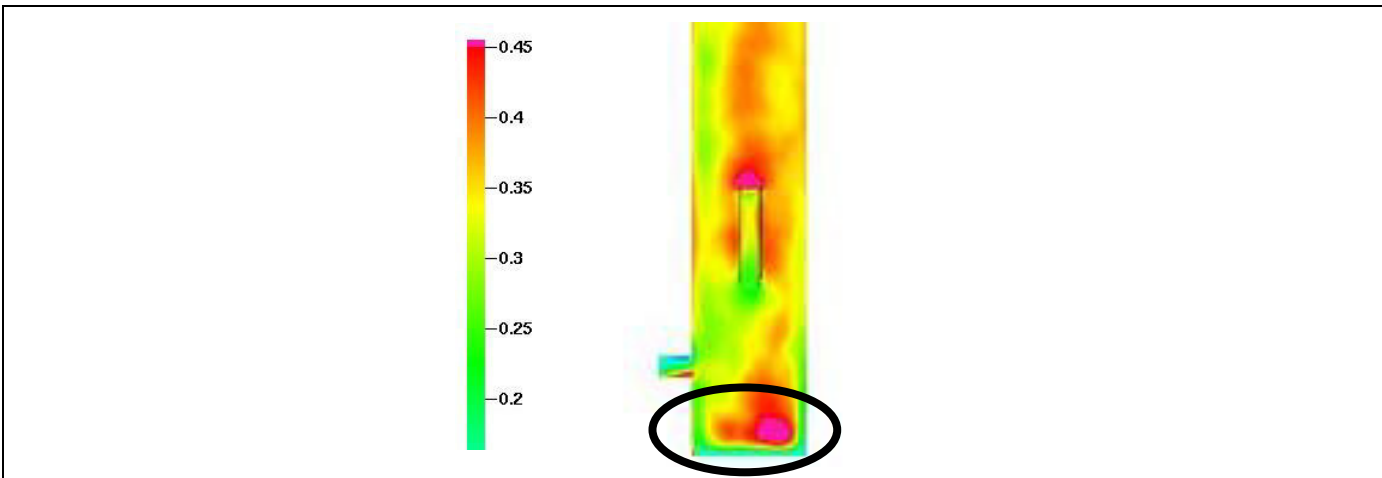


Figure V-9: Simulation n°2 Barracuda VR®, drag modified with multiplier, averaged solid volume fraction profile at the column bottom

One can see from this figure that at the bottom boundary condition the averaged solid volume fraction is lower close to the wall indicating that gas from the boundary condition is mainly flowing close to the walls. This explains the low solid volume fractions observed on the profiles of Figure V-8.

In the simulation n°3, the gas repartition through the bottom injections points was modified in order to inject less gas through the bottom outer ring where low solid volume fraction were observed on Figure V-9. Figure V-10 presents on the left side all the injection points and on the right side the injections points of the outer ring where the gas mass flowrate was reduced. From Figure V-9 the outer ring was defined from a radius of 0.08 m to the radius of the column walls.

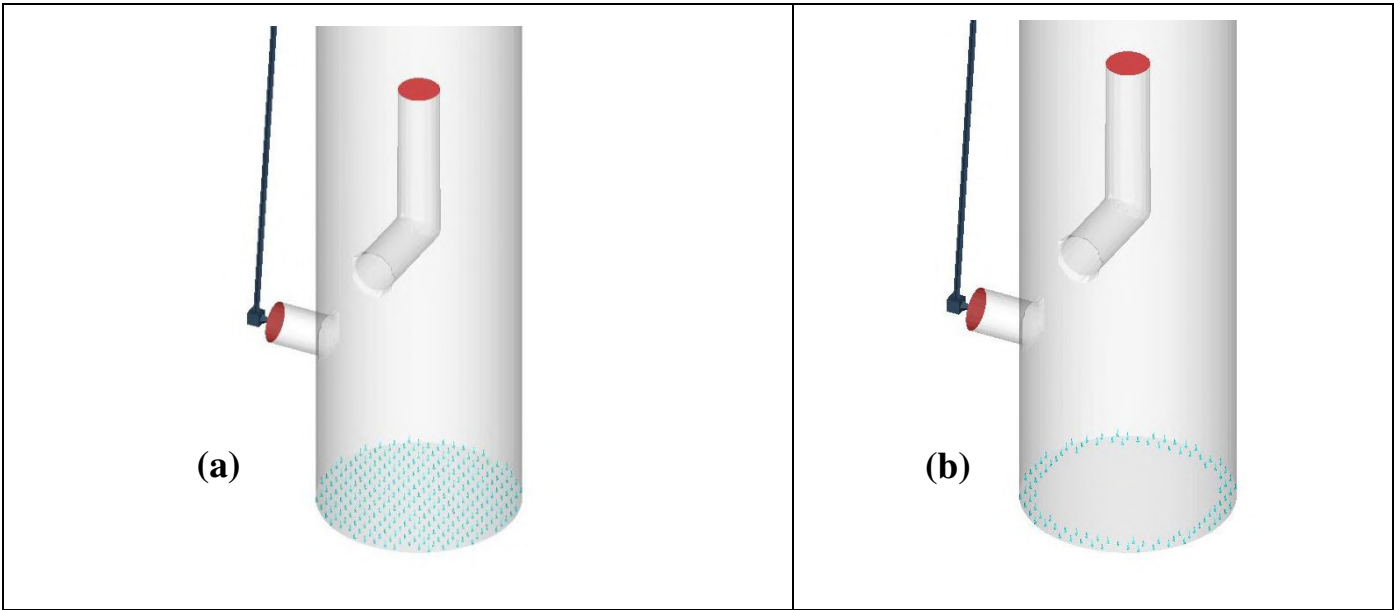


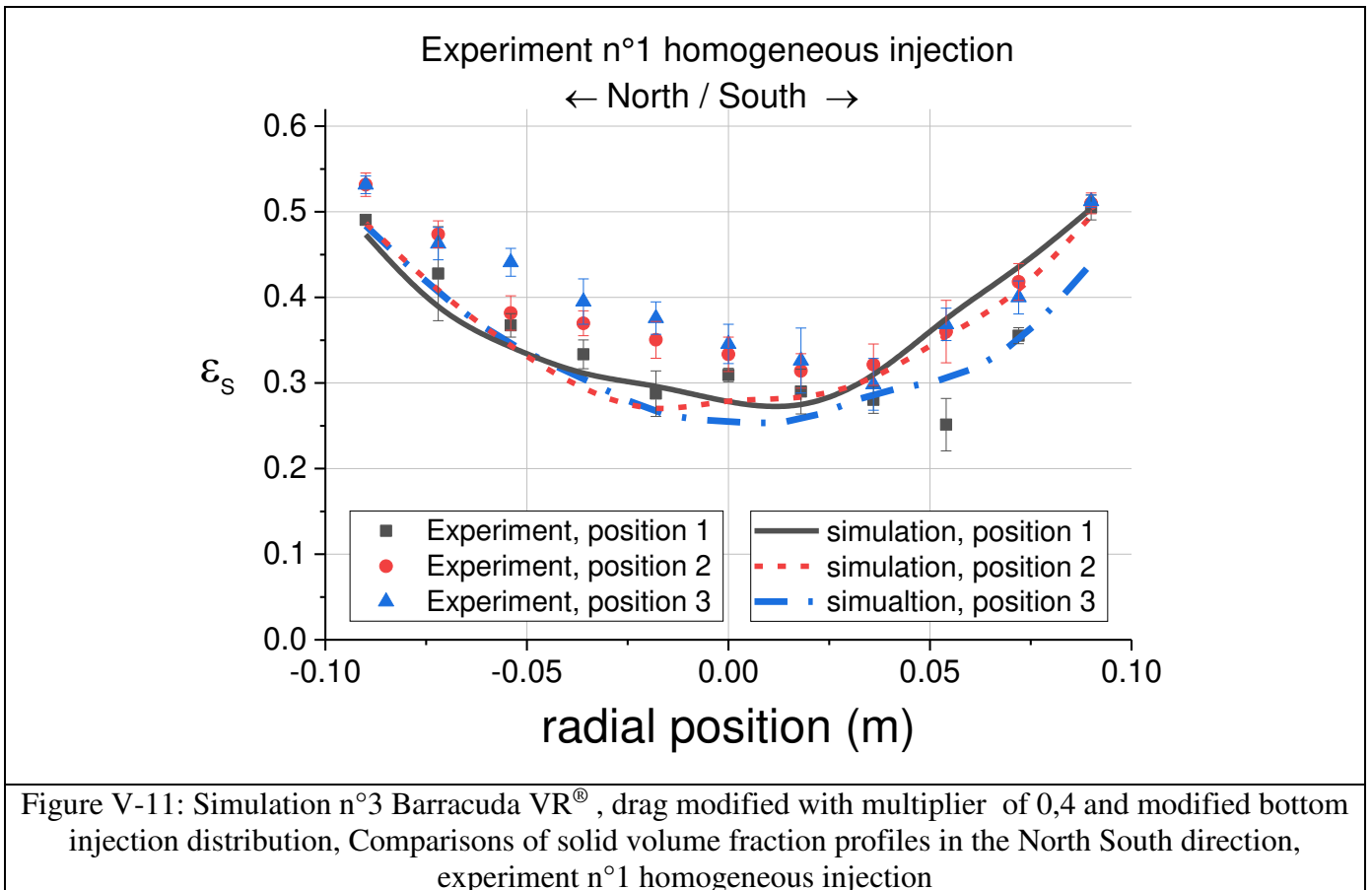
Figure V-10: (a) All bottom injection points, (b) injection points where gas mass flowrate was reduced

Table V-3 presents the difference in gas repartition between the uniform distribution and the distribution with gas reduced on the outer ring.

Table V-3 : Gas repartition among bottom injection points
uniform distribution and reduced gas flowrate on the outer ring distribution

	Uniform distribution	Distribution with gas flowrate reduced on the outer ring
percentage of gas through the outer ring of injection points	30%	5%
Percentage of gas through the rest of the injection points	70%	95%

Figure V-11 and Figure V-12 presents the comparison between experimental and simulation n°3 solid volume fraction profile in respectively the North-South and West-East directions. The predicted bed density and entrainment rate are presented in Table V-2. Finally, Figure V-6 presents the simulation average solid volume fraction in a plane crossing the column center.



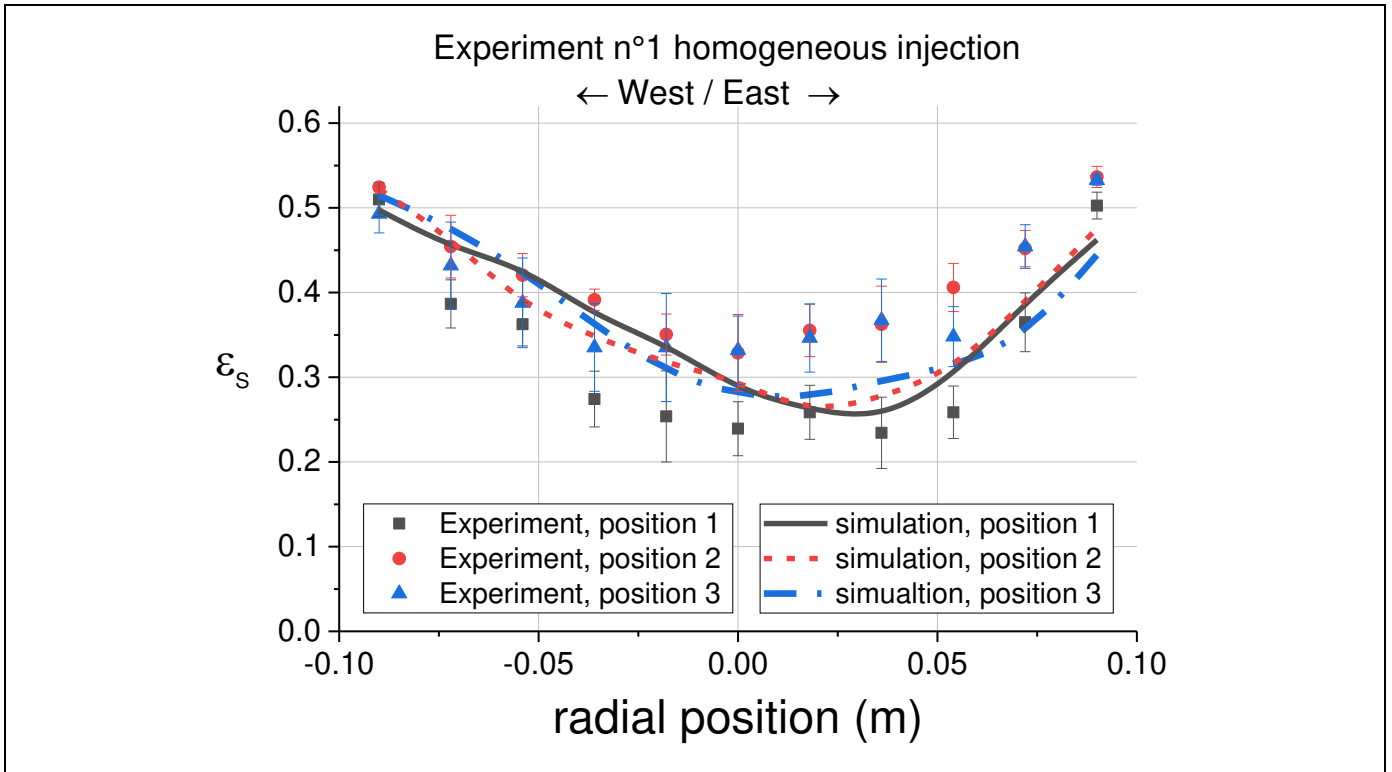


Figure V-12: Simulation n°3 Barracuda VR[®], drag modified with multiplier of 0,4 and modified bottom injection distribution, Comparisons of solid volume fraction profiles in the North South direction, experiment n°1 homogeneous injection

Different remarks can be pointed out regarding the results of simulation n°3:

- First the overall bed density is well predicted with a relative error compared to experiments of 1.8%.
- Second the entrainment predicted is in the range of the PSRI model prediction.
- Third, the solid volume fraction profiles are much better predicted compared to previous simulations. Indeed, the elliptical shape with higher values close to the wall and lower in the center are well captured. Then, in order to have a quantitative comparison between experimental and simulation profiles, the relative error between experiments and simulations was calculated for each experimental profile points according to Equation 88. The relative error obtained for each point was then averaged over all profiles in one direction. Results are presented in Table V-4. The averaged relative errors are around 14% for both directions.

$\text{Relative error for a profile point} = \frac{ \text{Experimental value} - \text{Simulation value} }{\text{Experiment value}}$	Equation 88
---	-------------

Table V-4 : Barracuda VR[®] Simulation n°3 averaged relative errors for profiles points in both directions

	North South direction	West –East Direction
Averaged relative error (%)	13.6	13.8

- Finally, the predicted profiles in the West-East direction tend to shift slightly toward the East direction which can be explained by the jet tube effect as discussed before.

Effect of the drag law multiplier was finally investigated with changing the previous value of 0.4 to 0.6. Comparison between experimental and simulation solid volume fractions profiles can be found in Appendix 7. The predicted bed density and entrainment rate are presented in Table V-2. One can see that the simulation with the 0.6 multiplier does not predict well the bed density compared to the simulation with the 0.4 multiplier and that solid volume fraction profiles shown in Appendix 7 are also underestimated

It is finally interesting to notice that Simulation n°2 and Simulation n°3 predict well the averaged bed density while predicted solid volume fraction profile are totally different with simulation n°2 profiles having the inverse shape compared to experimental values. This point highlights the fact that macro hydrodynamic descriptors like bed density are necessary but not sufficient to fully investigate CFD predictions. Then one can wonder about the bottom gas repartition modification that was implemented to match the experimental results: is it a real physical effect with gas flowing more preferably in the porous plate center due to the bed hydrodynamic or is it a simulation boundary condition artifact? This question is further discussed in Chapter V.2.4 based on additional elements presented afterwards.

To conclude, the parameters of simulation n°3 were considered satisfactory with good predictions of bed density and solid volume fraction profiles and with an entrainment rate in the range of the PSRI model. It was therefore necessary to modify the drag model and adjust the boundary conditions to match reasonably the experimental results. One can then wonder if these modifications have a physical meaning and can then be applied to other simulation conditions or if it is just a tuning effect for this single simulation. This question is investigated in the next simulation strategy steps.

2.2 Euler/Euler with KTGF approach: OpenFOAM

The same investigation presented in the previous chapter was carried out with the Euler/Euler KTGF approach using openFOAM.

The geometry considered was the same as the one taken for Barracuda VR[®] simulations shown in Figure V-2. The mesh cell size was also taken at 6mm with hexahedral cells, the mesh was however generated with a different software (Ansys Workbench meshing) since the mesh used in the Barracuda VR[®] simulations could not be exported to the OpenFOAM format. The total number of cells remains however similar with a difference in cells number lower than 1%.

The same boundary conditions philosophy than the Barracuda VR[®] simulations are applied except for the bottom gas plate gas injection where a uniform gas velocity is applied. Indeed, this difference is due to the fact that with OpenFOAM, it was not necessary to impose a specific gas profile at the bottom to get a good comparison with experimental data. This point is further discussed in Chapter V.2.4. Table V-5 presents the conditions imposed on the different boundaries for the air and particle velocity (U_{air} and $U_{particle}$), for the air and particles volume fraction (α_{air} and $\alpha_{particle}$), for the pressure and the granular temperature (P_{rgh} and $\Theta_{particles}$). It is interesting to point out that OpenFOAM being an open-source code, we actually have access to all the conditions imposed for all the simulation parameters as shown in Table V-5 which is not the case for commercial codes such as Barracuda VR[®].

Table V-5: Boundary conditions types for the gas and solid phases

	U.air	alpha.air	p_rgh
Bottom porous plate gas injection	interstitialInletVelocity;	zeroGradient;	fixedFluxPressure
jet injection inlet	same as walls	same than walls	same than walls
Dipleg return	InletVelocity Value changed dynamically with respect to entrainment rate	fixed value 0.52;	fixedFluxPressure
Top outlet	pressureInletOutlet Velocity	zeroGradient;	prghPressure; p uniform 107 000;
walls	fixedValue; uniform (0 0 0);	zeroGradient;	fixedFluxPressure

	U.particles	alpha.particles	Theta.particles
Bottom porous plate gas injection	fixedValue; uniform (0 0 0);	zeroGradient;	fixedValue; value uniform 1e-4;
jet injection inlet	same than walls	same than walls	same than walls
Dipleg return	InletVelocity Value changed dynamically with respect to entrainment rate	fixed value 0.48;	fixedValue; value uniform 1e-4;
Top outlet	pressureInletVelocity	zeroGradient;	zeroGradient;
walls	JohnsonJacksonParticlesSlip; specularityCoefficient 0.01; value uniform (0 0 0);	zeroGradient;	JohnsonJacksonTheta ; specularityCoefficient 0.01; restitutionCoefficient 0.85;

Different remarks can be point out from Table V-5:

- An “interstitial Inlet Velocity” condition is imposed for the air velocity of the bottom porous plate gas injection. This condition imposes a superficial velocity sets in order to have a superficial velocity at the top of the column of 0.65 m/s.
- For the particles velocity at the top outlet, a “pressure inlet velocity” is imposed in order to prevent particles backflow in the simulation.

Finally, contrary to the MP-PIC approach, the particle size distribution cannot be taken into account with this approach. Therefore, the simulation representative particle diameter was first taken equal to the particle size distribution average diameter dp_{50} of 75 microns as shown in Table III-1.

The same simulation strategy developed for the Barracuda VR[®] simulations was applied as shown in Table V-6, using first the Barracuda VR[®] Wen-Yu/Ergun drag model shown in Equation 59 (see Chapter II.2.4) and second the same drag law with a multiplier of 0.4 as shown in Equation 87.

Table V-6: OpenFOAM simulation n°1 and n°2 parameters

	Simulation n°1	Simulation n°2
Particle representative diameter (microns)	75	
Particle density (kg/m ³)	1 260	
Air temperature (°C)	20	
Bed mass (kg)	17	
Simulation time step (s)	1.10 ⁻⁴	
Simulation time (s)	20	
Drag Law model	Barracuda VR® Wen-Yu/Ergun	Barracuda VR® Wen-Yu/Ergun with multiplier of 0.4

Table V-7 presents simulations bed density and entrainment rate versus experimental and PSRI model values. Figure V-13 and Figure V-14 present the simulation instantaneous and average solid volume fraction profiles in a plane passing through the column center for respectively simulation n°1 and simulation n°2. And finally, Figure V-15 and Figure V-16 presents the comparison between experimental and simulations solid volume fraction profiles for respectively simulation n°1 and simulation n°2 in the North-South direction.

Table V-7 : Bed density and Particle entrainments from experiment and openFOAM simulations n°1 and n°2

Bed density (kg/m³)		
Experimental	Simulation n°1 with default parameters	Simulation n°2 with drag law multiplier of 0.4
504	245	319
Relative error	51%	37%

Particle Entrainment (kg/s)		
PSRI model	Simulation n°1 with default parameters	Simulation n°2 with drag law multiplier of 0.4
0.07	2.2	0.31

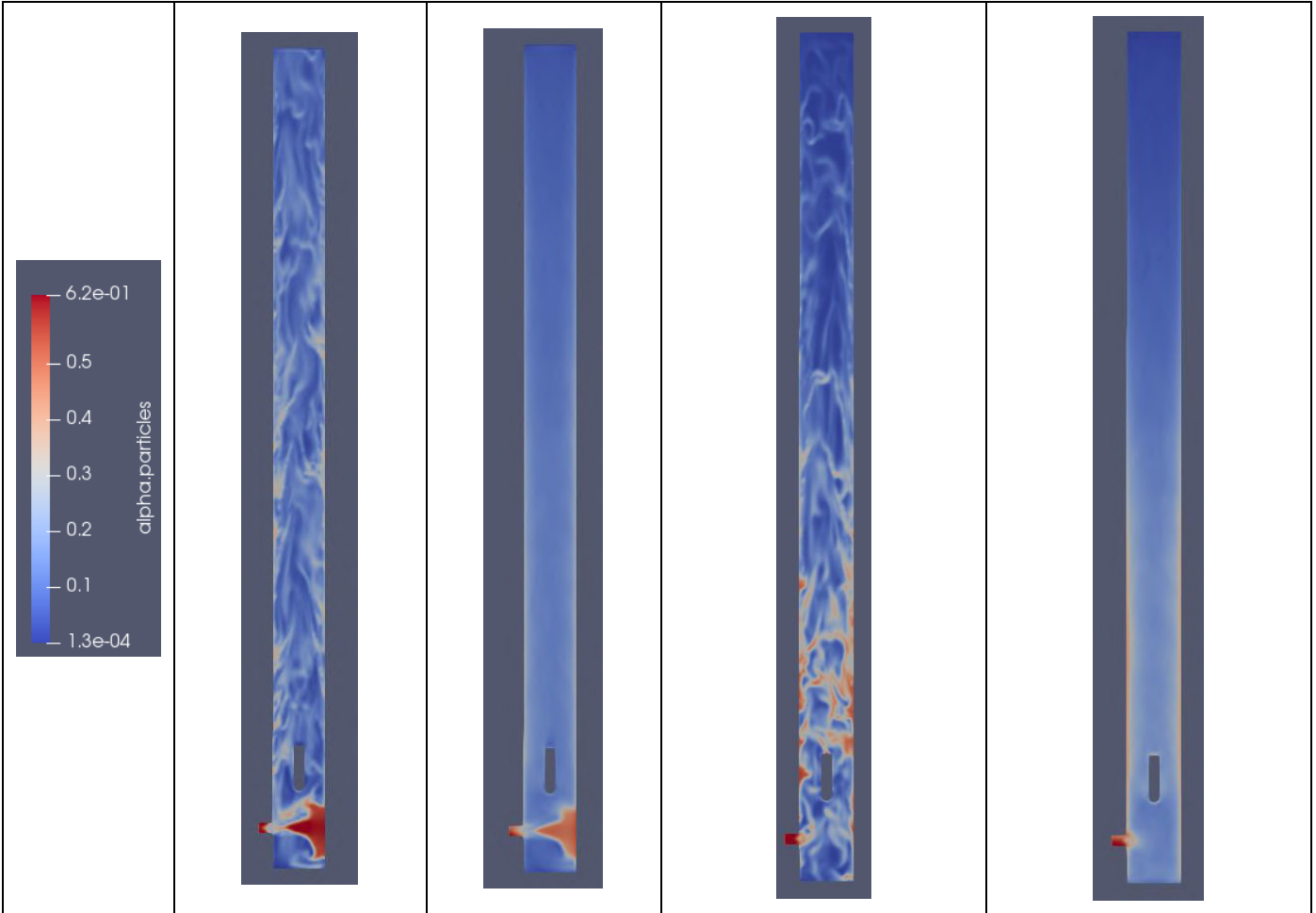


Figure V-13: Simulation n°1 openFOAM, default drag, instantaneous and averaged solid volume fraction profile

Figure V-14: Simulation n°2 openFOAM, default drag with multiplier of 0.4, instantaneous and averaged solid volume fraction profile

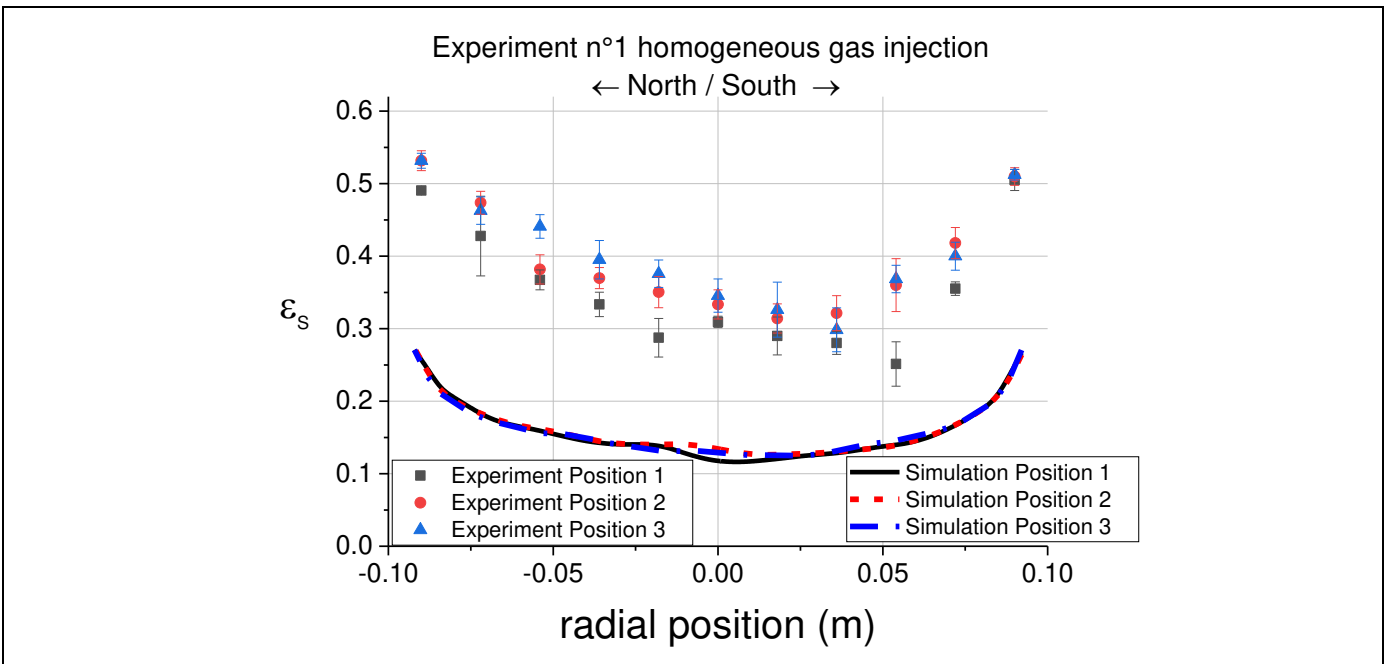


Figure V-15: Simulation n°1 OpenFOAM, default drag, Comparisons of solid volume fraction profiles in the North South direction, experiment n°1 homogeneous injection

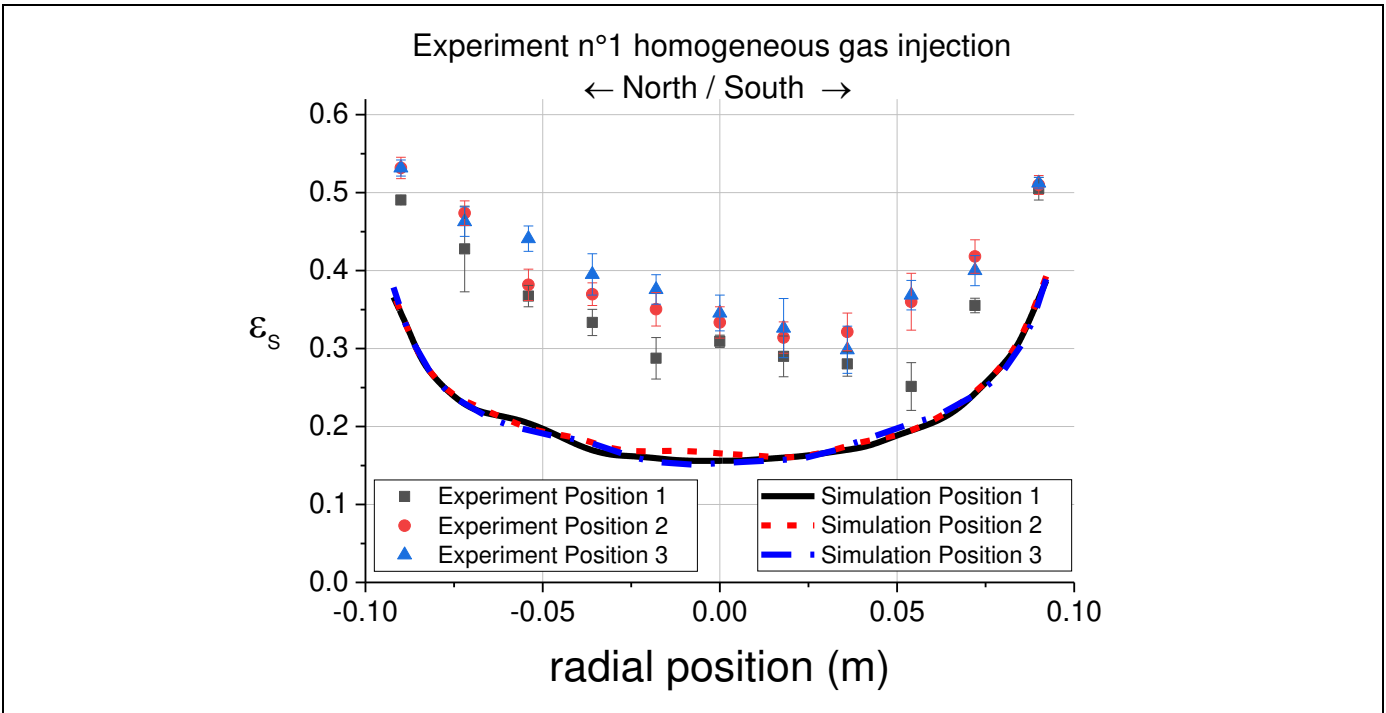


Figure V-16: Simulation n°2 OpenFOAM, default drag with multiplier of 0.4, Comparisons of solid volume fraction profiles in the North South direction, experiment n°1 homogeneous injection

Different remarks can be pointed out:

- First in both simulations, the bed density and the solid volume fraction profiles are clearly underestimated. Then the entrainment rate is overestimated especially for the first simulation where the high entrainment recreate an important solid flux in the cyclone dipleg return which causes a solid accumulation in the bottom of the column as shown in Figure V-15.
- Second, even if solid volume fraction profiles are underestimated, one can see that the profile shape is captured by the simulations with higher values close to the wall and lower value in the column center. Therefore, we concluded that contrary to Barracuda VR[®] simulations, there was no need to modify the bottom gas repartition in order to obtain the correct profile shape. This point raises the questions on why this repartition had to be modified with Barracuda VR[®]. This matter is further discussed in Chapter V.2.4.

The two codes at this stage do not give the same results. With openFOAM, the bottom boundary condition did not have to be modified in order to get an elliptical solid volume fraction profile shape; however the drag modification did not allow having a correct bed density prediction. One can then wonder if this difference is due to the fact that with OpenFOAM only a single representative particle diameter is taken into account. To investigate this issue, we then decided to use a different approach for the openFOAM drag model development with a model based on a more physical basis compared to the more empirical method with multiplier. For this purpose, the drag model developed by Li et al. [10] assuming clustering and equivalent diameters based on the solid volume fraction was used. In such approach, the actual simulation particle diameter is then replaced by alternative diameters trying to represent agglomeration and clustering in the different parts of the bed (as a function of the local solid volume fraction). It should be mentioned that the clustering model used by Li et al. [10] remains simple and correlative compared to more complex model with for example the approach developed by Motlagh

et al. [12] with particles clustering depending on a balance between hydrodynamic and inter-particle forces.

Based on Li et al. [10] work, three different equivalent diameters were defined according to three solid volume fraction classes corresponding to the dense, intermediate and dilute phases as shown in Table V-8. Two different equivalent diameters distribution were investigated in respectively simulation n°3 and simulation n°4. It is important to mention that for these two simulations, the Barracuda VR® Wen-Yu/Ergun drag model was kept, but used with representative particle diameter. As a reminder with this drag correlation the transition between the Wen-Yu and Ergun models occurs at higher solid volume fraction around 0.5 compared to the classic Gidaspow model where the transition occurs at a solid volume fraction of 0.2.

Table V-8 : Equivalent diameters versus solid volume fraction classes for OpenFOAM simulation n°3 and simulation n°4

	Solid Volume fraction	Equivalent diameter	Drag law model
Simulation n°3	dense: 0.62 to 0.08	400	Barracuda VR® Wen-Yu/Ergun model
	intermediate: 0.08to 0.02	150	
	dilute: 0.02 to 0	75	
	Solid Volume fraction	Equivalent diameter	Drag law model
Simulation n°4	dense: 0.62 to 0.08	500	Barracuda VR® Wen-Yu/Ergun model
	intermediate: 0.08to 0.02	150	
	dilute: 0.02 to 0	75	

Concerning the equivalent diameters presented in Table V-8, it is assumed that large clusters are formed for the highest solid volume fraction and that the equivalent diameter is equal to the mean diameter of the particle size distribution for the lowest particle size distribution. These assumptions are further discussed in Chapter IV-3.1.4.

Figure V-17 presents the experimental and simulation solid volume fraction for position n°1 and n°3 in the north-south direction. The other profiles can be found in Appendix 8. Table V-9 presents the simulations bed density and entrainment versus experimental and PSRI model data.

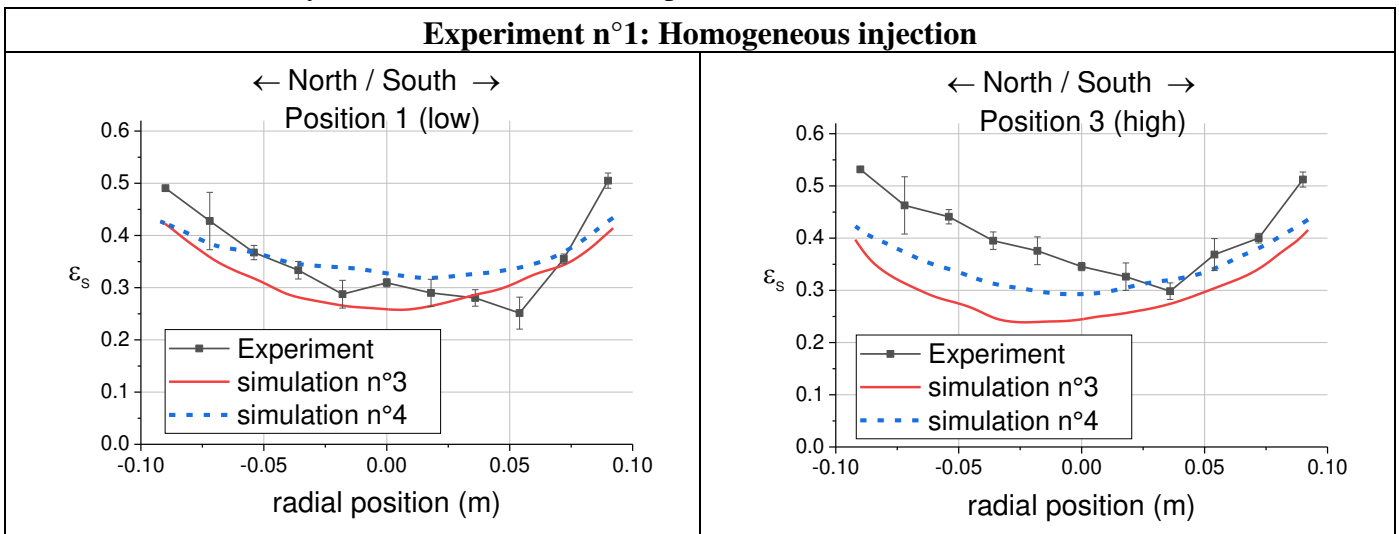


Figure V-17: Simulations n°3 and n°4 openFOAM, default Barracuda VR® drag, solid volume fraction profile at position 1 and 3, Experiment n°1 Homogeneous injection

Table V-9 : Bed density and Particle entrainments from experiment and openFOAM simulations n°3 and n°4

Bed density (kg/m³)		
Experimental	Simulation n°3	Simulation n°4
504	390	425
Relative error	23%	16%
Particle Entrainment (kg/s)		
PSRI model	Simulation n°3	Simulation n°4
0.07	0.42	0.36

One can clearly see that both simulations still underestimate the bed density and solid volume fraction profiles. From these results it was decided to then use the same drag law as Li et al. [10] which consists in a classic Gidaspow model with a transition between the Ergun and Wen-Yu correlation at a solid volume fraction of 0.2. Table V-10 presents the equivalent diameters versus solid volume fraction classes for the five simulations carried out.

Table V-10 : Equivalent diameters versus solid volume fraction classes for OpenFOAM simulation n°5 to simulation n°9

	Solid Volume fraction	Equivalent diameter	Drag law model
simulation n°5	dense: 0.62 to 0.08	400	Gidaspow
	intermediate: 0.08to 0.02	150	
	dilute: 0.02 to 0	75	

	Solid Volume fraction	Equivalent diameter	Drag law model
simulation n°6	dense: 0.62 to 0.08	400	Gidaspow
	intermediate: 0.08to 0.02	300	
	dilute: 0.02 to 0	75	

	Solid Volume fraction	Equivalent diameter	Drag law model
simulation n°7	dense: 0.62 to 0.08	500	Gidaspow
	intermediate: 0.08to 0.02	150	
	dilute: 0.02 to 0	75	

	Solid Volume fraction	Equivalent diameter	Drag law model
simulation n°8	dense: 0.62 to 0.08	500	Gidaspow
	intermediate: 0.08to 0.02	300	
	dilute: 0.02 to 0	75	

	Solid Volume fraction	Equivalent diameter	Drag law model
simulation n°9	dense: 0.62 to 0.08	500	Gidaspow
	intermediate: 0.08to 0.02	150 + drag multiplier of 0.31	
	dilute: 0.02 to 0	75	

Similarly to simulation n°3 and simulation n°4, it is assumed that large clusters are formed for the highest solid volume fraction and that the equivalent diameter is equal to the mean diameter of the particle size distribution for the lowest particle size distribution. Moreover, one can see in simulation n°9 that a drag multiplier of 0.31 is used for the second solid volume fraction class, in this case the drag correlation is calculated according to Equation 87 with the implementation of a multiplier in the drag model. It is important to notice that the value of 0.31 was found after a trial of different coefficient values with the same equivalent diameter of 150 microns. Figure V-18 presents the experimental and simulation solid volume fraction for position n°1 and n°3 in the north-south direction for simulation n°5 and n°9 which presented the most important results difference. The other profiles can be found in Appendix 8. Table V-11 presents the simulations bed density and entrainment versus experimental and PSRI model data.

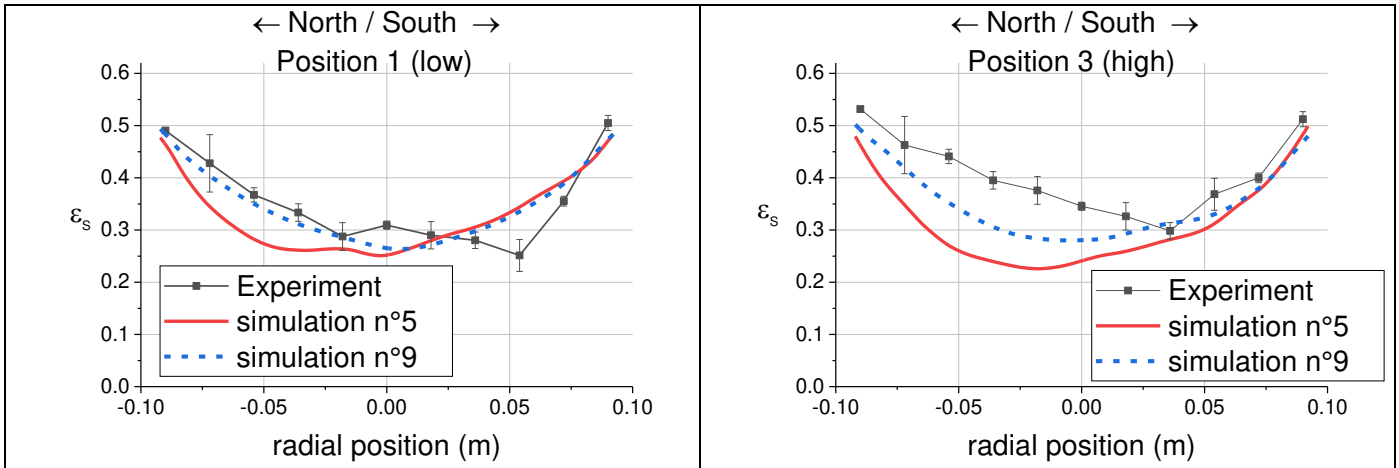


Figure V-18: Simulations n°5 and n°9 openFOAM, Gidaspow drag with clustering approach, solid volume fraction profile at position 1 and 3, Experiment n°1 Homogeneous injection

Table V-11 : Bed density and Particle entrainments from experiment and openFOAM simulations n°5 to n°9

	Bed density (kg/m3)	Relative error	Bed Entrainment (kg/s)
Experimental	504		0.07 (PSRI model)
simulation n°5	435	14%	0.28
simulation n°6	454	10%	0.2
simulation n°7	462	8%	0.29
simulation n°8	468	7%	0.14
simulation n°9	482	4%	0.12

One can see that among all simulations, simulation n°9 predicts better the experimental bed and solid volume fraction profiles with an entrainment rate in the same range than the PSRI model. It is also interesting to focus on the predicted entrainment rates of simulation n°7 and n°8. Indeed, the only difference between the two is the intermediate representative diameter which is 150 microns and 300 microns for respectively simulation n°7 and simulation n°8. The dense and dilute phase representative diameters (500 and 75 microns) remain the same. One can see that the entrainment rate of simulation n°7 is twice higher compared the simulation n°8 showing the influence of the intermediate representative diameter. Moreover when comparing simulation n°6 and n°8 where this time only the dense phase diameter differs with respectively 400 microns and 500 microns, the entrainment rate is higher for simulation n°6 showing the influence of the dense phase diameter on entrainment. These results therefore show that drag through the entire solid volume fraction range influences entrainment. It then interesting to

point out that when predicting better the solid void fraction, the bed entrainment is also better predicted which is promising.

Figure V-19 and Figure V-20 present the simulation n°9 solid volume fraction profiles versus experimental profiles. Table V-12 shows the average relative error of the profiles points in both directions and finally Figure V-21 present an instantaneous and average solid volume fraction profile in a plane passing through the column center.

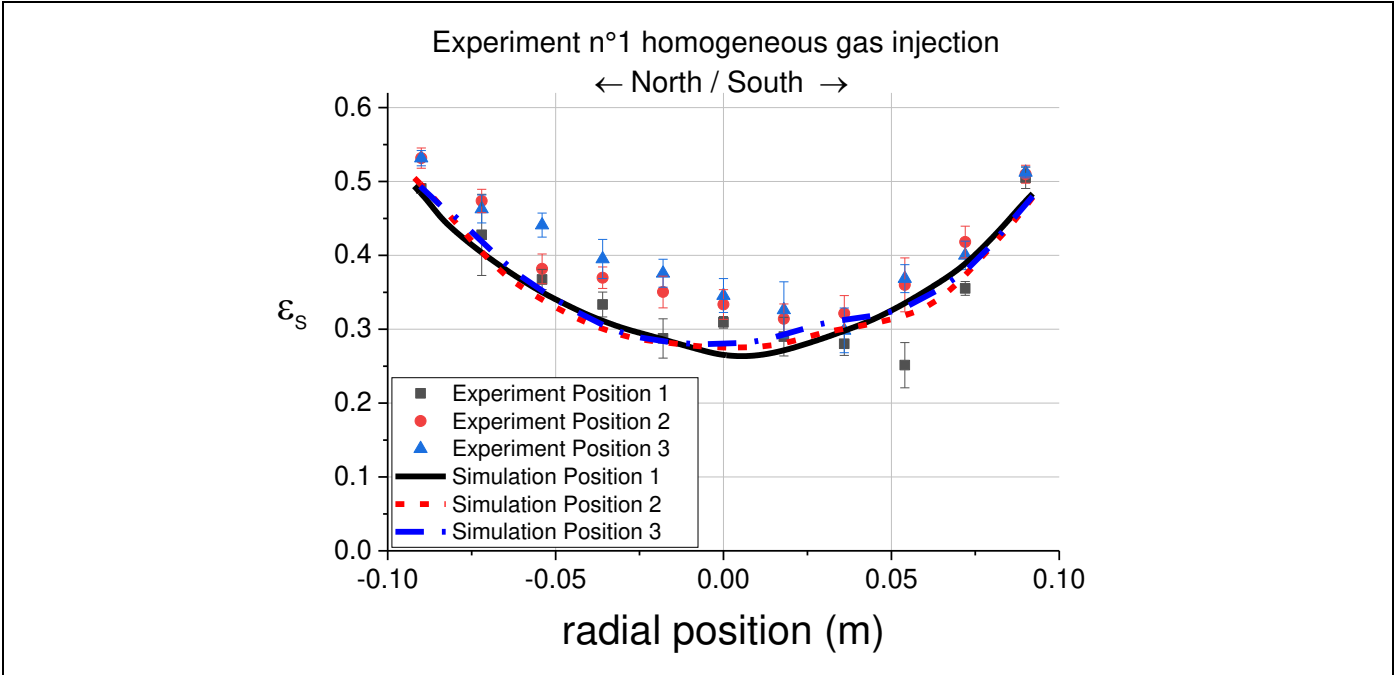


Figure V-19: Simulation n°9 OpenFOAM , Gidaspow drag with clustering approach, Comparisons of solid volume fraction profiles in the North South direction, experiment n°1 homogeneous injection

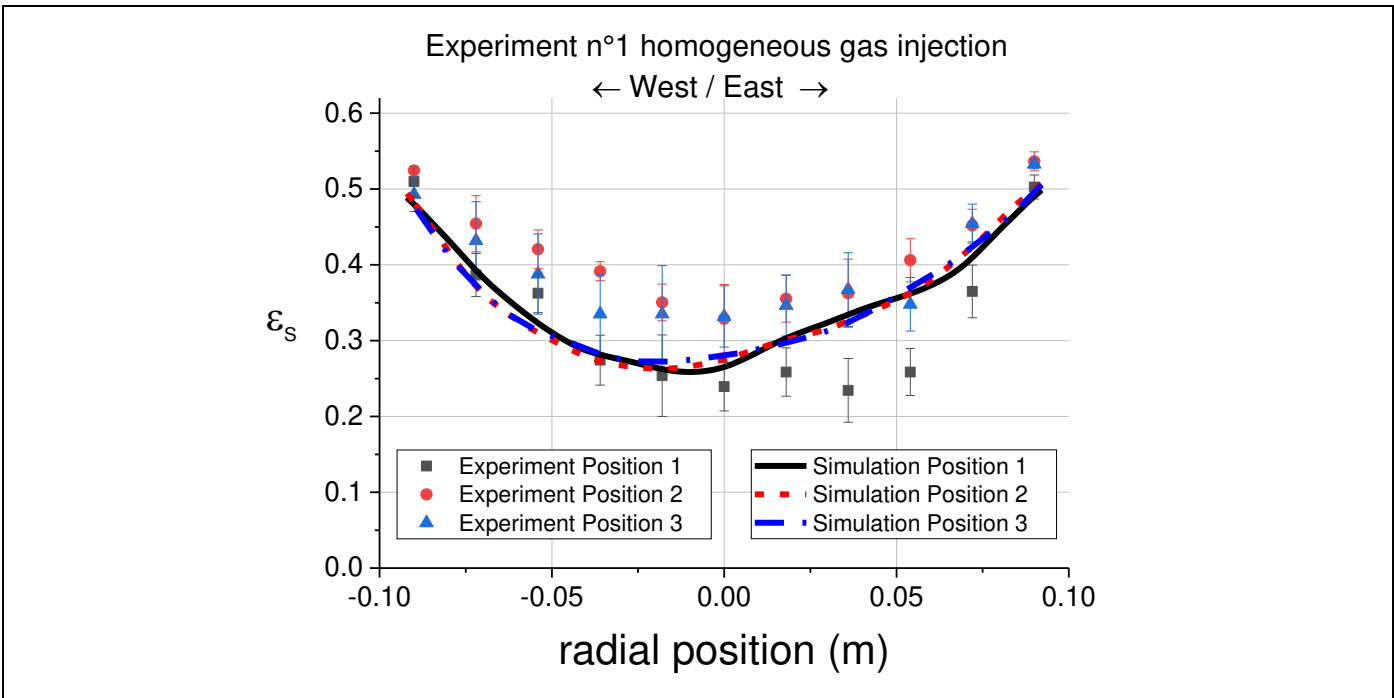


Figure V-20: Simulation n°9 OpenFOAM , Gidaspow drag with clustering approach, Comparisons of solid volume fraction profiles in the North South direction, experiment n°1 homogeneous injection

Table V-12 : OpenFOAM Simulation n°9 averaged relative errors for profiles points in both directions

	North South direction	West –East Direction
Averaged relative error (%)	11.6	14.1

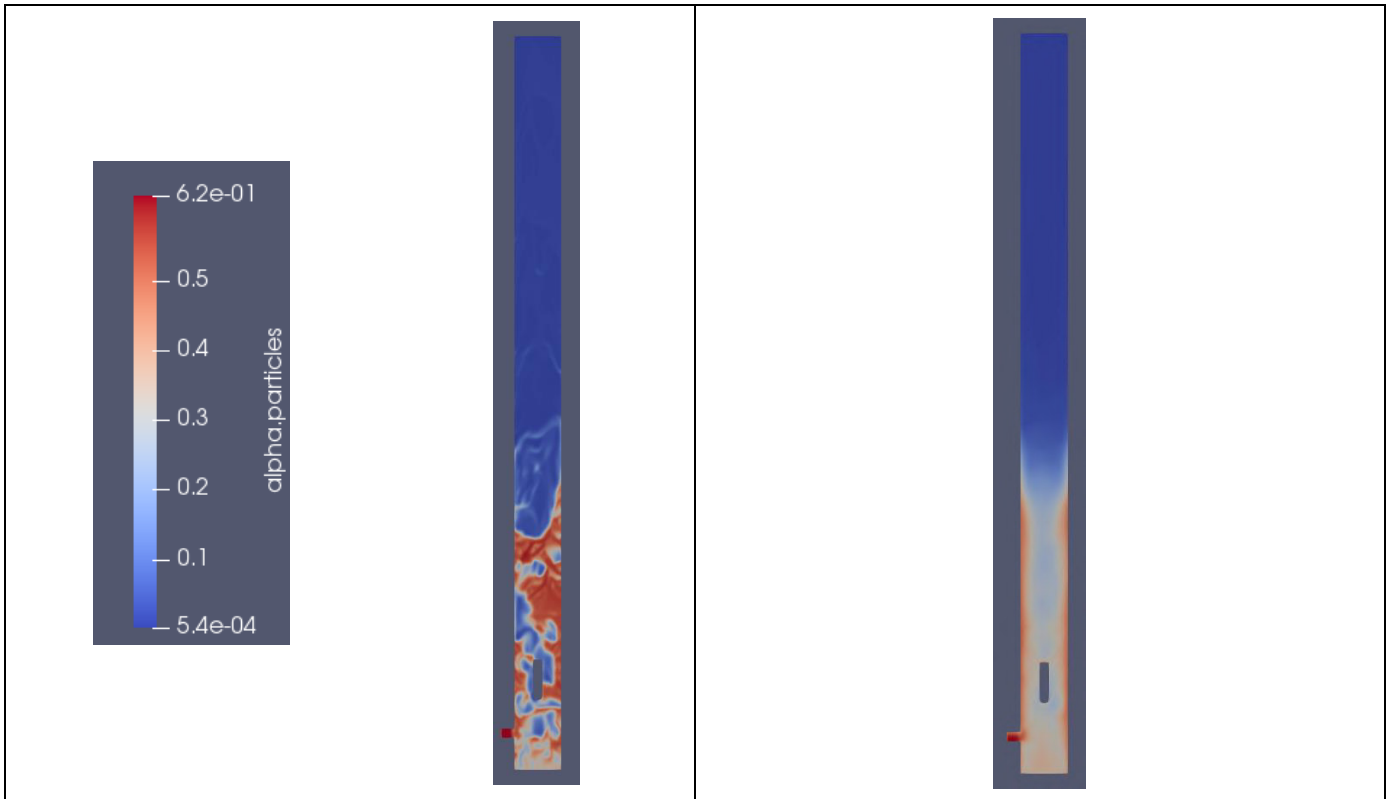


Figure V-21: Simulation n°9 openFOAM, Gidaspow drag with clustering approach, instantaneous and averaged solid volume fraction profile

The results obtained with the simulation n°9 parameters are considered satisfactory since the simulation predicts well the bed density with a relative error compared to the experiment of 4% and the entrainment rate is in the range of PSRI model. Moreover, the averaged relative errors for profiles points in both directions is around 14% which is considered satisfying and it is in the same range than the Barracuda VR® simulations. Again, this parameter should be taken as a qualitative indicator since the profile shape is a more pertinent parameter to validate the simulation compared to the quantitative solid volume fraction values.

To conclude, one can see that only the drag model had to be modified for the openFOAM simulation but the bottom boundary condition was kept uniform. The empirical drag modification with a multiplier did not give satisfying results and a more physical approach was used with the assumption of particle clustering in the bed. With these changes, a reasonable agreement was found between simulations and experiments in the 20 cm fluidized bed with homogeneous injection.

2.3 Effect of mesh size, cloud numbers and mesh type

At this point of the investigation, we now have two different CFD approaches with distinct optimized parameters presented in Table V-13 that give similar reasonable predictions of the experimental data investigated as shown in Table V-14.

Table V-13 : Final optimized parameters for Barracuda VR[®] and OpenFOAM simulations

MP-PIC approach, BarracudaVR parameters			
Particle size Distribution	From Figure III-2		
Gas particle interaction	Barracuda VR [®] Wen-Yu/Ergun + multiplier of 0.4 (Equation 59 and Equation 87)		
Bottom Boundary conditions	Injection points with specific distribution (less gas injected close to the wall)		
Euler/Euler with KTGF approach, OpenFOAM parameters			
Bottom boundary condition	Uniform gas injection		
Gas / particles interaction with clustering approach	Solid Volume fraction	Equivalent diameter	Drag law model
	0.62 to 0.08	500	Gidaspow (Table I-4)
	0.08to 0.02	150 + drag multiplier of 0.31	
	0.02 to 0	75	

Table V-14 : Barracuda VR[®] and openFOAM simulations results with optimized parameters

Bed density (kg/m³)		
Experimental	Barracuda VR[®]	OpenFOAM
504	513	482
Relative error	1.8%	4%
Particle Entrainment (kg/s)		
PSRI model	Simulation n^o3	Simulation n^o4
0.07	0.05	0.12
Averaged relative error for solid volume fraction points profiles		
	Simulation n^o3	Simulation n^o4
North-South direction	13.6	11.6
West-East direction	13.8	14.1

This chapter now investigates the effect of the mesh cell size for both codes, the effect of cloud numbers for Barracuda VR[®] and the effect of the mesh type for openFOAM keeping the same boundary conditions developed in Chapter V.2.1 and V.2.2

2.3.1 Effect of mesh cell size

As carried out in many CFD investigations, it is important to evaluate the solution mesh dependency. In this chapter, we evaluate two meshes effects as presented in Table V-15:

- First, the effect when refining the mesh. It is the most common effect investigated in the literature for CFD simulations where authors investigate that the physics implemented in the code is mesh independent. In this study, we generated a mesh with twice the number of cells compared to the default mesh.
- Second, the effect of using a coarse mesh cell size. The context behind this study is the use of CFD for extrapolation where coarser mesh cell sizes have to be used to simulate larger geometry. We therefore want to check the effect of using a large mesh cell size of 18 mm similar to the one that will be used for the 90 cm fluidized bed simulations.

Table V-15 : Meshes cells number and sizes investigated

	Cell size (mm)	Mesh cells number
Default Mesh	6	470 000
Refined mesh	5	1 000 000
Coarse mesh	18	20 000

Figure V-22 and Figure V-23 present the solid volume fraction profiles in the North-South direction for position 1 and position 3 for both Barracuda VR[®] and openFOAM simulations. The other profiles can be found in Appendix 7 and Appendix 8. Table V-16 presents the comparison between experimental and simulations data.

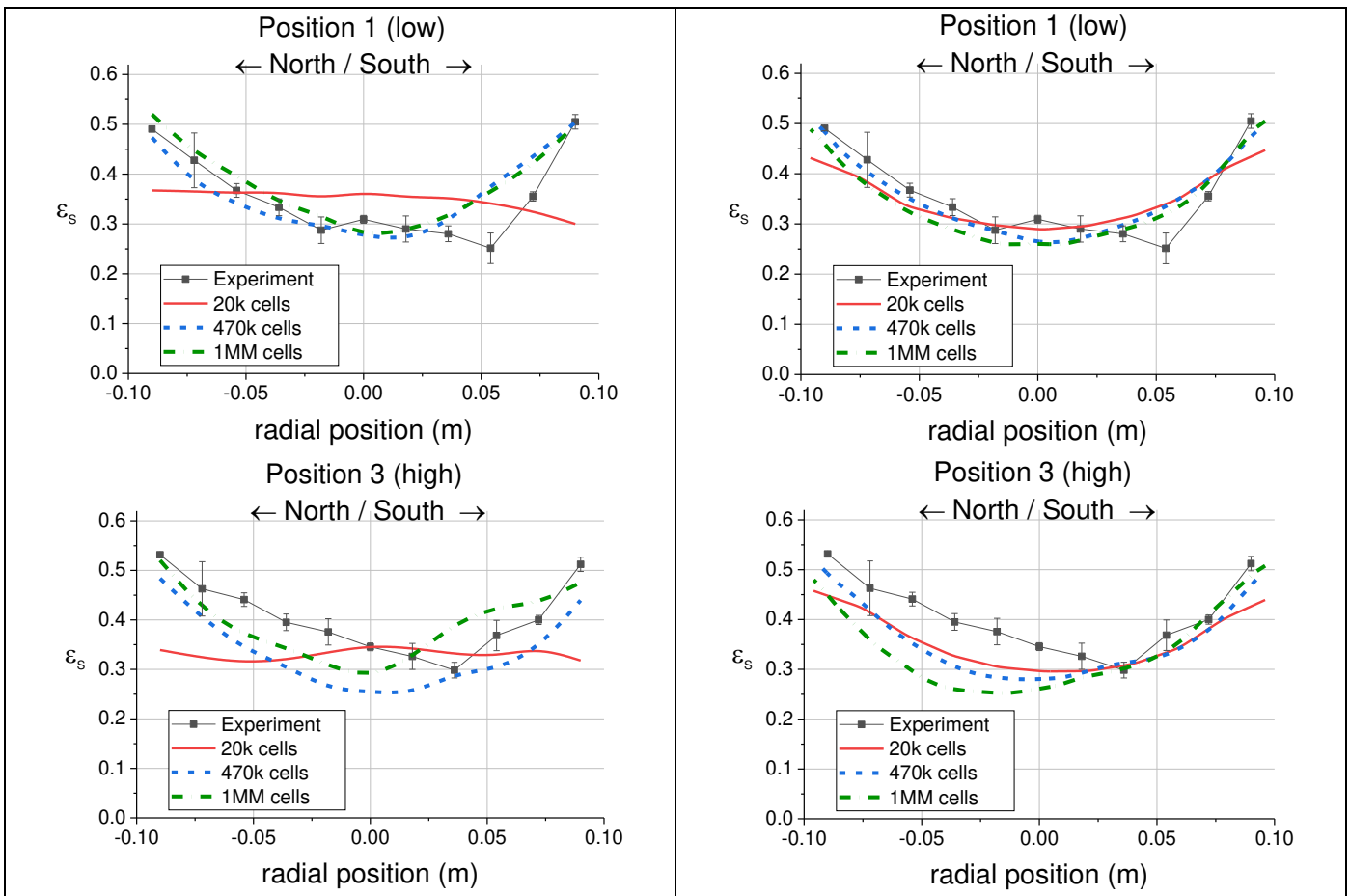


Figure V-22: Barracuda VR[®] simulations, effect of mesh, experiment n°1 20 cm fluidized bed

Figure V-23: openFOAM simulations, effect of mesh, experiment n°1 20 cm fluidized bed

Table V-16 : Simulations mesh effect, comparison with experimental data, 20 cm fluidized bed experiment n°1

Barracuda VR® simulations				
	Experimental	Simulation default mesh (470K)	Simulation refined mesh (1M)	Simulation coarse mesh (20k)
Bed density (kg/m ³) / relative error	504	513 (1.8%)	524 (3.9%)	445 (11.7%)
Particle Entrainment	0.07 (PSRI model)	0.05	0.03	0.12
Relative error north-south profile	-	13.6	10.9	18.4
Relative error West-East profile	-	13.8	13.4	25.5

openFOAM simulations				
	Experimental	Simulation default mesh (470K)	Simulation refined mesh (1M)	Simulation coarse mesh (20k)
Bed density (kg/m ³) / relative error	504	482 (4%)	478 (3%)	510 (1.1%)
Particle Entrainment	0.07 (PSRI model)	0.12	0.13	0.15
Relative error north-south profile	-	11.6	14.2	11.8
Relative error West-East profile	-	14.1	14.4	14.1

Different remarks can be made:

- For both codes, the mesh refinement has a limited effect on the simulations prediction with similar bed density, entrainment rates and profiles relative errors for the default simulation and the simulation with 1 million cells.
- The use of a coarse mesh has a different effect depending on the code. Indeed, with openFOAM the bed density and profiles relative error remains similar and the entrainment rate is not much affected. However for Barracuda VR® simulations, the bed density predicted becomes significantly lower with a relative error of around 12% compared to the experimental data while the solid volume fraction profiles become clearly flat which leads to higher profiles relative error. Concerning the flat profiles, one can wonder about the wall boundary conditions imposed in Barracuda VR® (see Chapter II.2.4 for more details on the particle wall boundary condition). Indeed, with openFOAM all the simulations give higher solid volume fraction at the wall which can be attributed to the wall boundary condition. This issue with Barracuda VR® could also explain why the bottom boundary conditions needed to be modify in order to match experimental results.

2.3.1 Effect of clouds number

As explained in Chapter I.4.2, Barracuda VR[®] and the MP-PIC approach discretizes the particle phase into clouds of particles having the same properties (size, density, velocity, ...). The average number of real particles per cloud therefore becomes a simulation parameter that can be adjusted. This chapter investigates the cloud number effect on the 20 cm fluidized bed experiment n°1 simulation with the coarse mesh configuration presented in Table V-15. Three configurations are investigated as shown in Table V-17. It should be pointed out that the coarse mesh configuration is chosen since it corresponds to the mesh cell size and the range of average number of particles per cloud that will be used for the 90 cm fluidized bed as shown in Table V-18.

Table V-17 : Simulations parameters with coarse mesh, number of clouds effect

	Number of Clouds	Averaged Number of particles per Cloud
Medium cloud number (default)	$3.36 \cdot 10^5$	$1.05 \cdot 10^6$
High cloud number	$2.35 \cdot 10^6$	$1.51 \cdot 10^5$
Low cloud number	$4.38 \cdot 10^4$	$8.09 \cdot 10^6$

Table V-18 : Clouds configurations for the 20 cm fluidized bed and the 90 cm fluidized bed

	Number of particles	Averaged Number of particles per Cloud	Number of Clouds
20 cm fluidized bed default coarse mesh simulation	$3.5 \cdot 10^{11}$	$3.36 \cdot 10^5$	$3.36 \cdot 10^5$
90 cm fluidized bed	$1.45 \cdot 10^{13}$	$1.3 \cdot 10^6$	$1.1 \cdot 10^7$

It is interesting to add that with the current computational power available for our simulations the maximum clouds number that the code can take into account is in the order of 10^7 - 10^8 . With the 90 cm fluidized bed simulation, the number of clouds shown in Table V-18 is close to the limit and therefore the average number of particles per cloud cannot be decreased below a value around 10^6 .

Table V-19 presents the simulations versus experimental data, while Figure V-24 presents the experimental and simulations solid volume fraction profile for position 1 and position 3 in the north-south direction, the other profiles can be found in Appendix 7.

Table V-19 : Barracuda VR[®] simulations cloud number effect, comparison with experimental data

	Experimental	Low number of clouds	Medium number of clouds (default)	High number of clouds
Bed density (kg/m^3) / relative error	504	453 (10.1%)	445 (11.7%)	456 (9.5%)
Particle Entrainment	0.07 (PSRI model)	0.001	0.12	0.13
Relative error north-south profile	-	30.9	18.4	23.8
Relative error West-East profile	-	34.6	25.5	29.1

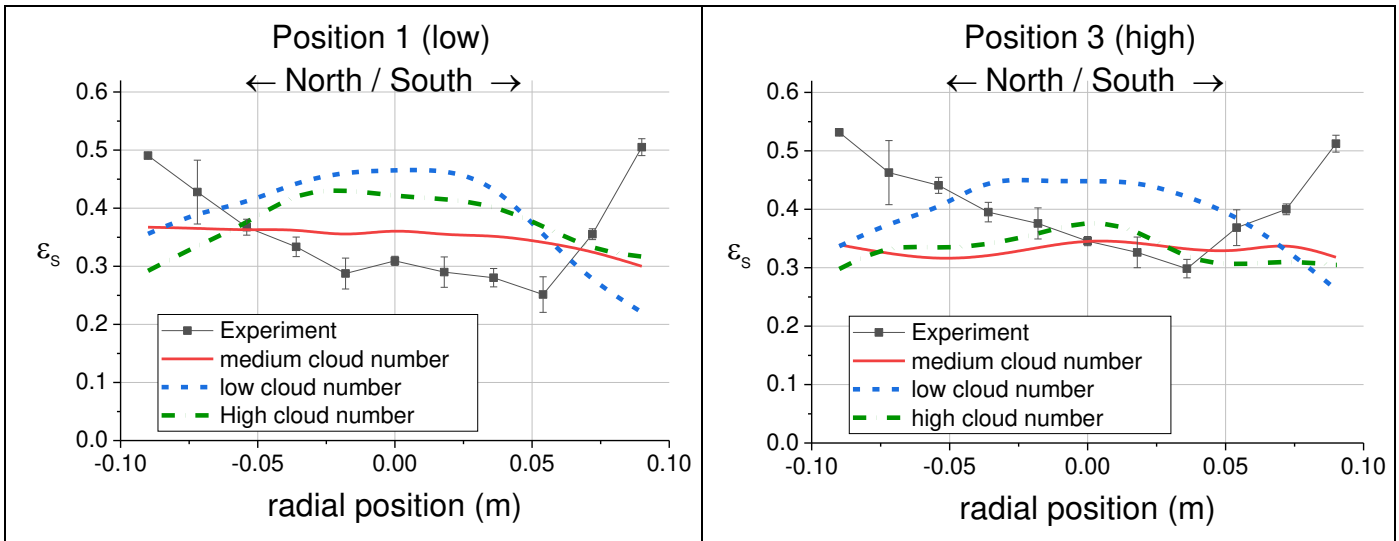


Figure V-24: Barracuda VR® coarse mesh simulations, cloud number effect, experiment n°1 20 cm fluidized bed

The following points can be made:

- First, the cloud number does not influence significantly the bed density prediction, with a predicted density still lower compared to the simulations with refined meshes.
- Surprisingly, the entrainment rate is dramatically influenced in the simulations with a low clouds number where almost no particles are entrained.
- Finally, the solid volume fraction experimental profile shape is not well captured in any of the simulations. Moreover, predicted profiles are affected by the clouds number effect with different shapes obtained especially in the simulation with a low clouds number.

It appears that the clouds number and therefore the average number of real particles per cloud have an influence on the simulations results. It is therefore a parameter to take into account when using the code for extrapolation to larger geometries and larger solid inventories.

It appears that the clouds number and therefore the average number of real particles per cloud have an influence on the simulations results but do not improve the quality of simulation at this stage with a coarse mesh. It could be interesting to evaluate also its impact with a refined mesh in the future, we did carry out this investigation since the objective of the PhD is the use of CFD for extrapolation with therefore coarse mesh cell sizes.

2.3.1 Effect of mesh cell type for openFOAM simulations

So far, only hexahedral type of cells has been used for all simulations. This chapter investigates the effect of the mesh cell type using tetrahedral cells for openFOAM only. Indeed, Barracuda VR® does not provide the option of using such a cell type.

Tetrahedral cells offer the advantage of meshing more precisely complex geometries. It is therefore important to check that results are independent when using them. For this purpose a first simulation with tetrahedral cells with about the same cells number of 470 000 cells than the default mesh was carried out. Pictures of the meshes can be found in Appendix 8. A second simulation was then carried out with larger

tetrahedral cells for with a total cell number of 80 000. The purpose of this simulation is to check the influence of the mesh cell size with tetrahedral cells. It should be highlighted that the number of 80 000 was used because it was the minimum number of cells that allows a correct meshing of the internal jet tube.

Figure V-25 presents the cell type effect investigation with a comparison between the simulation with hexahedral and tetrahedral mesh with 470 000 cells.

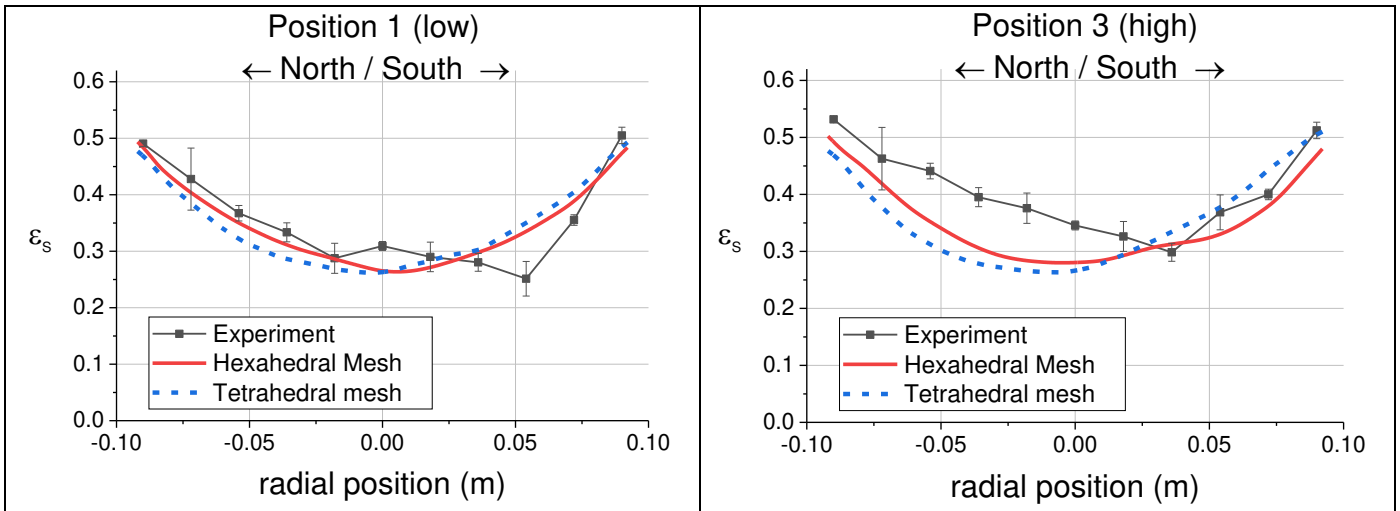


Figure V-25: openFOAM simulations, cell type effect, experiment n°1 20 cm fluidized bed

Figure V-26 presents the mesh size effect for tetrahedral cells.

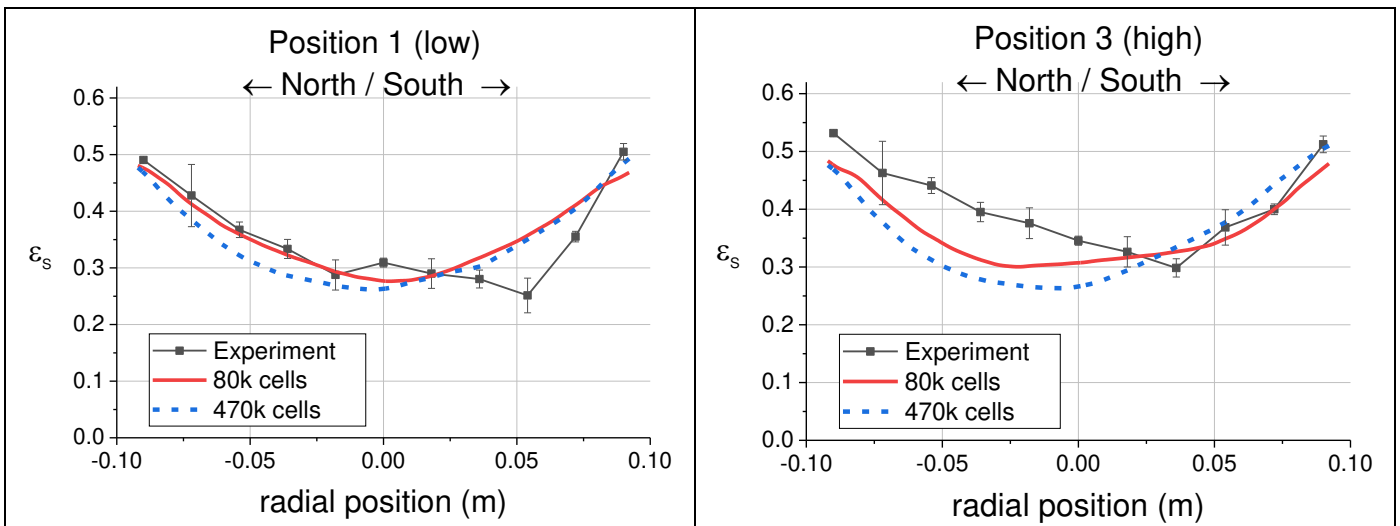


Figure V-26: openFOAM simulations, mesh size effect with tetrahedral cells, experiment n°1 20 cm fluidized bed

Table V-20 presents the comparison between simulations and experimental data.

Table V-20 : openFOAM simulations, cell type effect and cell size effect with tetrahedral cells, comparison with experimental data, experiment n°1

	Experimental	Hexahedral mesh (470k cells)	Tetrahedral mesh (470k cells)	Tetrahedral mesh (80k cells)
Bed density (kg/m ³) / relative error	504	482 (4%)	510 (1.2%)	513 (1.8%)
Particle Entrainment	0.07 (PSRI model)	0.12	0.11	0.14
Relative error north-south profile	-	14.1	13.5	13.9
Relative error West-East profile	-	11.6	10.5	11.2

One can clearly see that simulations results are not significantly affected either by the mesh type or by the mesh size for tetrahedral cells with predicted density, entrainment rate and profile relative errors in the same range.

2.4 Discussions

In this first simulation strategy step, we have used a simple fluidized bed experiment to evaluate and tune CFD codes. The amount of work conducted to reach acceptable results already shows that CFD is not a straight forward tool.

It is then important to remind that as presented in the literature review, the two CFD approaches considered in this study present some modeling advantages and drawbacks. The MP-PIC approach considers the full particle size distribution but presents a rather simplistic particle interactions model while the Euler/Euler with KTGF approach has a more complex and developed particle interactions model but taking into account only one representative diameter for the particles phase.

The first step presented in Chapter V.2.1 and V.2.2 was to study and find optimized parameters in term of drag model and boundary conditions to best match the 20 cm fluidized bed experiment n°1 data.

- With Barracuda VR[®] (MP-PIC approach), the default Barracuda VR[®] Wen-Yu/Ergun drag law was modified with a rather simplistic and correlative approach using a multiplier of 0.4. Moreover the bottom boundary condition was modified with a less gas injected close to the walls in order to obtain the correct solid volume fraction profiles shape.
- Concerning openFOAM and the Euler/Euler with KTGF approach, a uniform bottom boundary condition was sufficient to predict the solid volume fraction profiles shapes. Indeed, the correct solid volume fraction profiles shape was always obtained independently of the drag model used. Second, the drag model with multiplier used in Barracuda VR[®] did not provide satisfying results and the clustering approach of Li et al. [10] was implemented investigating different representative diameter classes distribution. After different simulations, the simulation n°9 distribution presented in Table V-10 gave the best matching results compared to experiments.

Different points can be discussed concerning this first step:

- First concerning the drag model modifications for the two codes, one can clearly notice that the Barracuda VR[®] modification is purely correlative and not based on physical phenomena. We indeed set one parameter to match the experimental data. Concerning openFOAM and the clustering approach, the approach is still correlative since we tested different representative diameter distribution in a trial and error scheme but it can be connected to physical phenomenon presented in the literature review. Indeed, Cocco et al. [44] put in evidence large particle structure inside a fluidized bed, while clustering was also observed in the dilute phase with entrained particles. Ozel et al. [8] also put in evidence the need of reducing the drag force due to the creation of large structures compared to the particle size which were not captured by classic mesh refinements similar to our simulation. Then the clustering approach used in this study is rather simplistic and more complex model (Motlagh et al. [12]) or the filtering approach (Ozel et al. [8]) or a combination of both could be tested in the future.
- Second, it is important to remind that Barracuda VR[®] simulation n°2 and simulation n°3 predicted similar averaged bed densities but different solid volume fraction profiles demonstrating that macro hydrodynamic descriptors such as bed density are necessary but not sufficient to investigate CFD codes predictions.
- Third, concerning the bottom boundary condition modification in Barracuda VR[®] with less gas injected close to the wall, one can wonder if this gas distribution occurs in the actual experiment or if it is a code boundary condition artifact. Unfortunately, we did not characterize experimentally the gas distribution at the outlet of the porous plate, so this question cannot be answered from an experimental point of view. However, as mentioned before, in the openFOAM simulations, correct profiles shape with higher solid volume fraction close to the wall was always obtained for all simulations independently of the drag model. Therefore, one can wonder if the wall boundary condition imposed in Barracuda VR[®] can be the cause of the wrong profile shape when imposing a uniform bottom distribution. This conclusion is also confirmed by the simulation using a coarse mesh where the correct profile shape is conserved with openFOAM while it is again not correctly predicted with Barracuda VR[®]. Unfortunately, no clear description of the Barracuda VR[®] particle wall boundary conditions is available for further analysis of this issue.
- Fourth, it is important to highlight that other parameters such as the gas turbulence model, the particles interaction models and the particles wall boundary conditions were not investigated in this work. Concerning the gas turbulence, one can wonder about the use of models developed from monophasic flows and about the effect of particles on the gas turbulence modeling. Tsuji et al. found that the presence of small particles decreased significantly the gas turbulence intensity [163]. Motlagh et al. [12] did not use a gas turbulence model in their turbulent fluidized bed simulations. Other authors used similar gas turbulence models than the one used in this study [127,164]. The influence of gas turbulence model therefore remains a topic to be investigated for future work. It is the same for the effect of particles interactions models and particle wall boundary condition model. Indeed, Fede et al. [13] demonstrated that these models can influence the results of fluidized bed simulations. It is therefore a point to be investigated in the future.
- Finally, this first step highlights the fact that a CFD simulation is an ensemble gathering different aspects such as an approach (MP-PIC, Euler/Euler with KTGF), sub-grid models (drag and particle interactions) and boundary conditions modeling. One could also add numerical methods and equation discretization. It is then important to point out that all these aspects are inter dependent and therefore when optimizing the drag law for one code with its own approach,

particle interactions model and boundary conditions, this drag law is not necessarily valid for the other code (with different approaches, boundary conditions, ...) as demonstrated in this study. This point highlights the difficulty to get intrinsic characterization of one physical phenomenon in a complex multiphasic flow. Indeed, in our case it is difficult to dissociate drag phenomena from particle interactions phenomena.

In a second step, simulations parameters such as mesh cell size and type as well as cloud numbers were investigated. It appeared that openFOAM predictions were quite independent from the mesh type and size while Barracuda VR[®] predictions were affected when using a coarse mesh and when reducing the number of clouds. Different points can be discussed:

- First from a point of using CFD for extrapolation and simulating larger geometry, it appeared that two parameters need to be investigated and taken into account for Barracuda VR[®] and the MP-PIC approach: the cell size and the number of real particles per cloud. On the other hand, only the cell size should be considered for openFOAM with the Euler/Euler with KTGF approach.
- Due to the limitation of computational power, we demonstrated that the average number of particles per cloud could not be lower than 10^6 in the simulation of the 90 cm fluidized bed with a total of 10^{13} particles. Therefore when simulating an industrial FCC regenerator with a total of 10^{15} particles, the average number of particles per cloud will necessarily be in the order of 10^8 . From this observation, it appears that the average number of particles per cloud is a parameter which is impossible to conserve when extrapolating simulation geometries and solid inventories. This is an issue whose consequences should be investigated in more details in a future study.

In a context of using CFD for extrapolation, from the different effects investigated in this study (cell size, cell shape, cloud numbers), openFOAM with the Euler/Euler KTGF approach seems to be the most pertinent tool. Indeed, with Barracuda VR[®] (MP-PIC approach), results were significantly affected by using larger cell sizes and the cloud number effect did not improve the predictions.

Finally, it is important to highlight that simulations optimized parameters were chosen based on a certain type and numbers of experimental data with macro descriptors (bed density) and local measurements (solid volume fraction profiles). Figure V-27 presents respectively a bubbling characterization of the Barracuda VR[®] and openFOAM optimized simulations showing area where the solid volume fraction is inferior to 0.01. Figure V-28 shows the mean solid axial velocity at an intermediate height of 0.6 m in bother directions for both simulations.

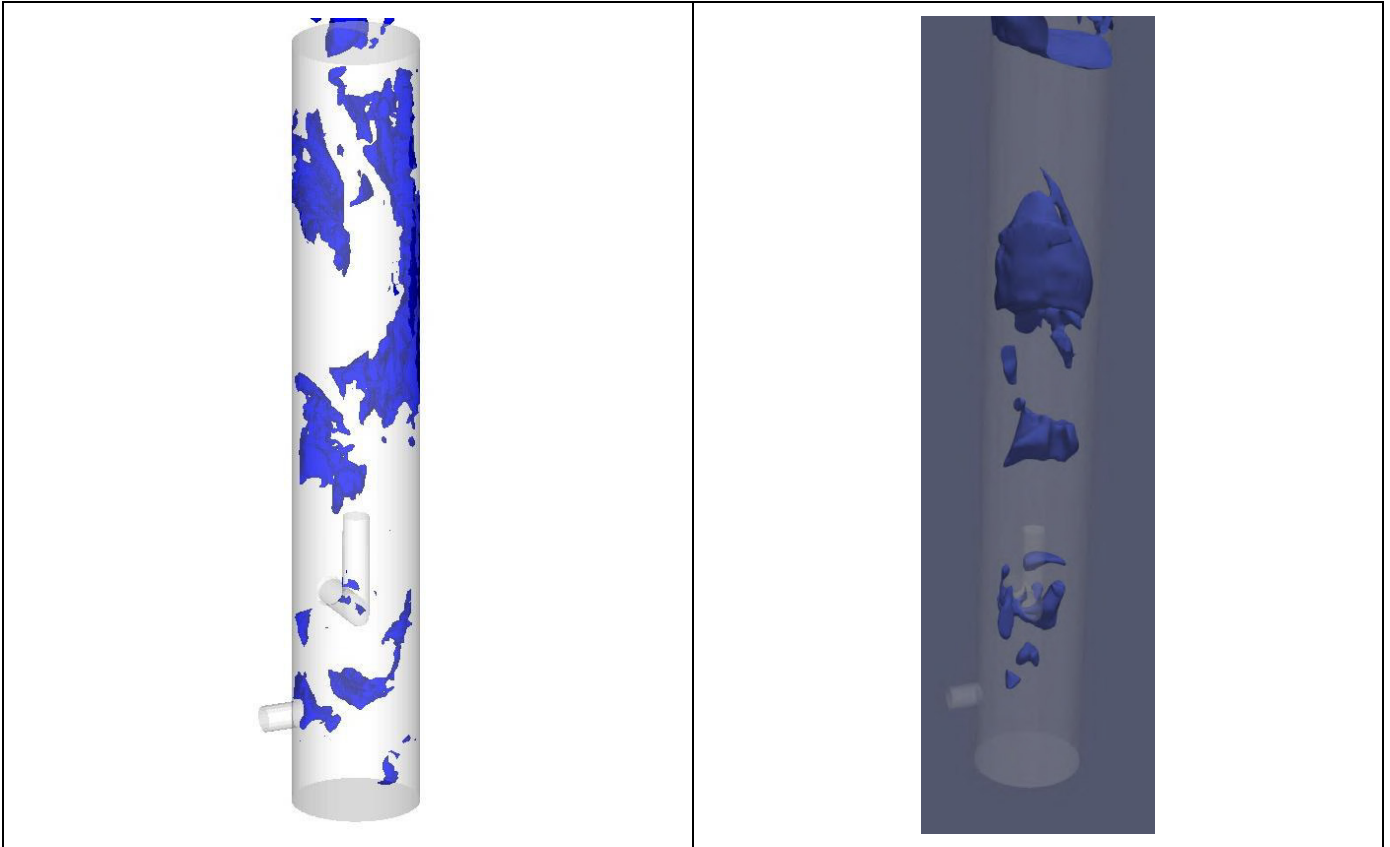


Figure V-27: Simulations bubbling characterization at a certain simulation time
 solid volume fraction < 0.01, mesh of 470k cells
 Optimized parameters, left: Barracuda VR[®] ; right: openFOAM

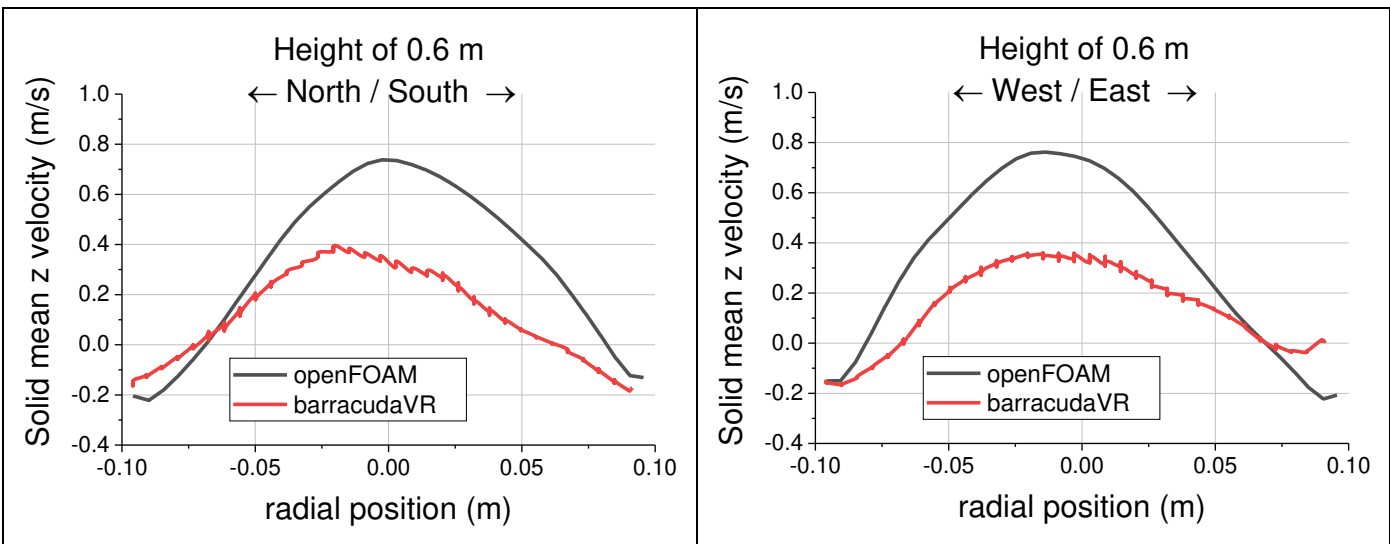


Figure V-28: Simulations solid mean axial velocity, mesh of 470k cells
 Optimized parameters, left: Barracuda VR[®] ; right: openFOAM

As shown in Figure V-27, openFOAM tends to predict the formation of large bubbles in the bed while the Barracuda VR[®] predicts heterogeneous gas structures. Then the particle mean axial velocities predicted in openFOAM are almost twice larger in the center of the column which results in a faster particles mixing. Other experimental data such as gas structure characteristics (size, velocity), particle velocity, gas and particles mixing are therefore necessary to fully investigate the CFD codes predictions. Among these

experimental data, particle and gas mixing are probably more accessible from an experimental point of view since local gas and particles velocity measurements can be challenging and instrumentation dependent as demonstrated by Tebianian et al. [98]. Moreover, gas and particles mixing can directly be connected to the local velocities. It is clearly a perspective for future work.

We have spent lots of effort to investigate and choose the CFD parameters and models for both Euler/Euler KTGF and MP-PIC approaches in order to simulate a simple fluidized bed experiment. We will now evaluate how the tuned CFD models behave when simulating larger scales, different operating conditions and other fluidization regimes.

3 Second simulation strategy step: CFD codes prediction when changing operating conditions

In the first step presented in the previous chapter, optimized parameters were found for both CFD codes to best match results from the 20 cm fluidized bed experiment n°1 with a homogeneous injection. As shown in Figure V-29, the second step of the simulation strategy consists in investigating the predictions of the two codes using the same optimized parameters on an experiment at the same scale with different operating conditions. The purpose is to put in evidence if the optimized parameters are case dependent or if they can be extrapolated to different operating conditions.

The 20 cm fluidized bed experiment n°2 with gas injected through the jet in the middle of the bed is used for this second step. It should be highlighted that the change of operating condition between the two experiments can be considered moderate since only the gas distribution is modified. However, as shown by experiments, it led to significant changes that can hopefully be captured by the CFD models developed in the first simulation strategy step.

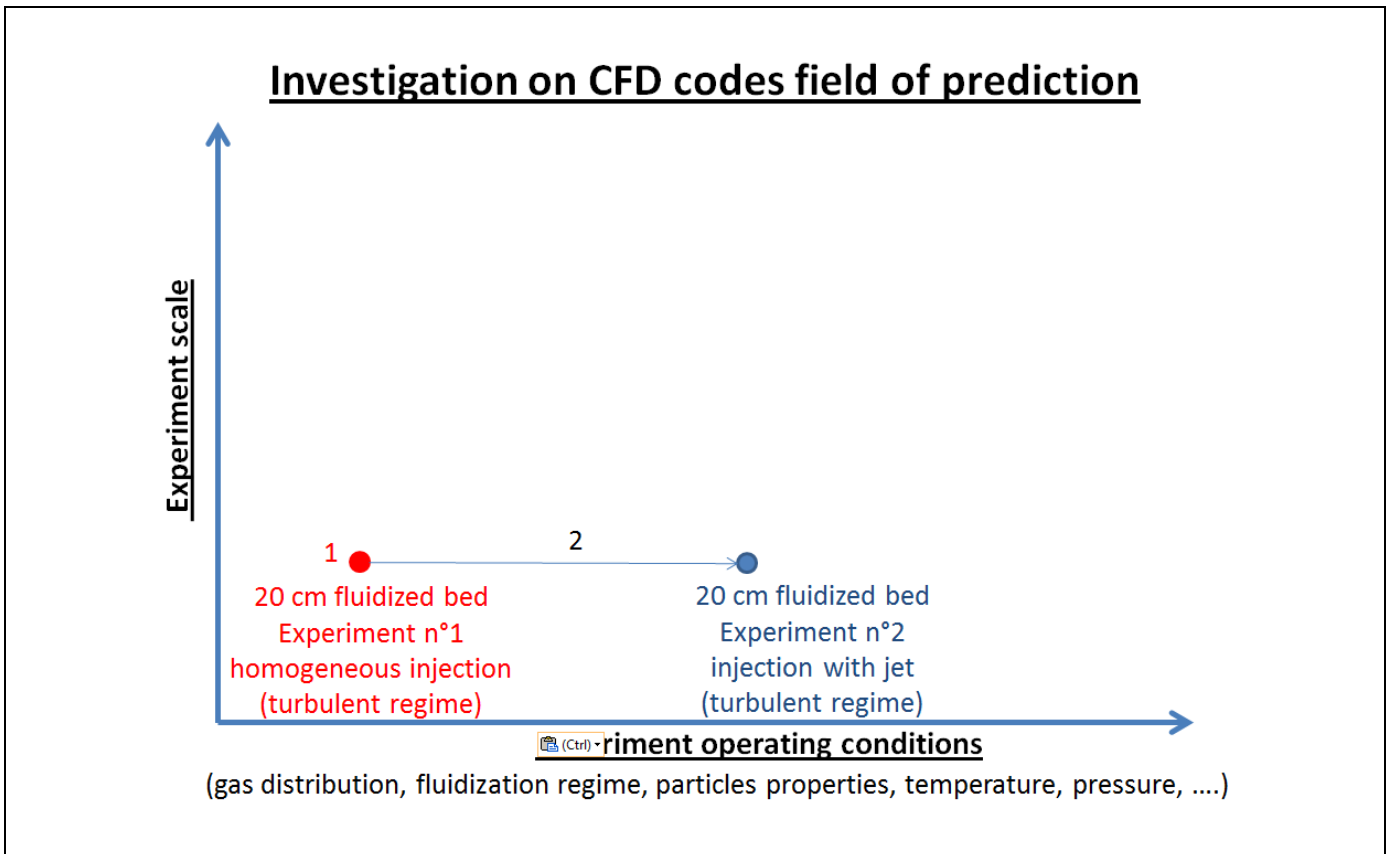


Figure V-29: Second step of the simulation strategy

3.1 Base case

The base case considered here consists in using the default mesh of 470 000 cells with the optimized parameters found in the first step and presented in Table V-13. Then, Table V-21 presents the other parameters required for the simulation of the 20 cm fluidized bed experiment n°2 with jet injection.

Table V-21 : Simulation parameters of the 20 cm fluidized bed experiment n°2 with jet injection

Mesh size	470 000 hexahedral cells
Cell size	6 mm
Particle density (kg/m ³)	1 260
Pressure at top boundary condition (kPa g)	6 kPag
Bottom gas flowrate injected through injection points (kg/s)	0.0060
Gas injected through the jet (kg/s)	0.0179
Air temperature (°C)	20
Bed mass (kg)	17
Simulation time step (s)	1.10 ⁻⁴
Simulation time (s)	20

The only modification compared to the previous simulations is for the jet boundary condition which was considered before as a wall and it is now considered for both codes as a uniform gas inlet. Table V-22 presents the comparison between experiment and simulation data. Figure V-30 and Figure V-31 shows the instantaneous and averaged volume fraction profile in a plane passing through the column center for respectively Barracuda VR[®] and openFOAM simulations. Finally, Figure V-32 and Figure V-33 present the solid volume fraction profiles in both directions for respectively the Barracuda VR[®]R and openFOAM simulations.

Table V-22 : Comparison between experiment and simulations data, 20 cm fluidized bed experiment n°2 with jet injection

	Experimental	Barracuda VR [®] Simulation	OpenFOAM simulation
Bed density (kg/m ³) / relative error	631	671 (6.3%)	666 (5.5%)
Particle Entrainment Experiment n°2	-	0.04	0.15
<i>Particle Entrainment Experiment n°1</i>	<i>0.07 (PSRI model)</i>	<i>0.05</i>	<i>0.12</i>
Relative error north-south profile		24.9	25.1
Relative error West-East profile		43.8	22.1

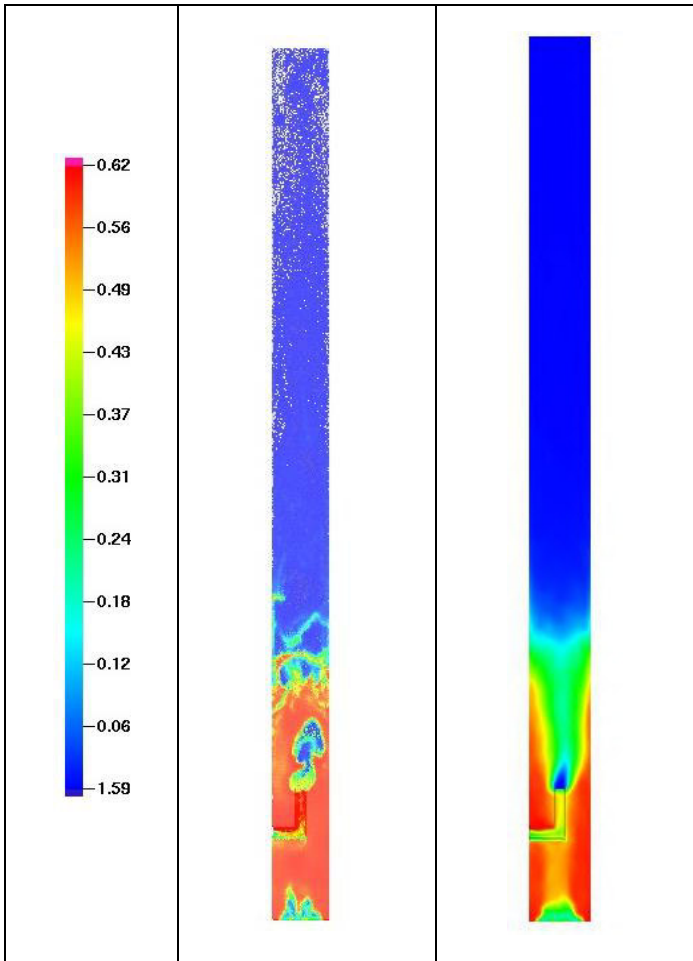


Figure V-30: Experiment n°2 Barracuda VR® simulation, instantaneous and averaged solid volume fraction profile

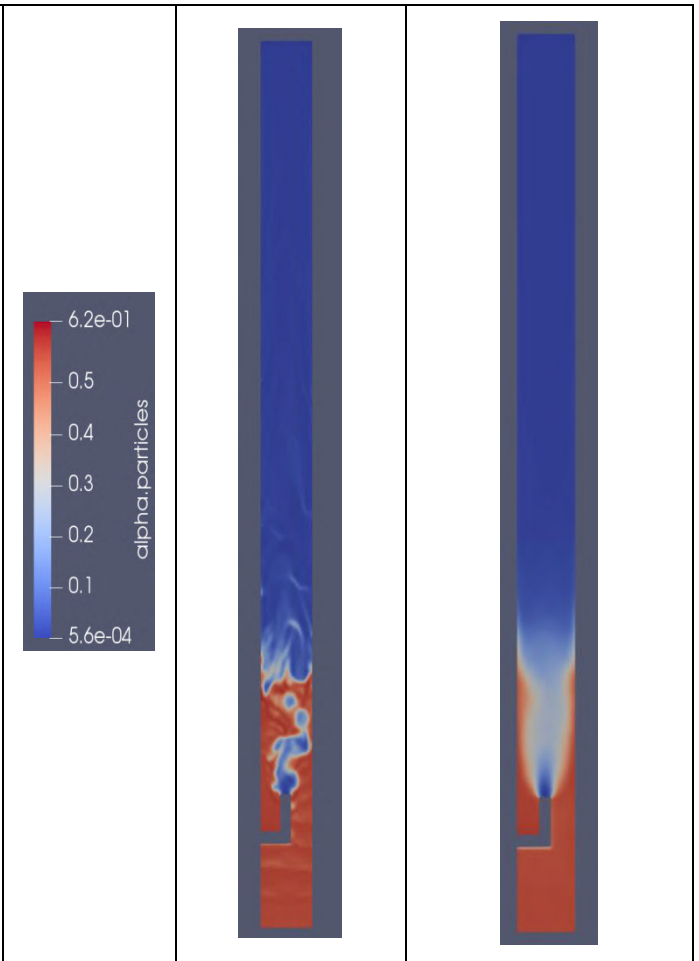


Figure V-31: Experiment n°2 openFOAM simulation, instantaneous and averaged solid volume fraction profile

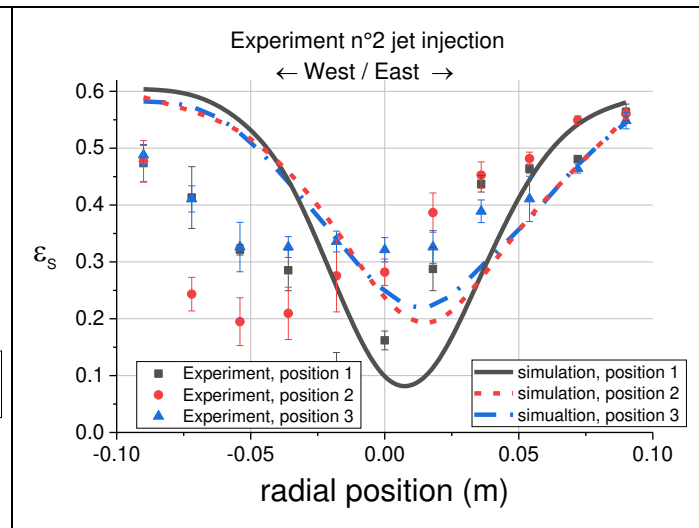
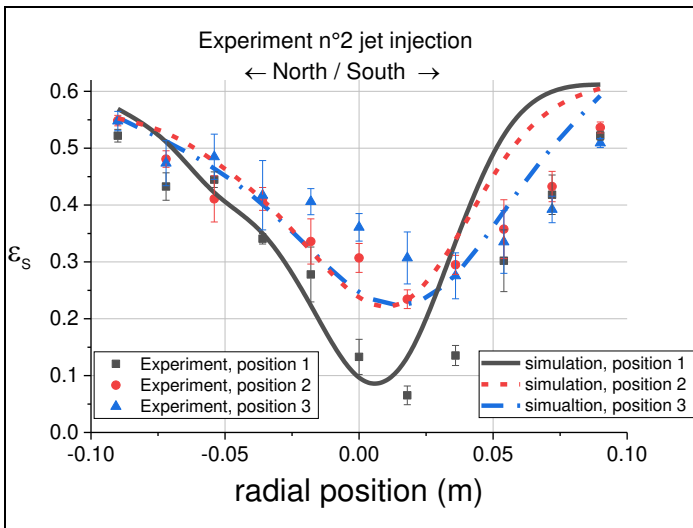


Figure V-32: Barracuda VR® simulations, default mesh of 470k cells, experiment n°2 20 cm fluidized bed

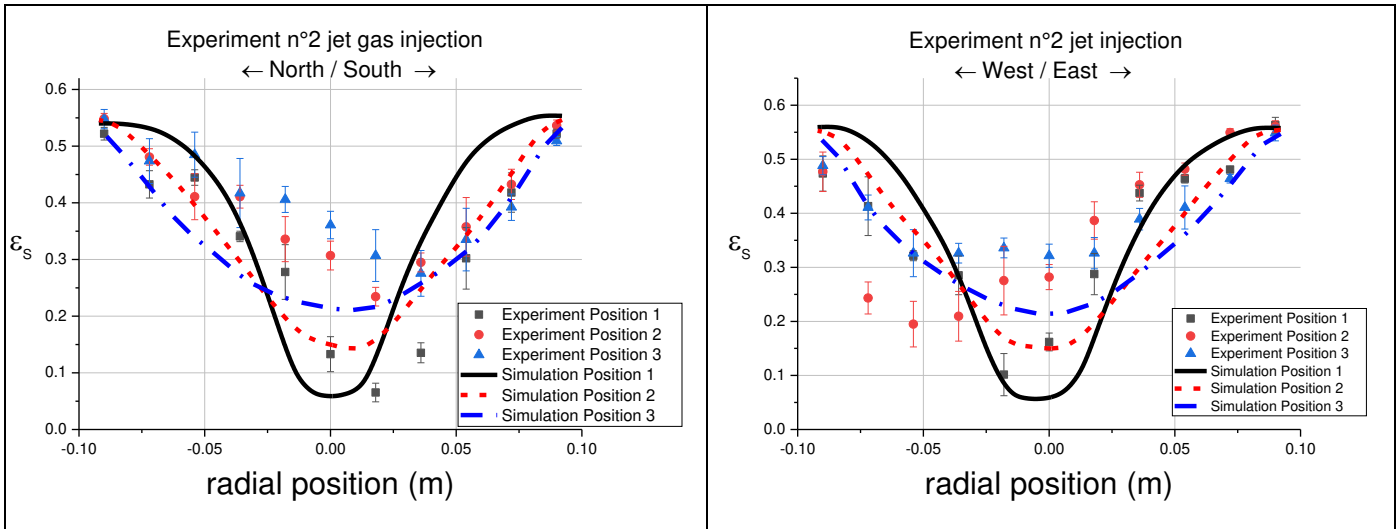


Figure V-33: openFOAM simulations, default mesh of 470k cells, experiment n°2 20 cm fluidized bed

Different points can be made:

- First both codes capture the change of bed density compared to experiment n°1 with a relative errors around 6% which is a satisfying result.
- Second, compared to experiment n°1, Barracuda VR® predicts a lower entrainment rate while openFOAM predict a higher entrainment rate. It would therefore be interesting to experimentally measure the entrainment rate for both experiments in a future work to assess which trend is the correct one.
- Third, concerning the profiles prediction:
 - o Both codes predict rather well the influence of the jet in the center of the column at the lowest position 1 with low solid volume fraction in the same range than the experimental value.
 - o Both codes fail to predict the position n°2 profile in the West-East direction shifting toward the west side, especially Barracuda VR® with a profile shifting on the other side. It is important to remind that this experimental profile shift was attributed to the jet side tube entering the column on the west side. Therefore, with Barracuda VR®, it seems that the side tube has the opposite effect while no effect is observed with openFOAM. The boundary condition imposed on the side tube wall could be investigated further in order to observe if it has an impact on the gas jet orientation (the same boundary conditions than the column wall were applied on the tube walls).
 - o We have also to keep in mind that the important experimental shift of the jet is surprising. It should therefore be confirmed with additional experiments, by moving for instance the side tube in another direction to observe if the gas shift goes in the same direction.
 - o For openFOAM, symmetrical profiles are obtained with respect to the column center for all positions in all directions while experimental profiles tend to shift toward the south and west directions. Then, the jet effect is attenuated progressively with predicted profiles showing elliptical shapes with higher solid volume fraction in the center especially for position n°3. Then, the solid volume fraction values on the sides are rather well captured while, in the center, values are underestimated. Average relative profiles points errors are around 25% which is higher than experiment n°1 predictions.
 - o For Barracuda VR®, the profile shift toward the south side seems to be captured however the West-Est direction the predicted shift goes in the opposite side compared to experiment. The

consequence is that the average relative profile points error goes to almost 50% in this direction. Then, the attenuation of the jet is less progressive compared to openFOAM with similar profiles obtained at position n°2 and n°3.

- It is also important to remind that experimental results should not be considered for the quantitative solid volume fraction value since we demonstrated that the optical probe signal can have a strong influence on the final quantitative results. Therefore the trend of profile shapes between experiment n°1 and n°2 is the important experimental result and from this point of view, simulation results can be considered rather satisfying since trends are captured between experiment n°1 and n°2 with elliptical profiles predicted for experiment n°1 and jet effect and jet dissipation rather well captured for experiment n°2 with openFOAM showing slightly better overall predictions.

Overall, the simulations results are considered quite satisfying for both codes since the trend of bed density and solid volume fraction profiles between experiment n°1 and n°2 are captured.

3.2 Influence of the mesh size and mesh type

The exercise of investigating the mesh size and mesh type effects was again carried out on the experiment n°2 simulation. The cloud effect was not investigated since we do not expect different conclusions compared to the work presented in Chapter V.2.3.1.

3.2.1 Mesh size

The same mesh sizes than the one presented in Chapter V.2.3.1 and Table V-15 were used for this study. Figure V-34 and Figure V-35 presents the solid volume fraction profiles for position 1 in the north-south direction and for position 3 in both directions for respectively the Barracuda VR[®] and openFOAM simulations. Other profiles can be found in Appendix 10 and Appendix 11. Table V-23 presents the comparison between experimental and simulation data.

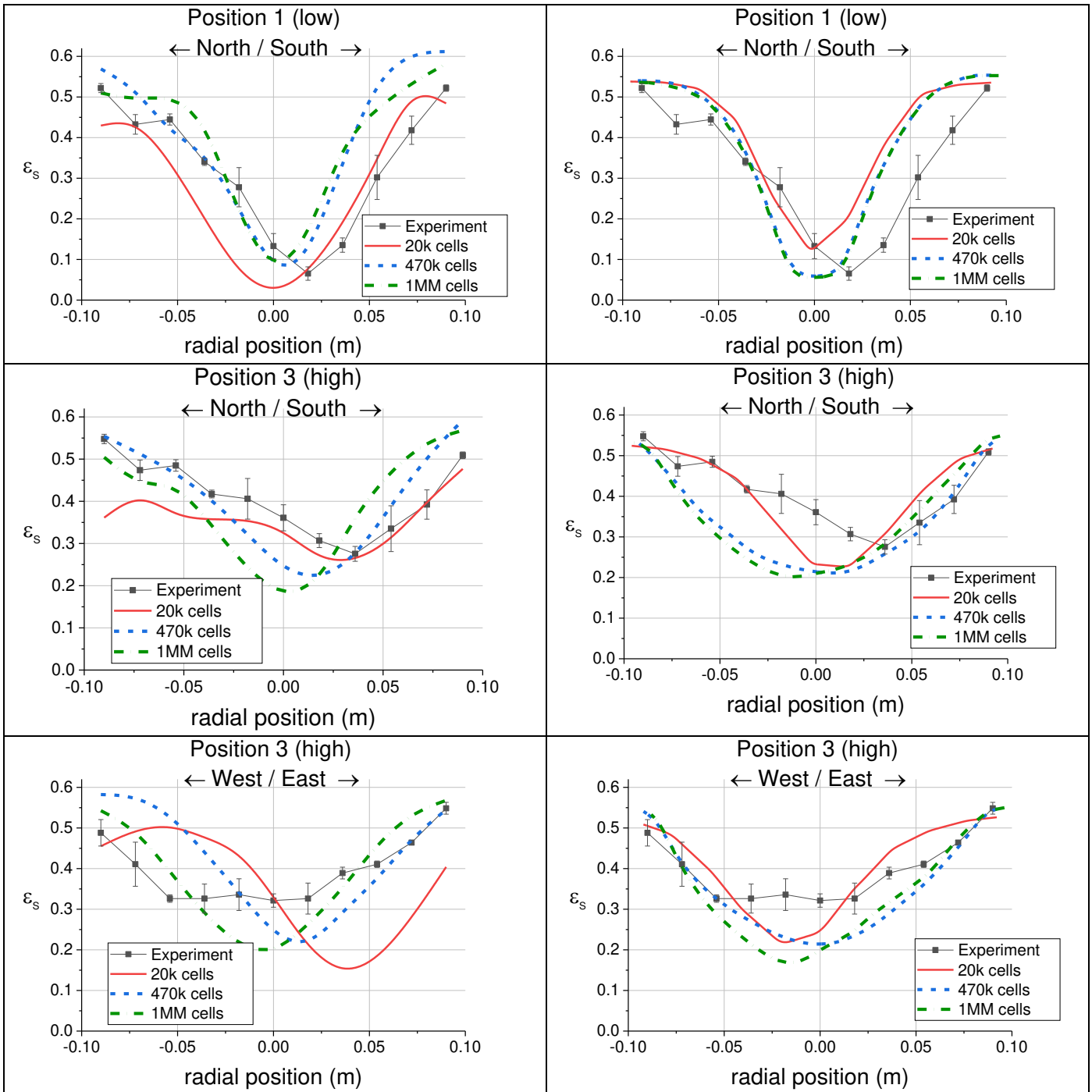


Figure V-34: Barracuda VR[®] simulations, effect of mesh, experiment n^o2 20 cm fluidized bed

Figure V-35: openFOAM simulations, effect of mesh, experiment n^o2 20 cm fluidized bed

Table V-23 : Simulations mesh effect, comparison with experimental data, 20 cm fluidized bed experiment n°2

Barracuda VR® simulations				
	Experimental	Simulation default mesh (470K)	Simulation refined mesh (1M)	Simulation coarse mesh (20k)
Bed density (kg/m ³) / relative error	631	671 (6.3%)	640 (1.4%)	520 (17.6%)
Particle Entrainment		0.04	0.02	0.09
Relative error north-south profile		43.8	31.8	22.4
Relative error West-East profile		24.9	31.4	51.7
openFOAM simulations				
	Experimental	Simulation default mesh (470K)	Simulation refined mesh (1M)	Simulation coarse mesh (20k)
Bed density (kg/m ³) / relative error	631	666 (5.5%)	664 (5.2%)	668 (5.9%)
Particle Entrainment		0.15	0.15	0.13
Relative error north-south profile		25.1	24.2	23.9
Relative error West-East profile		22.1	25.8	22.4

Results obtained lead to the same conclusions as with the mesh size effect study on experiment n°1 simulations. The mesh refinement with 1 million cells does not affect in a significant way the predicted results with prediction slightly improved for Barracuda VR® and with almost no changes for openFOAM. However the use of a coarse mesh leads to degraded prediction for Barracuda VR® with a bed density underestimated by 18% and solid volume fraction profiles highly modified especially in the West-East while openFOAM prediction remains in the same range with pretty good agreement obtained with experiment data. It is however interesting to point out that with the coarse mesh, the openFOAM profiles are less elliptical for position n°2 and n° 3 where the jet effect is more visible.

3.2.2 Effect of mesh cell type for openFOAM simulations

The use of tetrahedral cells and the size effect with this type of cells were also investigated for experiment n°2 simulations. Figure V-36 and Figure V-37 presents the experimental and simulations profiles for respectively the cell type effect investigation and for the mesh size effect with tetrahedral cells investigation. Table V-24 presents the comparison between simulations and experimental data.

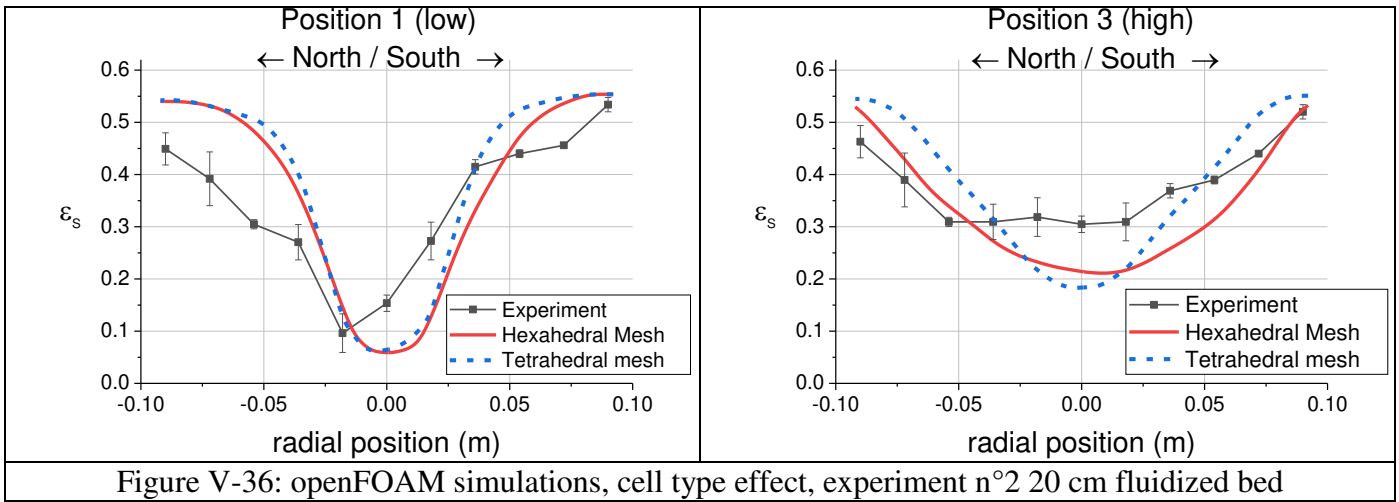


Figure V-36: openFOAM simulations, cell type effect, experiment n² 20 cm fluidized bed

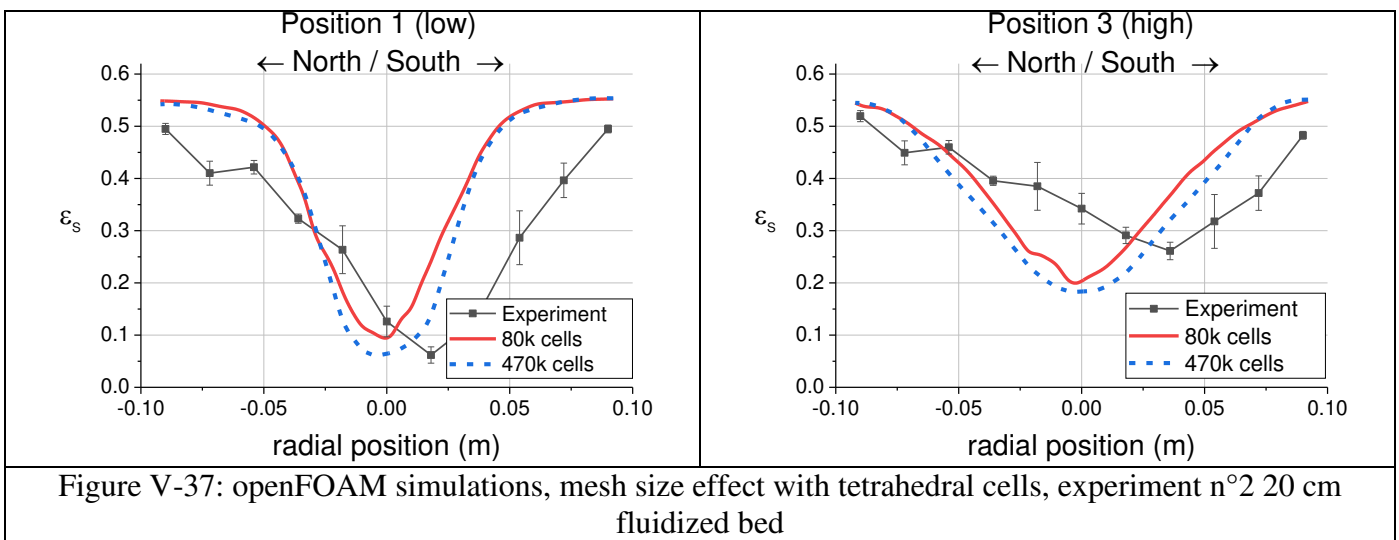


Figure V-37: openFOAM simulations, mesh size effect with tetrahedral cells, experiment n² 20 cm fluidized bed

Table V-24 : openFOAM simulations, cell type effect and cell size effect with tetrahedral cells, comparison with experimental data, experiment n²

	Experimental	Hexahedral mesh (470k cells)	Tetrahedral mesh (470k cells)	Tetrahedral mesh (80k cells)
Bed density (kg/m ³) / relative error	631	666 (5.5%)	667 (5.5%)	668 (5.9%)
Particle Entrainment		0.15	0.13	0.10
Relative error north-south profile	-	25.1	24.7	25.4
Relative error West-East profile	-	22.1	23.8	24.3

Conclusions remain the same with predictions rather independent of the mesh cell type and size. One can notice however a slightly lower entrainment with tetrahedral cells compared to hexahedral cells and when using larger cells.

3.3 Discussions

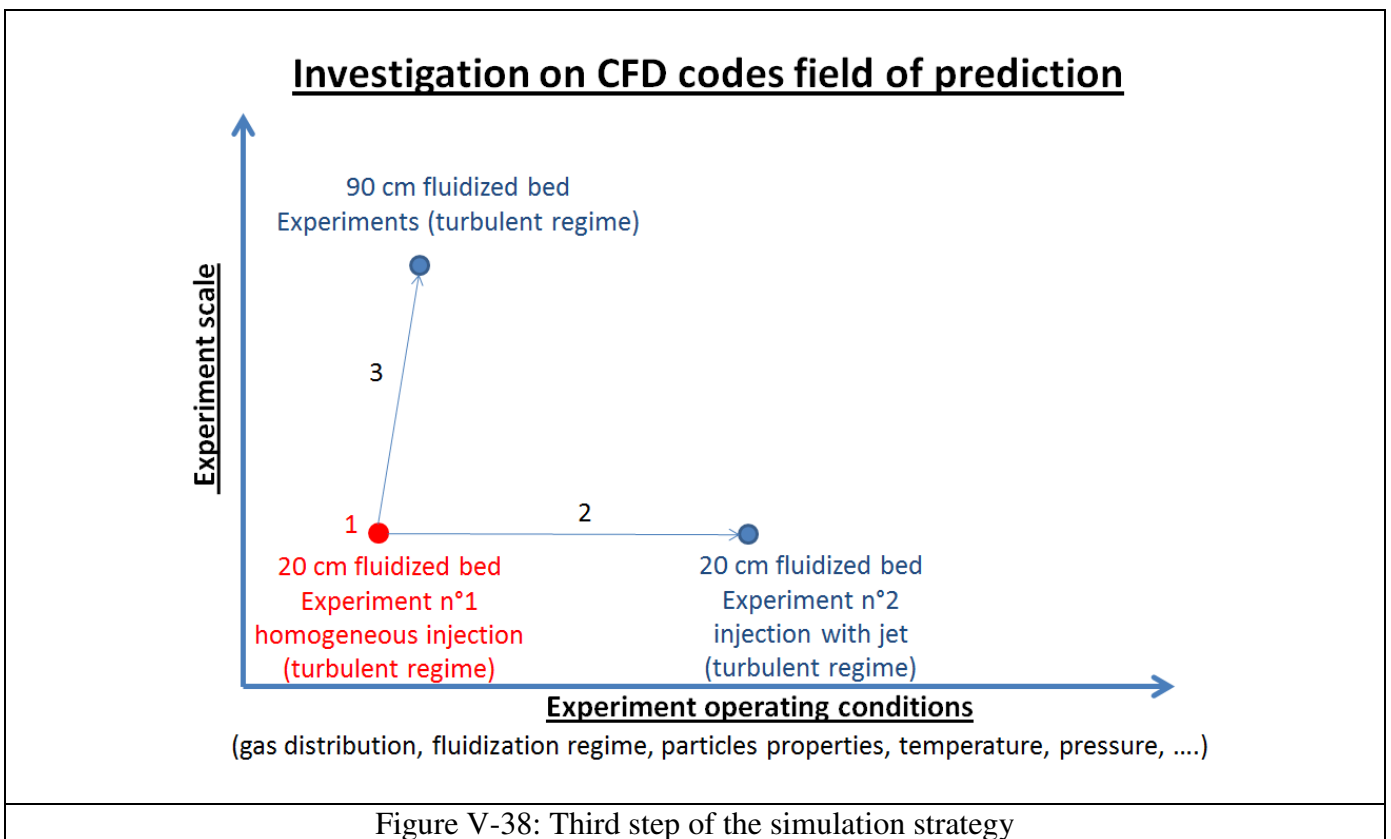
The main conclusion obtained from the jet simulations is that both CFD approaches predicted reasonably well the change of bed hydrodynamic compared to the homogeneous injection configuration. This result is satisfying and it shows that the parameters and models developed in the first simulation strategy steps allow reasonable prediction of other operating conditions at the same scale.

Then, similar results compared to the first simulation strategy step were obtained when investigating the effect of the mesh cell size. The predictions of the OpenFOAM approach (Euler/Euler KTGF) were not significantly affected which is not the case for the Barracuda VR[®] predictions (MP-PIC approach).

We are now going to investigate the use of both approaches for the simulation of a turbulent fluidized bed at a larger scale as described in the next chapter.

4 Third simulation strategy step: CFD codes predictions at larger scale

The first and second steps of this study consisted in finding optimized parameters for the simulation of a specified experiment at given operating condition and then in investigating the CFD prediction using the same parameter for another operating condition simulation with the same experiment. The results showed that both codes captured relatively well the change of bed density and solid volume fraction profile shape related to the change of gas distribution. This type of CFD exercise where different operating conditions on the same experiment are investigated is rather classical and can be found in many literature studies [10,12]. The next step of the simulation strategy we propose consists in investigating the CFD codes predictions when changing scale of experiments as shown in Figure V-38. For this purpose, the 90 cm fluidized bed experiments conducted at PSRI are used. It should be highlighted that to our knowledge, this type of study where CFD codes predictions of fluidized bed at different operating conditions and scales are evaluated against experimental data cannot be found in the literature.



4.1 Geometry, mesh and boundary conditions

This chapter presents the geometry, mesh and boundary conditions used for the Barracuda VR[®] and openFOAM simulations. First, the coarse mesh cell size of 18 mm used for the 20 cm fluidized bed was chosen. The goal is to keep a common cell size between the two experiments simulations. Table V-25 presents the mesh cell numbers for each scale of fluidized beds simulated with a hexahedral cell size of 18 mm, a projection for an industrial Fluidized Bed of 5 meters is also presented.

Table V-25 : Mesh cell numbers for fluidized beds at different scales with a hexahedral cell size of 18 mm

	20 cm fluidized bed experiment	90 cm fluidized bed experiment	Industrial fluidized bed (Diameter of 5 m and height of 10 m)
number of cells with a cell size of 18 mm	$20 \cdot 10^3$	$600 \cdot 10^3$	$33\,000 \cdot 10^3$

One can see that for the industrial fluidized bed, the mesh cell numbers using a cell size of 18 mm is in the order of 30 million which would imply a high computational power for a transient two phase flow simulation. It should be highlighted that from a computational power and parallelization point of view this simulation would be possible with openFOAM but not possible with Barracuda VR[®] which uses, at the time this manuscript is written, a calculation parallelization method with a single GPU card.

Two different meshes were used for Barracuda VR[®] and openFOAM simulations. This difference comes from the meshing of the bottom fluidized bed distributor shown in Figure V-39, one can refer to Appendix 3 for more details on this design.

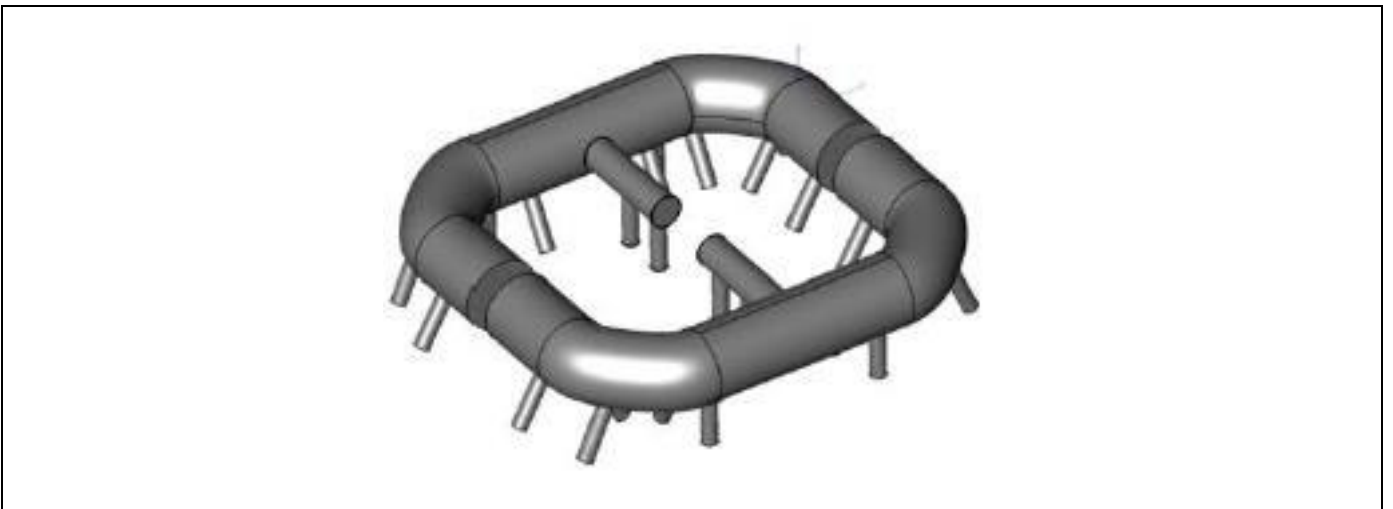
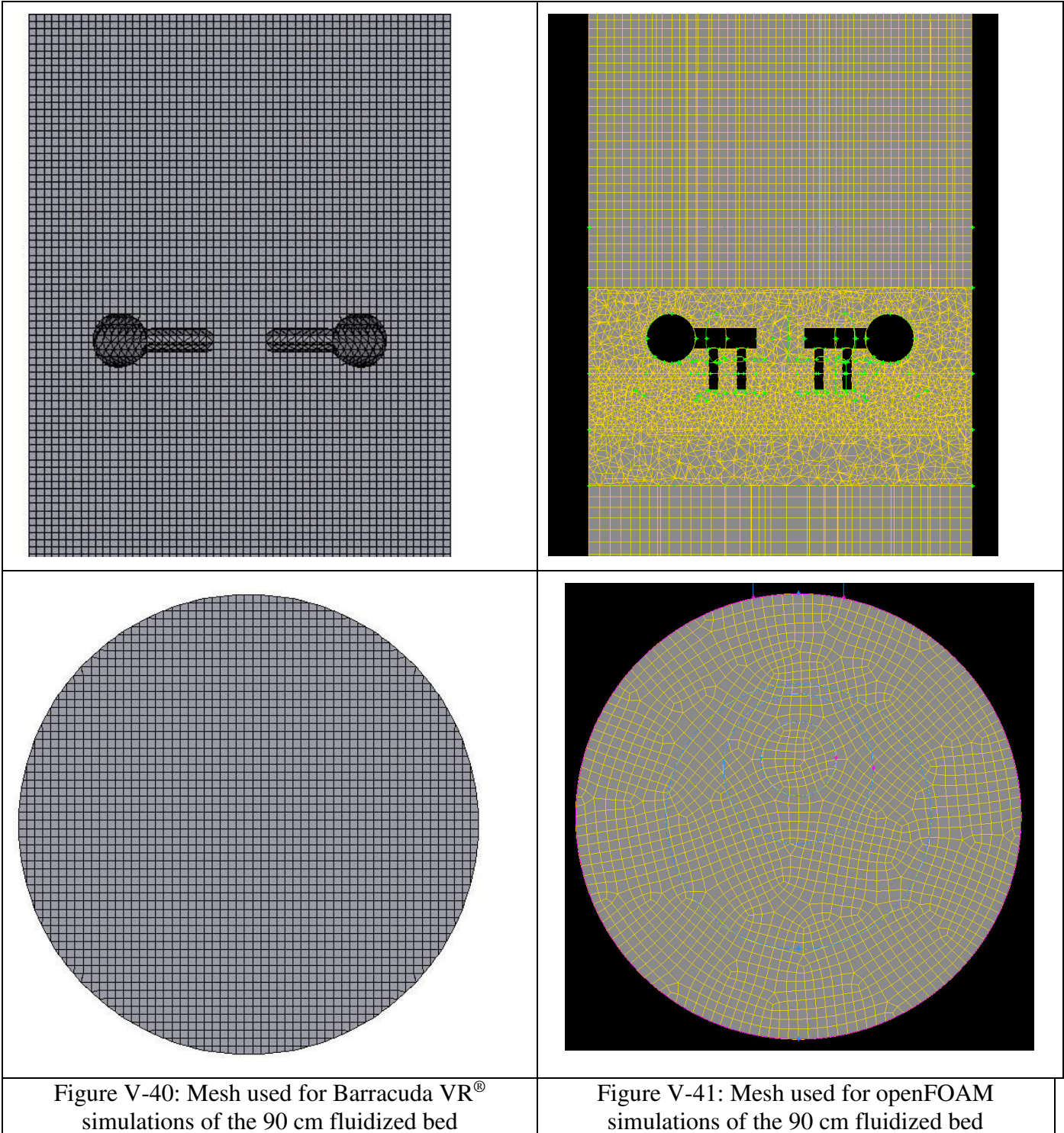


Figure V-39: 90 cm fluidized bed bottom distributor

As shown in Figure V-39, the distributor is composed of 36 nozzles with a diameter of 2.5cm connected to a main rectangular ring. The nozzles on the outside distribution ring are orientated with an angle of 30° with respect to the axial “z” axis. As explained in Chapter II.2.4, Barracuda VR[®] uses a structured hexahedral meshing method which in this case makes the meshing of the distributor impossible with a cell size of 18 mm. It would actually takes in the order of 10 million cells to mesh correctly the ring geometry. For this reason, the nozzles were not considered in Barracuda VR[®] simulations and injection points were used for the gas injection as explained below. On the other hand, openFOAM allows the use of non-structured hexahedral and tetrahedral cells which make possible the mesh refinement around the distributor.

Figure V-40 and Figure V-41 present the mesh used for respectively the Barracuda VR[®] and openFOAM simulations.



As discussed before, the cell size used above the distributor is the same for both meshes. Tetrahedral cells between 7 and 18 mm are used around the distributor for the openFOAM mesh. The total cell number is $600 \cdot 10^3$ and $800 \cdot 10^3$ for respectively Barracuda VR[®] and openFOAM meshes, the difference between the two being due to the refinement around the distributor of the openFOAM mesh.

Figure V-42 presents the geometry considered for openFOAM simulations, the geometry for Barracuda VR[®] simulation being the same except for the gas distributor as discussed below. In order to facilitate the geometry meshing with hexahedral cells, the first cyclone dipleg return is simulated with a squared surface having the same surface area than the real circular dipleg surface. The second cyclone dipleg is taken into consideration with a dead volume removed from the geometry. The top outlet real ring shape is the same than the experiment configuration.

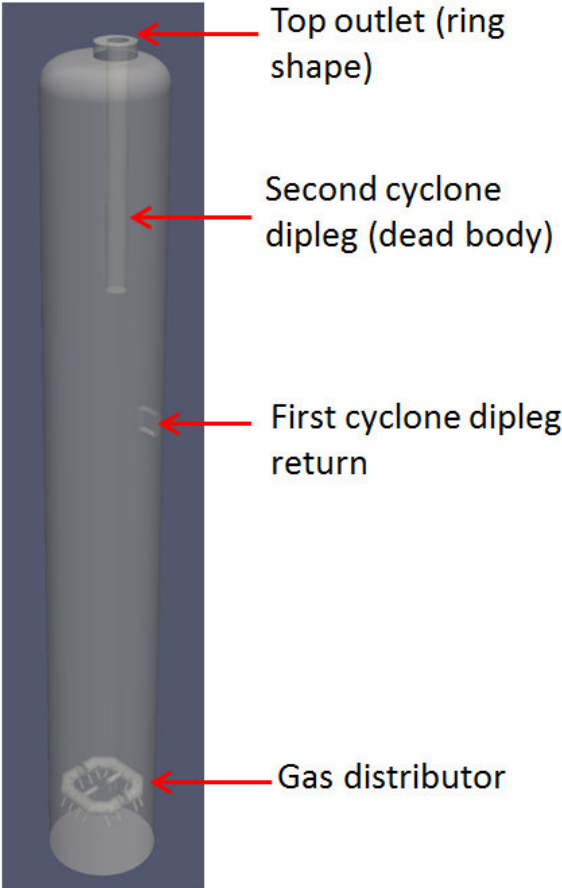
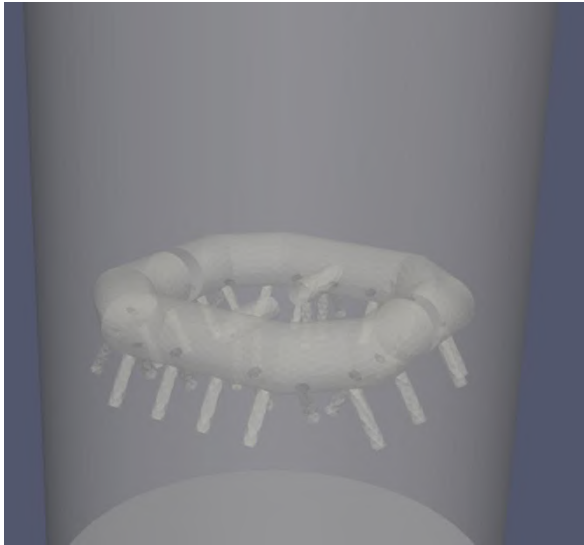
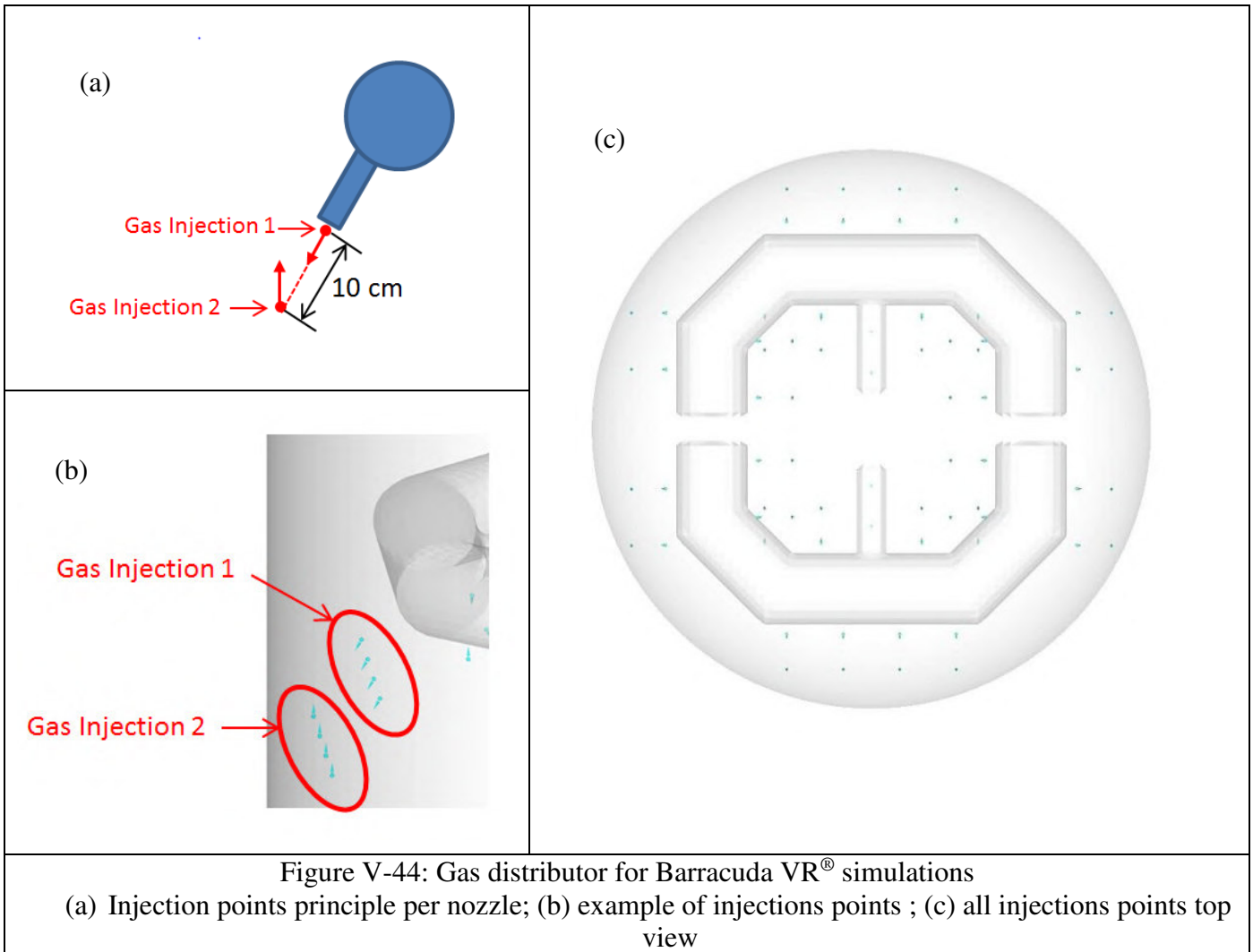
	
<p>Figure V-42: 90 cm fluidized bed geometry considered</p>	<p>Figure V-43: Gas distributor for openFOAM simulations</p>

Figure V-43 presents the gas distributor geometry in openFOAM simulations. Gas is injected through all the nozzles tips surfaces assuming a homogeneous distribution between all nozzles.

Figure V-44 presents the gas distribution used for Barracuda VR[®] simulations. Two injections points per nozzle were used with a distance of 10 cm between each other, this distance being calculated from an in-house jet penetration correlation. The reason of using two injections points is to make sure that the jet penetration is well represented. Indeed, a single injection point close to the nozzle with a mesh cell size of 18 mm was estimated as coarse condition to well represent the jet penetration. The gas flowrate is divided homogenously between all gas injection points. Figure V-44 (b) shows an example of injections points locations, it should be highlighted that the nozzles were not taken into in the geometry, only the main ring is considered. Figure V-44 (c) presents all injections points from a top view. One can see from this figure that the gas injection is rather uniform except in the column center.



It important to point out that the choice of the gas injection boundary conditions for the Barracuda VR[®] and openFOAM simulations was estimated as the best compromise in order to evaluate both codes on a similar basis. Indeed, injections point boundary condition is not available in openFOAM while Barracuda VR[®] does not allow meshing the distributor correctly. We could have assumed a uniform gas inlet boundary condition at the column bottom surface but this assumption was considered too strong since one objective is also to investigate potential gas distribution effects compared to the homogeneous injection porous media used in the 20 cm fluidized bed experiment.

The boundary condition imposed for both codes simulations are:

- Gas injection: Total gas mass flowrate calculated from the top superficial gas velocity and gas density with a temperature of 20°C and a pressure of 35 kPag
 - o Barracuda VR[®]: uniform distribution among all injection points, injection velocity equals to nozzle injection velocity divided by two (2 injection points per nozzle).
 - o openFOAM: uniform gas velocity at all nozzle tip surface.
- First cyclone dipleg return: all the solid escaping at the top outlet is re-injected through the first cyclone dipleg therefore assuming a 100% efficiency for the cyclone.
 - o Barracuda VR[®]: option used to connect the top outlet with the dipleg return. Gas flowrate calculated from Equation 86.
 - o openFOAM: uniform solid velocity adjusted to match solid flowrate escaping at the top and gas uniform velocity calculated from Equation 86.
- Top outlet, pressure imposed of 35 kPa g.
- Walls: same parameters than the 20 cm fluidized bed simulation for both codes.

For openFOAM, all boundary conditions imposed for all parameters (volume fraction, velocity, pressure, granular temperature) can be found in Appendix 12.

4.2 Base case

The first case investigated of the 90 cm fluidized bed experiments is the one with a superficial velocity of 0.6 m/s which is similar to the superficial velocity of the 20 cm fluidized bed experiments of 0.64 m/s. Table V-27 presents the simulation parameters for both code. The same optimized parameters found with the 20 cm fluidized bed simulations were applied. It is important to point out that particles used in both experiments have similar characteristics diameter but a density difference of 13% as shown in Table III-1 that is accounted for in the simulation particles description. It is therefore interesting to see if CFD can predict bed densities considering that particle density changes are taken into account.

Table V-26 : Simulation parameters of the 90 cm fluidized bed experiment, $U_{sg} = 0.6$ m/s.

	Barracuda VR [®]	openFOAM
Mesh size	600 000	800 000
Cell size above distributor	18 mm	
Particle density (kg/m ³)	1 490	
Particle size distribution	From Figure III-2	Representative diameters from Table V-13
Drag law	Default Barracuda VR [®] (Equation 59)	Gidaspow (Table I-4)
Pressure at top boundary condition (kPa g)	35 kPag	
gas flowrate (kg/s)	0.62	
Air temperature (°C)	20	
Bed mass (kg)	1 800	
simulation time step (s)	$5 \cdot 10^{-4}$	
Simulation time (s)	60	
Number of clouds	$1.1 \cdot 10^7$	-
Average Number of particles per cloud	$1.3 \cdot 10^6$	-

The first item checked was the gas distribution for both simulations. Figure V-45 presents the averaged solid volume fraction profile in a plane just above the nozzles tips, average carried over the 60 seconds of simulation time.

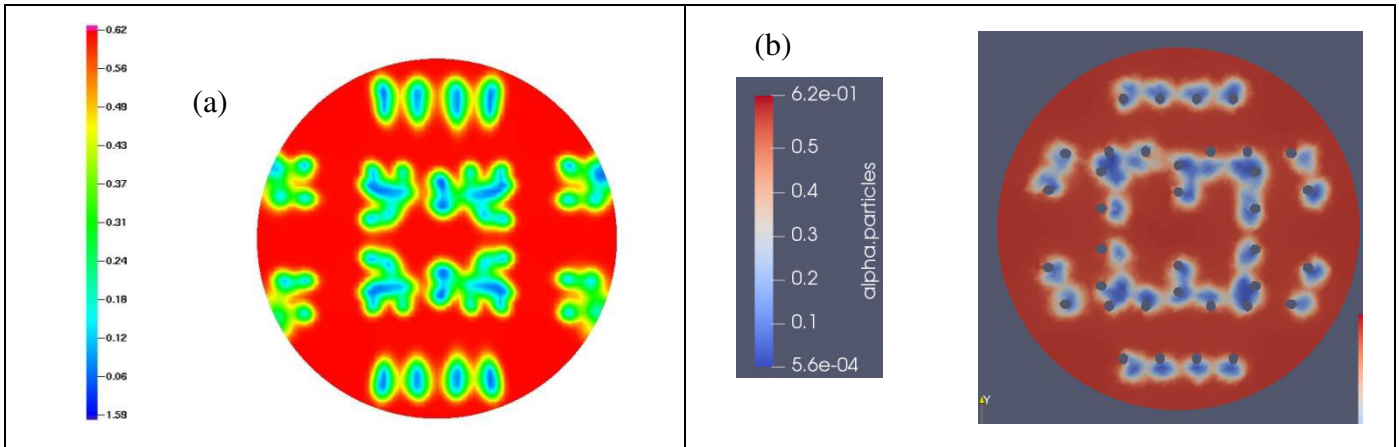


Figure V-45: Averaged solid volume fraction profile in a plane just above the nozzles tips
 (a) Barracuda VR[®] simulation ; (b) openFOAM simulation

One can see that Barracuda VR[®] gas distribution is more spread compared to openFOAM especially for the side nozzles. This comes from the fact that we assumed and imposed the jet penetration with Barracuda VR[®] which is not the case with openFOAM. However, we can consider that the difference between the two distributions is not significant and does not have an impact on the observations presented afterward.

The simulations steady state was considered when the pressure profile and particles entrainment reached stable values. For openFOAM simulations, steady state was reached at around 15 seconds of simulation time (as shown in Appendix 12), and simulations results presented were then averaged from 15 to 60 seconds of simulation time. Different results were obtained with the Barracuda VR[®] simulation. First it took about 25 to 30 seconds of simulation time to have a stable simulation pressure profile as shown in Appendix 12. Once steady state as considered was reached, no particle entrainment was obtained and finally large defluidized zone appeared during the course of the simulation. Figure V-46 and Figure V-47 present instantaneous solid volume fraction profiles in a plane passing through the column center at 10, 15 and 30 seconds of simulation time as well as the averaged solid volume fraction profile for respectively the Barracuda VR[®] and the openFOAM simulations.

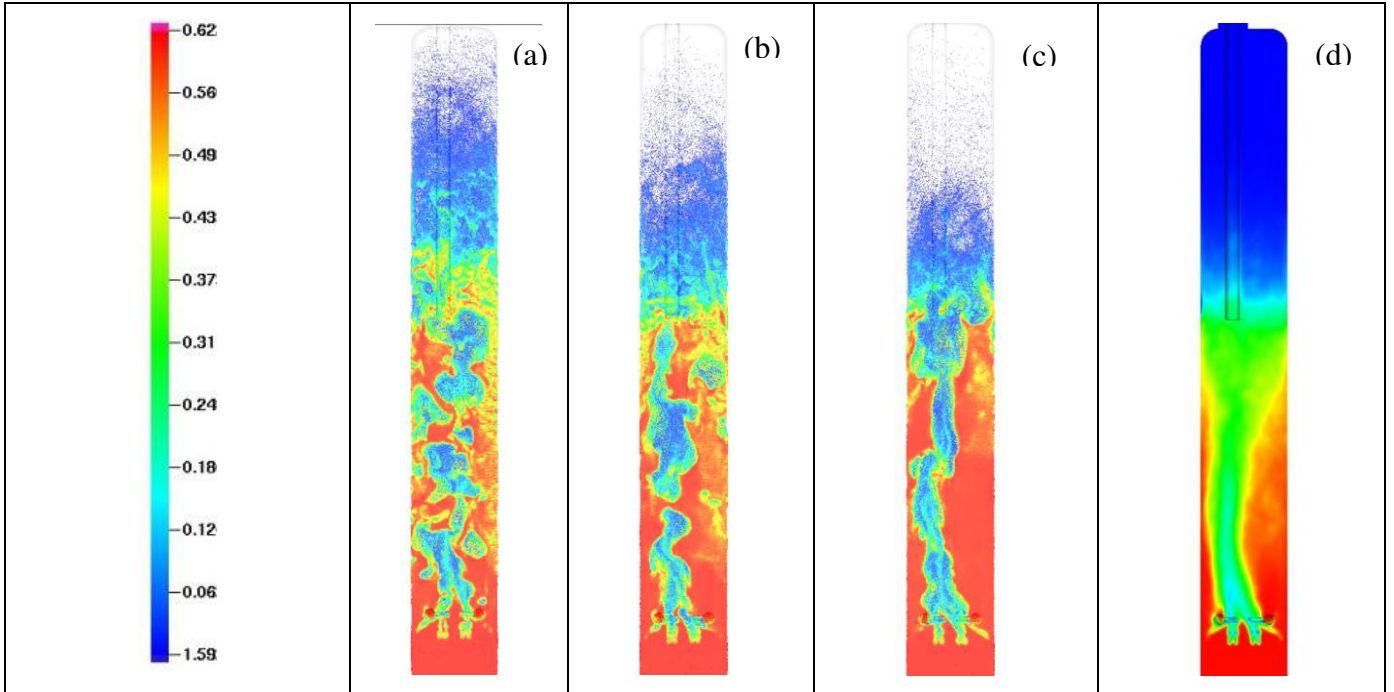


Figure V-46: Barracuda VR[®] simulation, gas velocity of 0.6 m/s
 a) instantaneous solid volume fraction at 10 seconds (b) instantaneous solid volume fraction at 15 seconds (c) instantaneous solid volume fraction at 30 seconds (d) averaged solid volume fraction

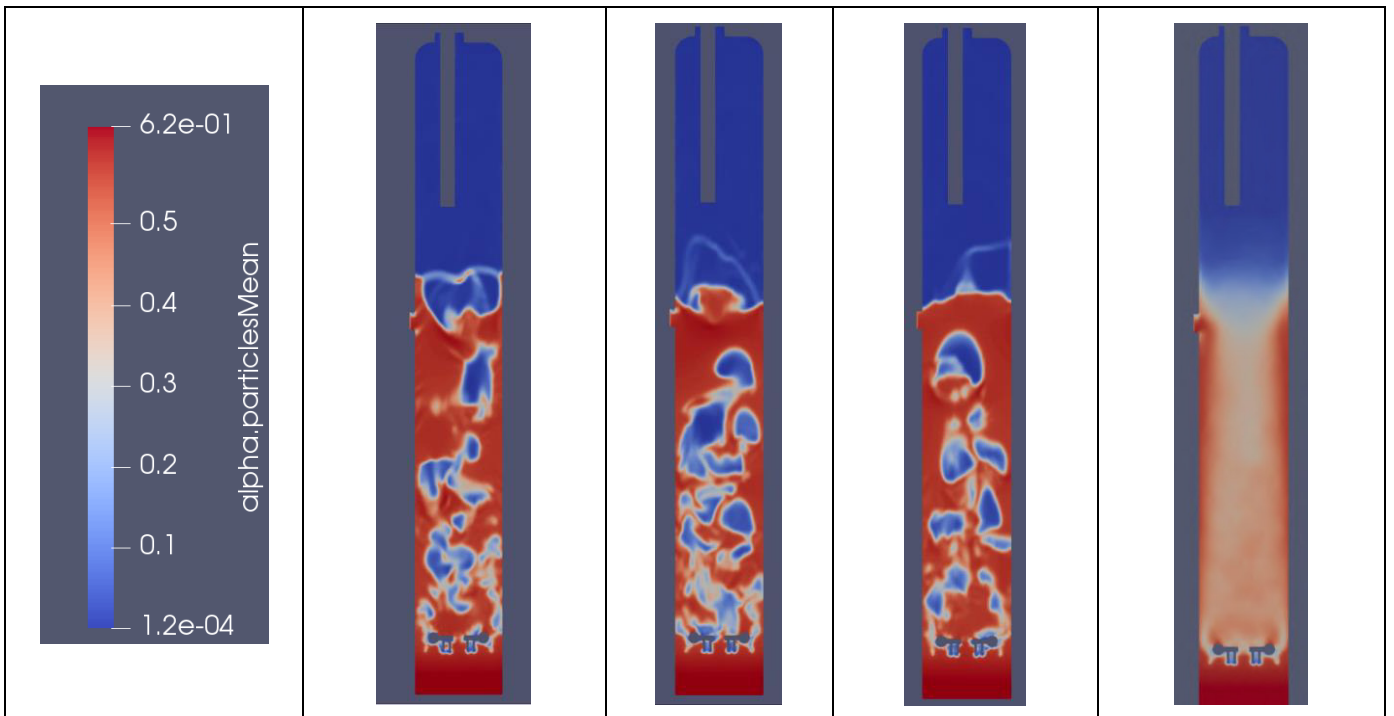


Figure V-47: OpenFOAM simulation, gas velocity of 0.6 m/s
 a) instantaneous solid volume fraction at 10 seconds (b) instantaneous solid volume fraction at 15 seconds (c) instantaneous solid volume fraction at 30 seconds (d) averaged solid volume fraction

One can clearly see the difference between the two simulations with steady conditions and similar instantaneous solid volume fraction profiles for openFOAM and with the creation of defluidized zones in the course of the simulation with gas by-passing the bed for Barracuda VR[®]. Figure V-48, Figure V-49

and Table V-27 presents respectively the experimental and simulations bed pressure profiles, the simulations average solid volume fraction profiles at a height of 1.5 meter above the distributor and the comparison between experimental and simulations data.

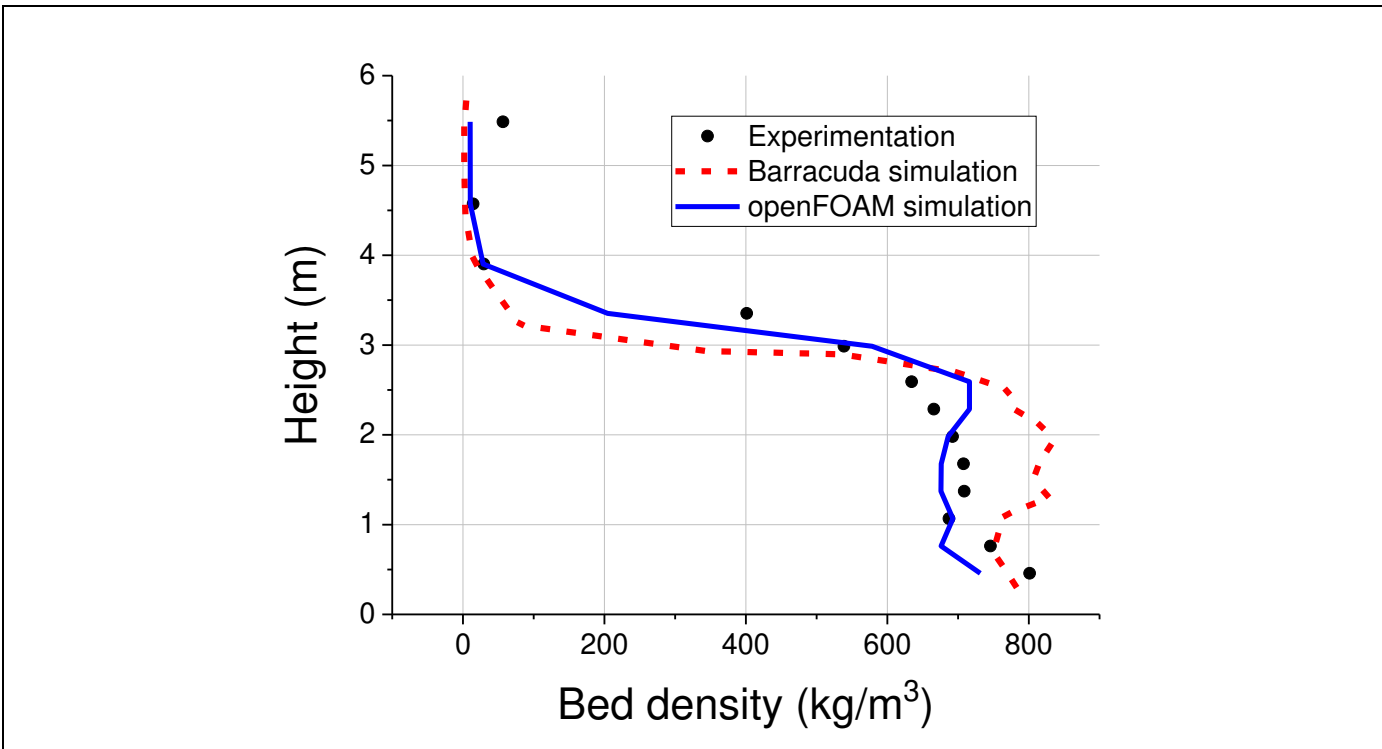


Figure V-48: Bed density profile from experiment and simulations

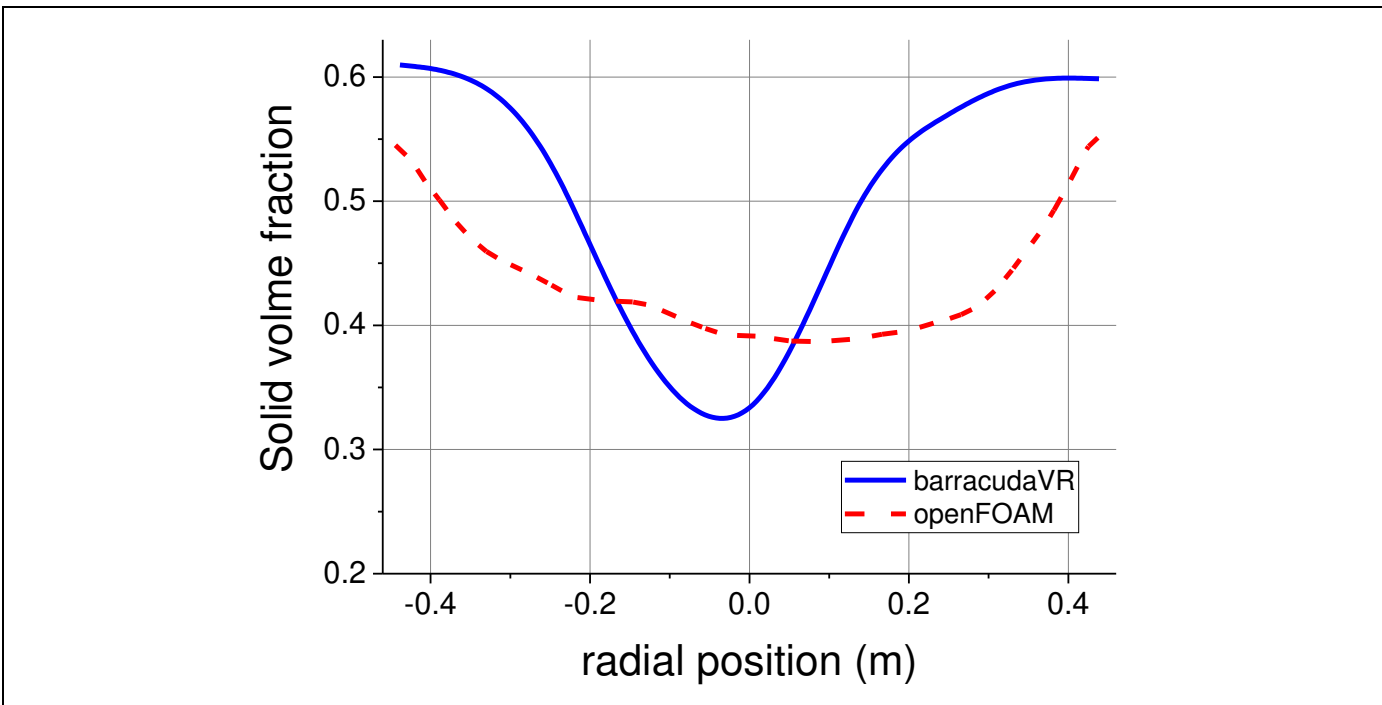


Figure V-49: Averaged solid volume fraction profiles from simulation at a height of 1.5 meter above the distributor

Table V-27 : Comparison between experimentation and simulations for the bed density

	Experimental	Barracuda VR [®] simulation	OpenFOAM simulation
Bed density (kg/m ³) (relative error with experimental)	706	777 (10%)	684 (2.8%)
Entrainment (kg/m ² /s)	1.21	0	5.8

Different remarks can be pointed out:

- First, the Barracuda VR[®] simulations overestimate by 10% the density and no entrainment is predicted.
- Second the openFOAM simulation predicts with accuracy the bed density while entrainment rate is highly overestimated with a factor 5 between experiment and simulation data.
- Third, the openFOAM solid volume fraction profile is symmetrical and similar to what was observed for the 20 cm fluidized bed experiment n°1 simulation while the Barracuda VR[®] profile clearly shows a gas-pass in the center of the bed. An experimental measurement is however necessary to fully validate this profile.

Barracuda VR[®] simulation results are considered unsatisfactory for different reasons:

- First, no entrainment is predicted while entrainment was observed for the 20 cm fluidized bed simulations at the same conditions. Experimentally, an entrainment of 1.21 kg/m/s was observed.
- Despite a good gas distribution (Figure V-45 shows that the gas distribution at the column bottom is more spread for BarracudaVR[®] simulation), gas ends-up by-passing the bed with large defluidization zone created within the bed which does not fit with openFOAM simulation. It also important to add that the same simulation was also performed in partnership with the Fluid Mechanic Institute of Toulouse (IMFT) using their code NEPTUNE_CFD and their filtered drag approach. This code also uses an Euler/Euler KTGF approach, one can refer to [165] for more details. In this simulation, the distributor nozzles are not represented and the gas is injected through the distributor squared central pipe. Results similar to the OpenFOAM simulation are obtained with elliptical solid volume profiles shape.
- The bed density is overestimated by 10% in the Barracuda VR[®] simulation. This is consistently linked with gas bypassing. It is interesting to point out that this overestimation can be considered as acceptable. Comparing only the overall bed density one could then consider the simulation as rather predictive. This point highlights the need of looking at the maximum number of experimental data to fully estimate the simulation predictions.

In general, the global “behavior” of the simulation is totally different from the 20 cm fluidized bed experiment n°1 where the Barracuda VR[®] parameters were optimized. This result can be attributed to the fact that these parameters are dependent of the scale and experimentation from which they were optimized and they cannot be used at larger scale with larger cell sizes. It is then interesting to remind that the 20 cm fluidized bed simulations with a coarse mesh having the same cell size than the one used for the 90 cm fluidized bed simulation already showed that simulations predictions were affected with Barracuda VR[®]. It would therefore be interesting to conduct simulations with the initial 20 cm fluidized

bed simulation cell size of 6mm. It however remains challenging with our current computational power with Barracuda VR[®].

Concerning openFOAM 90 cm fluidized bed simulation, results obtained are considered satisfactory with a global behavior similar to the results of the 20 cm fluidized bed simulation (symmetrical solid volume fraction and bed density well predicted). However, entrainment is highly overestimated at large scale. It was also overestimated for the 20 cm fluidized bed but not in the same proportion. This point is further investigated in the next simulations where the other operating conditions of the 90 fluidized bed experiments were simulated. However, due to the poor results obtained with Barracuda VR[®], **these other operating conditions simulations were carried out only with openFOAM.**

Finally concerning the comparison between both codes made from the 90 cm fluidized bed simulations, one can argue that we did not use the same boundary conditions for the gas distribution and that the comparison cannot directly be made. However, Figure V-45 clearly shows that at the level of the distributor, the gas distribution is better in the BarracudaVR[®] simulation. Therefore we considered that the bottom boundary conditions chosen for the BarracudaVR[®] simulation is not at the origin of the poor predictions obtained.

4.3 Other operating conditions

The other two operating conditions with a superficial gas velocity of 0.3 and 0.85 m/s where investigated in order to study the prediction trends of the openFOAM optimized parameters. The same boundary conditions were used with only the gas injection flowrate being modified to get the correct superficial velocity at the top.

In order to better predict the entrainment rate, two sets of representative diameters shown in Table V-28 were investigated to improve the drag model, defined originally in Table VI-8 in section VI.2.2. In the 2nd case, the solid volume fraction range for the smallest representative diameter is reduced from [0.02;0] to [0.01;0]. The purpose is to observe the influence of this minor modification on entrainment but also on the bed density predictions.

Table V-28 : Sets of representative diameter tested for the 90 cm fluidized bed experiments simulations

	Solid Volume fraction	Representative diameter
1st set default parameters	0.62 to 0.08	500
	0.08to 0.02	150 + multiplier
	0.02 to 0	75
2nd set	0.62 to 0.08	500
	0.08to 0.02	150 + multiplier
	0.01 to 0	75

The condition with a superficial gas velocity of 0.85 m/s was not simulated with the first set of representative diameters since the entrainment prediction with for the other condition was highly overestimated as shown below. Figure V-50 and Figure V-51 present respectively the average solid volume fraction and particle entrainment from experiments and simulations for the 90 cm and 20 cm fluidized beds.

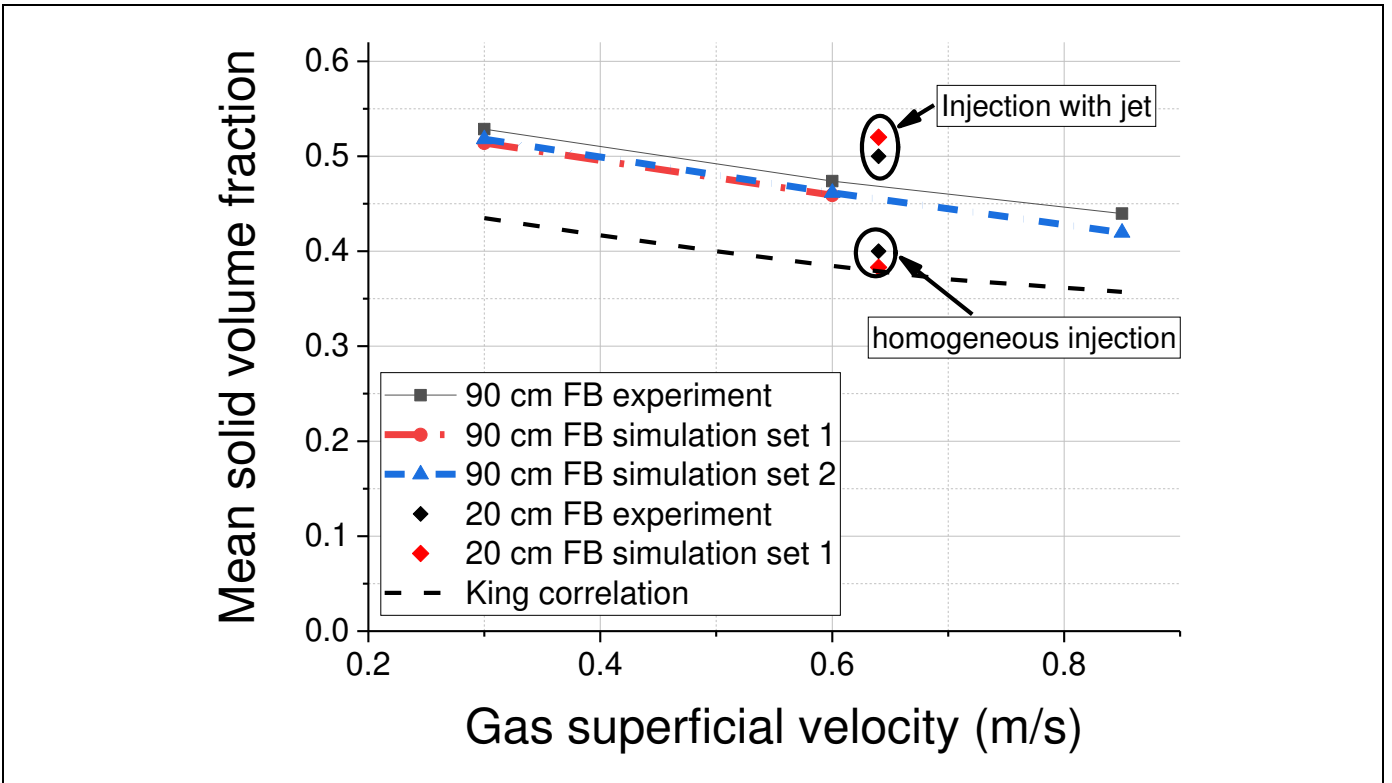


Figure V-50: Simulation and experimental overall bed densities, 90 cm fluidized bed experiments

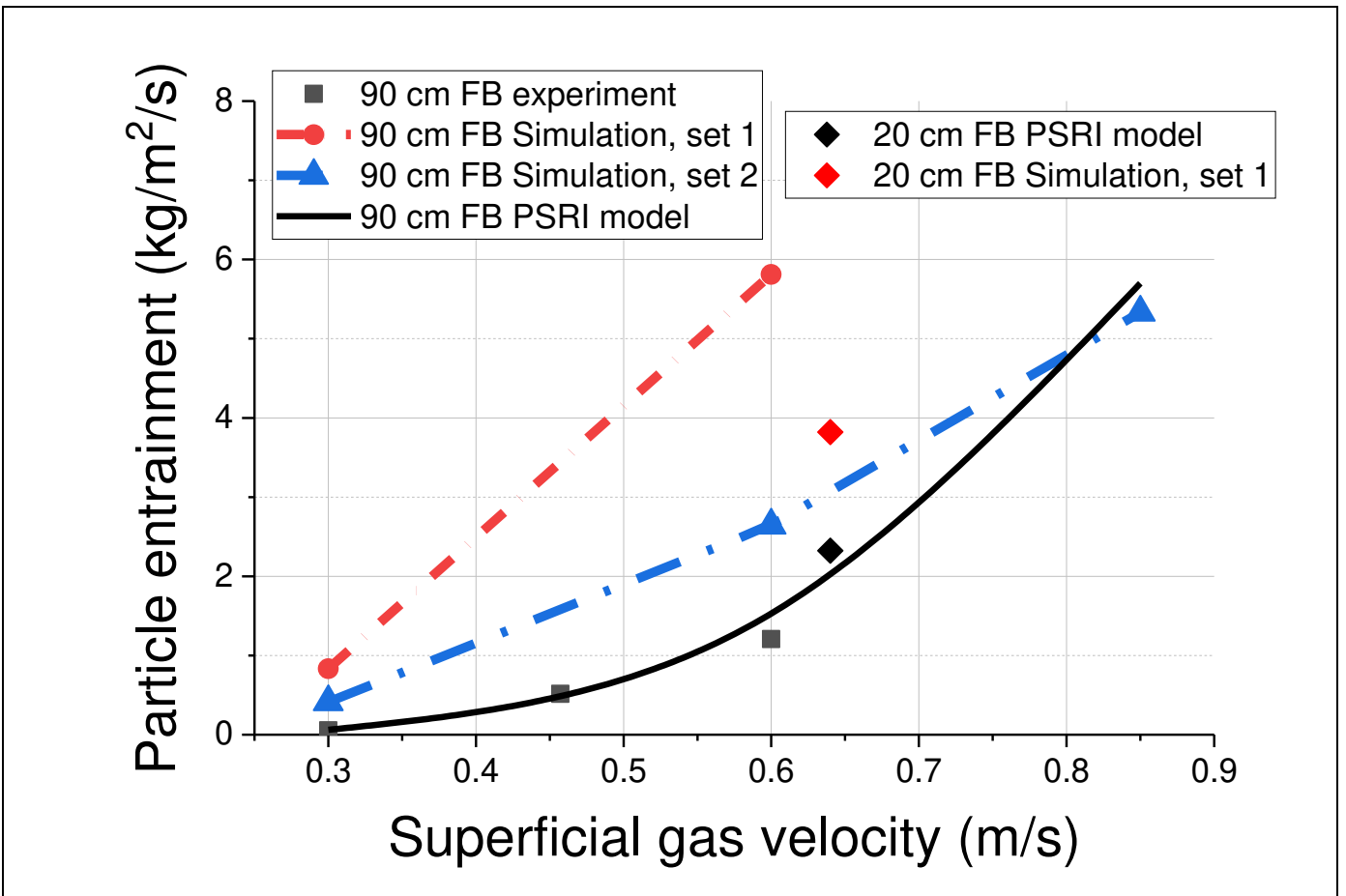


Figure V-51: Simulation and experimental particle entrainment, 90 cm fluidized bed experiments

Table V-29 presents the simulations and experimental data for the 90 cm fluidized bed.

Table V-29 : Simulations and experimental average solid volume fraction and entrainment rate

Superficial gas velocity (m/s)		Experimental	Set 1	Set 2
0.3	Solid volume fraction (relative error with experimentation)	0.53	0.51 (2.8%)	0.52 (2.0%)
	Entrainment (kg/m ² /s)	0.06	0.8	0.4
0.6	Solid volume fraction (relative error with experimentation)	0.47	0.46 (2.8%)	0.51 (2.5%)
	Entrainment (kg/m ² /s)	1.21	5.8	2.6
0.85	Solid volume fraction (relative error with experimentation)	0.44	-	0.42 (4.6%)
	Entrainment (kg/m ² /s)	-	-	5.3

Different points can be highlighted:

- First, the bed density trends and quantitative predictions are excellent with relative error lower than 5% for all 90 cm fluidized bed simulations. It is also interesting to notice that trends between the 20 cm and 90 cm fluidized bed are also captured which is also satisfying. As discussed in Chapter IV.3.1, the difference of experimental bed solid volume fraction between both experiments can be explained by scale and also distribution effects that are not taken into account in the King correlation indicated in Figure V-50. On the other hand, one can see that CFD managed in this case to predict the difference between experiments meaning that CFD captured somehow the scale and distribution effects.
- Concerning the entrainment for the 90 cm fluidized bed, results obtained are interesting. Indeed, the minor change of the solid volume fraction range for the smallest representative diameter in the drag model detailed description divided the entrainment predictions by 2. Entrainment rate is still overestimated for the lowest superficial velocity experiments but predicted values are closer to experimental data and the general trend over the full superficial velocity range experiments is rather well predicted. The most important remark concerning this point is that one can appreciate how entrainment predictions are sensitive and therefore difficult to model. Indeed, one can remember from the 20 cm fluidized bed simulations presented in Chapter V.2.2 that modifications in all classes of representative diameters affected the predicted entrainment rate. As discussed before, mesh size also affects entrainment calculation (see Table V-16 and Table V-24). Therefore predicting accurately entrainment remains more challenging than predicting bed hydrodynamics and density.
- Then concerning the diameter effect on entrainment, one can see when comparing the 90 cm and 20 cm fluidized bed simulations with the first set of representative diameter that a scale effect is predicted with lower entrainment rates for the smallest column. It should also be reminded that the PSRI model does not take into account a column diameter in its entrainment prediction above the TDH. It is therefore interesting for future work to measure experimentally entrainment at different scale to investigate this trend prediction.

Finally, Figure V-52 presents the experimental and simulation bed density profiles for the set n°2 if representative diameters. The profiles for the set n°1 can be found in Appendix 12.

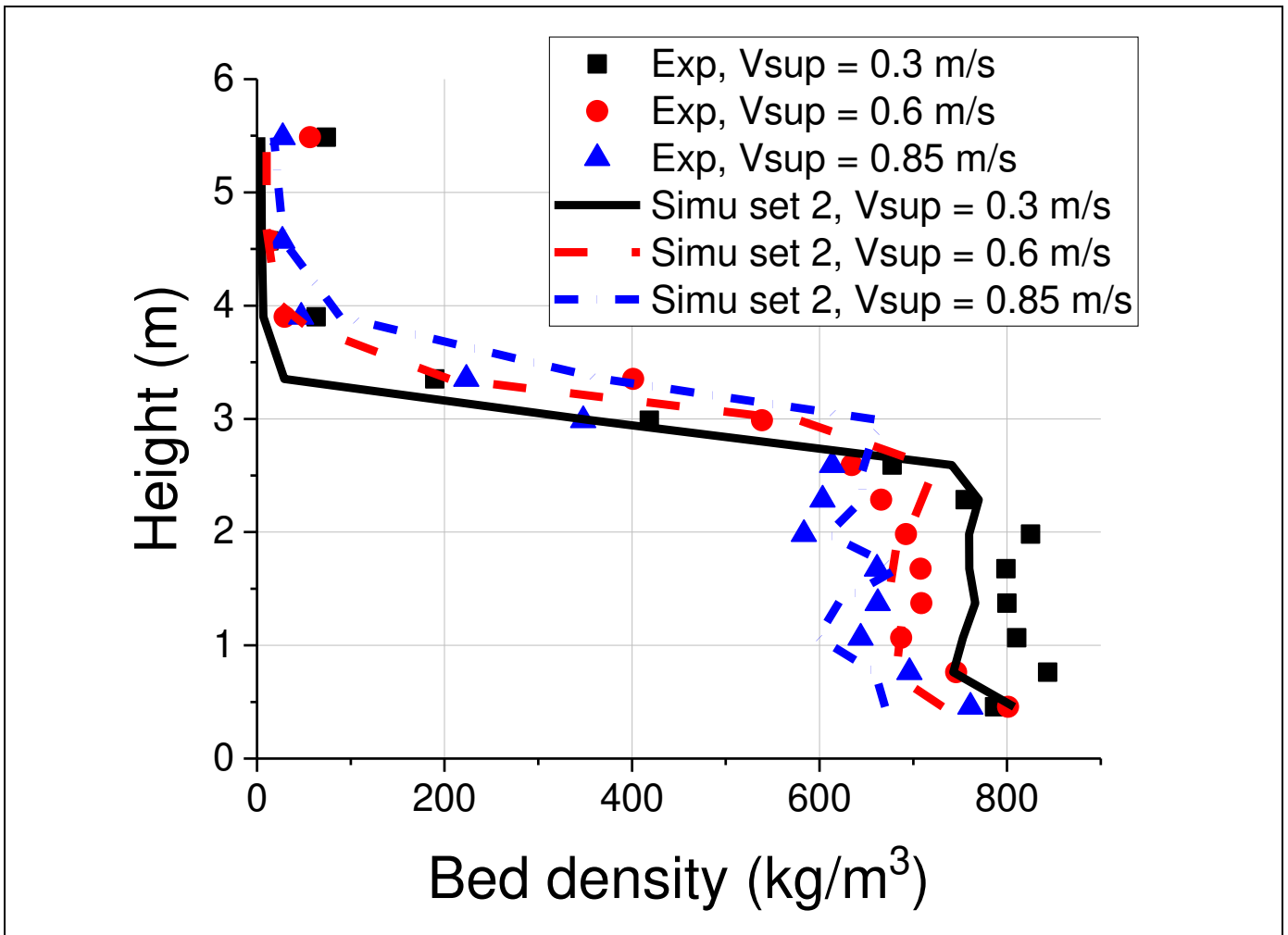


Figure V-52: Simulation and experimental bed density profiles, 90 cm fluidized bed experiments

The predicted pressure profiles are in good accordance with the experimental data with trends respected between the difference cases which confirm the results of the overall bed density. One can also notice a difference between experiments and simulation at the top of the bed, a problem of pressure experimental measurement is suspected at this position as explained in Chapter III.4.2.

4.4 Discussion

The first part of this chapter presented the comparison of openFOAM and Barracuda VR® simulations for the 90 cm fluidized bed experiment with a superficial gas velocity of 0.6 m/s. We can emphasize the following points:

- One could appreciate the difficulty of simulating accurately the bottom distributor at the bottom of the bed. Indeed the meshing method of Barracuda VR® does not allow to accurately describing the complex geometry and therefore assumptions had to be made related to the gas jet penetration and therefore the injected gas bed coverage. For future work, one could first simulate the nozzle jet penetration for a single nozzle and then integrate the result in the overall simulation. As shown in Figure V-45, the gas repartition close to the distributor between Barracuda VR® and openFOAM

simulations was slightly different it cannot clearly be the reason for the not satisfying behavior observed for the Barracuda VR[®] simulations.

- Second, the openFOAM simulations results were considered rather satisfactory with good bed density prediction even if the entrainment was overestimated (entrainment prediction was then revealed to be extremely sensitive to the representative diameters distribution). The main point is that openFOAM showed coherent predictions for the 20 cm fluidized bed simulations with refined and coarse mesh as well as for the 90 cm fluidized bed with the same cell size than the coarse mesh 20 cm fluidized bed simulation. By coherent prediction we mean that bed densities were well predicted and that solid volume fraction profiles were similar at both scale when for a homogeneous gas injection at the bottom.
- The same conclusions were not reached with Barracuda VR[®] simulations since results for the 90 cm fluidized bed simulation were considered unsatisfactory. No entrainment was obtained, large defluidized zone appeared in the bed with gas by-passing. A really important parameter to consider is the differences obtained along the simulation strategy developed. Indeed for Barracuda VR[®] simulations at small scale the bed density is well predicted and entrainment is observed when using optimized parameter on a refined mesh. Then it appeared that predicted results were affected when using large cells at small scale and finally results were not satisfactory at the large scale when using the same cell size. The simulation parameters used in Barracuda VR[®] are therefore considered not reliable for extrapolation at larger scales with large cell sizes. The result can be explained by the simple drag law modification carried out with the use of a multiplier. The multiplier of 0.4 is likely to be drag model, experiment, scale and approach dependent. One could also add that other parameters such as the simple particle interaction model could also be the cause of the particle accumulation observed in the Barracuda VR[®] simulation. Finally, it could also be interesting in the future with an improvement of computational power, to simulate the 90 cm fluidized bed with the 20 cm fluidized bed default mesh cell size of 6 mm in order to definitely conclude if the CFD scale-up issue is only connected to the cell size and cloud numbers.

Based on the openFOAM simulations of the 90 cm fluidized bed for different operating conditions, we can point out that:

- Satisfactory results were obtained in term of trends for the entrainment rate prediction and quantitative characterization for the bed density especially with the second set of representative diameter. Is also really important to point that trends between the 20 cm and 90 cm fluidized bed were also predicted showing that CFD captured the scale and distribution effects compared to the classic King correlation.
- The sensitivity of the entrainment prediction was demonstrated when changing the solid volume fraction range of the smallest representative diameter of 75 microns from [0.02;0] to [0.01;0]. Entrainment was decreased by a factor of 2 when using the second range, the value being still higher compared to experimental data, while bed hydrodynamics was not significantly affected. It is probably possible to “play” furthermore on this range to match better the experimental result and it could be done in future work. However, the model would probably be dependent on this experimental set of data and further validation should therefore be made by investigating entrainment with different column geometries and particle properties.

Finally, we can make the same remark already made for the 20 cm fluidized bed column simulation concerning the need of further experimental data to investigate the CFD predictions of the bed gas structure, particle velocity, gas and particle mixing. Figure V-53 presents an instantaneous solid volume

fraction profile for the simulation with a superficial gas velocity of 0.85 m/s. One can notice the creation of a large gas structure at the top of the bed that occupies almost the entire bed diameter. This type of structure is more characteristic of group B powder fluidized bed and could be attributed to the cluster approach we are using. Indeed as mentioned in the literature review, gas bubbles in Geldart group A powder fluidized bed tend to a maximum stable bubble size and large bubbles above 10 to 20 cm are not expected with FCC catalyst.

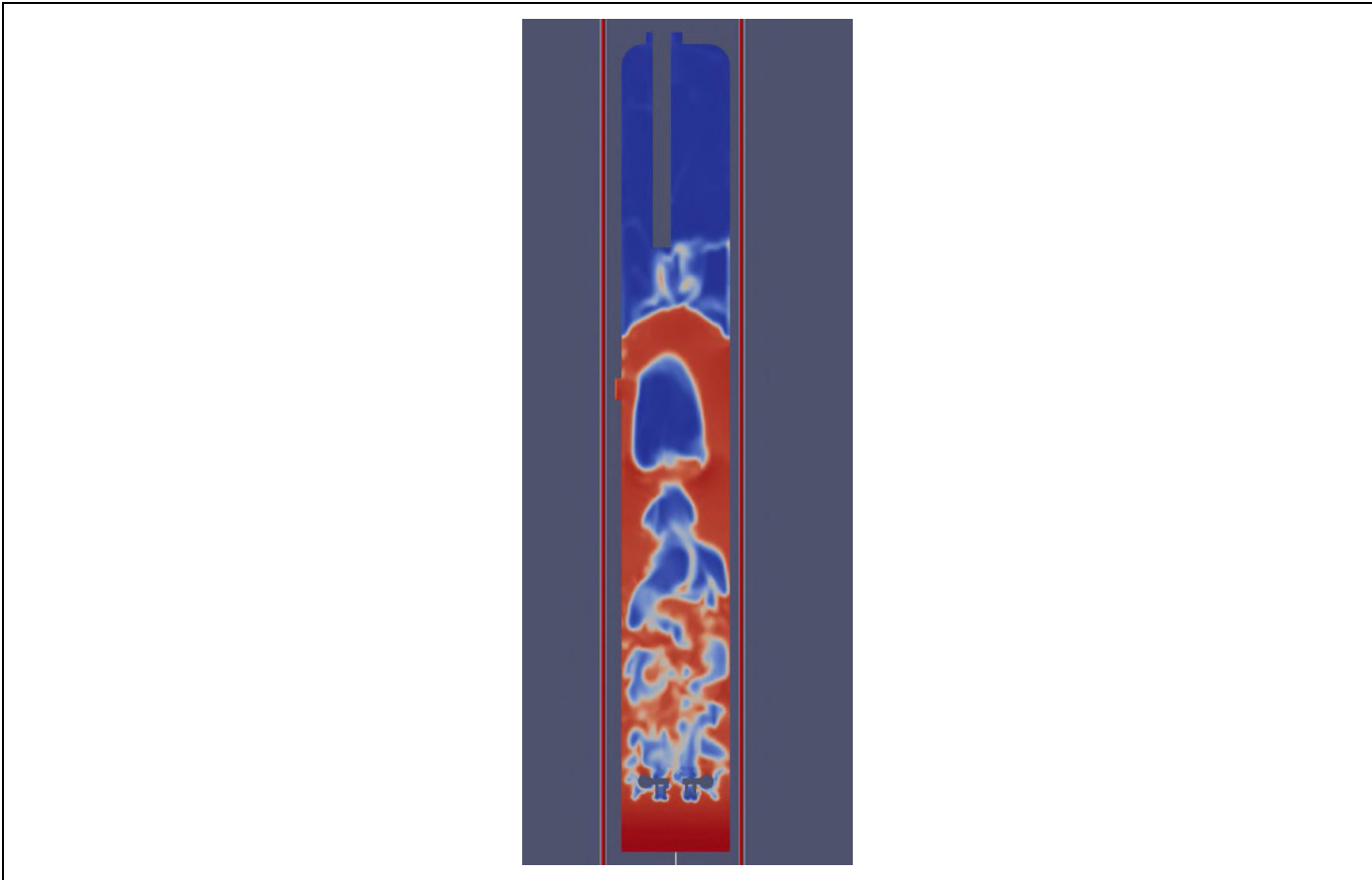


Figure V-53: Instantaneous solid volume fraction profile after 40 second of simulation time, OpenFOAM simulation , gas velocity of 0.85 m/s

This point shows that for fluidized bed CFD model development it is absolutely necessary to investigate many parameters at the same time with macro descriptors (bed density, entrainment, gas and particles mixing) but also local descriptors (volume fractions, bubble size and velocities). Indeed, our work was focused on bed density, local solid volume fraction and entrainment measurements but further work should also consider bubble characteristics. Our predictions were rather satisfactory. However what would happen if we now add the constraints of predicting smaller gas structure for all our previous simulations? It would be interesting in future work to investigate different ideas for this purpose. How to do this? We could for example modify the particles interaction model in order to have a more “viscous” solid phase. We could also add different particles classes to better represent the particles interactions. But then one could also wonder about the fact that smaller gas structure would have a lower velocity which would imply a lower bed density and the current model predictions would be affected. This would probably imply to modify again the drag model or other parameters. This highlights the fact that CFD model is dependent on the experimental data set that was used for development and validation, as it is always the case with modeling. It is therefore necessary to confront the model to many data characterizing

macro and local phenomena for both phases at different operating conditions in order to make the CFD model more physical and universal and less dependent on a specific set of data.

Finally, for future CFD model development and to investigate their extrapolation capability in fluidized beds, one could imagine two sets of experiments at different scales similar to the one presented in this PhD thesis. Then experimental data should be acquired on both experiments using the same particles and the same measuring techniques in order to remove the potential bias induced by the use of different experimental techniques and different particles. A wide range of operating conditions should be investigated from minimum fluidization regime to turbulent regime measuring macro descriptors such as bed density, entrainment, gas and particles mixing as well as local measurements such as local volume fractions, bubble size and velocities, particle velocity. This is however a considerable task and apart from modeling challenges, the challenge of measuring local characteristics should also be considered when confronting CFD and experimental results.

5 Fourth simulation strategy step: CFD code prediction at larger scale and different operating conditions (change of fluidization regime)

The study presented so far allowed investigating the extrapolation of CFD codes predictions for fluidized beds with simulations of experiments at different scales, different superficial velocities from 0.30 to 0.85 m/s and with different gas distribution configurations. The study clearly shows that, despite the two CFD codes using different approaches had similar good predictions for a given experiment at small scale, very different results were obtained when changing scale of experiments. Clearly, the simulations performed at a larger scale with openFOAM and the Euler/Euler KTGF represented much better the experiments that were considered.

In a last step presented in this chapter, we investigate the CFD predictions for experiments conducted with the same kind of solid materials (FCC equilibrium catalyst) but in a different fluidization regime characterized by very different operating conditions compared from the ones where the code parameters have been set. Indeed, the drag law models that have been used so far were adjusted on turbulent beds experiments. In a turbulent fluidized bed, hydrodynamics mostly relies on superficial gas velocity in the range of 0.3 to 1-1.3 m/s for FCC catalyst. A dense phase is observed and solid circulation is limited to entrainment which relies mostly on superficial velocity in the bed. Then in the transport regime, all particles are yet transported and hydrodynamics relies on gas superficial velocity, but also on solid flowrate (or mass flux). Since there is more gas flowing, the flow is therefore more dilute. Particles flow faster and take time to accelerate which results in axial and radial flow developments. One can then wonder if the model already tuned will apply in the transport regime or if it is operating condition dependent.

Figure V-54 presents the fourth and last step of the simulation strategy. It consists in simulating the riser experiments presented in Chapter IV.4. In these experiments the superficial velocity for transporting particles is in the order of 7 to 8 m/s which are well above the velocity used in the turbulent bed experiments. **Only openFOAM code predictions were investigated since we considered that the parameters chosen for barracudaVR failed for the simulation strategy third step.**

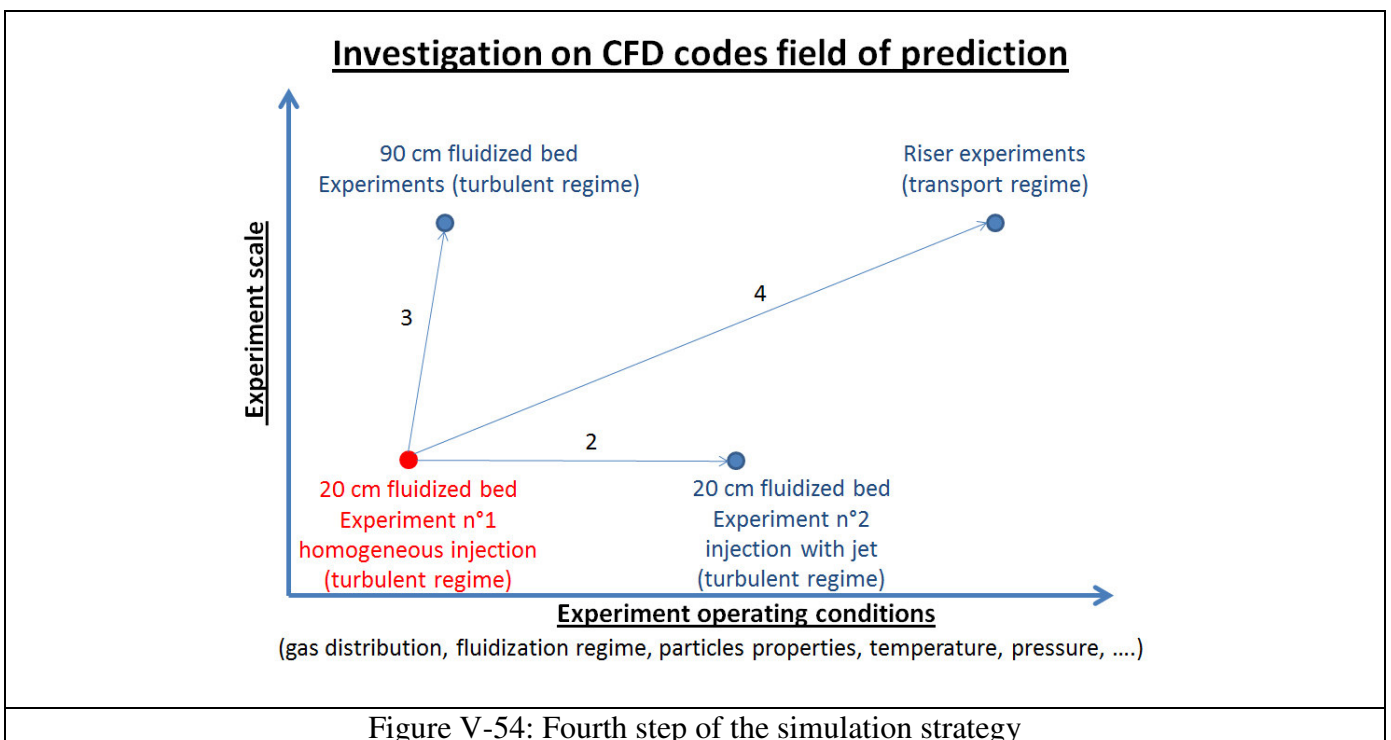


Figure V-54: Fourth step of the simulation strategy

5.1 Geometry, meshing and boundary conditions.

Figure V-55 presents the geometry considered and the boundary conditions applied.

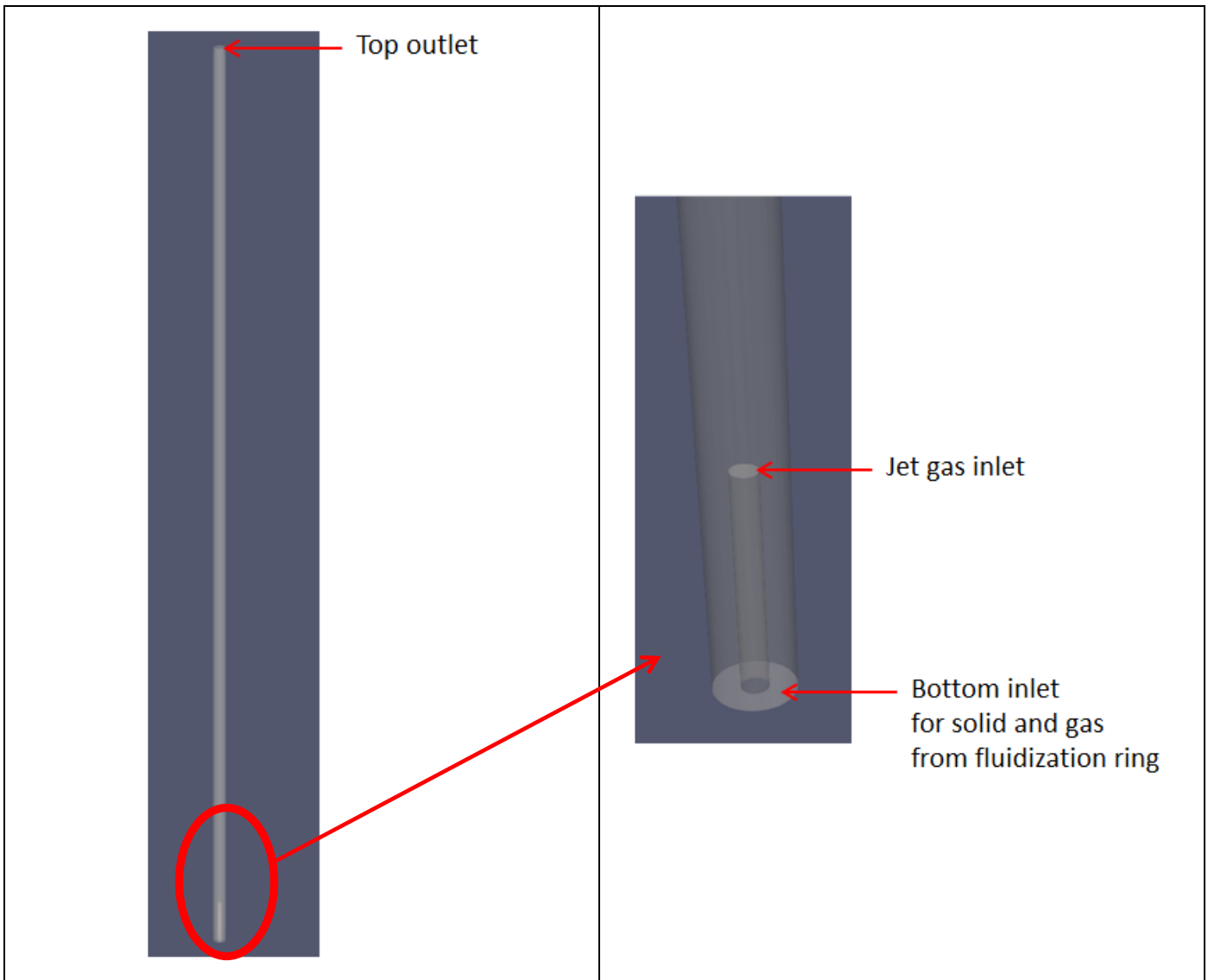


Figure V-55: openFOAM simulation, geometry and boundary conditions for riser simulation

Different remarks can be pointed out:

- First, the geometry is simplified compared to the real riser configuration presented in Chapter III.5.1. Indeed, the solid side inlet and outlet are not represented, the riser is considered straight. The main reason for this simplification is to have a regular mesh of hexahedral cells over the entire riser length as shown in Figure V-56 which presents the hexahedral cells in a vertical riser section. Most of the cells have a size of 18 mm to be consistent with the 90 cm fluidized bed simulations. However we chose from the beginning to refine the mesh close to the walls in order to better capture the physical phenomena at the wall as carried out in the work of Abdulkadir et al. [166]. The cells close to the wall have a size of about 3 mm.

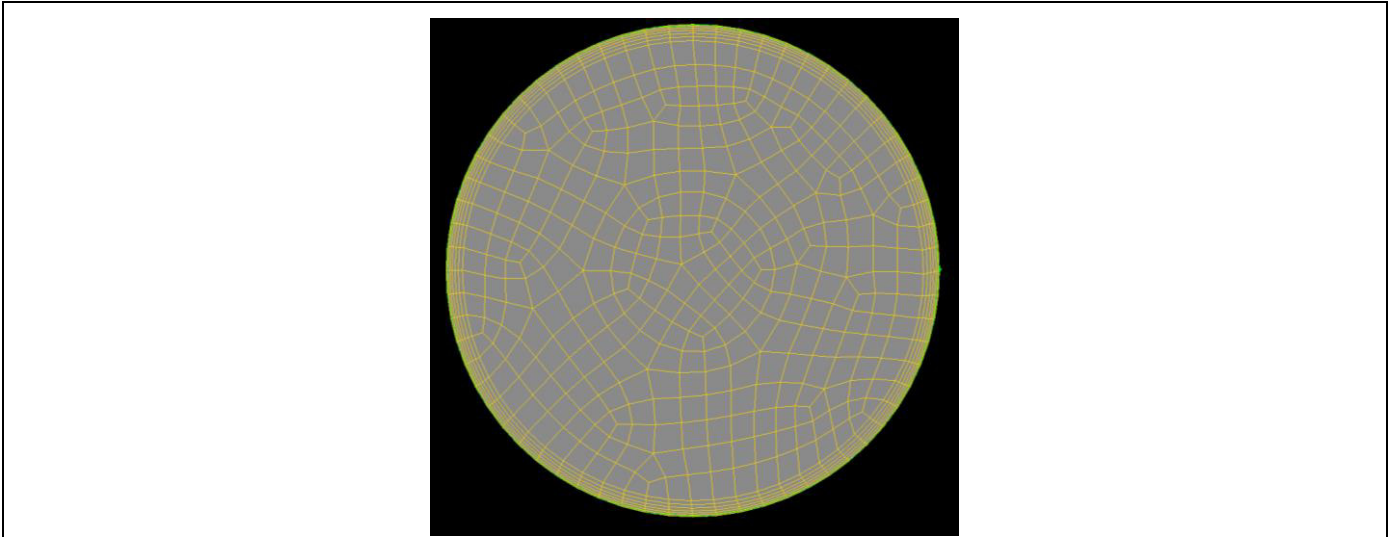


Figure V-56: openFOAM simulation , Mesh in a vertical riser section

- The second remark concerns the fact that the riser blind-T termination device is not taken into account in these simulations. For these reasons, pressure profiles will be compared only over a length of 15 meters in order to remove the termination device effects observed on the experimental profiles shown in Figure IV-8.
- Finally, we assume that the solid distribution is uniform through the bottom inlet surface while the solid arrives through a side inlet in the experiment. However, the solid inlet is located in the dense phase below the main gas injection point and we therefore take the assumption that the flow at the bottom of the riser behaves at a uniform moving fluidized bed. Pseudo-isokinetic profiles in different directions could be carried out in the future close to the main gas injection point to confirm the flow homogeneity.

The boundary conditions used are presented below. For more details on can refer to Appendix 13.

- Bottom inlet:
 - o Gas phase: Velocity imposed corresponding to the gas flowrate from the fluidization ring.
 - o Solid phase: Velocity imposed corresponding to the solid flowrate. The solid and gas volume fraction are imposed to have a mixture density of 700 kg/m^3 as measured on the cold flow pilot for all solid circulations.
- Jet gas inlet: Velocity imposed corresponding to the flowrate to have the superficial velocity at the top minus the flowrate from the ring.
- Top outlet: Pressure of 110 000 Pa abs imposed.

Table V-30 presents the riser simulations parameters.

Table V-30 : Riser simulations parameters

Mesh size	930 000
Cell size above distributor	3 to 18 mm
Particle density (kg/m ³)	1 450
Particle size distribution	Representative diameters from Table V-13 second set
Drag law	Gidaspow
Pressure at top boundary condition (Pa abs)	110 000
Air temperature (°C)	20
simulation time step (s)	1.10 ⁻⁴
Simulation time (s)	50

Simulations are considered at steady state when the pressure profile reaches stable values and that the solid mass in the system is constant which means that the solid going in is equal to the one going out. For more details one can go to Appendix 13. Steady state was always reached after 30 seconds of simulation time, results presented are therefore averaged from 30 seconds to 50 seconds of simulation time.

5.2 Base case

The experiment with the highest flux of 220 kg/m²/s was considered as the base case. Figure V-57 and Figure V-58 present the simulation and experimental data for respectively the riser pressure profile and mean solid local flux at the same height than the experimental isokinetic sampling. The mean local solid flux in each mesh cells is obtained from Equation 89.

$Flux_{MEAN} = \rho_S \times U_{s,z_MEAN} \times \alpha_{s_MEAN}$	Equation 89
---	-------------

Where: $Flux_{MEAN}$ is the local flux in the mesh cell (kg/m²/s)
 ρ_S is the particle density equals to 1450 kg/m³
 U_{s,z_MEAN} is the mean axial velocity in the mesh cell (m/s)
 α_{s_MEAN} is the mesh cell solid volume fraction

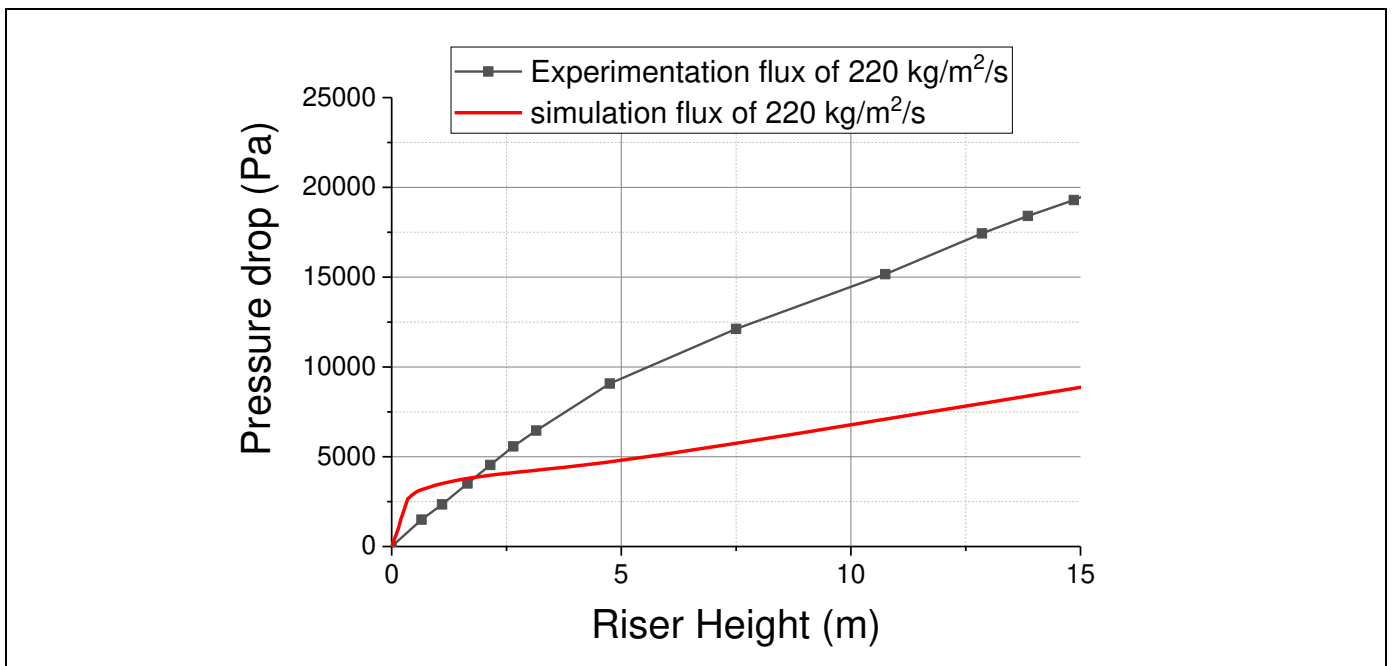


Figure V-57: openFOAM simulation and experimental pressure profile

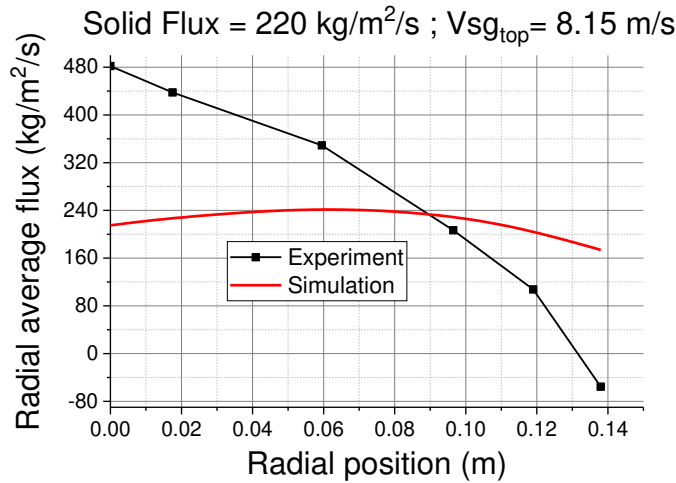


Figure V-58: openFOAM simulation and experimental local flux profile, drag model from 90 cm fluidized bed simulations

First, it is clear that the simulation failed predicting the pressure profile with a total pressure drop over 15 meters underestimated by 54%. Moreover, one can notice from Figure V-58 that the local solid volume fraction is flat which is in accordance with the fact that no solid recirculation was observed on the walls in the simulation. However, the experimental radial profile of local mass flux is very different, with very high flux (twice the average) toward the riser axis and light down flow at the wall.

Figure V-59 and Figure V-60 present respectively the mean velocity profile and an instantaneous and averaged solid volume fraction profile at the riser bottom.

Solid Flux of 220 kg/m²/s ; Vsg = 8.15 m/s

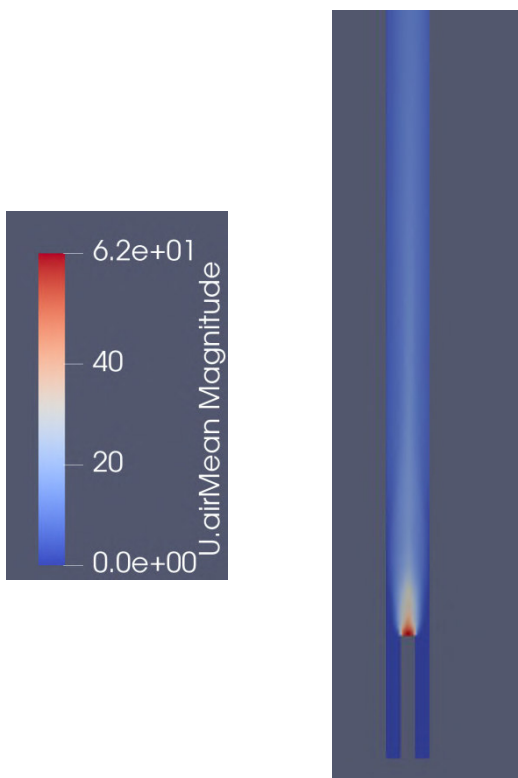


Figure V-59: openFOAM simulation mean velocity profile

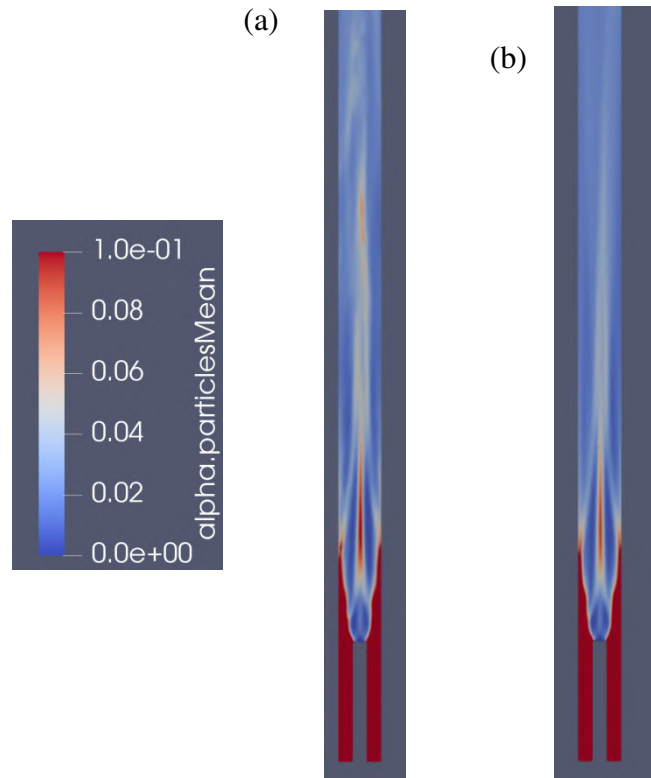
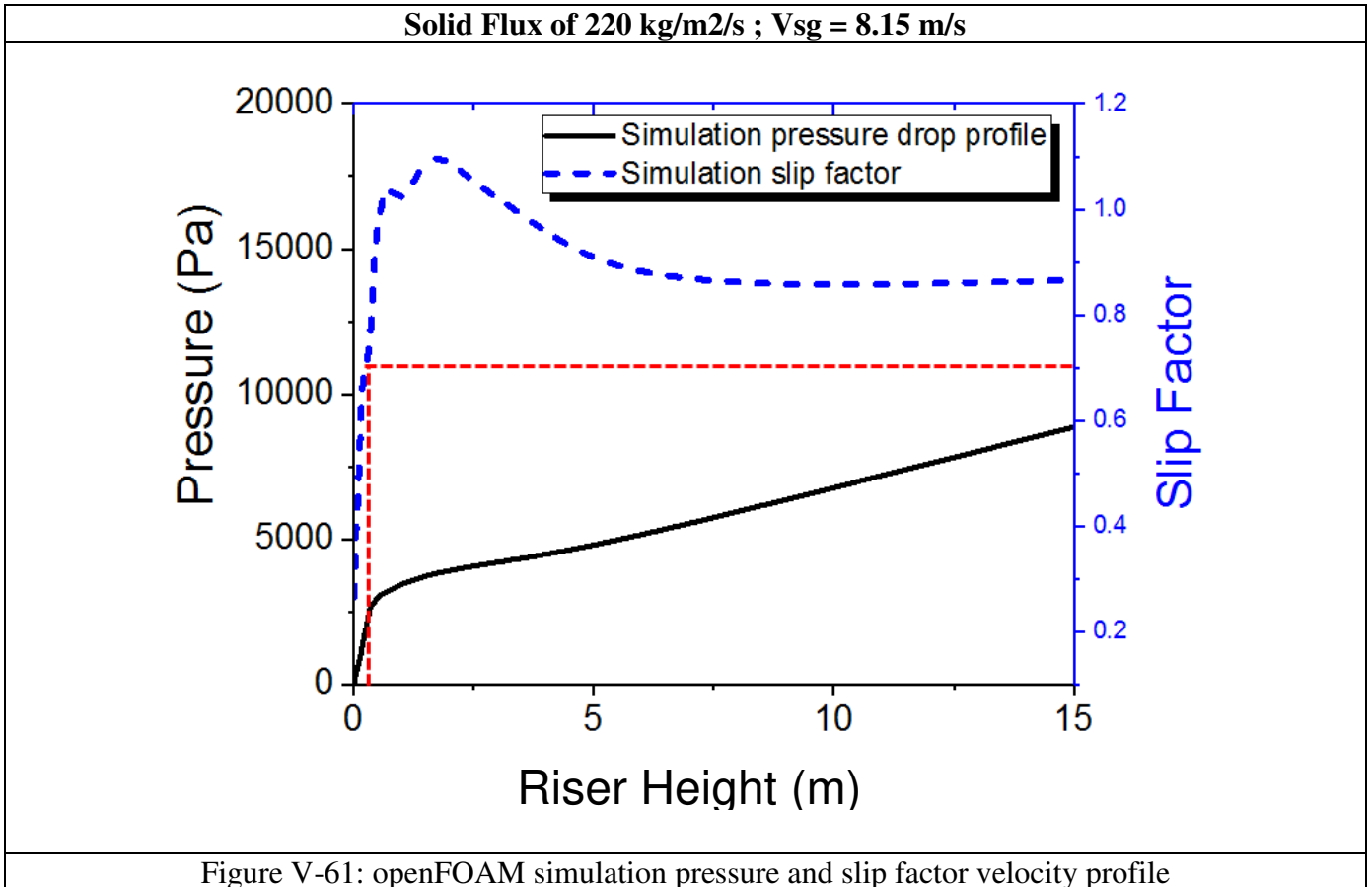


Figure V-60: openFOAM Simulation solid volume fraction (a) Instantaneous profile ; (b) averaged profile

One can see from Figure V-59 that gas velocity at the jet outlet is high with values in the order of 60 m/s. Then, from Figure V-60 we can see that there is no difference between instantaneous and averaged solid volume fraction profiles. The flow simulated therefore reaches a stable steady state really quickly after the gas injection with a fast acceleration of the particles. Finally, Figure V-61 presents the simulation pressure profile and the mean slip factor profile in the column center. The slip is defined in this case as the ratio of the solid mean velocity over the gas mean velocity.



It is interesting to notice that there is a really fast acceleration of the particles at the bottom of the riser which also corresponds to a fast increase of the pressure drop profile. From these observations, we concluded that the drag between the gas and the solid was overestimated at the riser bottom where high gas velocity in the range of 60 m/s occurs.

The first conclusion from this simulation is that the code parameters applied with a rather good success for the prediction of the fluidized bed experimental data investigated do not give good predictions for the riser experimental data. From the riser simulation results presented above, the drag overestimation at the riser bottom with high gas velocity is suspected. This results should be put in perspective with the fact that the predictions of the CFD model developed so far (including the approach, boundary conditions, mesh cell size, particle interaction and turbulence model) is dependent on the operating conditions simulated which means that some physical phenomena such as the drag or the particles/wall interactions are not well modeled through the entire range of operating conditions investigated and mesh cell size used.

5.3 Investigation on the drag model for the riser simulation

We then decided to investigate further if the drag overestimation could be a reason that explains the results presented in the previous chapter. It is important to point out that the study presented here is simply prospective with the aim to investigate a simple drag modification and better understand key modeling aspects based on numerical results.

From Figure V-61 showing the pressure and slip factor profiles, we first pointed out the fast pressure increase corresponding to the particle acceleration zone where the slip factor also increases dramatically. As shown with the red dotted lines in Figure V-61, the fast pressure increase stops for a slip factor value at around 0.7. We then decided to implement a modification in the model to reduce the drag in this fast pressure increase zone. For this purpose, we proposed the following modification:

$K_{d_modified_riser} = K_{d_fluidized_bed} * (Slip\ factor)^n \text{ if } Slip\ factor < 0.7$ $K_{d_modified_riser} = A * K_{d_fluidized_bed} \text{ if } Slip\ factor > 0.7$ $Slip\ factor = \frac{V_{particles}}{V_{gas}}$	Equation 90
---	-------------

When: $K_{d_fluidized_bed}$ is the drag model developed from the fluidized bed simulations, see Table V-13
 n and A are tuning factors.

With this modification, we first want to reduce the drag in the acceleration zone in function of the slip factor for slip factors values inferior to 0.7. The tuning factor n being superior to 1, drag will be reduced more for lowest slip velocity factor values occurring at the riser bottom. Then the decrease of drag is supposed to reduce momentum transfer between gas and particles and therefore particle acceleration will be slower. For slip factors higher than 0.7 where particles are accelerated in Figure V-61, the idea is to implement a simple drag modification with a multiplier. It is important to mention that this drag correlation modification is implemented to investigate the effect of the drag reduction and it is based only on numerical observations.

We then adjusted the tuning factor n and A in order to best match the experimental pressure profile based only on the simulation with a solid flux of 220 kg/m²/s. Figure V-62 presents the pressure profiles obtained for different values combinations of n and A

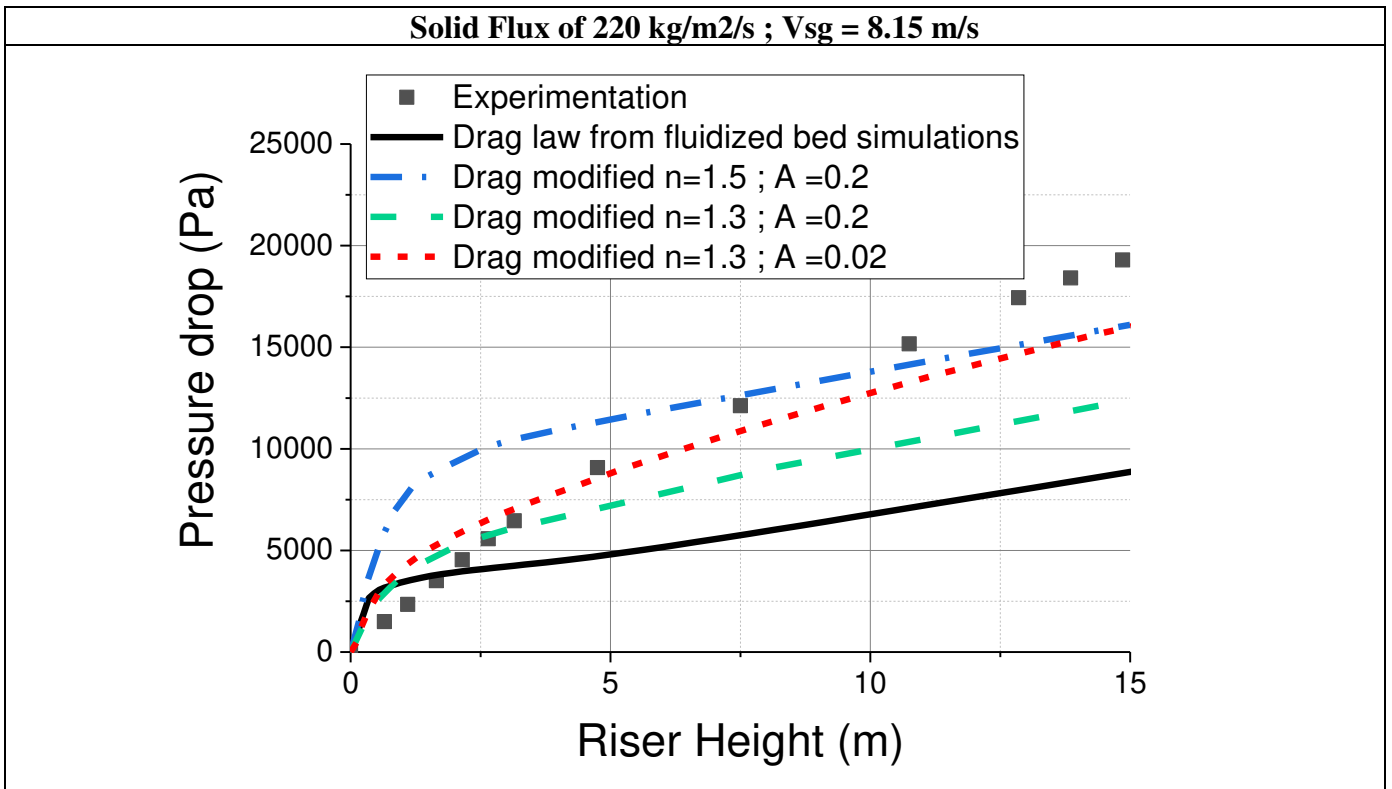


Figure V-62: openFOAM simulation and experimental pressure profiles

It is interesting to notice that a high “n” value overestimates the pressure drop in the bottom riser acceleration zone while a high “A” value underestimates the pressure increase in the upper riser accelerated zone. The best match was obtained with n equals to 1.3 and A equals to 0.02. Table V-31 presents the comparison between this simulation and the experimental data. The pressure increase versus height in the riser accelerated zone was calculated from a riser height of 5 meters.

Table V-31 : Riser simulations versus experimental data, solid flux of 220 kg/m²/s, V_{sg} = 8.15 m/s

	Experiment	Simulation with drag from fluidized bed simulations	Simulation with drag modified n=1.3 and A =0.02
Total pressure drop at 15 meters (Pa)	19 295	8 920 (53.7%)	16 000 (17%)
Pressure increase in the accelerated zone (Pa/m)	1 010	347 (65%)	750 (25.7%)

One can see that the simulation with the modified drag model has much better predictions than the default drag from the fluidized bed simulations. Relative errors compared with experiments remain however rather high with the total pressure drop underestimated by 17% and the pressure increase in the accelerated zone underestimated by 26%. At this point, these results were considered satisfactory since the main goal was to investigate the drag modification effect without reaching a perfect match with experimental data.

Figure V-63 presents the mean slip factor values in the column center for the default simulation with the drag law from fluidized bed simulations and for the riser modified drag model with n equals to 1.3 and A equals to 0.02. Figure V-64 and Figure V-65 present respectively the mean slip factor profile and the instantaneous slip factor profile for the simulation with the modified drag model.

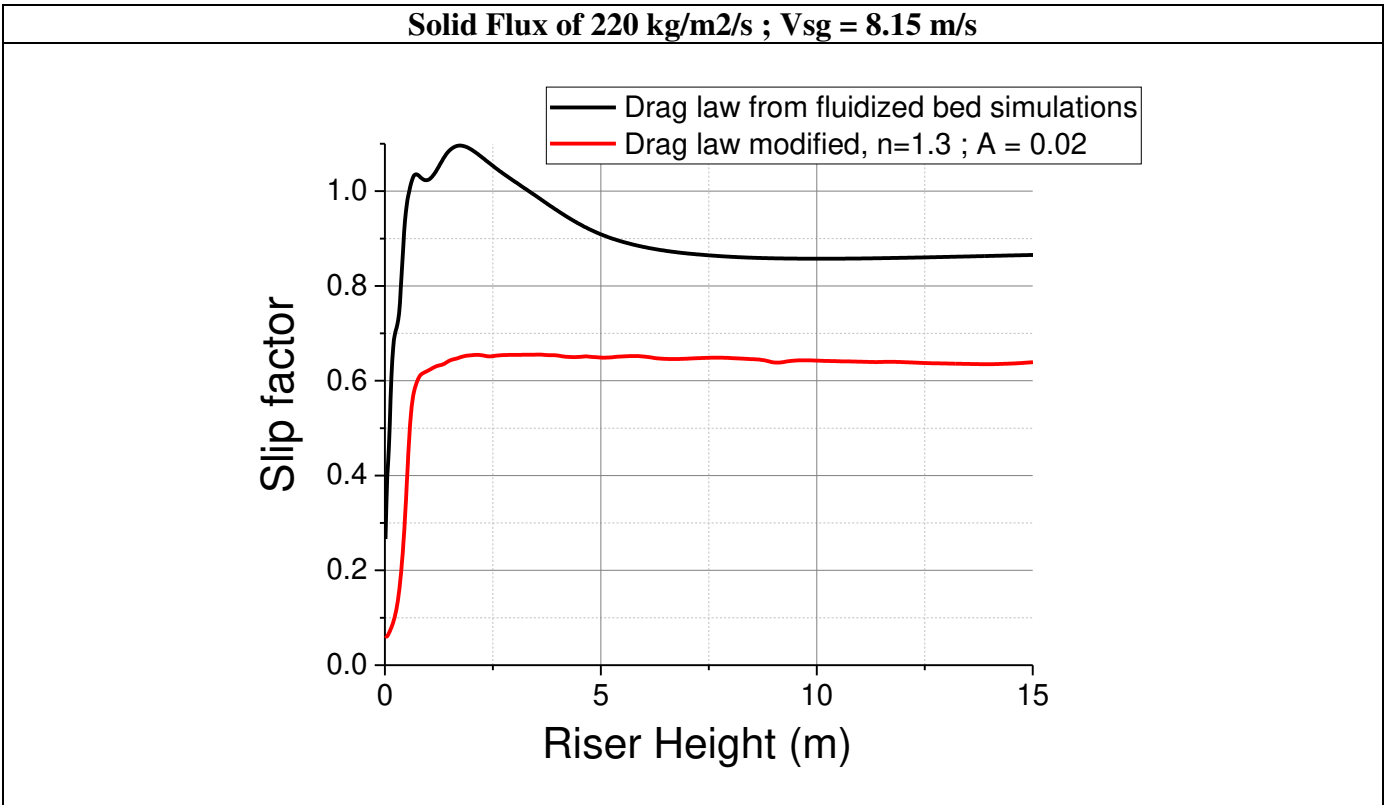


Figure V-63: openFOAM simulations, Slip factor profiles

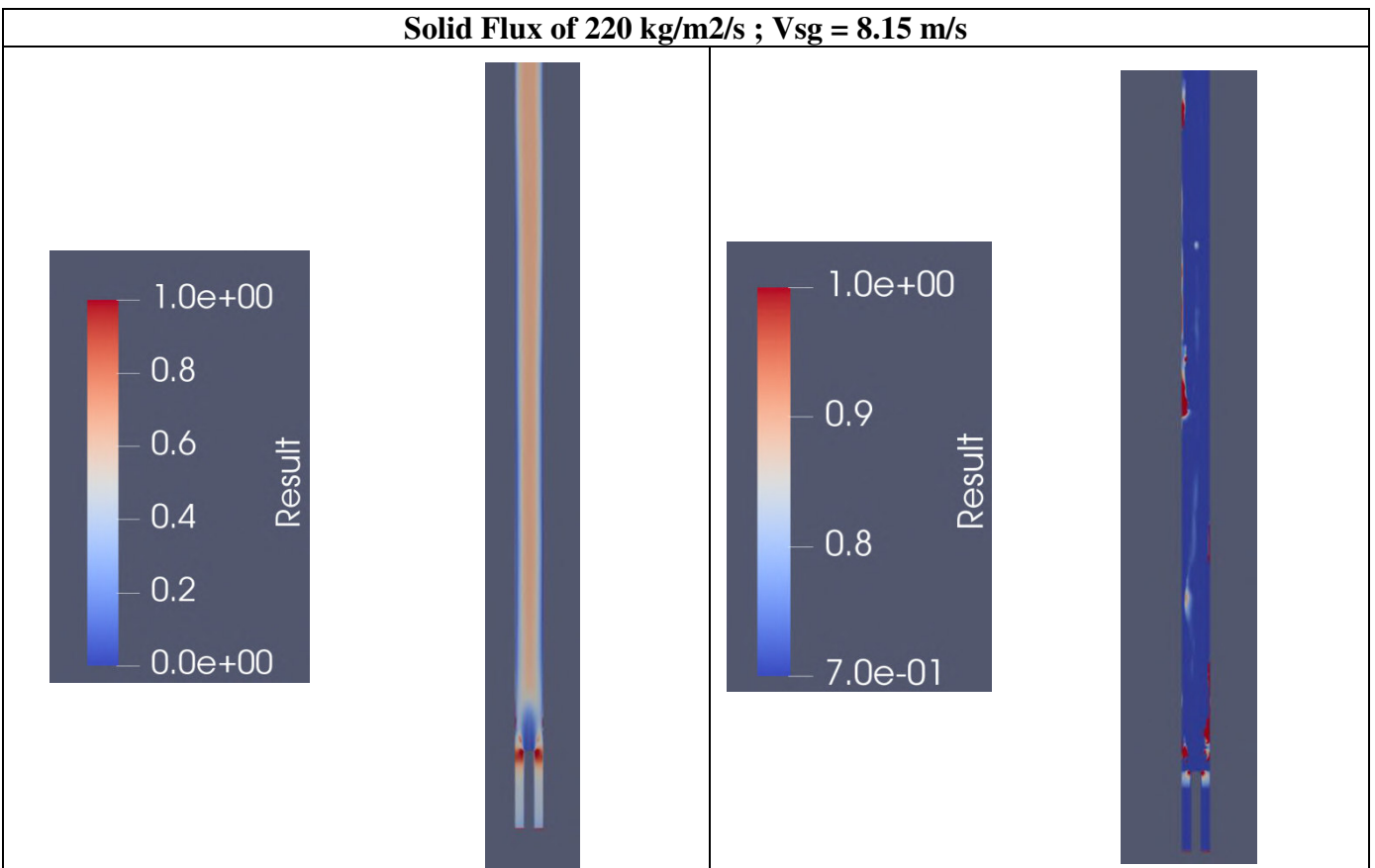


Figure V-64: openFOAM simulation Mean slip factor profile

Figure V-65: OpenFOAM, Instantaneous slip factor profile, focus on values above 0.7

Different remarks can be pointed out:

- First in Figure V-63 the mean slip factor increases sharply at the riser bottom, this sharp increase corresponding to the riser acceleration zone. The mean slip factor then reaches a stable value around 0.64 as shown in Figure V-63 and Figure V-64, this value being lower than the transition value of 0.7 set in the drag model. However, when looking at the instantaneous slip factor profile on Figure V-65, one can notice values higher than 0.7. It is finally worth pointing out that the Patience correlation presented in Equation 22 gives a lower mean slip factor value of 0.46.
- Second, it is interesting to look at the instantaneous slip factor profile at a given time in Figure V-65 which focuses on values higher than 0.7. One can see that slip factor values above 0.7 are mostly located close to the walls. As a reminder, a drag multiplier of 0.02 is used for slip factor values above 0.7 as shown in Equation 90. Therefore, this low multiplier value reduces drastically the drag close to the wall which allows having particles negative velocity and particles recirculation at the wall as shown in Figure V-67 which present the zones where the solid volume fraction is higher than 0.1 with solid negative velocities. One can also see from Figure V-66 which presents the instantaneous and average solid volume fraction profiles that unsteady structures are obtained with higher solid volume fractions at the wall.

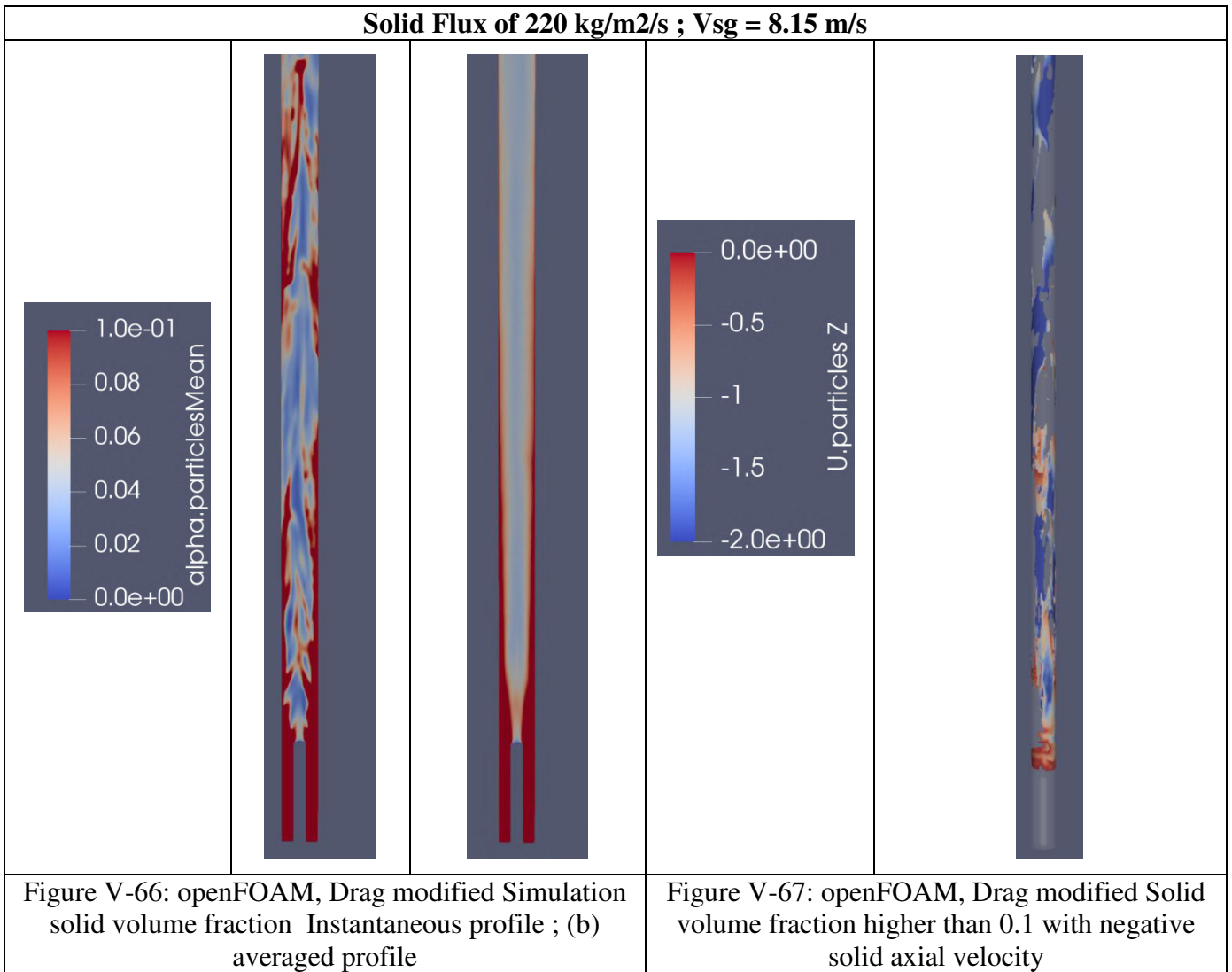
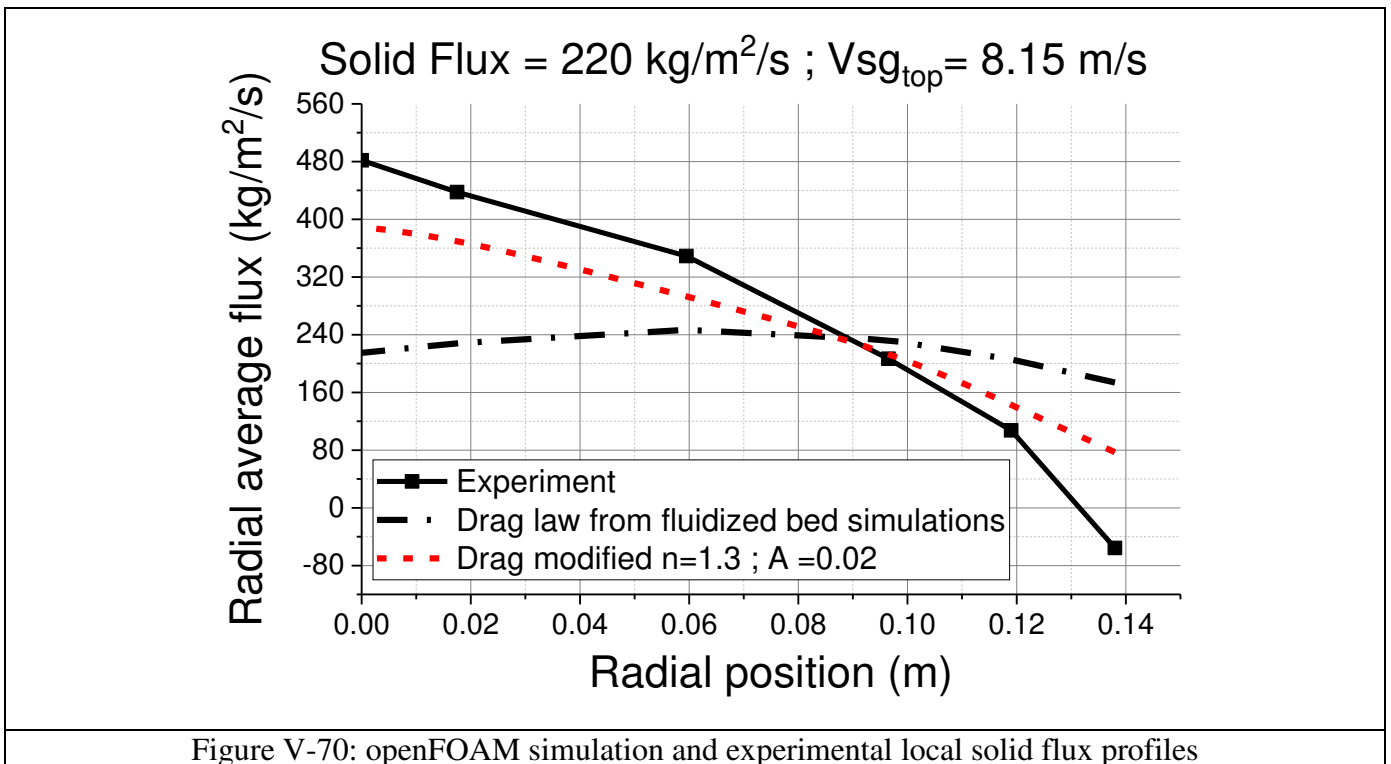
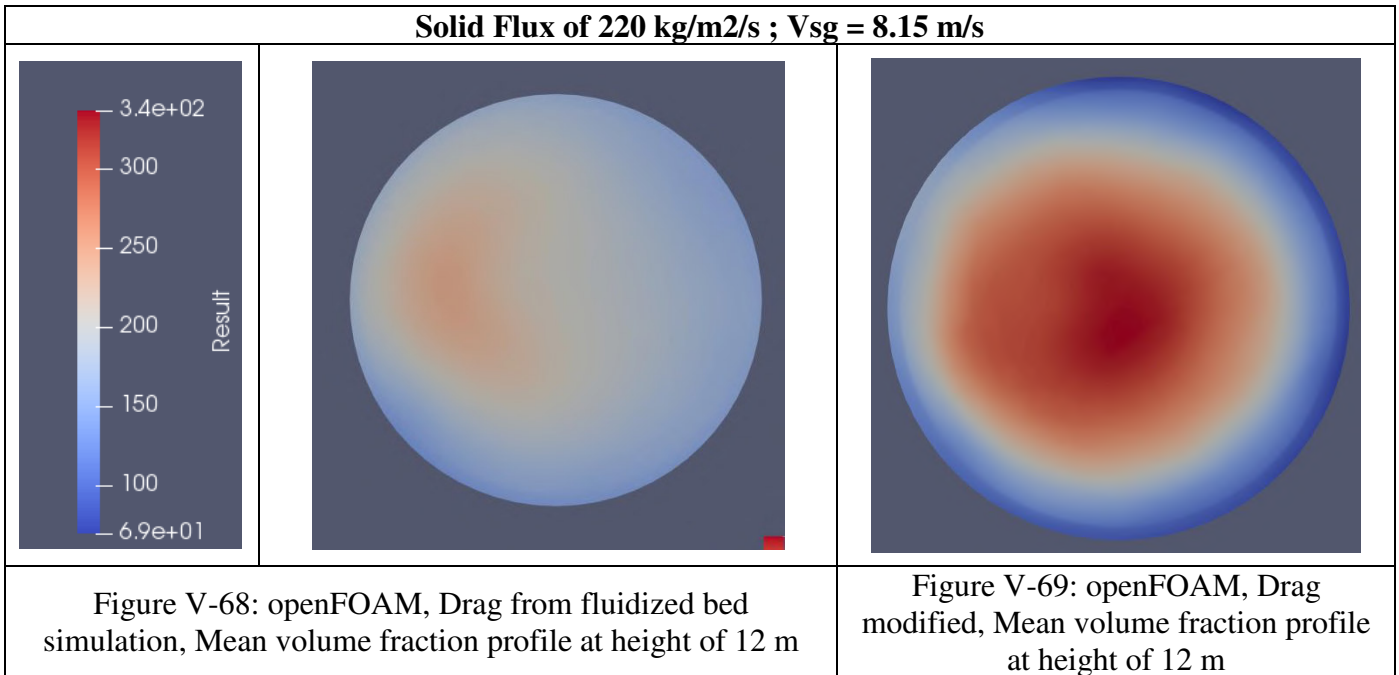


Figure V-68 and Figure V-69 present the local flux profiles for respectively the default drag from the fluidized bed simulation and the simulation with the riser modified drag. Figure V-70 presents the comparison between experimental and simulated local mass flux profiles.



One can see that the simulation with the modified drag predicts better the local flux profile shape with lower fluxes data close to the wall. This can be explained by the observations made earlier with the particles recirculation and the higher solid volume fraction at the riser wall when implementing the drag modification (one can refer to Appendix 13 to look at the mean volume fraction profiles at the height of 12 meters). However, one can notice that the experimental local flux close to the wall remains lower with

negative values indicating that the particles recirculation at the wall remains underestimated in the simulation.

The two other experiments with a flux of respectively 162 kg/m²/s and 77 kg/m²/s were then simulated using the modified drag model (as defined in Equation 90) Figure V-71 presents the comparison between experiments and simulations of the riser pressure profiles. Table V-32 shows the comparison of the experiments and simulations data of the total riser pressure drop and the pressure increase in the accelerated zone. The pressure profiles simulated fit the experiments reasonably well. Other simulations information can be found in Appendix 13. It should be noticed that the simulated local mass flux profiles obtained at this stage are not as symmetrical as the one obtained for the 220 kg/m²/s flux simulation (shown in Figure V-69). More work is needed to investigate this issue with two parameters to be investigated one being to average simulations over a longer duration since experimental results were also acquired on a longer duration as shown in Table III-12, the second parameter being the influence of the drag model parameters at the riser wall where solid concentration varies around the drag model transition solid volume fractions (see Table V-13).

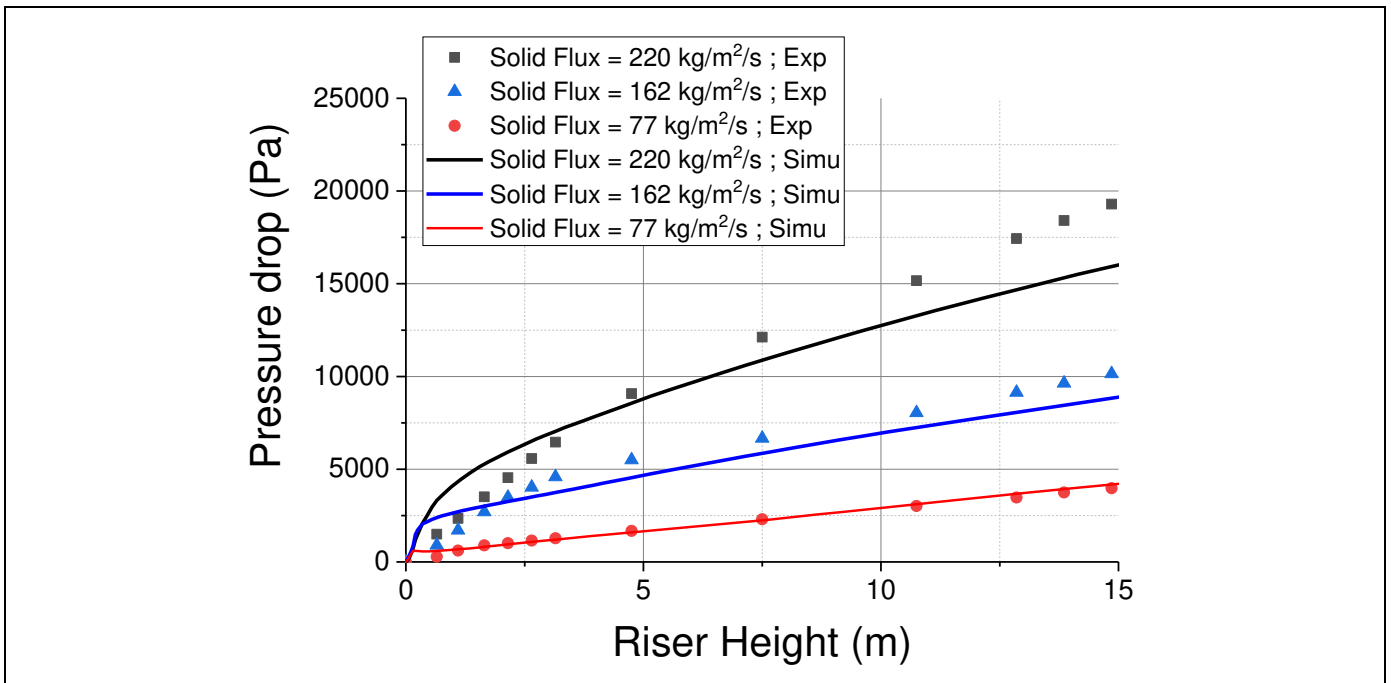


Figure V-71: Simulation and experimental pressure profiles for all fluxes

Table V-32 : Riser simulations versus experimental data for all fluxes

	Total pressure drop Experiment (Pa)	Total pressure drop Simulation (Pa)	Pressure increase in accelerated zone Experiment (Pa/m)	Pressure increase in accelerated zone Simulation (Pa/m)
Flux of 220 kg/m ² /s	19 295	16 000 (17%)	1 010	750 (25.7%)
Flux of 162 kg/m ² /s	10 146	8 900 (12.3%)	453	432 ((4.6%)
Flux of 77 kg/m ² /s	4 000	4 200 (4%)	224	250 (11.6%)

One can notice that pressure profile trend between experiments is rather well captured with better predictions for the lower flux experiments. The acceleration zone trend between experiments is also captured as well as the difference of slopes in the fully developed flow zone.

5.4 Discussions

The last part of this study consisted first in simulating the riser experiment with a flux of 220 kg/m²/s using the same CFD model developed from the turbulent fluidized bed simulations. The simulation failed predicting the experimental data investigated with a total pressure drop underestimated by 54% and a flat local flux profile. The overestimation of the drag was pointed out as a reason for these wrong predictions. This result shows that, based on the initial tuning, the CFD model and in particular the drag model developed from the turbulent fluidized bed simulation is operating condition dependent. It therefore means that some physical phenomena are not well captured or taken into account by the current CFD model with the mesh cell size used. This is the main conclusion of this last simulation strategy step. Indeed, in previous chapters we first demonstrated that CFD code extrapolation capacity between different scales with similar operating conditions should be investigated with care on experiments at different scales with relevant experimental data. We now point out that the operating condition prediction range should also be investigated to at least define the limit of the model, the final and idealistic goal being to develop a CFD model that can be predictive on the full operating condition range from minimum of fluidization regime to transport regime. One can wonder if this objective is realistic, our work at least shows that it is possible to adjust simulation parameters to predict experiments within the same fluidization regime at different scales.

In a second part, it was decided to investigate a drag model modification in order to reduce the particles acceleration observed in the first simulation. The slip factor was determined as the main flow characteristic and was then used to modify the drag model correlation. Different points can be discussed related to this study:

- First, the study presented is prospective. The main purpose was to show the effect of the drag reduction on the CFD code predictions but further work is absolutely necessary to well represent flows in transport regime. In particular, the investigation of the mesh cell size influence and other parameters such as wall functions and turbulence models need to be explored. A similar strategy with simulations of riser experiments at different scale should also be carried out to assess the extrapolation capacity of the CFD model developed.
- Second, it is interesting to notice that once the drag model was modified by tuning one riser pressure drop profile, we could then observe that the solid local flux profile was also better predicted and that other operating condition predictions were also satisfying. The modification carried out therefore has a certain physical meaning.
- Third, it was shown that the slip factor higher than 0.7 are observed mostly close to the walls. As a reminder, the drag model proposed reduces drastically the drag with a multiplier of 0.02. This drag modification then generates particle negative velocity and therefore particles recirculation which is in good accordance with experimental results. However, one can wonder about the physical meaning of this drag modification. Is drag coefficient really reduced at the wall or is the gas velocity at the wall overestimated which then force us to reduce the drag in order to have particle recirculation? This type of question shows again the difficulty to get intrinsic physical phenomenon characterization in a complex multiphase flow system. It also shows that other phenomena such as turbulence model and wall functions should absolutely be investigated in future work.

- Then, one can wonder if the approach using characteristic diameter for the drag model could also have been applied on the riser simulations using bigger diameter values. This question first highlights the need to get more precise local experimental characterization, it also highlights that different approaches might be used to get the same CFD predictions for a given experiment (as shown in V.2) and it is therefore necessary to test the CFD models on a wide range of operating conditions to evaluate their physical representation.
- Finally, one can wonder why the drag model had to be modified (with a high reduction implemented) between the turbulent fluidized bed and the transport riser simulations. Is it connected to the fact that drag is overestimated at low solid concentration or at high velocity gradient between gas and particles or both? Is it also an effect enhanced when using large mesh cells? These are questions that could be investigated in a multi scale approach with simulations using finer meshes and also other approaches such as CFD-DEM or Direct Numerical Simulations (DNS).

6 Use of CFD for extrapolation: Conclusions and perspectives

In this study, we have built a simulation strategy to evaluate CFD tools predictions on a multi scale basis in a wide range of operating conditions. For this purpose, we first presented the experiments carried out to collect data for the CFD investigation. Three experimental set ups were considered with first a 20 cm fluidized bed used to characterize different gas injection configurations, second a 90 cm fluidized bed where several gas superficial velocities were investigated and finally a 30 cm riser to characterize transport regime conditions. In the three experiments, FCC catalysts with similar physical properties were used in order to focus mainly on gas distribution, scale-up and fluidization regime effects. Local and global experimental flow characterizations were acquired. In this work, we demonstrated the challenges and complexity of acquiring experimental data for such gas/particle multiphase flows. All the information collected represents a rather important set of data for the evaluation of CFD prediction of gas distribution, multi scale and operating conditions effects.

We then developed our simulation strategy using two CFD approaches with first Barracuda VR[®] and the MP-PIC approach which takes into account a particle size distribution for a rather simplistic particle interactions model. Second, we worked with openFOAM and the Euler/Euler KTGF approach which uses a single representative diameter for the solid phase with a more complex particles interactions modeling. The main conclusions of this work are:

- We first found that the default CFD models parameters for both approaches failed predicting the hydrodynamic of the 20 cm fluidized bed and we therefore had to modify these models to capture the experimental data investigated. For this purpose, different drag laws were developed for each approach, the drag modification for Barracuda VR[®] being purely correlative, the one for openFOAM being based on a more physical approach with a simple clustering model.
- Both approaches with their modified parameters captured rather well the change of hydrodynamic due to the different gas distribution within the 20 cm fluidized bed. However, the predictions quality of Barracuda VR[®] was significantly affected when using a larger mesh cell size which was not the case for openFOAM.
- The simulations at a larger scale of the 90 cm fluidized bed showed the same trend with Barracuda VR[®] predictions failing to capture the bed hydrodynamic while openFOAM showed good bed density predictions and satisfactory entrainment trends for the different superficial gas velocities

experiments. **It is an important result since we demonstrated that scale effect is a clear differentiator between both CFD models and it therefore justifies the simulation strategy developed. We also demonstrated that CFD can be used for extrapolation with openFOAM capturing scale effects between the 20 cm and 90 cm fluidized bed simulations.**

- Finally, the riser simulations first showed that the CFD model developed from the fluidized bed experiments failed to predict the transport regime hydrodynamic. Second, we demonstrated that it was possible to modify again the drag law to capture the riser experimental data investigated. The drag law models developed have therefore limitations and for now we have to use a dedicated drag model for each fluidization regime investigated.

Different perspectives to this work can then be identified from an experimental point of view:

- First it is necessary even if challenging to collect more data to fully characterize the fluidized bed hydrodynamic such as bubbling, mixing and local particle velocities characterizations.
- For the evaluation of scale up effect, it would be ideal to perform experiments at different scales using the same catalyst, the same distribution system and the same experimental techniques in order to remove as much as possible experimental bias and characterize only scale up effects. In general, other extrapolation effects could be investigated experimentally using the same strategy with for example effects of temperature and pressure.
- Finally, it would be also interesting to characterize precisely the transition between turbulent and transport regimes. This set of experimental data could then be used to improve the modeling of CFD codes for the transition between these regimes in order to get the same CFD model being able to predict a wide range of operating conditions.

From a CFD point of view the perspectives are:

- First, it is necessary to develop the same simulation strategy based on a more complete set of experimental data with gas structures and local velocities characterization. Indeed all fluidized bed hydrodynamic aspects (bed density, entrainment rates, local volume fractions and velocities, mixing) should be investigated simultaneously to fully validate the CFD model hydrodynamic predictions in order to then implement the modeling of other physical phenomena (kinetic, mass and heat transfer, ...). Such a study would probably lead to the development of a more complex modeling of gas/particles interactions taking into account physical phenomena (particles clustering,) but also numerical issues with the change of mesh cell size for large scale simulations (filtered drag laws).
- Other simulation modeling parameters should be investigated such as wall boundary condition effects, turbulence effects especially for dilute transport conditions with the ambitious objective of predicting different fluidization regimes with a universal set of modeling parameters. The modeling could then be extended to other type of particles (Geldart Group B).
- Other extrapolation parameters such as temperature and pressure could also be investigated following a similar simulation strategy.
- Finally, the simulation of a real industrial configuration could be carried out, one should target an industrial unit with the maximum characterizing data available with possibly different operating conditions in order to be able to estimate the validity of the CFD predictions.

GENERAL CONCLUSIONS AND PERSPECTIVES

This dissertation focused on extrapolation issues for the development of circulating fluidized beds processes. Indeed, minimizing the risk of extrapolation is mandatory when developing such processes both from an economical and technology feasibility point of views [1]. Extrapolation relates in a first step to the understanding of physical phenomena at accessible scales through dedicated and focused experiments. In a second step, modeling is used to transpose observation from lab scale to an industrial perspective. In the first part of my dissertation, we focused on the first step of the extrapolation process with the use of CFD for a better understanding of physical phenomena at lab scale to then better interpret our results in a context of attrition extrapolation phenomena. In the second part of this dissertation, the use of CFD to directly extrapolate hydrodynamic phenomena was then investigated through a dedicated simulation strategy.

The investigation on the extrapolation of attrition phenomena first highlighted the challenges we have to face when developing the new Chemical Looping Combustion (CLC) process where particles attrition characterization on a long operation term basis is not available. We then presented a methodology to get a first preliminary attrition characterization of the potential oxygen carrier particles available. The method consists in comparing with a jet cup apparatus, the oxygen carriers attrition resistance with the one of Fluid Catalytic Cracking (FCC) catalyst for which attrition at lab and industrial scales is well characterized. This investigation then put in evidence how CFD tools allowed for a better understanding of the jet cup test with the characterization of the particles contacting frequency with the jet, parameter controlling the attrition generated in the apparatus. Experimental results then comforted the conclusion obtained from CFD with the attrition generated in the jet cup being inversely proportional to the initial sample volume. This CFD characterization step was therefore essential since without it the jet cup results could have been misinterpreted. The jet cup methodology developed then allowed comparing three solids of interest, with the fresh and equilibrium oxygen carriers performing respectively better and worse than the reference FCC equilibrium catalyst. With the oxygen carrier considered, the detrimental change of mechanical structure due to the CLC process condition was therefore clearly demonstrated. Other materials have therefore to be considered and can be evaluated at the early stage of the process development using the methodology developed in this work. We also demonstrated the importance of testing the solids after an exposure to the process conditions. For better quantitative predictions of attrition at industrial scales, we finally highlighted the need of a multi scale approach connecting the lab scale attrition testing results to the main sources of attrition in a CFB process for the implementation of a population balance model. A PhD in partnership with the university of Leeds and Total was launched in 2015 to develop such a multi-scale approach [146,147]

In the second part of this project, we focused on the use of CFD for the extrapolation of hydrodynamic phenomena in circulating fluidized bed with Geldart Group A FCC particles. Most of the CFD studies in the literature focus on CFD model development with validation carried out against experimental data on a specific lab scale equipment with a rather narrow ranges of operating conditions [10–13]. Authors also use CFD for industrial scale simulation with comparison of their results against few daily averaged macro experimental data often corresponding to one operating condition [9]. The CFD ability to predict scale effects when extrapolating is therefore usually not clearly investigated with comparisons against experimental data at different scales and operating conditions. Moreover, due to computational power limitations, CFD for large scale simulation impose the use of a coarser mesh compared to the lab scale simulation from which CFD models are evaluated. It is therefore also important to evaluate this parameter effect. Finally, it is also important to investigate the potential limits of CFD models in term of operating

conditions representativeness if one wants to model different fluidization regime in the same simulation. The simulation strategy presented in this project was developed to evaluate all these aspects.

We first carried out or used experiments at different scales and operating conditions using particles with the similar physical properties. Experiments on a 20 cm and a 90 cm turbulent fluidized beds experiments allowed characterizing scale and distribution effects. Experiments on a 30 cm riser were then carried out to characterize the hydrodynamic changes between turbulent and transport regimes. Local and global hydrodynamic characterization measurements were acquired and used for the CFD investigation. This first experimental step also highlighted the challenge to get local fluidized bed characterizations where data have always to be carefully validated against global hydrodynamic descriptors when possible.

Two CFD approaches were then evaluated with first Barracuda VR[®] and the MP-PIC approach and second openFOAM and the Euler/Euler KTGF approach. Default CFD models parameters failed predicting the 20 cm fluidized bed experimental data investigated. Dedicated drag models and boundary conditions were then developed for both CFD approaches with success for the predictions of the two gas injection configurations of the 20 cm fluidized bed. We then demonstrated that scale effect was a clear differentiator between the two CFD approaches with the parameters chosen for Barracuda VR[®] failing to predict the 90 cm fluidized bed hydrodynamic while openFOAM parameters predicted with success the bed density and entrainment trends for the different superficial gas velocities experiments. It is an important result which first justifies the proposed simulation strategy and second it shows that CFD can be used for extrapolation purposes with openFOAM predicting the effect of scale on the bed density. Finally we demonstrated that the model developed from fluidized bed experiments failed to predict the transport regime hydrodynamic and that a different drag model had to be developed to well capture the riser experimental data. Therefore at this stage it is possible to develop a dedicated drag model for each fluidization regime but the development of a universal model is complicated and requires further investigations with probably many efforts.

As a perspective, a wider set of experimental data could be used to fully cover all hydrodynamic aspects of a fluidized bed (characterization of local gas structures, local velocities, mixing) to then apply the same simulation strategy. It is however important to realize that data collection is a large and complex amount of work. It should not be neglected and clearly, availability of experimental set of data for CFD development and validation is an issue. Then, it is also necessary to investigate all modeling parameters such as gas turbulence model, wall boundary conditions, particles interactions models with the confrontation of the CFD models against a wide range of operating conditions in order to make the models less operating conditions dependent and therefore more physical. Other extrapolation aspects to industrial operating conditions such as pressure and temperature could be investigated following a similar experimental and simulation strategy. Finally, a real industrial configuration could be simulated as a last step of our simulation strategy.

Extrapolation remains a complex and difficult challenge for multiphase flow reactors. We therefore have to use all the tools available with lab scale experimentation, exploitation of industrial units data and of course modeling. This work shows that CFD can be used for the understanding of local phenomena as well as for extrapolation purposes. However, it remains a practical tool where universal theoretical models for gas/particles and particles/particles interactions are not available. We therefore cannot use CFD tools without a careful validation and determination of their limits in order to better interpret their results and use them efficiently. The work carried out in this dissertation is an illustration of this last statement.

VI. REFERENCES

- [1] T.Gauthier, J.Bayle, P.Leroy, *Oil & Gas Science and Technology – Rev. IFP*, (2000).
- [2] W.-c. Yang, *HANDBOOK of FLUIDIZATION and FLUID-PARTICLE SYSTEMS*.
- [3] T. Gauthier, M. Yazdanpanah, A. Forret, B. Amblard, A. Lambert, S. Bertholin, CLC, a promising concept with challenging development issues, *Powder Technology* 316 (2017) 3–17. <https://doi.org/10.1016/j.powtec.2017.01.003>.
- [4] R. Cocco, Y. Arrington, R. Hays, J. Findlay, S.B.R. Karri, T.M. Knowlton, Jet cup attrition testing, *Powder Technology* 200 (3) (2010) 224–233. <https://doi.org/10.1016/j.powtec.2010.02.029>.
- [5] Raynal, L., Augier, F., Bazer-Bachi, F., Haroun, Y., Pereira da Fonte, C., *Oil & Gas Science and Technology – Rev. IFP*, (May–June 2016).
- [6] J. Wang, M.A. van der Hoef, J.A.M. Kuipers, Why the two-fluid model fails to predict the bed expansion characteristics of Geldart A particles in gas-fluidized beds: A tentative answer, *Chemical Engineering Science* 64 (3) (2009) 622–625. <https://doi.org/10.1016/j.ces.2008.09.028>.
- [7] D. Gidaspow, *Multiphase flow and fluidization: Continuum and kinetic theory descriptions*, Academic Press, London, 1994.
- [8] A. Ozel, P. Fede, O. Simonin, Development of filtered Euler–Euler two-phase model for circulating fluidised bed: High resolution simulation, formulation and a priori analyses, *International Journal of Multiphase Flow* 55 (2013) 43–63. <https://doi.org/10.1016/j.ijmultiphaseflow.2013.04.002>.
- [9] B. Amblard, R. Singh, E. Gbordzoe, L. Raynal, CFD modeling of the coke combustion in an industrial FCC regenerator, *Chemical Engineering Science* 170 (2017) 731–742. <https://doi.org/10.1016/j.ces.2016.12.055>.
- [10] P. Li, X. Lan, C. Xu, G. Wang, C. Lu, J. Gao, Drag models for simulating gas–solid flow in the turbulent fluidization of FCC particles, *Particuology* 7 (4) (2009) 269–277. <https://doi.org/10.1016/j.partic.2009.03.010>.
- [11] C. Chen, J. Werther, S. Heinrich, H.-Y. Qi, E.-U. Hartge, CFPD simulation of circulating fluidized bed risers, *Powder Technology* 235 (2013) 238–247. <https://doi.org/10.1016/j.powtec.2012.10.014>.
- [12] A.H. Ahmadi Motlagh, CFD simulation of two- and three-phase flow in FCC reactors, 2015.
- [13] P. Fede, O. Simonin, A. Ingram, 3D numerical simulation of a lab-scale pressurized dense fluidized bed focussing on the effect of the particle-particle restitution coefficient and particle–wall boundary conditions, *Chemical Engineering Science* 142 (2016) 215–235. <https://doi.org/10.1016/j.ces.2015.11.016>.
- [14] D.M. Snider, An Incompressible Three-Dimensional Multiphase Particle-in-Cell Model for Dense Particle Flows, *Journal of Computational Physics* 170 (2) (2001) 523–549. <https://doi.org/10.1006/jcph.2001.6747>.
- [15] Chad Eric Rollins, *Development of Multiphase Computational Fluid Dynamics Solver in OpenFOAM*, PhD thesis, North Carolina State University.
- [16] Daizo Kunii, O. Levenspiel, *Fluidization Engineering*, Butterworth-Heinemann Ed., Boston (1991).
- [17] R. Mülhaupt, Catalytic Polymerization and Post Polymerization Catalysis Fifty Years After the Discovery of Ziegler's Catalysts, *Macromol. Chem. Phys.* 204 (2) (2003) 289–327. <https://doi.org/10.1002/macp.200290085>.
- [18] P. Basu, Combustion of coal in circulating fluidized-bed boilers: A review, *Chemical Engineering Science* 54 (22) (1999) 5547–5557. [https://doi.org/10.1016/S0009-2509\(99\)00285-7](https://doi.org/10.1016/S0009-2509(99)00285-7).
- [19] S.R.A. Kersten, X. Wang, W. Prins, W.P.M. van Swaaij, Biomass Pyrolysis in a Fluidized Bed Reactor. Part 1: Literature Review and Model Simulations, *Ind. Eng. Chem. Res.* 44 (23) (2005) 8773–8785. <https://doi.org/10.1021/ie0504856>.
- [20] IEA Statistics, Key trends in CO2 emissions, 2019, www.iea.org/publications.
- [21] Technology Roadmap Carbon capture and storage - 2013 edition. IEA (2013), www.iea.org/publications.

- [22] T.Gauthier, F.Guillou, S.Bourgeon, H.Stainton, la combustion en boucle chimique, *L'Actualité chimique*, 371-372: 52-56.
- [23] B. Moghtaderi, Review of the Recent Chemical Looping Process Developments for Novel Energy and Fuel Applications, *Energy Fuels* 26 (1) (2011) 15–40. <https://doi.org/10.1021/ef201303d>.
- [24] L.-S. Fan, L. Zeng, S. Luo, Chemical-looping technology platform, *AIChE J.* 61 (1) (2015) 2–22. <https://doi.org/10.1002/aic.14695>.
- [25] V. Barišić, E. Coda Zabetta, T. Eriksson, A. Hotta, S. Kokki, K. Nuortimo, J. Palonen, CFB technology provides solutions for reducing CO₂ emissions, IFSA (2008), *Industrial Fluidization South Africa*, 3-23. Edited by T. Hadley and.
- [26] Sofia DA SILVA RODRIGUES, Riser hydrodynamic study with Group B particles for Chemical Looping Combustion, Chemical engineering. Université Claude Bernard - Lyon I, 2014. English. <https://tel.archives-ouvertes.fr/tel-01127251>.
- [27] Mohammad Mahdi Yazdanpanah, Investigation of a Chemical Looping Combustion (CLC) Configuration with Gas Feed, Other [cond-mat.other]. Université Henri Poincaré - Nancy 1, 2011. English. NNT 2011NAN10118 tel-01746270.
- [28] J. Adanez, A. Abad, F. Garcia-Labiano, P. Gayan, L.F. de Diego, Progress in Chemical-Looping Combustion and Reforming technologies, *Progress in Energy and Combustion Science* 38 (2) (2012) 215–282. <https://doi.org/10.1016/j.pecs.2011.09.001>.
- [29] R. Sadeghbeigi, Fluid catalytic cracking handbook: An expert guide to the practical operation, design, and optimization of FCC units, Elsevier; Butterworth-Heinemann, Amsterdam, Boston, Heidelberg etc, 2011.
- [30] A.A. Avidan, R. Shinnar, Development of catalytic cracking technology. A lesson in chemical reactor design, *Ind. Eng. Chem. Res.* 29 (6) (1990) 931–942.
- [31] T. Gauthier, J. Bayle and P. Leroy, FCC: Fluidization Phenomena and Technologies, *Oil & Gas Science and Technology – Rev. IFP*, Vol. 55 (2000), No. 2, pp. 187-207 (2000).
- [32] T. Gauthier, Current R&D Challenges for Fluidized Bed Processes in the Refining Industry, *International Journal of Chemical Reactor Engineering* 7 (1) (2009). <https://doi.org/10.2202/1542-6580.1857>.
- [33] W. Letzsch, J.-L. Mauleon, S.Long, Total Petroleum Inc., Advances in Fluid Catalytic Cracking, Symposium on advances in catalytic cracking presented before the division of petroleum chemistry, Inc. American Society Washington D.C. Meeting, August 28 - September 2 (1983).
- [34] Sabine Rode, Opérations polyphasiques en génie des procédés, hydrodynamique, transferts, réactions, séparations mécaniques, édition ellipses.
- [35] J.R. Grace, G. Sun, Influence of particle size distribution on the performance of fluidized bed reactors, *Can. J. Chem. Eng.* 69 (5) (1991) 1126–1134. <https://doi.org/10.1002/cjce.5450690512>.
- [36] T.Allen, Particle Size Measurement, 3rd Ed. Terence Allen. Chapman and Hall/Methuen, New York, 1981. 678 pp. \$55. Paul Becher Wilmington, *Journal of Dispersion Science and Technology* 3 (4) (1981) 465–466. <https://doi.org/10.1080/01932698208943652>.
- [37] H. Masuda, K. Higashitani, H. Yoshida, Powder technology handbook, 3rd ed., Taylor & Francis, Boca Raton, 2006.
- [38] K.-I. Mukaida, Density measurement of small porous particles by mercury porosimetry, *Powder Technology* 29 (1) (1981) 99–107. [https://doi.org/10.1016/0032-5910\(81\)85008-5](https://doi.org/10.1016/0032-5910(81)85008-5).
- [39] J. Visser, Van der Waals and other cohesive forces affecting powder fluidization, *Powder Technology* 58 (1) (1989) 1–10. [https://doi.org/10.1016/0032-5910\(89\)80001-4](https://doi.org/10.1016/0032-5910(89)80001-4).
- [40] J. Israelachili, (Second Edi.). Santa Barbara: Academic (1992).
- [41] Y. Chen, J. Yang, R.N. Dave, R. Pfeffer, Fluidization of coated group C powders, *AIChE J.* 54 (1) (2008) 104–121. <https://doi.org/10.1002/aic.11368>.
- [42] B.M. Kaye, R.P. Boardman, in Proc. Symp. on the Interaction between Fluids and Particles, Institution of Chemical Engineers London (1962) 17–21.

- [43] A. Cahyadi, A. Anantharaman, S. Yang, S.R. Karri, J.G. Findlay, R.A. Cocco, J.W. Chew, Review of cluster characteristics in circulating fluidized bed (CFB) risers, *Chemical Engineering Science* 158 (2017) 70–95. <https://doi.org/10.1016/j.ces.2016.10.002>.
- [44] R. Cocco, F. Shaffer, R. Hays, S.B. Reddy Karri, T. Knowlton, Particle clusters in and above fluidized beds, *Powder Technology* 203 (1) (2010) 3–11. <https://doi.org/10.1016/j.powtec.2010.03.023>.
- [45] D. Geldart, Types of gas fluidization, *Powder Technology* 7 (5) (1973) 285–292. [https://doi.org/10.1016/0032-5910\(73\)80037-3](https://doi.org/10.1016/0032-5910(73)80037-3).
- [46] G. Bruni, P. Lettieri, D. Newton, J. Yates, The influence of fines size distribution on the behaviour of gas fluidized beds at high temperature, *Powder Technology* 163 (1-2) (2006) 88–97. <https://doi.org/10.1016/j.powtec.2006.01.007>.
- [47] A.R. Abrahamsen, D. Geldart, Behaviour of gas-fluidized beds of fine powders part I. Homogeneous expansion, *Powder Technology* 26 (1) (1980) 35–46. [https://doi.org/10.1016/0032-5910\(80\)85005-4](https://doi.org/10.1016/0032-5910(80)85005-4).
- [48] P.N. Rowe, Prediction of bubble size in a gas fluidised bed, *Chemical Engineering Science* 31 (4) (1976) 285–288. [https://doi.org/10.1016/0009-2509\(76\)85073-7](https://doi.org/10.1016/0009-2509(76)85073-7).
- [49] Hillgardt K., Werther J., Influence of temperature and properties of solids on the size and growth of bubbles in gas fluidized beds, *Chem. Eng. Technol.* 10 (1987) 272-280.
- [50] Darton C., LaNauze R., Davidson, Harrison D., Bubble growth due to coalescence in fluidised beds, *Transactions of the Institution of Chemical Engineers* (1977).
- [51] X. Li, A.J. Jaworski, X. Mao, Bubble size and bubble rise velocity estimation by means of electrical capacitance tomography within gas-solids fluidized beds, *Measurement* 117 (2018) 226–240. <https://doi.org/10.1016/j.measurement.2017.12.017>.
- [52] D. Geldart, The size and frequency of bubbles in two- and three-dimensional gas-fluidised beds, *Powder Technology* 4 (1) (1970) 41–55. [https://doi.org/10.1016/0032-5910\(70\)80007-9](https://doi.org/10.1016/0032-5910(70)80007-9).
- [53] Werther J., *Fluidization Technology: Vol. I* (edited by Keairns D.L.), p. 215. Hemisphere, Washington.
- [54] Matsen J.M., *A.I.Ch.E. Symp. Ser. No. 128*, 69 30-33.
- [55] D. Geldart (Ed.), (1977). *Gas Fluidization, short course*,
- [56] M. Rhodes, What is turbulent fluidization? *Powder Technology* 88 (1) (1996) 3–14. [https://doi.org/10.1016/0032-5910\(96\)03093-8](https://doi.org/10.1016/0032-5910(96)03093-8).
- [57] J. Yerushalmi, N.T. Cankurt, Further studies of the regimes of fluidization, *Powder Technology* 24 (2) (1979) 187–205. [https://doi.org/10.1016/0032-5910\(79\)87036-9](https://doi.org/10.1016/0032-5910(79)87036-9).
- [58] Cai P, Chen SP, Jin Y, Yu ZQ, Wang ZW (Eds.), Effect of operating temperature and pressure on the transition from bubbling to turbulent fluidization.
- [59] H.T. Bi, J.R. Grace, Effect of measurement method on the velocities used to demarcate the onset of turbulent fluidization, *The Chemical Engineering Journal and the Biochemical Engineering Journal* 57 (3) (1995) 261–271. [https://doi.org/10.1016/0923-0467\(94\)02875-B](https://doi.org/10.1016/0923-0467(94)02875-B).
- [60] Allan Issangya, S. B. Reddy Karri, Ted Knowlton, and Ray Cocco, Effects of Bed Diameter, Baffles, Fines Content and Operating Conditions on Pressure Fluctuations in Fluidized Beds of FCC Catalyst Particles, *The 14th International Conference on Fluidization – From Fundamentals to Products*", J.A.M. Kuipers, Eindhoven University of Technology R.F. Mudde, Delft University of Technology J.R. van Ommen, Delft University of Technology N.G. Deen, Eindhoven University of Technology Eds, *ECI Symposium Series*, (2013). https://dc.engconfintl.org/fluidization_xiv/77.
- [61] D. King, Estimation of dense bed voidage in fast and slow fluidized beds of FCC catalyst *Fluidization VI*, Grace, J.R. and Bergougnou, M.A. (Eds.), Engineering Foundation, New York, (1989), p. 1-8.
- [62] H.T. Bi, N. Ellis, I.A. Abba, J.R. Grace, A state-of-the-art review of gas–solid turbulent fluidization, *Chemical Engineering Science* 55 (21) (2000) 4789–4825. [https://doi.org/10.1016/S0009-2509\(00\)00107-X](https://doi.org/10.1016/S0009-2509(00)00107-X).

- [63] A.S. Issangya, S.B. Reddy Karri, T. Knowlton, R. Cocco, Use of pressure to mitigate gas bypassing in fluidized beds of FCC catalyst particles, *Powder Technology* 290 (2016) 53–61. <https://doi.org/10.1016/j.powtec.2015.08.043>.
- [64] G.E. Klinzing, F.Rizk, R.Marcus, L.S. Leung, *Pneumatic conveying of solids, a theoretical and practical approach*, third edition, particle technology series.
- [65] H.T. Bi, J.R. Grace, Flow regime diagrams for gas-solid fluidization and upward transport, *International Journal of Multiphase Flow* 21 (6) (1995) 1229–1236. [https://doi.org/10.1016/0301-9322\(95\)00037-X](https://doi.org/10.1016/0301-9322(95)00037-X).
- [66] H. Yang, M. Gautam, Experimental study on the interface of core-annulus flow in the riser of a circulating fluidized bed, *Powder Technology* 85 (1) (1995) 57–64. [https://doi.org/10.1016/0032-5910\(95\)02998-H](https://doi.org/10.1016/0032-5910(95)02998-H).
- [67] M. Rhodes, H. Mineo, T. Hirama, Particle motion at the wall of a circulating fluidized bed, *Powder Technology* 70 (3) (1992) 207–214. [https://doi.org/10.1016/0032-5910\(92\)80055-2](https://doi.org/10.1016/0032-5910(92)80055-2).
- [68] R.Karri, T.Knowlton, paper presented at the Seventh International Conference on Circulating Fluidized Beds, 2002.
- [69] J.J. Nieuwland, E. Delnoij, J.A.M. Kuipers, W.P.M. van Swaaij, An engineering model for dilute riser flow, *Powder Technology* 90 (2) (1997) 115–123. [https://doi.org/10.1016/S0032-5910\(96\)03205-6](https://doi.org/10.1016/S0032-5910(96)03205-6).
- [70] Garic-Grulovic R, Grbavcic Z, In: E.T.Berg, editor. *Fluid Transport: Theory, Dynamics and Applications*. Nova Science Publishers, Inc; 2011. p. 1-43.
- [71] H. KQNNO, S. SAITO, PNEUMATIC CONVEYING OF SOLIDS THROUGH STRAIGHT PIPES, *J. Chem. Eng. Japan / JCEJ* 2 (2) (1969) 211–217. <https://doi.org/10.1252/jcej.2.211>.
- [72] G.S. Patience, J. Chaouki, F. Berruti, R. Wong, Scaling considerations for circulating fluidized bed risers, *Powder Technology* 72 (1) (1992) 31–37. [https://doi.org/10.1016/S0032-5910\(92\)85018-Q](https://doi.org/10.1016/S0032-5910(92)85018-Q).
- [73] E.K. Levy, H.S. Caram, J.C. Dille, S. Edelstein, Mechanisms for solids ejection from gas-fluidized beds, *AIChE J.* 29 (3) (1983) 383–388. <https://doi.org/10.1002/aic.690290306>.
- [74] M. Colakyan, O. Levenspiel, Elutriation from fluidized beds, *Powder Technology* 38 (3) (1984) 223–232. [https://doi.org/10.1016/0032-5910\(84\)85005-6](https://doi.org/10.1016/0032-5910(84)85005-6).
- [75] S.M. Tasirin, D. Geldart, Entrainment of FCC from fluidized beds — A new correlation for the elutriation rate constants $K_{i\infty}^*$, *Powder Technology* 95 (3) (1998) 240–247. [https://doi.org/10.1016/S0032-5910\(97\)03343-3](https://doi.org/10.1016/S0032-5910(97)03343-3).
- [76] J.H. Choi, J.E. Son, S.D. Kim, Solid entrainment in fluidized bed combustors, *J. Chem. Eng. Japan / JCEJ* 22 (6) (1989) 597–606. <https://doi.org/10.1252/jcej.22.597>.
- [77] C.L. Briens, M.A. Bergougnou, T. Baron, Prediction of entrainment from gas-solid fluidized beds, *Powder Technology* 54 (3) (1988) 183–196. [https://doi.org/10.1016/0032-5910\(88\)80077-9](https://doi.org/10.1016/0032-5910(88)80077-9).
- [78] C.L. Briens, M.A. Bergougnou, I.I. Inculet, T. Baron, J.D. Hazlett, Size distribution of particles entrained from fluidized beds: Electrostatic effects, *Powder Technology* 70 (1) (1992) 57–62. [https://doi.org/10.1016/0032-5910\(92\)85054-Y](https://doi.org/10.1016/0032-5910(92)85054-Y).
- [79] I.H. Chan, T.M. & Knowlton, United States: American Institute of Chemical Engineers. (1984).
- [80] M. Sciężko, J. Bandrowski, J. Raczek, On the entrainment of solid particles from a fluidized bed, *Powder Technology* 66 (1) (1991) 33–39. [https://doi.org/10.1016/0032-5910\(91\)80078-W](https://doi.org/10.1016/0032-5910(91)80078-W).
- [81] A. Cahyadi, A.H. Neumayer, C.M. Hrenya, R.A. Cocco, J.W. Chew, Comparative study of Transport Disengaging Height (TDH) correlations in gas–solid fluidization, *Powder Technology* 275 (2015) 220–238. <https://doi.org/10.1016/j.powtec.2015.02.010>.
- [82] J.-H. Choi, I.-Y. Chang, D.-W. Shun, C.-K. Yi, J.-E. Son, S.-D. Kim, Correlation on the Particle Entrainment Rate in Gas Fluidized Beds, *Ind. Eng. Chem. Res.* 38 (6) (1999) 2491–2496. <https://doi.org/10.1021/ie980707i>.

- [83] J.W. Chew, A. Cahyadi, C.M. Hrenya, R. Karri, R.A. Cocco, Review of entrainment correlations in gas–solid fluidization, *Chemical Engineering Journal* 260 (2015) 152–171. <https://doi.org/10.1016/j.cej.2014.08.086>.
- [84] D. Geldart, A.C.Y. Wong, *AIChE Symposium Series* 255 (1987) 1.
- [85] J. Baeyens, D. Geldart, S.Y. Wu, Elutriation of fines from gas fluidized beds of Geldart A-type powders — effect of adding superfines, *Powder Technology* 71 (1) (1992) 71–80. [https://doi.org/10.1016/0032-5910\(92\)88006-4](https://doi.org/10.1016/0032-5910(92)88006-4).
- [86] T. Knowlton (Ed.), *Fluidization, Solids Handling, and Processing, Pressure and Temperature Effects in Fluid-Particle Systems*, Elsevier, 1999.
- [87] P.N. Rowe, P.U. Foscolo, A.C. Hoffmann, J.G. Yates, (Kunii and Toei, eds.), p. 53 (1984).
- [88] J.S.M. Botterill, Y. Teoman, K.R. Yüregir, The effect of operating temperature on the velocity of minimum fluidization, bed voidage and general behaviour, *Powder Technology* 31 (1) (1982) 101–110. [https://doi.org/10.1016/0032-5910\(82\)80009-0](https://doi.org/10.1016/0032-5910(82)80009-0).
- [89] H. Cui, J. Chaouki, Effects of temperature on local two-phase flow structure in bubbling and turbulent fluidized beds of FCC particles, *Chemical Engineering Science* 59 (16) (2004) 3413–3422. <https://doi.org/10.1016/j.ces.2004.05.006>.
- [90] J. Werther, Measurement techniques in fluidized beds, *Powder Technology* 102 (1) (1999) 15–36. [https://doi.org/10.1016/S0032-5910\(98\)00202-2](https://doi.org/10.1016/S0032-5910(98)00202-2).
- [91] J.R. van Ommen, R.F. Mudde, Measuring the Gas-Solids Distribution in Fluidized Beds -- A Review, *International Journal of Chemical Reactor Engineering* 6 (1) (2008). <https://doi.org/10.2202/1542-6580.1796>.
- [92] J.G. Yates, S.J.R. Simons, Experimental methods in fluidization research, *International Journal of Multiphase Flow* 20 (1994) 297–330. [https://doi.org/10.1016/0301-9322\(94\)90076-0](https://doi.org/10.1016/0301-9322(94)90076-0).
- [93] S.U. Sane, H.W. Haynes, P.K. Agarwal, An experimental and modelling investigation of gas mixing in bubbling fluidized beds, *Chemical Engineering Science* 51 (7) (1996) 1133–1147. [https://doi.org/10.1016/S0009-2509\(96\)80012-1](https://doi.org/10.1016/S0009-2509(96)80012-1).
- [94] P. Ege, A. Grislingås, H.I. de Lasa, Modelling turbulent fluidized bed reactors: Tracer and fibre optic probe studies, *The Chemical Engineering Journal and the Biochemical Engineering Journal* 61 (3) (1996) 179–190. [https://doi.org/10.1016/0923-0467\(95\)03039-5](https://doi.org/10.1016/0923-0467(95)03039-5).
- [95] R.A. Cocco, S.R. Karri, T.M. Knowlton, J. Findlay, T. Gauthier, J.W. Chew, C.M. Hrenya, Intrusive probes in riser applications, *AIChE J.* 63 (12) (2017) 5361–5374. <https://doi.org/10.1002/aic.15892>.
- [96] S. Tebianian, Comparison of alternative advanced experimental techniques for measurement of hydrodynamic characteristics of gas-fluidized beds, 2015.
- [97] J.-M. Schweitzer, J. Bayle, T. Gauthier, Local gas hold-up measurements in fluidized bed and slurry bubble column, *Chemical Engineering Science* 56 (3) (2001) 1103–1110. [https://doi.org/10.1016/S0009-2509\(00\)00327-4](https://doi.org/10.1016/S0009-2509(00)00327-4).
- [98] K. Dubrawski, S. Tebianian, H.T. Bi, J. Chaouki, N. Ellis, R. Gerspacher, R. Jafari, A. Kantzas, C. Lim, G.S. Patience, T. Pugsley, M.Z. Qi, J.X. Zhu, J.R. Grace, Traveling column for comparison of invasive and non-invasive fluidization voidage measurement techniques, *Powder Technology* 235 (2013) 203–220. <https://doi.org/10.1016/j.powtec.2012.10.031>.
- [99] J. Liu, Particle and gas dynamics of high density circulating fluidized beds, 2001.
- [100] P.M. Herbert, T.A. Gauthier, C.L. Briens, M.A. Bergougnou, Application of fiber optic reflection probes to the measurement of local particle velocity and concentration in gas—solid flow, *Powder Technology* 80 (3) (1994) 243–252. [https://doi.org/10.1016/0032-5910\(94\)02859-1](https://doi.org/10.1016/0032-5910(94)02859-1).
- [101] Y.P. Tsuo, D. Gidaspow, Computation of flow patterns in circulating fluidized beds, *AIChE J.* 36 (6) (1990) 885–896. <https://doi.org/10.1002/aic.690360610>.
- [102] J. Ding, D. Gidaspow, A bubbling fluidization model using kinetic theory of granular flow, *AIChE J.* 36 (4) (1990) 523–538. <https://doi.org/10.1002/aic.690360404>.
- [103] V. Ranade, *Computational Flow Modeling for Chemical Reactor Engineering Volume 5* (2001).

- [104] Euzenat Florian, Simulation numérique directe et analyse des transferts de chaleur dans les lits de particules fixes et mobiles. PhD, Dynamique des fluides,, Institut National Polytechnique de Toulouse, 2017.
- [105] M.W. Baltussen, K.A. Buist, E.A.J.F. Peters, J.A.M. Kuipers, Multiscale Modelling of Dense Gas–Particle Flows, in: Bridging Scales in Modelling and Simulation of Non-Reacting and Reacting Flows. Part II, Elsevier, 2018, pp. 1–52.
- [106] Venier, Cesar & Márquez Damián, Santiago & Ramajo, Damian & Nigro, Norberto. (Ed.), (2013). NUMERICAL ANALYSIS OF MULTIPHASE SOLID-GAS FLOW WITH EULERIAN MODELS AND KINETIC THEORY CLOSURE.
- [107] M.J. Andrews, P.J. O'Rourke, The multiphase particle-in-cell (MP-PIC) method for dense particulate flows, *International Journal of Multiphase Flow* 22 (2) (1996) 379–402. [https://doi.org/10.1016/0301-9322\(95\)00072-0](https://doi.org/10.1016/0301-9322(95)00072-0).
- [108] S.E. Harris, D.G. Crighton, Solitons, solitary waves, and voidage disturbances in gas-fluidized beds, *J. Fluid Mech.* 266 (1994) 243–276. <https://doi.org/10.1017/S0022112094000996>.
- [109] G. Ferschneider, P. Mege, Eulerian Simulation of Dense Phase Fluidized Beds, *Rev. Inst. Fr. Pét.* 51 (2) (1996) 301–307. <https://doi.org/10.2516/ogst:1996026>.
- [110] J. Wang, A Review of Eulerian Simulation of Geldart A Particles in Gas-Fluidized Beds, *Ind. Eng. Chem. Res.* 48 (12) (2009) 5567–5577. <https://doi.org/10.1021/ie900247t>.
- [111] W. Wang, B. Lu, N. Zhang, Z. Shi, J. Li, A review of multiscale CFD for gas–solid CFB modeling, *International Journal of Multiphase Flow* 36 (2) (2010) 109–118. <https://doi.org/10.1016/j.ijmultiphaseflow.2009.01.008>.
- [112] J. Wang, Y. Liu, EMMS-based Eulerian simulation on the hydrodynamics of a bubbling fluidized bed with FCC particles, *Powder Technology* 197 (3) (2010) 241–246. <https://doi.org/10.1016/j.powtec.2009.09.022>.
- [113] S. Ergun, *Chem. Engng. Progr.* 48 (1952), pp. 89–94.
- [114] C.Y. Wen, Y.H. Yu, *Chemical Engineering Progress Symposium Series*, 62 (1966), pp. 100-111.
- [115] Syamlal M., O'Brien T.J., *AIChE Symp.* 85 (1989), pp. 21–31.
- [116] Ray Cocco, Allan Issangya, S.B. Reddy Karri, Tim Freeman, Heinrich M. Jaeger, Ted M. Knowlton, Small-Scale Particle Interactions Are Having Significant Effects on Global Fluidized Bed Behavior KONA Powder and Particle Journal 2017 Volume 34 Pages 155-167.
- [117] J.-F. Parmentier, O. Simonin, O. Delsart, A functional subgrid drift velocity model for filtered drag prediction in dense fluidized bed, *AIChE J.* 58 (4) (2012) 1084–1098. <https://doi.org/10.1002/aic.12647>.
- [118] J. Li (Ed.), 1987. Multi-scale modeling and method of energy minimization in two-phase flow. Doctor Dissertation.
- [119] W. Wang, J. Li, Simulation of gas–solid two-phase flow by a multi-scale CFD approach—of the EMMS model to the sub-grid level, *Chemical Engineering Science* 62 (1-2) (2007) 208–231. <https://doi.org/10.1016/j.ces.2006.08.017>.
- [120] E. Ghadirian, H. Arastoopour, CFD simulation of a fluidized bed using the EMMS approach for the gas-solid drag force, *Powder Technology* 288 (2016) 35–44. <https://doi.org/10.1016/j.powtec.2015.10.034>.
- [121] Davidson J.F, In: Guazzelli E., Oger L. (eds) *Mobile Particulate Systems*. NATO ASI Series (Series E: Applied Sciences), vol 287. Springer, Dordrecht.
- [122] C.G. Philippssen, A.C.F. Vilela, L.D. Zen, Fluidized bed modeling applied to the analysis of processes: Review and state of the art, *Journal of Materials Research and Technology* 4 (2) (2015) 208–216. <https://doi.org/10.1016/j.jmrt.2014.10.018>.
- [123] Lee et al, Fluidized-bed Catalyst Cracking Renenerator Modelling and Analysis, *The Chemical Engineering Journal*, 40 (1989), p.71-82 (1989).

- [124] R.M. Filho, L.M.F. Lona Batista, M. Fusco, A fast fluidized bed reactor for industrial FCC regenerator, *Chemical Engineering Science* 51 (10) (1996) 1807–1816. [https://doi.org/10.1016/0009-2509\(96\)00039-5](https://doi.org/10.1016/0009-2509(96)00039-5).
- [125] S. Soundararajan, A.K. Dalai, F. Berruti, Modeling of methanol to olefins (MTO) process in a circulating fluidized bed reactor, *Fuel* 80 (8) (2001) 1187–1197. [https://doi.org/10.1016/S0016-2361\(00\)00182-4](https://doi.org/10.1016/S0016-2361(00)00182-4).
- [126] G.C. Lopes, L.M. Rosa, M. Mori, J.R. Nunhez, W.P. Martignoni, CFD Study of Industrial FCC Risers: The Effect of Outlet Configurations on Hydrodynamics and Reactions, *International Journal of Chemical Engineering* 2012 (6) (2012) 1–16. <https://doi.org/10.1155/2012/193639>.
- [127] T. Engen, CFD analysis of gas-particle flow in a scaled circulating fluidized bed, master thesis master thesis (2016).
- [128] S. Shah, K. Myöhänen, S. Kallio, T. Hyppänen, CFD simulations of gas–solid flow in an industrial-scale circulating fluidized bed furnace using subgrid-scale drag models, *Particuology* 18 (2015) 66–75. <https://doi.org/10.1016/j.partic.2014.05.008>.
- [129] J. Werther, J. Reppenhagen, Attrition in Fluidized Beds and Pneumatic Conveying Lines, in: *Fluidization, Solids Handling, and Processing*, Elsevier, 1999, pp. 435–491.
- [130] J. Werther, E.-U. Hartge, A population balance model of the particle inventory in a fluidized-bed reactor/regenerator system, *Powder Technology* 148 (2-3) (2004) 113–122. <https://doi.org/10.1016/j.powtec.2004.09.005>.
- [131] M. Kramp, A. Thon, E.-U. Hartge, S. Heinrich, J. WERTHER, The Role of Attrition and Solids Recovery in a Chemical Looping Combustion Process, *Oil Gas Sci. Technol. – Rev. IFP Energies nouvelles* 66 (2) (2011) 277–290. <https://doi.org/10.2516/ogst/2010035>.
- [132] M. Ghadiri, J.A.S. Cleaver, V.G. Tuponogov, J. WERTHER, Attrition of FCC powder in the jetting region of a fluidized bed, *Powder Technology* 80 (2) (1994) 175–178. [https://doi.org/10.1016/0032-5910\(94\)80014-6](https://doi.org/10.1016/0032-5910(94)80014-6).
- [133] P.C. Knight, J. Bridgwater, Comparison of methods for assessing powder attrition, *Powder Technology* 44 (1) (1985) 99–102. [https://doi.org/10.1016/0032-5910\(85\)85028-2](https://doi.org/10.1016/0032-5910(85)85028-2).
- [134] M. Rydén, P. Moldenhauer, S. Lindqvist, T. Mattisson, A. Lyngfelt, Measuring attrition resistance of oxygen carrier particles for chemical looping combustion with a customized jet cup, *Powder Technology* 256 (2014) 75–86. <https://doi.org/10.1016/j.powtec.2014.01.085>.
- [135] ASTM D5757-11, Standard Test Method for Determination of Attrition of FCC Catalysts by Air Jets, ASTM, Philadelphia, United States, 2011.
- [136] A. Knight, N. Ellis, J.R. Grace, C.J. Lim, CO₂ sorbent attrition testing for fluidized bed systems, *Powder Technology* 266 (2014) 412–423. <https://doi.org/10.1016/j.powtec.2014.06.013>.
- [137] W. Xu, D.S. DeCroix, X. Sun, Mechanistic based DEM simulation of particle attrition in a jet cup, *Powder Technology* 253 (2014) 385–392. <https://doi.org/10.1016/j.powtec.2013.11.031>.
- [138] Y. Tsuji, T. Tanaka, T. Ishida, Lagrangian numerical simulation of plug flow of cohesionless particles in a horizontal pipe, *Powder Technology* 71 (3) (1992) 239–250. [https://doi.org/10.1016/0032-5910\(92\)88030-L](https://doi.org/10.1016/0032-5910(92)88030-L).
- [139] M.M. Yazdanpanah, A. Forret, T. Gauthier, A. Delebarre, An experimental investigation of L-valve operation in an interconnected circulating fluidized bed system, *Powder Technology* 221 (2012) 236–244. <https://doi.org/10.1016/j.powtec.2012.01.007>.
- [140] Thierry Gauthier, Florent Guillou, Stéphane Bourgeon, Hélène Stainton (Eds.), *La combustion en boucle chimique Un procédé en rupture pour le captage du CO₂*.
- [141] B. Amblard, S. Bertholin, C. Bobin, T. Gauthier, Development of an attrition evaluation method using a Jet Cup rig, *Powder Technology* 274 (2015) 455–465. <https://doi.org/10.1016/j.powtec.2015.01.001>.
- [142] J. SMAGORINSKY, GENERAL CIRCULATION EXPERIMENTS WITH THE PRIMITIVE EQUATIONS, *Mon. Wea. Rev.* 91 (3) (1963) 99–164. [https://doi.org/10.1175/1520-0493\(1963\)091<0099:GCEWTP>2.3.CO;2](https://doi.org/10.1175/1520-0493(1963)091<0099:GCEWTP>2.3.CO;2).

- [143] S. Clark, D.M. Snider, J. Spenik, CO₂ Adsorption loop experiment with Eulerian–Lagrangian simulation, *Powder Technology* 242 (2013) 100–107. <https://doi.org/10.1016/j.powtec.2013.01.011>.
- [144] James Parker PhD Chief Technology Officer, CPF_D software, Personal communication.
- [145] T. Nelson, J.G. van der Watt, D. Laudal, H. Feilen, M. Mann, S. Srinivasachar, Reactive jet and cyclonic attrition analysis of ilmenite in chemical looping combustion systems, *International Journal of Greenhouse Gas Control* 91 (2019) 102837. <https://doi.org/10.1016/j.ijggc.2019.102837>.
- [146] F. Fulchini, W. Nan, M. Ghadiri, M. Yazdan Panah, S. Bertholin, B. Amblard, A. Cloupet, T. Gauthier, F. Radjai, S. Nezamabadi, S. Luding, J.Y. Delenne, CFD-DEM Analysis of Particle Attrition in a Jet in a Fluidised Bed, *EPJ Web Conf.* 140 (2017) 7017. <https://doi.org/10.1051/epjconf/201714007017>.
- [147] F. Fulchini, M. Ghadiri, A. Borissova, B. Amblard, S. Bertholin, A. Cloupet, M. Yazdanpanah, Development of a methodology for predicting particle attrition in a cyclone by CFD-DEM, *Powder Technology* 357 (2019) 21–32. <https://doi.org/10.1016/j.powtec.2019.08.101>.
- [148] Y. Liu, X. Lan, C. Xu, G. Wang, J. Gao, CFD simulation of gas and solids mixing in FCC strippers, *AIChE J.* 58 (4) (2012) 1119–1132. <https://doi.org/10.1002/aic.12646>.
- [149] T. Patureaux, D. Barthod, Usage of Cfd Modelling for Improving an Fcc Riser Operation, *Oil Gas Sci. Technol. – Rev. IFP Energies nouvelles* 55 (2) (2000) 219–225. <https://doi.org/10.2516/ogst:2000014>.
- [150] R. Sadeghbeigi, *Fluid catalytic cracking handbook: Design, operation and troubleshooting of FCC facilities*, 2nd ed., Gulf Publ. Co, Houston, Tex., 2006.
- [151] Wen-Ching Yang, Ted M. Knowlton, L-valve equations, *Powder Technology* 77 (1) (1993) 49–54. [https://doi.org/10.1016/0032-5910\(93\)85006-U](https://doi.org/10.1016/0032-5910(93)85006-U).
- [152] T.M. Knowlton, *Non-mechanical solids feed and recycle devices for circulating fluidized beds*, Pergamon, 2013.
- [153] Zhengyang Wang, Shaozeng Sun, Hao Chen, Qigang Deng, Guangbo Zhao, Shaohua Wu, Experimental investigation on flow asymmetry in solid entrance region of a square circulating fluidized bed, *Particuology* 7 (6) (2009) 483–490. <https://doi.org/10.1016/j.partic.2009.07.004>.
- [154] Herbert P, The application of single fiber optic probes for the measurement of particle velocity and concentration in dilute gas-solid flows, MESC Thesis, The University of Western Ontario (1996).
- [155] Allan S. Issangya, S.B. Reddy Karri, Ray A. Cocco, Ted Knowlton, 12th International Conference on Fluidized Bed Technology CFB12At: Krakow, Poland (May 2017).
- [156] B.E. Launder, D.B. Spalding, The numerical computation of turbulent flows, *Computer Methods in Applied Mechanics and Engineering* 3 (2) (1974) 269–289. [https://doi.org/10.1016/0045-7825\(74\)90029-2](https://doi.org/10.1016/0045-7825(74)90029-2).
- [157] P.C. Johnson, R. Jackson, Frictional–collisional constitutive relations for granular materials, with application to plane shearing, *J. Fluid Mech.* 176 (-1) (1987) 67. <https://doi.org/10.1017/S0022112087000570>.
- [158] T. Li, J. Grace, X. Bi, Study of wall boundary condition in numerical simulations of bubbling fluidized beds, *Powder Technology* 203 (3) (2010) 447–457. <https://doi.org/10.1016/j.powtec.2010.06.005>.
- [159] T. Li, S. Benyahia, Evaluation of wall boundary condition parameters for gas-solids fluidized bed simulations, *AIChE J.* 59 (10) (2013) 3624–3632. <https://doi.org/10.1002/aic.14132>.
- [160] C. Jayarathna, B. Moldestad, L.-A. Tokheim, Validation of results from Barracuda CFD modelling to predict the minimum fluidization velocity and the pressure drop of Geldart A particles, Linköping University Electronic Press, 2017, pp. 76–82.
- [161] Taxil Isabelle, *Etude hydrodynamique des lits fluidisés turbulents*, thèse de Doctorat, Université technologique de Compiègne (1996).
- [162] Allan S. Issangya, Ted Knowlton, S. B. Reddy Karri, The 12th International Conference on Fluidization (2007).
- [163] Tsuji T, Morikawa Y, Shioni H., *Journal of Fluid Mechanics* 139, pp. 417–434 (1984).

REFERENCES

- [164] J. Peltola, MSc Thesis Juho Peltola - Dynamics in a Circulating Fluidized Bed: Experimental and Numerical Study (2019).
- [165] W. Yu, P. Fede, M. Yazdanpanah, B. Amblard, F. Euzenat, O. Simonin, Gas-solid fluidized bed simulations using the filtered approach: Validation against pilot-scale experiments, *Chemical Engineering Science* (2020) 115472. <https://doi.org/10.1016/j.ces.2020.115472>.
- [166] M. Abdulkadir, V. Hernandez-Perez, S. Lo, I.S. Lowndes, B.J. Azzopardi, Comparison of experimental and Computational Fluid Dynamics (CFD) studies of slug flow in a vertical riser, *Experimental Thermal and Fluid Science* 68 (2015) 468–483. <https://doi.org/10.1016/j.expthermflusci.2015.06.004>.

APPENDIX

Appendix 1 Jet cup attrition testing

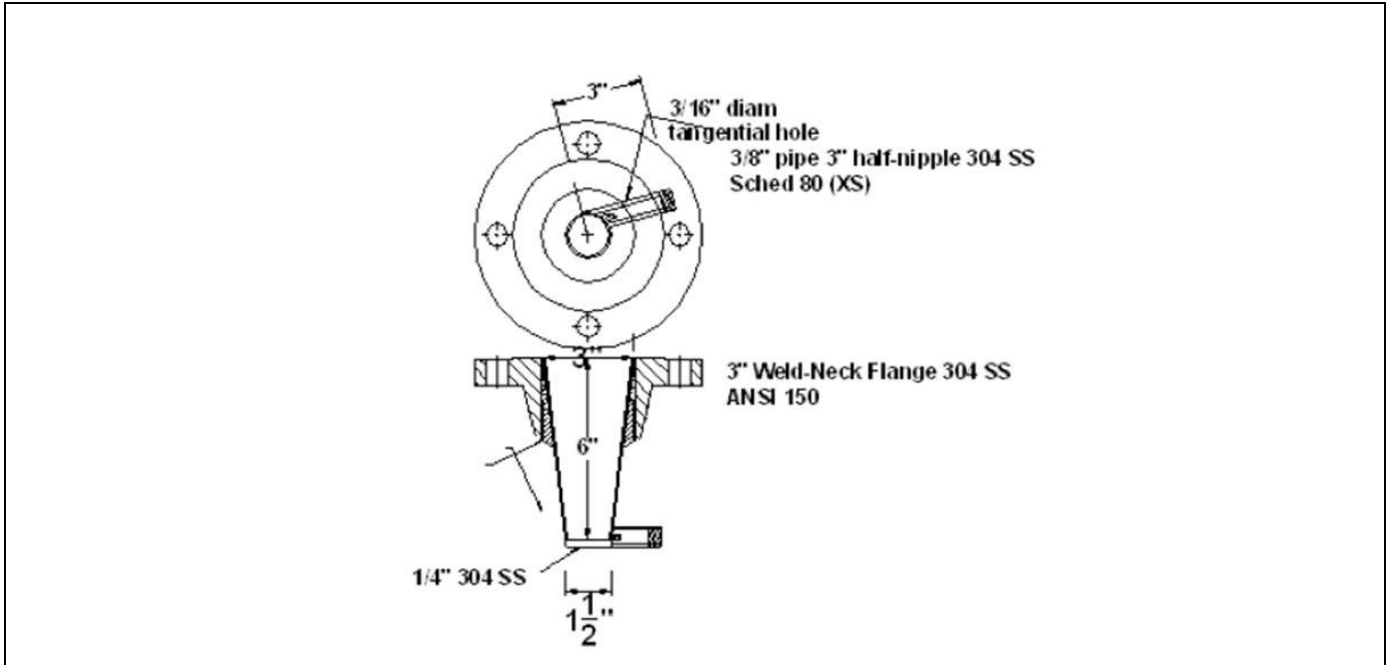


Figure 0-1: Sketch of the jet cup (dimensions are in inches)

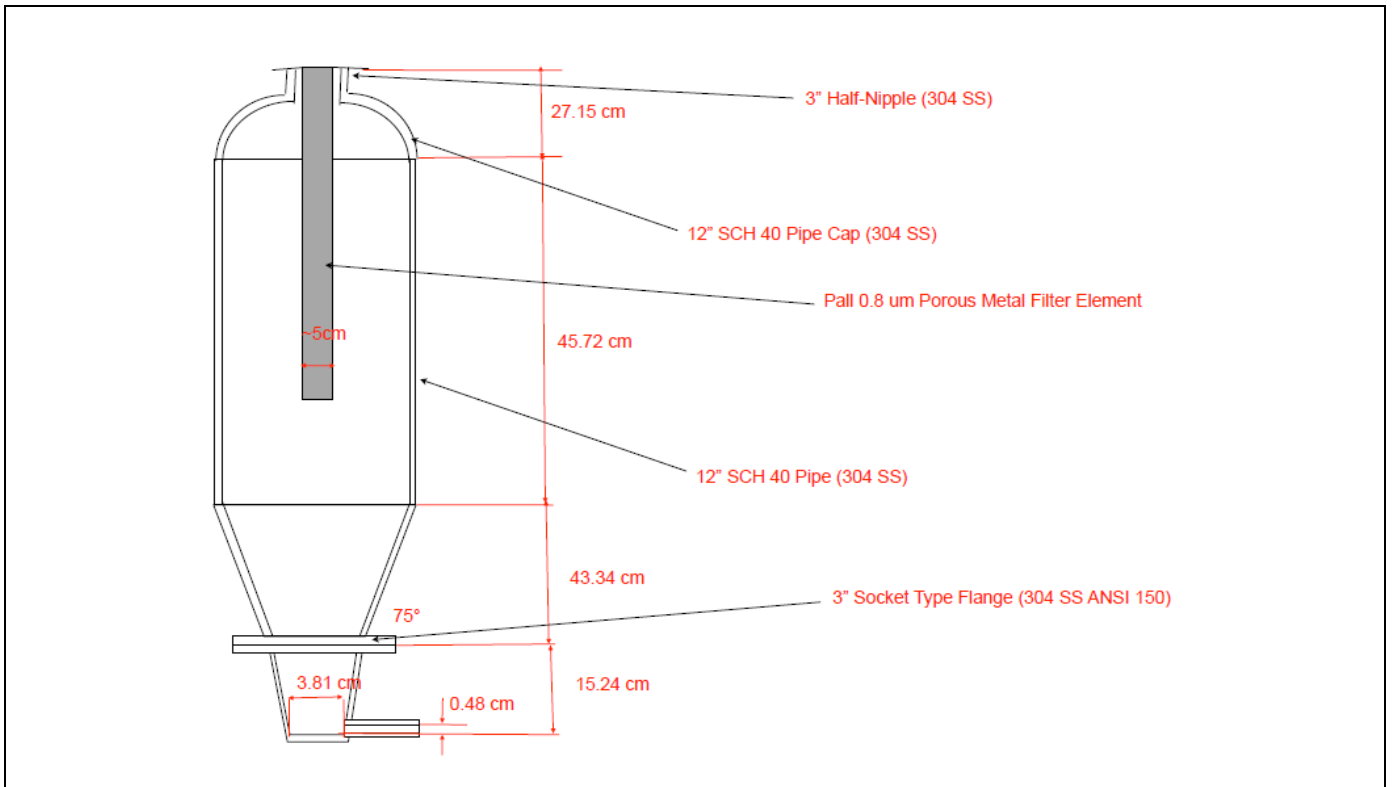


Figure 0-2: Sketch of the overall configuration

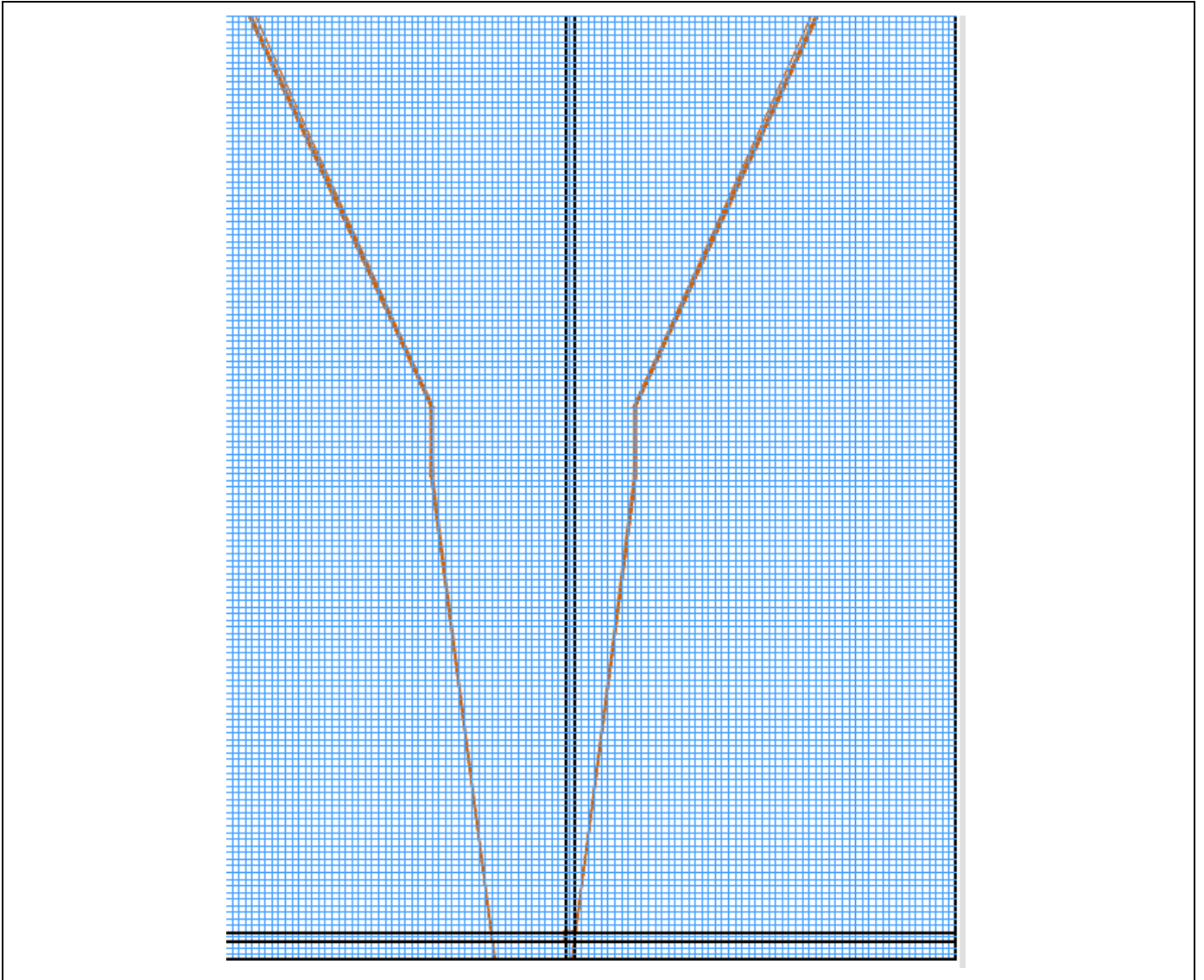


Figure 0-3: Jet cup hexahedral structure mesh

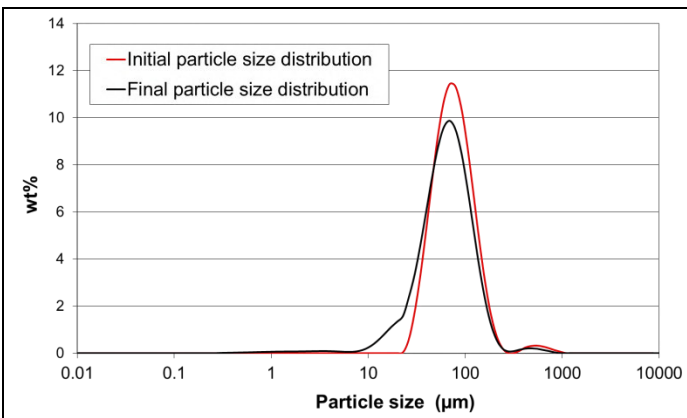


Figure 0-4: Initial and Final Particle Size Distribution for a test with 100 grams of Group A equilibrium FCC particles during one hour ; Air Injection velocity = 90 m/s

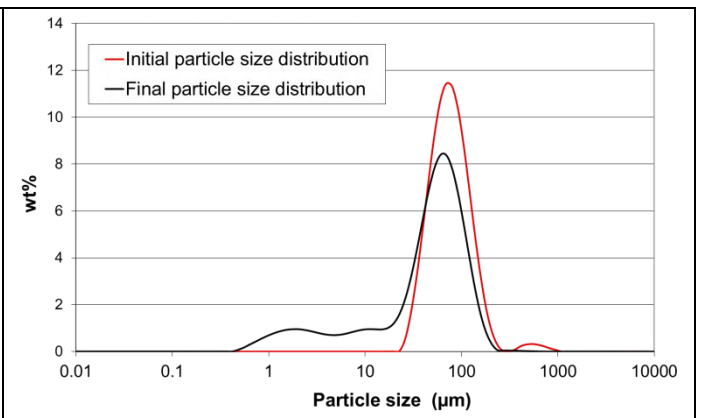


Figure 0-5: Initial and Final Particle Size Distribution for a test with 100 grams of Group A equilibrium FCC particles during one hour ; Air Injection velocity = 180 m/s

Table 0-1: Results for jet cup testing repetitions on the three solids of interest

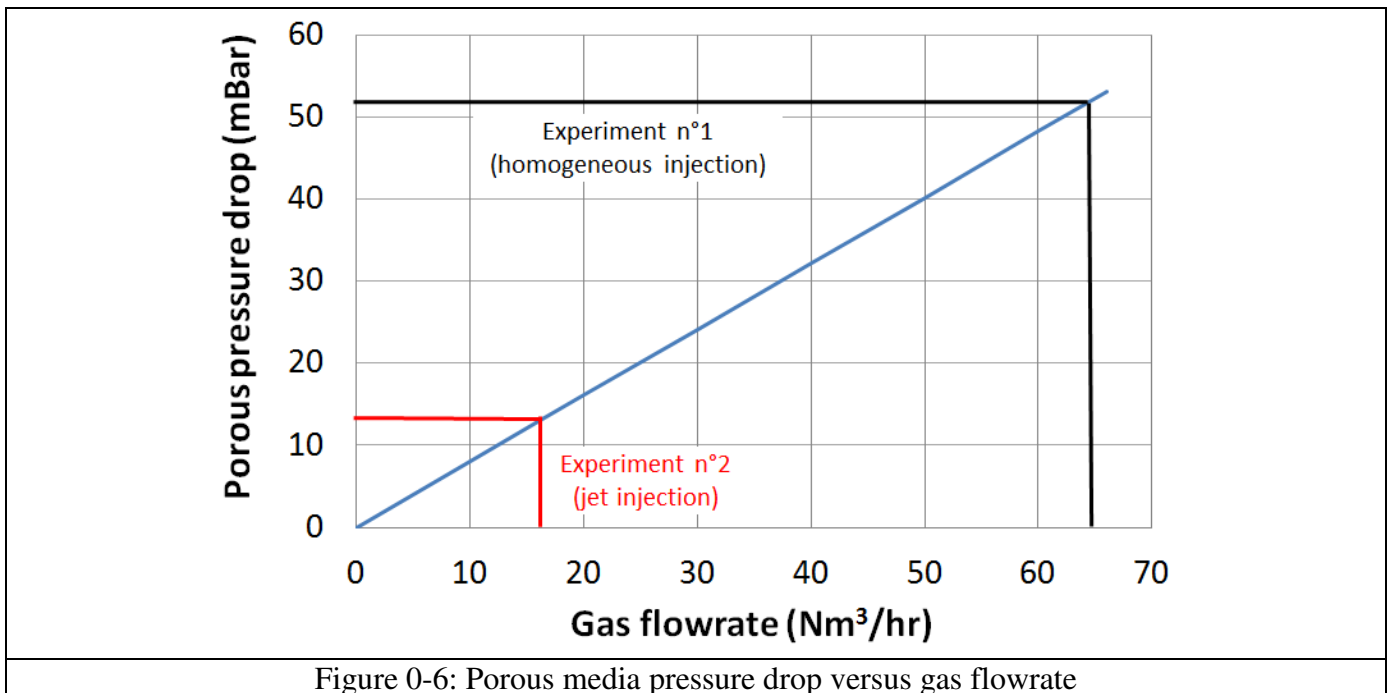
Solids	Test number	Coefficient D	Coefficient E
Group A equilibrium FCC	Test 1	15.2	5.8
	Test 2	11.5	6.1
	Test 3	13.3	6.9
	Test 4	13.6	7
	Test 5	13.5	6.8
	Test 6	14.2	6.7
	<i>Average / Standard deviation</i>	<i>13.5 / 1.2</i>	<i>6.5 / 0.5</i>
Group B fresh oxygen carrier	Test 1	12.9	1.2
	Test 2	11.2	3.2
	Test 3	11.9	2.8
	Test 4	13.3	0.5
	Test 5	11.3	2.1
	Test 6	12.3	2
	<i>Average / Standard deviation</i>	<i>12.15 / 0.8</i>	<i>2 / 1</i>
Group B equilibrium oxygen carrier	Test 1	34.7	6.9
	Test 2	31.8	7.2
	<i>Average / Standard deviation</i>	<i>33.2 / 2</i>	<i>7.1 / 0.2</i>

Appendix 2 20 cm fluidized bed experiments characteristic

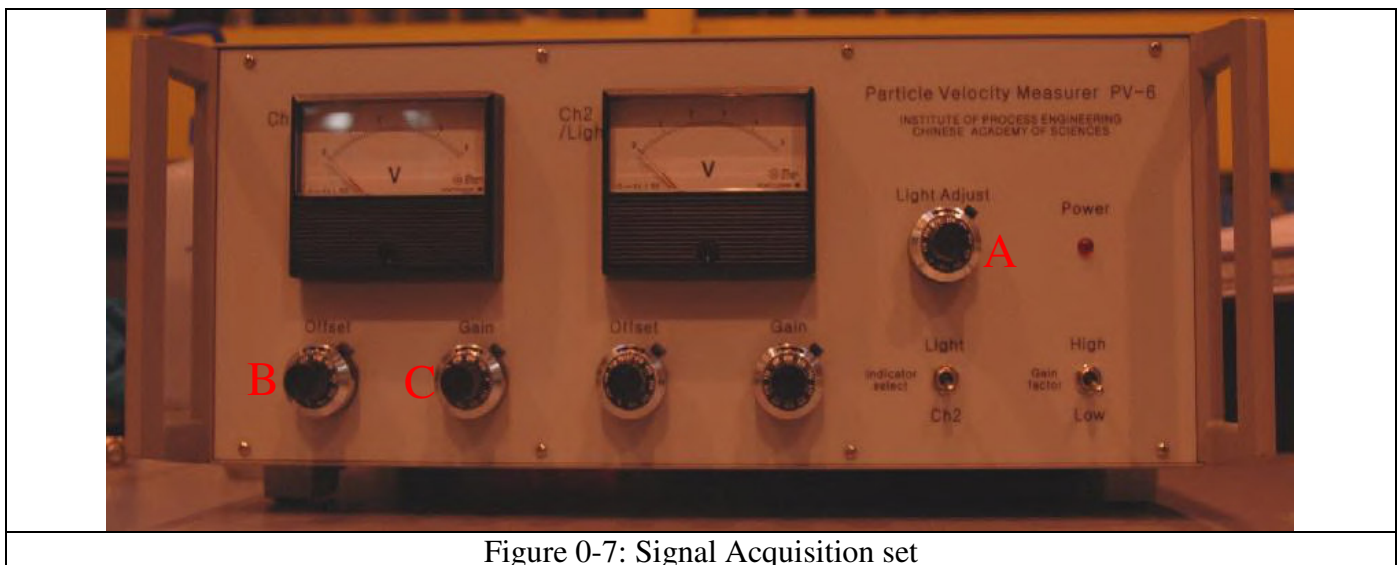
Characteristic of the porous media used for gas injection at the column bottom

- Characteristics: Poral in copper, class 15, diameter 212 mm, thickness 5 mm

http://sintertech.org/fr/wp-content/uploads/sites/10/2014/08/2016_04_Brochure-SINTERTECH-PORAL-compressed.pdf



Fiber probes acquisition system used at IFPEN



- A: Light intensity adjustment
- B: Signal Offset adjustment
- C: Signal Gain adjustment

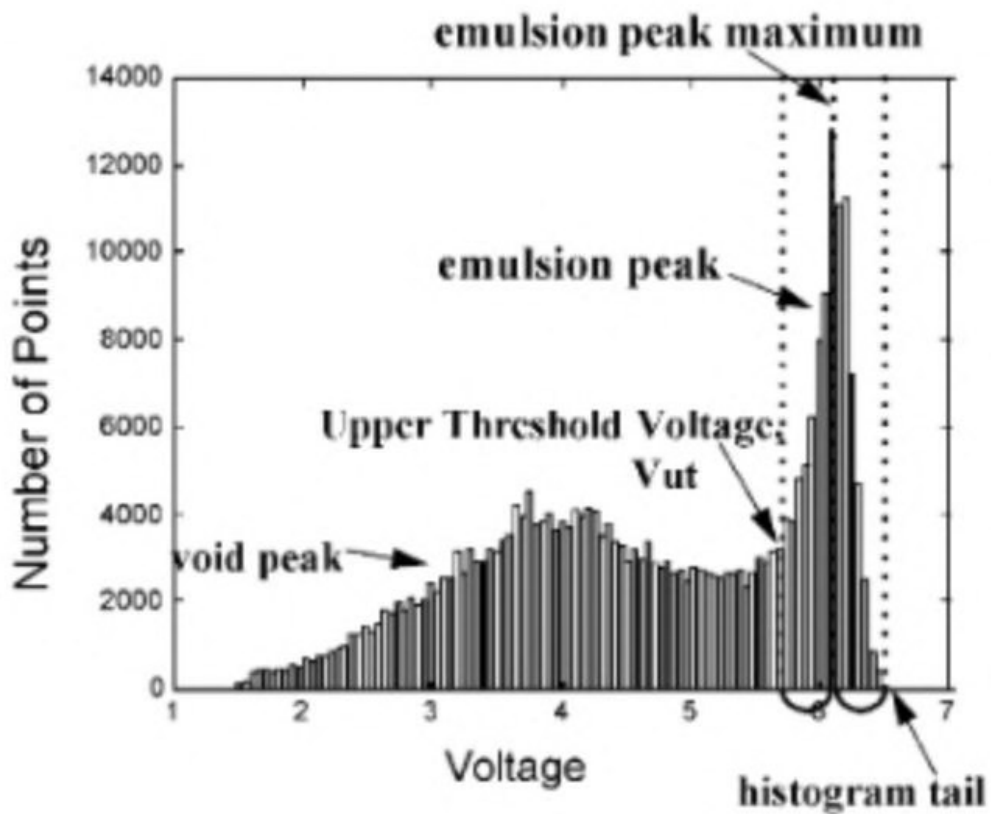
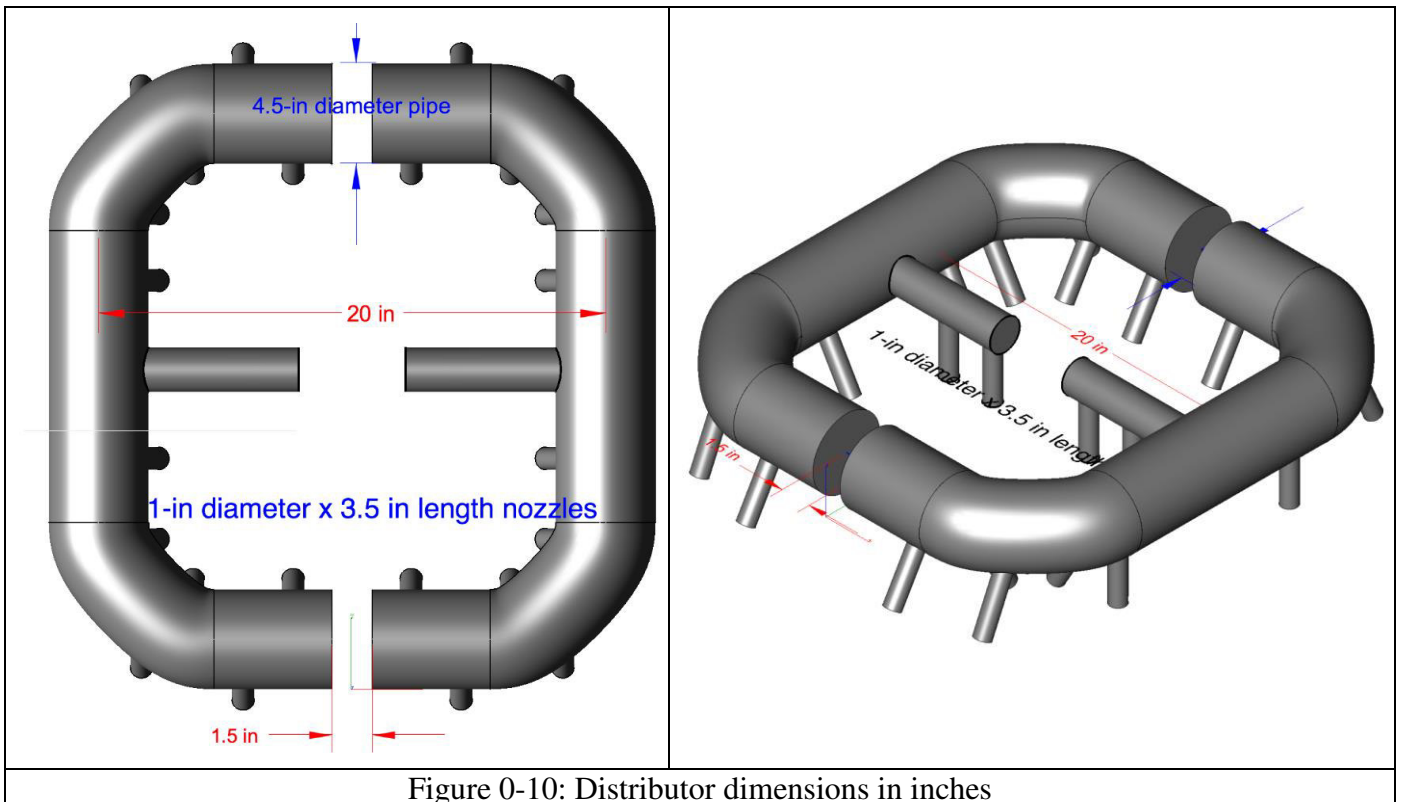
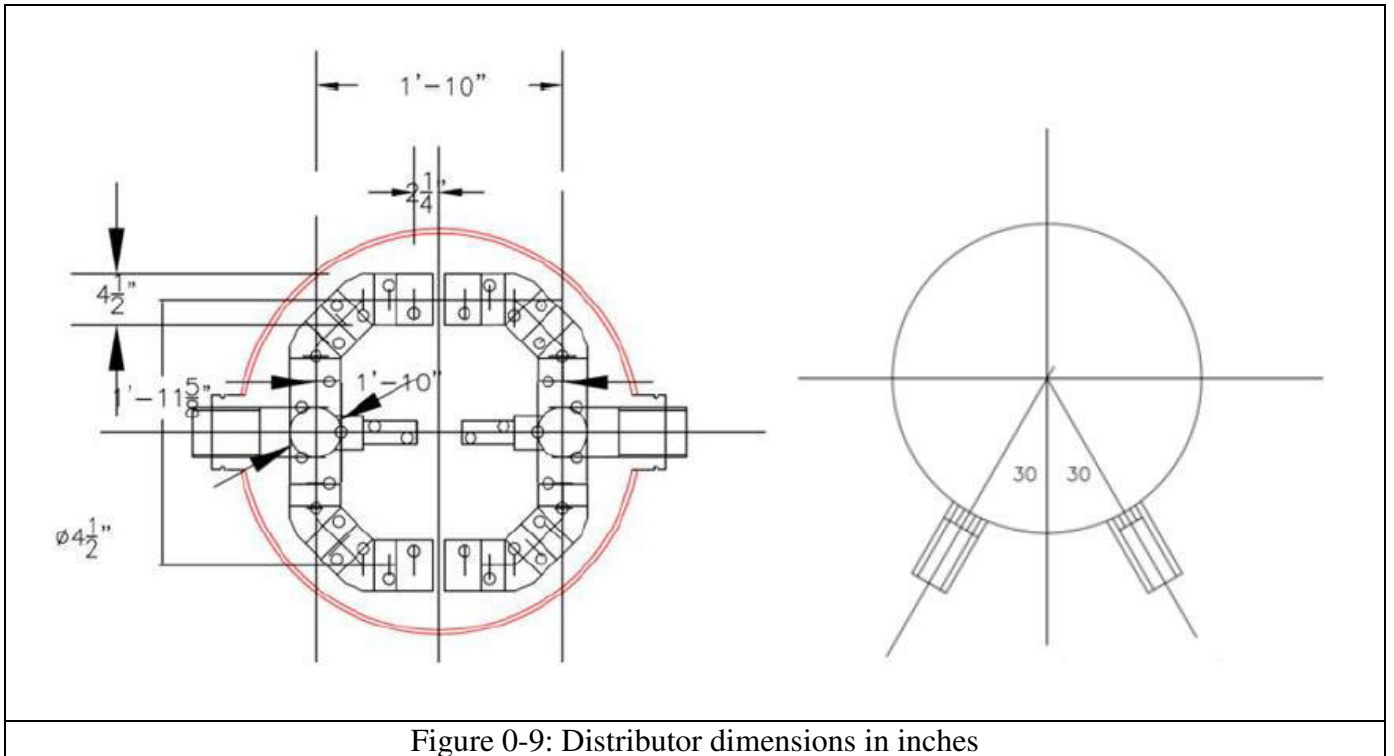
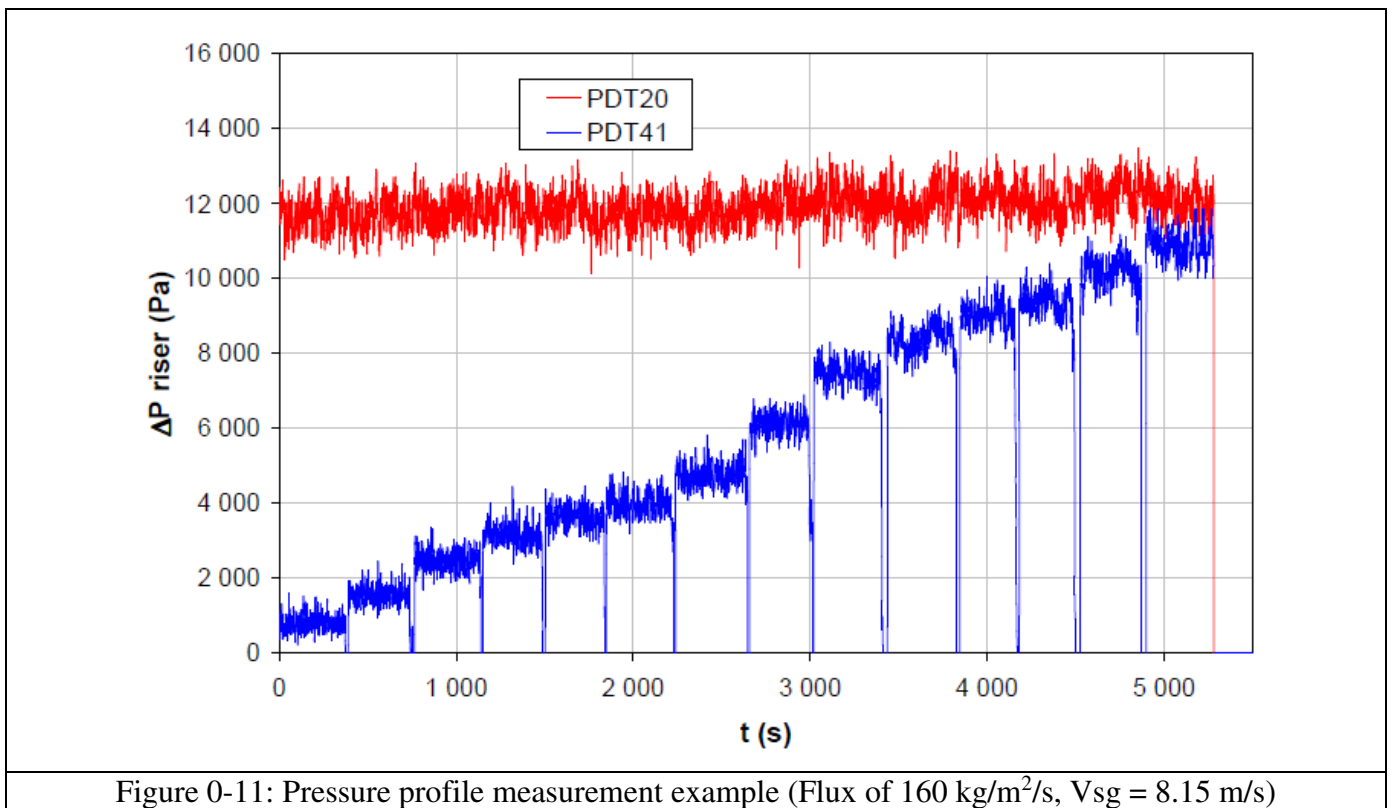


Figure 0-8: Schweitzer et al., Method to determine the transition between emulsion and bubble phases from the optical probe histogram signal values

Appendix 3 PSRI 90 cm fluidized bed distributor design



Appendix 4 30 cm riser experiments



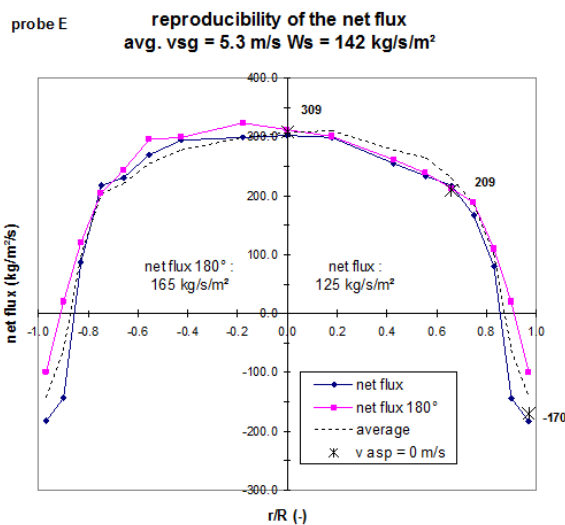
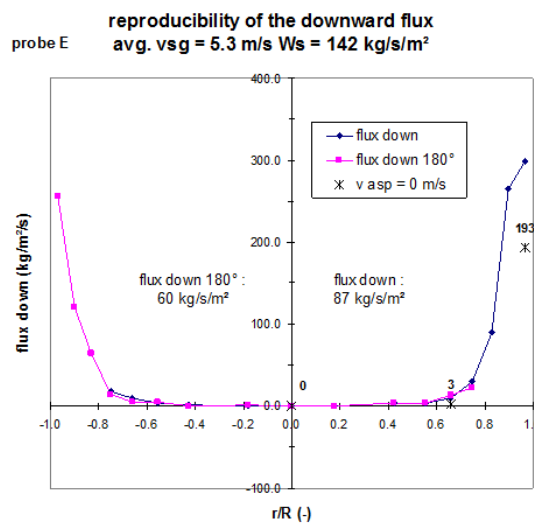
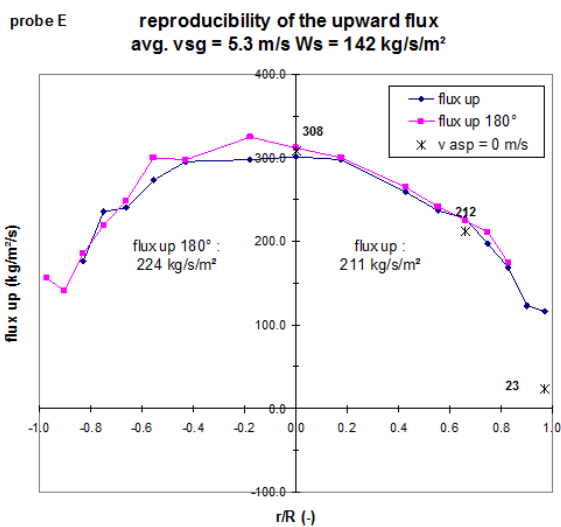
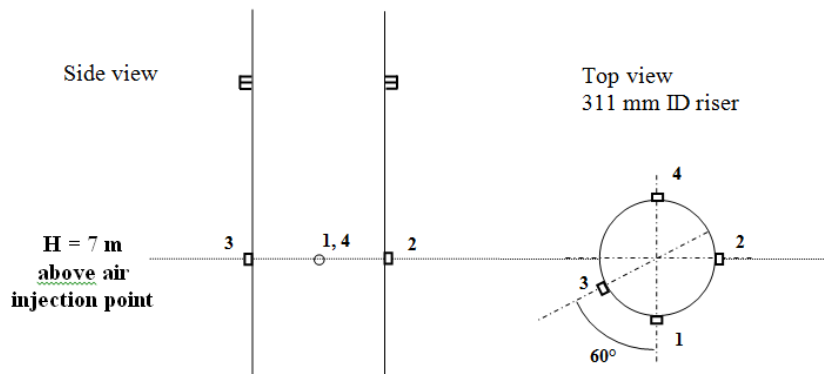


Figure 0-12: Riser experiments carried out at IFP Energies Nouvelles in 2001 on a 31 cm riser with FCC particles. Investigation of the pseudo isokinetic probe profile repeatability using two riser ports opposite to each other (port 1 and port 4)

Appendix 5 fvSolution file for OpenFOAM simulations

```
FoamFile
{
  version 2.0;
  format  ascii;
  class   dictionary;
  location "system";
  object  fvSolution;
}
// *****

solvers
{
  "alpha.*"
  {
    nAlphaCorr 1;
    nAlphaSubCycles 2;

    smoothLimiter 0.1;

    implicitPhasePressure yes;
    solver        smoothSolver;
    smoother      symGaussSeidel;
    tolerance     1e-9;
    relTol        0;
    minIter       1;
  }

  p_rgh
  {
    solver        GAMG;
    smoother      DIC;
    tolerance     1e-8;
    relTol        0;
  }

  p_rghFinal
  {
    $p_rgh;
    relTol        0;
  }

  "U.*"
  {
    solver        smoothSolver;
    smoother      symGaussSeidel;
    tolerance     1e-5;
    relTol        0;
    minIter       1;
  }

  "(h|e).*"
  {
    solver        smoothSolver;
    smoother      symGaussSeidel;
    tolerance     1e-6;
    relTol        2;
    minIter       0;
    maxIter       0;
  }
}
```

```

}

"Theta.*"
{
  solver      smoothSolver;
  smoother    symGaussSeidel;
  tolerance   1e-6;
  relTol      0;
  minIter     1;
}

"(k|epsilon).*"
{
  solver      smoothSolver;
  smoother    symGaussSeidel;
  tolerance   1e-5;
  relTol      0;
  minIter     1;
}
}

PIMPLE
{
  nOuterCorrectors 3;
  nCorrectors      1;
  nNonOrthogonalCorrectors 0;
}

relaxationFactors
{
  equations
  {
    ".*"      1;
  }
}

```

Appendix 6 fvSchemes file for OpenFOAM simulations

```
FoamFile
{
  version 2.0;
  format  ascii;
  class   dictionary;
  location "system";
  object  fvSchemes;
}
// *****

ddtSchemes
{
  default Euler;
}

gradSchemes
{
  default Gauss linear;
}

divSchemes
{
  default none;

  "div(phi,alpha.*)"      Gauss vanLeer;
  "div(phir,alpha.*)"    Gauss vanLeer;

  "div(alphaRhoPhi.*,U.*)"  Gauss limitedLinearV 1;
  "div(phi.*,U.*)"         Gauss limitedLinearV 1;

  "div(alphaRhoPhi.*(h|e).*)" Gauss limitedLinear 1;
  "div(alphaRhoPhi.*,K.*)"  Gauss limitedLinear 1;
  "div(alphaPhi.*,p)"      Gauss limitedLinear 1;

  div(alphaRhoPhi.particles,Theta.particles) Gauss limitedLinear 1;

  "div(alphaRhoPhi.*(k|epsilon).*)" Gauss limitedLinear 1;

  div((((alpha.air*thermo:rho.air)*nuEff.air)*dev2(T(grad(U.air)))) Gauss linear;

  div((((thermo:rho.particles*nut.particles)*dev2(T(grad(U.particles))))+(((thermo:rho.particles*lambda.particles)*div(phi.particles))*I))) Gauss linear;
}

laplacianSchemes
{
  default Gauss linear uncorrected;
  bounded Gauss linear uncorrected;
}

interpolationSchemes
{
  default linear;
}
```



```
snGradSchemes
{
  default uncorrected;
  bounded uncorrected;
}
```

Appendix 7 20 cm fluidized bed experiment n°1 Barracuda VR® simulations

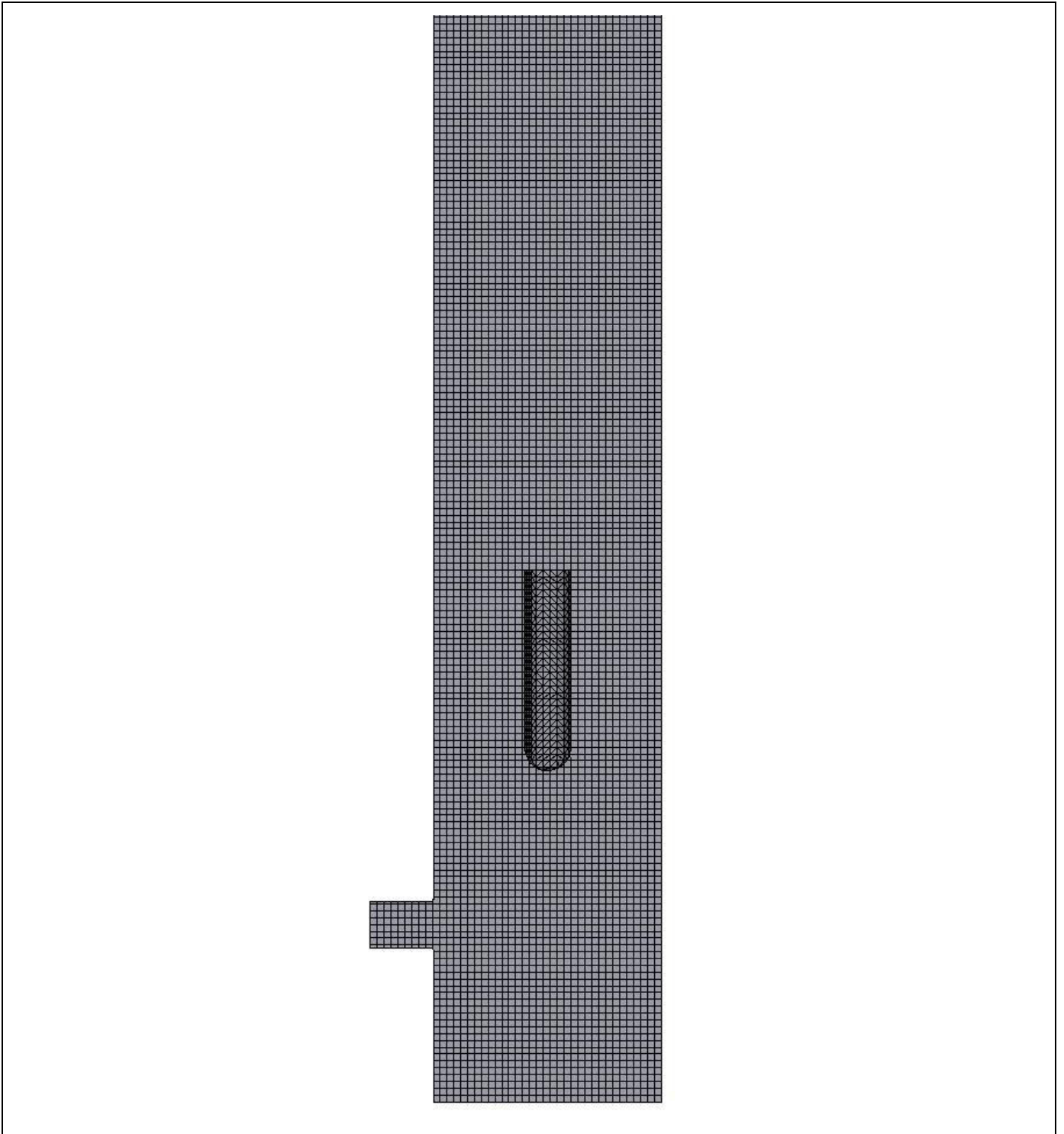


Figure 0-13: 470 000 cells Barracuda VR® mesh, cell size of 5mm

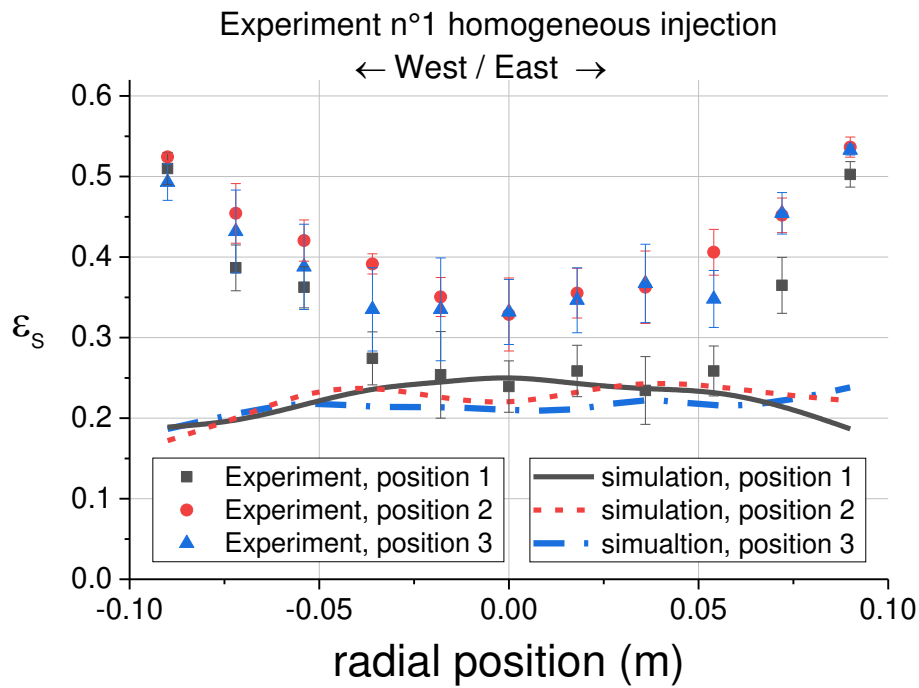


Figure 0-14: Simulation n°1 Barracuda VR[®], Default Barracuda VR[®] parameters, Comparisons of solid volume fraction profiles in the North South direction, experiment n°1 homogeneous injection

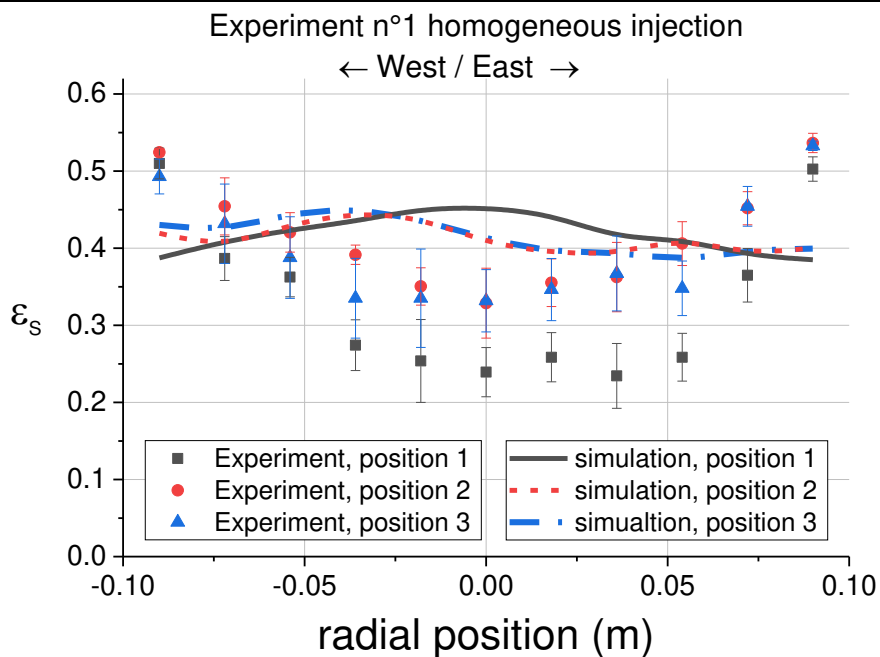


Figure 0-15: Simulation n°2 Barracuda VR[®] drag modified with multiplier of 0.4, Comparisons of solid volume fraction profiles in the North South direction, experiment n°1 homogeneous injection

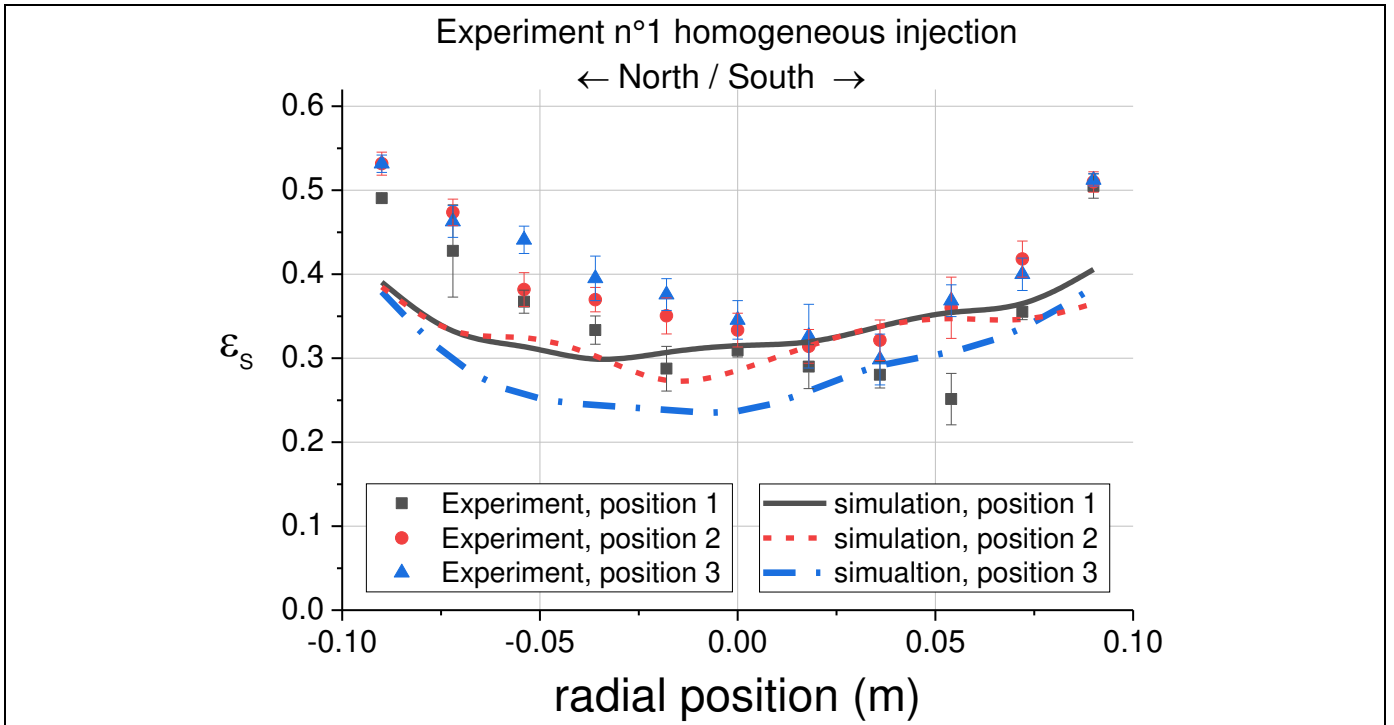


Figure 0-16: Simulation n°3bis Barracuda VR® drag modified with multiplier of 0.6 and modified bottom injection distribution, Comparisons of solid volume fraction profiles in the North South direction, experiment n°1 homogeneous injection

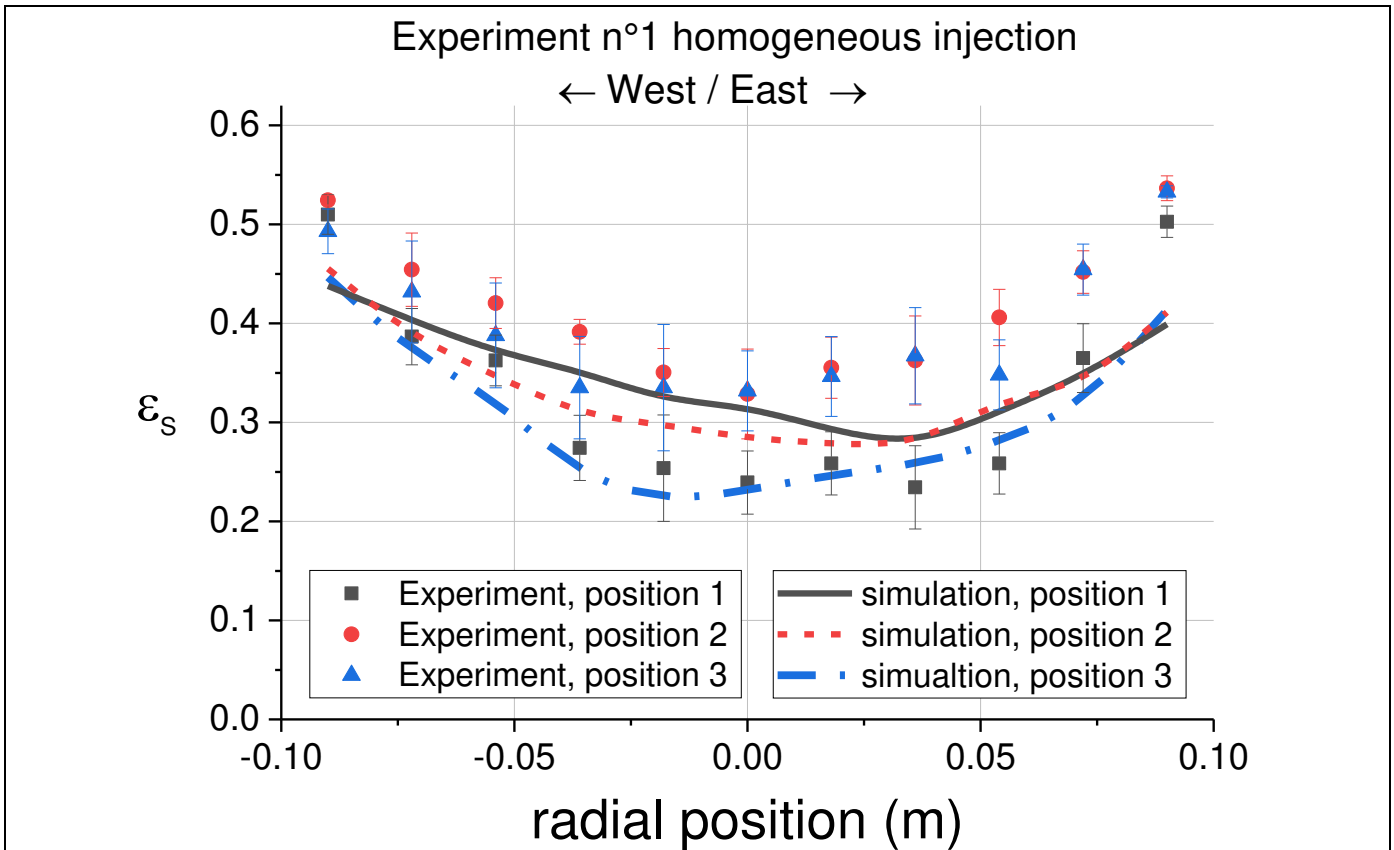


Figure 0-17: Simulation n°3bis Barracuda VR® drag modified with multiplier of 0.6 and modified bottom injection distribution, Comparisons of solid volume fraction profiles in the West East direction, experiment n°1 homogeneous injection

Experiment n°1: Homogeneous injection

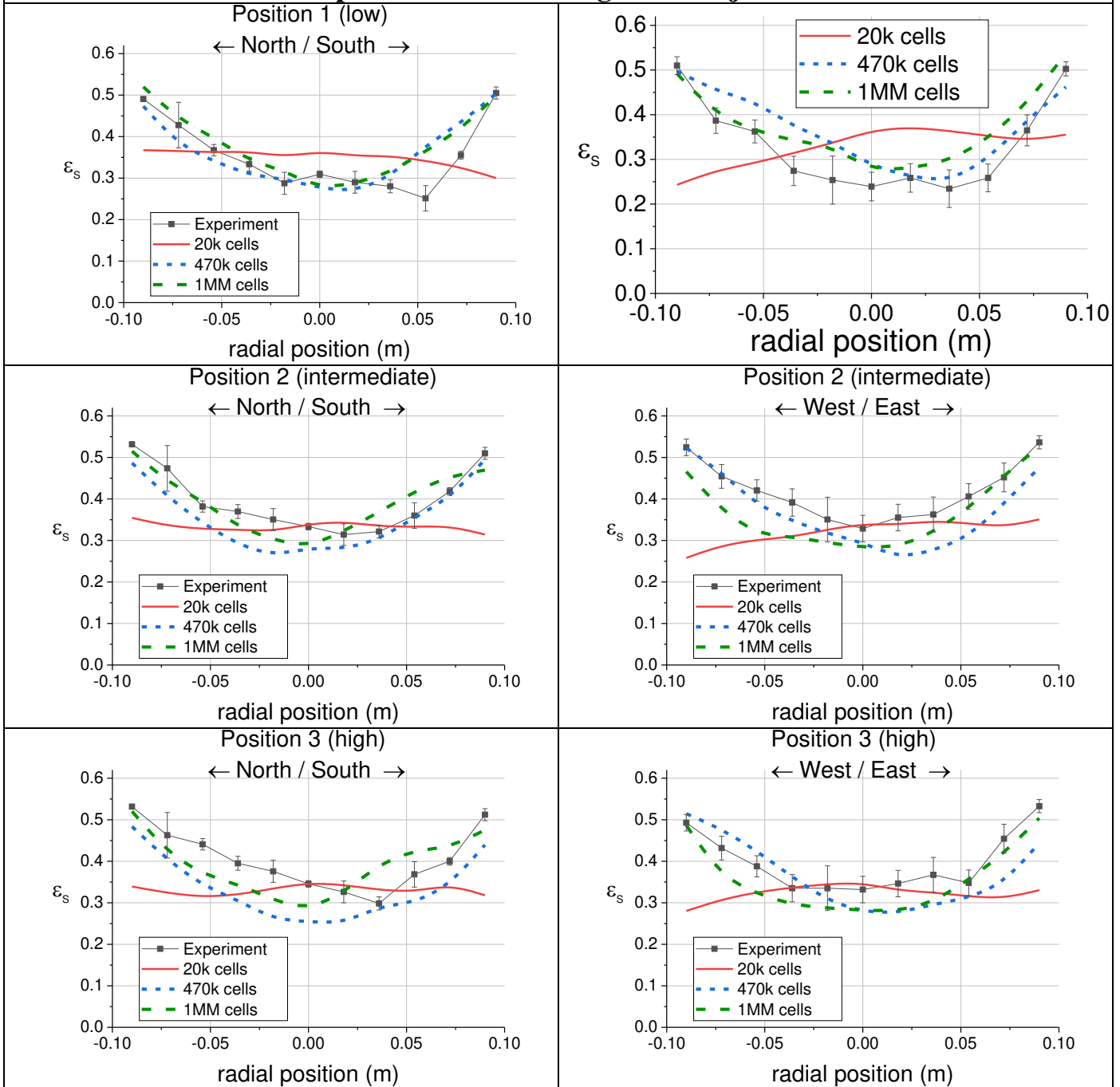


Figure 0-18: Effect of mesh size Barracuda VR[®], default Barracuda VR[®] drag multiplier of 0.4 and modified bottom injection distribution, Comparisons of solid volume fraction profiles

Experiment n°1: Homogeneous injection

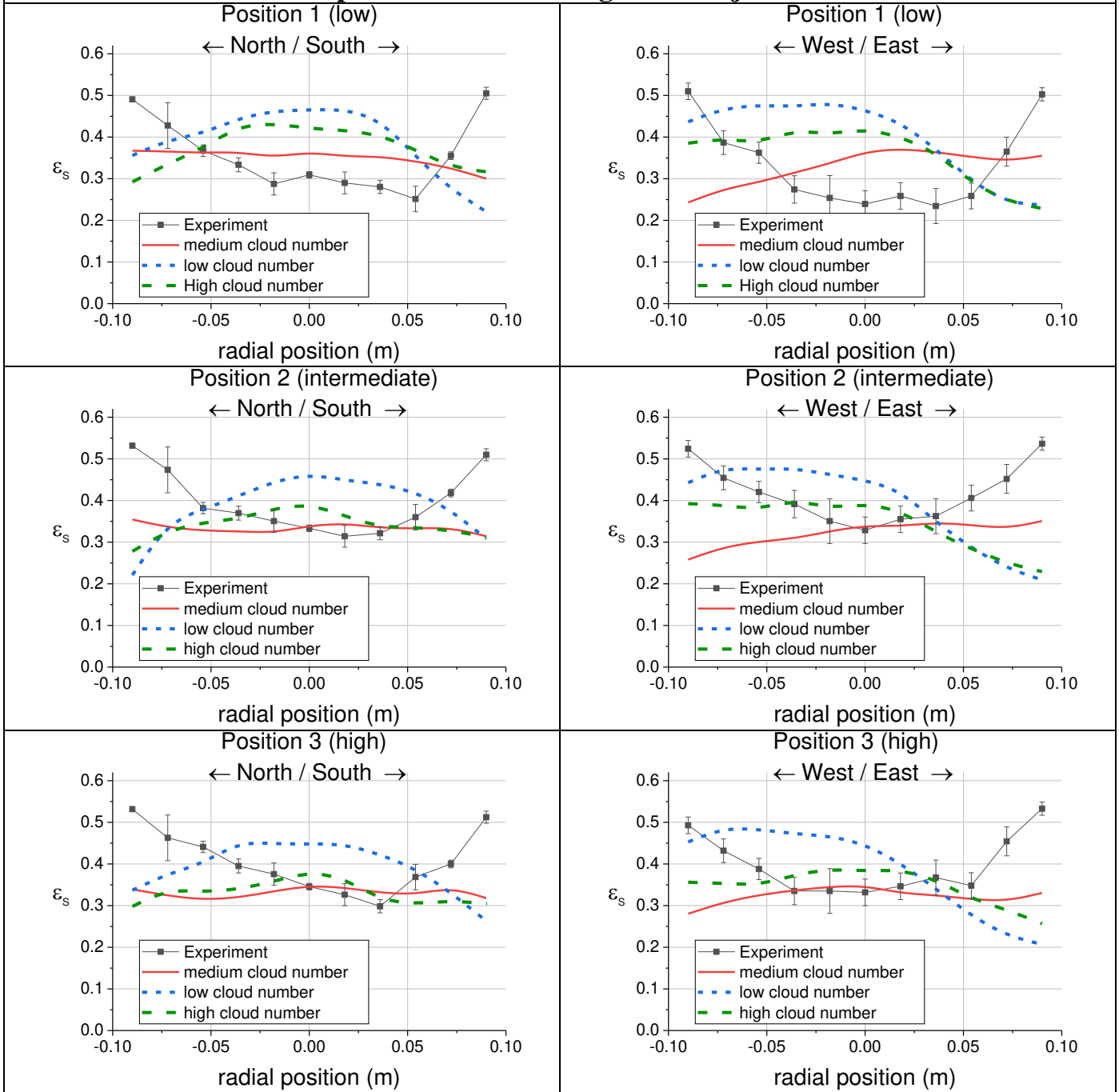
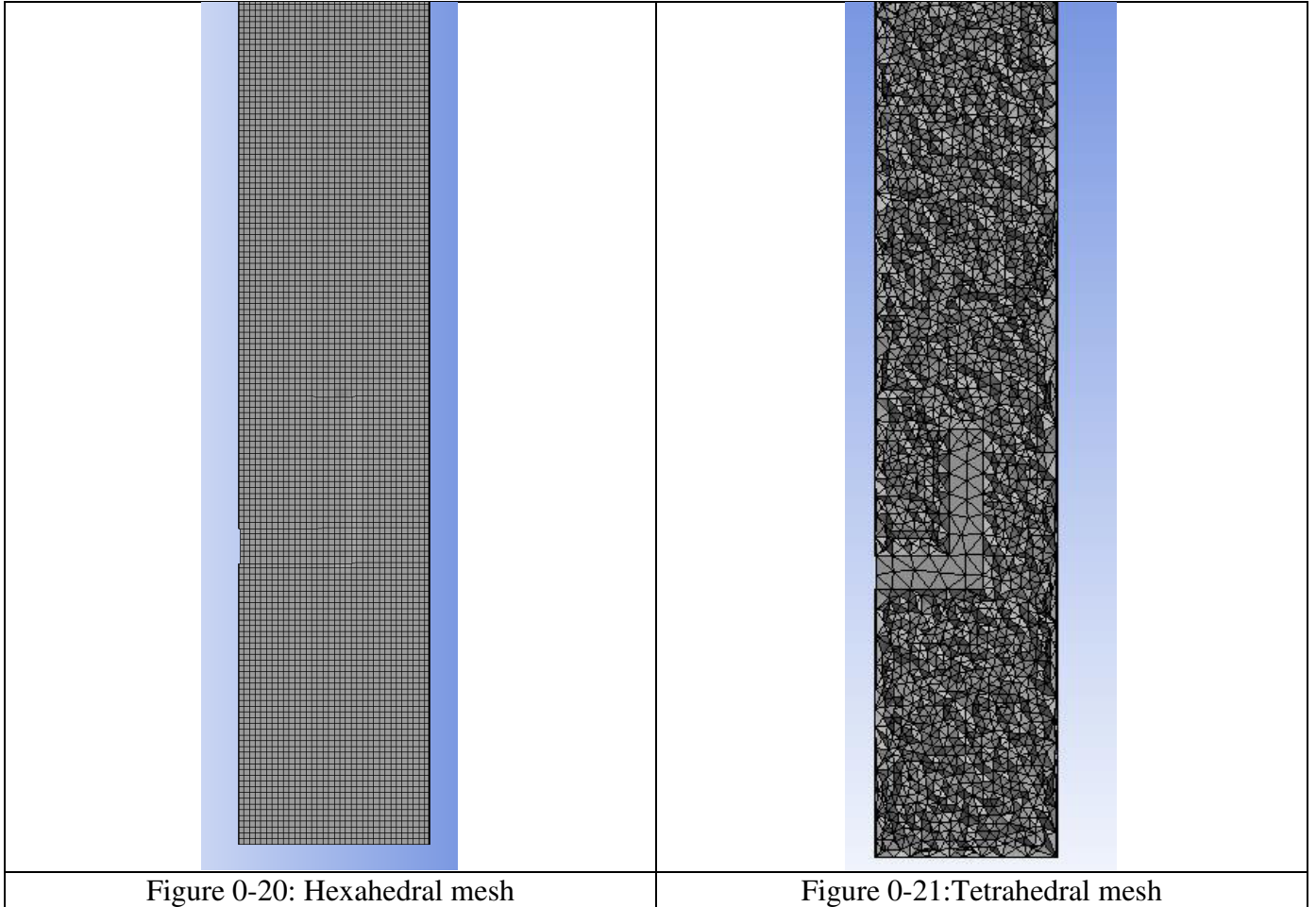


Figure 0-19: Barracuda VR[®] coarse mesh, Effect of clouds number VR, default Barracuda VR[®] drag multiplier of 0.4 and modified bottom injection distribution, Comparisons of solid volume fraction profiles

Appendix 8 20 cm fluidized bed experiment n°1 OpenFOAM simulations



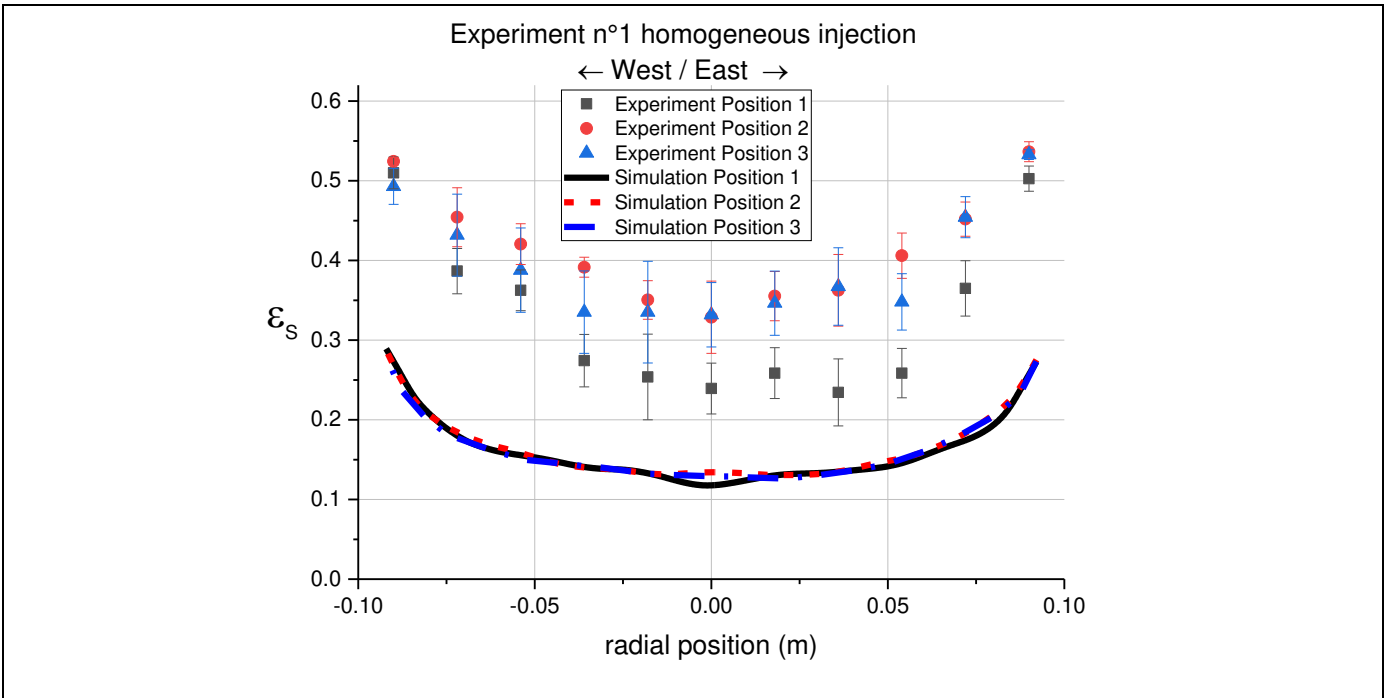


Figure 0-22: Simulation n°1 openFOAM, default Barracuda VR[®] drag, Comparisons of solid volume fraction profiles in the West East direction, experiment n°1 homogeneous injection

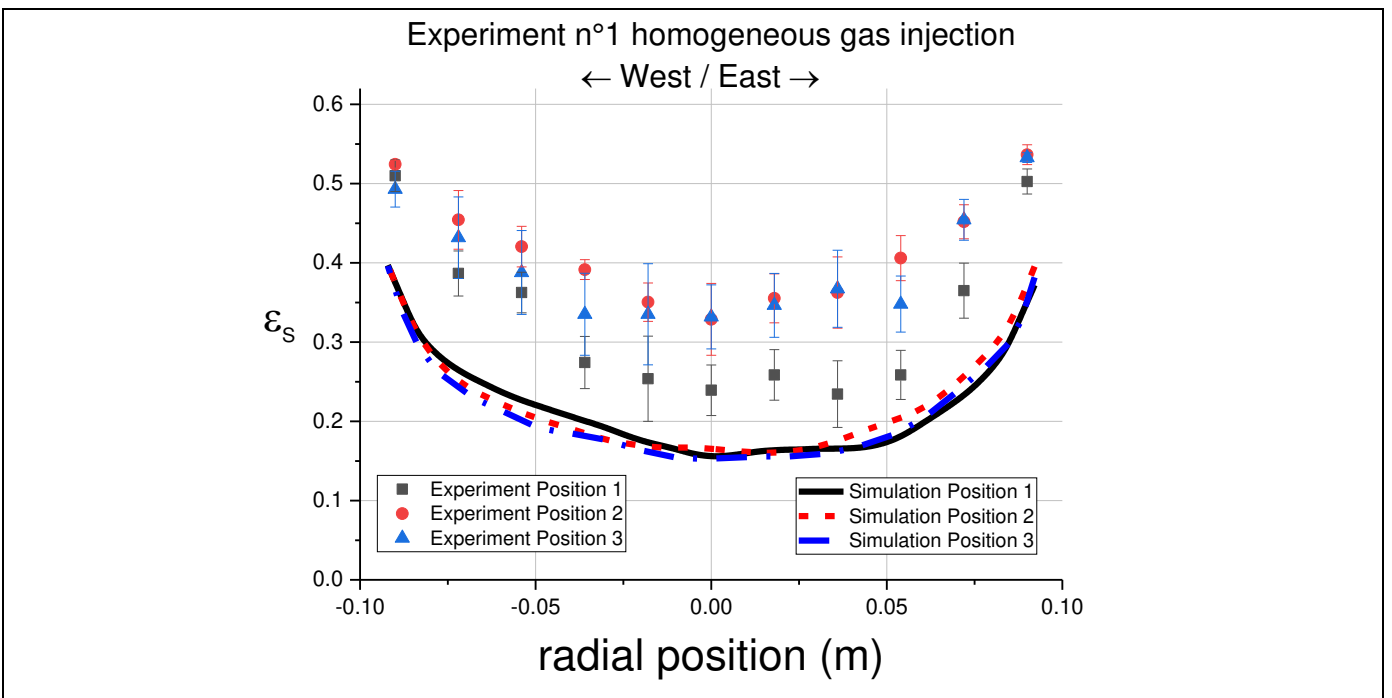


Figure 0-23: Simulation n°2 openFOAM, default Barracuda VR[®] drag with multiplier of 0.4, Comparisons of solid volume fraction profiles in the West East direction, experiment n°1 homogeneous injection

Experiment n°1: Homogeneous injection

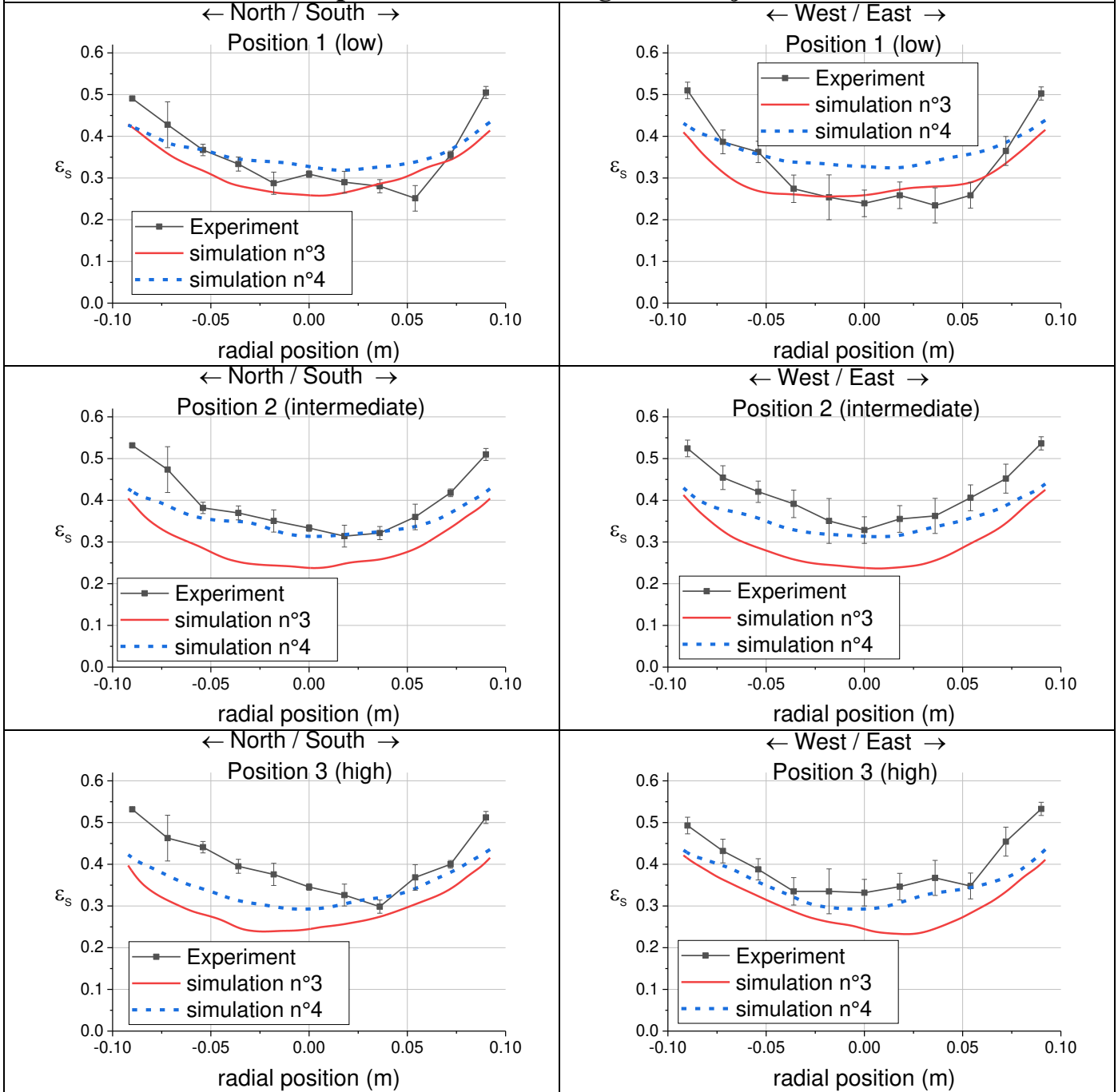


Figure 0-24: Simulation n°3 and simulation n°4 openFOAM, default Barracuda VR[®] drag with clustering approach, Comparisons of solid volume fraction profiles in the West East direction, experiment n°1 homogeneous injection

Experiment n°1: Homogeneous injection

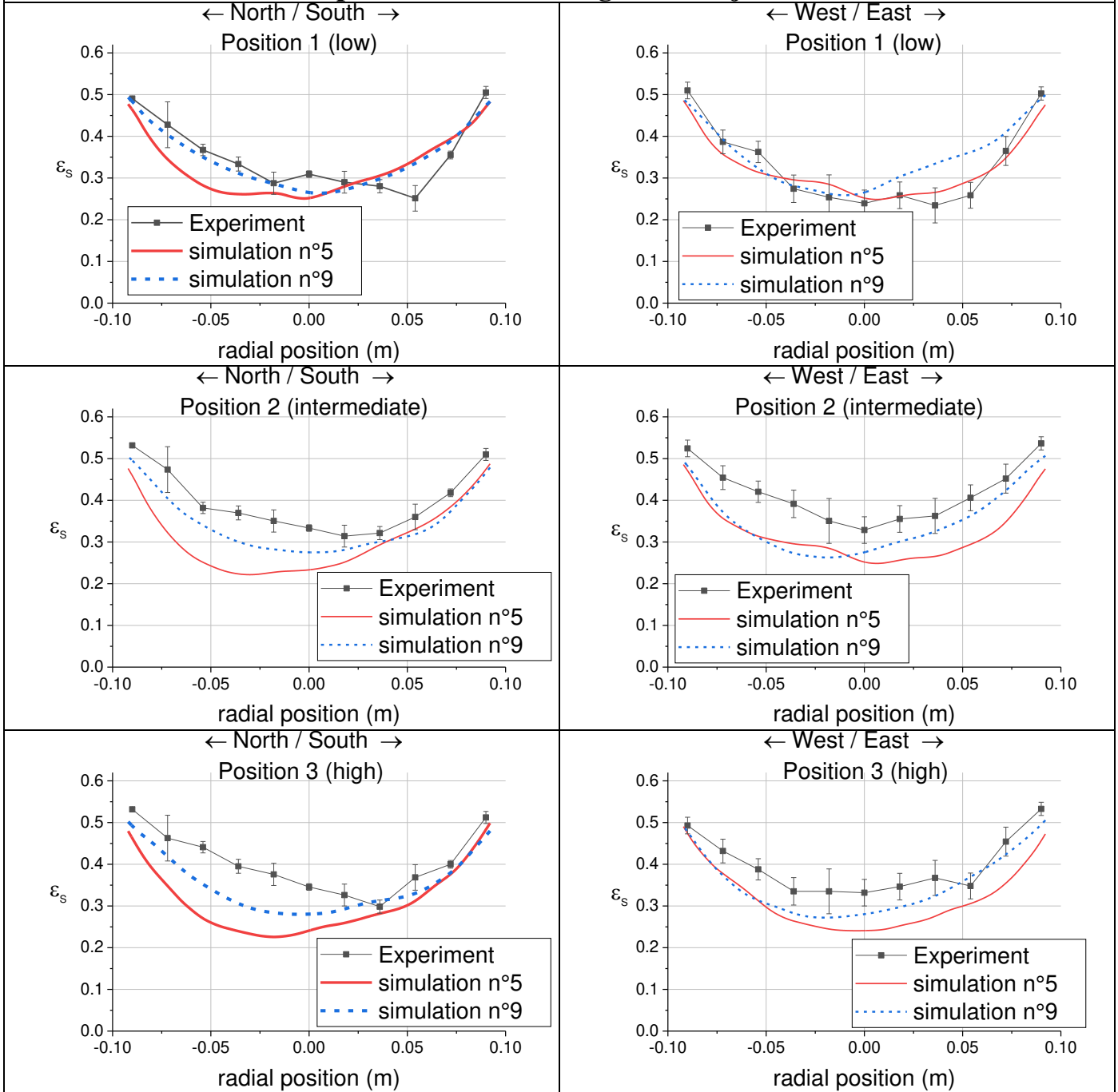


Figure 0-25: Simulation n°5 and simulation n°9 openFOAM, Gidaspow drag law with clustering approach, Comparisons of solid volume fraction profiles in the West East direction, experiment n°1 homogeneous injection

Experiment n°1: Homogeneous injection

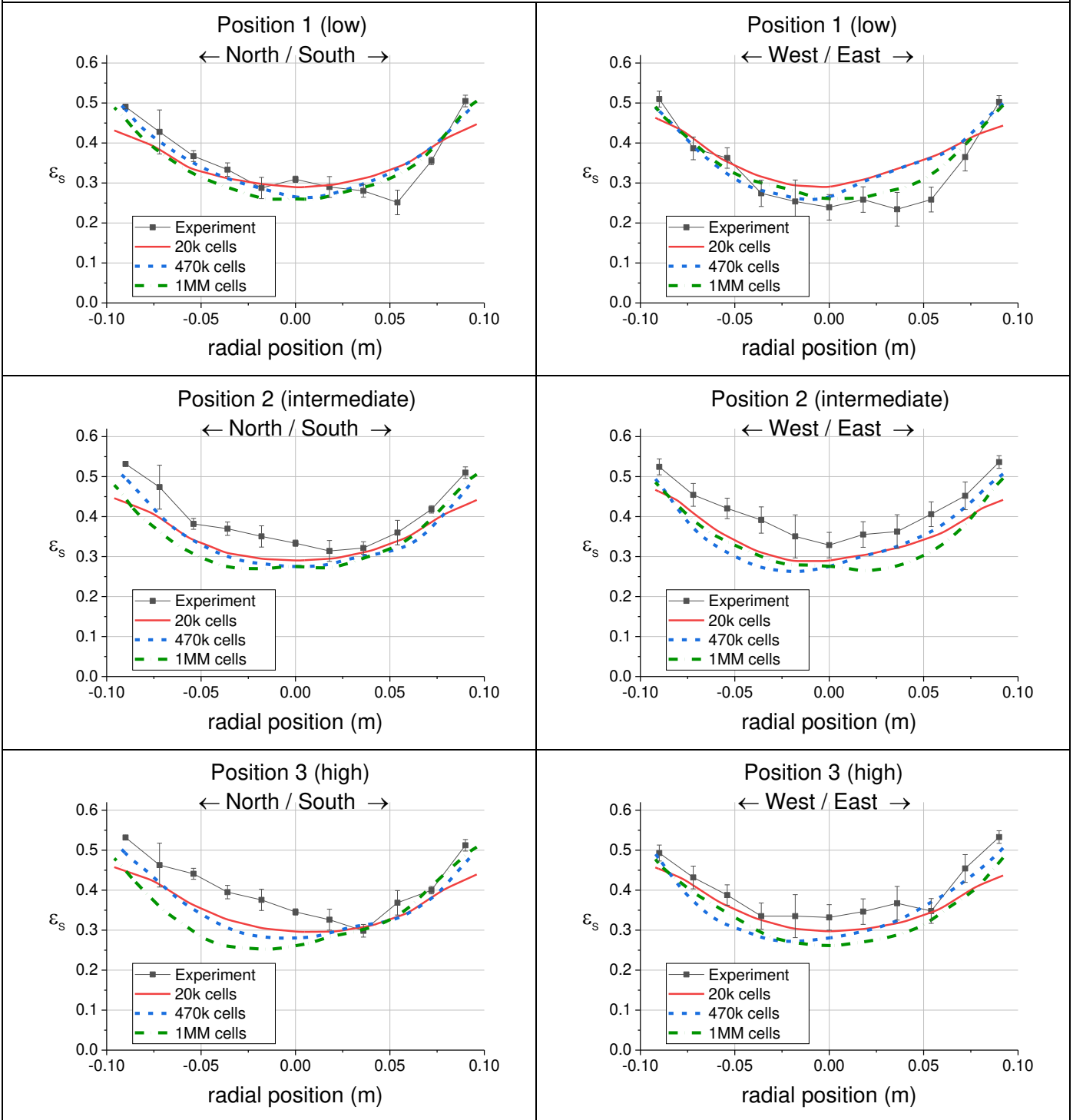


Figure 0-26: Mesh effect openFOAM, Gidaspow drag law with clustering effect, Comparisons of solid volume fraction profiles in the West East direction, experiment n°1 homogeneous injection

Experiment n°1: Homogeneous injection

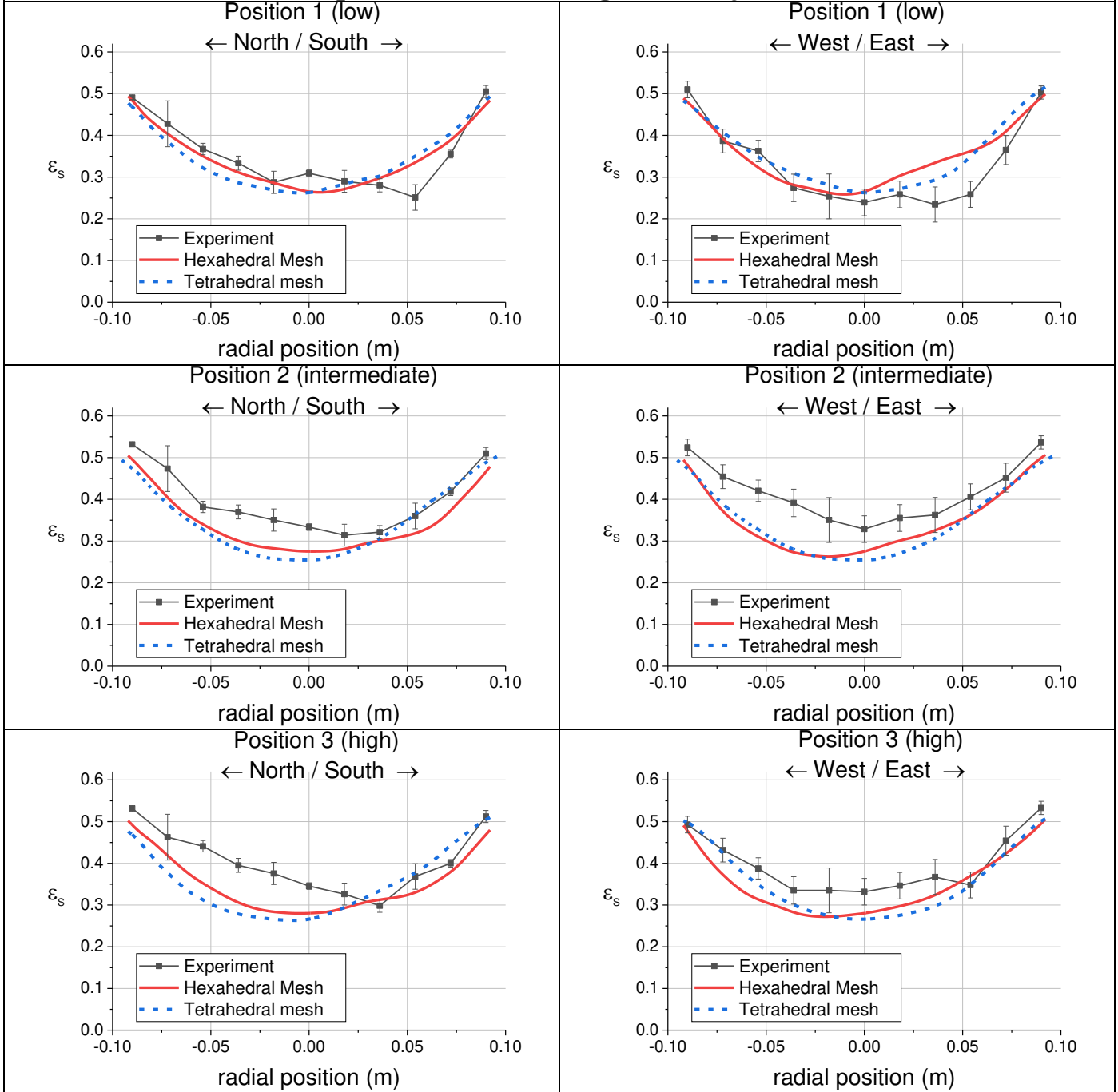


Figure 0-27: Cell type effect openFOAM, Gidaspow drag law with clustering effect, Comparisons of solid volume fraction profiles in the West East direction, experiment n°1 homogeneous injection

Experiment n°1: Homogeneous injection, tetrahedral cells

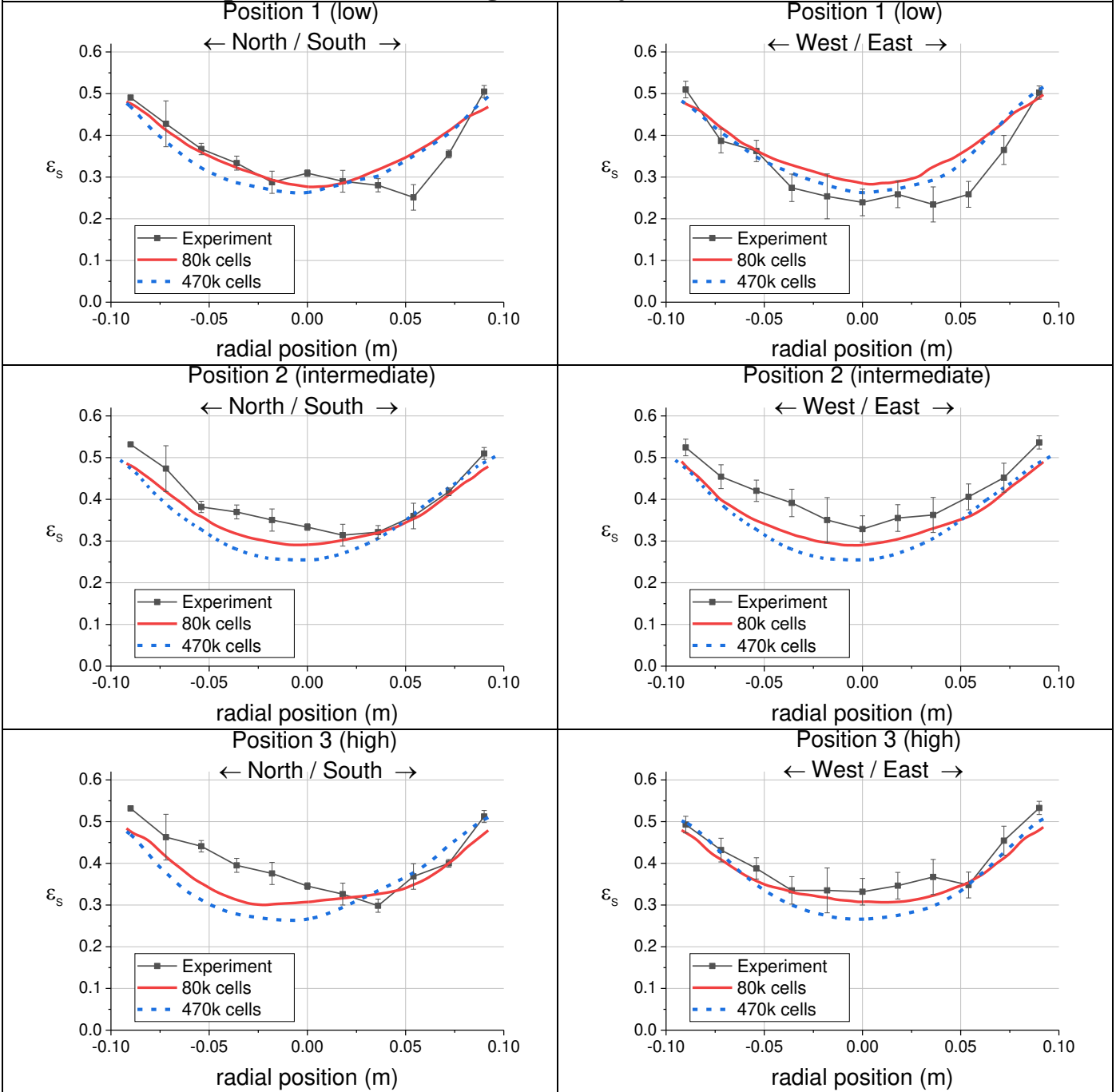


Figure 0-28: Size effect with tetrahedral cells openFOAM, Gidaspow drag law with clustering effect, Comparisons of solid volume fraction profiles in the West East direction, experiment n°1 homogeneous injection

Appendix 9 20 cm fluidized bed experiment n°1 Barracuda VR® simulations, analysis to define simulation steady state

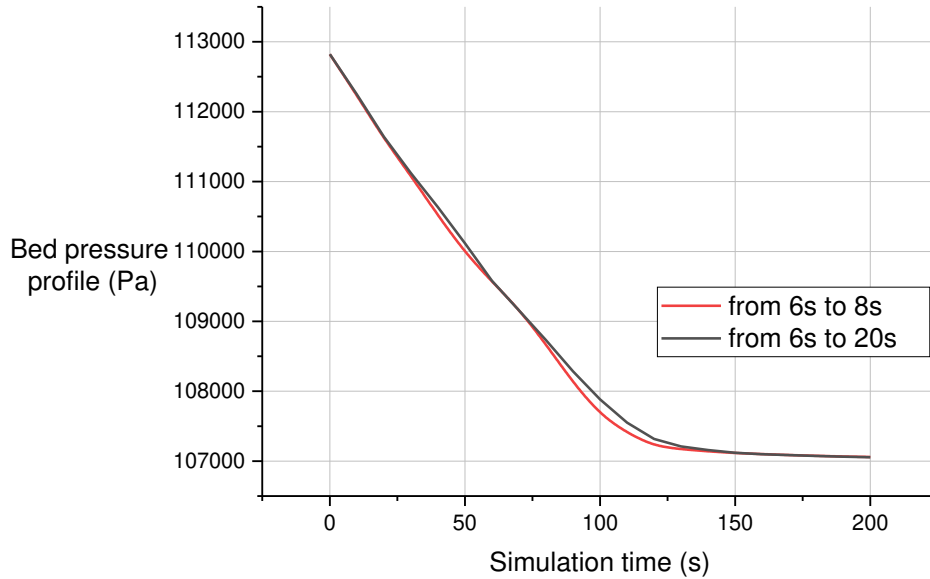


Figure 0-29: Simulation n°3 drag modified with multiplier of 0.4 and modified bottom injection distribution, Pressure profile, influence of the average period

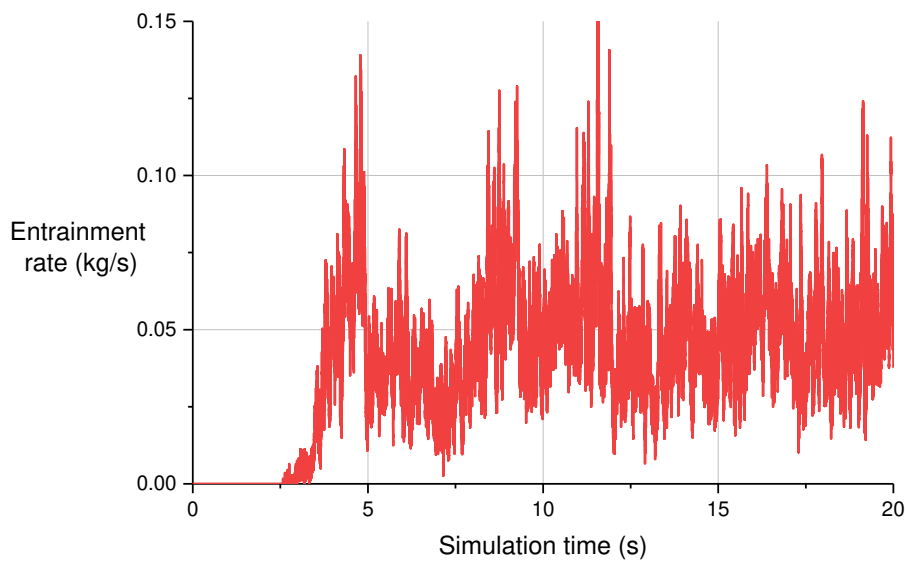


Figure 0-30: Simulation n°3 drag modified with multiplier of 0.4 and modified bottom injection distribution, Entrainment rate versus simulation time (s)

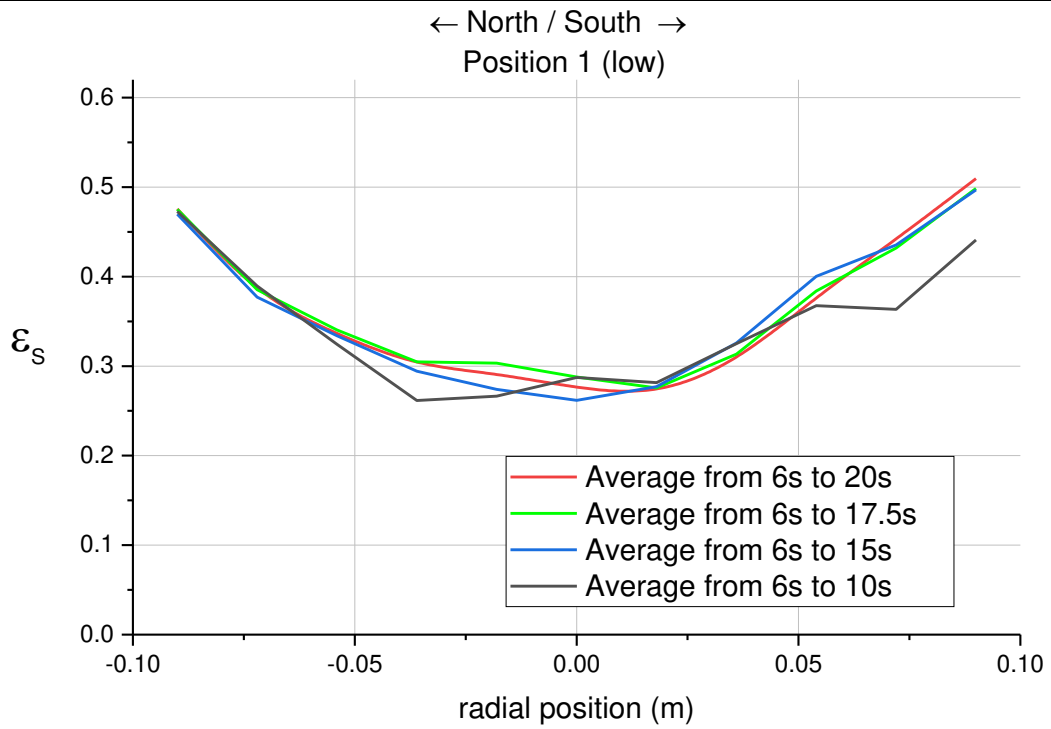


Figure 0-31: Simulation n°3 drag modified with multiplier of 0.4 and modified bottom injection distribution, Effect of time average period on solid volume fraction profile result, north south direction, position 1

Appendix 10 20 cm fluidized bed experiment n°2 Barracuda VR® simulations

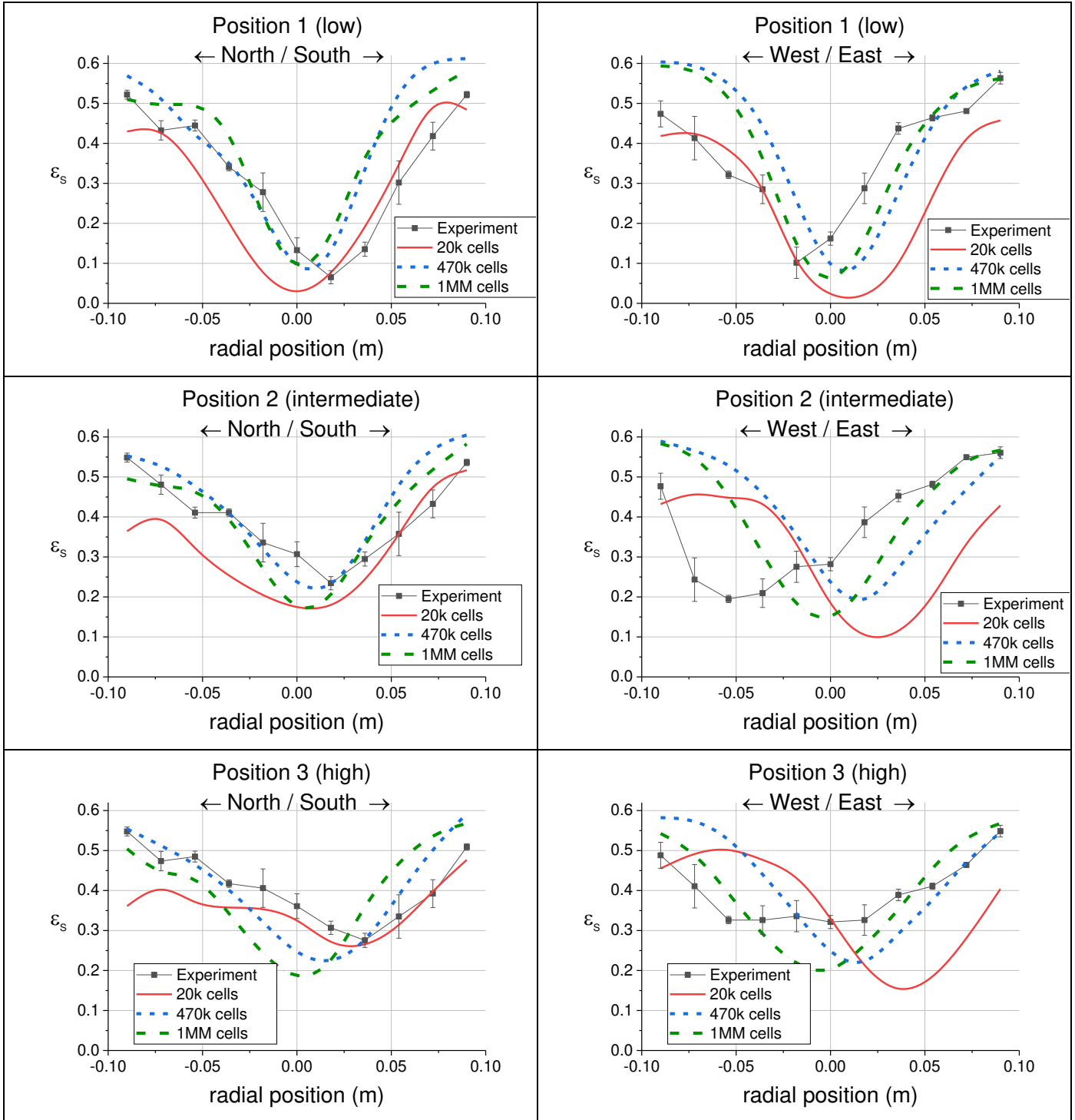


Figure 0-32: Barracuda VR® simulations, optimized parameters, mesh size effect, 20 cm fluidized bed experiment n°2

Appendix 11 20 cm fluidized bed experiment n°2 openFOAM simulations

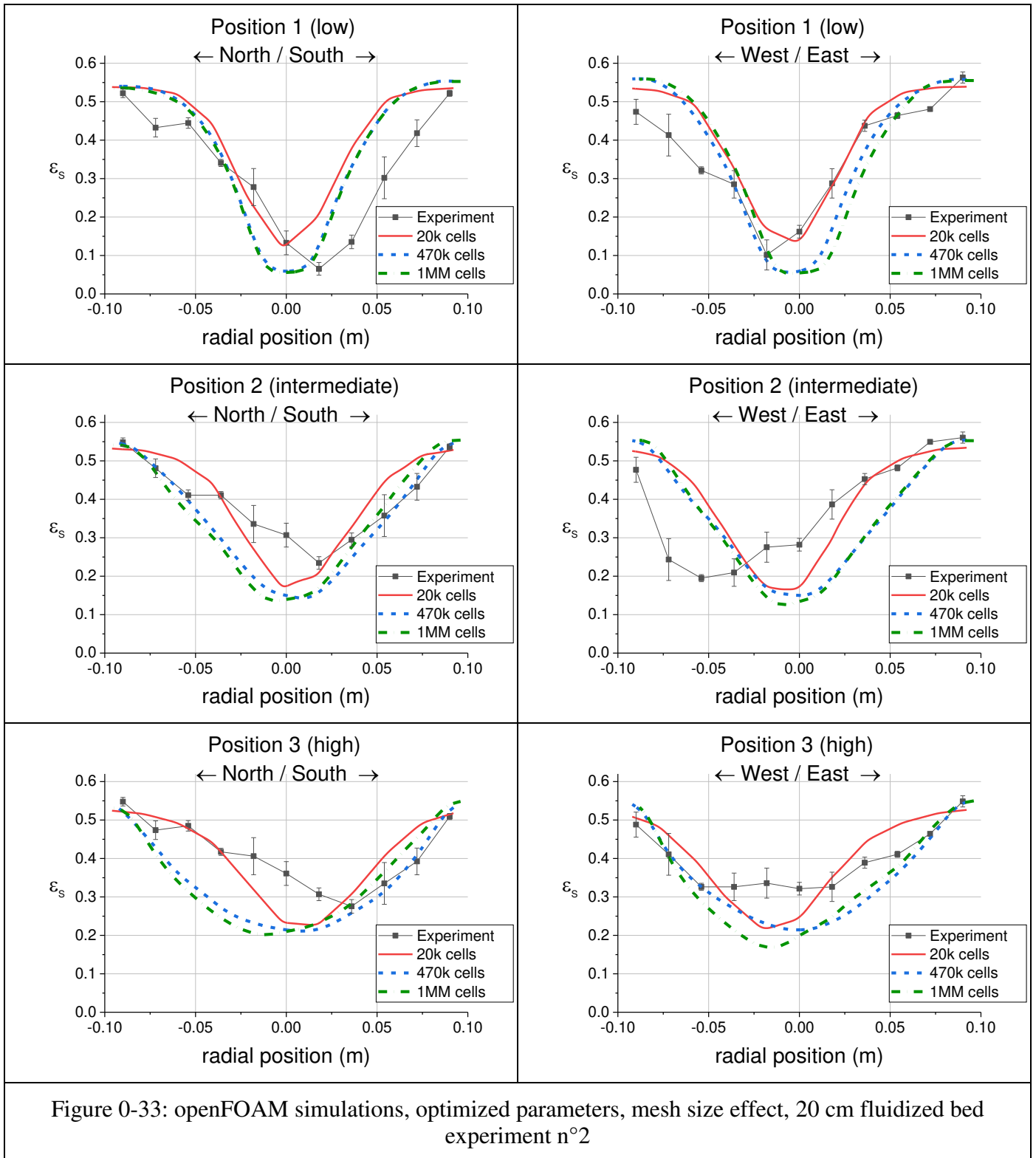


Figure 0-33: openFOAM simulations, optimized parameters, mesh size effect, 20 cm fluidized bed experiment n°2

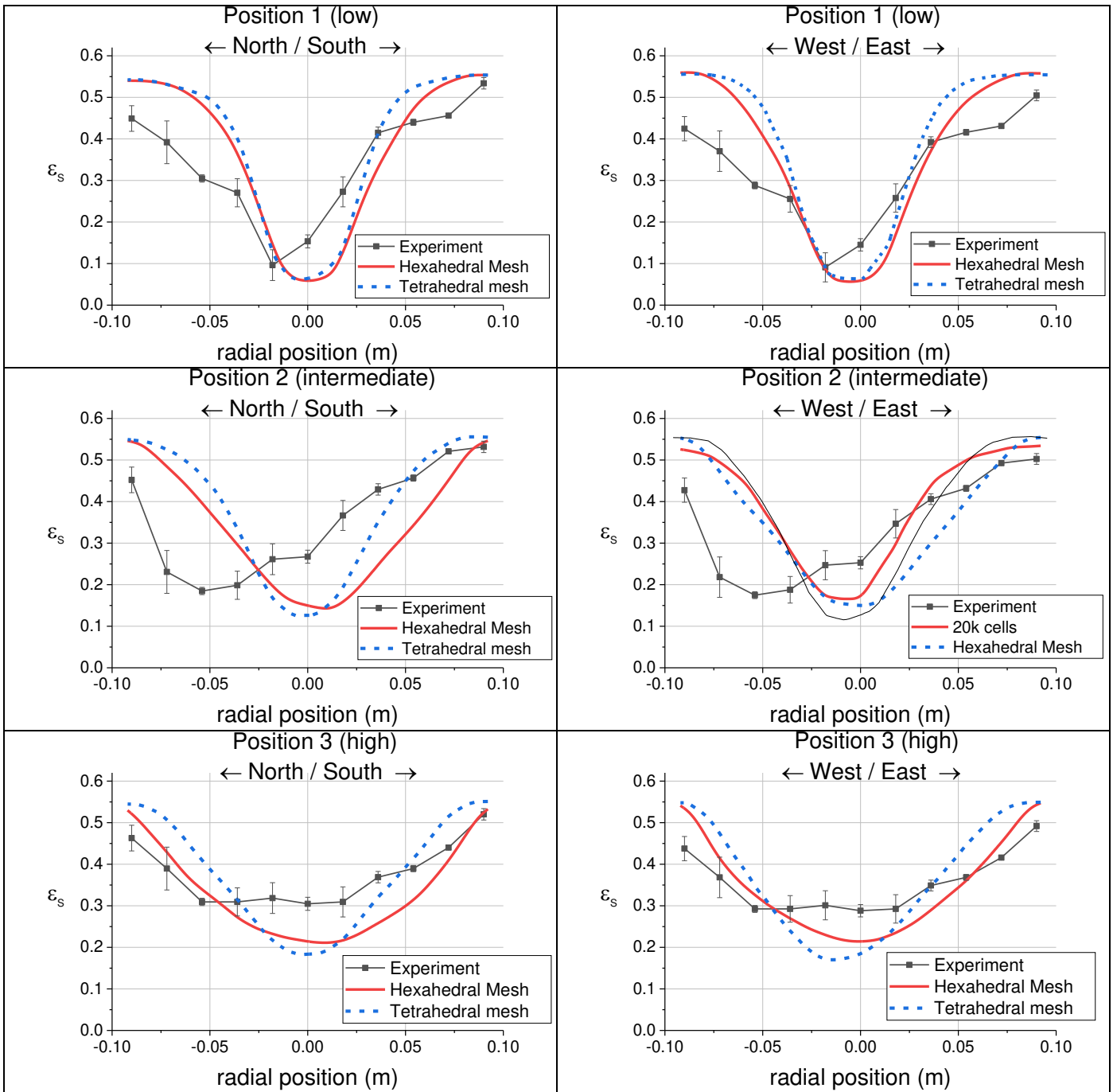


Figure 0-34: openFOAM simulations, optimized parameters, mesh type effect, 20 cm fluidized bed experiment n°2

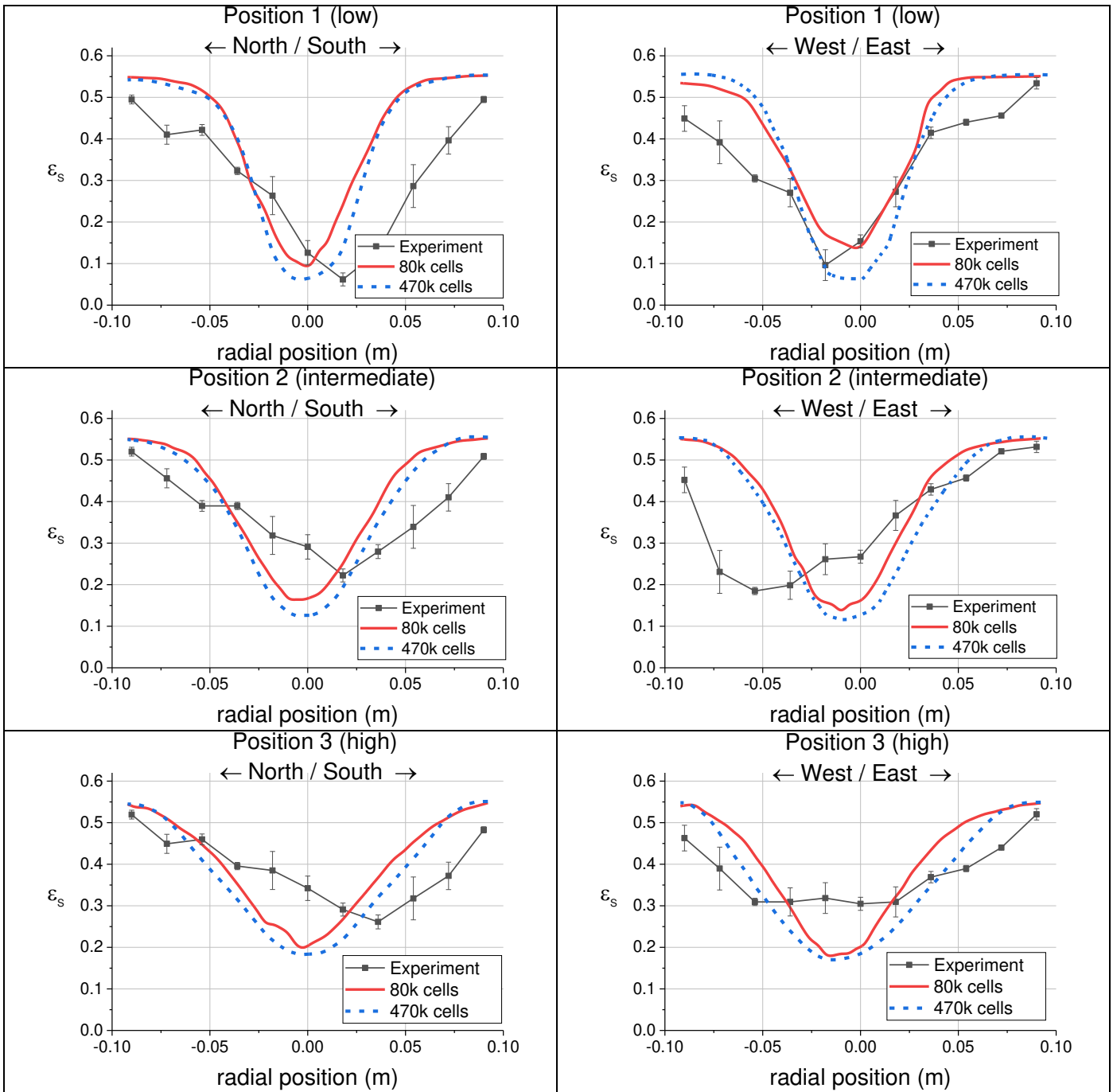


Figure 0-35: OpenFOAM simulations, optimized parameters, mesh size effect with tetrahedral cells, 20 cm fluidized bed experiment n°2

Appendix 12 90 cm fluidized bed simulation

Table 0-2: OpenFOAM Boundary conditions types for the gas and solid phases

	U.air	alpha.air	p_rgh
Nozzles tip	InletVelocity calculated from Nozzle tip velocity	fixed value 1;	fixedFluxPressure
Dipleg return	InletVelocity Value changed dynamically with respect to entrainment rate	fixed value 0.52;	fixedFluxPressure
Top outlet	pressureInletOutlet Velocity	zeroGradient;	prghPressure; p uniform 136 325;
walls	fixedValue; uniform (0 0 0);	zeroGradient;	fixedFluxPressure

	U.particles	alpha.particles	Theta.particles
Nozzles tip	fixedValue; uniform (0 0 0);	fixed value 0;	fixedValue; value uniform 1e-4;
Dipleg return	InletVelocity Value changed dynamically with respect to entrainment rate	fixed value 0.48;	fixedValue; value uniform 1e-4;
Top outlet	pressureInletVelocity	zeroGradient;	zeroGradient;
walls	JohnsonJacksonParticlesSlip; specularityCoefficient 0.01; value uniform (0 0 0);	zeroGradient;	JohnsonJacksonTheta ; specularityCoefficient 0.01; restitutionCoefficient 0.85;

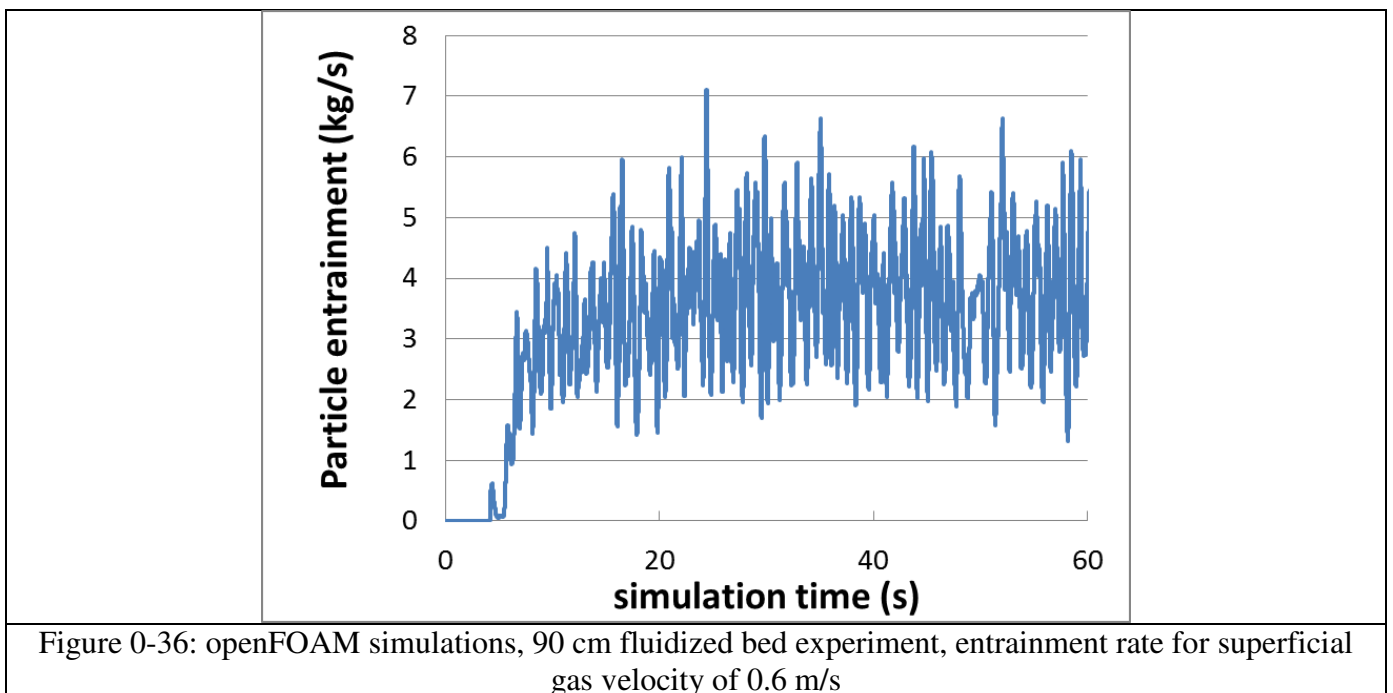


Figure 0-36: openFOAM simulations, 90 cm fluidized bed experiment, entrainment rate for superficial gas velocity of 0.6 m/s

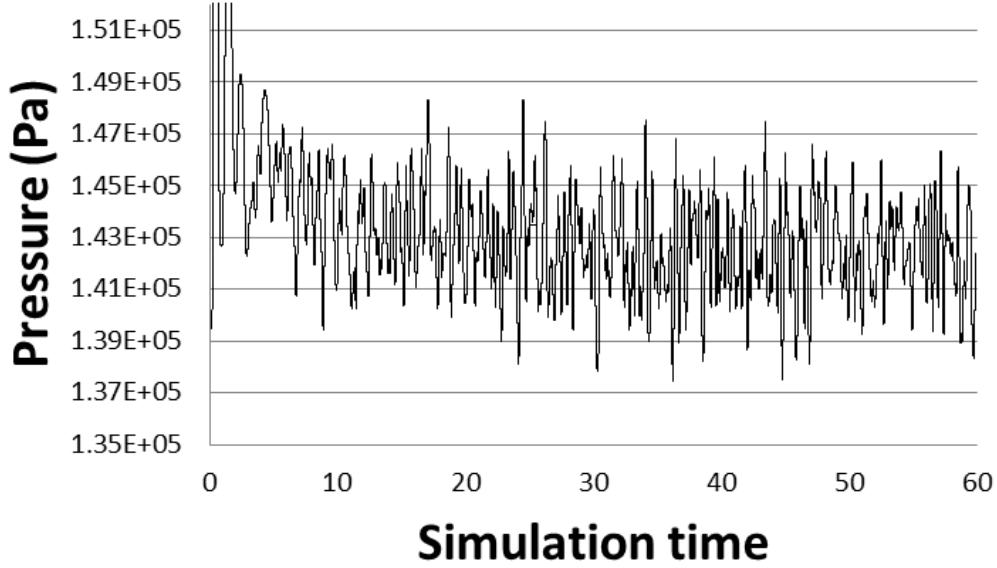


Figure 0-37: Barracuda VR[®] simulations, 90 cm fluidized bed experiment, pressure at a bed height of 3 meters superficial velocity of 0.6 m/s

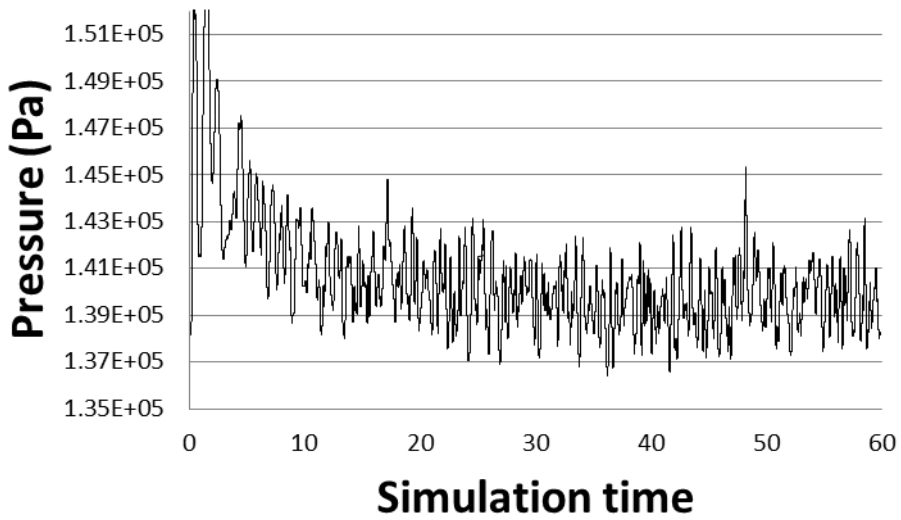


Figure 38: Barracuda VR[®] simulations, 90 cm fluidized bed experiment, pressure at a bed height of 3.2 meters superficial velocity of 0.6 m/s

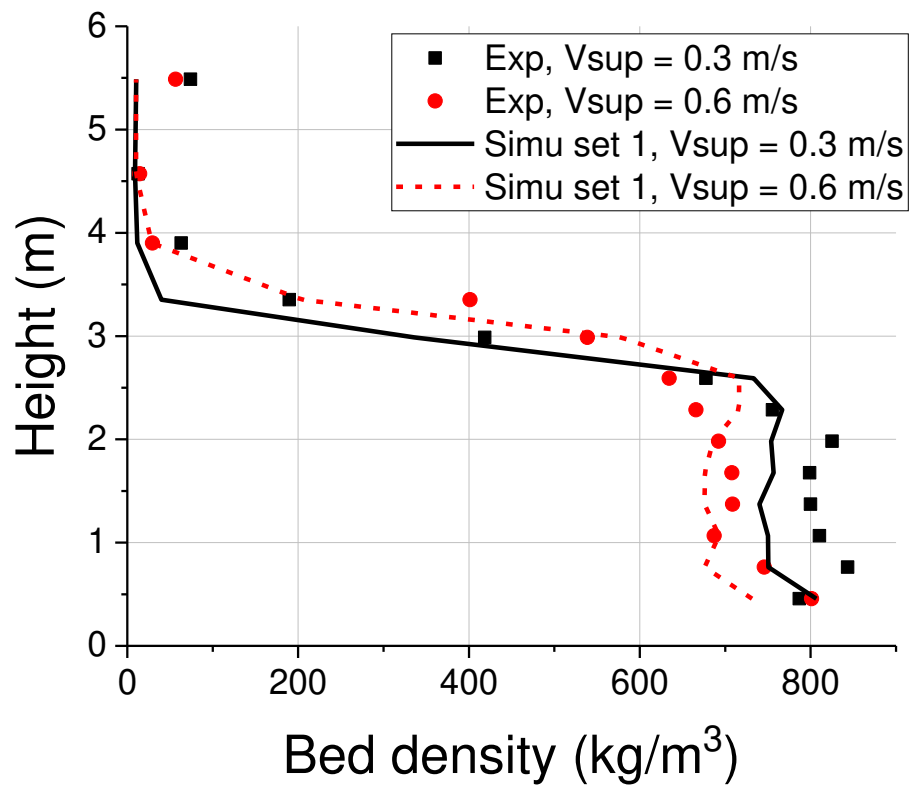


Figure 0-39: openFOAM simulations, 90 cm fluidized bed experiment, bed density profiles, set n°1 default representative diameters distribution

Appendix 13 Riser simulations with openFOAM

Table 0-3: OpenFOAM Boundary conditions types for the gas and solid phases

	U.air	alpha.air	p_rgh
Bottom inlet	InletVelocity calculated from fluidization ring velocity	fixed value 0.48;	fixedFluxPressure
Jet gas inlet	InletVelocity calculated to match superficial gas velocity at the riser top	fixed value 1;	fixedFluxPressure
Top outlet	pressureInletOutlet Velocity	zeroGradient;	prghPressure; p uniform 110 000;
walls	fixedValue; uniform (0 0 0);	zeroGradient;	fixedFluxPressure

	U.particles	alpha.particles	Theta.particles
Bottom inlet	InletVelocity calculated from solid flowrate	fixed value 0.52;	fixedValue; value uniform 1e-4;
Jet gas inlet	fixedValue; uniform (0 0 0);	fixed value 0;	fixedValue; value uniform 1e-4;
Top outlet	pressureInletVelocity	zeroGradient;	zeroGradient;
walls	JohnsonJacksonParticlesSlip; specularityCoefficient 0.01; value uniform (0 0 0);	zeroGradient;	JohnsonJacksonTheta ; specularityCoefficient 0.01; restitutionCoefficient 0.85;

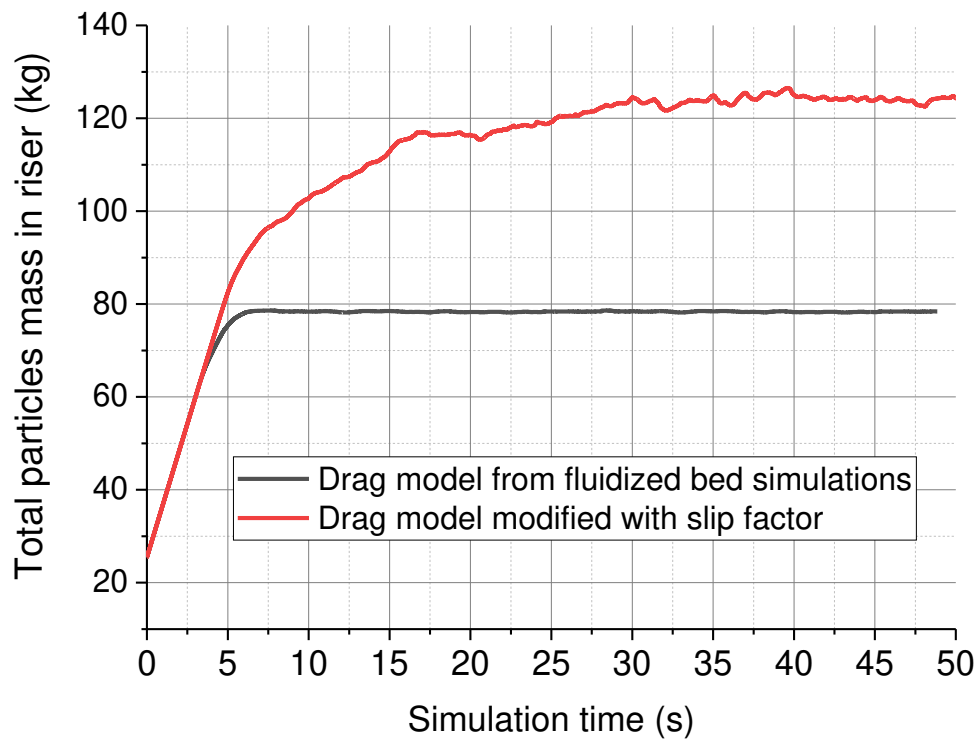


Figure 0-40: Riser simulation with a solid flux of 220 kg/m²/s, drag from fluidized bed simulations and drag modified n=1.3 ; $\beta = 0.02$, total particles mass in the riser versus time

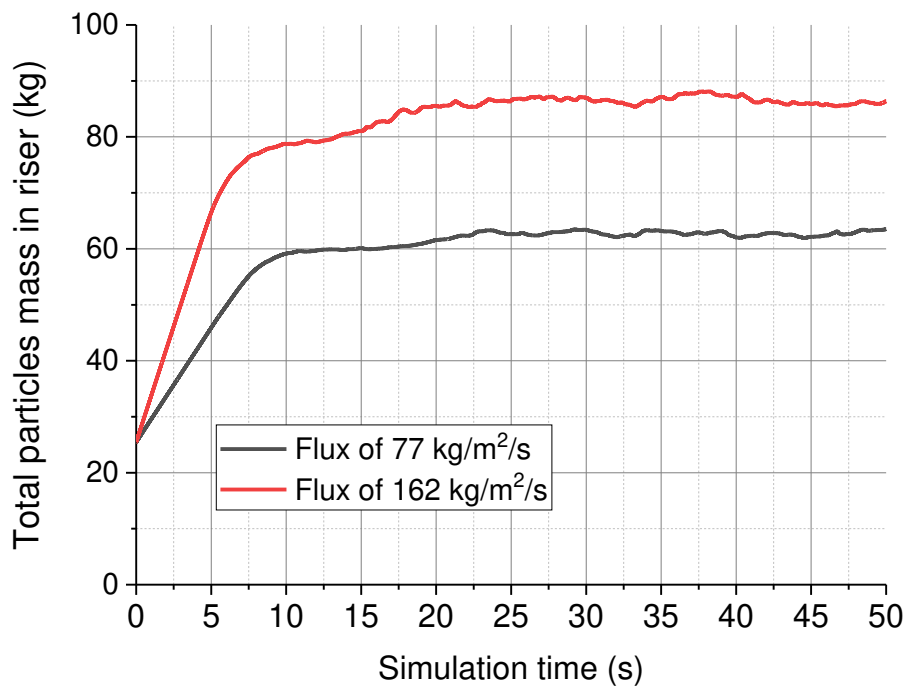


Figure 0-41: Riser simulations; drag modified n=1.3 ; $\beta = 0.02$, total particles mass in the riser versus time

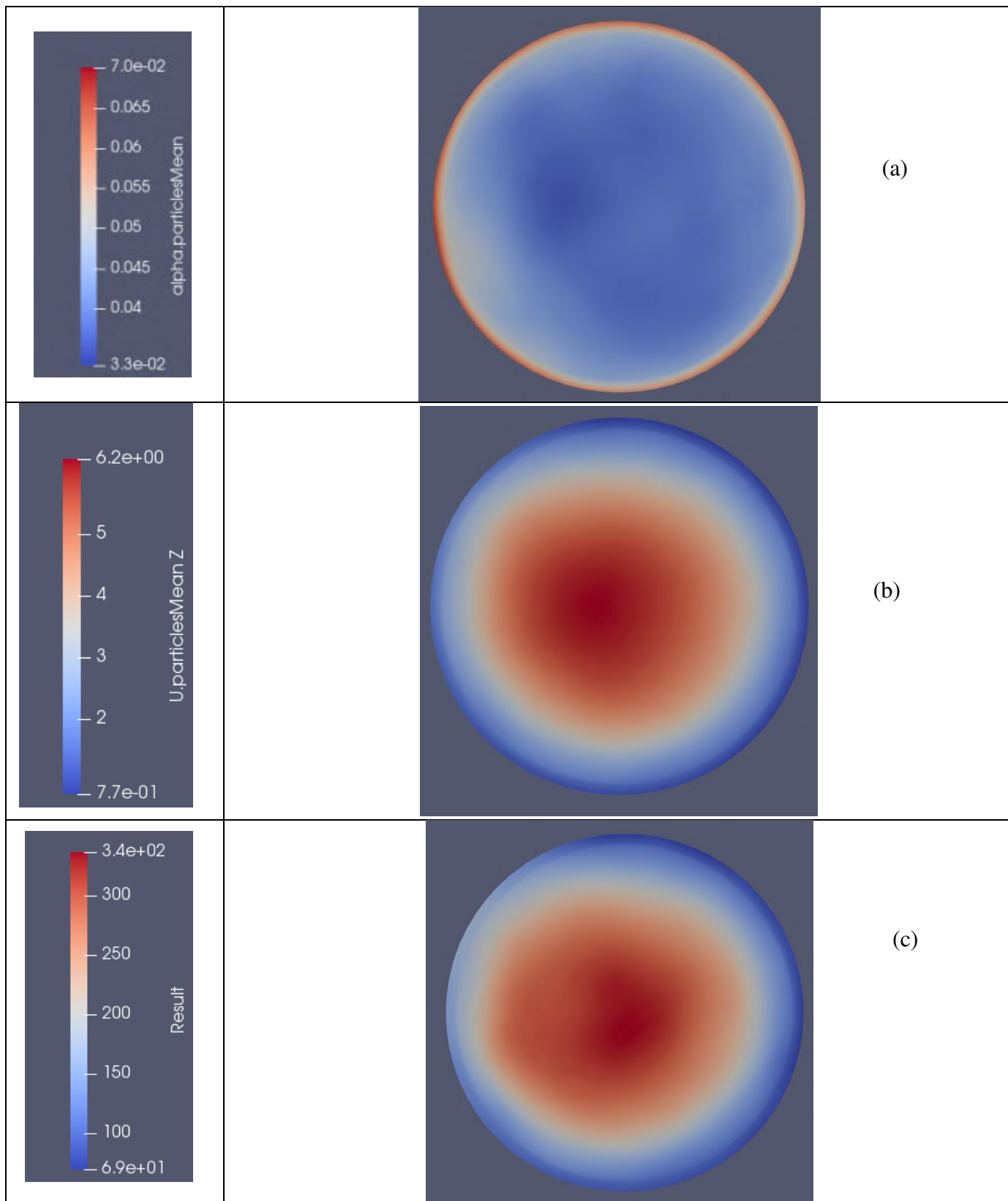


Figure 0-42: Riser simulation with a solid flux of $220 \text{ kg/m}^2/\text{s}$, drag modified $n=1.3$; $\beta=0.02$, local flux reconstruction; (a) mean solid volume fraction ; (b) mean solid axial velocity ; (c) local solid flux

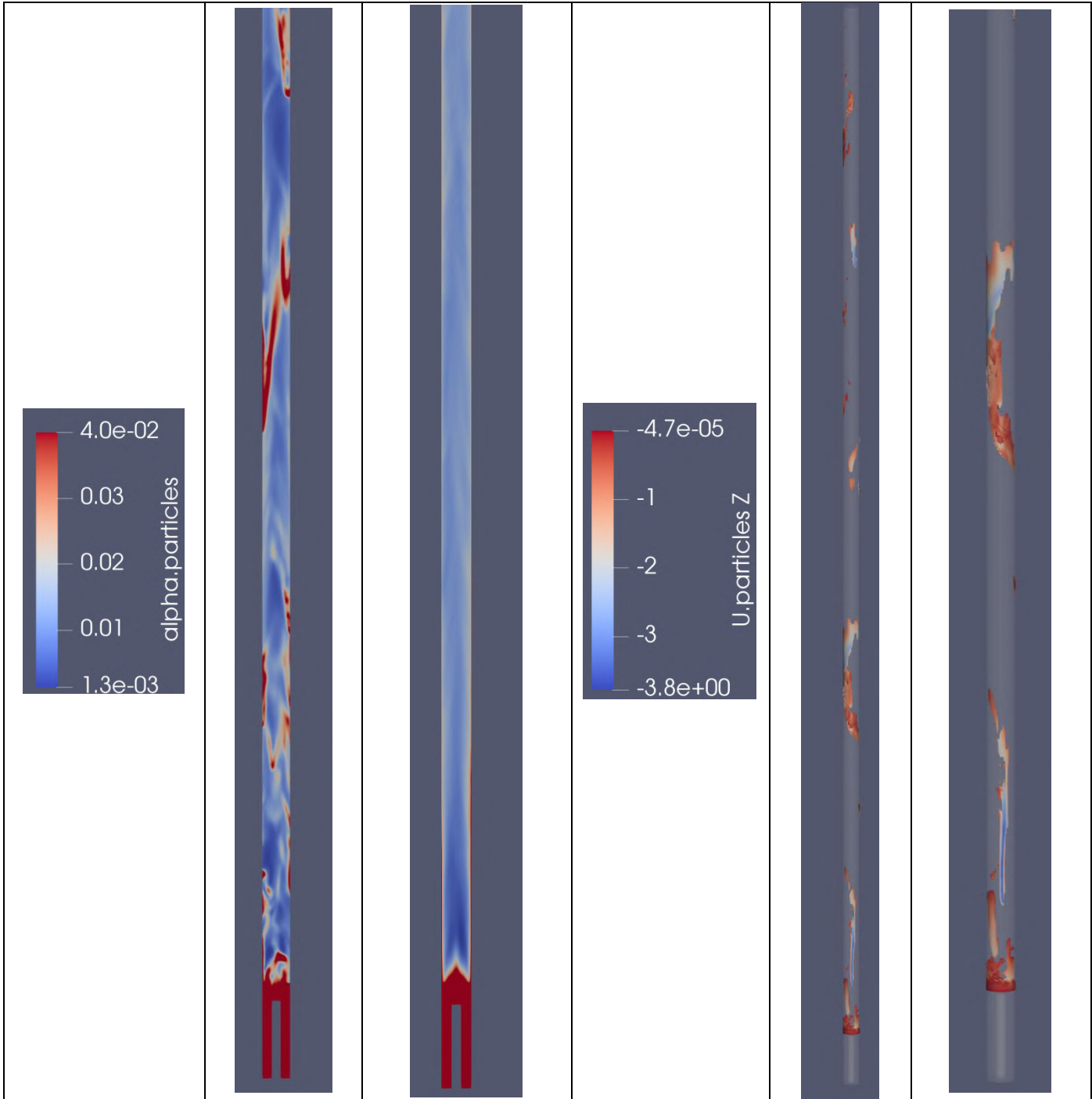


Figure 0-43: Simulation with a flux of $77 \text{ kg/m}^2/\text{s}$, Drag modified $n=1.3$ and $A = 0.02$ solid volume fraction instantaneous and averaged profiles

Figure 0-44: Simulation with a flux of $77 \text{ kg/m}^2/\text{s}$ Drag modified $n=1.3$ and $A = 0.02$ Solid volume fraction higher than 0.03 with negative solid axial velocity

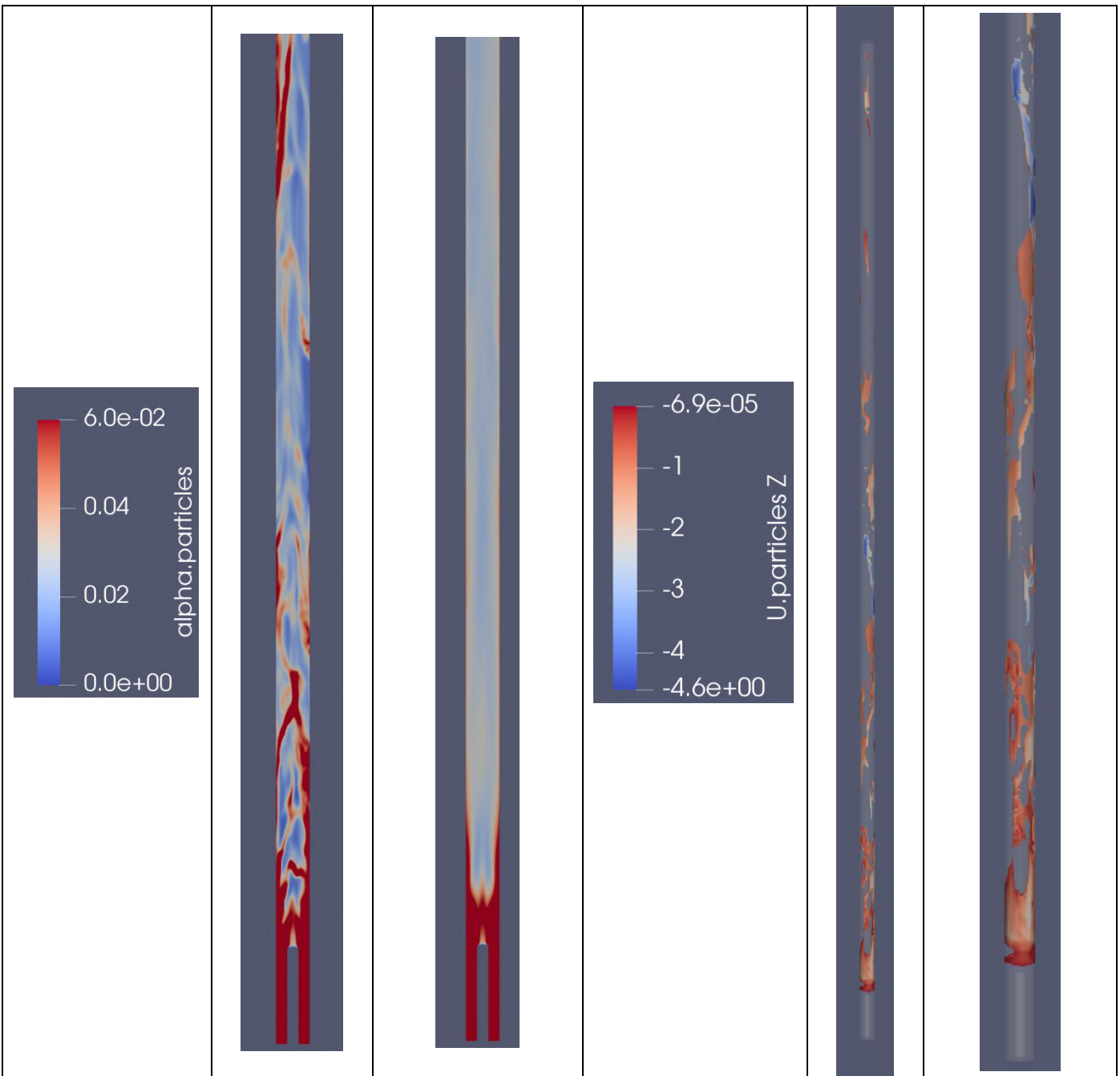


Figure 0-45: Simulation with a flux of $162 \text{ kg/m}^2/\text{s}$, Drag modified $n=1.3$ and $A = 0.02$ solid volume fraction instantaneous and averaged profiles

Figure 0-46: Simulation with a flux of $162 \text{ kg/m}^2/\text{s}$ Drag modified $n=1.3$ and $A = 0.02$ Solid volume fraction higher than 0.06 with negative solid axial velocity

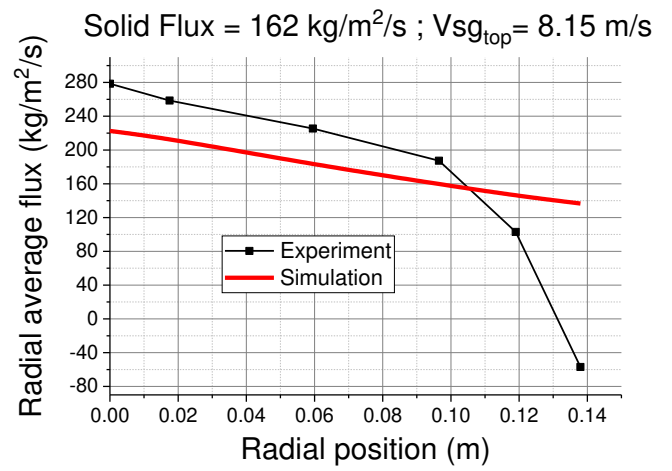
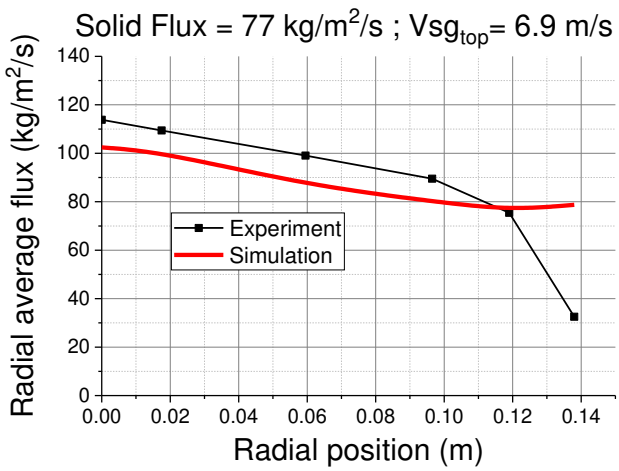
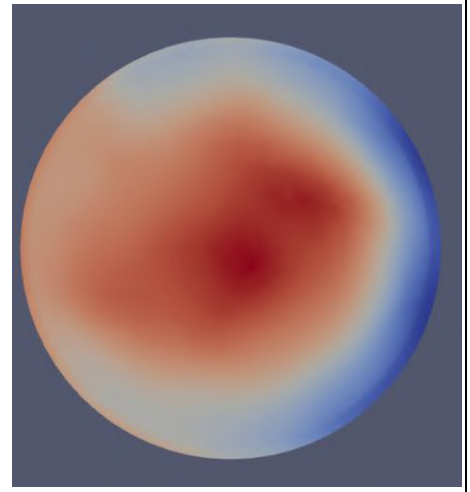
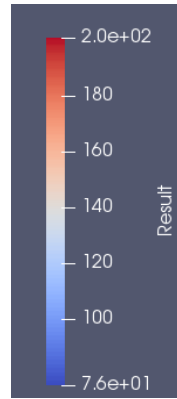
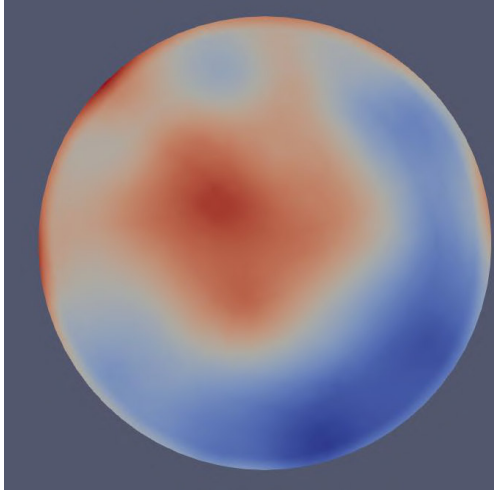
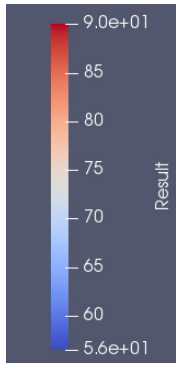


Figure 0-47: Simulation and experimental local flux profile at a height of 12 meters, flux of 77 kg/m²/s

Figure 0-48: Simulation and experimental local flux profile at a height of 12 meters, flux of 162 kg/m²/s

CURRICULUM VITAE

Benjamin AMBLARD
20 rue Claude Veyron 69007 Lyon
benjamin.amblard@ifpen.fr
phone: 04 37 70 27 24

French nationality
Driving License
date of birth: 25/10/1983
2 children

Researcher in chemical engineering

Graduated from the French National Institute of Applied Sciences (INSA) in 2007

Professional experiences:

- Since 2011 : **Research engineer in the chemical engineering department of IFP Energies Nouvelles**
- Process and technology development: Investigations on gas/particles and gas/liquid flows with experimentation and CFD simulation studies. Management of trainees, PhD student and post-docs.
 - Processes investigated: catalytic cracking FCC (refining), hydrocracking in ebullated beds (refining), chemical looping combustion (CO₂ capture), biomass conversion in fluidized bed (petro chemistry).
 - Member of the technical committee of the Particulate Solid Research Incorporation (PSRI) in Chicago for 6 years: orientation of the research program carried out by the consortium.
 - Teaching at the IFP School on the catalytic cracking process (master 2).
- 2009-2011 : **Process engineer at Axens**
- Conception and design of industrial units for refining
- PRO-II simulations, preparation of PFDs and P&IDs.
 - Design of pumps, columns, drums, heat exchanger, and instrumentation.
 - Process book writing
- 2007-2008 : **Research engineer for Total in North America**
- Experimentation on cyclones for gas/particles separation at PSRI in Chicago with T. Knowlton, R.Karri and R. Cocco.
 - Experimental study for the detection of agglomerates in a fluidized bed of polyethylene at the university of Western Ontario with C.Briens.
- 2006 : **Research Engineer at Total as a trainee**
- CFD simulations of bubbles columns for the Fischer-Tropsch process.

Languages and computer skills

Languages - English: Fluent - French: Fluent - Italian: Fluent - Spanish: Good level

Computer skills - CFD simulations: GAMBIT, Workbench Fluent, Barracuda, OpenFoam
- Process simulation : PRO-II
- Programming : Fortran, visual basic and C ++
- CAD: CATIA v5, Solidworks.
- Operating systems: Windows, Linux, Mac-OS.
-:Desktop software: Word, Excel, Power Point.

Publications and congresses

- Publications :
- **B.Amblard**, S.Bertholin, C.Bobin et T.Gauthier, Development of an attrition evaluation method using a Jet Cup rig, **Powder Technology**, Elsevier, 2015, 274, pp.455-465
 - **B.Amblard**, R.Singh, E. Gbordzoe, L. Raynal CFD modeling of the coke combustion in an industrial FCC regenerator, **Chemical Engineering Science** 170 (2017) 732 – 742
 - W.Yu, P.Fede, M. Yazdanpanah, **B. Amblard**, F.Euzenat, O.Simonin, Gas-solid fluidized bed simulations using the filtered approach, **Chemical Engineering Science**, 2020, 115472
 - T.Gauthier, M.Yazdanpanah, A.Forret, **B.Amblard**, A.Lambert, S.Bertholin, CLC, a promising concept with challenging development, **Powder Technology**, Elsevier, 2017, 316, Pages 3-17
 - F. Fulchini, M. Ghadiri, A. Borissova, **B. Amblard**, S. Bertholin, A. Cloupet, M. Yazdanpanah, Development of a methodology for predicting particle attrition in a cyclone by CFD-DEM, **Powder Technology** 357 (2019) 21–32.
 - F.Fulchini , W. Nan, M. Ghadiri, M. Yazdan Panah , **B. Amblard**, T.Gauthier, CFD-DEM Analysis of Particle Attrition in a Jet in a Fluidised Bed, **EPJ Web of Conferences** 140,(2017)
- Congresses
- 2017: Organization of the «8th World Congress on Particle Technology AIChE» in Orlando United States.
 - 2017: Oral presentation at the « 13th International Conference on Gas–Liquid and Gas–Liquid–Solid Reactor Engineering (GLS-13)»,Bruxelles. “CFD modeling of the coke combustion in an industrial FCC regenerator”
 - 2016: Oral presentation at the congress «2016 Frontiers in Particle Science and Technology », Houston. “Attrition Testing Using a Jet Cup Rig for the Chemical Looping Process Development »
 - 2014: Oral presentation at the congress « Industrial Fluidization conference South Africa », Johannesburg “Method for the evaluation of particles attrition using a Jet Cup apparatus”

Student supervisions

- 2015-2019 Supervision of a PhD student in partnership with the university of Leeds and Total on attrition for the development of the chemical combustion process
- 2017-2019 Supervision of a post-doctoral fellow in partnership with Total and the Institut of Fluid Mechanic of Toulouse on the CFD simulation of fluidized bed with combustion chemical reactions

Patents

- US2019321753A - NEW DEVICE FOR GAS-LIQUID SEPARATION, INTENDED FOR THREE-PHASE FLUIDISED BED REACTORS SUCH AS THOSE USED IN THE H-OIL PROCESS
- US2019270941A - NEW DEVICE FOR GAS-LIQUID SEPARATION, INTENDED FOR THREE-PHASE FLUIDISED BED REACTORS SUCH AS THOSE USED IN THE H-OIL PROCESS
- US2019351350A - DEVICE FOR LIMITING VORTICES AND SOLID DEPOSITS
- WO19091736A1 - NOVEL GAS-SOLID SEPARATOR FOR CATALYTIC CRACKING UNITS HAVING AN EXTERNAL RISER NOUVEAU SEPARATEUR GAZ SOLIDE POUR LES UNITES DE CRAQUAGE CATALYTIQUE POSSEDANT UN RISER EXTERNE
- US2019374920A - DEVICE FOR DISTRIBUTING A POLYPHASE MIXTURE IN A CHAMBER CONTAINING A FLUIDIZED MEDIUM
- WO18215364A1 - NOVEL PACKING FOR IMPROVING CONTACT BETWEEN A GAS PHASE AND A DISPERSED SOLID PHASE MOVING IN COUNTER-CURRENT FLOW NOUVEAU GARNISSAGE POUR AMELIORER LE CONTACT ENTRE UNE PHASE GAZ ET UNE PHASE SOLIDE DISPERSE CIRCULANT A CONTRE-COURANT
- WO18202554A1 - NOVEL DEVICE FOR DISTRIBUTING A POLYPHASE MIXTURE IN A CHAMBER COMPRISING A FLUIDISED MEDIUM NOUVEAU DISPOSITIF DE DISTRIBUTION DE MELANGE POLYPHASIQUE DANS UNE ENCEINTE COMPORTANT UN MILIEU FLUIDISE
- US2019112536A - DEVICE COMPRISING LATERAL INJECTIONS OF LIQUID FOR LIMITING THE PHENOMENA OF SOLID DEPOSITS IN ITEMS OF EQUIPMENT WITH A CONICAL BOTTOM